THE INELASTIC SEISMIC RESPONSE OF STEEL PLATE SHEAR WALL WEB PLATES AND THEIR INTERACTION WITH THE VERTICAL BOUNDARY MEMBERS

David J. Webster

A dissertation
submitted in partial fulfillment of the
requirements for the degree of

Doctor of Philosophy

University of Washington

2013

Reading Committee:

Jeffrey W. Berman, Chair

Laura N. Lowes

Charles W. Roeder

Program Authorized to Offer Degree:
University of Washington Civil & Environmental Engineering

University of Washington

Abstract

THE INELASTIC SEISMIC RESPONSE OF STEEL PLATE SHEAR WALL WEB PLATES AND THEIR INTERACTION WITH THE VERTICAL BOUNDARY MEMBERS

David J. Webster

Chair of the Supervisory Committee:
Associate Professor Jeffrey W. Berman
Civil & Environmental Engineering

The steel plate shear wall (SPSW) is a building lateral force resisting system that comprises a moment frame (the boundary frame) and slender steel diaphragms (web plates) welded or bolted inside the boundary frame. The system resists lateral load primarily through tension field action in the web plates. Web plate forces are anchored by the boundary frame members. The Seismic Provisions currently require the boundary members to be capacity designed assuming the web plate has fully yielded in tension and forms a pure tension field at a prescribed angle computed from an elastic analysis. In design, web plates are frequently modeled as a series of parallel, inclined tension-only truss elements.

This research focused on the development and magnitude of in-plane web plate stresses due to seismic demands and how these are transferred to and resisted by the boundary frame, specifically the vertical boundary members, or elements (VBEs). The evolution of web plate stress is controlled by the material properties, slenderness ratio, hardening behavior, web plate aspect ratio and cyclic drift history. Several small-scale cyclic tests of steel web plates were conducted to investigate the hardening, pinching and snap-though behavior, and to validate observations made in numerical studies that the tension field inclination angle migrates to a fixed value close to 45 degrees as the web plate is loaded plastically. Using statistical methods, the magnitude of hardening expected for typical web plate ma-

terials was then estimated for the MCE level earthquake.

The results of the experiments and ABAQUS analyses of single story SPSWs are used to develop and implement a new OpenSees uniaxial material model, SPSW-WP, to be applied to truss elements, specifically for SPSW applications. The material was designed to mimic the effects of in-plane web buckling and accurately capture the effects of material hardening, stiffness degradation, residual shear strength, web plate slenderness and correctly model the reloading drift under cyclic loading conditions. The model is calibrated using ABAQUS analyses of single story SPSWs with a range of material hardening characteristics and geometries. It is then validated using both ABAQUS models and with cyclic test data.

Finally the new material model is incorporated into the analyses of two six-story SPSWs; one utilizing slender A36 steel web plates, and one with stocky, low yield point LYP100 steel web plates. The story drift demands and VBE demands are compared and contrasted with ABAQUS analyses of the equivalent structures for four DBE and four MCE level ground motions.

Web plate hardening and changes in the tension field inclination angle were found to be significant but had only a moderate influence on VBE demands. The use of stocky web LYP plates enhances lateral stiffness, reduces story drifts and reduces VBE demands when compared with more commonly used slender A36 web plates of lower net tensile strength.

TABLE OF CONTENTS

Page

LIST OF FIGURES

LIST OF TABLES

ACKNOWLEDGMENTS

I would like thank my adviser, Jeff Berman, for his unwavering support and accessibility throughout the duration of this work. I would also like to thank Laura Lowes for her assistance and very constructive contributions in preparation of this document and Charles Roeder for his frank commentary and valuable insight. Many thanks also to the National Science Foundation for its funding of this project, without which it would not have been possible.

Lastly, but certainly by no means least, I would like to acknowledge my wife, Caroline, for her seemingly infinite patience and support.

DEDICATION

For Caroline, Andy and Kyle

Chapter 1

INTRODUCTION

This dissertation has been prepared as a component of a research project on Steel Plate Shear Walls (SPSWs) titled "NEESR-SG: Smart and Resilient Steel Walls for Reducing Earthquake Impacts". Financial support for this study was provided by the National Science Foundation as part of the George E. Brown Network for Earthquake Engineering Simulation under award number CMMI-0830294. The document presents research related primarily to the behavior of SPSW web plates and their interaction with the boundary frame members.

This research was part of a larger effort that has been undertaken by various researchers in the U.S and Taiwan. A series of reduced scale tests designed to examine self-centering SPSWs has been undertaken at the University of Washington and at the University of Buffalo. A series reduced scale coupled SPSW tests have been undertaken at the University of Illinois at Urbana Champagne using the MAST-SIM lab. At NCREE,a pseudo-dynamic test of a full scale self-centering SPSW was undertaken.

1.1 General Background

SPSWs are a type of building "lateral system", the building frame system that is primarily responsible for resisting wind and earthquake loading; an example is shown in Fig. 1.1. The focus of the research is on seismic response, although the behavior under wind loading is also addressed. There are two primary components of a Steel Plate Shear Wall: 1) A boundary frame, typically a single bay multi-story moment frame, consisting of wide flange (WF) section beams and columns; and 2) un-reinforced steel panels (web plates) which are welded or bolted into the space formed by the beams and columns via a continuous steel tab (fish plate). The beams in a SPSW are referred to as horizontal boundary elements

(HBEs) and the columns as vertical boundary elements (VBEs). The HBEs are typically moment connected to the VBEs with detailing similar to special moment resisting frame (SMRF) connections. This is currently a system requirement in US building codes for use as a ductile seismic force resisting system. The web plates in a modern SPSW are relatively slender, and made from mild steel sheet or plate. The height to thickness ratio (h/t_w) of a panel varies with demand but is usually between 300 to 3000. This results in a web plate thicknesses that may range from as little as 1 mm to as much as 25 mm.

Figure 1.1: SPSW During Construction

The SPSW only recently emerged as a viable building lateral system in the United States when it was included in the 2005 American Institute of Steel Construction's Seismic Provisions for steel buildings (AISC 2005) where they are called Special Plate Shear Walls. Despite its many advantages over other lateral systems, it is yet to attract broad acceptance by the design and construction community in the United States. SPSWs are often described as a vertically oriented plate girder, but the similarities between plate girders and SPSWs are mostly superficial, and their performance is certainly quite different. The comparison does however provide a visual concept of the basic principal.

1.2 SPSW System Behavior

The seismic behavior of SPSWs is perhaps not as well understood as other commonly used systems, such as concentrically braced frames, as there are a limited number of buildings with SPSW lateral systems that have been subjected to large earthquakes. Consequently, there is limited data available on actual earthquake performance. However, a considerable amount of analytical end experimental research from countries including Japan, Iran, Turkey, Canada, the United Kingdom, and the United States, has been undertaken since the early 1970s, the bulk of which has occurred over the last ten years. The consensus of this body of research is that the system is ductile and has good energy dissipation capacity, and is cost effective as both a new building lateral system and as a potential retrofit scheme. SPSW systems do however require a little more effort to model and analyze correctly when compared to some of the other commonly adopted lateral systems and the design process often requires a significant amount of iteration.

The analytical difficulty results from the complex web plate behavior and its interaction with the HBEs and VBEs. The web plate is the primary lateral load resisting component of the wall, typically resisting 50-80% of the story shear. The plate will buckle in shear at very low load and resist lateral load through tension field action, hence the plate girder analogy. The tension field is anchored by the boundary elements which complete the load path to the ground. Figure 1.2 schematically illustrates how the tension field is anchored and how the load delivered to the wall at each floor level is transferred to the base.

As the wall is loaded laterally, and prior to elastic buckling of the web plates, the boundary frame and plates behave elastically with the web plates resisting pure in-plane shear. The demands on the boundary members at this stage are very low. As the lateral load increases, the web plates progressively buckle and the stress fields change from a state of almost pure shear to one where the tensile stresses dominate, resulting in tension field action. At this load, bifurcation theory predicts an abrupt change in lateral stiffness of the plate, although the real change in lateral stiffness is a little less obvious because of the initial out-of-plane imperfections in the web plate. The behavior of the plate up to and just beyond the point

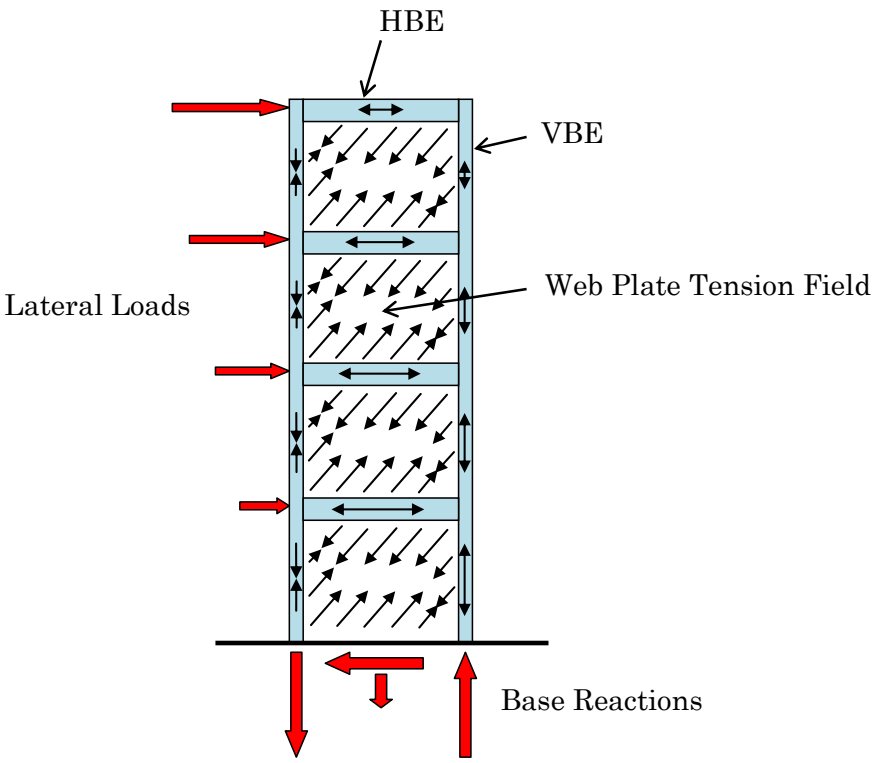

Figure 1.2: SPSW Load Paths

of elastic buckling is of secondary concern. Of more importance for seismic response is the behavior of the plate and anchoring boundary frame after the plate buckles and the wall is subjected to significant inelastic demands. Furthermore, after the first inelastic cycle the panel will have residual out-of-plane distortions that will accumulate on further cycling. The demands on the anchoring boundary frame can be quite severe even for a low rise structure. The frame, particularly the VBEs, will experience transverse bending resulting from pull-in of the web plates in addition to the bending associated with lateral displacement of the frame. The frame members also have significant axial load demands.

1.3 Research Objectives

This research focuses on SPSW web plate behavior and the VBE demands resulting from web plate anchorage forces. The main objectives are:

1. to characterize web plate behavior under lateral load for a range of plate aspect ratios, slenderness ratios and material properties using experimental data and numerical analyses

2. to develop a phenomenological model for a SPSW web plate that accurately and reliably approximates the these behaviors

3. to examine the influence of the web plate anchorage forces on the vertical boundary elements

4. to identify any economic benefits (reduced material costs, etc) associated with any particular design assumptions or strategies that may be adopted in light of 1, 2 and 3 above.

The focus of this effort, with regard to boundary element demands, is on the VBEs. Some global system performance measures, specifically story drifts, are also examined. The focus on the VBE demands is motivated mostly by economics. The section sizes required for VBEs can become an economic disincentive when selecting a building lateral system. Very large sections need to be fully welded at the splice locations. With jumbo sections the welding operation alone can become prohibitively expensive and difficult to achieve. It is not uncommon to require the largest W14 section (W14x730) for even a nine story SPSW if using capacity design (either pushover analysis, the Indirect Capacity Design approach proposed by the CSA 2001). Force demands on the VBEs can be very high but capacity design procedures may over-estimate demands for high rise structures, resulting in oversized sections that may make an otherwise viable lateral system economically unattractive. For this reason alone it is worthwhile examining VBE demands. Another consequence of static procedures is their inability to capture the effects of higher modes on the structure. Thus the need for a reliable and accurate means of estimating VBE demands (that is not overly conservative) appears to be worthwhile. Since the web plate strength and cyclic response is a primary determinant of VBE demand, a model that accurately describes the web plate behavior and adequately accounts for all of the material and geometric parameters is needed.

1.3.1 Web Plate Behavior

There are two methods commonly used in research and in practice to model SPSW web plates, however each method has limitations. The methods are:

- Tension-only strip method
- Continuum or shell method

The tension-only strip method is analytically simple, but is time consuming to incorporate into a multi-story model if the model building process is not automated. It is also a rather crude approximation of a structure (the web plate) that has very complex behavior, and deviates considerably from actual behavior when the plate slenderness h/t ratio gets small, i.e., the plate is stocky. As shown in this research and by others, this model fails to accurately capture some significant aspects of web-plate response and how the web plate interacts with the boundary members. The shell or continuum approach is capable of matching the behavior more realistically but is computationally very expensive and only an option if using sophisticated research software. An alternative model must be simple to implement and adequately capture global and local behaviors at low and high drift levels. Ideally the model could be used with both linear (modal and linear static) and non-linear (pushover and response history) analyses. The results of an experimental program on a suite of reduced scale web plates, together with analytical parametric studies, will contribute to the development of this model.

1.3.2 Vertical Boundary Element Performance

Accurately predicting the performance of the VBEs in a SPSW is of paramount importance. VBEs are the primary component for resisting wall overturning through axial load and are simultaneously subjected to high flexural and shear demands from transverse forces delivered by the web plate. The current method for determining VBE demand may lead to a design that is conservative or unconservative, depending on the geometry of the structure,

the controlling load case and the assumptions used in the analysis. By analyzing single and multi-story sub-assemblies it should be possible to extract useful information about "actual" VBE performance. The results of the experimental program on the reduced scale web plate will also contribute to this effort.

1.4 Scope of Work

The scope of work for this research is as follows:

1. Examine the current body of knowledge related to SPSW web plate modeling and identify any gaps in the knowledge base or issues that may require further study

2. If appropriate, develop a computationally efficient alternative to the shell modeling approach that is capable of mimicking the behavior observed in both web plate specimens and nonlinear FE analyses of web plates modeled with shells.

3. Examine the influence of material hardening, snap-through behavior, web plate slenderness and other phenomena on system response and on VBE demands.

1.5 A Note on Terminology

Throughout this document, many terms will be used that are particular to the Steel Plate Shear Wall. For the sake of clarity these will be defined here. SPSW means *steel plate shear wall* or more specifically, an *un-reinforced* steel plate shear wall. HBE and VBE are *horizontal boundary element* and *vertical boundary element* respectively. A sub-assembly is defined as a single story of a multi-story SPSW comprising a top and bottom HBE, VBEs and a web plate. A WF is an AISC *wide flange* beam section. The terms *web plate* and *panel* may be used interchangeably.

1.6 Overview of this Document

After an introduction to the basics of the system and the broad objectives of the research in Chapter 1, the motivation for the research program and some of the issues surrounding contemporary SPSW analysis are presented. A literature review of past research and other

publications related to SPSW analysis and design is then presented in Chapter 2. Chapter 3 presents a selection of preliminary studies that were carried out before the testing program was initiated. Chapter 4 presents a detailed description and documentation of an experimental program designed to investigate web plate hardening, post-buckling response, tension field inclination and VBE demand. An analysis and discussion of the experimental results is presented in Chapter 5. Chapter 6 presents the results of computational models of the Phase II experiments. Chapter 7 presents the results of numerical simulations of the experiments. Chapter 8 introduces a new *OpenSees* material model for SPSW web plates and provides background on the calibration and performance of the model for single panels. In Chapter 9, Monte-Carlo simulations are used to quantify the magnitude and and examine the influence of web plate hardening under design level earthquakes. Chapter 10 presents the results of OpenSees analysis of two six-story SPSWs using the new material model and contrasts this with the results of *ABAQUS* analyses of the same structure. Chapter 11 provides a summary of the findings and a discussion of recommended future research.

Chapter 2
RELEVANT PRIOR RESEARCH

2.1 Introduction

This literature survey will start with a cursory review of some early analytical studies of thin metallic plates and a general introduction to SPSW web plate behavior and modeling techniques. A very brief discussion of plate girder research is included because it was often cited by pioneering SPSWs investigators. Lastly, some significant contributions to SPSW analysis and design from various authors will be presented. Not all aspects of the SPSW will be addressed, instead the focus will be on those aspects that are within the stated scope of research. These include but are not limited to:

1. **Web plate stress field development**
2. **Analytical web plate modeling techniques**
3. **Hysteretic models for web plates including hardening**
4. **VBE demands due to web plate pull-in and frame action**

Although the SPSW has been used in building construction since the late 1960's, by 1983 still very few structures had been built with this lateral system and very little research had been performed. The system was only included in the AISC Seismic Provisions in 2005 (henceforth referred to as simply the *Provisions*). Much of the research prior to 1983 was carried out in Japan and concerned reinforced SPSWs, where the web plate is thicker and is fitted with stiffeners to prevent elastic buckling. These structures are fundamentally different from the modern un-reinforced SPSW because they behave more like a deep beam. A substantial amount of analytical and experimental work focusing on un-reinforced SPSW systems has been done since the early 1980's. The majority of this has occurred in the last fifteen years in Canada and the US, and to a lesser extent in Iran, Turkey, South Korea,

India and the United Kingdom.

A characteristic feature of the SPSW is the buckling and post-buckling behavior of the web plate in shear. The contemporary model for this behavior is founded largely on research activity into thin plate buckling that predates the SPSW system by several decades. This early research into the buckling and post-buckling behavior of thin rectangular metallic plates is quite extensive but only a brief review will be provided because the essence of it has already been documented by many other investigators of SPSWs. In 1986 the Swiss Federal Institute of Technology's Technical Working Group No. 8 (TWG8) produced a booklet [29] which was the culmination of around eleven years of continuous research into the behavior of thin plate structures. This is an incredibly rich source of information on the historical development of thin plate theory, analysis techniques and design and provides an excellent appraisal of significant milestones since the time of Saint Venant and up to 1986.

2.2 Early Analytical Studies of Thin Metal Plates Loaded in Shear

The majority of the research that has influenced the development of SPSWs came from the aeronautical engineering industry of the 1930's and concerns in-plane loading of thin metallic plates. One of the earliest works relevant to modern SPSW design was introduced by Wagner in 1931 [75] in a series of technical memos for the National Advisory Committee for Aeronautics (NACA), now NASA, and later modified by Kuhn in 1933 [41]. Wagner postulated that the post-buckled state of a thin plate loaded in shear can be approximated as a series of parallel uniaxial tension members inclined in the direction of the theoretical principal tension stress, typically around forty-five degrees. Each tension member had an area equal to the product of the plate thickness and the spacing of the members. He argued that as the plate span/thickness ratio approached infinity, the amplitude of the post-buckled corrugations approached zero and the "contemporary" principal compressive stresses also approach zero. This became known as *tension field theory* and was used in the aerospace industry and eventually applied to plate girder design. He also developed an equation that predicts the inclination angle of the elastic tension field.

Another justification for the use of truss members in post-buckling analysis of thin web plates loaded in shear comes from the nature of the buckling itself. The nonlinear behavior of an imperfect structure can be categorized as either imperfection sensitive, or as imperfection insensitive. Imperfection sensitive structures are those that display a dependency of the ultimate load on the level of initial imperfection in the structure. These structures typically soften on the application of load and never actually reach their bifurcation load. The maximum load that can be applied depends on the magnitude and shape of the initial imperfection. An example of this is a hydro-statically compressed cylinder [39], the load carrying capability of which is severely compromised by slight imperfections. The imperfections lead to in-plane bending stresses that amplify under second order effects and do not otherwise occur in a perfect structure.

An imperfection insensitive structure is one which on monotonically increasing load there is no discernible critical load and the post-buckling ultimate strength is insensitive to the level of initial imperfection. Thin rectangular plates loaded with in-plane shear generally fall into this category. The ultimate shear capacity of a ductile metallic plate is largely governed by the yield strength of the material, and to a lesser extent h/t, regardless of the critical shear buckling stress which varies with $(h/t)^2$.

The outcome of much of this early analytical work was closed-form or tabulated solutions for elastic critical loads of thin plates under various loading and boundary conditions. These solutions were, and still are, an important component of the design of many aerospace structures. Timoshenko [69], [70] provided several exact and approximate solutions for determining the elastic critical load of thin plates subjected to various in-plane loads. Much of the work that followed this either modified Timoshenko's approximate solutions, such as Stein and Neff [63], included post-critical elastic buckling, such as Levy [43], or expanded the data base of boundary and loading conditions. In the late 1940's Stowell [64],[65] included material plasticity in his analysis of thin plates loaded in shear. These analyses are instructive and the results can be useful when checking computational models. However, the development of analytic solutions to post-buckling problems clearly was developed from

a need to provide solutions to these problems without the benefit of powerful computational tools. Consequently they can be exceedingly complex even for the simplest of loading and boundary conditions. They have limited utility today compared to computational methods such as FEA that can easily accommodate practically any geometry and boundary conditions and also incorporate material and geometric nonlinearities. Furthermore, all of this analytical work was limited to monotonically increasing load.

2.3 Plate Girder Research

In Civil Engineering, researchers including Basler [5], Rockey [57] and Skaloud [61] found applications in civil structures, specifically plate girder design. Although plate girders bear a resemblance to SPSWs, they are fundamentally different in their behavior. Plate girders typically have relatively stocky webs compared to SPSW web plates. The boundary elements that anchor plate girder webs (flanges and stiffeners) are much more flexible than their SPSW analogues (VBEs and HBEs respectively). Plastic failure mechanisms in plate girders are based on incomplete tension field development and the yielding of the girder flanges under monotonically increasing load. On the other hand, plastic mechanisms normally developed in SPSWs include full plastification of the web plate under repeated cyclic loading and preclude VBE plastic hinging by instead allowing the boundary structure to yield only at the HBE ends. For these reasons it is believed the plate girder analogy is not generally appropriate and plate girder research, though obviously important in the early years of SPSW development and in its own right, is of limited value to the SPSW design now. A similar point was asserted by TWG8 [29] with respect to plate girder analysis: "The pure tension field proposed by Wagner...is suitable only for aircraft structures where extremely thin plates attached to very rigid boundary elements are encountered". By extension, it could be argued this also applies to SPSW design.

2.4 SPSW Web Plate Modeling Techniques

The first modern day research into SPSW behavior and modeling, such as that by Timler [67] in 1983, Tromposch [73] in 1987, Chen [16] in 1991 and Driver [27] in 1997, was achieved through physical testing. With one notable exception, Roberts [55] 1991, the web plate be-

havior in these studies was itself not the primary focus. Rather, it was system behavior (including the boundary frame) such as peak strength, initial and post-buckling stiffness and pushover response. In these studies the models used to verify the test results were simple and ultimately constrained by the limitations of the available computational tools. In 1983 Timler and Kulak [67] adapted the tension field strip model originally developed by Wagner [75] for the analysis of SPSWs. As the database of system behavior accumulated, alternative strip models were proposed and verified against existing test data, although in principle the method did not change appreciably. These modified strip models included features such as supplemental degradation elements [27] or semi-empeircal material and hysteretic models to achieve a better match with the available test data. Eventually the continuum models such as those used by Elgaaly [30] and Driver [27] attracted more widespread use as computer speed and software advances permitted. This remains the case.

The strip method has been adopted and implemented by many investigators of SPSWs and is still commonly used. It has generally been found to capture global load-displacement response well but under-predicts initial stiffness as has been noted by Driver [27] and Topkaya [72]. As a research tool, its capacity to accurately capture true hysteretic behavior of a web plate and its interaction with the boundary members ultimately depends on the sophistication of material model adopted for the truss elements. A strip model utilizing bilinear, tension-only truss elements is a crude approximation of a complex continuum structure.

Accordingly, SPSW web plate models can be separated into two broad categories: 1) those that use uniaxial truss elements (strip models) and, 2) those that use some form of continuum element, such as shells or orthotropic plates. The use of orthotropic plates has not gained much traction, but in some respects it may be preferable to the strip model for pushover analysis [26]. The typical continuum model utilizes a mesh of non-linear shell elements for the web plate. Shells have been used more extensively since 2000 due to advances in computational speed and commercial software capabilities, but their application has been restricted mostly to research. The strip method has been (and still is) used extensively by researchers because it can handle both monotonic loading and cyclic loading if the strips are

added in both directions. Each method requires careful implementation of an appropriate material model.

In the absence of a more attractive modeling alternative, the strip model will prevail as the preferred method for analyzing SPSWs in commercial practice. As a design tool it is simple but can be time consuming to implement, particularly if rigid offsets are modeled and even more so if the engineer rigorously applies Eq. F5-2 of the 2010 Seismic Provisions [1] and inclines the strips accordingly. As long as practicing engineers are designing SPSWs using strip methods, there will be a need for up-to-date strip method modeling techniques, such as those currently proposed by the AISC Seismic Provisions [1], and recommendations that reflect the latest research findings. Fig. 2.1 illustrates the geometry of two three-story SPSWs with and without rigid offsets between the web plate and the boundary members.

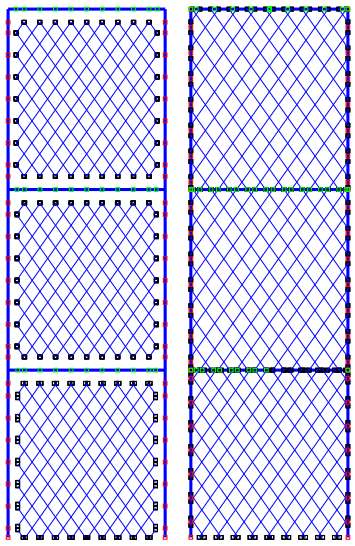

(a) (b)

Figure 2.1: SPSW Strip Model for 3-Story Building, (a) with Rigid Offsets, and (b) without Rigid Offsets

The continuum model can capture aspects of the true behavior that can only be approximated with the strip method such as Normal Plastic Contraction (discussed later in Section

5.5.1 and in detail in Section 8.5.1), out-of-plane flexural strength and shear strength parallel with the strips. However, the continuum approach suffers from numerical instabilities if implicit time stepping solvers are used because of the complex snap-through type buckling that invariably occurs. This is more so the case with reversed cyclic loading as many past researchers have found, e.g., [77],[54] and [6]. These difficulties can be avoided using explicit time stepping methods and reduced integration elements to speed up the analysis. Advances in computational speed will make the continuum approach more attractive for research purposes. Fig. 2.2 shows a five story continuum model of an SPSW modeled using $ABAQUS$ shell elements.

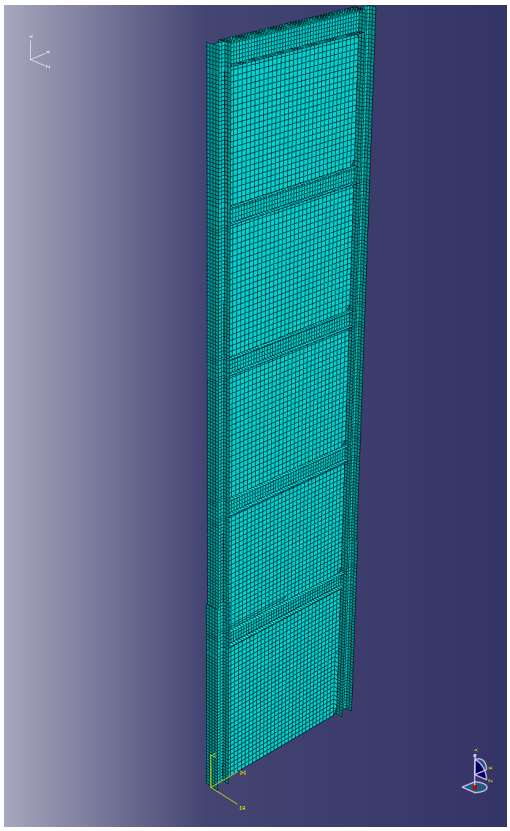

Figure 2.2: Continuum Model of SPSW

2.4.1 Material Hardening

Neither the AISC Provisions [1] nor the Canadian Standards Association - Design of Steel Structures CAN/CSA S16-09 [22] require consideration of material hardening when designing the boundary elements for web plate strength, although the influence of hardening should be considered. Kinematic hardening was typically assumed in the research studies reviewed in this survey, but this may not be appropriate for inelastic reversed cyclic loading of web plates and may tend to underestimate the maximum strength of the plate, and consequently the demand it imposes on the boundary frame. Of the more than seventy documents reviewed for this literature survey, only six proposed a specific hardening model for cyclic analyses.

Two other aspects of material hardening that are worth consideration are strain aging effects and strain rate effects. Strain aging of steel can considerably increase the yield strength and reduce the ductility of A572, A993 and A36 steels. With 10 hours of strain aging, the yield strength of A36 steel may increase by 25% with 2% plastic pre-strain and by as much as 100% with 12% plastic pre-strain [37]. Ultimate strengths may also increase by as much as 25%. This may have a bearing on the aftershock performance of not only SPSWs but all steel and reinforced concrete lateral systems after a large seismic event. High strain rates also increase the yield strength of steels. The influence of strain rates on SPSWs was investigated in a study undertaken by Bhowmick *et al* [11].

2.4.2 Alternative Web Plate Models

The strip method has evolved over the last two decades on two fronts. The first is through modifications to the configuration of the strips, such as with the multi-directional strip model proposed by Rezai[54] and the compression strut and deterioration strip added by Shishkin *et al* [60]. The other is through modifications to the material model that describes the element behavior such as by Roberts [55], Driver *et al* [27], Elgaaly [30] & [31] and Choi *et al* [21]. Some of the proposed modeling changes include both geometric and material modeling adaptations in an effort to reliably capture the behavior of the continuum web

plate.

2.5 Contributions from Various Authors

2.5.1 Levy, Fienup and Woolley 1945

The assumption of a pure tension field is a convenient but somewhat conservative one, as was recognized by Levy *et al* [43] in 1945. It circumvents analytical difficulties by substituting a post-buckled thin plate with a tension-only membrane. Levy presented an elastic post-buckling analysis of a thin square web plate loaded in shear. The motivation for this analysis was to minimize structural weight by taking advantage of the actual elastic post-buckling strength and stiffness. Starting with von Karmen's large deflection equations and using a lengthy and cumbersome iterative successive approximation procedure he computed an "equivalent width" of the unbuckled panel along the diagonal tension band that is formed on loading. This is done for two cases, one with axially flexible vertical stiffeners ($r = 0.25$), the other with infinitely rigid stiffeners ($r = \infty$). The flanges are assumed infinitely rigid. He also computes the in-plane stress components at the corner and at the center of the plate at various stages of loading. These are plotted in Fig. 2.3.

An interesting feature of Levy's analysis is the conclusion that the mid-line in-plane principal compressive stress at the center of the panel is maintained at very close to the shear buckling stress, even as the tension field increases in magnitude. Although he does not show it, the compressive stress at other locations on the plate will (on average) be higher than this. At approximately twice the critical buckling load for the $r = \infty$ case, the principal compressive stress reaches a maximum value around 20% greater than the magnitude of the critical buckling stress. At eight times the critical buckling load the compressive stress decreases to less than a quarter of the critical buckling stress. At the corner of the plate the principal stresses had approximately equal magnitude at all loads (not shown on this plot), signifying a condition of pure shear.

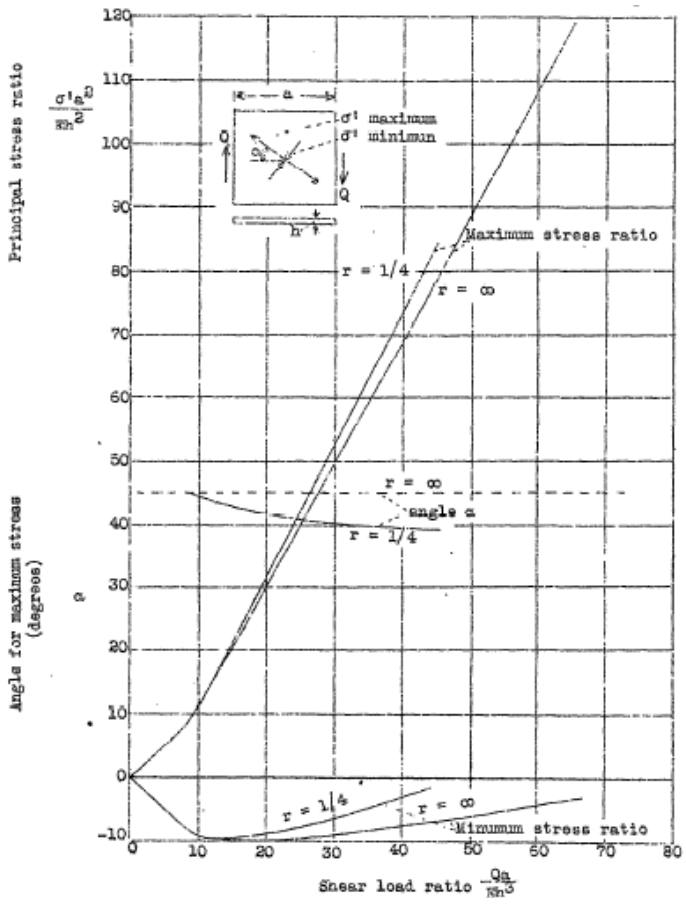

Figure 2.3: Post-buckled stress components for square plate loaded in shear after Levy [43]

2.5.2 Thornburn, Kulak and Montgomery 1983

In 1983, Thornburn *el al* [66] prepared one of the first reports to address the behavior and modeling of steel plate shear walls and extend the concept of the "pure diagonal tension" strip model originally proposed by Wagner in 1931. Thornburn *el al* states that "after buckling, the compressive principal stress cannot increase any further". This common assumption echoes Levy's conclusion about the stress state at the center of the plate. It legitimizes the use of the tension strip model when the plate span to thickness ratio h/t is high, as is typically the case for a normally proportioned SPSW.

By examining a single story panel of an SPSW and introducing a series of simplifications, Thornburn derived a simple closed form solution for the tension field inclination angle based on the theorem of least work. However, the solution did not include the contribution of strain energy from the columns. This was later included by Timler *el al* [67] the same year. In the original derivation Thornburn did not explicitly state that the derivation of the inclination angle is valid only when panel stresses are in the elastic range. However, he did state that the un-reinforced SPSW system is "not recommended where significant inelastic load reversals are expected". This implies that the equation was really only intended for predominantly elastic behavior and is quite contrary to its present application.

Thornburn determined the minimum number of strips required to adequately capture the post buckling behavior of a panel and its interaction with the boundary frame. The strip spacing was varied and a minimum of ten equally spaced strips was found to adequately represent the tension field action. This recommendation is still made by the AISC [1]. The new web plate model was then applied to a ten story shear core but only to examine differences between deflections computed one story at a time, compared to a fully assembled model.

In an effort to provide the design engineer with an easily implementable modeling approach, Thornburn also developed the "equivalent truss" concept. This model replaces multiple inclined strips with a single equivalent diagonal brace that has an equivalent stiffness. With some careful implementation, this method has some validity when considering story drifts and global behavior of a large SPSW system, although it does not capture the demands on the boundary elements resulting from anchorage of the tension field stresses. Several parametric studies were undertaken to examine the effect on panel stiffness contributed by panel aspect ratio, panel thickness, column stiffness and tension field inclination angle.

Many of Thornburn's observations and conclusions form the basis of contemporary modeling and design of SPSWs.

2.5.3 Timler and Kulak 1983

An experimental program conducted by Timler [67] followed directly from the analytical work of Thornburn [66] and was designed to test some of the modeling methods and theoretical work derived by Thornburn. As mentioned previously, the tension field inclination formula derived by Thornburn was re-derived in this study to account for the flexural strain energy of the columns.

The test specimen consisted of a symmetrically arranged two-panel wall sub-assembly. The rationale behind the test setup was that the middle beam serves as a boundary frame beam with essentially infinite flexural stiffness. This is consistent with the modeling assumption used to derive the inclination angle. The two panels offered the researchers the opportunity to study, in effect, two specimens in one setup. To simplify the fabrication and to reduce the boundary frame deflection in the absence of the panels, the center-line beam to column connections were moment connected. All other connections were pinned.

The web plate was specified as G40.21 300w (f_y = 43.5 ksi) hot rolled plate and was 5 mm thick, quite thick for this application. The columns and beams were built-up sections approximately equivalent to AISC W12x87 and W18x97 sections respectively.

The specimen was loaded vertically in the middle of the specimen with tension and compression loading sequences to the serviceability limit deflection of $h/400$ or 6.25 mm, followed by two full cycles to the same load and then a single excursion to failure in compression and tension. Seventeen equally spaced strain rosettes were mounted on the near and far side of one web plate along the entire height of the plate. Additional rosettes were mounted on both web plates at other locations. Strain gauges were also mounted on the boundary frame members to track bending and axial deformations.

The out-of-plane deformations of one web plate were continuously monitored throughout the test by a custom built device that ran along a rail mounted across the diagonal of the panel,

normal to the expected direction of the tension field. The data obtained from the tests included the magnitude and direction of the principal in-plane strain components of the web plate, and the axial force and bending moments in both the column and beam sections at several locations. The panel strain gauge rosette readings were used to determine in-plane stresses. This was done only after the effect of flexural strains due to the buckling waves was removed by averaging the near side and far side strain gauge readings at each point. The averaged principal stress components, representing the mid section in-plane stresses, show a lot of scatter in both magnitude and direction, particularly at the top of the panel. Although the authors state that the computed angle of inclination (51 degrees) is within the observed range of readings (44 to 56 degrees), the scatter observed in the orientation of the tension field suggests that any attempt to validate the inclination angle calculation using the results of this experiment would be rather difficult.

Though it was not a stated objective of this test, it is difficult to deduce from these plots the ratio of principal tensile stress to principal compressive stress at each point because the arrow head obscures the true length of the stress vector. The authors do state that there was an observed compressive stress present in the plate and that this is to be expected, although this was a qualitative statement and no data was provided in the report.

Timler's report includes several plots that compare the expected and observed boundary member axial strain and flexural strain demands at several locations at different load levels and in different loading directions. Two section locations where these strains are recorded are symmetrically arranged. The recorded strains are expected to be similar in magnitude and sense, but this was not observed. The explanation provided is that initial imperfections in the panels and boundary members resulted in one panel attracting more load than the other and creating an unbalanced stress distribution. This seems to be a likely reason for the discrepancy but it makes it difficult to draw any conclusions about how the magnitude of the stresses in the boundary members compared with the results of analytical models. To validate the use of an average alpha in the 9 story strip models of the prototype buildings, Timler [68] noted significant differences in the VBE demand resulting from "noticeable vari-

ations" in alpha but argued that since the angle differences between the stories was small, the weighted average value could be used.

2.5.4 Tromposch and Kulak 1987

This well documented report focused on the results of an experimental program, similar to that performed by Thornburn *et al.* The objectives of this experiment were to study, in more detail, the cyclic hysteretic behavior of a near full-scale SPSW sub assembly with bolted connections and axially pre-loaded columns, and to validate the strip model approach proposed by Thornburn. Some modifications were introduced that differed from the tests conducted by Thornburn, including the pre-loading of the columns, the bolted connections, and the full cyclic loading protocol. The cyclic loading amplitudes were also much larger than those tested by Thornburn and were well into the inelastic range of the structure. The beam sections were also a little larger, with AISC equivalent W24x162 sections, the columns were the same. The web plates were 3.25 mm (1/8 inch) thick and were welded to the 5 mm thick fish plates.

Welding distortions presented some practical and analytical challenges for the researchers, including curling of column flanges and bowing of members. An attempt was made to compensate for strains introduced into the assembly resulting from connection fit-up and weld shrinkage, but the methods used were very approximate, and the authors recognized this fact.

Strains were measured on the near and far side of both web plates and also at several locations around the boundary frame. As with the Thornburn test, the panel strain gauge rosettes were used to measure the strain field magnitude and inclination of the principal strains and were averaged to eliminate the contribution from panel out-of-plane bending. Principal in-plane stresses were deduced from these strains using the conventional plane-strain to plane-stress transformation equations. The boundary member strain gauges were used to determine both axial and flexural demands in the boundary members. The out-of-

plane buckled deformations of the west panel, resulting from compression loading only, were measured at discrete intervals during the test. These deformations were also measured at the completion of the monotonic load sequence. Beam-to-column joint rotations were also measured.

The web plates behaved in a manner consistent with expectations, with some crimping and minor tearing present at the completion of the test. The tension field formed at an angle close to 45 degrees in each of the loading directions, but the scatter in orientation was high. The strain gauges recorded data well beyond yield of the plate and showed the angle of inclination to roughly coincide with the computed angle. There was some scatter in both magnitude and direction of the principal tensile strains. It is worth noting that the average computed principal compressive stress in the web plates, at the completion of cycle 14, was approximately 38% of the computed tensile stress but it should be pointed out that the method used to compute these stresses is not clear. The authors appear to have used a linear elastic 2D plane-stress constitutive model to determine stresses from the strain rosette data, and capped the stress at 192.5 MPa (the theoretical yield stress minus the presumed pre-stress from welding). This approach does not correctly account for accumulated plastic strains in the calculation of the in-plane stress field or the inclination of the principal tensile stresses.

As with the earlier study conducted by Thornburn, the test was simulated using a simple incremental plane-frame strip model. Due to symmetry, the model represented only half of the structure. Ten tension strips were used to model the web plate. Rigid off-sets were not used to account for the eccentricity of connection of the web plate to boundary members. The connection between boundary members was modeled both as pinned and as moment connected to investigate the influence of each on specimen strength and flexibility.

2.5.5 Roberts and Sabouri-Ghomi 1991

This appears to be the first modern study devoted exclusively to the behavior of an unreinforced SPSW web plate. In this study several small rectangular aluminum and steel panels were tested within a pinned frame. The purpose of the study was to develop a simple hysteresis model for SPSW panels based on the results of an experimental program. The panels had a height h of 300 mm had aspect ratios h/L equal to 1 and 1.5, and plate thicknesses t_w equal to 0.54 mm (aluminum), 0.83 mm (steel) and 1.23 mm (steel). The h/t_w ratios for these panels range from approximately 244 to 556. The elastic modulus and 0.2% proof stress for each specimen are provided but no stress-strain data are provided, so it is not known if the steel exhibits a distinct yield plateau. The panels were mounted inside a pin-connected frame and bolted to the frame using high-tensile *M8* bolts. It was not explicitly stated that the bolts were pre-tensioned so that slip would not occur at the connection.

Loads were applied to the frame by applying an actuator force along one panel diagonal and this is the force reported in the hysteresis plots, an example of which is shown in Fig. 2.4. For all of the tests the loads were applied until a target displacement was reached. The first target displacement was at approximately two times the panel yield stress, or approximately 1.6 mm. The amplitude of the displacements were increased progressively up to a peak of around 2.8 mm. It is unclear if the displacement is measured across the diagonal dimension or as a drift, but the authors do say that "tensile forces were applied along one panel diagonal until the corresponding displacement reached a prescribed value, generally 1.6 mm". In order to get an equivalent drift angle or inter-story drift this figure would clearly need to be adjusted. In all of the tests, the peak displacement was between three and five times the yield displacement. This corresponds to an approximate inter-story drift of just over 1%.

The hysteresis curves for all six specimens show stable behavior up to the peak displacement. This is not surprising given the modest drift levels. Before the tension field is re-established the thin aluminum panels exhibit severe pinching with a post-buckling strength of between

10 and 15% of the peak load. The thicker and stronger steel panels also have pinched hystereses but the pinching is less severe and tends to reduce further for the thickest plate (1.23 mm). The thickest plate has a post-buckling strength in excess of 50% of the peak strength. All of the panels display considerable softening and non-linearity upon unloading where linearity would be expected.

The author develops a hysteresis model on the basis of the experimental results and on the assumption that during cyclic loading the shear stress in the panel prior to tension field re-alignment is maintained at the elastic buckling stress of the plate, τ_{cr}. In order to account for the presence of in-plane shear stress when computing the amount of plastic contraction normal to the plastic tensile strains, an expression for the plastic strain increments on the diagonals is formulated in terms of the yield stress of the material, the assumed yield function (von Mises) and the critical buckling stress of the plate.

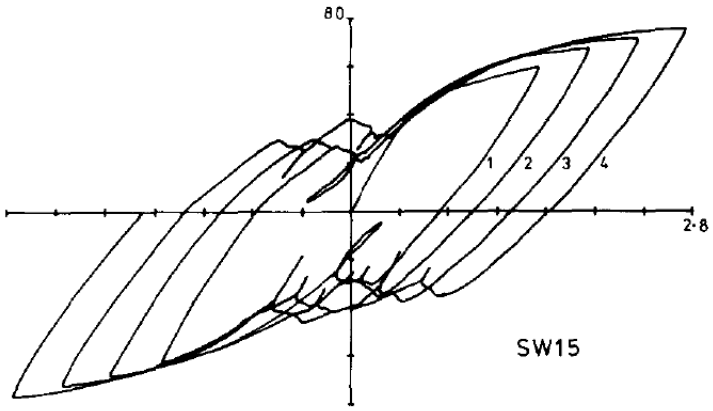

Figure 2.4: Roberts test SW15: 450 mm x 300 mm x 1.23 mm thick Steel with F_y of 152 MPa

Using the equation provided by Roberts, the plastic strain increment ratio, β, which is used to compute the drift at reloading (e.g., point H1 on Fig. 2.5) will vary between 0.5 for a pure tension field to about 0.56 for the extreme case of a square web plate with an h/t of 300. For most practical situations β will be less than 0.54. Roberts simplifies the

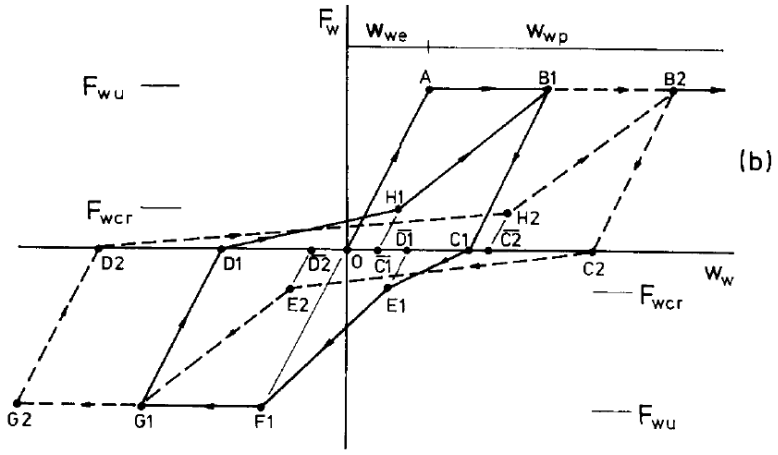

Figure 2.5: Roberts hysteresis model

hysteresis model by effectively delaying the development of the tension field on reloading. The branch D1-H1 on Fig. 2.5 has substantially lower strength than the true hysteresis curve. Furthermore, as the plate reloads after the first cycle the tension field may in fact be fully re-established before the point B1 is reached. The model assumes for simplicity that the plate loads along H1-B1.

An interesting feature of the hysteresis curves for specimens SW3 and SW15 (shown in Fig. 2.4) is the apparent isotropic hardening. This is not observed in the aluminum plate specimens (SW1 and SW13) or the other steel web plate specimens (SW2 and SW14). The ratio of actual plastic load capacity to predicted plastic load capacity, using $0.5F_y t_p L$, averages 1.61 for SW3 and SW15 but only 1.30 for SW2 and SW14. SW2 and SW14 did not display isotropic hardening behavior. It is difficult to draw any conclusions from this without additional stress-strain data which was not provided in the paper.

2.5.6 Sabouri-Ghomi and Roberts 1991

Sabouri-Ghomi [59] presents a macro modeling approach for the dynamic response of a multi-story SPSW that takes into account both shear and flexural deformations over a full story height. The starting point for the analysis is an idealized continuous Timoshenko beam. The solution to the dynamic equilibrium problem is then formulated in terms of finite difference equations with mass lumped at the story level and with shear and flexural stiffness defined over the story. The model incorporates plastic yielding of web plates and uses an idealized multi-linear hysteretic relationship for the web plate which includes plastic contraction. This is the same hysteresis model developed by Roberts [55]. The model also includes a elasto-plastic hysteresis model for hinging of the boundary frame which is a function of the global shear deflection component.

The model is geometrically linear and so does not include the effects of $P - \Delta$, local instabilities associated with boundary element hinging, buckling or other similar phenomena. The model implicitly assumes that the web plate yielding is not influenced by boundary element flexibility and that HBE hinging is not influenced by the axial force in the HBE because the HBEs are not explicitly modeled. These effects could however be included in this type of model and it could be quite useful for determining many response quantities of interest such as drift demand, residual drift, story accelerations and story shear force and overturning moment. Through some simple relationships it could also be used to compute VBE axial and flexural demands (assuming the VBEs remain elastic).

2.5.7 Chen 1991

In 1991 Chen [16] performed two three-story quarter scale tests of SPSWs, one with thin panels, the other with relatively thick panels. Both tests were carried out with a single lateral load at top of the specimens. Stable hysteresis was observed for the thick plate specimen with flexible BEs although severe pull-in for 1st story VBEs resulted in pinched hysteresis. The load was applied cyclically over twenty-four cycles (3 at each drift level) ramping up to a maximum of 2% drift. For both tests, 45 degree rosettes were used to

measure strains but results were not reported in thesis (only in supplement). The author also computed and recorded the initial stiffness, cumulative energy dissipation and ductility factors for specimens. The author observed out-of-plane buckling corrugations and these were generally observed to be inclined at approx 45 degrees, but these were not actually measured.

2.5.8 Elgaaly, Caccese and Du 1993

Shortly after Chen's tests, Elgaaly [30] developed a hysteretic model and calibrated it to the Chen tests. In his simplified piecewise linear model, Elgaaly assumed zero compression capacity on unloading and also assumed strain on reloading corresponds to half way point between loading strain from previous cycle (in same direction) and total strain from that cycle. This is a simplification but it is a little easier to implement and appeared to satisfactorily matched test data.

Elgaaly then performed FE analysis of the three story Chen specimen with 6x6 shell element mesh using NONSAP. The model over-predicted the stiffness by 30 to 40% and strength by 18 to 26% from test. The tension field inclination determined from the FEM model was 40-50 deg. Elgaaly also analyzed the Caccese [14] tests using a modified strip model. In this model the strips were given tri-linear stress strain properties and are inclined at the elastically predicted inclination angle. The tri-linear material model is based on the results of three test specimens. The model initially presented appears to consider compression development in the truss element but is later simplified to be tension only. Plastic contraction is handled in an approximate way by setting the plastic strain increment from the current cycle to half the plastic strain from the previous cycle. The model is compared to the test results and reasonable agreement is observed, although the web plate response in analysis and test is obscured by frame action. Furthermore, the limited test data makes a thorough comparison difficult.

2.5.9 Roberts 1995

Roberts [56] uses the results of his 1991 study to formulate a model for hysterestic behavior of unstiffened perforated and un-perforated steel plate shear walls. The model accounts for the presence of shear stress in the panel in the post-buckling range by assuming a uniform distribution of the elastic critical buckling stress is maintained over the plate as it yields. This critical stress is used to locate the reloading point on an idealized piecewise linear hysteresis curve. He does not discuss the nature of the residual post-buckling strength that is evident in his test results, nor does he attempt to reconcile this effect with his model. The author then presents a method for analyzing the seismic performance of a multi-story SPSWs using a shear deformable Timoshenko beam analogy. This approach appears to have some value as a diagnostic tool for global performance provided the boundary element frame contribution to the strength and stiffness can be included.

2.5.10 Xue 1995

In 1995 Xue [77] performed one the earliest purely analytical studies of multi-story SPSWs using continuum finite elements. The Kulak and Elgaaly specimens were modeled using the ADINA software to check the feasibility of shell elements in capturing the elastic and plastic post-buckling behavior of web plates. A bilinear material model with isotropic hardening was used for the monotonic analysis of these specimens. After experiencing numerical difficulties with ADINA in the cyclic analysis, the finite element package ULSAS was adapted by Xue to ULSAS-GE whereby cyclic loading of 3D SPSW structures could be performed. The ULSAS-GE package was validated against the Kulak specimen although only to a very limited drift range and only through two cycles up to approximately half the peak lateral load of the test.

Xue analyzed (using ADINA) and designed a twelve story prototype SPSW using the 1988 UBC equivalent lateral force procedure. Beams and columns were modeled using elastic line elements and web plates were modeled with a 6x6 mesh of shell elements. The motivation for this design was to identify sensible ranges of design parameters to be used for paramet-

ric studies, by carrying out actual designs with different framing configurations. These are shown in Fig. 2.6. The P-G system is identified as the optimal configuration with respect to overall performance of the system and utilizes a partial moment frame with the web plates connected to the girders only.

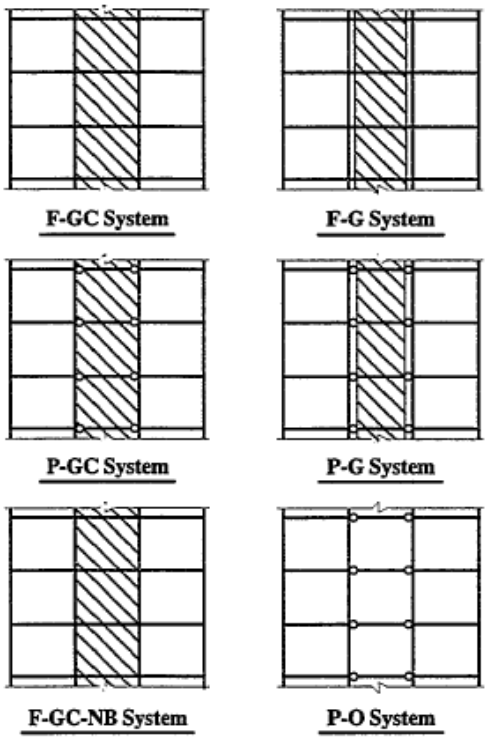

Figure 2.6: Xue systems types investigated as part of prototype design

A parametric study of a single story sub-assembly of a P-G type system was undertaken by Xue using monotonic loading. The panel aspect ratio, h/t ratio, girder rigidity and connection arrangements are varied to establish a set of empirical formulas that are used to predict behavior of a P-G system under monotonic loading. Using ULSAS-GE, cyclic analyses are performed for eight separate sub-assembly designs. A bilinear material model is used for both the beam-columns and web plates with combined isotropic and kinematic hardening. The mesh size used for the web plates was typically 12x12. Using the results

of these cyclic analyses, a hysteresis model is developed. After reviewing several hysteretic modeling techniques, a four parameter version of the the Masing (1971) method is implemented. This model is complex but appears to match the ULSAS-GE analysis response quite well, except for some notable differences at low drift levels where tension field loading predicted by the hysteresis models occurs very late in the cycle.

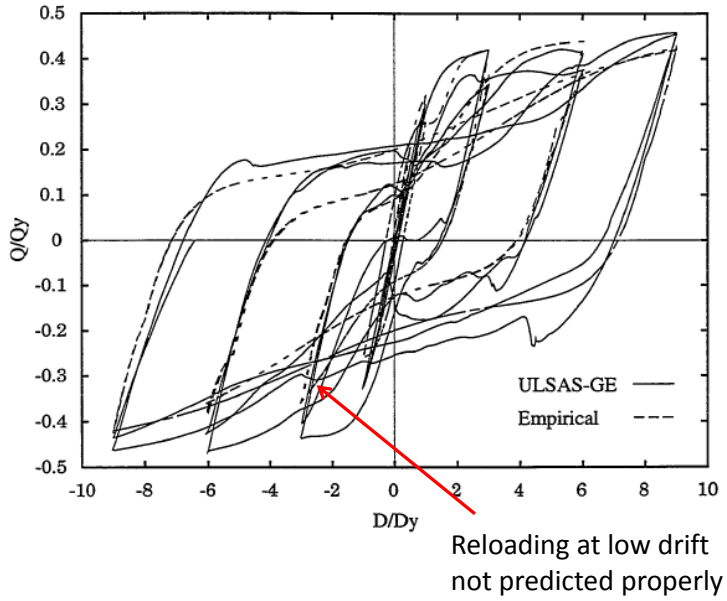

Figure 2.7: Xue [77]: ULSAS-GE and Masing Hysteresis

2.5.11 Elgaaly and Lui 1997

In 1997 Elgaaly introduced the "strip-gusset" concept into a web plate model to account for the variation in strain observed in the direction of the tension field. These strain variations were measured in tests by Elgaaly in 1993 [30] were motivated by Marsh's findings in 1982, that for plate girders the post-buckling strength is defined by "local yielding and redistribution of yield stresses at plate boundary". Elgaaly's proposed modification to the conventional strip model is based on the assumption that the web plate will undergo significant shear yielding close to the panel boundaries and that the size of this gusset zone is a

function of the plate critical buckling stress. The result is a non-uniform axial strain distribution along the length of the truss element having an assumed parabolic distribution, with a maximum value occurring at the ends of the strip and a minimum at midspan. This strain distribution is used to compute an effective initial yield stress, σ_{y1}, and a tangent elastic modulus, E_1, between σ_{y1} and the material yield strength σ_y. The result of this modification is a web plate that softens more gradually upon lateral loading. Significant premature shear yielding at the plate boundary is not observed in FEM models analyzed by the Elgaaly.

2.5.12 Driver, Kulak, Kennedy and Elwi 1997

In 1997 Driver [27] physically tested a four story one-half scale SPSW. This test has been well document by other investigators so the setup will not be detailed here. The author applied the ATC-24 displacement history load sequence using the yield drift, δ_y, at 1st story as the controlling parameter and equal lateral forces at each level. Gravity loads were applied by pretensioning. Ten strain rosettes were attached to the 2^{nd} story panel near the corner to measure stress field development. Five rosettes were placed on the near-side and five on the far-side. Strain gauges were also attached to the VBEs 300 mm (11.8 inches) above and below the beam column joint on the outsides of the beam flanges. The strain gauge locations can be seen on Fig. 2.8.

The test was simulated using both a strip model and a continuum model. The strip model comprised ten uniaxial truss elements per panel and used line elements with the facility for concentrated P-M interaction plastic hinges to form anywhere in the VBEs and HBEs. Rigid offsets were not included in the model. Driver found that ten strips were adequate for web plate strip modeling and that peak strength is relatively insensitive to inclination angle. He concluded that the strip model consistently under predicted the stiffness of the specimen but it is approximately the same when the load is about 60 percent of peak. The continuum model used a coarse 6x9 mesh of *ABAQUS* S8R5 elements for web plates and continuum elements for the beams and columns.

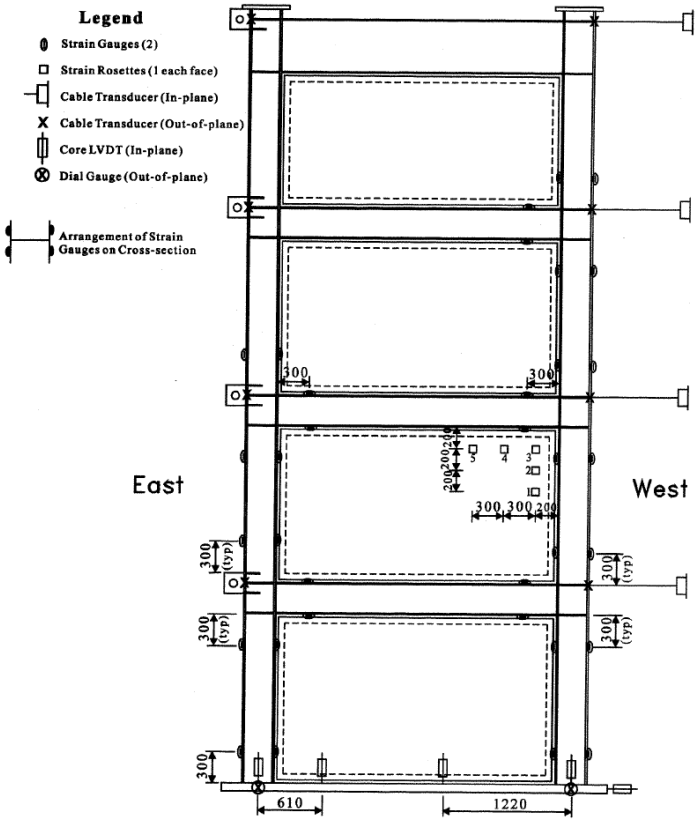

Figure 2.8: Driver [27]: test strain gauge arrangement

The magnitude of the principal compressive stresses determined from strain gauge data exceeded the principal tensile stress magnitude by an average factor of 1.90. However the same ratio determined from the FEA analysis is 0.70. The correlation between experimental and numerically estimated web plate tensile stresses was reasonable ($R_{\sigma 1} = 0.911$), but it was not very good for the compressive stress estimate ($R_{\sigma 2} = 0.677$). σ_1 and σ_2 are the tensile and compressive principal stresses respectively. This is not surprising given the coarseness of the mesh and the high strain gradients that would have occurred in the test and in the numerical simulation.

Table 2.1: Driver Test and FEA alpha prediction

Load Level	α_{Test} **(deg)**	α_{FEA} **(deg)**
Low	55.6	50.6
Medium	50.8	47.5
High	50.4	45.1

Comparisons between the experimental and numerical estimates of VBE axial and flexural demand reveal that the experimental estimates of VBE flexure are less than the numerically predicted estimates and substantially less for the 2^{nd} floor VBEs. The strip models (both 42 degree and 50 degree) consistently predict higher flexural demands than the continuum model.

The correlation between the measured and predicted inclination angle also shows some dispersion but is generally positive with $R_\alpha = 0.891$. The mean measured and numerically predicted angles are shown in Table 2.1. Some migration of the strain gauge derived angle does occur when progressing from a low to a high load level, although the author doesn't suggest this is due to plasticity. The angle predicted by the FEA analysis appears to approach 45 degrees at high load level, which is consistent with plastic behavior, but the method used to determine α from the strain gauge data is not provided. Equation F5-2 from the *Provisions* predicts an α of 41.8 degrees.

In the subsequent cyclic analysis of the web plate and frame, which did not include geometric non-linearity and subsequently did not exhibit any pinching behavior, Driver used a kinematic hardening rule. Driver also proposed that up to moderate load levels, a pure shear model of a web plate, that is an inelastic plane-stress model,"provides a reasonable approximation of true behavior". Driver modeled test specimen with plane stress elements, without geometric non-linearity, and no hysteretic pinching is evident in analysis results.

Driver introduces a hysteretic model that separates the contribution to hysteretic response form the boundary frame and web plate. As with Elgaaly's hysteretic model, it includes a simplification for determining the drift at reloading. It is assumed that the inelastic stretching of the panel in the previous half cycle begins when the drift is zero. The author concedes that this is a simplification of the actual behavior. This may lead to significant error in the cyclic response when the drift history is severely asymmetric. The proposed model is compared with the hysteretic response of the four story specimen that was tested as part of the same research project. A reasonable match is achieved between the model and the test, however the proposed model under-predicts dissipated energy and there are obvious differences in the shape of the predicted and actual load-displacement response. It is not clear how well this model would capture the real response to asymmetric loading, e.g., the Steel SAC Near-Fault Protocol [40].

2.5.13 Lubell 1997

In 1997 Lubell [48] used 9 strain gauge rosettes on each side of the 1^{st} and 2^{nd} story of a 4 story quarter scale specimen to measure the in-plane principal strain characteristics and tension field inclination. The specimen was loaded cyclically under the ATC-24 protocol using displacement control up to a target drift of $7\times\delta y$. The rosettes were positioned each side of the first and second story web plates near the boundary elements. Once again, as for the Tromposch [73] tests, the strain data was used to compute tension field inclination for inelastic cyclic loading. Although it is feasible to do this when the strains are elastic, and for the case of monotonic loading that is moderately plastic, it is not easily or directly applicable to cyclic loading at large inelastic drifts.

2.5.14 Timler, Ventura, Prion and Anjam 1998

Timler et al [68] performed study using strip models as part of an effort by UBC and UA and the Canadian Institute of Steel Construction to provide succinct guidelines for SPSW design, he compared SPSW systems of ordinary, nominally ductile and ductile capacity to

equivalently ductile concrete moment frame systems. The work of Driver [27], Rezai [54] and Lubell [48] were part of this effort. A cost comparison was made between the SPSW and concrete alternatives and the differences were minimal.

2.5.15 Rezai 1999

In 1999 Rezai [54] conducted the first comprehensive shake table testing program of a reduced scale, multi-story SPSW. Rezai analyzed the data from a quasi-static test of a similar four story reduced scale specimen by Lubell.

A salient feature of both the four story specimens (and an unfortunate drawback) is the excessive flexibility of the VBE sections. The VBEs for the quasi-static tests were S75x8 (AISC S3x5.7) and for the shake table tests B100x9 sections (AISC M4x6) were used. The shake table specimen VBEs had only 55% of the flexural stiffness required by the Provisions and insufficient strength using capacity design principles. The quasi-static specimen was even weaker and those VBEs ultimately failed in weak axis buckling at the first level at only twice the yield drift.

The strain gauge layout for the quasi-static test is shown in Fig. 2.9. The first story elastic tension field orientation angle is low on account of the very flexible VBEs. The computed α from the web plate strain gauges is shown in Fig. 2.10. This plot also shows some characteristics of the migration of alpha towards 45 degrees, however in general the inclination angle appears to be variable, particularly in the center of the plate where the transition on load reversal is very gradual. The excessive inelastic behavior of the VBEs makes any direct comparison with Eqn. F5-2 of the *Provisions* inappropriate.

The shake table program included nine individual runs of real and synthetic scaled ground motions. It is understood that the structure was unaltered from test to test and damaged components were not replaced, though it is not explicitly stated otherwise. The tension field orientations were computed from strain gauge data and appeared to vary between 37

and 42 degrees for all of the reported load histories (the computed α for this test is 38.8 degrees) but it is not possible to determine from the plots how α changed on each cycle. The 1^{st} story drift did not exceed 0.8% or about $1.5\delta_y$ for this structure. Plots of bending moment and shear force were shown for the first floor VBEs and indicate that the bending demand from web plate pull-in ($M_{vbe,web}$) is very small compared to frame action demands. An accurate assessment of the relationship between base shear and $M_{vbe,web}$ is not feasible. However, at low drifts $M_{vbe,web}$ is significantly lower than would be predicted assuming a fully engaged and moderately plastified tension field, as would be expected at $1.5\delta_y$.

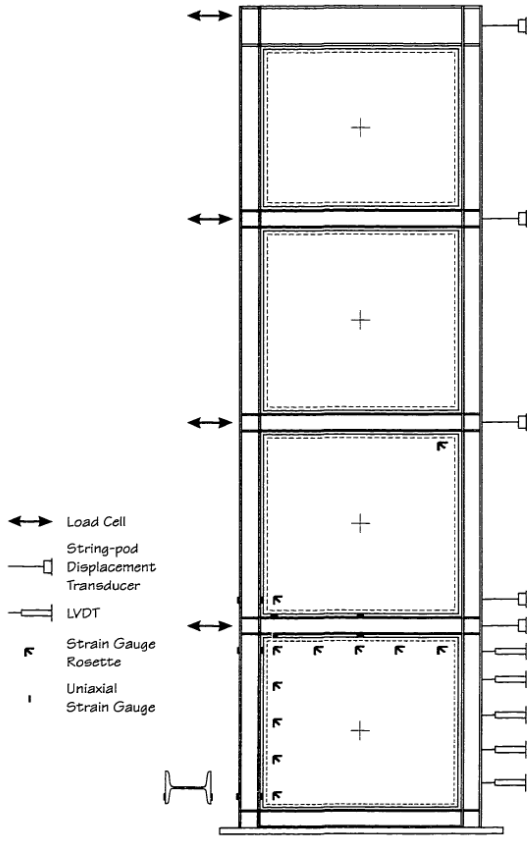

Figure 2.9: Rezai [54]: Shake table test strain gauge layout

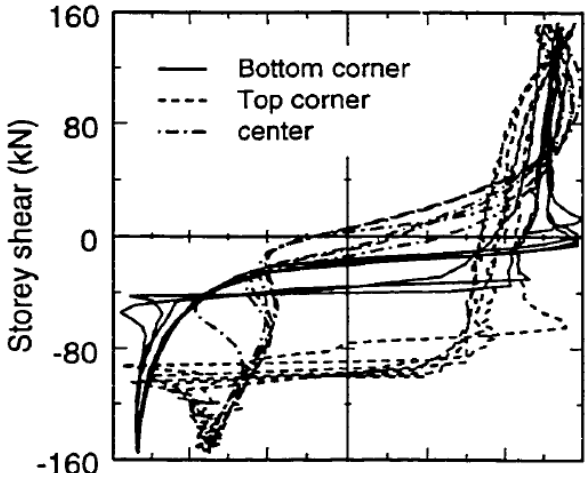

Figure 2.10: Rezai [54]: Inclination of principal strains from shake table test

Rezai investigated the influence of various parameters (including column and beam cross-sectional area A_c and A_b, column moment of inertia I_c, web plate length L, web plate height h and and web plate thickness t_w) on the tension field inclination angle α. He analyzed the geometry of the 1^{st} story of five reduced scale tests that had been performed up to that time (including his own) and plotted the relationship between alpha and variations in each of the parameter in turn, holding all others constant. There is no discussion about how plastification of the web plate may precipitate changes in the tension field orientation when all other geometric parameters are held constant.

A modified strip model is proposed which includes a limited number of strips inclined at various angles, shown in Fig. 2.11. The objective is presumably to capture the variable nature of the web plate tension field and its interaction with the boundary frame with a minimum of modeling effort. The strip width is determined by equating work terms for a conventional tension field to that of a single diagonal truss element at 45 degrees using the same equations presented by Timler [67]. This effective strip width is apportioned equally to the strips.

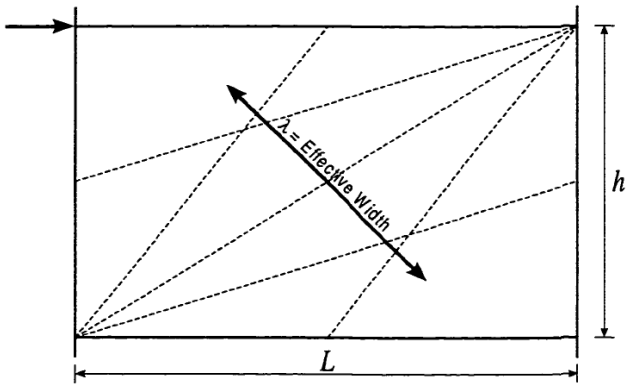

Figure 2.11: Rezai's proposed strip model

The proposed model predicts peak strength from pushover analyses reasonably well, but only on one of the tests specimens it is compared with. Furthermore, pushover strength is not very sensitive to tension field inclination. It is questionable whether the model can adequately predict VBE demands, partly because there is only one point of attachment at mid-height of the VBE and also because the inclination of the shallow strips (and consequently the transverse force demand) is highly sensitive to the L/h ratio. The model was not used to predict cyclic response.

2.5.16 Lubell 2000

Lubell [49] summarizes and discusses results of a four story testing program, in the discussion he suggests that a better match of experimental elastic stiffness can be obtained by reducing the angle to 22 deg (elastic predicted alpha = 37) without cautioning that this would also lead to unconservative VBE demands. He does recommend though that boundary elements should be capacity designed.

The author performed quasi-static test of two single story and one four story specimen

prior to shake table testing carried out by Rezai [54]. Severe pull-in was observed on these tests. Severe in-plane and out-of-plane plastic deformations of boundary elements were observed in single story and four story tests. The BEs were not capacity designed and had very low weak axis flexural strength which resulted in inelastic buckling. In this test the panels had equal thickness over all stories. The load was applied equally to all four stories which resulted in large inelastic demands at the first floor while the other remained relatively undamaged.

2.5.17 Behbahanifard 2003

In 2000 the top three stories of the Driver test specimen were salvaged and re-tested at C-FER. The specimen was subjected to cyclic lateral loading using an ATC-24 loading protocol with the δ_y at the 2^{nd} floor level once again set as the controlling parameter. The lateral loads applied at each floor were of equal magnitude, as for the original Driver test. Gravity loads were simulated with pre-stressing.

In addition to measuring applied lateral loads and horizontal displacements at each level, the specimen was instrumented with strain gauges on the flanges and webs of the first and second story VBEs and HBEs. The gauges were placed at several stations along the length of the member and were used to compute member axial and flexural demands.

At the peak displacement of cycles ten through twenty-four the web plate tension field inclination on the second and third story were determined by measuring the orientation of the buckled corrugations. There is wide scatter in the measured direction of the buckled waves in the first story web plate for both the push and pull cycle, with a reported range of 12 degrees. The second story panel has less scatter with a range of 6 degrees. The average angle for the first story panel stabilizes after cycle number fifteen to approximately 51 degrees. The average angle determined for the second story panel fluctuates a little more but settles to a value of around 46 degrees.

Using *ABAQUS Explicit* [25], the author modeled the four story Driver [27] specimen and modified three story salvaged portion he tested. He concluded that for the four story Driver test at ultimate load there was excellent agreement between the FEA predicted tension field orientation and that derived by Timler and Kulak [67]. It should be noted that the equation predicts an angle very close to 45 degrees for levels one, two and three of the specimen so a good match between the model and the equation is expected. *ABAQUS* predicts an angle closer to 45 degrees. For the three story specimen he concludes that the match is excellent for story one but found FEA under predicts the second story angle by 15%. It is not clear how the author is computing the angle derived from the FEA analysis as it is not discussed. The author also analyzes the trajectory of the buckling corrugations in the three story test and compares this to the FEA result.

A dimensional analysis is carried out to determine key parameters that influence the performance of SPSWs. He examined three models with different column flexibility parameters computed per [22] of 1.5, 2.5 and 3.5 (holding the other parameters constant) and plotted this against normalized base shear and found that there is a strong dependence of base shear capacity on column flexibility. However, analysis of the modeling parameters reveals that the columns with high flexibility (2.5 and 3.5) also have low strength and will yield at midspan well before the plate has reached it full capacity. This implies that high flexibility cannot necessarily be correlated with low system strength. Had the VBEs not yielded at midspan, only a small reduction in lateral capacity should have been observed.

2.5.18 Shishkin, Driver and Grondin 2005

In Structural Engineering Report #261 from the University of Alberta [60], Shishkin *et al* propose a modified strip model that includes deterioration strips to capture the effects of local plate tearing at the panel corners and a single diagonal compression strut to mimic the observed effective compression resistance offered by the plate. Two deterioration strips are included in each panel and intersect with the beam-column joints. Fig. 2.12 shows the modified model applied to the Driver specimen. The deterioration strips are modeled as

elastic-perfectly plastic and hinge at a drift of $5\Delta_y$, dropping to zero load once the drift exceeds $9\Delta_y$. Beam-column rotational plastic hinges and strip axial hinges are modeled using multi-linear load-displacement properties. The compression strut stiffness is computed using the equivalent brace equation derived by Thornburn *et al* and has a single axial plastic hinge within its span. The compression hinge is set to yield at 8% of the tensile stress of the web plate and has no tensile strength.

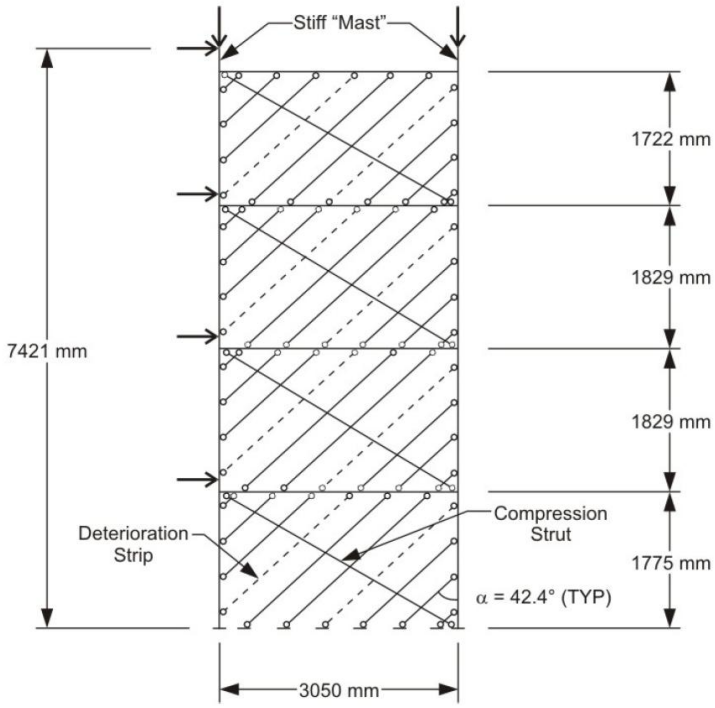

Figure 2.12: Shishkin's modified strip model of the 1997 Driver test specimen

The model was calibrated against the Driver test of 1997 and a pushover analysis was performed using SAP2000. The load-displacement response of the modified tension strip model closely matched the cyclic envelope of the Driver experimental hysteresis curve, although it was calibrated to do so. The force demands on the boundary elements did not match the test results very well but there was significant shear yielding and inelastic flange

buckling of the VBEs in the test specimen, so the bending and axial demands determined form strain gauge data would be highly suspect. A slightly simplified version of the modified model was validated against three other SPSW tests; the Timler and Kulak specimen from 1983 [67], the single story Lubell specimen from 2000 [49], and the four story Lubell specimen from 1997. This simplified version of the model used bilinear material properties for the strips and beam-column plastic hinges. The modified strip model did not appear to predict the pushover response any better than a conventional strip model. The inclusion of the compression strut slightly over-predicted initial stiffness in the Timler specimen and the deterioration strips result in under-predicted strength of the four story 1997 Lubell specimen at large drifts. Though not stated by the author, the deterioration in push-over strength may also be attributed to the observed VBE inelastic deformation near the base of the four story specimen. Severe shear-flexure yielding of the VBE would lead to a reduction in lateral strength.

The modified model can be used to adequately predict the strength and stiffness of an SPSW test, however it needs to be carefully calibrated. As a design tool it has some utility in that it can capture panel degradation and global lateral strength of the panel reasonably well. More importantly though, the model is not designed to be used in cyclic analysis as it is purely a push-over capacity tool, and is not calibrated to accurately predict boundary element demands.

2.5.19 Kharrazi 2005

Kharrazi [38] performed quasi-static and dynamic shake table tests of single story, 60% scale specimens of SPWs at the University of British Columbia. The specimen frames were moment connected and had an L/h ratio of 0.75, less than the AISC Provisions minimum permitted value of 0.8. The VBEs were constructed of a pair of HSS 102x102x8 sections (HSS 4x4x5/16). The top and bottom HBEs were W200x86 (W8x58) sections. Two web plate materials were tested, both 22 Ga cold formed steel sheet, with actual F_y of 246 MPa and 153 MPa. The VBEs had an effective I_c of 76.3×10^6 mm^4 (18.3 in^4) also less than the

AISC Provisions minimum, computed to be $189.3 \times 10^6\ mm^4$ ($45.4\ in^4$). The quasi-static model was tested to validate the analytical Modified Plate-Frame Interaction (M-PFI) models developed by the author, to obtain performance data for the shake table tests and to study the post-buckling behavior of the web plates.

Three quasi-static tests were performed using the ATC-24 loading protocol with displacement controlled loading. Two were carried out on specimens with web plates, DSPW-1 (246 MPa) and DSPW-2 (153 MPa), and one bare frame test, SF-1. Strain gauges were mounted on the boundary frame and on the web plate, although only three of the seventeen web plate mounted rosettes had matching front and backside gauges to eliminate flexural strains due to plate buckling. Elimination of these strains is not discussed. Fig. 2.13 shows the locations of the web plate rosettes.

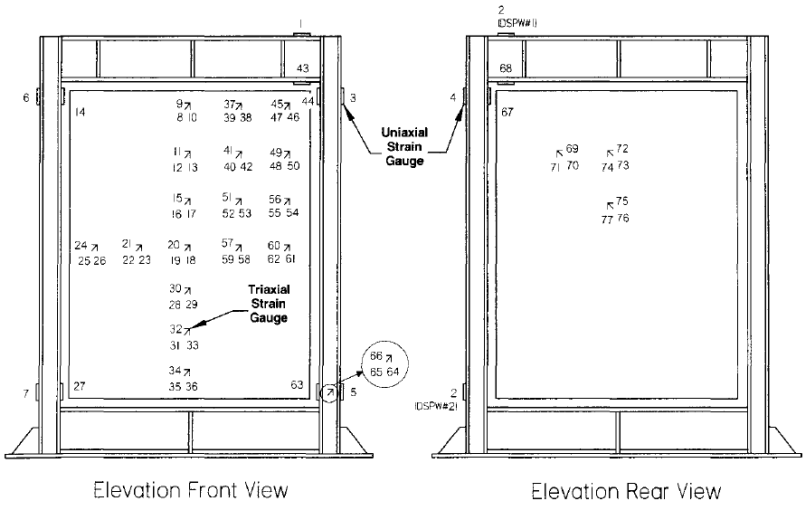

Figure 2.13: Kharrazi test specimen showing strain rosette locations

The specimens showed stable hysteretic behavior to drift levels exceeding 6% with mini-

mal pinching, however the plastic capacity of the boundary frame was between 60 and 80% of the specimen capacity, so the hysteresis is heavily influenced by the strength of the frame. Surprisingly, in both tests with web plates, the VBEs started developing flexural hinges at very high drifts of approximately 4%.

The tension field inclination angle was measured in both DSPW-1 and DSPW-2 at 0.25%, 0.5%, 1.0% and 2.0% using the strain gauges, and also by observation of the inclination of the buckling corrugations. The buckles were oriented at an angle of between 37 and 39 degrees. The average angle determined by the strain gauges was 38.1 degrees for drifts greater than or equal to 0.5%, although it appears that the total strain is used in this calculation as it is not explicitly stated otherwise.

Kharrazi introduces a modified plate-frame interaction (M-PFI) methodology for analyzing SPSWs and applies it to a 3-story, a 9-story and a 27-story SPSW design which is then validated using $ABAQUS$ pushover analyses. This method is intended to be used as a performance based design tool that can be implemented independently of structural analysis software. Simple closed form equations are developed, based in part on parametric studies carried out by Behbahanifard [6], that assess the strength and stiffness of a story as being the sum of the boundary frame and web plate contributions, modified to account for overturning effects. The web plate modified strength is assumed to be defined by an elliptical interaction equation for flexure and shear. The effective flexural strength of the web plate assumes a uniform shear stress of τ_{cr} at yield and bending stresses based on plane section behavior of the wall. The equations are very complex and to some extent belie the simplistic nature of the assumed mechanics.

2.5.20 Park, Kwack, Jeon, Kim and Choi 2007

Park *el al* [51] tested five, three story, one-third scale SPSWs. Each specimen was subjected to increasing cyclic loading with a single concentrated lateral load at the top of the frame, up to a maximum displacement of $8\delta_y$. Two of the specimens were purposefully designed

to have weak VBEs (WC series) with each specimen having different web plate thicknesses, the remaining three (SC series) had strong columns but also with different web plate thicknesses. The main objective was to assess ductility capacity of the systems.

Each of the SC series specimens displayed large inelastic drift capacity with very limited pinching and shear yielding was distributed at all levels. The displacement ductility reduced as the web plate thickness increased. Both of WC series specimens had significant inelastic behavior concentrated in the first floor VBEs, with significant inelastic flange buckling. Rapid strength deterioration occurred after yield drift. The ductility capacity of the WC specimens was comparable to the SC specimens with the thicker web plates. More damage occurred in the WC specimen with the thicker plate and the energy dissipated was no greater than the WC specimen with the thin plate. Several weld fractures were noted in the framing connections for all of the tests. Some tearing was noted in the web plates but was stable and not believed to contribute to system strength degradation.

The lateral strength and VBE capacities were determined with a simple capacity design approach, but it only included the pull-in demand from the web plate assuming a column with built-in ends, with no contribution from frame drift. Capacities were checked using the AISC equations which roughly correlated with the test observations.

2.5.21 Choi and Park 2008

This series of experiments was similar to the Park *et al* [51] one-third scale tests the previous year. The objective this time was to test the energy dissipation and ductility capacity of three story specimens with thin plates and with different panel aspect ratios. Two of the specimens (FSPW1 and FSPW2) had identical web plate thicknesses and member sizes, but with aspect ratios of 1.5 and 2.2 respectively. Both were designed so that the VBEs remained elastic using capacity design principals, although as for Park [51] the frame drift contribution was not counted in the VBE demands. The third specimen (FSPW3) had the identical plate thickness and an aspect ratio of 2.2, however in order to study the effects of

shear yielding in the VBEs, FSPW3 was purposefully designed to resist only 60% of the web plate tension field force. All three SPSW specimens had HBEs and VBEs with compact sections per AISC requirements. A CBF and a MRF specimen were also constructed and tested as part of the same experimental program for comparative purposes. The loading arrangement and protocol were identical to Park *et al.*

All three SPSW specimens had stable hysteresis with some pinching but limited strength degradation. Specimen FSPW3 had considerable inelastic shear yielding in the VBE web. Most of this shear deformation occurred within the top third of the first story. By contrast, FSPW2 had limited inelastic deformation in the first floor VBEs and maintained close to its peak strength up to a drift of 5.3%. The damping modification factor (κ_{pred}, the ratio of the total energy dissipated at $3\delta_y$ to that of an ideal elasto-plastic system) was computed for all specimens. The three SPSW specimens had superior κ_{pred} compared with the CBF and this increased with aspect ratio and with increasing flexural to shear strength ratio of the wall. κ_{pred} for the SPSWs was lower than the MRF, although the MRF had significantly lower peak strength ($< 30\%$ than for SPSWs).

2.5.22 Qu and Bruneau 2008

A two-phase experiment on a single full-scale two story SPSW was carried out by Qu *et al* [52] in 2008. The objective of these tests was to establish the replace-ability of web plates in a system already subjected to large ground motions. All HBE and VBE sections were compact and capacity designed per Berman *et al* [7] recommendations. The panel aspect ratio was 1.0 for both stories. At each floor level the specimen was built integrally with a section of concrete/metal deck slab. All HBEs had RBS sections designed per FEMA 350. The specimen was instrumented with strain gauges on the boundary element flanges and web at several stations. LVDTs were placed across the panel diagonal to measure web plate elongation. No web plate strain gauges were used to measure plate strain. Various other instruments were used to measure joint tilt and lateral in-plane displacement.

In the Phase I tests, the specimen was subjected to pseudo-dynamic loading from three ground motions of progressively decreasing intensity (MCE, DBE and "service" level EQ). In Phase II the specimen was pseudo-dynamically tested to a single MCE level earthquake and then cyclically tested to failure with drifts exceeding 5%.

The specimen showed stable hysteresis for both pseudo-dynamic tests but the response was extremely pinched. The Phase II cyclic test shows stable hysteresis out to approximately 3% drift, after which there is significant strength degradation (loss of about 45%) at 5% drift. The strength degradation was attributed to complete fracture of the intermediate HBE shear tab which led to additional shear tab and flange fractures in these connections and ultimately changed the load paths.

The Phase II pseudo-dynamic test was modeled using a simple tension strip model. The model included 15 bi-directional strips (each way) for the web plate. These were not rigidly offset form the HBEs and VBEs. Nominal material strengths were obtained from coupon tests results and isotropic hardening was assumed. A good match was obtained between the strip model and the test hysteresis although the model over predicted the strength at the lower drift levels, and the energy dissipated. A monotonic pushover analysis of the specimen was conducted using a comprehensive FEA shell model which included the slabs, also in *ABAQUS*. The shell model very slightly over-predicted the peak strength of the specimen but significantly over-predicted the stiffness due to the significant web plate deformations.

2.5.23 Bhowmick, Driver and Grondin 2009

Bhowmick, Driver and Grondin[11] used *ABAQUS Standard* to perform response history analyses on two hypothetical buildings located in Vancouver B.C, one four story and one fifteen story building. The models include leaning columns to assess the significance of including P-delta effects. The buildings are designed using the CAN/CSA-S16-01 equivalent static force procedure, although they are purposely designed without considering P-delta effects. The boundary elements and the web plate are modeled using a bilinear material

with an F_y of 350 MPa and an E_s of 200,000 MPa. The material model incorporates the Cowper-Symonds overstress power law to predict dynamic yield strength of the steel. The buildings are subjected to a small suite of NBCC design spectrum compatible earthquake ground motions and various response quantities are evaluated.

The results of the response history analyses showed that:

- Story drifts were considerably lower than the code prescribed maximum, averaging less than 1% for the fifteen story building.
- Peak story shear forces were up to four times larger than the shears determined from NBCC equivalent static forces.
- Average base shear was 47% higher in the fifteen story building. Much of this overstrength is attributed to the shear strength of the columns.
- Low code estimated probable base shear results in a concomitant underestimate of the column axial and bending demands.
- Axial forces and bending moments in the columns are both significantly underestimated by the CAN/CSA S16-01 capacity design approach.
- If strain rate effects are included, the system ductility is reduced and the average flexural demand at the base of the wall is increased.
- P-delta effects have a negligible impact on the story drifts.

This paper revealed a number of interesting attributes of tall SPSWs, although some of the details are unclear. The plots generated for VBE (column) bending moment show "dynamic moment envelopes" but only one point is plotted at each floor so this moment is presumably the maximum that occurs over the story height. It would be interesting to know how this moment varied over the story height and what the peak axial-flexure and axial-shear interaction values were at each level. Since the model included all of the features needed for a comprehensive non-linear analysis, including the effects of shear-flexure-axial

interaction in the VBEs and localized inelasticity and residual story drifts, it would be useful to know how these quantities compare with equivalent strip models. The paper doesn't note the mesh density for the *ABAQUS* model. Other research on web plate continuum models recommend a minimum of thirty elements be used on the short side of a web plate or five elements over the buckled wave length. Less than this may result in an artificially stiff model.

2.5.24 Topkaya 2009

Topkaya presented a series of papers in 2009 addressing the stiffness [72] and period determination of SPSWs [71]. The motivation was to provide a simple method for determining stiffness without having to resort to complex nonlinear FE modeling. Since prescriptive force based design procedures use the fundamental period for lateral force determination, and stiffness for drift determination, an accurate assessment of both is needed.

Topkaya and Atasoy 2009

The lateral stiffness of ten previously tested SPSWs is determined using the strip method and the continuum method. It was found that the continuum method provides an upper bound on stiffness while the strip method provides a lower bound when compared to the experimental results. A simplified approach for determining lateral stiffness is proposed that utilizes a single diagonal brace. This is a modified version of the equivalent brace model proposed by Thornburn [66]. The modified equivalent brace member takes account of shear-flexure interaction on lateral stiffness. The area of the VBE section is also modified in this approach. The equivalent brace model was validated by comparing the results against 80 continuum and strip models with a broad range of aspect ratios and panel slenderness values and was found to be 8% stiffer than the average of the continuum and strip methods for each case.

Topkaya and Kurban 2009

The prescriptive code equations for building period are often expressed as a scalar function of the building height (in feet or meters) raised to an index which has been calibrated from experimental and field measurements. In this study, a total of 20 SPSW wall systems and 44 dual systems (SPSWs with moment frames) are analyzed using both linear and nonlinear FE models. The results are compared with the code equation for period and a simple hand calculation method is proposed for estimating the period. An equation for estimating the period elongation as a function of inter-story drift is also proposed for systems with uniform properties along the height of the wall. It was found that the code based equations sometimes significantly underestimate the period and lead to overly conservative designs. The period obtained from the geometrically nonlinear analyses was observed to be 17% greater than that from linear analysis.

2.5.25 Choi and Park 2010

Choi and Park [**?**] develop a hysteretic model of a web plate based entirely on the results of FEM continuum analyses of a cyclically loaded web plate. The model is validated against the results of various experimental results. Choi's model is based on an analysis of a single panel with bi-linear material properties and kinematic hardening. The panel aspect ratio (L/h) is 1.5 and the slenderness ratio (h/t) is 250; a very stout plate for SPSW applications. The model comprises a 40x60 mesh of $ABAQUS\ S4R$ shell elements and a rigid, pin-connected boundary frame. To equate the behavior of this model to that of an equivalent strip model, Choi extracts the stresses in the web plate elements at each point in time and determines the normal stress components in the direction of the theoretical tension field, in this case 45 degrees. This operation is carried out for both directions. As the plate unloads and then buckles prior to reloading in the opposite direction, the normal stress is observed to significantly exceed the buckling stress at low drift levels but appears to converge to τ_{cr} as the drift magnitudes increase. Fig. 2.14 shows the average stress in the diagonal direction for one loading direction.

In the proposed hysteretic model, the web plate compressive strength normal to the

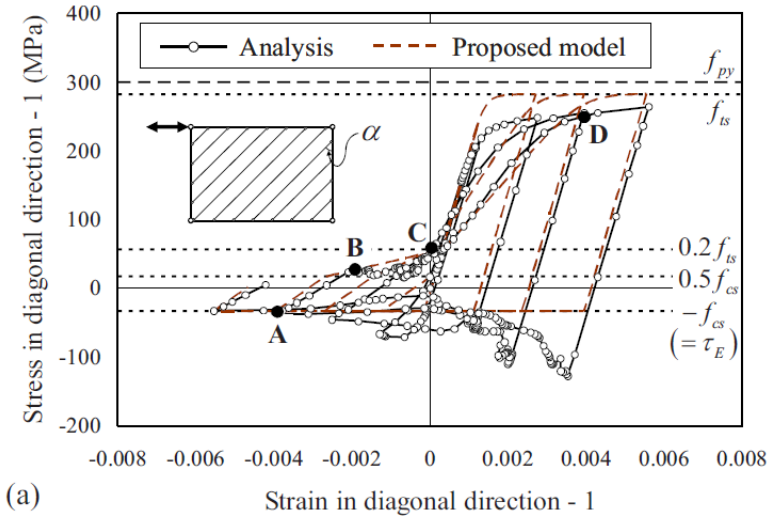

Figure 2.14: Choi's analysis of web plate showing mean normal stress at 45 degrees.

tension field is assumed to be the buckling stress, τ_{cr}. This compressive stress magnitude is maintained in the strip element until reloading in tension has resumed. On reloading in tension the tangent stiffness is set to $0.2E_s$. This is presumably based on the computed slope from the *ABAQUS* model, although this slope is observed to be higher than $0.2E_s$ at low drifts. Fig. 2.15 shows the proposed hysteresis model. Choi does not discuss how the model handles tension reloading occurring after only a short excursion in the compression direction, i.e., between points CG and CA or between points TH and TC in Fig. 2.15.

The other key features of the hysteresis curve, i.e., the pivot points at σ_s equals $0.5f_{cs}$ and $0.2f_{ts}$ are also presumed to be based entirely on observation of the analytical model results, rather than having some kinematical or mechanical justification. The remaining reloading point that deserves scrutiny is the point TB. When the plate reloads after completing one full cycle, the tangent stiffness E_t, is defined by TF and TB, with TB being the point where the tension field is deemed to have been fully re-established, simply because it

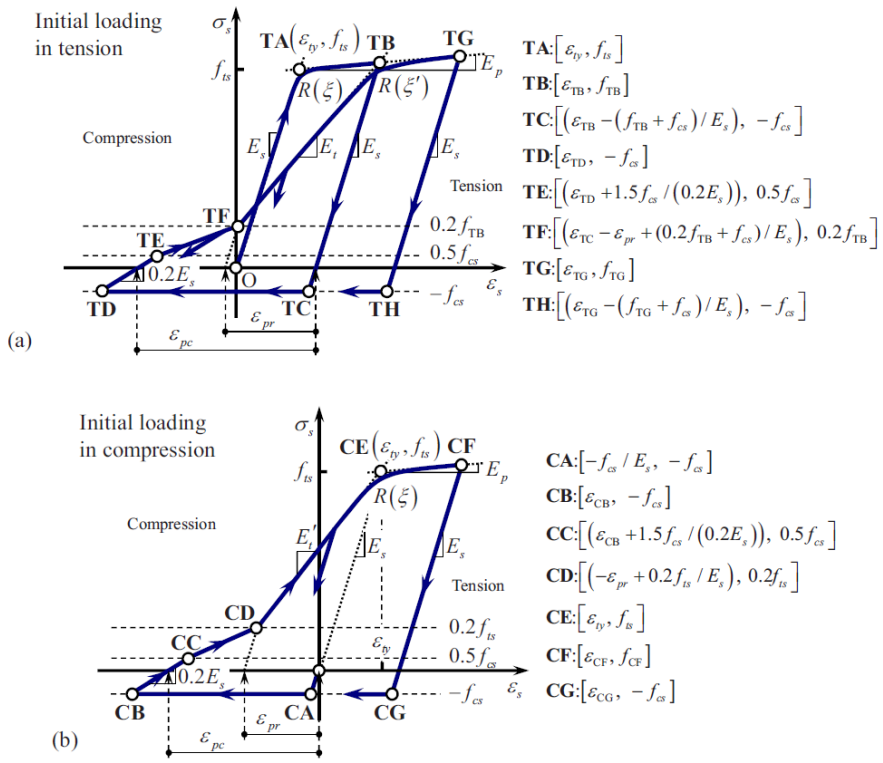

Figure 2.15: Choi's proposed hysteretic model.

was the point of tension unloading in the last cycle. This however is not generally the case because it depends on the amount of plastic strain accumulated in the last half cycle. If this plastic strain is significant it would push the reloading point back towards TA. This is undoubtedly a simplification.

After developing the hysteretic model, Choi applies it to a tension brace model and a conventional strip model to be used in the model validation process. In both cases the models are generated assuming the tension field operates at the angle determined by Eq. F5-2 of the *Provisions*, which is the conventional assumption. This introduces an obvious inconsistency between the analytical model from which the hysteresis model was developed and how it is applied. If for a particular SPSW the elastically predicted inclination angle

is significantly more or less than 45 degrees, the lateral strength and stiffness of the panel and the boundary element demands will not be correct.

In summary, the Choi hysteresis model is well developed and appears to perform reasonably well, although only the Roberts [55] test from 1991 for a pin framed SPSW web plate provides a fair comparison. The proposed model does tend to produce fatter hysteresis curves than the tests, although this may be due to frame action. The other tests presented in the model validation would have had considerable contribution to the hysteresis from the boundary frame action. Lastly, the FE model that the proposed hysteresis model was calibrated from is for a single aspect ratio and web plate slenderness.

2.6 Summary of Literature Survey and Conclusions

Many aspects of SPSW behavior have been examined by researchers since the pioneering work of Timler and Kulak. A variety of physical experiments have been conducted and analytical models have been developed to describe their behavior. However, some common themes and assumptions have persisted in the literature and deserve further scrutiny.

1. **The Tension Field Inclination Angle**

   The validity of a tension field inclination angle (α) predicted using elastic analysis for applications in plastic analysis and capacity design is questionable. With few exceptions, the angle predicted by Eq F5-2 of the *Provisions* has been used in strip modeling. The only justifications cited for using 45 degrees in lieu of Eq. F5-2 (or a similarly derived elastic based equation) are: a) simplicity of modeling or b) that the lateral strength of the web plate is not very sensitive to α in the range 38-50 degrees and 45 degrees, though not perceived as being strictly correct, can be justified. While it is true that the lateral strength of the web plate is relatively insensitive to angles in this range, the forces delivered to the boundary elements may not be.

2. **Web Plate Hardening.**

When cyclic inelastic analyses were undertaken, it was typically assumed that the hardening of a SPSW web plate can be adequately characterized using a kinematic model ([27],[6],[38] and [20]), whereas only two used an isotropic hardening model for the web plate ([52] and [10]). Many did not include hardening at all, presumably because it is not required in design. From a design standpoint, it is a simple matter to account for hardening, provided some basic guidelines are available for estimating its contribution. Though it is included in seismic design of other systems, e.g., EBFs and SMRFs, it is not considered in the design of SPSWs, yet its effect may be of a similar magnitude. If steel web plates hardened by even as much as 20% beyond $R_y F_y$, the expected yield strength of the plate, the resulting force demands on the VBEs may alter the pattern of damage in the structure and potentially concentrate too much inelastic behavior at one level. Severe pull-in of the VBEs resulting from web plate hardening may not induce collapse but it could concentrate deformation at that level and force the wall to behave more like a concrete shear wall with a flexural hinge. The philosophy behind the design of the SPSW is to have distributed shear yielding over as many stories as possible and this concentrated inelastic behavior would not be capable of dissipating a lot of energy. Furthermore, this type of behavior is not consistent with the design intent.

3. **Web Plate Residual Strength Prior to Reloading.**

   After several excursions of reversed cyclic loading the web plate was frequently assumed to have zero or negligible strength prior to tension field reloading (defined as the *residual* shear strength in the chapters that follow). This is a fair assumption for very slender plates and is commonly made by those who have developed web plate hysteretic models. However, for many plate slenderness ratios, a considerable proportion of hysteretic energy may be dissipated in this part of the cycle. The extent to which it influences the overall response, from a response history analysis standpoint, is probably modest but should be investigated.

Chapter 3

PRELIMINARY ANALYSES AND MOTIVATION FOR EXPERIMENTAL PROGRAM

Past research activity has captured the global lateral strength and stiffness of SPSWs using the strip model approach with reasonable success, but equally accurate prediction of the frame-plate interaction and web plate hysteretic behavior have so far not been achieved with this type of model. The computational tools now available make it possible to develop a more realistic and robust model that, it is hoped, can be used to accurately model other significant behaviors.

There are a number of key assumptions that have been used in design, and in the development of web plate models, that persist and should be reviewed. These are:

1. **the constancy/stability of the web plate tension field orientation.**
2. **the post-buckled (elastic or inelastic) web plate can be adequately modeled as a pure tension field.**
3. **a previously plastically deformed web plate has essentially zero shear strength prior to reloading.**
4. **a cyclically loaded web plate hardens kinematically.**

This chapter presents four studies that influenced the experimental and analytical program presented in this document. These studies address each of the above to some degree but they alone do not represent a complete and thorough analysis of the limitations of contemporary SPSW models. Without doubt, there remain many aspects of the SPSW modeling that require revision and improvement and are not directly addressed in this chapter. However, this chapter lays the groundwork for experimental and numerical detailed in the later chapters.

Before a brief discussion of the assumptions listed above, or presenting the results of the preliminary studies, some background information is provided on the finite element models and analyses that were used for many of the preliminary studies presented in this chapter and used for the experimental verification presented in Chapter 4.

3.1 Finite Element Modeling and Analysis

The *ABAQUS* platform was used for all of the continuum modeling of the web plates. Preliminary *ABAQUS* analyses of the Driver [27] test raised some questions about how best to model web plates and how different assumptions might affect the response of an SPSW, both globally (load displacement response) and locally (demand on the boundary elements).

The majority of experimental programs carried out on SPSWs up to this time have incorporated complete SPSW sub-assemblies. These past experiments have assessed the strength and stiffness of a complete SPSW system, typically less than four stories, or a single story sub-assembly. These systems often had fully or partially restrained boundary frame member connections that contributed to the lateral strength. Extracting a precise description of panel behavior from this data is impossible because the hysteretic response of the assembly includes the response of both the web plate and the boundary frame. Many aspects of the web plate behavior, such as the residual strength and the nature of the cyclic hardening, cannot be determined from such tests unless the load displacement response of the frame can be fully and accurately characterized, and then deducted from the total response.

To provide improved understanding of web plate behavior and modeling, a series of analyses of SPSW sub-assemblies was undertaken. The analyses were conducted using *ABAQUS* version 6.9 produced by Dassault Systemes Simulia Corp (DSS) (http://www.3ds.com). Details of the models, such as the element types, material models, solution strategies employed, etc, were chosen based in part on the recommendations of other researchers who have studied SPSWs, and in part on the observed stability of the chosen solution algorithm.

3.1.1 Shell Elements Used to Model the Web Plate

The *ABAQUS S4R* element was used to model web plates and has been used successfully by many researchers of SPSW web plates. The S4R is a four-noded doubly curved, reduced integration shell element with hourglass control. It can accommodate finite strains and large rotations. Nine Gauss integration points were used though the thickness of the shell to accurately capture inelastic out-of-plane bending behavior of the web plate. Preliminary analyses of web plates with different mesh densities showed that a minimum of thirty elements along a panel edge is required to obtain reliable results, i.e., to not over-predict strength or stiffness by more than approximately 5%. The aspect ratio of the shell elements was kept as close to unity as possible.

3.1.2 Wire Elements Used to Model Boundary Frames

Boundary frames were modeled using B31 wire elements. This element is a two-noded Timoshenko (by default) beam-column element with finite strain, large rotation capability and a single midspan integration point, as is typical for the shear deformable beam-column element. The VBE and HBE cross-sections are modeled as I-sections with the default number of integration points across the flanges (five) and through the depth of the web (thirteen total).

3.1.3 Solution Algorithm

When a web plate is loaded cyclically it will undergo "snap-through" behavior as the plate unloads elastically and commences reloading in the opposite direction. Implicit line search methods, such as Riks method, were attempted in the early stages of the preliminary modeling but were abandoned due to recurring issues with solution convergence.

Consequently all of the analyses were carried out using *ABAQUS Explicit* [25]. This solver uses an explicit central difference time stepping solution strategy for displacement updating and is generally advantageous for very short duration transient dynamic analysis and contact problems. However, the explicit solver can also be used successfully for quasi-

static processes.

There are advantages to using the dynamic explicit procedure over the implicit methods that are available with *ABAQUS* Standard. The dynamic explicit procedure does not require the formation of a global stiffness matrix, so matrix inversion is not required; nor is iteration required at the end of each time increment. The mass matrix is diagonal so inversion is a trivial operation. Acceleration components ($\ddot{u}_i^N$) are computed at each nodal degree-of-freedom using the out-of-balance residual force vector. Velocities and displacements ($\dot{u}_i^N$ and u_i^N) are computed from the nodal accelerations. The solution is stable provided the time step is sufficiently small.

The central difference equations used by *ABAQUS* are provided below:

$$\dot{u}^N_{(i+\frac{1}{2})} = \dot{u}^N_{(i-\frac{1}{2})} + \left(\frac{\Delta t_{(i+1)} + \Delta t_{(i)}}{2}\right)\ddot{u}^N_{(i)} \tag{3.1}$$

$$u^N_{(i+\frac{1}{2})} = u^N_{(i)} + \Delta t_{(i+1)}\dot{u}^N_{(i+\frac{1}{2})} \tag{3.2}$$

$$\ddot{u}^N_{(i)} = (M^{(NJ)})^{-1}(P^J_j - I^J_j) \tag{3.3}$$

where u^N is a displacement or rotational degree of freedom and i is the time increment number. The $(i+\frac{1}{2})$ and $(i-\frac{1}{2})$ subscripts represent plus and minus half time increments respectively. M^{NJ} is the mass matrix, P^J is the applied load vector and I^J is the internal force vector.

These advantages come at the expense of an extremely small time increment required to keep the method numerically stable. The time step is a function of the smallest element size and the highest natural frequency of the model, and is shown in Eq. 3.4.

$$\Delta t \leq \frac{2}{\omega_{max}} \tag{3.4}$$

where ω_{max} is the highest natural frequency of the structure. Δt may be estimated by computing the travel time of a dilatational wave, with speed c_d, through the smallest element with a characteristic length equal to L_{min}.

$$\Delta t \cong \frac{L_{min}}{c_d} \tag{3.5}$$

The dilatational wave speed, c_d, is proportional to the square root of the material elastic modulus and inversely proportional to the square root of the the mass density. It can be expressed using Eq. 3.6 for systems with no damping. The solution will remain stable provided the time increment is kept below a maximum threshold value, Δt, computed per Eq. 3.5.

$$c_d = \sqrt{\frac{\hat{\lambda} + 2\hat{\mu}}{\rho}} \tag{3.6}$$

where $\hat{\lambda}$ and $\hat{\mu}$ are the Lamé's constants, and ρ is the material density.

Mass Scaling

A common strategy for reducing solution time in quasi-static explicit analyses is to scale the mass up to achieve a lower wave speed and thus reduce the stable time increment. By scaling the mass by a factor of fifty the solution time can be reduced by a factor of approximately seven. Some care must be exercised when scaling mass if using force control so the inertial loads do not become excessive. For all of the analyses, unless stated explicitly otherwise, a mass scaling factor of fifty was adopted. The displacement ramp time was computed so that the inertial loads remained below approximately 1% of the expected peak strength of the structure. Both the monotonic and cyclic analyses of the the quasi-static problem utilized displacement control.

3.1.4 Material Modeling Including Hardening

Preliminary analyses of cyclically loaded plates using *ABAQUS* revealed that the response is quite sensitive to whether a kinematic or isotropic hardening evolution law is adopted

for the material, even for relatively modest accumulated plastic strains. This aspect of the material model was investigated as part of the preliminary analyses presented in this chapter.

3.1.5 Stress-Strain Data

In ABAQUS, stress-strain data pairs provided by the user must be converted to log-plastic strain and Cauchy (true) stress, ϵ_{ln}^{pl}-σ_{true}. The transformation is carried out using Eqs. 3.7 and 3.8.

$$\sigma_{true} = \sigma_{eng}(1 + \epsilon_{eng}) \tag{3.7}$$

$$\epsilon_{ln}^{pl} = ln\big(1 + \epsilon_{eng}\big) - \frac{\sigma_{true}}{E_s} \tag{3.8}$$

where σ_{eng} and ϵ_{eng} are the engineering stress and strain. The engineering stress-strain data are typically determined from coupon tests, as was done for the numerical analyses of the experimental tests presented in Chapter 4.

Yield Criterion and Flow Rule

For the preliminary studies, and for the modeling carried out as part of the test verification process, a general rate and pressure independent plasticity model (J_2) with von-Mises yield criteria and an associated flow rule was implemented. The material properties used in the analyses were derived from the coupon tests and were provided as "half-cycle" data in the *ABAQUS* input file. The von Mises yield surface is defined by the function:

$$F = f(\boldsymbol{\sigma} - \boldsymbol{\alpha}) - \sigma^0 \tag{3.9}$$

where σ^0 is the yield stress and $f(\boldsymbol{\sigma} - \boldsymbol{\alpha})$ the equivalent von Mises stress defined by:

$$f(\boldsymbol{\sigma} - \boldsymbol{\alpha}) = \sqrt{\frac{3}{2}(\mathbf{S} - \boldsymbol{\alpha}^{dev}) : (\mathbf{S} - \boldsymbol{\alpha}^{dev})} \tag{3.10}$$

where $\mathbf{S}$ is the deviatoric stress tensor and $\boldsymbol{\alpha}^{dev}$ is the deviatoric component of the backstress tensor which defines the kinematic shift of the yield locus in stress space. The associated flow rule for J_2 plasticity is defined by:

$$\dot{\boldsymbol{\epsilon}} = \dot{\bar{\epsilon}}^{pl} \frac{\partial F}{\partial \boldsymbol{\sigma}} \tag{3.11}$$

where $\dot{\boldsymbol{\epsilon}}$ is the plastic strain increment tensor and $\dot{\bar{\epsilon}}^{pl}$ is the equivalent plastic strain rate defined by:

$$\dot{\bar{\epsilon}}^{pl} = \sqrt{\frac{2}{3}\dot{\boldsymbol{\epsilon}} : \dot{\boldsymbol{\epsilon}}} \tag{3.12}$$

Hardening

Nonlinear kinematic hardening is modeled as the superposition of a linear Ziegler term and a *recall* term, which introduces the non-linearity and may include several components. The general form of the nonlinear kinematic hardening (using $ABAQUS$ nomenclature) is as follows:

$$\dot{\boldsymbol{\alpha}}_k = C_k \frac{1}{\sigma_0}(\boldsymbol{\sigma} - \boldsymbol{\alpha})\dot{\bar{\epsilon}}^{pl} - \alpha_k \gamma_k \dot{\bar{\epsilon}}^{pl} \tag{3.13}$$

where C_k and γ_k are terms to be calibrated from test data. α_k is the k^{th} component of the backstress. The total backstress is computed using:

$$\boldsymbol{\alpha} = \sum \dot{\boldsymbol{\alpha}}_k \tag{3.14}$$

When isotropic hardening is used in conjunction with kinematic hardening, $ABAQUS$ uses the following relationship for the evolution of the isotropic hardening component:

$$\sigma^0 = \sigma|_0 + Q_\infty\left(1 - e^{-b\dot{\bar{\epsilon}}^{pl}}\right) \tag{3.15}$$

Where $\sigma|_0$ is the initial size of the yield surface. The terms Q_∞ and b in Eq. 3.15 are determined by the user and describe the increase in the size of the yield surface at saturation and the rate of saturation respectively. For pure isotropic hardening, these need not

be specified because *ABAQUS* will use the provided stress-strain data.

If Q_∞ is set to zero the combined hardening will reduce to nonlinear kinematic hardening. In this case the user nominates only the number of backstress components (α_k) and *ABAQUS* internally computes the parameters required to best match the provided stress-strain data. The backstress components have a form equivalent to the term in Eq. 3.15 inside the parentheses (See Fig. 3.1). Some care must be exercised when using the nonlinear kinematic hardening option. It was found that the function describing the stress-strain data pairs must have negative curvature (second derivative of the stress-strain function had to be less than zero throughout), i.e., no saddle or inflection points, and the stress must monotonically increase with increasing strain.

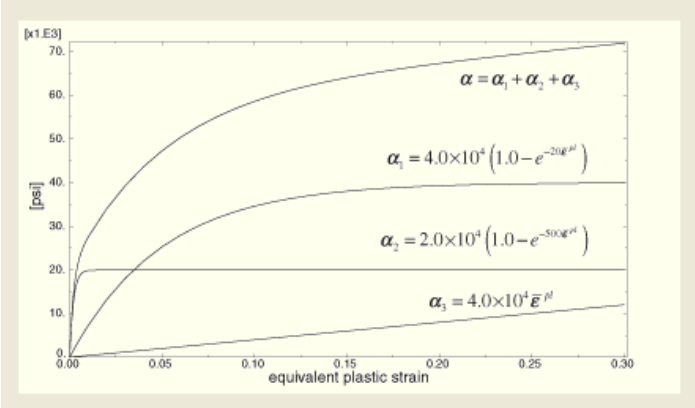

Figure 3.1: Example backstress component functions. Taken from [25]

Kinematic hardening is characterized by translation of the yield surface (in stress space) when plastic load occurs. As mentioned above, *ABAQUS* uses Ziegler's [78] hardening rule for the linear component of the kinematic hardening to determine the direction of this translation. Zeigler's rule assumes that the translation occurs in the same direction as the reduced stress vector (total stress minus the back-stress). Fig. 3.2 graphically depicts the

change in the von Mises yield surface in principal stress space for kinematic and isotropic hardening. Fig. 3.3 graphically depicts how the yield surface for a cyclically loaded web plate translates in principal stress space using Zeigler's rule. Isotropic hardening is characterized by growth or expansion of the yield surface in stress space, but with no translation. Kinematic hardening occurs in many metals when loaded cyclically, including mild steel, although the loading schemes that have demonstrated this behavior are predominantly uniaxial and this is not the case for a cyclically loaded web plate. Isotropic hardening can also be observed in cyclic loading response of metals. The extent to which each of these contributes to the total response of a cyclically loaded web plate is not well established and may vary considerably depending on steel grade and plate thickness. *ABAQUS* has a combined hardening capability which enables the modeling of materials with both kinematic and isotropic hardening characteristics.

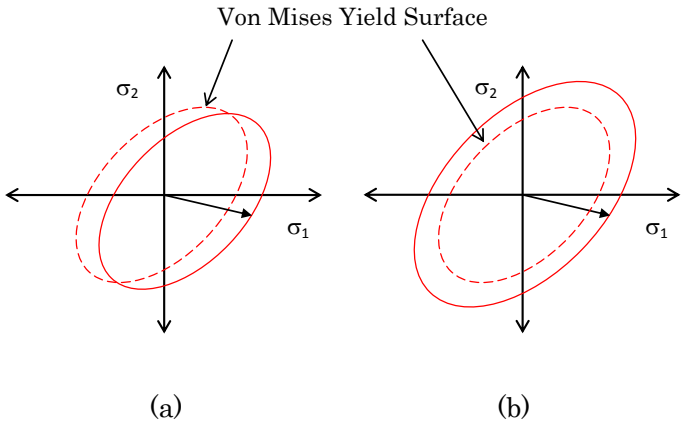

Figure 3.2: (a) Kinematic and (b) Isotropic hardening with von Mises Yield Surface

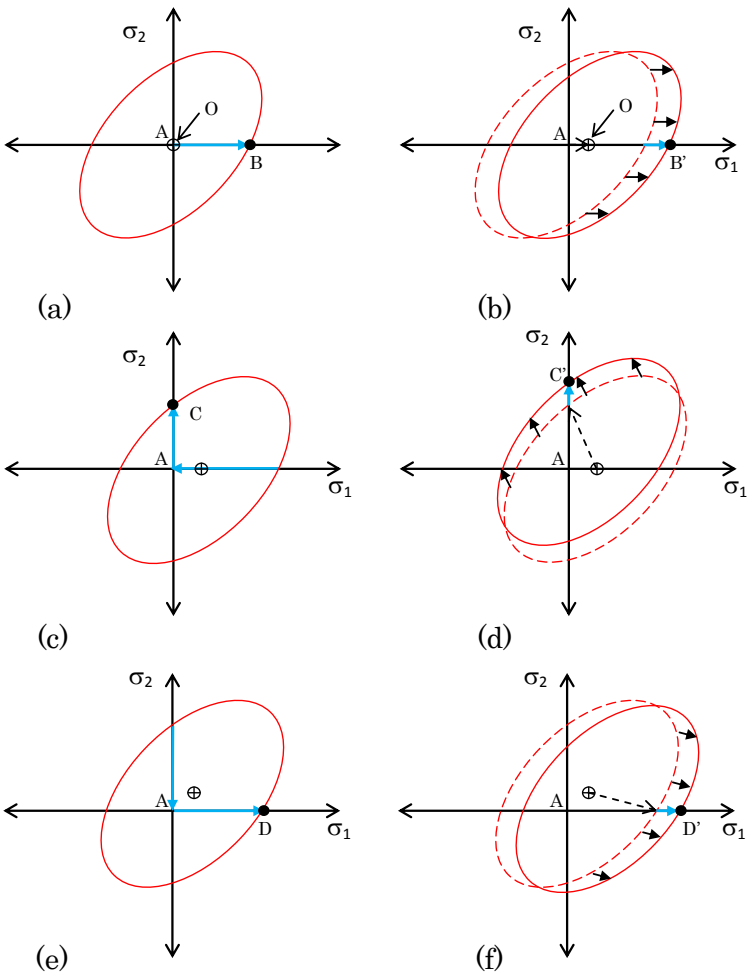

Figure 3.3: Kinematic hardening of cyclically loaded web plate with von Mises yield surface and Ziegler's rule

3.2 Review of Conventional Assumptions

3.2.1 The Constant Web Plate Tension Field Orientation

The assumed tension field orientation directly affects the computed lateral strength and stiffness of an SPSW panel and, because the anchorage forces are a function of the assumed angle, the angle significantly affects boundary element design. Fig. 3.4 shows screen captures of a preliminary *ABAQUS* model for a single story sub-assembly which has an elastically predicted tension field inclination angle of approximately 37 degrees. The *ABAQUS* stress trajectories at yield drift and at 3% drift are shown in the figure. For this case, and others like it, the angle changes once plastification commences.

Current practice is to incline the tension strips (should they be used) in accordance with the angle determined by equation F5-2 of the *Provisions*. If not utilizing shell elements, this provision effectively requires the design engineer to model web plates using a tension strip model with a strip inclination governed by the bay geometry and relative elastic stiffness of the sourounding boundary frame members. This provision has since been modified to allow a single angle and will be discussed further in the sections that follow.

3.2.2 Pure Tension Field

The standard model for web plate behavior utilizes a pure tension field. i.e., a uniaxial stress field in 2D space that is principally inclined to the vertical axis of the frame, usually close 45 degrees. The pure tension field assumption is an approximation and is generally conservative for design purposes. Preliminary analyses indicate that compressive stress magnitudes can be significant and their inclusion will increase the predicted lateral strength and decrease the VBE transverse force demand. The extent to which the compressive stresses influence the lateral strength and VBE demand depends on a number of factors including, web plate slenderness, aspect ratio, drift level and drift history. Directly measuring web plate principal compressive stresses in an experiment (through strain measurement) would be extremely challenging, however the influence of it on boundary element forces could feasibly be measured.

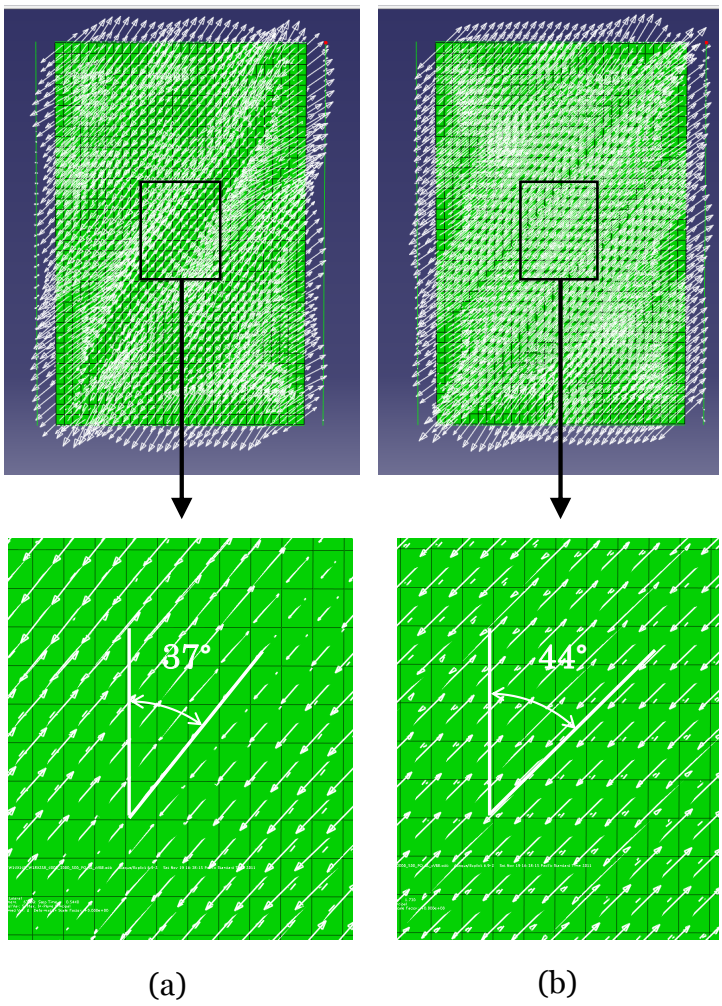

Figure 3.4: Preliminary *ABAQUS* model showing inclination of principal stress trajectories at a) yield drift and b) 3% drift.

3.2.3 Zero Shear Strength Prior to Reloading

The preliminary numerical analyses identified that the strength a web plate has as it is unloaded and then subsequently reloaded in the opposite direction (referred to from here on as *unloaded shear strength*) can be quite significant, particularly for relatively thick plates ($h/t < 500$). This can be seen in Fig. 3.5 where it is approximately 25-30% of the peak strength for a web plate with h/t of 930. It is conventionally assumed that the plate has

limited or zero load carrying capacity when transitioning from elastic unloading to elastic reloading in the opposite direction. The nonlinear *ABAQUS* models identified significant unloaded shear strength during this phase which should be accounted for when estimating energy dissipation capacity and when performing response history analyses.

3.2.4 Cyclic Kinematic Hardening

One of the motivations for the experimental program presented in Chapter 4 was to understand the hardening response of cyclically loaded steel web plates and whether there is a way to relate a simple metric of steel material properties to the observed hardening behavior. Preliminary analyses of web plates using *ABAQUS* revealed significant differences in the cyclic load-displacement response for the two most commonly adopted hardening models.

Fig. 3.5 shows the results of two analyses where isotropic and nonlinear kinematic hardening laws were used. This analysis illustrates that there can be potentially significant differences in the peak force response of a web plate, but this difference obviously depends on the loading history and the material properties of the plate. This has implications for design in terms of maximum demands on the boundary elements and on the amount of energy that will be dissipated through cyclic loading. These analyses, which used actual coupon test data, reveal a difference in peak force response of approximately 20% between the kinematic model and the isotropic model. The actual experimental results from tests described later are also shown and are observed to be somewhere between these two idealized responses.

The precise nature of this behavior in cyclically loaded steel web plates has been largely overlooked, presumably because a) it is assumed the response will be insensitive to the hardening law used, or b) since the loading is cyclic, kinematic hardening is naturally assumed. With regard to the first assumption, this is certainly the case when the inelastic demands on the web plate are limited, as would occur in a design level wind event or a small earthquake. Cyclic plastic demands on a web plate can be very significant for large seismic events and the degree of accumulated plastic strain will make the selection of the

appropriate hardening rule at least as important as the material yield strength and R_y factor.

Nonetheless there appears to be no clear consensus on which hardening rule is appropriate, although it appears to be at least as important as any other aspect of the web plate behavior because it directly affects VBE demand.

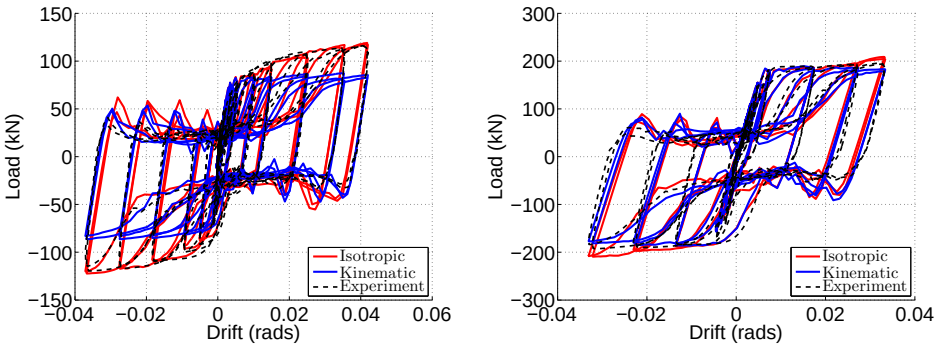

(a) 18 Ga web plate

(b) 16 Ga web plate

Figure 3.5: ABAQUS hysteretic response of (a) 18 Ga A1008 steel and (b) 16 Ga A36 steel with different hardening evolution laws

3.2.5 Need for Research Program into Web Plate Behavior

The issues raised by the review of some conventional modeling assumptions leads naturally to the need for an experimental program and additional numerical simulations designed to investigate some of these issues.

3.3 Preliminary Analytical Studies

A number of analytical studies were undertaken to investigate the behavior of SPSW subassemblies and examine the interaction between geometry and loading on various response quantities such as VBE demand, tension field orientation, VBE flexibility, web plate unloaded shear strength and web plate compressive stress.

3.3.1 Study #1

It has been demonstrated by several researchers that the assumed orientation of the web plate tension field has only a modest impact on the lateral strength of a web plate, as will be demonstrated in Section 3.3.2. However, the effect on the vertical boundary elements is more substantial.

The 2010 Provisions include an equation defining the angle of the web-plate tension field. This equation is often quoted in the literature and is used frequently for pushover and cyclic analyses. The equation, F5-2 in the Provisions, is reproduced here as Eq. 3.16.

$$\tan^4 \alpha = \frac{1 + \frac{t_w L}{2A_c}}{1 + t_w h\left(\frac{1}{A_b} + \frac{h^3}{360 I_c L}\right)} \tag{3.16}$$

where t_w is the plate thickness, A_b is the HBE section area, A_c is the VBE section area, I_c is the VBE section moment of inertia, h is the story height and L is the bay length between VBE center-lines.

This equation was originally derived using elastic least-work principles and only strictly applies to very thin elastic web plates in the post-buckling stage of loading. The assumptions that underpin the equation are reasonable and reflect a balance between the need for an accurate mathematical representation of the problem and ease of the derivation. They are as follows:

1. **The web plate extends to the boundary element (BE) center-lines.** This is a reasonable assumption when the BE depths are small in comparison with the web plate dimensions.

2. **The web plate behaves as a pure tension field.** The post-buckled web plate stress field is complex and non-uniform. For thin plates the pure uniform tension field assumption provides a reasonable measure of the web plate strain energy. For thick

plates, the contribution of compressive and flexural stresses in the web plate are more significant and should not be ignored.

3. **VBE shear deformation is ignored.** The additional deformation resulting from shear stress in the VBEs should be considered under certain circumstances. Shear deformation may be more significant than the effects of bending deformation for deep sections.

4. **VBE flexural demands are based on VBE rotational end fixity.** This assumption is reasonably consistent with actual behavior except for cases where there is a large change in plate thickness, VBE section stiffness, or story height above (or below) the story of interest. Should this be the case, the fixed end assumption is only a very rough approximation of the actual condition and the actual angle of inclination will deviate from Eq. 3.16.

5. **HBE axial stiffness does not include influence of composite slab.** The effective area of the HBE section is influenced by the tributary area of the composite concrete slab that is typically part of this type of building construction. It is difficult to assess this contribution accurately so it is generally ignored.

6. **HBEs do not store flexural strain energy and are pin-ended.** Under the assumption that the plates above and below the story of interest are approximately equal in thickness to the plate being studied, and that they are subjected to approximately the same transverse load, the flexural demand on the HBEs due to vertical out-of-balance loading will be small. However, this is rarely the case. The web plates on adjacent floors frequently differ in thickness. For the extreme case where there is no plate above or below the story of interest the estimation of the tension field angle changes modestly for short HBEs and significantly for long HBEs.

The elastically predicted inclination angle typically varies from 35 to 50 degrees for most practical SPSW configurations. The result of this particular provision is a structural model with a complicated geometry that is extremely tedious to assemble manually using most commercial software packages, and one which potentially changes on each iteration of the

design.

As discussed, Eq. 3.16 (Eq. F5-2 in the *Provisions*) is based on an elastic analysis and was not originally recommended for situations where large inelastic demands are likely [66]. However, it can be argued and will be shown in this study, that for moderate to large inelastic strains the angle of inclination approaches 45 degrees regardless of system geometry and frame stiffness. Animations of laterally loaded web plate models with elastic α (α_{el}) considerably less than 45 degrees, demonstrate noticeable changes in principal stress trajectories as the drift increases into the plastic range (See Fig. 3.4). These trajectories were observed to abruptly change shortly after yielding had initiated and stabilize as the drift continued to increase monotonically. Should this always be the case, it would considerably simplify the modeling and design process. It also has ramifications for design of the boundary members.

Eq. 3.16 can be re-written including the term $\frac{E_t}{E}$ which is the ratio of the web plate tangent modulus to the elastic modulus.

$$\tan^4\alpha(E_t) = \frac{1+\frac{(\frac{E_t}{E})t_w L}{2A_c}}{1+(\frac{E_t}{E})t_w h\left(\frac{1}{A_b}+\frac{h^3}{360I_c L}\right)} \tag{3.17}$$

The angle is of course unchanged for elastic loading. Taking the limit of this function as E_t approaches zero (a fully plastic plate) yields:

$$\lim_{E_t\to 0}\left\{\tan^4\alpha(E_t)\right\} = 1 \Rightarrow \alpha = \frac{\pi}{4} \tag{3.18}$$

Where E_t is the tangent modulus of the web plate and E is the elastic modulus. As the plate stretches plastically and the boundary frame remains elastic, α approaches 45° in the limit as E_t/E approaches zero. A similar argument can be made by maintaining elastic material properties throughout the system but reducingt_ww to reflect the reduced plate stiffness as the plate yields. This suggests that as the web plate stiffness reduces relative to the boundary frame, the angle will change accordingly. This makes no prediction as to

the rate or full extent of this change but it is logical to assume that as the drift increases beyond the yield drift, an initially low α value (¡40 degrees) or high α value (¿50 degrees) will asymptotically approach an angle governed by Eq. 3.17.

Migration of the principal stress trajectories can be observed in the results of non-linear finite element analysis of laterally loaded elasto-plastic web plates. The impact of this change is subtle for many SPSW geometries but it should not be ignored when the computed angle (using Eq. 3.16) is very low. This occurs when the VBEs are flexible in flexure and stiff axially, and/or if the HBEs are axially flexible.

It will be shown that, when loaded in shear (either monotonically or cyclically), a slender metallic plate that is anchored by an elastic boundary frame, and which has a post-buckled tension field inclination angle less than 45 degrees, will undergo a change in this angle upon plastification of the web plate. The angle will migrate rapidly towards a steady-state value governed approximately by the tangent modulus of the plate.

To test the migrating α hypothesis, a series of pushover analyses were performed in *ABAQUS* for a small suite of SPSW sub-assemblies. The SPSW sub-assembly model was constructed such that it reflected the assumptions employed in developing Eq. 3.16. A total of six sub-assemblies were modeled with varying panel aspect ratio, plate thickness and VBE stiffness.

Fig. 3.6 shows a schematic of the basic *ABAQUS* model. The model incorporated the element formulations and mesh size as described previously and used an elasto-plastic web plate material. No rigid offset was modeled between the boundary element (HBEs and VBEs) center-lines and the edge of the web plate. The plates were seeded with a simple bi-harmonic imperfection with an amplitude of approximately span/1000. The boundary conditions and kinematic constraints were enforced so that they were consistent with the assumptions embedded in Eq. 3.16, this way a direct comparison with Eq. 3.16 could be made. The rotations at the top and bottom of each VBE were constrained to be equal. This ensures the VBEs behave as fixed end beams but can rotate as a rigid bodies as the

Table 3.1: Data for *ABAQUS* Models Alpha Migration

Assembly #	**VBE**	**HBE**	**(m) h**	**(m) L**	**h/t**	**(deg) α_{AISC}**	**(deg) α_{min}**	**(deg) $\alpha_{2\%}$**
1	W14x159	W14x550	4.66	3.97	419	37.1	39.5	45.5
2	W14x159	W14x605	4.83	3.97	434	37.0	39.7	45.6
3	W14x159	W14x665	4.83	3.97	434	37.1	39.7	45.6
4	W14x159	W14x665	5.49	4.82	576	37.0	38.3	45.3
5	W14x159	W14x730	4.83	3.97	434	37.2	39.6	45.7
6	W14x159	W14x730	5.49	4.82	576	37.1	38.2	45.3

assembly drifts laterally. The top and bottom HBEs are pinned to the VBEs and permitted to shorten axially. A slider constraint was introduced along the length of each HBE such that a straight profile is maintained, ie. no flexure. Each assembly was monotonically pushed to a drift of 2%.

Table 3.1 lists the critical design parameters for each sub-assembly as well as the computed inclination angle per AISC and the elastic (α_{min}) and plastic angle ($\alpha_{2\%}$) determined form the *ABAQUS* analysis. The angle is the mean angle determined by first computing the principal tensile stress trajectory for each element in the web plate, and then averaging over the web plate at each drift amplitude. The frame geometry and stiffness parameters were contrived to limit the AISC predicted α to fall between 37 and 38 degrees. All of the assemblies satisfied the code limits for panel aspect ratio, VBE flexibility and VBE strength.

The progression of the web plate tension field inclination angle with increasing drift is presented in Fig. 3.7. This angle was observed to vary a few degrees over the area of the plate. The standard deviation (SD) of the *ABAQUS* computed inclination angle peaked at around 11 degrees at a drift of 0.2%, just as the plate tension field is established after elastic buckling. As the drift increased to 1%, the SD rapidly decreased to around 4.5 degrees and was 3.1 degrees at 2% drift. Clearly there is a tendency for the mean computed

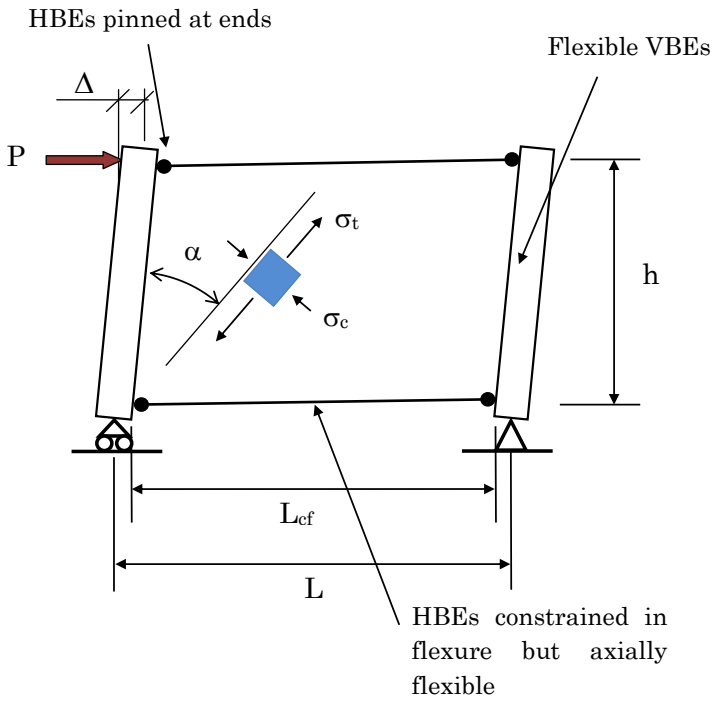

Figure 3.6: Schematic of *ABAQUS* model used to test migrating alpha hypothesis

tension field angle to rapidly progress towards 45 degrees. Prior to elastic buckling the angle is around 45 degrees, which is consistent with theory describing a plane-stress membrane. After buckling the tension field behavior starts to dominate and the mean computed angle is observed to drop to a value close to that predicted by Eq. 3.16. The match between theory and the continuum model is quite good around yield drift, differing by 2.1 degrees on average, but the angle derived from the continuum model is consistently higher than that predicted assuming a pure tension field. Once the drift increases to two times the yield drift the computed mean exceeds 40 degrees. At four times yield drift (approximately 1%) all of the web plates have a computed mean α exceeding 43 degrees. It is reasonable therefore to expect that this behavior will prevail with a real structure under monotonic loading.

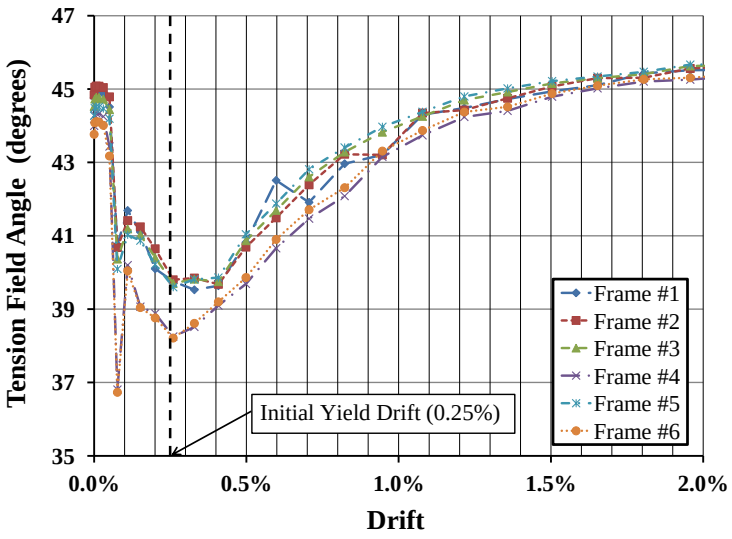

Figure 3.7: Migration of tension field orientation for *ABAQUS* web plates with computed α between 37 and 38 degrees per AISC

Conclusions for Study #1

This study demonstrated that for a small selection of SPSW sub-assemblies subjected to monotonically increasing shear force into the inelastic range, the tension field orientation migrated towards 45 degrees as the plate plastified.

It is difficult to state conclusively how this phenomenon affects a real structure under reversed cyclic loading, as would occur in a seismic or wind event.

3.3.2 Study #2

To illustrate the sensitivity of various force quantities to the tension field inclination angle, a simple analysis of the conventional tension field equations was undertaken. In this study, the elastic tension field angle, α^{el}, as predicted by Eq. 3.16 was varied between 34 and 44 degrees and the resulting lateral strength, $\hat{V_n}$, and the imposed VBE transverse distributed forces, w_x, were computed using Eqs. 3.19 and 3.20 respectively. These forces are normalized by setting the yield stress F_y, web plate thickness t_w, panel height h and clear distance between VBE inside flanges, L_{cf} equal to 1.0. Only the dependence on α is examined.

$$\hat{V_n} = \frac{1}{2} R_y F_y t_w L_{cf} sin(2\alpha) = \frac{1}{2} sin(2\alpha) \tag{3.19}$$

$$w_x = R_y F_y t_w sin^2\alpha = sin^2\alpha \tag{3.20}$$

where R_y is the ratio of expected to nominal yield strength of the web plate and the other terms are as previously defined. Eq. 3.19 and 3.20 are identical to the AISC equations except that the 0.42 factor is dropped in favor of 0.5.

An assumed material stress-strain relationship was used that results in the normalized tensile stress v's drift response shown in Fig. 3.8. The yield drift was set to 0.4% for all cases. Since the effect of hardening had not been examined, it was not included in this model. The variation in the actual inclination angle was approximated with a smooth function computed using Eq. 3.21, which is loosely based on the shapes observed from preliminary numerical analyses (See Fig. 3.7).

$$\alpha = 45 - \hat{A} sin\left(\pi \frac{\Delta}{0.03}\right) e^{-250\Delta} \tag{3.21}$$

where Δ is the drift and $\hat{A}$ is an amplitude function approximated using

$$\hat{A} = \frac{45 - \alpha^{el}}{0.15} \tag{3.22}$$

where α^{el} is equal to the elastically predicted angle per Eq. 3.16. This function is plotted in Fig. 3.9 for the values of α^{el} mentioned previously.

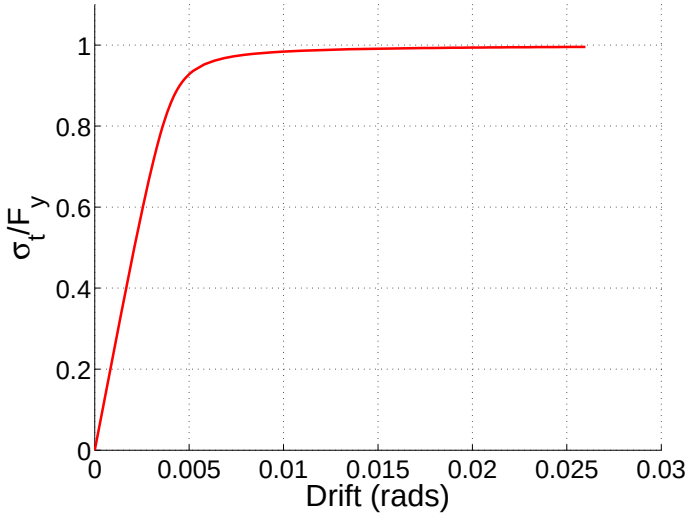

Figure 3.8: Synthetic lateral load v's drift.

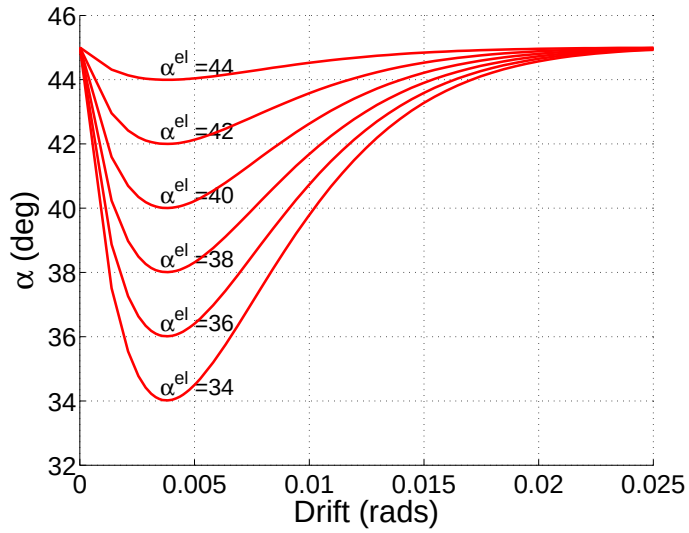

Figure 3.9: Synthetic tension field inclination angle v's drift for various values of α^{el}.

Although the material model and inclination angle function used in this study are en-

tirely synthetic, they capture the real non-linear behavior reasonably well and are instructive for examining trends. Fig. 3.10 shows the ratio, $R_{\hat{V}n}$, of $\hat{V}_n$ computed using α from Fig. 3.9 to that using a constant α^{el} predicted using Eq. 3.16. From this plot it is clear that the lateral capacity is not very sensitive to the assumed inclination angle. $R_{\hat{V}n}$ varies from 0.95 to only 1.06 for all cases. This is equivalent to comparing the result from a strip model with strips inclined per Eq. 3.16 to that of a model where the inclination of the strips that varies as a function of drift magnitude. The exact same relationship emerges for the longitudinally distributed vertical load delivered to the VBE from the web plate, which is largely responsible for VBE axial force; i.e., the axial force in the VBEs resulting from web plate anchorage forces is not very sensitive to the actual inclination angle.

The transverse force on the VBEs, and a significant proportion of the axial force in the HBEs (often denoted $P_{hbe,vbe}$), both result from web plate transverse or "pull-in" forces. The ratio between w_x computed using α from Fig. 3.9 to that using a constant α^{el}, denoted here as R_{wx}, are plotted in Fig. 3.11. In contrast to the lateral capacity $R_{\hat{V}n}$, the result of plastification of the web plate clearly has a large impact on the transverse force demands, even at modest drift levels. For example; at 1% drift, a strip model with strips inclined at a computed α^{el} of 36 degrees under-predicts the transverse force on the VBEs by a factor of approximately 1.2. The converse is true for the transverse force on the HBEs, where a low value of α^{el} will over-predict the demand.

Conclusions for Study #2

This study used a synthetic material model and an approximation of the relationship between the tension field inclination angle and drift to examine the effect of varying the angle on lateral strength and on the transverse force demand on the VBEs.

The sensitivity of the lateral strength to the inclination angle is found to be small, in accordance with studies done in the past [27], [8]. The transverse force on the VBEs is however substantially affected by changes in the inclination angle, with the ratio R_{wx} exceeding

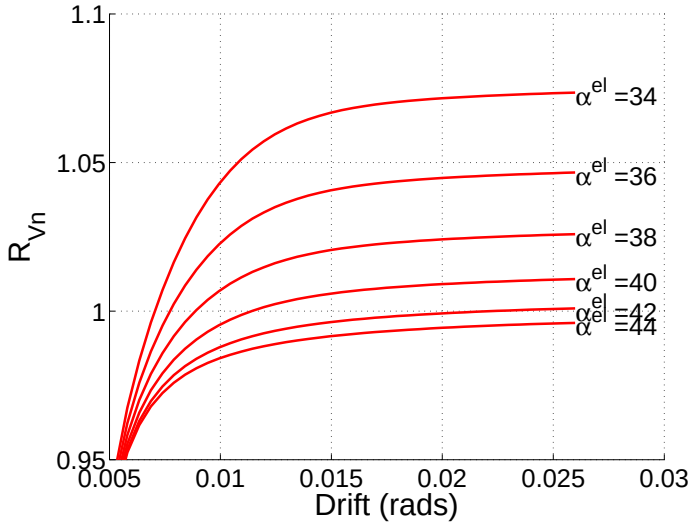

Figure 3.10: Ratio of V_n predicted using strips inclined at true (synthetic) α to V_n predicted using α^{el} per Eq. F5-2 of the *Provisions*.

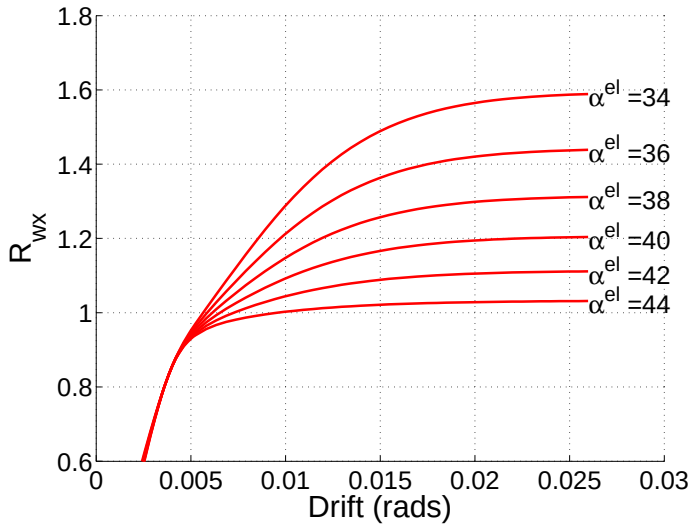

Figure 3.11: Ratio of VBE transverse force, w_x, predicted using strips inclined at true (synthetic) α to w_x predicted using α per Eq. F5-2 of the *Provisions*.

1.4 for angles less than 36 degrees at 2% drift.

3.3.3 Study #3

A series of analyses was conducted under cyclic loading to examine the influence of web plate slenderness and aspect ratio on:

- Mean tensile and compressive stress at peak load of each cycle (normalized by σ_y)
- VBE flexural demand (normalized by bending moment equivalent demand from 45 deg strip model)
- Residual lateral strength (normalized by V_y)

For this third preliminary study, a model very similar to that used in Study #1 was used (See Fig 3.6). A total of sixteen sub-assemblies were analyzed, each had a height of 3.5 m with the sub-assembly length assigned to $0.8h$, $1.3h$, $1.7h$ and $2.3h$ and the web plate thickness set equal to $h/300$, $h/500$, $h/700$ and $h/900$ for each value of L. The offset between the VBE center-line and the panel edge was included and the model incorporated very stiff boundary elements. The stiff VBEs would ensure that the moment demands from web-plate pull-in forces represented a reasonable upper bound for a given L, h and t_w.

Each model comprised W14x730 VBEs and HBEs with the HBEs pinned at each end to the VBEs. The net deflection of the HBEs at midspan was restrained to mimic the presence of equivalent tension fields above and below the assembly. The section sizes were chosen to approximate a rigid boundary frame so that α would be maintained close to 45 degrees at both the elastic and plastic stages of loading and consequently the VBE flexural demand could be normalized using a 45 tension field.

The web plate material was modeled as elasto-plastic with a yield stress of 250 MPa (36.3 ksi) with an elastic modulus of 205,000 MPa (29,730 ksi). It is recognized that some response quantities may be dependent upon the ratio of F_y to E but for the purposes of this analysis this dependency was not considered.

A displacement history comprising a single positive and negative stroke at drifts of 0.25%,

0.5%, 1%, 2% and 3% was applied. Fig. 3.12 shows this history diagrammatically. These drifts correspond approximately to δ_y, $2\delta_y$, $4\delta_y$, $8\delta_y$ and $12\delta_y$. The element formulation, mesh refinement and material model were as for Study #1. To reduce computational effort, panel stresses were sampled at each time increment over an evenly spaced, eight by eight, grid of sixty-four sample points. The average tension field angle determined at these locations was found to be very close to the average computed over the entire web plate, with the vast majority falling between 44 and 46 degrees.

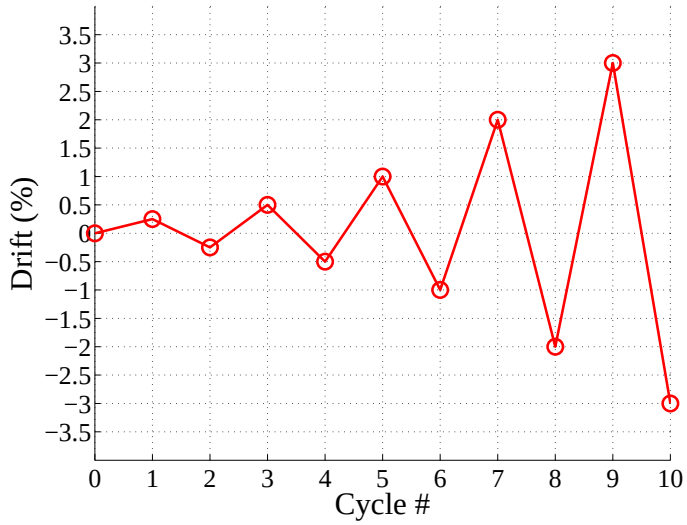

Figure 3.12: Cyclic Drift Amplitudes for Study # 2 Model

Hysteresis Curves and Lateral Strength

The hysteresis curves for each of the sixteen models are shown in Figs. 3.13 through 3.16. The sub-assembly strength has been normalized by V_y, the theoretical lateral strength of the panel assuming a pure tension field inclined at the angle α, which is computed using the following equation:

$$V_y = 0.5 F_y t_w L sin(2\alpha) \tag{3.23}$$

where F_y is the panel yield strength and all other parameters are as previously defined. When α equals 45 degrees, this simplifies to:

$$V_y = 0.5 F_y t_w L \tag{3.24}$$

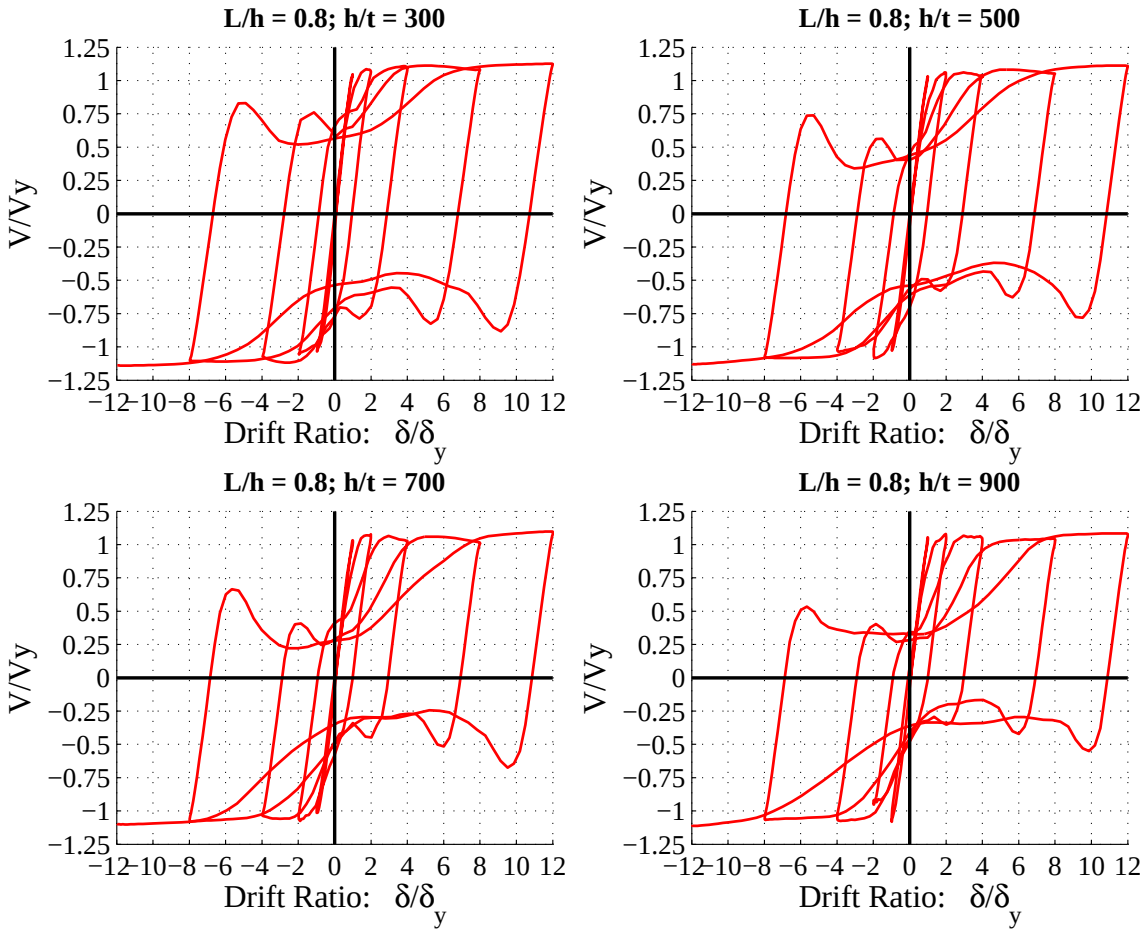

Figure 3.13: Hysteresis curves normalized by V_y: L/h = 0.8

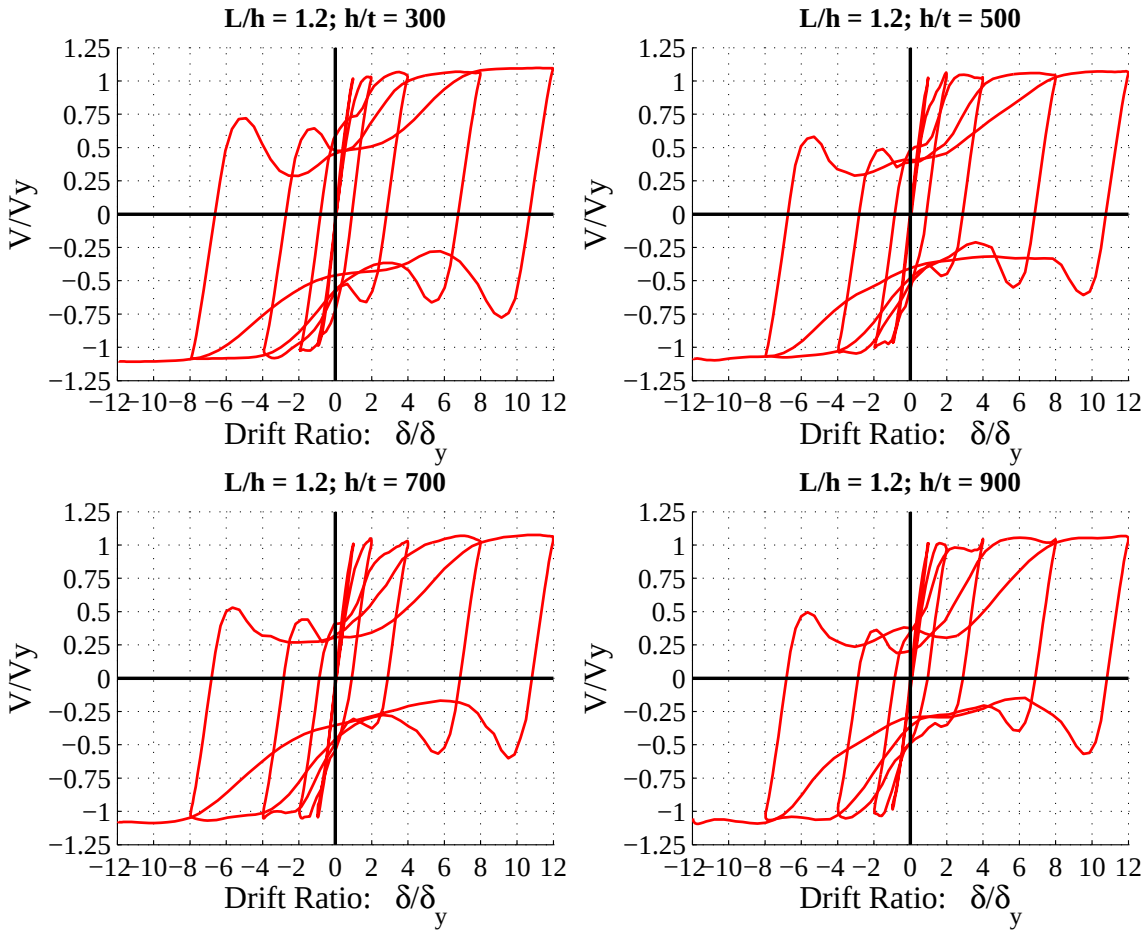

Figure 3.14: Hysteresis curves normalized by V_y: L/h = 1.2

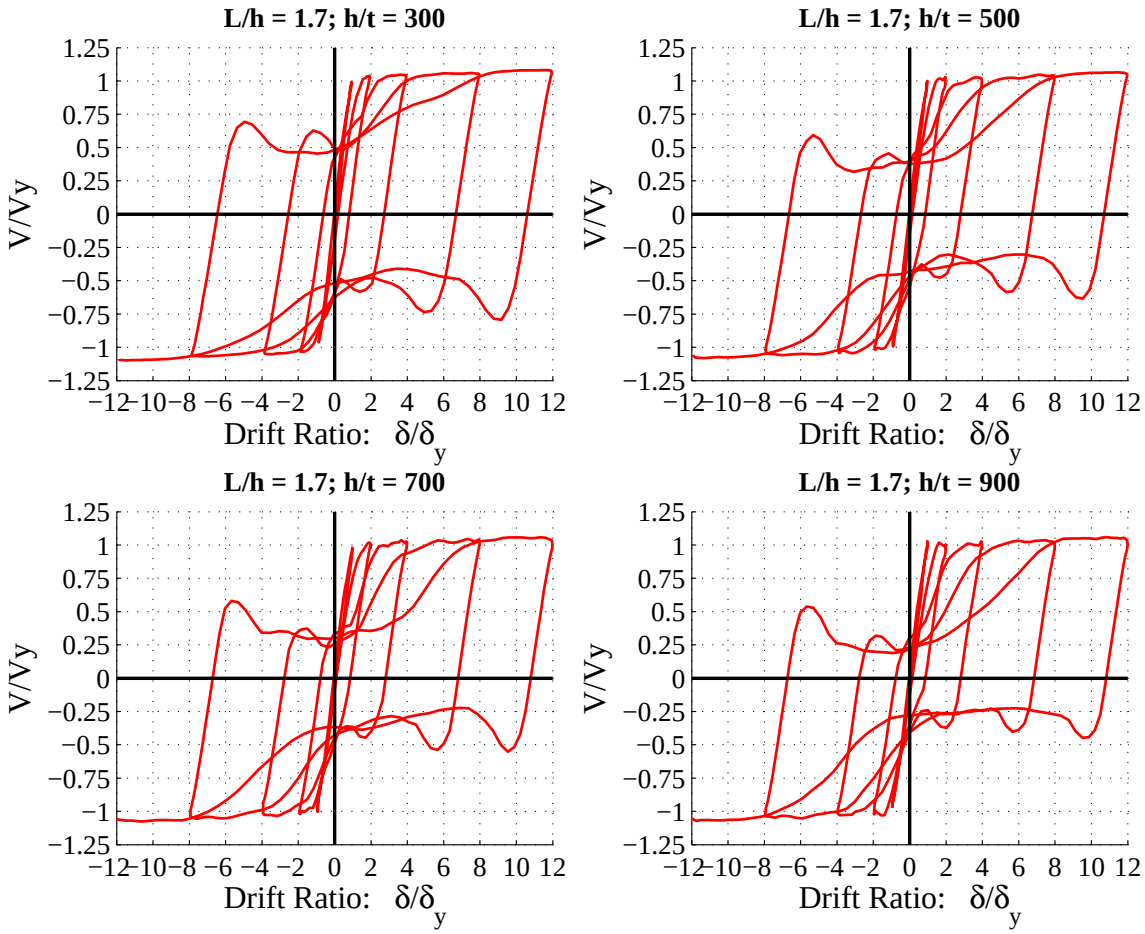

Figure 3.15: Hysteresis curves normalized by V_y: L/h = 1.7

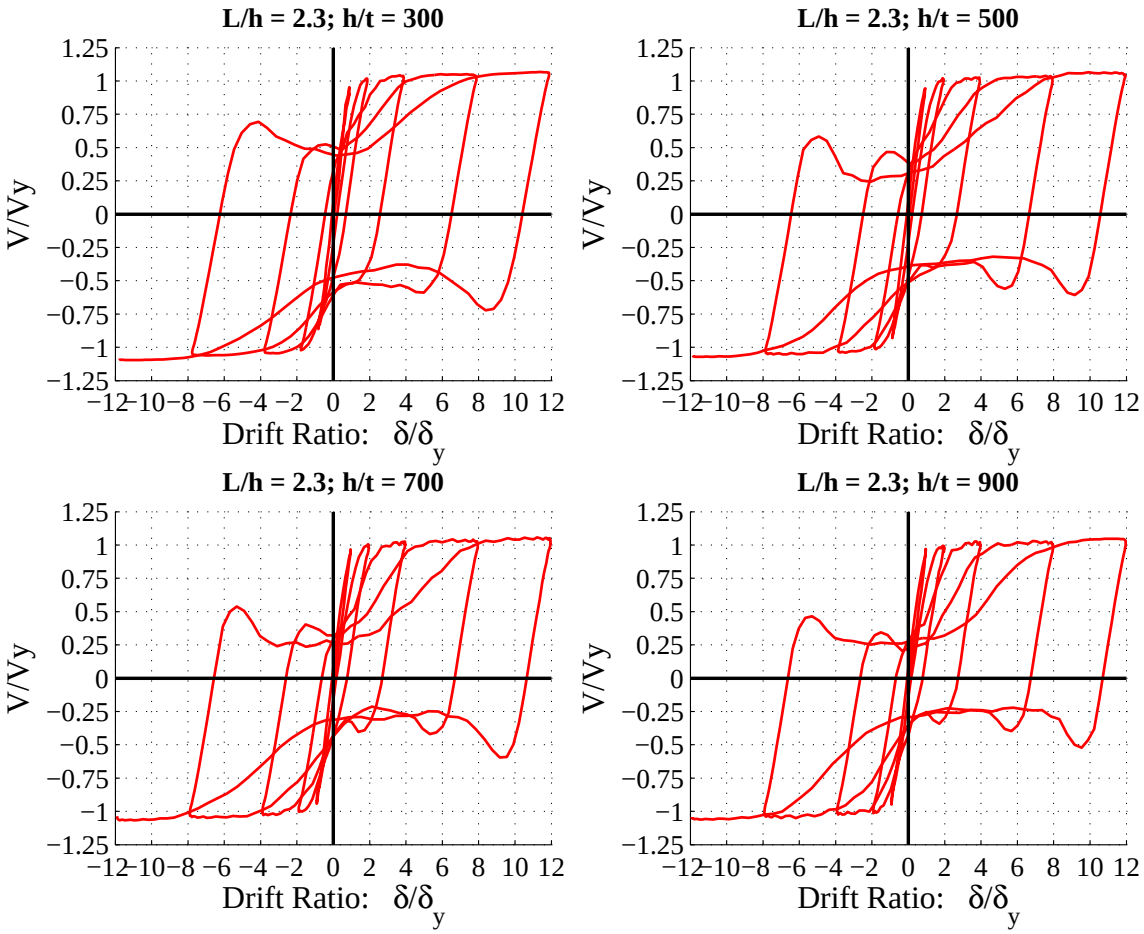

Figure 3.16: Hysteresis curves normalized by V_y: L/h = 2.3

Examination of these figures reveals the following trends:

- The normalized peak strength is highest for low panel aspect ratios (L/h) and low panel slenderness (h/t), exceeding 1.1 for $L/h = 0.8$ and $h/t = 300$, but approaches unity rapidly as these parameters increase.

- The normalized unloaded shear strength of the web plate increases with increasing L/h and h/t but appears to stabilize once L/h exceeds 1.2

- The normalized snap-through strength sometimes exceeds 75% of the peak lateral strength for low slenderness and is consistently greater than 40% of the peak lateral strength. (*This particular aspect of the simulated response was later found to consistently over-estimate actual snap-through strength when compared to experimental results and is believed to be related to mesh size, element formulation and solution method.*)

Eq. F5-1 of the *Provisions* defines the nominal strength of a panel. It is reproduced here as Eq. 3.25.

$$V_n = 0.42 F_y t_w L_{cf} sin(2\alpha) \tag{3.25}$$

As discussed in the *Commentary* of the *Provisions*, the 0.42 factor ($0.5\ \frac{1}{1.2}$) is included to account for the assumed difference between system over-strength and nominal strength, however it is not clear why this modification is required for SPSW design but an equivalent modification is not required for other systems. L_{cf} is the clear distance between inside VBE flanges and is used instead of L, the distance between VBE center-lines. It can be argued that L_{cf} should only be used if the kinematics of the deformed panel account for the rigid offset between the column center-line and the panel edge. Assuming a panel yield mechanism as shown in Fig. 3.17, the shear strain in the panel is γ_c for a lateral drift of γ_a

The lateral force V_y required to develop this mechanism becomes:

$$V_y = 0.5 F_y t_w (L - d_c)\left(1 + \frac{d_c}{L - d_c}\right) \tag{3.26}$$

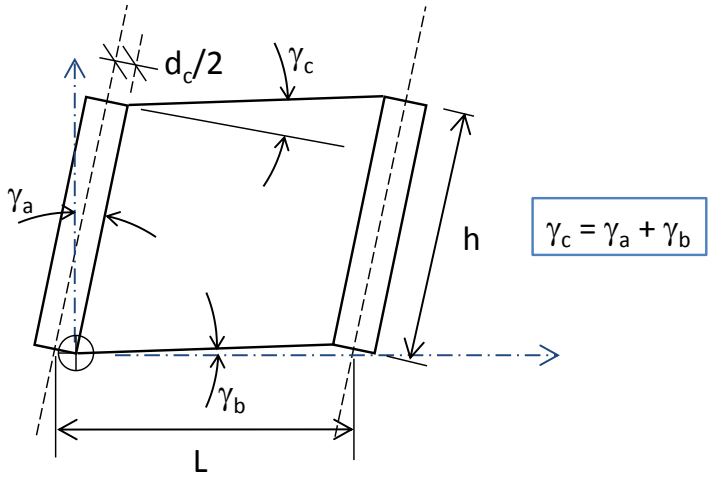

Figure 3.17: Kinematics of deformed SPSW web plate

where d_c is the depth of the VBE section. Recognizing that $L_{cf} = L - d_c$, this can be re-written as:

$$V_y = 0.5F_y t_w L_{cf}\left(1 + \frac{L - L_{cf}}{L_{cf}}\right) = 0.5F_y t_w L \tag{3.27}$$

When the depth of the VBE section is a significant proportion of the overall wall length, Eq. 3.25 considerably under-predicts the lateral strength of the panel. Fig 3.18 shows the plate strength determined from the *ABAQUS* analysis normalized by Eq. 3.25. In each of these plots the VBE depth is held constant at 0.569 m (22.4 inch) and the height is 3.5 m (137.8 inch). The strength discrepancy is most pronounced in the first plot of Fig. 3.18 (with $L/h = 0.8$, $d_c/L = 0.20$) where Eq. 3.25 under-predicts the lateral strength by approximately 40%. The effect diminishes as the panel aspect ratio increases. If the *ABAQUS* results are normalized by Eq. 3.24 instead of Eq. 3.25, the curves generally fall between 1.0 and 1.1 for all panel geometries. Material hardening is *not* included in these models so the strength discrepancy results entirely from the 5/6 reduction factor, the assumed versus actual deformation kinematics of the panel in the plastic analysis, and the presence of non-negligible compressive stresses.

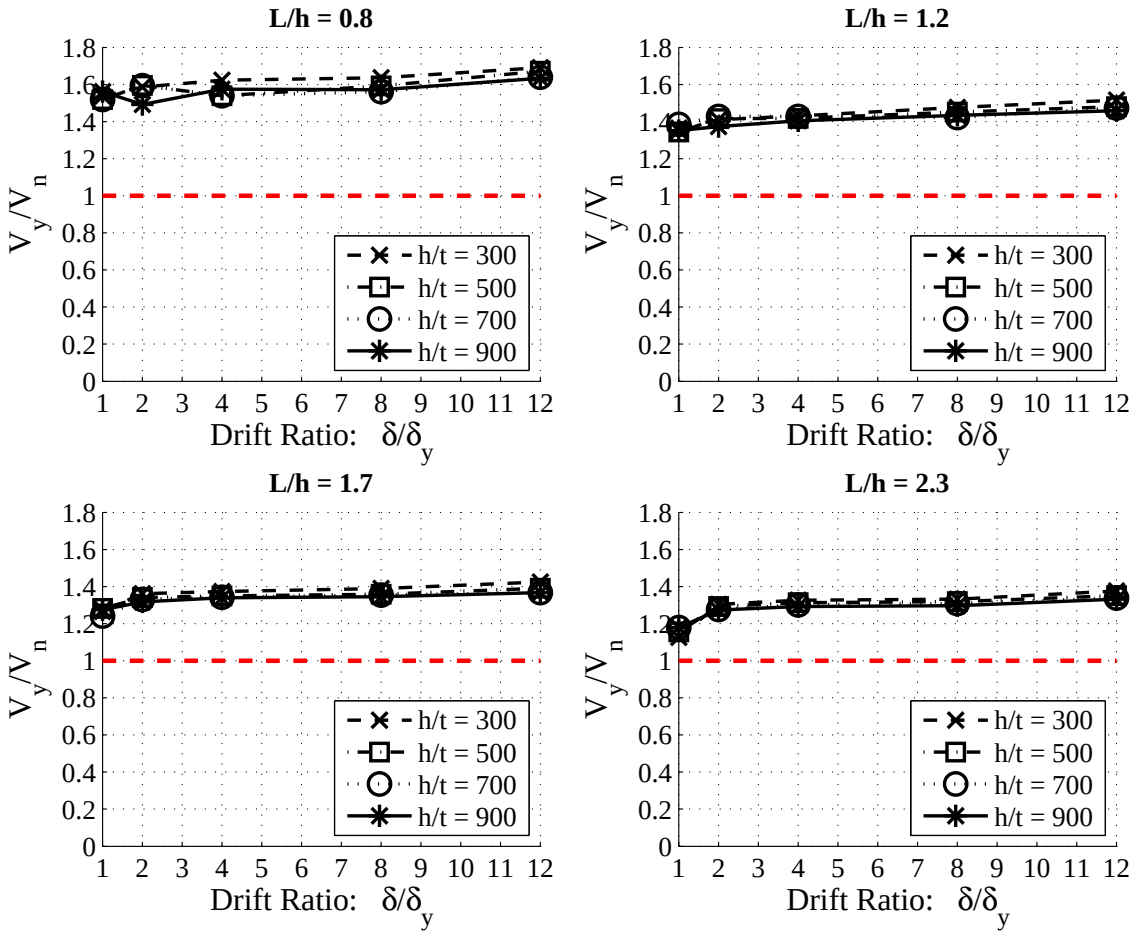

Figure 3.18: Lateral load capacity normalized by AISC V_n

Mean compressive stress

Web plates loaded into the post-buckling range also develop compressive stresses normal to the direction of the principal tensile stresses (See Figure 3.19). Preliminary analyses show these stresses are lower in magnitude than the tensile stresses, but are often significantly higher in magnitude than the critical buckling stress. As the plate is loaded monotonically beyond the critical buckling stress, the average compressive stresses will increase in order to stabilize the tension field. Preliminary analyses also indicate that the stresses normal to the principal tensile stresses are highly variable and in some areas may be positive (tension).

The compressive stresses tend to have higher magnitude in zones near the panel boundaries where the plate exhibits high double curvature, than in the central portion of the plate where the buckling corrugations predominantly in single curvature. The average magnitude of the compressive stress also varies with panel aspect ratio L/t. Fig. 3.20 shows a screen capture of the bottom three stories of a five story continuum model at 2% drift. The dark shaded regions on the plate represent areas where the magnitude of the mid-plane principal compressive stress exceeds 10% of the material yield stress. The minimum principal stress deminishes, and actually becomes tensile, along bands roughly coincident with the post-buckling web plate corrugations. In the discussions that follow, σ_y and F_y both denote yield stress.

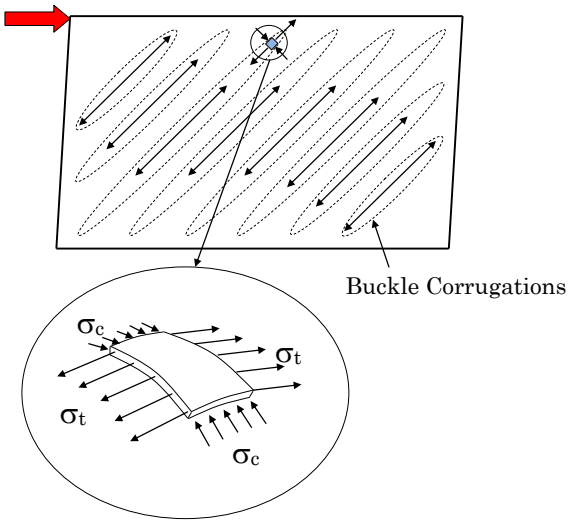

Figure 3.19: Post-Buckled Panel

Fig. 3.21 shows the relative magnitudes of the mean principal tensile stress and mean principal compressive stress in the web plate at various drift levels, normalized by the plate yield strength. As can be seen from Fig. 3.21, the mean compressive stress is a significant fraction of the yield stress at δ_y for all plate thicknesses. The wall with an aspect ratio of 0.8 has a compressive stress ranging from $0.15F_y$ for the $t_w = h/900$ plate to $0.36F_y$ for the $t_w = h/300$ plate. At $12\delta_y$ these values drop to approximately $0.07F_y$ and $0.11F_y$ respectively.

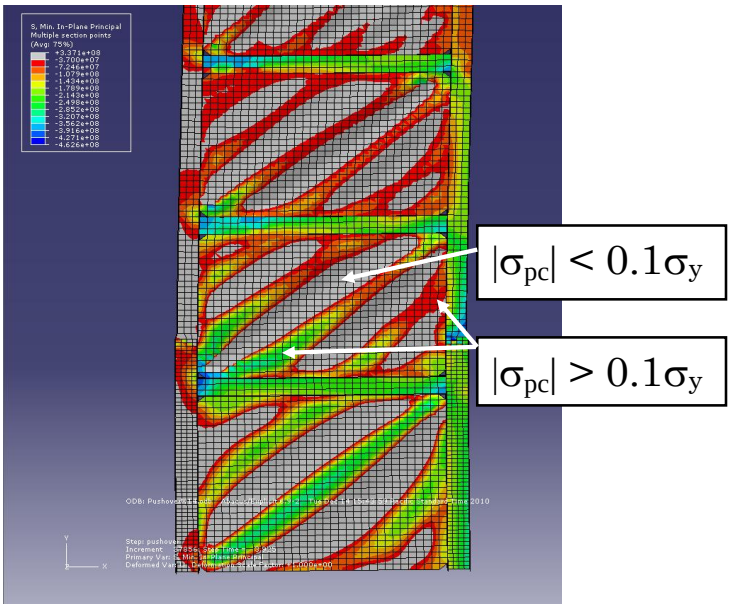

Figure 3.20: Bottom three stories of five story $ABAQUS$ model at 2% drift showing regions of principal compressive stress magnitude $|\sigma_{pc}|$ in excess of 10% σ_y

As the aspect ratio of the web plate increases to 2.3, the mean compressive stress drops but is still approximately $0.06F_y$ for the thinnest plate at maximum drift. These results indicate that there is a significant compressive stress presence, even at high inelastic drifts for a very thin plate.

The web plate compressive stresses tend to increase the lateral load capacity slightly beyond that predicted by a 45 degree tension field model. Assuming a uniform stress field and employing a von Mises yield criterion again with k being the ratio of mean principal compressive stress σ_c to mean principal tensile stress σ_t, gives

$$F_y^2 = \sigma_t^2 + k\sigma_t^2 - k^2\sigma_t^2 \tag{3.28}$$

$$\sigma_t = \frac{F_y}{\sqrt{1+k+k^2}} \tag{3.29}$$

$$\sigma_c = \frac{kF_y}{\sqrt{1+k+k^2}} \tag{3.30}$$

By integrating stresses along the bottom boundary of the web plate assuming a 45 degree tension field, the modified lateral load is then

$$V_y = 0.5F_y t_w L\left(\frac{1+k}{\sqrt{1+k+k^2}}\right) \tag{3.31}$$

Recognizing that for small k, the term $\sqrt{(1+k+k^2)}$ is approximately equal to $(1+\frac{k}{2})$, this gives

$$V_y \cong 0.5F_y t_w L\left(1+\frac{k}{2}\right) \tag{3.32}$$

When $k = 0.06$, the increase in the lateral strength is therefore only around 3%, a modest difference and arguably negligible. The upper limit on the increase is approximately 15.5% for the case of a very thick plate that does not buckle.

VBE demand resulting from web plate "Pull-in"

Web plate compressive stresses also affect VBE demands. Fig. 3.22 shows how the VBE flexural demand changes with increasing drift, web plate thickness and aspect ratio. The VBE demands are extracted from the *ABAQUS* model and modified to produce an equivalent moment demand that can be associated with a uniform load on a simply supported beam. To do this, the bending moment at the top and bottom of the VBE are averaged and subtracted from the midspan bending moment. This moment, denoted M_{eq}, is then normalized by the bending moment derived from a 45 degree tension field model with the full tensile yield strength activated, denoted M_{tf}.

$$M_{eq} = \frac{1}{2}\left(M_{top} + M_{bot}\right) - M_{mid} \tag{3.33}$$

$$M_{tf} = \frac{1}{2}F_y t_w \frac{\hat{h}^2}{8} \tag{3.34}$$

where $\hat{h}$ is the VBE span measured between where the points M_{top} and M_{bot} are sampled.

The data in Fig. 3.22 show that normalized VBE demand increases with increasing aspect ratio and increasing slenderness. This can be attributed to the lower mean compressive stress for high aspect ratio and high slenderness. At yield drift the normalized VBE demand varies from approximately 0.5 to 0.9. As the drift increases, the effective compressive stress diminishes and the normalized demand approaches and sometimes exceeds 1.0.

Fig. 3.23 shows the VBE moment, M_{eq}, normalized by the moment computed using the full stress field, denoted M_{sf}. M_{sf} is calculated using the mean engineering tensile and compressive stress field magnitudes at the various drifts, rather than a simple tension field. M_{sf} is defined as

$$M_{sf} = \frac{1}{2}\left(\bar{\sigma}_t + \bar{\sigma}_c\right) t_w \frac{\hat{h}^2}{8} \tag{3.35}$$

where $\bar{\sigma}_t$ and $\bar{\sigma}_c$ are the mean tensile and compressive (Cauchy) stresses extracted from the analysis at the drift level of interest, converted to engineering stress by dividing the reported stress by $(1 + \bar{\epsilon}^{pl})$.

Since the actual demand from $ABAQUS$ normalized by M_{sf} exceeds 1.0, this bending moment underestimates the actual demand, but it does result in a more uniform estimate across all drift levels. Close examination of many sub-assemblage panels analyzed as part of this study, and of analysis performed by Kharrazi [38], reveals that the tension field inclination in a fully plastified plate is greater than 45 degrees near the connection to the VBE and may be more than 50 degrees. This results in an increase in the transverse load of approximately 17% beyond what a 45 degree tension field would predict. This is consistent with the result observed in Fig. 3.23.

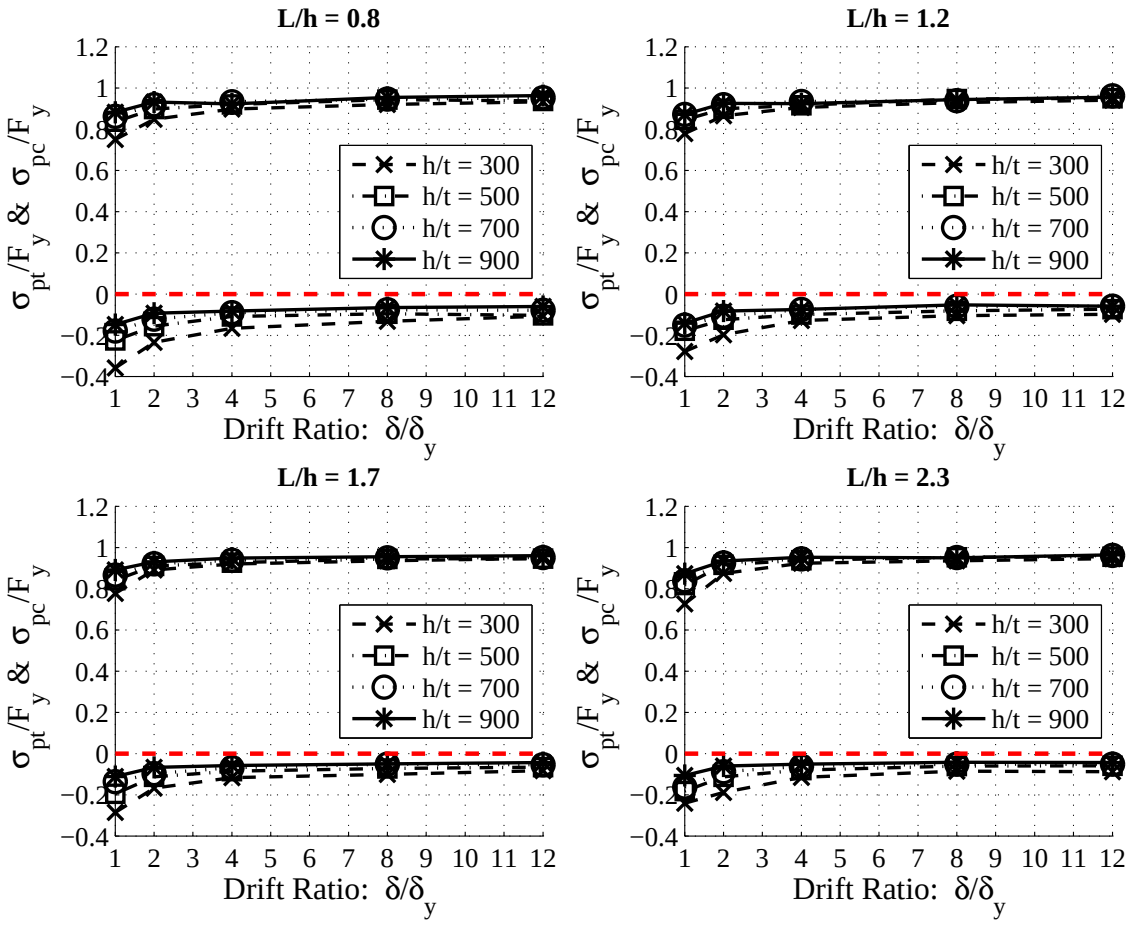

Figure 3.21: ABAQUS mean nominal principal stresses (σ_{pt} & σ_{pc}) normalized by plate nominal yield stress (F_y)

Web Plate Unloaded Shear Strength

The web plate unloaded shear strength, defined here as the shear strength achieved by the plate after it has elastically unloaded and is undergoing load reversal, but before the plate tension field is re-established in the opposite direction, has a bearing on the energy dissipation capacity. To date, this strength has not been studied or quantified but it could have a notable influence on the dynamic response of an SPSW.

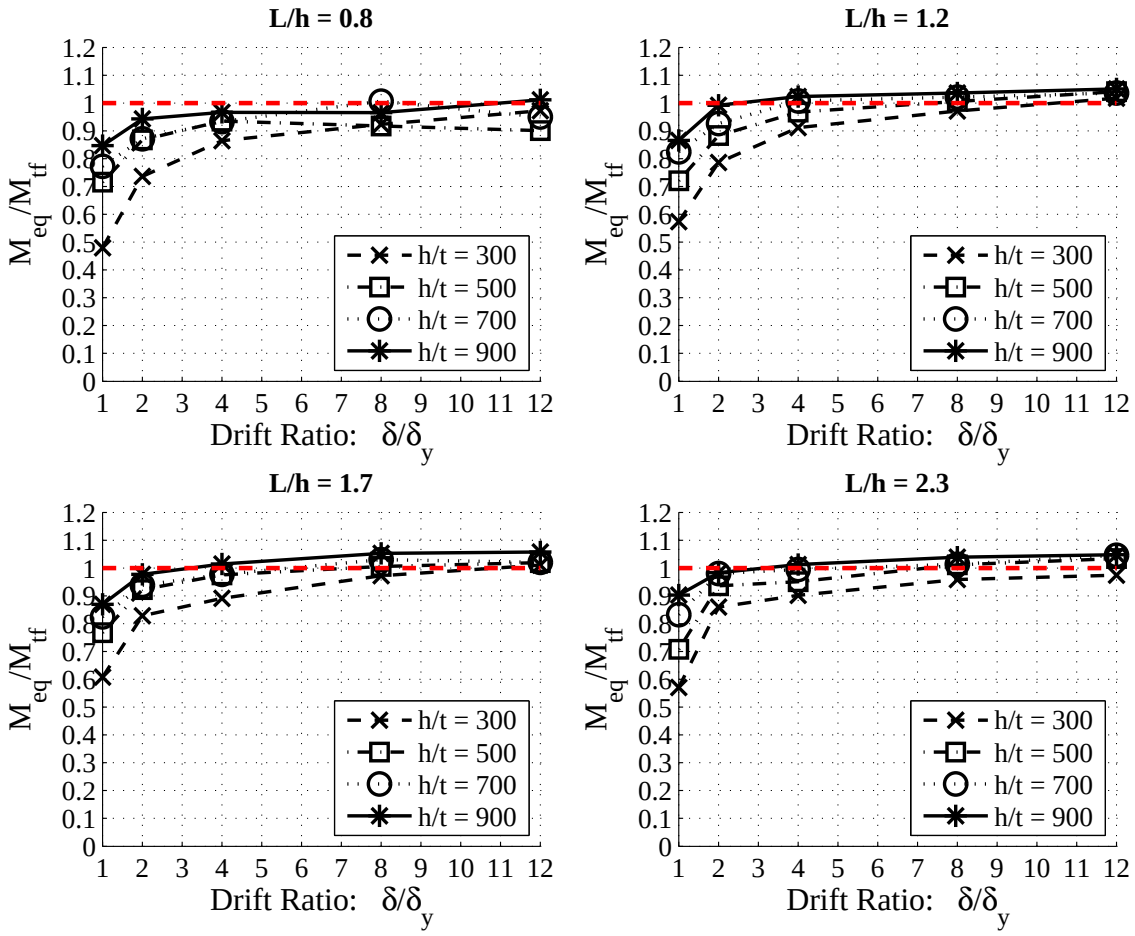

Figure 3.22: ABAQUS VBE moment demand (M_{eq}) normalized by moment demand from 45 degree tension field model (M_{tf})

This value is taken as the minimum strength that occurs post "snap-through", prior to re-loading. In Fig. 3.24 the unloaded shear strength is normalized by the plastic strength of the plate, V_y. This figure also shows how the unloaded shear strength is determined from the hysteretic data. It is evident from this plot that the unloaded shear strength is considerably higher than the critical buckling strength of the plate, τ_{cr}, which is often assumed to be the post buckling strength of a web plate but is typically less than 6% of the plate lateral yield strength. The unloaded shear strength appears to be sensitive to the panel

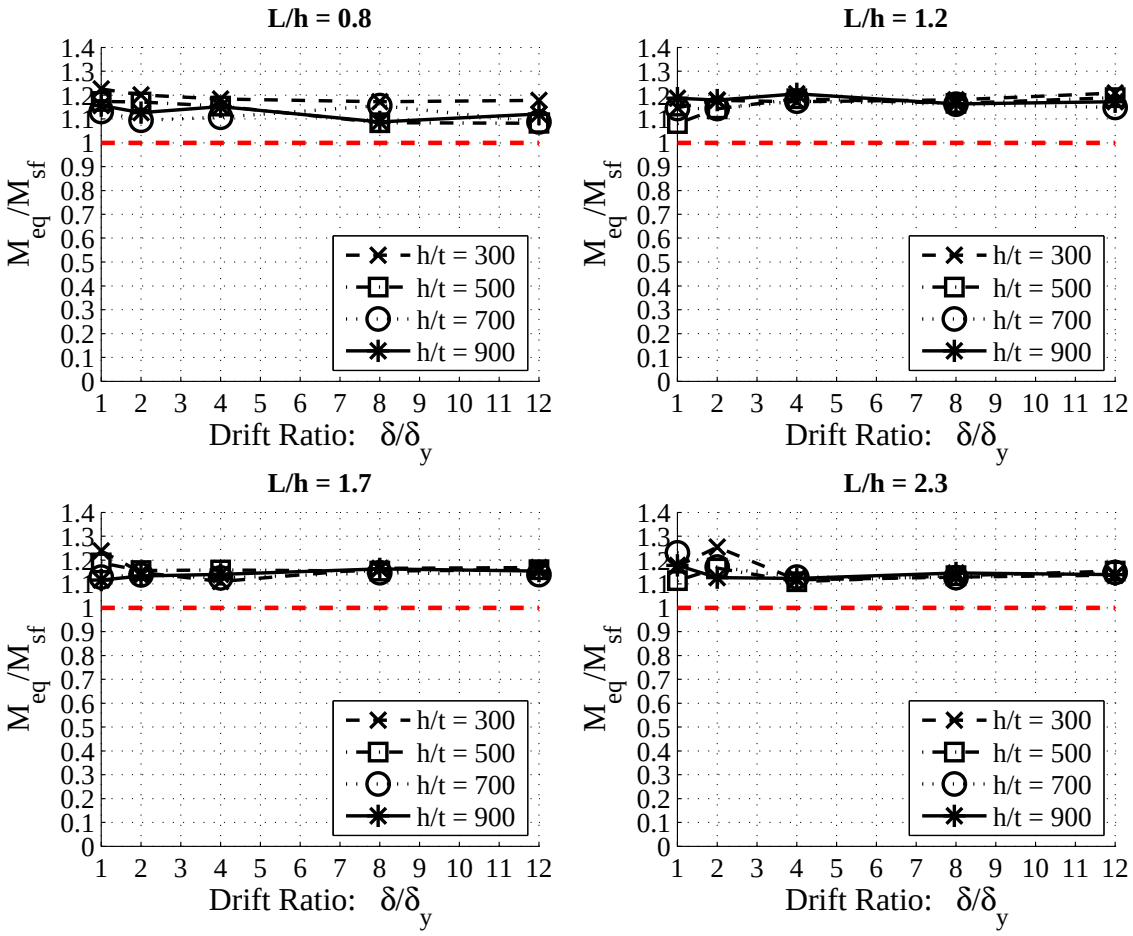

Figure 3.23: ABAQUS VBE moment demand (M_{eq}) normalized by moment demand using mean principal stresses (M_{sf})

aspect ratio, L/h, when the ratio is less than approximately 1.0, otherwise the ratio of the unloaded shear strength to the lateral yield strength, V_{res}/V_y, is stable and is correlated only with the slenderness, h/t.

Conclusions for Study #3

This study focused on the behavior of sixteen sub-assemblies with varying aspect ratio, panel slenderness and very and stiff boundary elements. The results indicate that there are

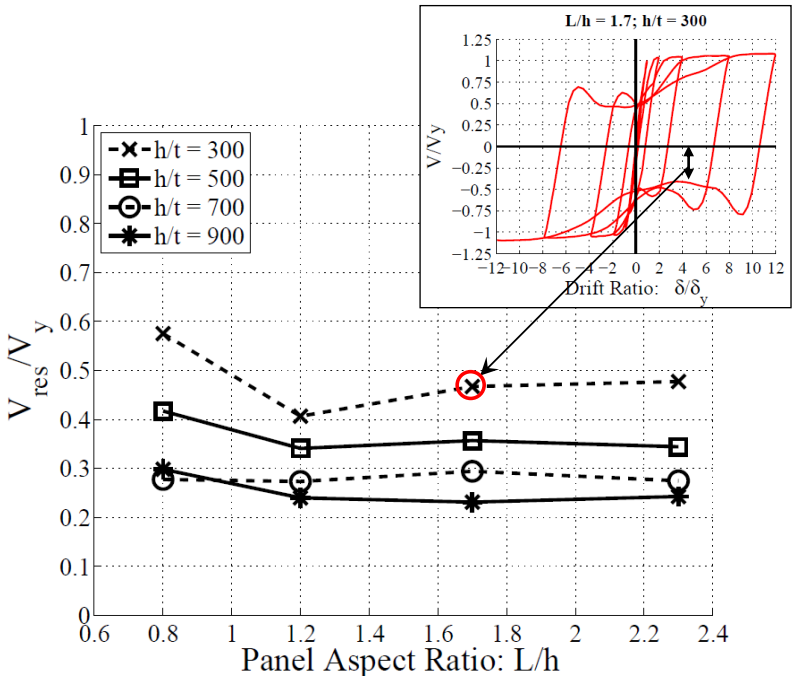

Figure 3.24: ABAQUS Residual Shear Strength (V_{res}) Normalized by (V_y)

significant compressive stresses developed in the plate upon cyclic loading and these stresses have an influence on the lateral strength of the plate and on VBE demand. The following broad conclusions can be drawn.

- The lateral strength of a web plate should be determined using L instead of L_{cf}.
- The 0.42 factor in Eq. 3.25 should be reviewed.
- Compressive stresses in thick web plates with low aspect ratio and low slenderness should be considered.
- The web plate unloaded shear strength may be predicted and could be included in the development of a more comprehensive hysteretic model

3.3.4 Study #4

The fourth study addresses the impact of VBE flexibility on the distribution and development of the web plate stresses. This study was performed as part of a larger study [76] of the interaction between the web plate and boundary frame.

Both the Canadian [22] and US codes [1] require that the VBE flexural stiffness exceed a prescribed minimum value, which is a function of the height, length and thickness of the web plate. The minimum I_c required by the *Provisions* is:

$$I_c = 0.0031 t_w \frac{h^4}{L} \tag{3.36}$$

The minimum VBE stiffness was introduced so that adequate system ductility be provided [49]. The VBEs must have stiffness sufficient to anchor the web plate and enable a uniform stress field to develop. If the VBEs are too flexible, the stress field will be highly non-uniform and plasticity will be concentrated only in certain regions of the web plate. The analysis used to develop Eq. 3.36 was based on an idealized elastic plate girder. The model was extended to seismic response prediction of SPSWs; however it is not consistent with many aspects particular to the SPSW system. Furthermore, although the established threshold for stress field uniformity embedded in the code equation is reasonable (i.e., that the ratio of minimum to maximum web plate tensile stress be no less than 0.8), the limit was selected arbitrarily and has since been found to be uncorrelated with available test data on VBE performance [52].

The *ABAQUS* analyses performed to investigate VBE flexibility were similar those presented in the previous sections, but differed in a number of respects. First the computational model is presented, followed by the SPSW sub-assemblies that were analyzed and finally the results of the analyses and a discussion.

Computational Model

The *ABAQUS* model developed for this study, shown schematically in Fig. 3.25, was devised so that several phenomena could be examined with particular attention focused on the web plate and the VBE behavior. The model represents an arbitrary single story subassembly of a multi-story SPSW, with wide flange HBE and VBE sections. The HBEs are moment connected to the VBEs, as is required by the *Provisions*. The HBE and VBE sections are determined so that, for a prescribed geometry, the members satisfy the strength and compactness requirements of the *Provisions*. The HBE cross-sectional area A_g and elastic section modulus S_x are set to half of that required for a continuous SPSW system; in this way the HBE will deliver a similar flexural demand to the VBEs, as would occur for a continuous system with an equal panel thickness and story height above and below. The halving of A_g accounts for the absence of plate pull-in force contribution from the adjacent story. Therefore the axial shortening of the HBE in the model will be compatible with a continuous system. The geometry can be modified to suit a prescribed bay length (L), story height (h), web plate thickness (t_w), boundary element section properties and applied moment-shear demand ratio (M_{OT}/V). Neither dead nor live loads were included in the analyses. Stresses and strains were sampled over an evenly spaced grid of one hundred points.

The boundary conditions were modeled so that they approximate, as closely as possible, the boundary conditions in a continuous wall system. To approximate the effect of having continuous VBEs through the beam-column joint, the top and bottom of each VBE are constrained to have equal in-plane rotation. The VBEs are otherwise unconstrained except that the left VBE bottom node is pinned while the right VBE bottom node has a roller boundary condition. The HBEs are rigidly connected to the VBEs with a half column depth offset that maintains normality. VBE panel zone flexibility is not modeled. The mid-point of both the top and bottom HBE is constrained to lie on a straight line between opposite ends of the HBE member. This ensures that the HBE can flex near the ends where moment demand is typically highest, can shorten axially, but it is prevented from deflecting

vertically at mid-span. This constraint attempts to capture the axial and localized flexural demands on the HBE without permitting excessive center span deflection for cases of large HBE span-depth ratios, which would influence the web-plate stress field. In a real system the HBE is largely (though not entirely) prevented from deflecting vertically by the presence of the web plate in the adjacent story.

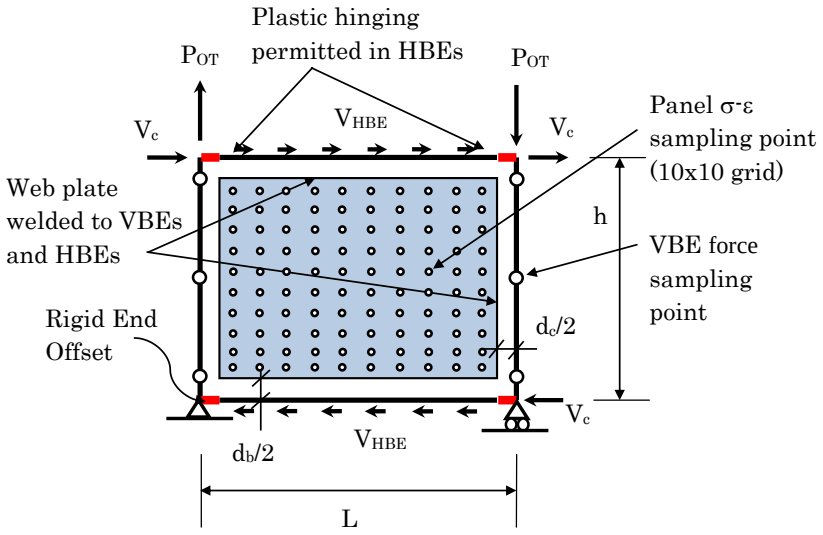

Figure 3.25: Schematic diagram of *ABAQUS* model used for VBE flexibility analysis

Selection of Model Parameters

To examine the effect of VBE slenderness, two suites of models were analyzed; one suite comprised flexurally slender VBE sections (limited to W12 or W14), the other with deeper and typically lighter sections (limited to W24 through W40). For the first suite, and for a given geometry, the most flexurally slender section was adopted for the model, regardless of whether or not the VBE satisfied the AISC minimum stiffness limit. As previously discussed, this was done to examine this particular provision. For the second suite of models, the most efficient section (by weight) was selected.

Designs were selected on the basis that they satisfy capacity-design requirements for various M_{OT}/V ratios. The resulting designs are in shown in Table 3.2. A total of sixty-seven sub-assemblies were analyzed with a broad range of α, β and M_{OT}/V values. A sample of thirty-five of these is shown in Table 3.2.

The VBE flexibility ratio (β), defined for this study as I_c provided divided by I_c required by Eq. 3.36, ranged from 0.80 to 28.1, with a mean of 6.4. Three of the sixty-seven combinations had a β less than unity.

The VBE forces were extracted from the simulations at 2% drift and the capacities checked using the AISC interaction equations to validate the use of elastic member properties. The mean value of member interaction for all of the assemblies was computed to be 1.069, slightly higher than the code limit of 1.00, but still within the realm of substantially elastic behavior.

Influence of VBE Flexibility on Stress Uniformity and Plastic Strain

The influence of VBE flexibility on the web plate ductility demand was explored using two metrics: a) the coefficient of variation of the principal tensile stress (Cσ_{pt}) prior to significant yielding and b) the coefficient of variation of the equivalent plastic strain (Cϵ_{PEEQ}) at 2% drift.

Fig. 3.26 shows Cσ_{pt} plotted against β at drifts of $0.5\delta_y$ and δ_y respectively. At $0.5\delta_y$, assembly #1 and #2 (both with β values less than unity) have a Cσ_{pt} of 0.28 and 0.32 respectively; significantly above the mean value of 0.22 (with SD = 0.028). The situation is similar, although slightly less obvious, when the drift is at δ_y with Cσ_{pt} values of 0.26 and 0.27 (mean = 0.20, SD = 0.025). For assemblies with $\beta \geq 1.0$, there appears to be no relationship between β and the uniformity of the stress field. This observation is consistent with the code provision, and with expectation.

Fig. 3.27 shows the relationship between Cϵ_{PEEQ} and β at a drift of 2%. At this drift level there has been significant plastic strain throughout the plate, variations in membrane

Table 3.2: Data for *ABAQUS* Models Examining VBE Flexibility

Assm #	VBE	HBE	(m) L	(m) h	(mm) t_w	(m) M_{on}/V	(Eq. H1-1) AISC Int	β	(deg) AISC α
1	W14x730	W30x211	5.69	6.15	9.5	24.3	0.984	0.81	37.26
2	W14x730	W30x235	4.88	6.1	8.1	24.3	0.962	0.83	37.74
3	W14x605	W21x111	4.57	5.72	3.8	12.1	0.956	1.63	38.78
4	W14x605	W27x178	4.57	5.72	5.1	6.0	0.983	1.22	38.92
5	W14x550	W24x146	3.66	4.57	6.1	12.1	0.998	1.74	39.15
6	W14x500	W27x178	3.66	4.57	6.1	6.0	0.964	1.51	39.52
7	W14x370	W24x146	3.66	4.57	4.1	24.3	0.967	1.50	39.89
8	W14x500	W21x93	4.57	4.35	3.8	24.3	0.973	3.68	40.05
9	W14x665	W36x256	5.49	5.23	6.1	6.0	0.956	2.01	40.59
10	W14x455	W27x194	4.57	4.35	5.1	6.0	0.983	2.42	41.06
11	W14x665	W24x146	6.4	4.13	5.3	12.1	0.995	6.87	41.23
12	W14x730	W36x302	6.4	4.92	7.1	12.1	0.963	2.94	41.44
13	W14x665	W40x278	6.4	4.92	5.3	24.3	0.962	3.40	41.86
14	W14x605	W40x264	6.4	4.13	5.3	6	0.991	5.98	42.68
15	W36x800	W21x122	3.66	4.57	6.1	24.3	0.971	11.93	39.64
16	W27x539	W30x211	5.49	5.23	9.1	6.0	0.976	2.77	39.99
17	W36x652	W30x211	6.4	6.1	7.1	24.3	0.986	4.43	40.32
18	W36x487	W30x211	6.4	6.1	7.1	12.1	0.963	3.15	40.43
19	W30x261	W18x86	3.66	4.57	3	12.1	0.978	4.83	40.68
20	W33x387	W24x146	4.57	5.72	3.8	24.3	0.985	3.67	40.75
21	W36x800	W36x256	6.4	4.92	10.7	24.3	0.964	8.87	40.88
22	W40x372	W27x178	3.66	4.57	6.1	6.0	0.991	5.46	41.15
23	W30x211	W21x111	3.66	4.57	3.0	6.0	0.971	3.80	41.36
24	W36x395	W24x146	4.57	4.35	5.1	6.0	0.971	9.58	41.48
25	W27x539	W36x256	5.49	5.23	6.1	12.1	0.955	4.15	41.6
26	W40X593	W24X146	6.4	4.13	5.3	12.1	0.972	27.92	41.71
27	W40X593	W36X256	6.4	6.1	5.3	12.1	0.997	5.88	41.73
28	W36X487	W40X278	6.4	6.1	5.3	6.0	1	4.2	41.90
29	W36X652	W40X264	6.4	4.92	7.1	12.1	0.983	10.40	42.06
30	W40X503	W36X256	6.4	4.13	10.7	12.1	0.995	11.52	42.29
31	W36X361	W24X162	5.49	4.22	4.6	24.3	0.966	13.05	42.43
32	W36X487	W27X235	6.4	4.92	5.3	24.3	0.966	9.87	42.51
33	W40X503	W36X302	6.4	4.92	7.1	6.0	0.99	8.55	42.67
34	W40X431	W36X256	5.49	4.22	6.1	6.0	0.984	13.26	42.98
35	W36X487	W40X294	6.4	4.13	7.1	24.3	0.994	14.96	43.27

stresses have been largely eliminated and plastic strain demands are evening out. There is no observable trend in this data and statistical analysis reveals the same. Interestingly, the $C\epsilon_{PEEQ}$ for assembly #1 and #2 are below the mean of the group, signifying that for this measure of ductility demand the low β value had no impact on the uniformity of the plastic strains.

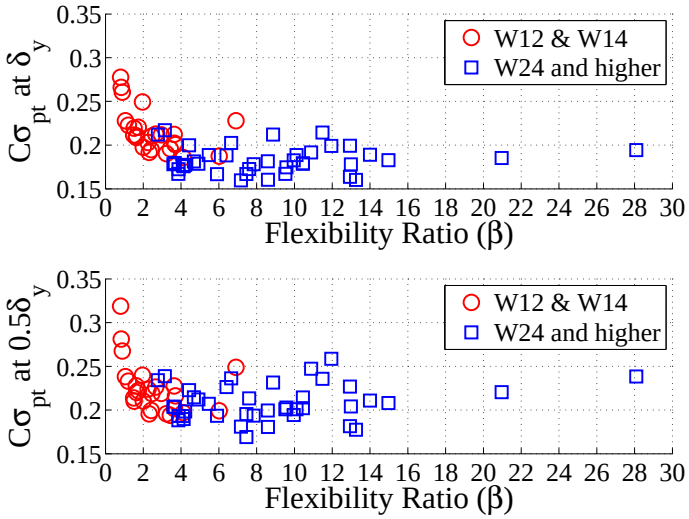

Figure 3.26: Relationship between β and the measured coefficient of variation of σ_{pt} ($C\sigma_{pt}$) at $0.5\delta_y$ and δ_y

Compression field magnitude

The computed ratio of mean compressive stress to mean tensile stress is shown in Fig. 3.28 for yield drift, Δ_y, and for a drift of 3% for a broad range of D/t ratios. For the monotonic load case the magnitude of the compressive stress generally falls between about 6% and 30% of the corresponding tensile stress for the typical range of of SPSW panel D/t ratios. The relationship between these stress magnitudes and their dependance on drift level is more important under cyclic loading. This will be addressed in the chapters that follow.

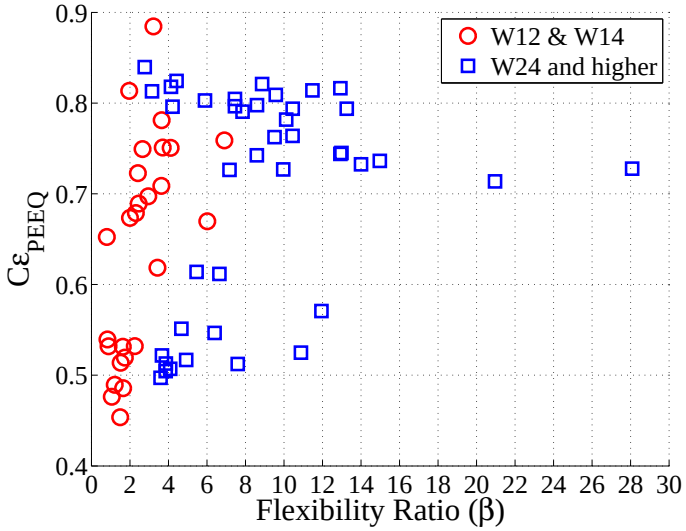

Figure 3.27: Relationship between β and the measured coefficient of variation of ϵ_{PEEQ} (Cϵ_{PEEQ}) at 2% drift

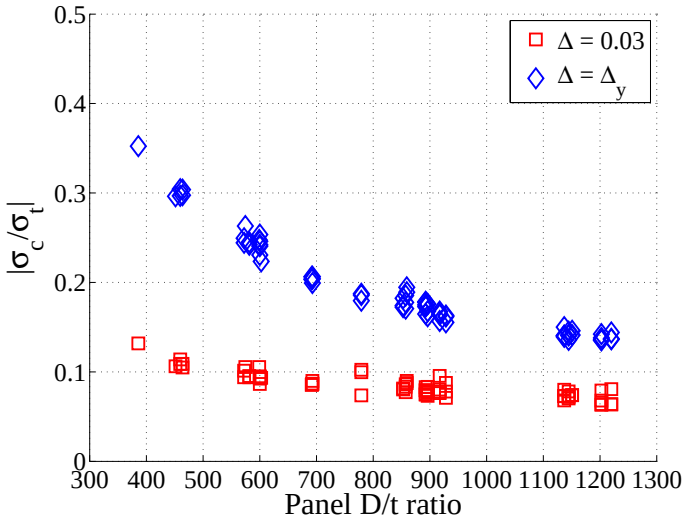

Figure 3.28: Ratio of σ_c to σ_t magnitudes predicted by ABAQUS

Tension Field Inclination Angle

As part of the larger study [76], the angle of the tension field was also examined. Table 3.2 provides for each sub-assembly the α computed using Eq. 3.16. The mean α extracted

from $ABAQUS$ was recorded at the end of each time increment. The relationship between the predicted inclination angle using the AISC equation (α_{AISC}) and the α predicted by $ABAQUS$ (α_{ABQ}) at the elastic and plastic phases of loading is shown if Fig. 3.29. This figure presents the correlation between the two measures at δ_y, where α is close to its minimum value and the plate is not yet fully yielded, and at 2% drift where the web plate is completely plastic. It also shows a line representing the ideal relationship where the two measures would be perfectly correlated. It is clear that there is a relationship between the α_{AISC} and α_{ABQ} at the end of the elastic range, although α_{ABQ} is usually closer to 45 degrees than α_{AISC}. However, in the fully plastic condition the correlation completely breaks down and no relationship exists (correlation coefficient = -0.089). The mean α_{ABQ} at 2% drift for the sixty-seven sub-assemblies modeled was computed to be 43.4 degrees.

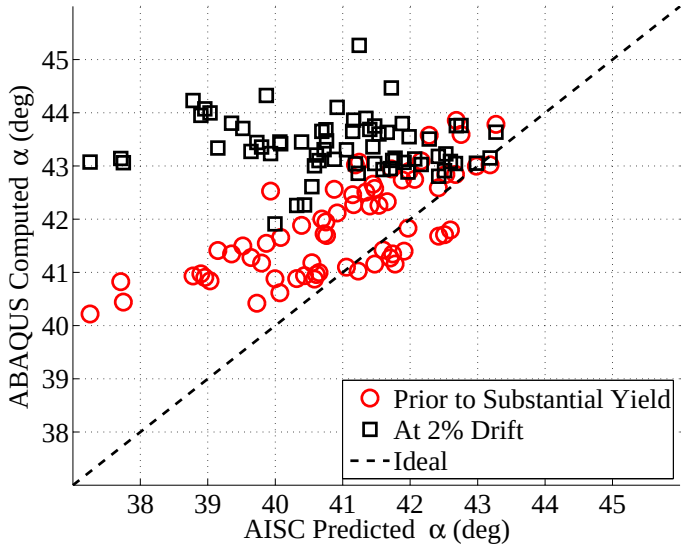

Figure 3.29: Correlation between α predicted by AISC Eq. 3.16 and α predicted by ABAQUS

Conclusions for Study #4

This study identified that for monotonic loading, the inclination of the web plate tension field approached 44 degrees for a broad range of panel geometries, VBE stiffnesses and M/V ratios. It was also found that the code minimum required VBE slenderness signifies a point where, at elastic drift levels, the uniformity of web plate stress is significantly reduced, indicating that the slenderness limit is a good predictor of stress uniformity. The minimum slenderness however does not correlate with the uniformity of plastic strains at large drifts, which is arguably a more important metric for determining ductility demand.

This study also examined the migration of the tension field. The primary difference between this study and study #1 is the inclusion of variable M/V ratios and a broader range of panel geometries. The objective of this part of the study was to argue for the use of a single value of α that provides a better representation of the inelastic condition and will considerably simplify the design process.

The analysis did not address cyclic loading and how this form of loading may affect the web plate stress field and VBE demand. Additional analyses and experimentation are required to identify how cyclic loading may influence these.

3.3.5 Overall Summary and Conclusions

After presenting the particulars of the *ABAQUS* models used in many of the parametric studies, this chapter detailed four analytical studies concerning SPSW web plate behavior. These studies collectively provided the motivation for an experimental program designed to test and verify some of the findings and ultimately provide justification for simplifications and modifications to the existing design equations contained in the Provisions. It is also hoped that the results of these studies will aid the development of an alternative hysteretic model.

Chapter 4

EXPERIMENTAL DESIGN AND SETUP

4.1 Overview

The tests carried out for the experimental program were conducted between December 2010 and May 2011 at the University of Washington Structural Research Laboratory (UW SRL). The main objective is to examine the strength and deformation behavior of shear loaded thin steel web plates in the absence of boundary frame contribution to the lateral load resistance. This was accomplished by using a true pin for the VBE to HBE connections.

The experimental program was broken into two distinct phases as shown in Table 4.1. In the Phase I tests (Tests #1-16 to #3-18), the goal is to associate various aspects of web plate hysteretic response to the mechanical properties derived from tensile coupon tests (F_y, F_u, E, ϵ_{sh}), and the panel L/t ratio. Large and essentially rigid HBE and VBE sections will be used for this purpose. The Northern Digital Instruments (NDI) optical tracking system, OptoTrak (described later) will be used to assess web plate deformation for Tests #1-18 and #1-16. In the Phase II tests (Tests #1-22 to #3-22), the web plate tension field orientation and VBE demand will be studied using strain rosettes and optical tracking. In this phase, the rigid VBEs are replaced with flexible VBEs and strains are measured in both the VBEs and the web plate. Figs. 4.1 and 4.2 show the experimental setup for the Phase I and Phase II tests respectively. The setup and specimens are described later in this chapter.

Key features of the hysteresis and stress field development will be identified and eventually incorporated into multi-story SPSW models using *ABAQUS* and OpenSees through *ABAQUS* parametric studies.

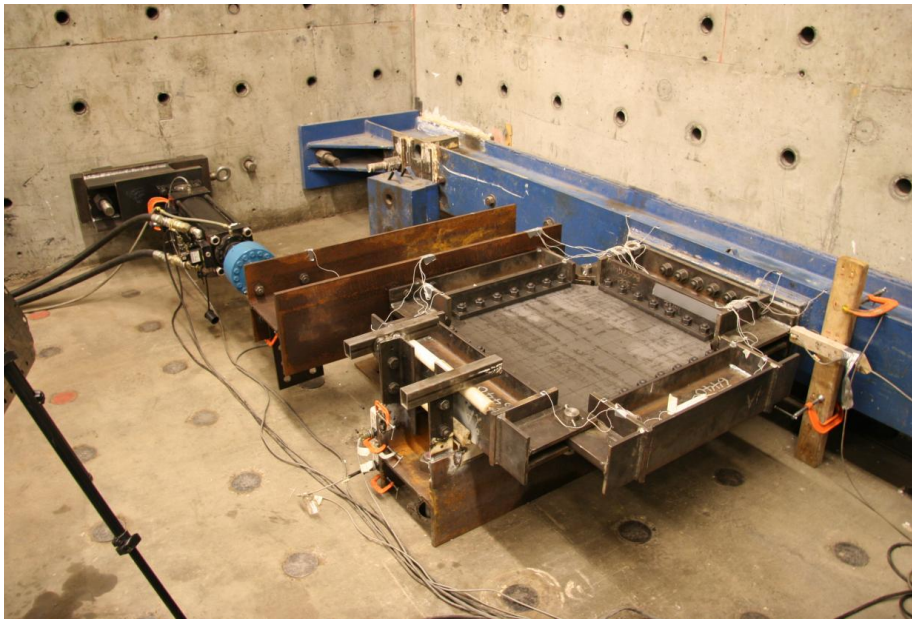

Figure 4.1: Phase I Test Setup

A one-sixth scale boundary frame assembly was designed and assembled by the author. The components, including the HBEs, VBEs, and clamping plates, were fabricated by a local commercial steel fabricator. The frame was designed so that it could be used for multiple tests using a variety of plate thicknesses and material properties. The web plates were anchored to the boundary frame so they could be easily removed and replaced after each test. The frame members and connections for both phases of the experiment were designed to remain entirely elastic after being subjected to multiple cycles of inelastic web plate loading, but would not resist lateral load. This was achieved through the use of pure pin connections between the boundary frame members. A single actuator loaded the top of the frame, subjecting the web plate specimen to a state of pure shear.

4.2 Experimental Objectives

The key objectives of the experimental program are enumerated below. As shown in Chapter 2, there are aspects of SPSW web-plate behavior that are not well understood and deserve

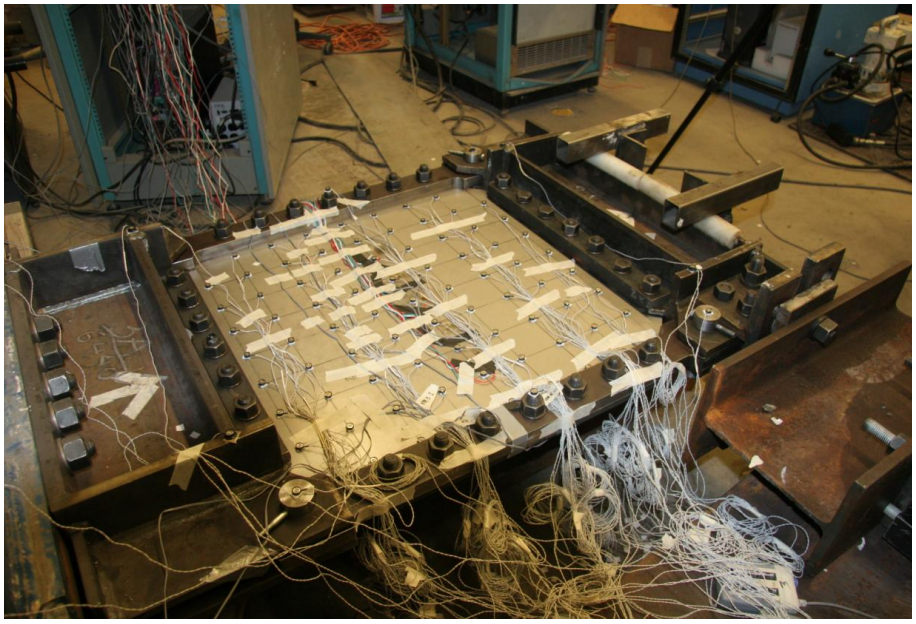

Figure 4.2: Phase II Test Setup

further examination.

1. **To characterize the cyclic hysteretic response of steel web plates typically used in SPSWs.** The hardening evolution for a web plate loaded cyclically in shear can be modeled using a kinematic or isotropic hardening law, or a combination of the two. The response of a web plate for these hardening laws is quite different and there appears to be a lack of clarity in the existing literature as to which is appropriate. The post-buckled compressive strength of a web plate V_c (normal to the tension field), is often assumed in the literature to be the critical buckling load, V_{cr}. FE analyses indicate that mean value of V_c may considerably exceed V_{cr}.

2. **To measure the tension field inclination for the case of slender VBE sections.** When a web plate is loaded monotonically from the elastic post-buckled state to the fully plastic state there is a significant change in the direction of the principal tensile stresses where the elastic value is initially much less or greater than 45 degrees. The potential exists that for small angles (computed per Eq. 3.16), un-conservative

Table 4.1: Testing Program

Phase	Test Ref #	Plate Gage	Material Spec
1	1-16	16	A36
1	2-16	16	A36
1	3-16	16	A36
1	1-18	18	A1008
1	2-18	18	A1008
1	3-18	18	A1008
2	1-22	22	A1008
2	2-22	22	A1008
2	3-22	22	A1008

force demands on the VBE will result due to the change in the principal stress trajectories upon web plate plastification. A constant angle would simplify the design process.

3. **To compare the inclination of the buckled waves and principal strain trajectories and compare this to numerical simulations.** The orientation and magnitude of the buckled waves have been studied before ([6], [73]) but no comparison has yet been made between the direction of the tension field, as measured by the direction of the buckled waves, and the direction as measured through strain gauges mounted on the surfaces of the web plate. Since it is easier to measure the direction of the buckles than the direction of principal strains, this comparison may be useful to other researchers.

4. **To measure VBE demand.** The change in the tension field angle, the effect of accompanying compressive stresses normal to the direction of the principal tensile stresses, and of the nature of the web plate hardening are not generally considered in conventional SPSW modeling, but all of these can influence the force demand on the

VBEs.

4.2.1 A note on Plastic Strain Accumulation

Throughout this chapter, frequent reference is made to the accumulated plastic strain and estimated values of accumulated plastic strain. The methods for doing this are covered in detail in Chapter 7, Section 7.2.2.

4.3 Practical Experimental Design Considerations and Constraints

The materials and equipment available were sufficient to carry out the tests, but not without challenges regarding the anchorage of the test frame to the reaction beam, connection of the actuator to the test frame and connection of the actuator to the strong wall. This was all achieved by utilizing materials and resources around the lab so that minimal additional expense was incurred in acquiring additional shop fabricated components. The space, time and resources available for testing the specimens introduced many practical challenges.

4.3.1 Specimen Orientation and Base Support

The boundary frame and specimen were oriented in a horizontal plane, parallel with the floor. Figs. 4.3 and 4.4 show plan views of the Phase I and II tests respectively. An existing reaction beam which was anchored to the concrete strong-wall served as the "rigid base" for the test specimen. The bottom W8x58 HBE was connected to the reaction beam with ten 31.8 mm (1 1/4 inch) diameter A490 pre-tensioned bolts. The reaction beam was connected to the concrete strong-wall with 51 mm (2 inch) diameter post-tensioned threaded rods spaced at approximately 914 mm (3 feet) along its entire length. Prior to the first test, it was believed the reaction beam would provide an essentially rigid base. However, when the specimen was fully loaded it displaced elastically more than was anticipated. This had to be accounted for when processing the results and will be discussed in a later section.

4.3.2 Specimen Size Limitations

The overall dimensions of the steel web plates were limited by the desired web plate length-to-thickness ratio (L/t) and by the available actuator capacity. The actuator used in the experiments was rated to ±244.6 kN (±55 kips), with a maximum stroke of ±254 mm (±10 inches). A practical maximum load limit of 222.4 kN (50 kips) and an assumed plate ultimate tensile stress of 413.7 MPa (60 ksi) were used to determine the optimal panel dimensions for the test specimen. A web plate length of 711 mm (28 inches) was determined and appeared to be optimal. The panel L/t ratios were selected so that they would be representative of what would be encountered in a typical design. There are no code limits on the L/t ratios for SPSW panels but most practical designs fall between 2000 and 500. The Seismic Specification does set lower and upper limits on the panel aspect ratio (L/h) of 0.8 and 2.5 respectively. A square web plate was chosen simply because it satisfied the code prescribed limits without introducing unnecessary excess strength in the assembly that would not benefit the stated test objectives. Since the lateral strength of a web plate is primarily a function of the plate length, thickness and yield strength, a higher aspect ratio would reduce the maximum testable height of the VBEs and make it more difficult to reliably measure flexural deformation. The web plate specimen dimensions are shown in Fig. 4.12.

The actuator capacity and the thinnest readily available hot-rolled sheet (16 Ga A36) were used to determine the overall scale of the testing frame. The 16 Gage sheet is approximately 1.52 mm (0.060 inch) thick. On the basis of this panel strength and the available actuator capacity, a web plate length of 711 mm (28 inches) was determined. The 18 Ga A1008 sheet was chosen because it resulted in a L/t typically seen in design and because its material properties are quite different to the A36 specification. The 22 Ga A1008 sheet was chosen specifically for the purpose of measuring changes in the web plate tension field orientation. The thinner plate was necessary because thick plate would have required a stronger and stiffer VBE section and would have resulted in a less reliable assessment of VBE deformation using the optical tracking system. The web plate L/t ratios are 466 and 583 and 889

for the 16 Ga, 18 Ga and 22 Ga plate respectively.

4.3.3 Boundary Frame Members and Connections

In order to accurately assess the behavior of steel web plate loaded in shear, it was necessary that the supporting boundary frame have zero or negligible lateral strength and stiffness when subjected to lateral load, that way the applied load was resisted only by the web plate. For both phases of the experiment, the boundary frame was designed so that its members remained entirely elastic under the highest expected loading. For the Phase I tests, the VBEs had very high flexural and axial stiffness with respect to the web plate so that the boundary frame approximated a pin connected rigid frame and their deformations under web plate anchorage forces were negligible. For the Phase II tests the VBE stiffness was tuned to achieve a particular web plate tension field inclination angle when loaded elastically.

The boundary frame was pin connected at each of the four corners with a single 36.5 mm (1 7/16 inch) diameter steel pin. The center of each pin was aligned with the center-line of the bolt rows connecting the web plate to the boundary frame fish plate. This was done to promote a uniform strain distribution in the plate under lateral load, without excessive crimping in the corners. A large diameter pin was utilized so that no bearing or plowing deformation would occur in the connection, even at loads well in excess of the maximum expected load. The pins were machined so that each connection had less than 0.08 mm (0.003 inches) of play between the pin and the hole, thereby reducing the deformation of the assembly due to looseness in the connections to a negligible level.

4.3.4 Web Plate to Boundary Frame Connection

The plane of the web plate aligned with the center line of the HBE and VBE boundary elements so that out-of-plane rotational forces were minimized at the pinned connections. The

connection of the web plate to the boundary frame was designed so that the full strength of the plate could be developed prior to failure of the connection, and also that removal and replacement of a web plate could be carried out quickly and easily. A bolted slip-critical type connection was selected because it offered both of these advantages. Reliably welding the edge of thin steel sheet was viewed as problematic because it requires a great deal of skill. It was believed this could not be achieved for thin plates without introducing severe panel warping, and/or material embrittlement in the heat affected zone (HAZ) of the web plate near the weld. There were concerns that this type of connection may prematurely fail due to large out-of-plane deformations of the panel and low cycle fatigue tearing in the HAZ. Furthermore, removal of the plate after testing would be a laborious task requiring weld grinding and other surface preparation activities.

The adoption of a bolted connection had its share of challenges also, and these had to be weighed against those for a comparable welded connection option. The bolted connection required the punching of holes for the plate and the pre-tensioning of each of the twenty-eight bolts. Since the plates were small, the hole-punching operation was simple and could be carried out with minimal preparation. A template was fabricated out of plywood so that the holes could be located easily on each of the web plate specimens.

4.4 Design and Construction of Web Plate Test Frame

The testing frame members and connections were designed according to the LRFD principles. The "expected" strength of the web plates were used to determine demands. All members and connections were designed to remain entirely elastic for both phases of the testing program.

4.4.1 Geometry and Layout

The web plate testing frame was bolted directly to the reaction beam and was positioned with the web plate approximately 400 mm (16 in) above the strong floor surface. The plane geometry can be seen in Figs. 4.3 and 4.4 for the Phase I and Phase II tests respectively. The

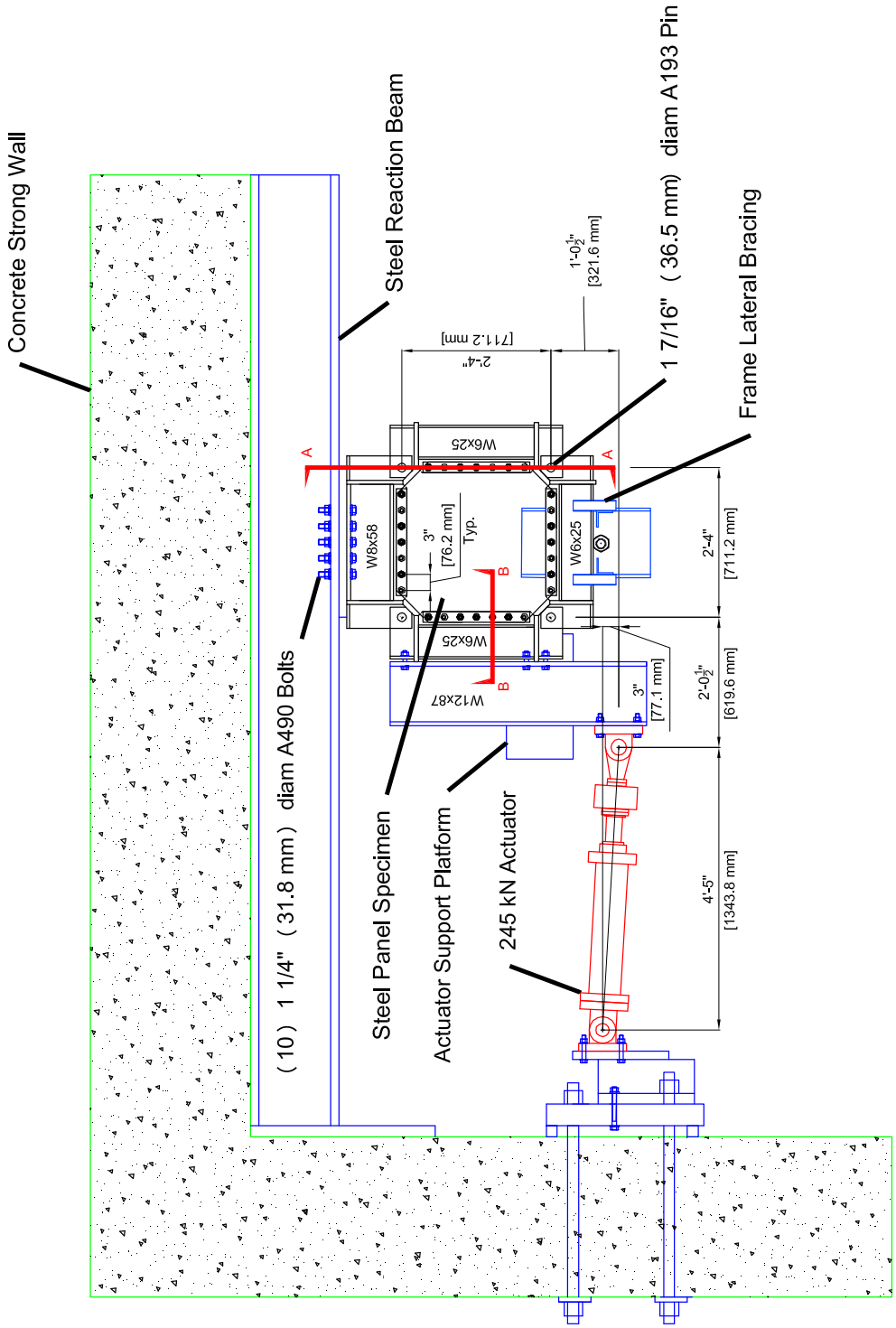

Figure 4.3: Test Assembly for the Phase I Panel Tests

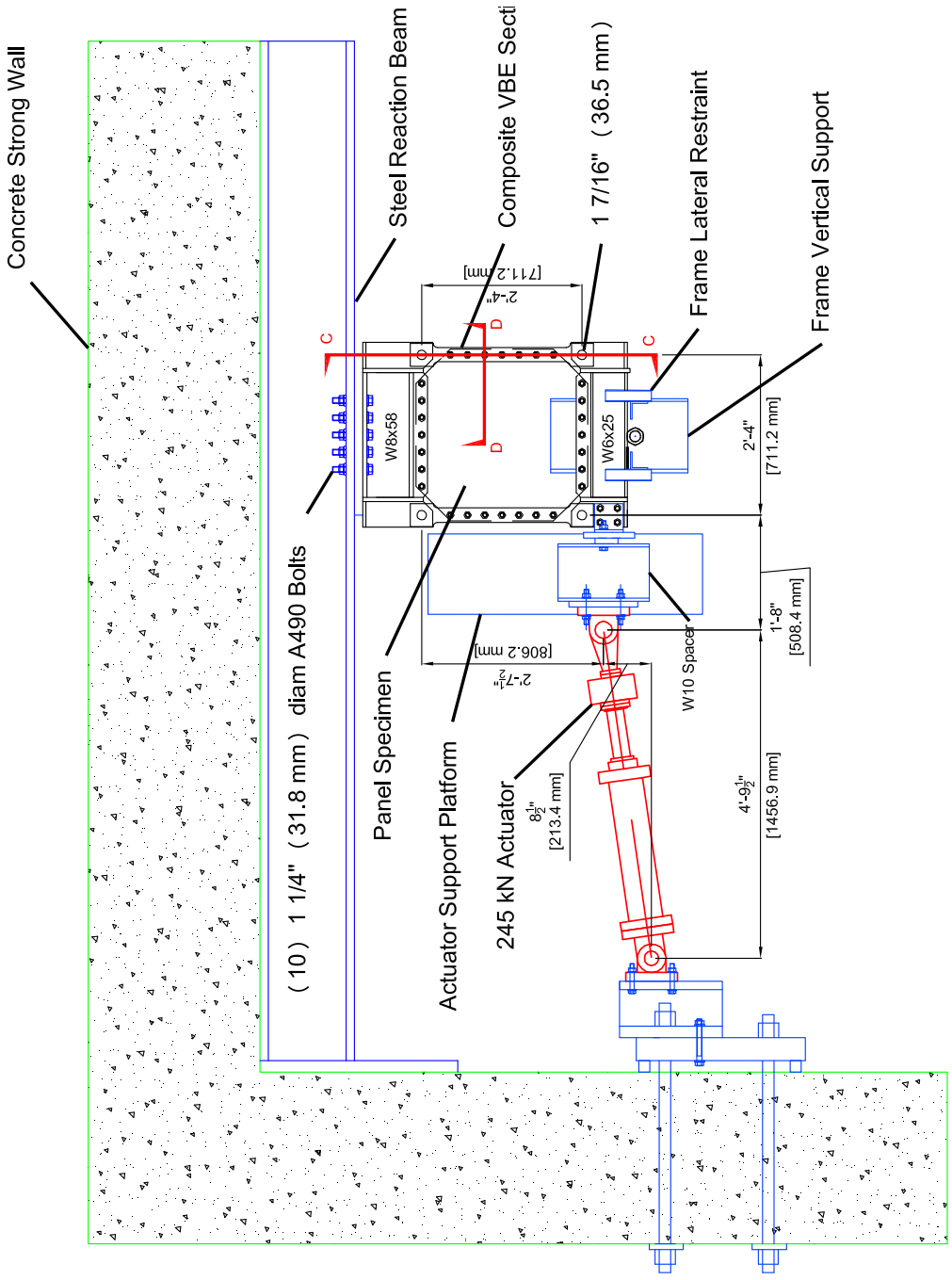

Figure 4.4: Test Assembly for the Phase II Panel Tests

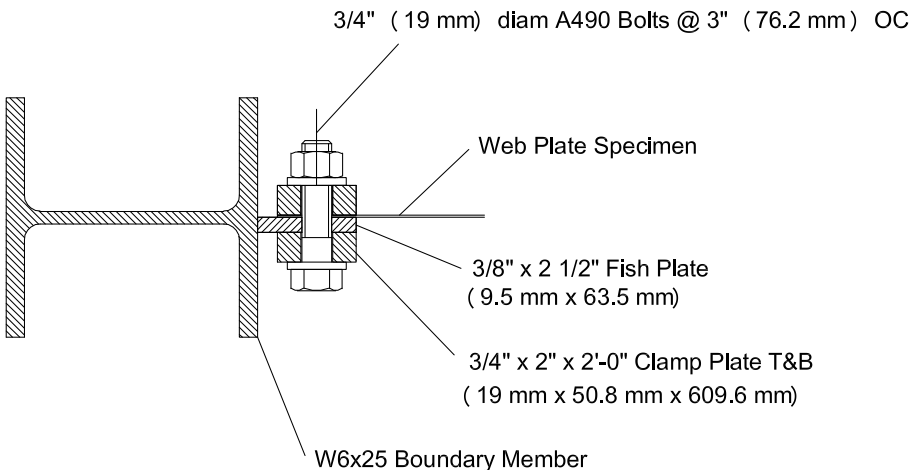

Figure 4.5: VBE Section for the Phase I Panel Tests

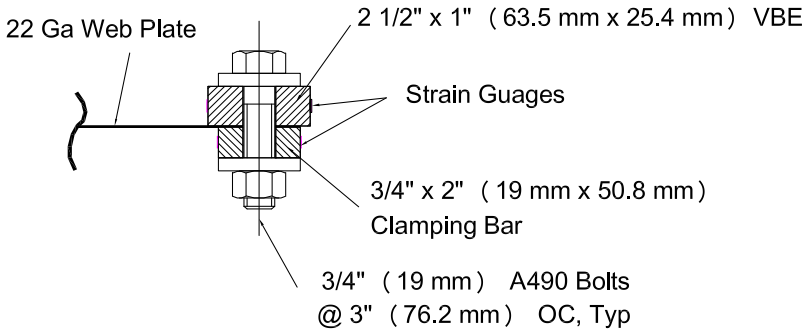

Figure 4.6: VBE Section for the Phase II Panel Tests

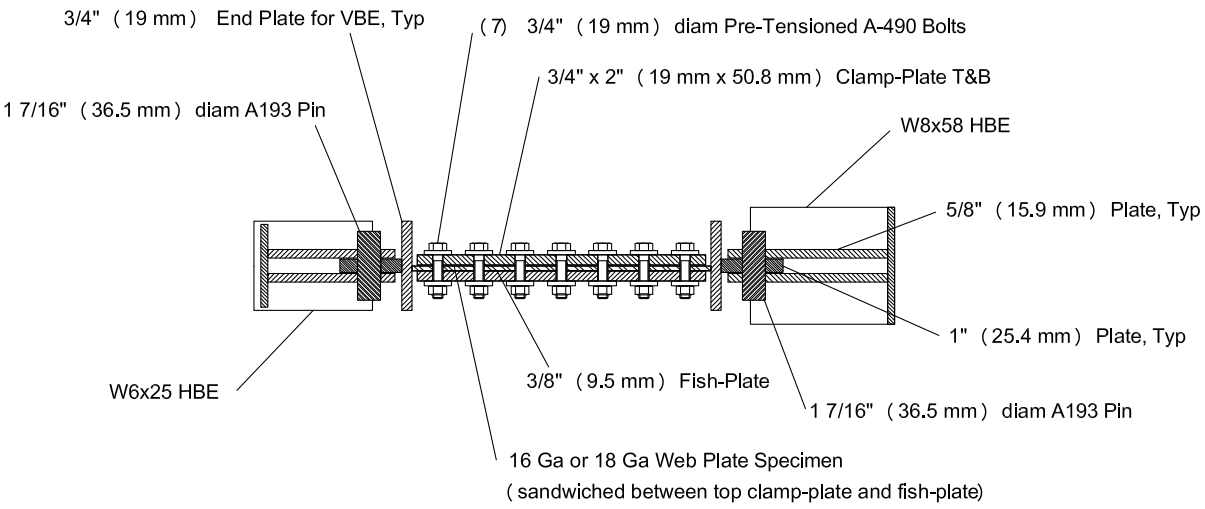

Figure 4.7: VBE Long Section for the Phase I Panel Tests

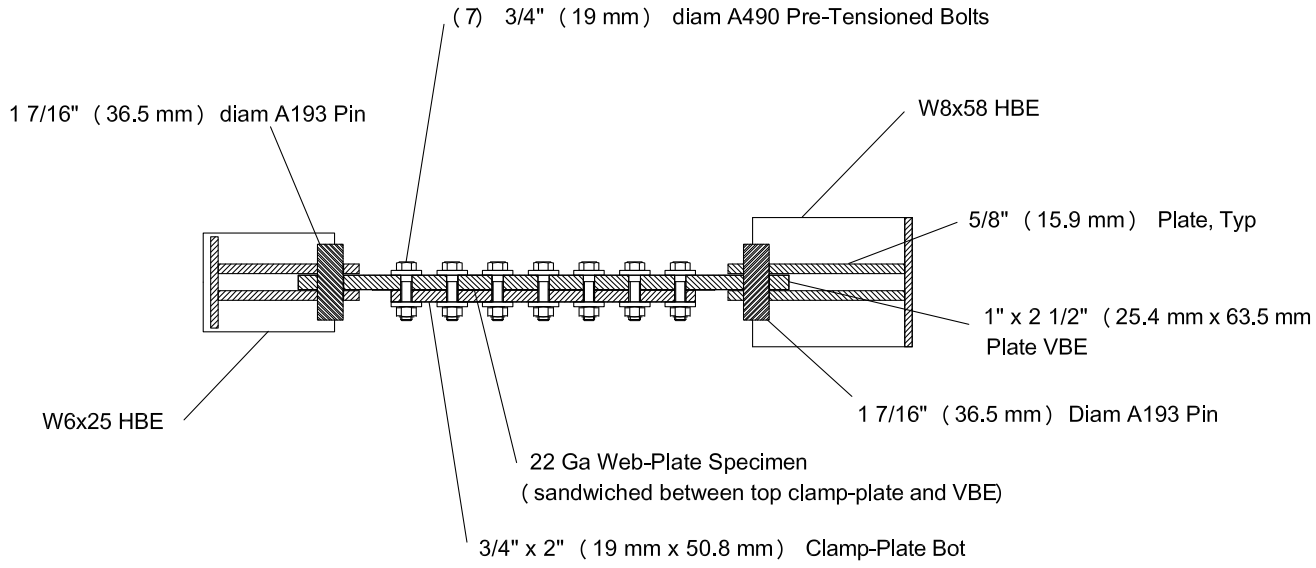

Figure 4.8: VBE Long Section for the Phase II Panel Tests

Figure 4.9: OptoTrak LED Locations for the Phase I Panel Tests

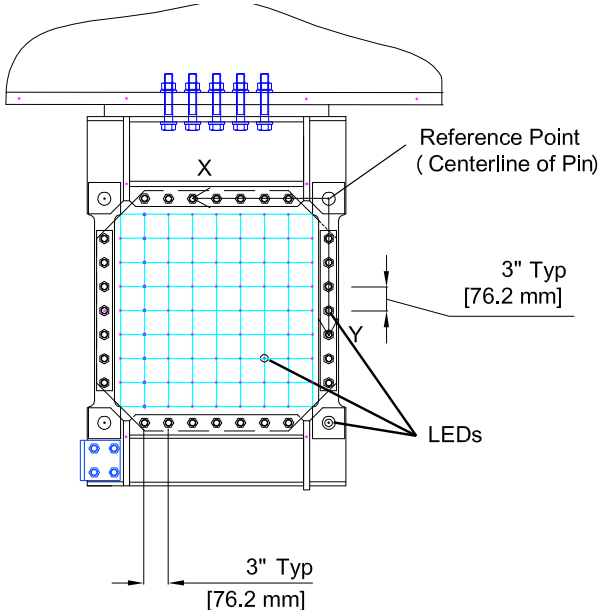

Figure 4.10: OptoTrak LED Locations for the Phase II Panel Tests

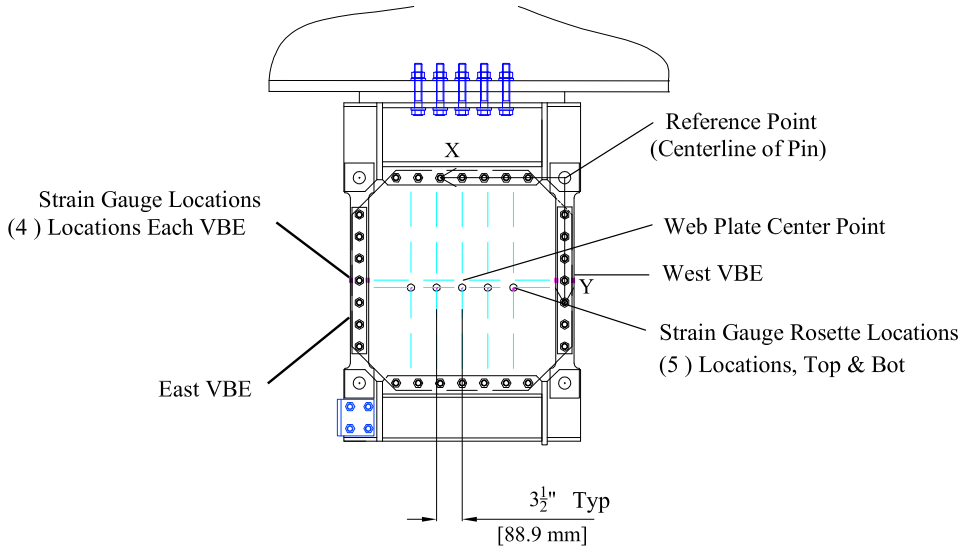

Figure 4.11: Strain Gauge Locations for the Phase II Panel Tests

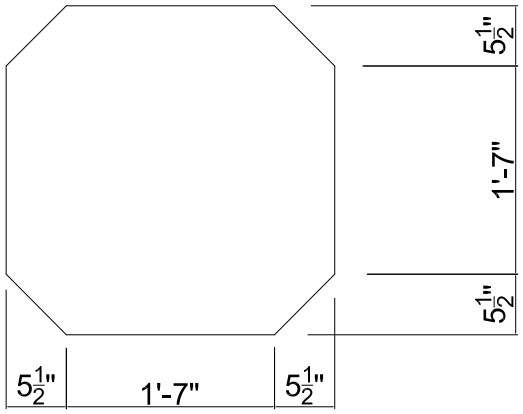

Figure 4.12: Panel Specimen Dimensions

web plate clear span between clamping plates was 648 mm (26.5 in) and the panel aspect ratio was maintained at 1.0 for all tests. The trimmed corners of the web plate resulted in a cut-out condition, which is common in SPSW construction. The free edge of the cutouts extended approximately 100 mm (4 in). This results in locally unconstrained out-of-plane behavior at the free edge when the plate buckles. Consequently, under lateral load the plate may have a tendency to fold along the diagonal of the web plate. The actuator mounting point was controlled by the available space, the location of anchorage holes in the strong wall and the the existing bolt hole group in the reaction beam.

4.4.2 Boundary Frame Connections

The boundary frame members were connected using a single 31.8 mm (1 7/16 inch) diameter by 100 mm (4 inch) long A-193 steel pin at each corner. The pins were held in place with a single 6.4 mm (1/4 inch) diameter bolt that prevented the pin from dropping through the hole. Prior to machining the pins, the holes in the W6 and W8 boundary member end plates were drilled. Each pin was then machined in an iterative manner so as to ensure a snug fit

in the final assembly. On installation, the pins were lubricated to minimize resistance to the applied displacements. See plan Figs. 4.3 and 4.4 and long section Figs. 4.7 and 4.8 showing pin locations.

4.4.3 Web Plate to Boundary Frame Connection

The web-plate to fish-plate connections were designed to prevent slip of the plate specimen at the the connection using "expected" ultimate strength, $R_t F_u$, rather than service level forces. The connection incorporated a 9.5 mm (3/8 inch) thick fish plate and a 19.1 mm (3/4 inch) thick by 50.8 mm (2 inch) wide clamping bar (CB) used to clamp the web plate to the fish plate and provide a uniform clamping pressure. The plate was attached using 19.1 mm (3/4 in) diameter A-490 bolts at 76 mm (3 in) spacing. The bolts were first installed in a snug tight condition and then fully pre-tensioned per using turn-of-the-nut method the AISC [2] using a hydraulic torque wrench. The faying surfaces in contact with the web plate specimen did not receive any special surface treatment, however this was considered in computing the slip resistance capacity of the connection. A conservative slip coefficient of 0.35 was assumed. See Fig. 4.5 for connection of the web plate to the HBEs and VBEs for the Phase I tests and for the web plate connection to the HBEs on the Phase II tests. See Fig. 4.6 for the web plate to VBE connection for the Phase II tests.

Phase II VBEs

The VBEs for the Phase II tests were flexurally very slender in comparison to the W6x25 VBEs used for the Phase I tests. These members were designed so that they remained elastic when the 22 Ga web plate strength was fully developed, and that they satisfied the intent of the minimum I_c requirement of the *Provisions*. Since the code minimum I_c is based on a fixed-end condition and the Phase II VBEs were pin ended, the minimum permissible stiffness needed to be increased by a factor of three. The 51 mm x 19 mm (2 in x 3/4 in) clamping bars used to attach the web plate to the VBEs were included in the stiffness calculation since they will bend as the VBE bends. See Fig. 4.6 for a section through the VBE. It was particularly important in these tests that the bolts be fully pre-tensioned at

the VBE connection so that no flexural slip occurred between the VBE and the clamping plate. Strain gauges were mounted on the inside and outside of the clamping bars, as well as the VBEs, to check strain levels and compute total flexural demand.

The VBEs were designed so that the elastic tension field angle, as predicted by a modified form of Eq. 3.16, is significantly less than 45 degrees. This is often the case for an SPSW designed using an approach similar to AISC Design Guide 20 [58]. The rationale behind the use of slender sections is:

- The change in the tension field angle as the plate plastifies can be measured experimentally.
- The demand on the VBEs can also be measured through experiment. This is achieved in two ways: 1) by tracking the deflected profile of the VBEs using the optical tracking system, and 2) by measuring the strains at the extreme fiber of the VBE section at midspan. Should the VBE section be too stiff, this becomes difficult to measure accurately and is obscured by experimental noise.

The modified form of Eq. 3.16 is:

$$\tan^4 \alpha = \frac{1 + \dfrac{t_w L}{2A_c}}{1 + t_w h\left(\dfrac{1}{A_b} + \dfrac{h^3}{60 I_c L}\right)} \tag{4.1}$$

The difference is a result of the change in flexural strain energy stored in the VBEs, which increases by a factor of six for the pin-ended condition. The VBE stiffness is tuned so that the predicted elastic tension field angle will be no more than approximately 37 degrees. This was verified with an *ABAQUS* model of the test prior to actually testing the plate.

4.4.4 Boundary Frame to Reaction Beam Connection

An existing bolt hole group in the reaction beam was utilized to secure the base of the boundary frame. See Fig. 4.3. The existing bolt holes are arranged in two rows of five and accommodate 31.8 mm (1 1/4 inch) diameter A-490 bolts at approximately 89 mm (3 1/2 inch) spacing. A matching arrangement of holes was provided in the W8x58 base. Ten 1 1/4 inch diameter, fully pre-tensioned A-490 bolts were used for the connection. Calculations indicated that the connection would easily accommodate the maximum expected forces with all components remaining elastic, although the amount of deformation at the connection and at the reaction beam were not computed. The elastic deformation was found to be significant enough that it needed to be accounted for when determining the actual drift and actual applied lateral load. However, the influence of this deformation on the lateral load was small.

4.4.5 Bracing and Lateral Stabilization

The boundary frame needed support and lateral restraint as the panel specimen was loaded for a maximum drift range of approximately ±6%. The frame was vertically supported at the outermost flange of the top HBE by an assembly which was anchored to the strong-floor. Figure 4.13 shows the lateral bracing scheme used for all of the tests.

The lateral bracing assembly consisted of a support made from a section of 600 mm long W12x87, with the flanges normal to the plane of the floor, with two L3x3x1/4 by 250 mm angles welded to the flanges. One leg of each angle lay in a horizontal plane. Each angle had a section of stainless steel bent plate welded to the horizontal leg to form a 75 mm by 200 mm shelf. The underside of the outermost flange of the top HBE had a profiled section of PTFE secured to it that would then bear on the stainless steel platform and allow the frame to slide over the support assembly with minimal resistance. The top side of the HBE flange was then restrained from out-of-plane (vertical) movement by a pair of 50 mm by 250 mm HSS outrigger restraints. The HSS restraints were bolted to two vertically oriented sections of L3x3x1/4 angle that were welded to the W12x87. The bolted connection

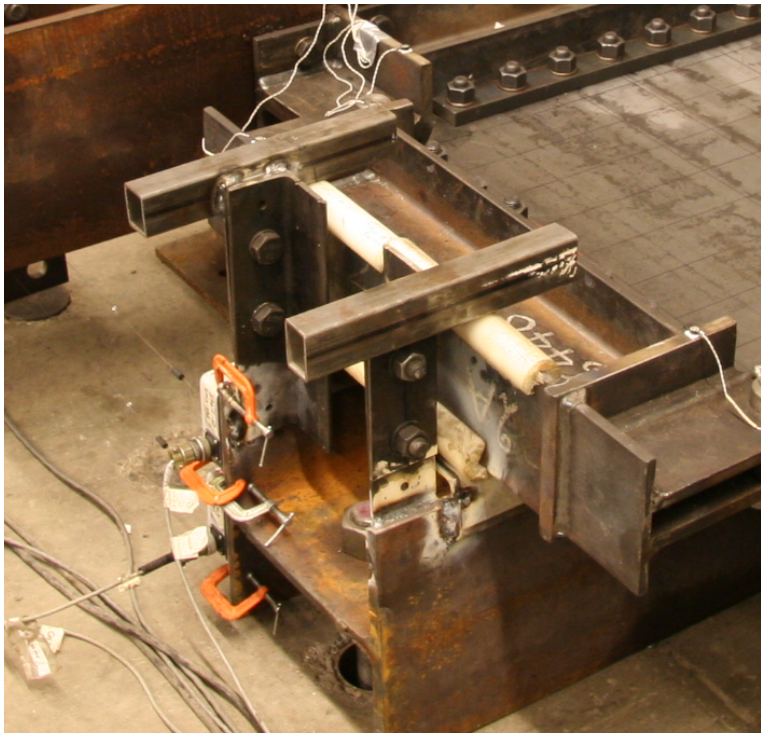

Figure 4.13: Lateral Bracing for Boundary Frame

facilitated removal of the boundary frame and for a snug fit between the restraint assembly and the boundary frame HBE. Another profiled section of PTFE was located between the top edge of HBE flange and the HSS restraints. This arrangement did not prevent all out-of-plane movement but it did ensure that the system was stable. Observations made during testing revealed that some vertical movement did occur when the thicker plates experienced snap-though behavior, but it was generally less than 2 or 3 mm.

4.4.6 Actuator Support and Mounting

Phase I

In order to efficiently transfer the actuator load to the boundary frame, a four foot long section of W12x87 was utilized. The W12x87 (referred to as the "W12 arm") was connected to the boundary frame with 19.1 mm (3/4 inch) diameter fully pre-tensioned A490 bolts

at the top and bottom of the left W6x25 VBE. Four bolts connected the W12 arm to the VBE closest to the actuator, where tensile forces on the connection would be highest. Two bolts were used to connect the W12 arm to the VBE at the bottom connection, closest to the reaction beam. See Fig. 4.3. This loading mechanism was advantageous because the long lever-arm reduced the actuator load required to yield the web plate specimen, it closed the gap between the testing frame and the actuator clevis, and permitted the actuator to be oriented almost parallel with the top W25 HBE. The flange edges of the W12 arm were supported by a rigid steel bearing plate which was secured to the strong floor. A large section of stainless steel sheet was clamped to the top of the bearing plate and functioned as the bottom surface of a frictionless bearing pad. A 6.4 mm (1/4 inch) thick sheet of PTFE was placed between the W12 arm and the stainless steel bearing surface. A generous application of lubricant was applied between the PTFE and the stainless steel bearing pad.

The actuator clevis was anchored to the outer flange of the W12 arm using four 19.1 mm (3/4 inch) diameter A36 threaded rods. The nuts were torqued with full effort of a spud wrench. At the remote end, the clevis was connected to a steel bracket mounted on the concrete strong wall with four similar A36 threaded rods. The nuts for this connection were also tightened manually to a snug condition.

Phase I

In the Phase II setup, the W12 Arm was removed and the actuator was connected to the top VBE via a 305 mm (12 inch) long section of W10x48, labeled the W10 spacer in Fig. 4.4. The W10 spacer was bolted, using a pair of 19.1 mm (3/4 inch) diam A490 fully pre-tensioned bolts, to a pair of L5x3X1/2x3/4 x 127 mm (5 inch) long angles. The angles were bolted to the end of the W6x25 VBE using four 19.1 mm (3/4 inch) diam A490 fully pre-tensioned bolts. The W10 spacer was vertically supported by the Actuator support platform with a sandwich of PTFE and stainless steel sheet between the support platform and the W10 spacer providing a low-friction gliding bearing surface.

4.5 Materials

The critical components of the test specimen, boundary frame and connecting elements are detailed below. These were selected to ensure that the testing frame remained elastic under extreme load conditions. Support platforms, brackets, bent plates and miscellaneous items were cut and assembled in the lab from available material and no material specification was available. Components that carried substantial load and were fabricated from lab stock material were designed assuming A36 material properties.

4.5.1 Boundary Frames

The top HBE and the VBEs were W6x25 sections. The bottom HBE, which was bolted to the reaction beam, was a W8x58. The HBE and VBE sections were fabricated from ASTM A992 Gr 50 steel. All other shop fabricated material, including clamping bars, fish plates, end plates and shear tabs were ASTM A36 Gr 36 steel.

4.5.2 Bolts, Pins and Rods

All bolts connecting the web plate to the boundary frame and the boundary frame to the reaction beam were ASTM A490 and utilized F436 hardened washers. All threaded rods used to connect the actuator clevis to the test frame and to the strong wall, were ASTM A36. The pins used for the pin connections between the boundary frame members were ASTM A193 Gr B7 (F_u = 100 ksi).

4.5.3 Web Plates

The web plates for the Phase I tests were 16 Ga ASTM A36 and 18 Ga ASTM 1008 SS Gr. 40. For the Phase II tests the web plates were 22 Ga ASTM A1008 SS Gr. 40. The sheet was purchased from a single commercial sheet steel supplier in 914 mm (36 inch) square sections. This allowed for some error in specimen preparation and for taking coupon samples in both directions.

Hot-rolled A36 steel sheet and cold-rolled A1008 steel sheet were used because both are

ductile and are suitable for steel plate shear wall construction. The cold-rolled A1008 sheet has mechanical properties enhanced ductility over conventional cold-rolled sheet. Hot-rolled A36, A572 and A1011 steels have been used in SPSW construction and are common steel grades used in building construction in the United States. The A1008 sheet used in these tests has very similar mechanical properties to A1011. Cold rolled sheet has been tested experimentally [7] and used in actual SPSW design but it generally has very limited ductility and is prone to fracture at relatively low strain levels.

Most commercial suppliers specify cold-rolled sheet as A366 or as A366/A1008. The ASTM A1008 specification superseded A366 after A1008 was withdrawn in 2000. The A366 specification was for commercial steel (CS). The equivalent A1008 variant appears to be A1008 CS A, B or C. This steel sheet has a broad range of specified yield strengths with a typical range specified by A1008 of 138-276 MPa (20-40 ksi). The yield strength in this case is non-mandatory, so the actual yield strength of A1008 steel may be outside this range and still satisfy the specification. The elongation at fracture for the A1008 is greater than 0.30, but once again this is a typical characteristic of this steel and is non-mandatory. The A36 specification allows for a very broad range of mechanical properties also, but has an expected yield strength of $R_y F_y$ of 323 MPa (47 ksi).

4.6 Coupon Tests

Two coupons were cut from each panel, one from each direction. The coupons were cut by water jet to a size and shape specified by ASTM A370-07a. They were tested using an Instron 600 DX Static Hydraulic Universal Testing System apparatus. The strain gauge extensometer used was an Instron 2630-115 with a gauge length of 50.8 mm (2.0 inches). This particular extensometer does not operate post-peak so no information was recorded beyond the ultimate load. For the purposes of these tests, this limitation was of no concern since accumulated plastic strains in the web plate are not expected to exceed 0.2. Furthermore, the strains measured by extensometer become less meaningful once necking initiates,

Table 4.2: Web Plate Material Properties

Test Ref	**Material**	**F$_y$ (MPa)**	**F$_u$ (MPa)**	**F$_u$/F$_y$**	**E (MPa)**
1-16	A36	388	450	1.161	202,000
2-16	A36	391	450	1.151	196,000
3-16	A36	367	438	1.193	179,800
1-18	A1008	218	322	1.475	153,700
2-18	A1008	218	326	1.496	151,100
3-18	A1008	298	364	1.221	173,400
1-22	A1008	285	378	1.327	190,000
2-22	A1008	287	382	1.330	151,000
3-22	A1008	287	373	1.300	163,500

and this generally happens well before the ultimate load is attained. Coupon dimensions are shown in Table 4.3. The plate material properties determined by analyzing coupon test results are shown in Table 4.2 and the stress-strain curves for the 16 Ga and 18 Ga coupons are shown in Figs. 4.14(a) through 4.14(f). The 22 Ga coupons are shown in Figs. 4.15(a) through 4.15(c). The F_y reported for the 16 Ga plate is the lower yield point and is computed as the average of the stress values on the plateau. The F_y reported for the 18 Ga plate is the 0.2% proof stress because there is no discernible yield plateau. Both the yield stress F_y and the ultimate stress F_u are engineering or nominal stress quantities. The Elastic modulus is computed by determining the initial slope of each stress-strain function.

Table 4.3: Coupon Data

Coupon Ref	**Gage**	**w (mm)**	**t (mm)**	**Material Spec**
16-1T	16	12.80	1.47	A36
16-1L	16	12.88	1.47	A36
16-2T	16	12.78	1.46	A36
16-2L	16	13.03	1.46	A36
16-3T	16	13.03	1.46	A36
16-3L	16	12.85	1.46	A36
18-1T	18	12.85	1.12	A1008
18-1L	18	12.95	1.12	A1008
18-2T	18	12.98	1.14	A1008
18-2L	18	12.95	1.14	A1008
18-3T	18	12.98	1.12	A1008
18-3L	18	12.88	1.12	A1008
22-1T	22	12.59	0.71	A1008
22-1L	22	12.52	0.71	A1008
22-2T	22	12.62	0.71	A1008
22-2L	22	12.62	0.71	A1008
22-3T	22	12.64	0.71	A1008
22-3L	22	12.62	0.71	A1008

Prior to testing, the thickness and width of each coupon was measured using a digital micrometer. These measurements are shown in Table 4.3. The thickness of each of the specimens was generally consistent with the gauge designation, although some variability is noted. This is partly attributable to variations in actual thickness, and partly due to the imprecise nature of dial gauge measurements.

Since careful application of material properties is important to the objectives of this experimental program, the stress-strain data are presented in tabular and graphical form for both directions in each panel. The stress-strain curves are presented as engineering stress versus engineering strain.

16 Ga Plate:

The stress-strain curves for the 16 Ga plates tested show some unusual behavior, not typical of A36 steel: 1) the yield plateau for all specimens is very long, generally between 0.04 and 0.05 mm/mm. Typical A36 steel has a strain at initiation of strain hardening ε_{sh} between 0.01 and 0.015 mm/mm. 2) although the shape and magnitude of the upper yield point is typical of A36 steel, the yield plateau is not very stable and tends to fluctuate excessively compared to normal A36 behavior. This effect will tend to average out over the whole plate and with the presence of residual stresses, material impurities and microscopic imperfections will soften the transition from the elastic to the plastic state. 3) the ratio of ultimate stress F_u to the averaged yield stress F_y is very low. Typical A36 steel has an F_u to F_y ratio between 1.3 (sheet) and 1.5 (plate). The 16 Ga specimens tested had ratios between 1.15 and 1.19, well below typical range for A36 steel.

18 and 22 Ga Plate:

The stress-strain curves for the 18 Ga and 22 Ga specimens indicate typical behavior exhibited by cold-rolled A1008 carbon steel sheet. It is worth noting that for the 18 Ga sheet there is no discernible yield point or plateau but the 22 Ga sheet appears to have a distinct yield plateau. There is some softening visible prior to the first yield and the length of the

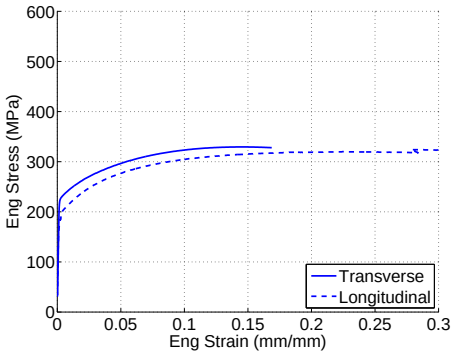

(a) Test #1-18

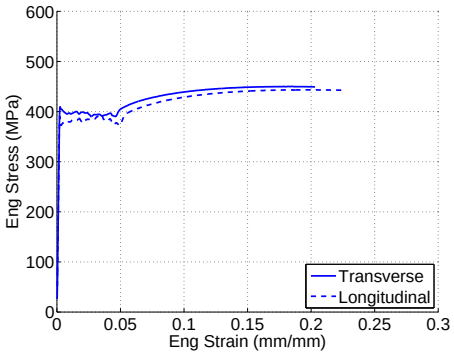

(b) Test #1-16

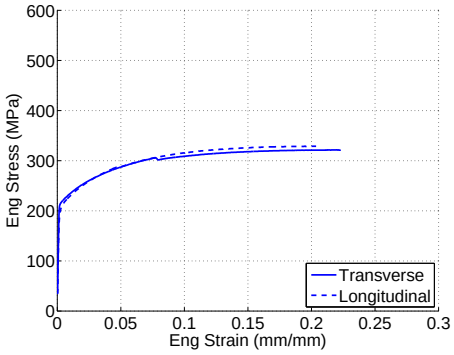

(c) Test #2-18

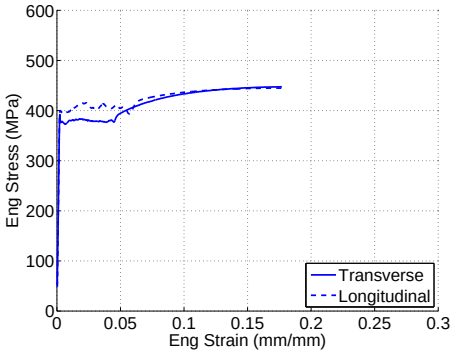

(d) Test #2-16

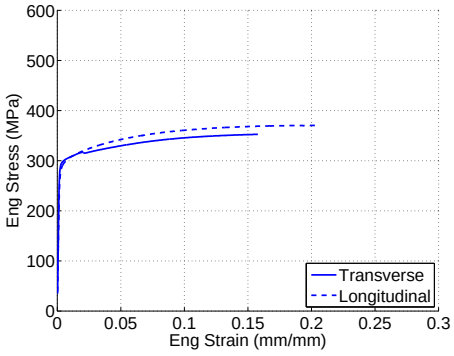

(e) Test #3-18

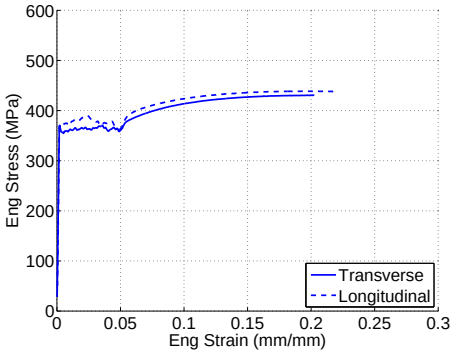

(f) Test #3-16

Figure 4.14: Stress-strain curves for 16 Ga and 18 Ga specimens

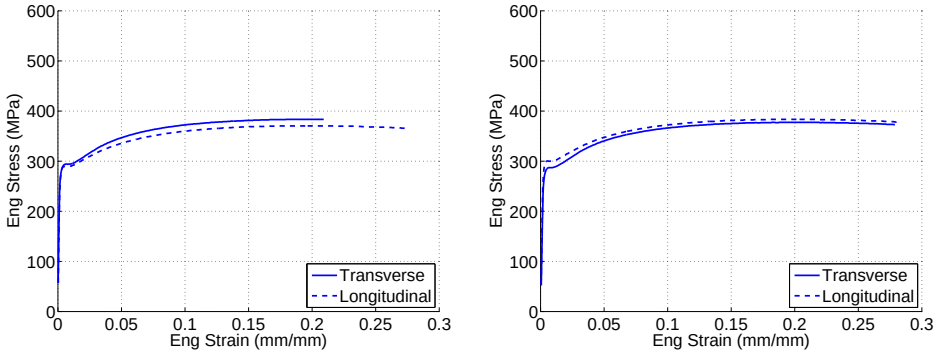

(a) Test #1-22

(b) Test #2-22

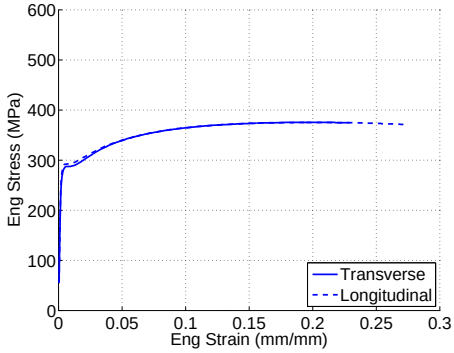

(c) Test #3-22

Figure 4.15: Stress-strain curves for 22 Ga specimens

yield plateau is between approximately 0.005 and 0.01 mm/mm. Cold-rolled plate can be quite brittle with a very low strain at failure, so it was important to test steel panels that exhibited good ductility.

4.7 Control, Data Acquisition and Instrumentation

Each phase of testing utilized a custom-built load frame equipped with a 245 kN (±55 kip) actuator having a ±127 mm (±5 inch) stroke and built-in displacement transducer. The actuator was controlled by an MTS 442 controller. A 489 kN (110 kip) load cell was mounted between the clevis and the actuator piston. Two string pot (spec) extensometers were also used to measure displacements of the frame but served only as a backup. The string pots proved to be unreliable and were abandoned part way though the experimental program in favor of the OptoTrak optical tracking system.

4.7.1 Instrumentation

The instrumentation consisted of the Northern Digital Instruments (NDI) OptoTrak system, two string pot extensometers, one Duncan linear extensometers, and high elongation strain gauges.

4.7.2 Data Acquisition System

The data acquisition system was controlled through a personal computer using Windows based software LabVIEW version 7.l. The instrumentation controlled through LabVIEW included strain gauges, potentiometers, and a single 445 kN (100 kip) load cell. The information from the OptoTrak was controlled through another computer that housed the NDI software. Calibration factors were necessary for the strain gauges, potentiometers, and load cell to convert the measured changes in voltage to physical quantities of strain, displacement, and axial load. The available data channels were organized and labeled within the program and stored for each test for efficient data analysis. Data was recorded at a rate of

2 Hz. All recorded values were stored in a tab delimited data file, which was then processed and analyzed with Matlab and Microsoft Excel. National Instruments hardware was used for the data acquisition of the instrumentation controlled through LabVIEW.

4.7.3 Optical Tracking

Lateral in-plane displacements of the frame and out-of-plane displacements of the panels were measured in real time using the *Certus HD OptoTrak* optical tracking system manufactured by NDI. This system utilizes a position sensor which triangulates the position of several light emitting diodes (LEDs) using three infrared cameras mounted on a tripod. The system has an accuracy of 0.1 mm RMS (0.00394 inch) for the x and y directions (in the plane of the web plate) and 0.15 mm (0.0059 inch) in the z direction, normal to the plane of the web plate.

The system comprised a single position sensor, a system control unit (SCU), infrared light emitting diodes (LEDs), and devices referred to as strobers which connect the markers to the SCU. The LED markers were fixed to the web plate and boundary frame using double sided tape. Markers were also placed on the reaction beam to measure deflection away from the strong-wall as load was applied to the test specimen.

Once the user has positioned the markers appropriately, the OptoTrak system is connected. The NDI software is then started using the configured host computer which is linked to the SCU and communicates with the connected strobers and position sensors. The strobers then activate the markers and the position sensors detect their infrared light emissions. The position sensors then return the position data of the markers to the SCU, at which point the SCU processes this raw data and returns it to the host computer (NDI 2005).

The NDI OptoTrak system was utilized for all of the tests carried out as part of this experimental program and Table 4.4 shows the location of the LEDs for each test. Test #1-18 and #1-16 included a symmetrical 76 mm (3 inch) grid of LEDs on the web plate

Table 4.4: NDI OptoTrak LED Locations

Phase	**Test Ref #**	**LED Locations**
1	1-16	On frame and web plate
1	2-16	On frame only
1	3-16	On frame only
1	1-18	On frame and web plate
1	2-18	On frame only
1	3-18	On frame only
2	1-22	On frame and web plate
2	2-22	On frame and web plate
2	3-22	On frame and web plate

in addition to several LEDs placed around the boundary frame and on the reaction beam. Tests #1-22 through #3-22 had a similar arrangement of LEDs. The remaining tests (three through six) had LEDs only on the boundary members and the reaction beam so that drift and displacements could be tracked.

Frame drift was calculated by measuring the change in angle between the north-south and east-west oriented boundary members. This method enabled an accurate assessment of the true frame drift and permitted easy and accurate real-time updating of the effective lateral load based on current deformed geometry, which included rigid body rotation of the assembly about the base.

4.7.4 Strain Gauges

High elongation strain gauges were used for the Phase II Tests (#1-22 through #3-22) with the 22 Ga web plate. The gauges were 5 mm long, high elongation type YFLA-5-5L manufactured by Tokyo Sokki Kenkyujo Co, Ltd. The gauges are rated to a strain of $\pm 2\%$.

All surfaces to receive strain gauges were cleaned with several applications of emery paper and a water based alkaline cleaning solution followed by an application of water based acid cleaning solution and emery paper. The surface was then cleaned with distilled water and dried to remove excess moisture. The gauges were adhered using Cyanoacrylate adhesive (type CN) for TML strain gauge applications. Great care was taken to ensure that the strain gauge rosettes were installed at exactly the same location on the top and underside of each web plate. Precise marks were made on each side so that the gauges could be positioned correctly.

Web Plate Strain Gauge Rosettes

Five strain gauge rosettes were mounted on the top and under-side of each panel to measure in-plane membrane strains. Each rosette comprised three individual 5 mm high elongation strain gauges arranged in a 45 degree rosette configuration with zero degrees oriented parallel with the HBEs. The curvature of the buckled plate significantly influences the strains measured at the surface of the plate when the out-of-plane deformations are high. At a drift of 1.5% it is estimated that the flexural strain associated with the primary buckles can have a magnitude as high as 40% of the strain in the direction of the principal tension. Only the in-plane component of web plate strain was of interest. It was therefore necessary to install rosettes on the underside of the panel in exactly the same location as those positioned on top of the panel. The in-plane strain was then computed as the average of the two strain readings, theoretically eliminating the strain associated with out-of-plane flexural deformations of the plate. The rosettes were installed 25.4 mm (1 inch) below the mid-height of the panel, at a spacing of 88.9 mm (3 1/2 inch) with the middle gauge located centrally as shown in Fig. 4.11. The reason for moving the gauges down slightly from the middle of the plate was to avoid obstructing the OptoTrak LEDs that were arranged on a symmetrical 76.2 mm (3 inch) grid.

VBE Strain Gauges: Phase II tests only

Strain gauges were installed at midspan on the inside and outside of the VBE bar and clamping plate to measure flexural and axial strains in the VBEs. These strains would then be used to compute stresses and later converted to midspan axial force and bending moment.

4.7.5 String Potentiometers

Two string potentiometers (POTs) were installed at the underside of the boundary frame and oriented parallel with the direction of frame HBE. The POTs were placed in parallel and positioned to measure the total displacement at the top of the frame. Two devices were used to ensure data would still be collected should one fail. The ends of the POTs were connected to the W12 arm and the housing was clamped to the top of the stationary support frame. Data was recorded only for Tests #1-18, #1-16 and #2-18. The POTs proved to be time consuming to install and calibrate, and did not give entirely reliable results. Both POTs had a tendency to stick-slip and sometimes recorded jagged data. Although the potentiometers recorded uninterrupted data, the displacements measured by the two instruments differed by as much as 10% in some instances, even when the frame drift was moderate. This discrepancy was unacceptable and resulted in the abandonment of the string potentiometers in favor of the OptoTrak which could measure real-time displacements in 3D to an accuracy of 0.1 mm. Furthermore, the string potentiometer is only capable of measuring linear displacement and could not be used to simultaneously track boundary frame base rotation, nor could it directly measure the small but not insignificant displacement components perpendicular to the axis of the string, which was an unavoidable consequence of the test configuration. This behavior would have required several more string and/or Duncan pots, and confidence in the performance of the OptoTrak system was high.

Chapter 5

EXPERIMENTAL OBSERVATIONS AND PRELIMINARY DATA ANALYSIS

The experimental program consisted of nine individual cyclic tests. The first six tests were designed to examine material hardening and hysteretic behavior. Tests #1-18, #2-18 and #3-18 used 18 Ga A1008 web plate. Tests #1-16, #2-16 and #3-16 used the 16 Ga A36 plate. Tests #1-22, #2-22 and #3-22 were designed to examine the tension field re-orientation behavior and VBE demand and required the substitution of the slender VBE section and the 22 Ga A1008 plate.

Each test was carried out quasi-statically using saw-toothed displacement patterns under displacement control. The time required for a full cycle varied depending on the amplitude of the cycle and the test, but it was generally kept between forty seconds and five minutes. The long cycle time made it easy to capture abrupt changes in the tension field. The actuator control permitted manual interruption and continuation of loading at the discretion of the operator. The tests were frequently paused to examine the specimen, take photographs and note significant changes.

An analysis and summary of the snap-through and unloaded shear strengths of the web plates is presented at the end of the chapter.

5.1 Bare Frame Testing

The bare frame for Tests #1-16 through 3-18 was loaded to verify that the resistance offered by the pinned frame was negligibly small in comparison to the peak loads observed in the 22 Ga plate test, the weakest of the panel specimens. The frame resistance was observed to be of constant magnitude with varying displacement (approximately 0.60 kN) up to 0.06 radians drift in each direction.

5.2 Loading Protocol

Since the goal of the experimental program was to establish a link between fundamental material properties and observed behavior, no established displacement protocol was followed for the cyclic tests. Many loading protocols have been developed for steel components and many of these would have been acceptable for this experimental program. However, since web plate fracture and accumulated damage were not to be included in the numerical model, the number of cycles at each drift level was set to two, rather than the typical three cycles used in many loading protocols. As implied, the reduced number of cycles was purposely selected to reduce the risk of plate fracture and load degradation observed in past experiments allowing investigation of the fundamental behavior of the web plate over a larger range of drifts. Furthermore, the experiments were not used to assess component behavior for development of seismic response quantities so the need for close adherence to an established protocol, though preferable in some ways, was not strictly necessary.

For the Phase I tests, a displacement sequence was chosen that resembled the ATC 24 protocol [4] but with only two cycles at each amplitude. The target displacements for Tests #1-18 through to #3-16, as a fraction of the expected yield displacement, are shown in Table 5.1. The target displacements for Tests #1-22, #2-22 and #3-22 through to #3-16 are shown in Tables 5.2, 5.3 and 5.4 respectively.

Table 5.1: Target Displacement Amplitudes for Tests 1-18 to 3-16 (Phase I)

Half Cycle #	**(fraction of δ_y) Amplitude**
1-4	0.25
5-8	0.50
9-12	0.75
13-16	1.00
17-20	1.5
21-24	2.0
25-28	3.0
29-32	4.0
33-36	5.0

Table 5.2: Target Displacement Amplitudes for Test 1-22 (Phase II)

Half Cycle #	**(fraction of δ_y) Half Cycle Amplitude**
1-2	$\pm$0.25
3	3.0
4	0
5-10	$\pm$4.0

Table 5.3: Target Displacement Amplitudes for Test 2-22 (Phase II)

Half Cycle #	**(fraction of δ_y) Half Cycle Amplitude**
1-2	±0.25
3-8	±6.0

Table 5.4: Target Displacement Amplitudes for Test 3-22 (Phase II)

Half Cycle #	**(fraction of δ_y) Half Cycle Amplitude**
1-6	±0.25
7-12	±0.50
13-16	±0.75
17-22	±1.0
23-28	±1.5
29-34	±2.0
35-40	±3.0
41-46	±4.0

5.3 Base Rotation, Load and Drift Correction (Transfer Functions)

On examination of photgraphs taken during the second test (Test #1-16), movement of the reaction beam was clearly visible when comparing the position of the assembly at maximum push stroke to that at maximum pull stroke. Some flexing in the W8 flanges at the bolted connection was also observed. The total movement at peak load was small, typically less than 2-3 mm away from the strong-wall but equated to an equivalent base rotation of as much as ±0.4 %, and a net translation away from the strong-wall of approximately 1 mm. Due to this base movement, it was not possible to precisely match the target drifts shown

in Table 5.1, particularly at low drift levels. The actual drifts attained were invariably lower than the target drifts. Adjustments were made for subsequent tests to compensate for this movement but an exact match between target drift and actual drift was not achieved. Both the reaction beam movement and the W8 flange flexing were entirely elastic and the deformation was fully recovered when the load was removed. Figures 5.1 and 5.2 show an exaggerated state of frame deformation for the Phase I tests (16 & 18 Ga plate) and the Phase II tests (22 Ga plate) respectively. Table 5.5 shows the target and actual drift levels attained for Test #1-18 and Test #1-16.

The movement at the support also had to be accounted for when computing the effective applied web plate shear force, because the movement influenced the orientation of the actuator axis with respect to the frame HBE axis. The effect on force was not substantial, but it was relatively easy to implement the correction. It was possible to accurately compute every aspect of the frame deformation at a user specified sampling frequency, typically 2 Hz, by placing LED markers at specific points on the boundary frame members. The drift, α, was computed at every time point by deducting the mean inclination angle of the HBEs, β, from the mean inclination angle of the VBEs, θ.

For both phases of the experiment the axis of the actuator rotated slightly as the frame displaced from the positive and negative directions of loading. The amount of rotation could have been minimized, and the effect neglected, by setting the initial position of the actuator parallel with the top HBE in the zero displacement (neutral) position. It was neither practical nor feasible to position the actuator so that it was exactly parallel with the top HBE when in the neutral position, and the initial inclination, γ, was different for the Phase I and Phase II tests. In the neutral position γ is approximately 3.24 degrees for Phase I, and 8.41 degrees for Phase II tests. This was an unavoidable consequence of the geometric constraints associated with the attachment of the actuator to the strong wall, but could be accommodated though a transformation of the load (recorded by the actuator load cell) to a web plate shear force. The change in the applied force due to the actuator

Table 5.5: Target and Actual Drift Amplitudes for Tests #1-18 and #1-16 (Phase I)

		Test #1-18	**Test #1-16**
Cycle #	**Target Drift (%)**	**Actual Drift (%)**	**Actual Drift (%)**
1	0.25	0.0806	0.077
1	-0.25	-0.0179	-0.0528
2	0.25	0.0766	0.0797
2	-0.25	-0.0175	-0.0517
3	0.5	0.186	0.1459
3	-0.5	-0.044	-0.0789
4	0.5	0.2205	0.1482
4	-0.5	-0.0417	-0.0749
5	0.75	0.349	0.2266
5	-0.75	-0.0661	-0.0989
6	0.75	0.3722	0.2267
6	-0.75	-0.0615	-0.0969
7	1	0.5365	0.3103
7	-1	-0.1364	-0.1489
8	1	0.5532	0.314
8	-1	-0.1315	-0.1398
9	1.5	1.0334	0.4796
9	-1.5	-0.5098	-0.2417
10	1.5	1.0059	0.4808
10	-1.5	-0.5082	-0.2446
11	2	1.4995	0.7494
11	-2	-0.9429	-0.455
12	2	1.4913	0.756
12	-2	-0.9313	-0.4493
13	3	2.5184	1.7335
13	-3	-1.8347	-1.3529
14	3	2.4997	1.7426
14	-3	-1.8124	-1.3386
15	4	3.5291	2.7331
15	-4	-2.7494	-2.2489
16	4	3.5455	2.6879
16	-4	-2.7616	-2.3006
17	5	4.1995	3.3365
17	-5	-3.6738	-3.2175
18	5	4.1806	3.319
18	-5	-3.7076	-3.3029

orientation change was very small ($< 1\%$). At each stage of the displacement time-history, the geometry of key points were computed using the NDI system and the applied load measured by the load cell appropriately modified. The result is a non-linear relationship between the load-cell load and the actual applied load that would be observed if the panel were loaded along an axis colinear with the axis of the top HBE. This calculated load is used in reporting load-displacement history.

The equation used for the Phase I tests to convert the load in the load cell to an equivalent panel load F_{panel}, is as follows:

$$F_{panel} = F_{Act}\frac{R\big(\cos(\Omega-\alpha)\cos(\beta-\gamma)+\sin(\Omega-\alpha)\sin(\beta-\gamma)\big)}{C\cos\alpha} \tag{5.1}$$

The Phase II tests have the following relationship between F_{panel} and F_{Act}:

$$F_{panel} = F_{Act}\cos(\beta-\gamma) \tag{5.2}$$

Where F_{panel} is the lateral force resisted by the panel and reported in the hysteresis curves, and F_{Act} is the force measured in the load cell. Refer to Figs. 5.1 and 5.2 for definition of the angles and dimensions.

5.3.1 Drift Calculation

Frame drift was computed using data collected from LED markers placed in several locations on the boundary frame. In this way that the orientation of each member could be computed at each point in time. For Tests #1-18 and #1-16 however, markers were placed only on the left VBE and top HBE. On all other tests they were placed on all members and the HBE and VBE orientations were averaged to obtain the "true" drift.

The frame drift was calculated as the difference in the change in orientation of the HBEs with respect to the VBEs. To do this it was necessary to compute the change in orientation of each HBE with respect to its initial configuration, and find the mean of the two angles. The same was done for both VBEs. The drift was then simply the difference between these

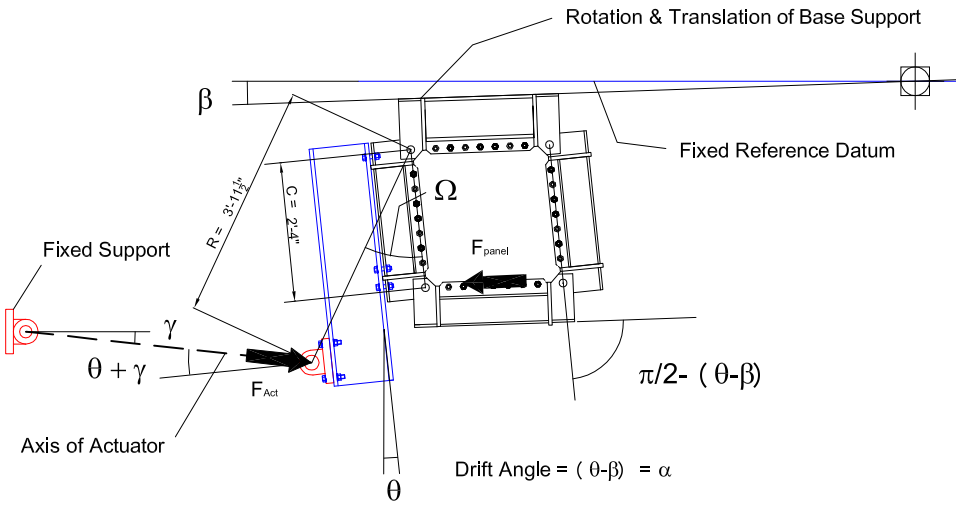

Figure 5.1: Frame Drift Kinematics for the Phase I Tests

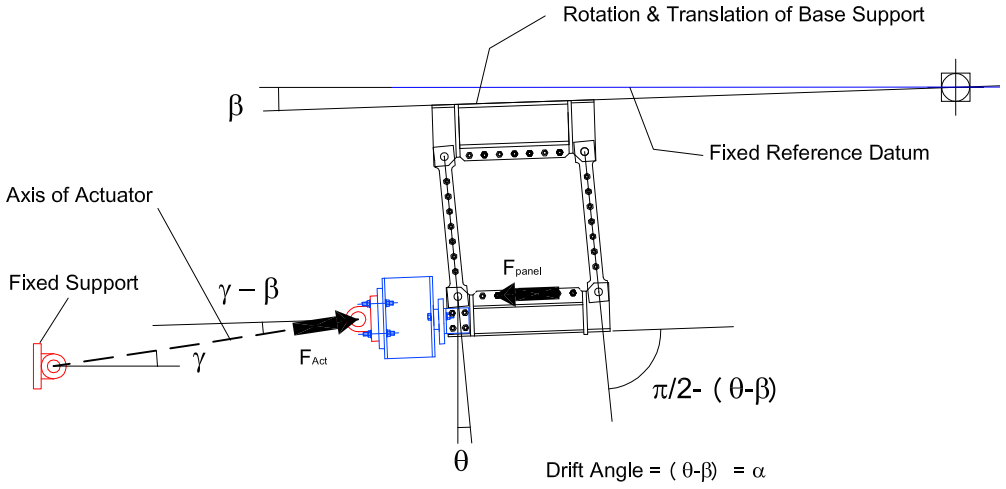

Figure 5.2: Frame Drift Kinematics for the Phase II Tests

two mean values. The HBEs and VBEs remained essentially parallel, so it should have been possible to do this calculation with only one VBE and the HBE closest to the actuator. However, slight differences were observed in the computed orientation of each VBE (the same was observed of the HBEs), consequently the mean value was used.

5.4 Phase I Test Results and Observations

Tests #1-18 and #1-16 are documented in detail. The NDI optical tracking system was used to track out-of-plane web plate deformations for both tests. The deformation was processed and the results presented as a series of contour plots at various stages of the loading sequence. These contour plots are presented in several figures that are included in the body of the discussion on experimental observations. Deformation amplitudes (z direction) are shown on the plots in mm units, and are measured with respect to the original unloaded configuration, ie. the initial imperfection was deducted from the deformed shapes. The positive and negative values represent displacement vertically up and down respectively. The x and y plan units are also presented in mm and are measured with respect to the X-Y axes shown on Fig. 4.9 with the origin at the corner LED.

As discussed, the web plate initial imperfections were removed from the contour plots. Fig. 5.3 shows the imperfections as measured using the OptoTrak system prior to testing for Tests #1-18, #1-16, #2-22 and #3-22. These imperfections are measured with respect to a plane which may not be parallel with the plane of the plate. (In this figure, and the contour plots that follow, the out-of-plane deformations were measured using the OptoTrak system using the grid of LED targets that are shown in Fig. 4.10. The contours are generated using the contour function in Matlab.) The geometry of the fish plate boundary has a bigger influence on the state of initial imperfection than any inherent plate imperfection. This is clear on examination of these plots. The imperfections generally range from 1 to 3 mm over the span of the web plate.

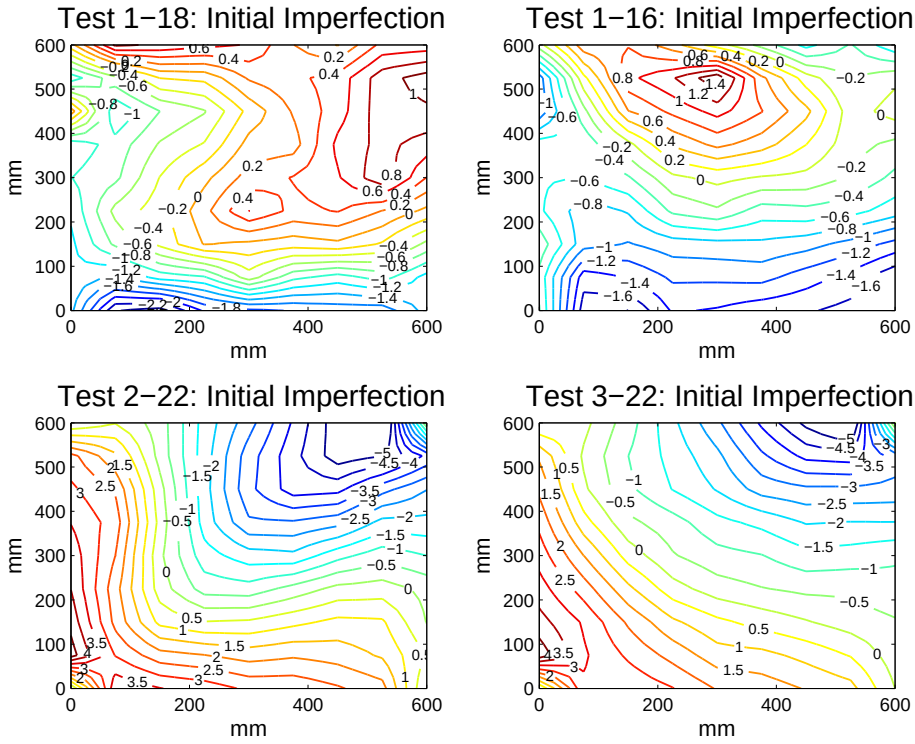

Figure 5.3: Web plate initial imperfections

Pertinent details of Tests #2-18, #3-18, #2-16 and #3-16 will be presented where the behavior differed from the first test for each plate thickness. The OptoTrak system was not used to track web plate deformation for these tests.

5.4.1 Test #1-18

Test #1-18 was the first of the Phase I tests for the 18 Ga plate. The OptoTrak target LED layout for this test can be seen on Fig. 4.9. The actual drift amplitude history in Fig. 5.4 shows an asymmetric shift towards the pull (positive) direction with limited drift in the push (negative) direction of loading before cycle #10 and an offset of approximately 0.5% towards the push direction for the cycles that follow. The running median also tends to migrate towards the pull direction. This is not a serious limitation given the objectives of the testing program, but needs to be accounted for when modeling the response in ABAQUS.

The hysteresis curve for Test #1-18 is shown in Fig. 5.5. The red circles indicate occurrences of snap-through behavior which was determined by an algorithm that detects significant and rapid changes in out-of-plane deformations recorded by the LEDs on the web plate. The hysteresis shows pinched but stable behavior. The strength of the plate appears to have not been fully activated, even at 4% drift, as no load degradation is evident. The unloaded shear strength of the plate is between 16 kN and 25 kN depending on the cycle number, or approximately 14 to 21% of the peak load attained. An analysis of unloaded shear and snap-through strength ratios is provided at the end of the chapter.

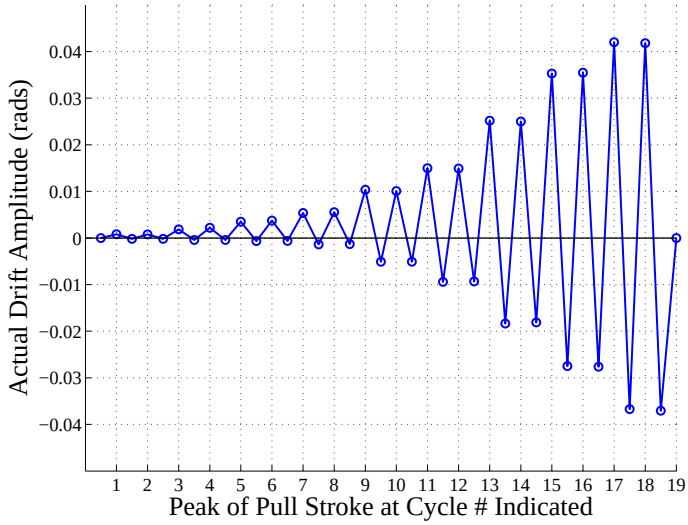

Figure 5.4: Test #1-18 Actual Frame Drift History

The asymmetry is attributed to a pre-load of approximately 5.8 kN (1.3 kips) that existed in the actuator prior to the first cycle and represents the zero displacement position. This was not noticed until after the test was complete. Examination of the LVDT record and the displacement of key LED markers shows that the desired displacement protocol was successfully applied, and very accurately. However, imposing a symmetric displacement protocol does not necessarily result a symmetric frame drift (due to movement at the base support). The pre-load will advance nonlinearities on the pull stroke more than on the

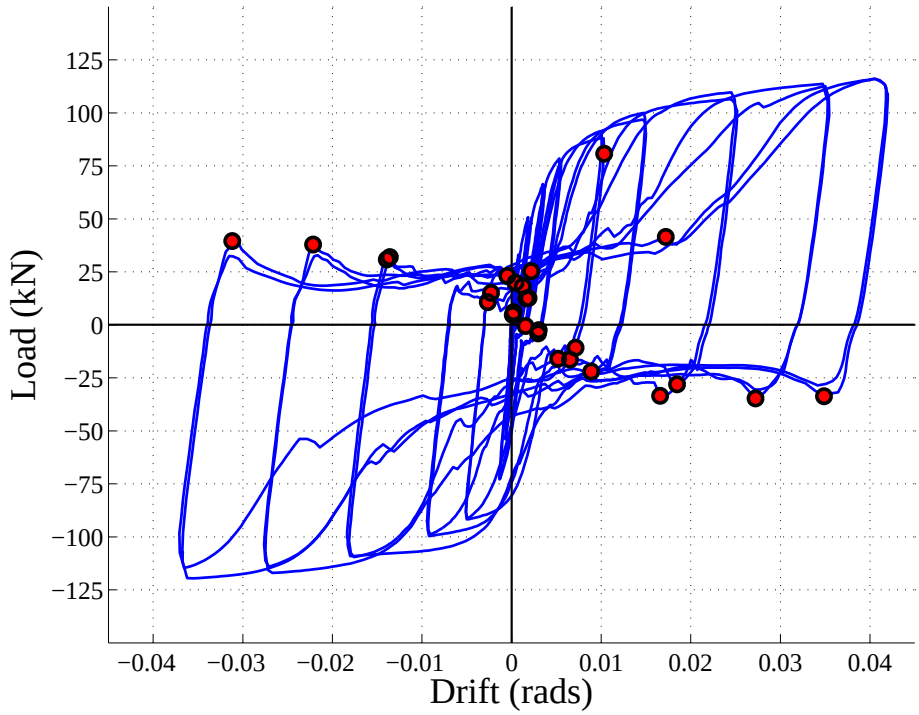

Figure 5.5: Hysteresis Curve for Test #1-18 (Snap-through events shown)

push stroke and will result in a subtle ratcheting behavior in the load-drift response.

Test #1-18 utilized only three LED markers on the frame, therefore the drift angle could only be computed using the angle change between a single HBE and a single VBE. This may have contributed to slight inaccuracies in the computed drift for this test. Different combinations of LED markers at the periphery of the web plate were used to try and improve the accuracy of the drift calculation, but there was no significant change in the result.

Observations

All buckling corrugations were observed to form at approximately 45 degrees, however the amplitude and frequency of the waves varied depending on the drift level and on the extent of the accumulated plastic strain. No slip was observed between the web plate and the fish plate at any stage of the test. The first two cycles of load were at a target drift of 0.25%,

however because of the base rotation this drift was not actually achieved and was closer to 0.08% on the pull stroke. The actual drift is shown in Fig. 5.4. There was a small amount of out-of-plane deformation at the peak load of these cycles but the amplitude was very small at approximately -3 mm (-1/8 in). The plate appeared to remain entirely elastic. No slip was observed at the web plate connections.

On Cycles #3 and #4 (0.5% target drift; 0.22% actual) the web plate was visually observed to buckle and deformed into a single diagonal corrugation with an amplitude of approximately -5 mm (3/16 in), and two minor corrugations on either side with an amplitude of approximately +3 mm (1/8 in). Audible popping sounds were noted as the plate buckled. Slight perturbations in the recorded load were observed on unloading as the plate snapped through to a new configuration, prior to re-establishment of a tension field. The deformed shape is noticeable in the photograph Fig. 5.6. The deformed contours at the pull and push of cycles #3 and #4 are shown in Fig. 5.7. It is clear form these plots that there is a significant difference in the applied load. The pull strokes have more corrugations, but with slightly lower amplitude, than the push strokes. This is indicative of higher lateral force.

On cycles #5 and #6 (0.75% target drift; 0.37% actual) the behavior was similar to cycles #3 and #4 but the amplitude of the buckled corrugations at peak load increased slightly. The increased strain energy resulted in louder popping sounds on snap-through when load changed direction. The backbone curve used to track load-displacement in real time throughout the test displayed a noticeable change in stiffness between cycles #5 and #6. This signified the start of yielding. At the completion of cycle #6, in the neutral displacement position, a residual out-of-plane web plate deformation with an amplitude of approximately -7 mm (1/4 in) was observed. See Fig. 5.11

The observed behavior for cycles #7 and #8 (1.0% target drift; 0.55% actual) was sim-

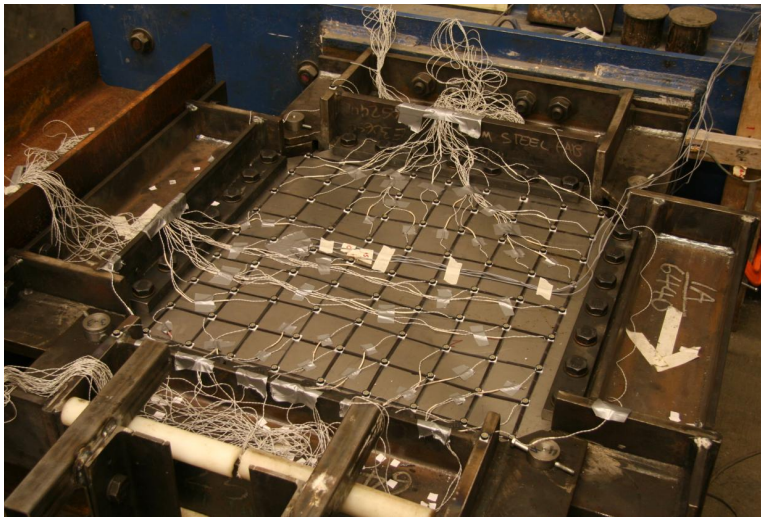

Figure 5.6: Test # 1-18 web plate deformation at valley of cycle # 6.

ilar to cycles #5 and #6, but with slightly tighter buckling corrugations. 1% drift is two to three times higher than typical yield drift. Figs. 5.8 and 5.9 show images of the test at the peak of cycle #8 pull stroke and the residual web plate deformation at the end of cycle #8 in the neutral position.

At the pull stroke of cycles #9 and #10 (1.5% target drift; 1.03% actual) the web plate buckled shape consisted of three ridges and two valleys. The amplitude of the diagonal ridge was approximately 6 mm (1/4 in). On unloading from cycle #12 there was a loud popping sound which corresponded with a reduction in measured load of approximately 9 kN. (2 kips). The residual out-of-plane web plate deformation at the completion of cycle #12 had an amplitude of approximately 21 mm (13/16 in). See Fig. 5.11. No tearing was yet evident although some localized crimping was detected near the cut-outs.

At cycles #11 and #12 (2% target drift; 1.50% actual) the plate had substantially yielded although there was still no sign of tearing anywhere on the plate. The number

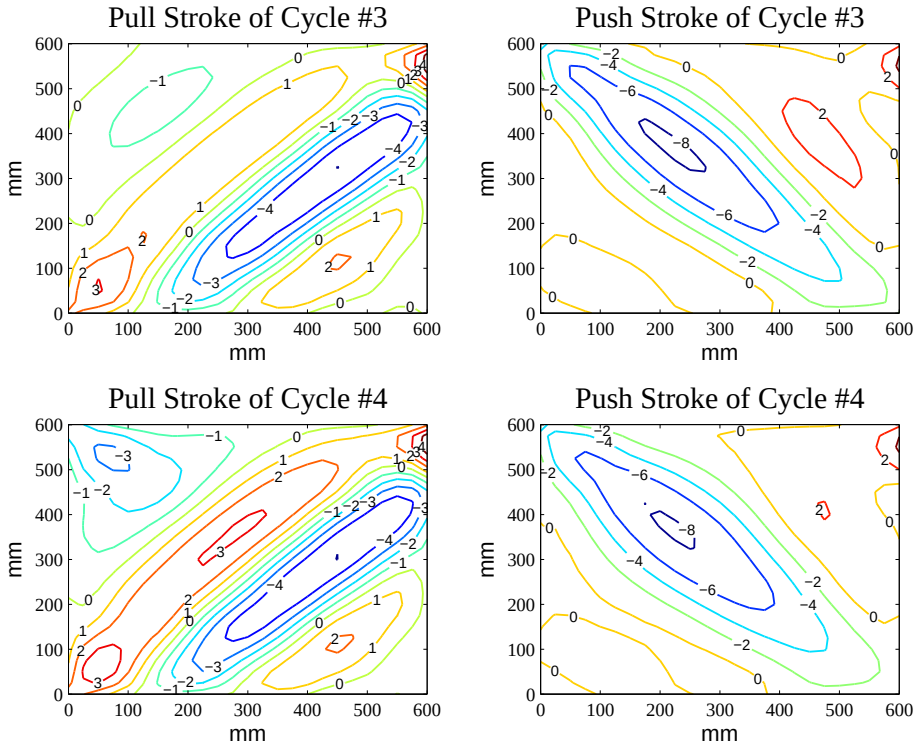

Figure 5.7: Web plate deformed shapes: Test #1-18

of buckling corrugations remained the same as for the previous two cycles. The residual out-of-plane web plate deformation at the completion of cycle #11 had an amplitude of approximately 15 mm (5/8 in). The formation of a distinct pyramid shaped residual web plate deformation was starting to emerge. This shape was observed in many of the tests.

At cycles #13 and #14 (3% target drift; 2.50% actual) localized pinching and crimping behavior was now noticeable over the plate, yet still no tearing or other brittle behavior could be observed. Six buckling corrugations were formed at peak load with the main diagonal having an amplitude of approximately 8 mm (5/16 in). No evidence of slip at the web plate connection was observed. The residual deformation at the completion of cycle #14 had an amplitude of approximately 35 mm (1 1/4 in). See Fig. 5.12

The last four cycles, two at 4% target drift (3.53% actual) and two at 5% target drift

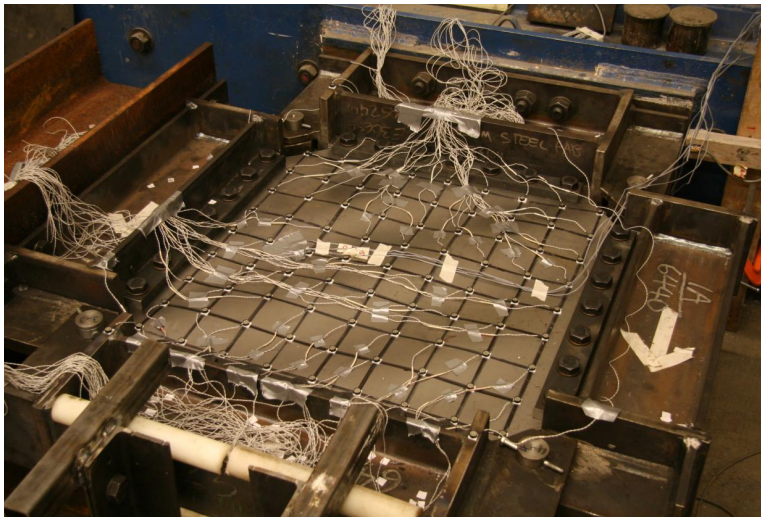

Figure 5.8: Test # 1-18 web plate deformation at peak of cycle # 8 pull stroke.

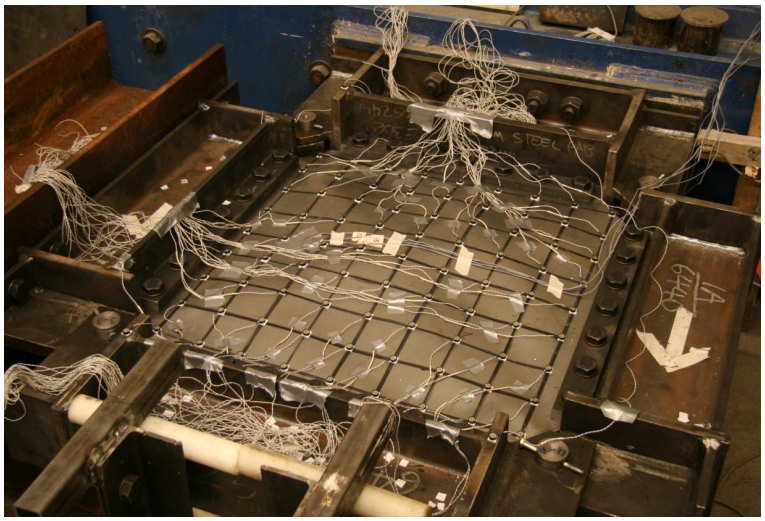

Figure 5.9: Test # 1-18 residual web plate deformation at end of cycle # 8.

(4.20% actual), remained stable with no noticeable reduction in peak load. At the completion of cycle #20 there was still no evidence of tearing or slip at the connections, except at the very end of the clamping plate where the plate edge was unrestrained.

Figure 5.10: Test # 1-18 residual web plate deformation at completion of test.

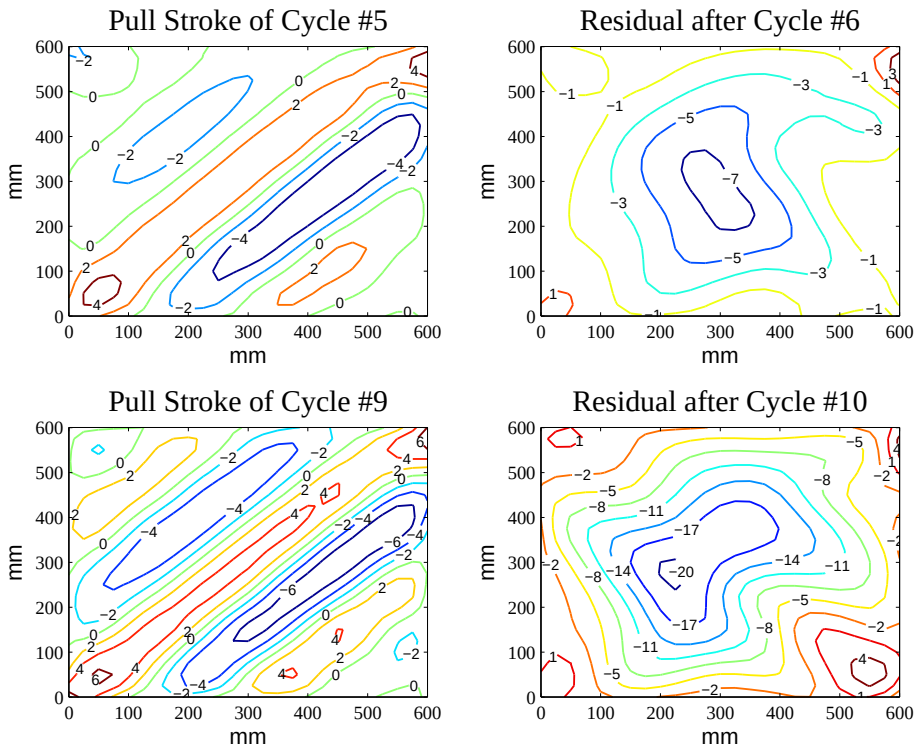

Figure 5.11: Web plate deformed shapes: Test #1-18

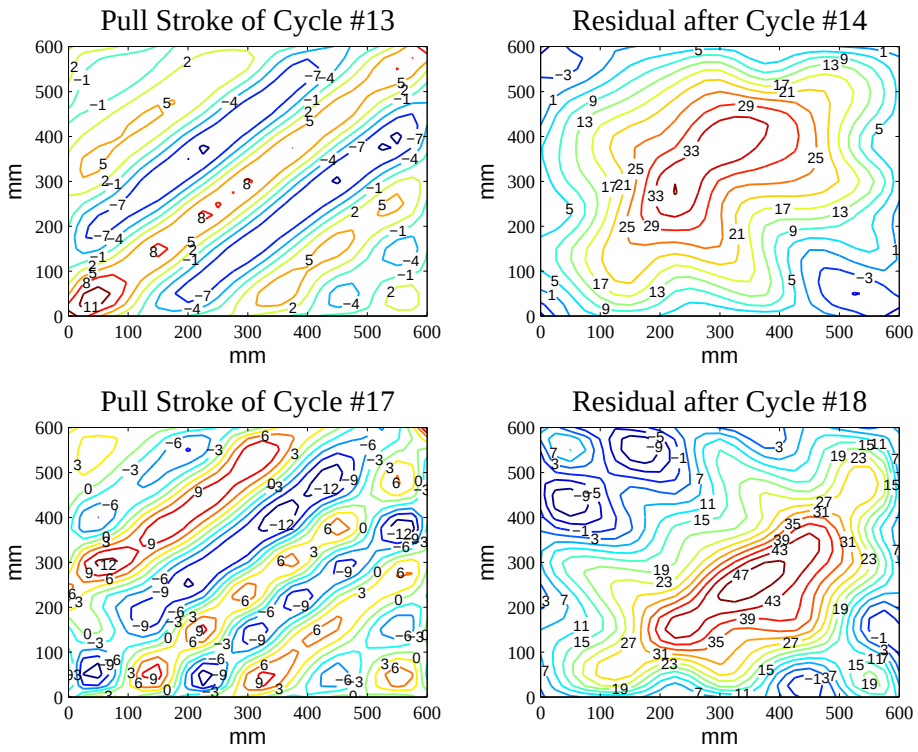

Figure 5.12: Web plate deformed shapes: Test #1-18

5.4.2 Test #1-16

This test was carried out after Test #1-18 and was the first test of a 16 Ga plate. The NDI optical tracking system was used to track web plate deformation and frame drift.

The hysteresis curve for Test #1-16 is shown in Fig. 5.13. The solid circles indicate occurrences of snap-through behavior detected by the OptoTrak system. The backbone of this hysteresis is visibly different from that of Test #1-18 because material has different hardening characteristics than the 18 Ga plate. After reaching substantial yield, the peak load does not increase very much on subsequent cycles. There is a visible increase in load of approximately 4-5% beyond an observable plateau once drifts move beyond around 2%. The material used for test #1-16 has an F_u/F_y ratio of 1.14 and has a very long yield plateau which delays progression into the strain hardening region. The total estimated accumulated plastic strain for this test is approximately 0.08; well beyond the strain at strain hardening. See Table 4.2.

The unloaded shear strength of the plate appears to be between 25 kN and 35 kN depending on the cycle, or approximately 13-20% of the peak load attained. See section at end of this chapter for analysis and discussion of unloaded shear and snap-through strength.

Observations

All buckling corrugations were observed to form at approximately 45 degrees. No slip was observed between the web plate and the fish plate at any stage of the test. The first two cycles of load (0.25% target drift) did not produce any unexpected or noteworthy behavior. Some creaking and popping could be heard as the plate loaded and unloaded but the plate did not appear to deform. Fig. 5.15 shows the panel deformations at the peak of the the pull stroke for cycles #1, #3, #5 and #7. The actual drift achieved at the peak of the pull stroke of cycle #7 is 0.31%, around 75% of yield drift. One main buckled corrugation, with an amplitude of approximately 8 mm (5/16 in) was observed. Other very minor corrugations each side of this were also visible.

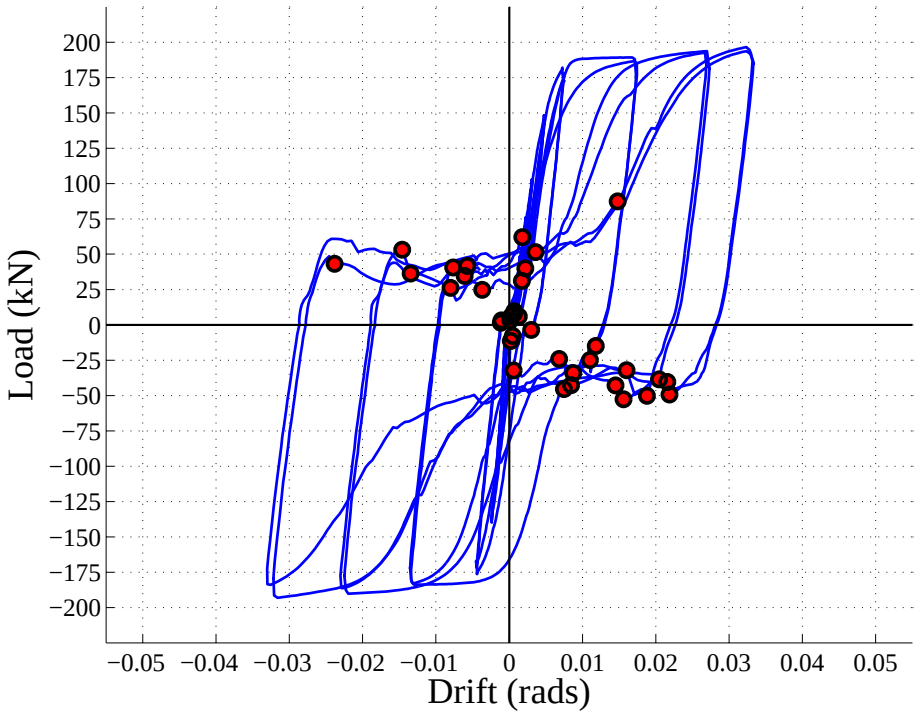

Figure 5.13: Hysteresis Curve for Test #1-16 (Snap-through events shown)

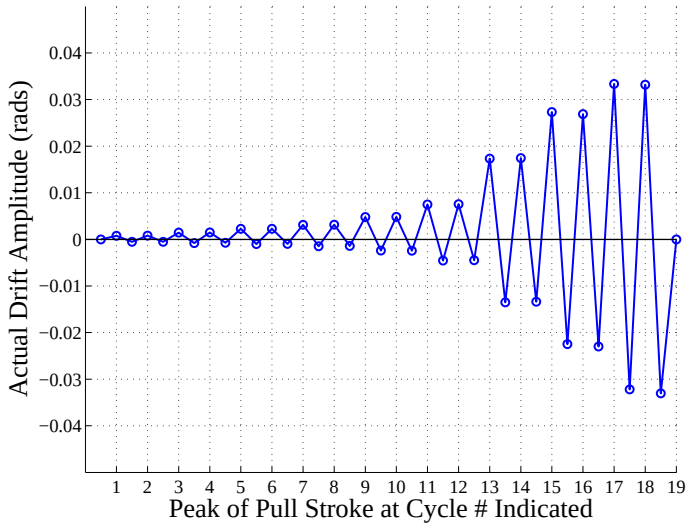

Figure 5.14: Test #1-16 Actual Frame Drift History

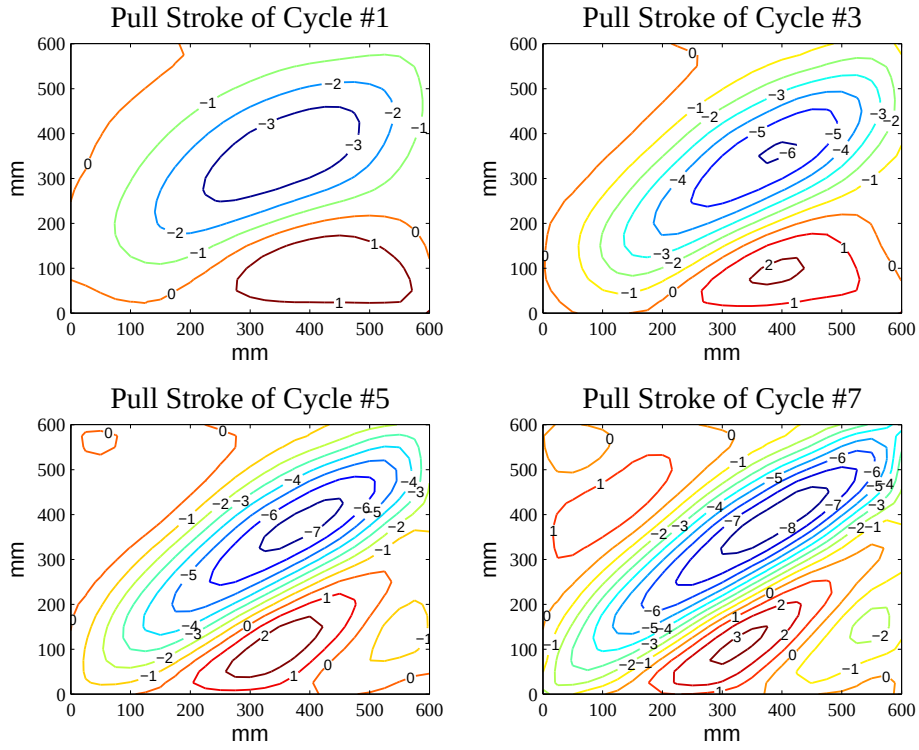

Figure 5.15: Web plate deformed shapes: Test #1-16

The residual web plate deformations after cycles #2, #4, #6 and #8 are shown in Fig. 5.16. After cycle #2 the magnitude of the peak deformation is less than 0.5 mm. It is clear from this plot that even after cycle #6 there has been very limited inelastic demand on the web plate, with a peak residual amplitude of only 1 mm. After cycle #8 it increased to 2 mm.

At cycles #9 and #10 (1.5% target drift; 0.48% actual) there still has not been substantial yielding even though the actual drift exceeded the theoretical yield drift by about 16%. The load at the peak of the pull stroke for cycle #10 is approximately 150 kN, or about 79% of the peak lateral force attained for the specimen. See Fig. 5.13. At cycle #9, the first of several very loud snap-through transitions occurred as the plate unloaded and reloaded in the opposite direction. The intensity of these sounds was significantly greater than for the first 18 Ga test (Test #1-18).

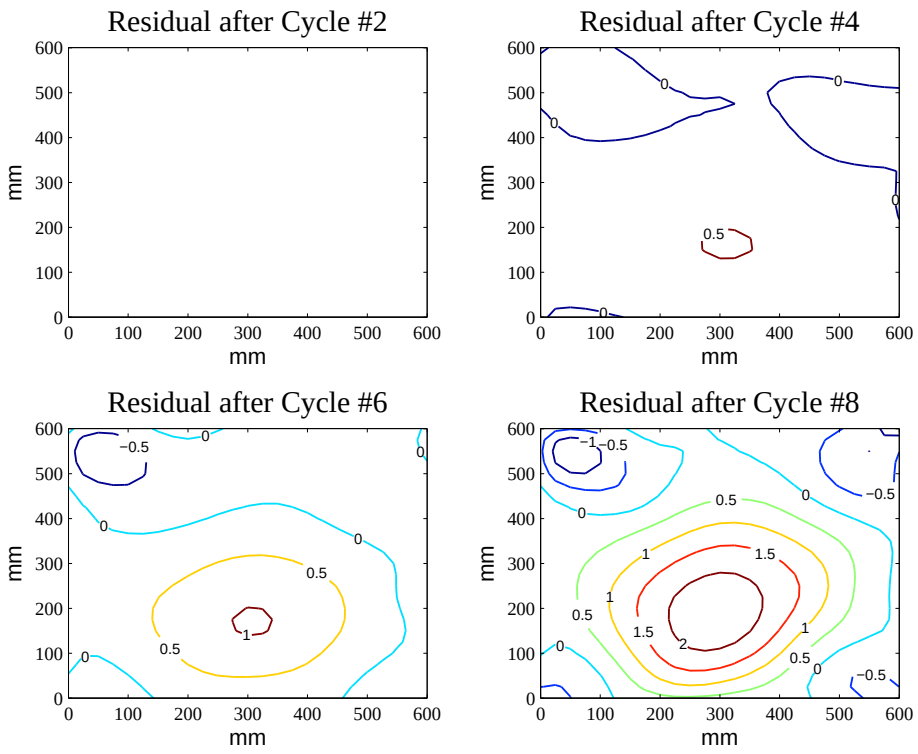

Figure 5.16: Web plate deformed shapes: Test #1-16

At cycles #11 and #12 (2% target drift; 0.76% actual) the lateral load started to plateau and the plate had fully yielded at the peak of the pull stroke. On the push stroke of cycle #12 the drift was still at only 0.45% and so the plate had only just started to yield (175 kN).

Cycles #13 and #14 showed significant inelastic action in the web plate (3% target drift; 1.74% actual). At the peak of the pull stroke for cycle #13 the actual drift exceeded $4\delta_y$. On the push stroke it exceeded $3\delta_y$. Three corrugations with magnitudes of approximately 5-10 mm were now visible in the plate at peak drift in each direction. Fig. 5.18 shows the buckled shape for the peak of the pull stroke for cycles #11, #13, #15 and #17. (and Fig. 5.19 for Cycle # 18). As the load increased there is clearly an increase in the number of corrugations, with two or three visible at cycle #11 and four distinct ridges at cycle #17.

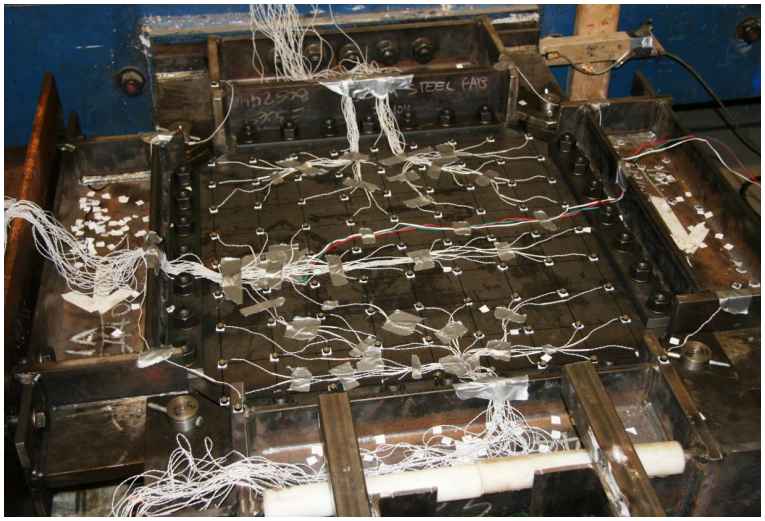

Figure 5.17: Test # 1-16 web plate deformation at peak of cycle # 8 pull stroke.

The residual out-of-plane deformations at the ends of cycles #11, #13, #15 and #17 can be seen in Fig. 5.20. The plate was observed to bow up or down with the direction of the residual amplitude being quite random. The progression of residual amplitudes is 10 mm (3/8 in), -32 mm (1 1/4 in), -41 mm (1 5/8 in) and 49 mm (1 15/16 in) for the four cycles noted. The 49 mm displacement at the end of cycle #18 represents approximately 7% of the web plate span. This deformation is obviously dependent on the load history, but it is worth emphasizing the magnitude. This deformation corresponds approximately to a plastic drift of 2.9%. No tearing was observed at any point on the plate and no slip was detected at any of the connections. There were some regions where the plate had undergone significant localized flexural yielding and displayed very tight curvature or folding. See Fig. 5.22. This is common for SPSW web plates under reversed cyclic loading. These areas are often the first to fracture.

5.4.3 Tests #2-18 and #3-18

Tests #2-18 and #3-18 were the second and third 18 Ga plate tests in Phase I. The OptoTrak system was used only to track frame drift. No LEDs were mounted on the web plate. The

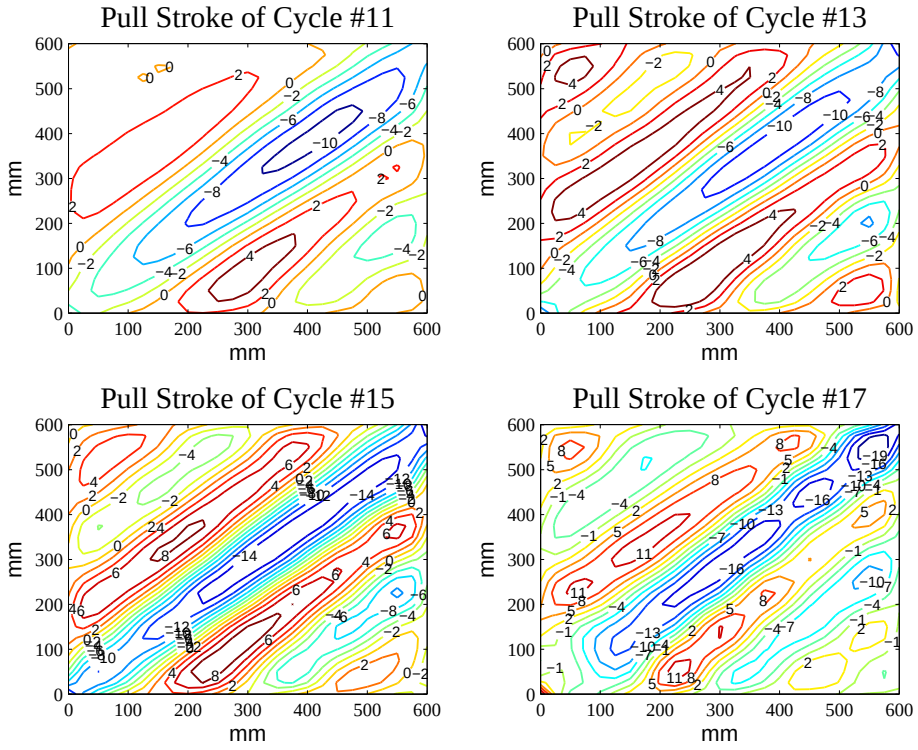

Figure 5.18: Web plate deformed shapes: Test #1-16

displacement protocols for these tests were the same, however, as discussed previously the actual drifts were slightly different from the target drifts and from one another. It is also noteworthy that the stress-strain response of the coupon specimens is significantly different.

Observations

As for Test #1-18, all buckling corrugations were observed to form at approximately 45 degrees and the observed buckling behavior was very similar to Test #1-18 with no notable differences. No slip was observed between the web plates and the fish plate at any stage of either test. No tearing occurred in either web plate.

Figs 5.23 through 5.26 show hysteresis curves for the two tests. There are some notable differences in these curves. Test #3-18, with slightly higher total accumulated drift than

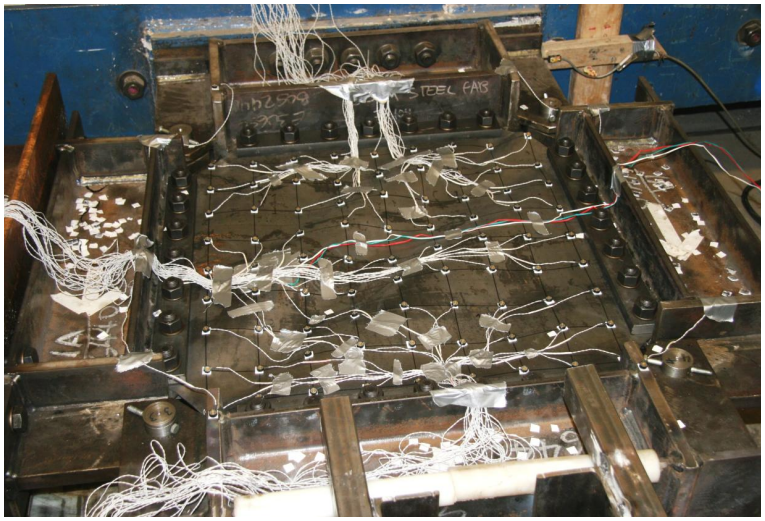

Figure 5.19: Test # 1-16 web plate deformation at peak of cycle # 18 pull stroke.

Test #2-18, shows less hardening. Test #3-18 appears to yield at a lateral load of around 90 kN, whereas Test #2-18 is closer to 75 kN. The maximum lateral load attained for each test is very nearly the same, at about 115 kN in both the push and pull directions. Examination of the coupon tests results in Table 4.2 and Fig. 4.14 reveal significant differences in the material properties of these plates. Test #1-18 and #2-18 are very similar. F_u for the Test #3-18 coupon is about 8% higher than that of Test #2-18 and F_y is about 33% higher than Test #2-18. On the basis of the coupon results, there should be noticeable differences in the hysteretic response but since the average accumulate plastic strain for each of these tests is estimated to be around 0.10, the peak lateral load should be primarily a function of F_u, not F_y. The peak load for Test #3-18 should therefore be approximately 8% higher than Test #2-18. The peak load attained for these tests is however nearly equal, differing by less than 1%. This suggests that these specimens had different hardening behaviors.

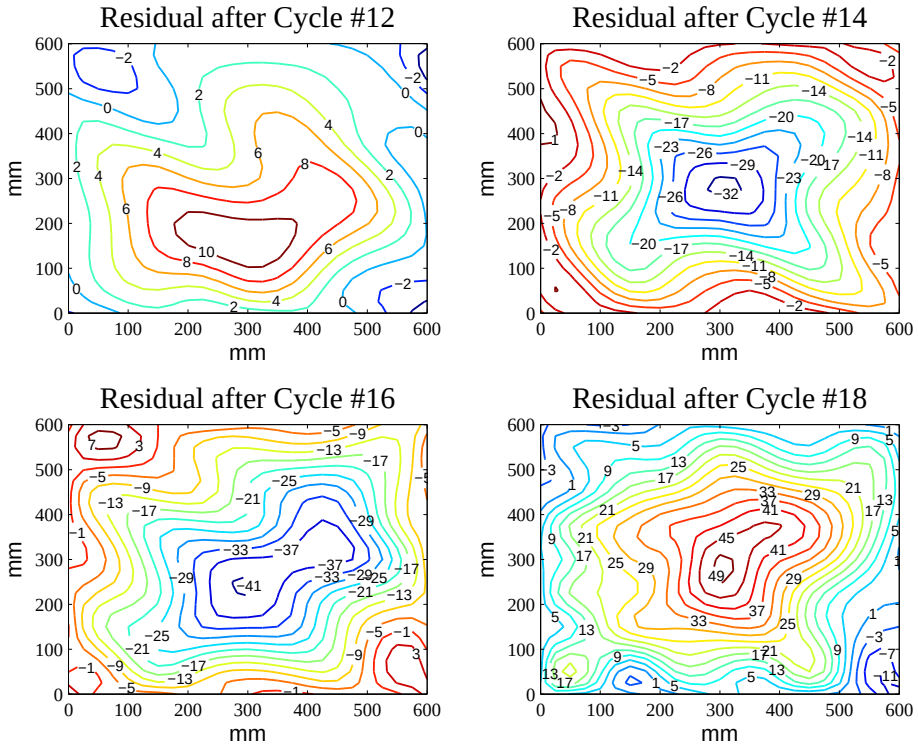

Figure 5.20: Web plate deformed shapes: Test #1-16

5.4.4 Tests #2-16 and #3-16

Tests #2-16 and #3-16 were the second and third 16 Ga plate tests for Phase I. Figs 5.27 and 5.28 show hysteresis curves for the two tests. The OptoTrak system was used only to track frame drift. No LEDs were mounted on the web plate. As for Test #1-16, all buckling corrugations were observed to form at approximately 45 degrees and the observed buckling behavior was similar to Test #1-16 with no notable differences in development of the plate tension field.

Figure 5.21: Test # 1-16 web plate residual deformation after cycle # 18.

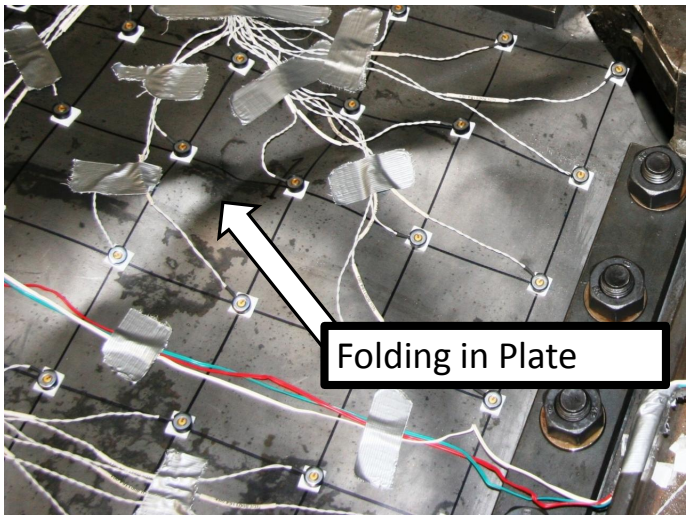

Figure 5.22: Test # 1-16 web plate folding after cycle # 18.

Observations

In Tests #2-16 and #3-16, the intent was to cycle out to larger drifts than the first 16 Ga test so that hardening could be observed and measured. The actuator reached maximum

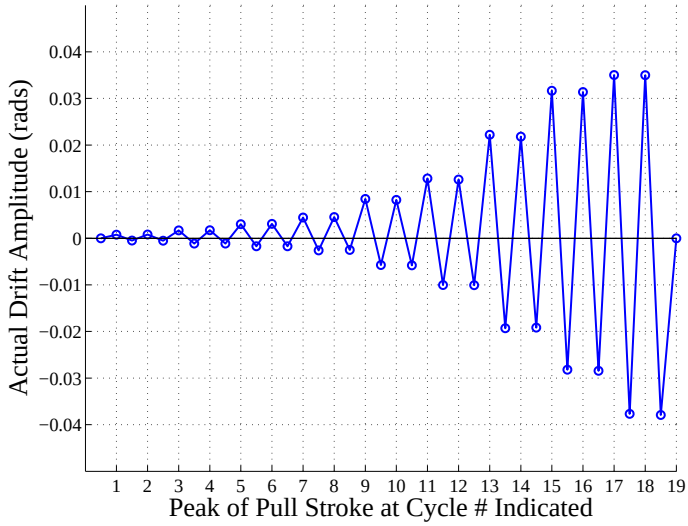

Figure 5.23: Test #2-18 Actual Frame Drift History

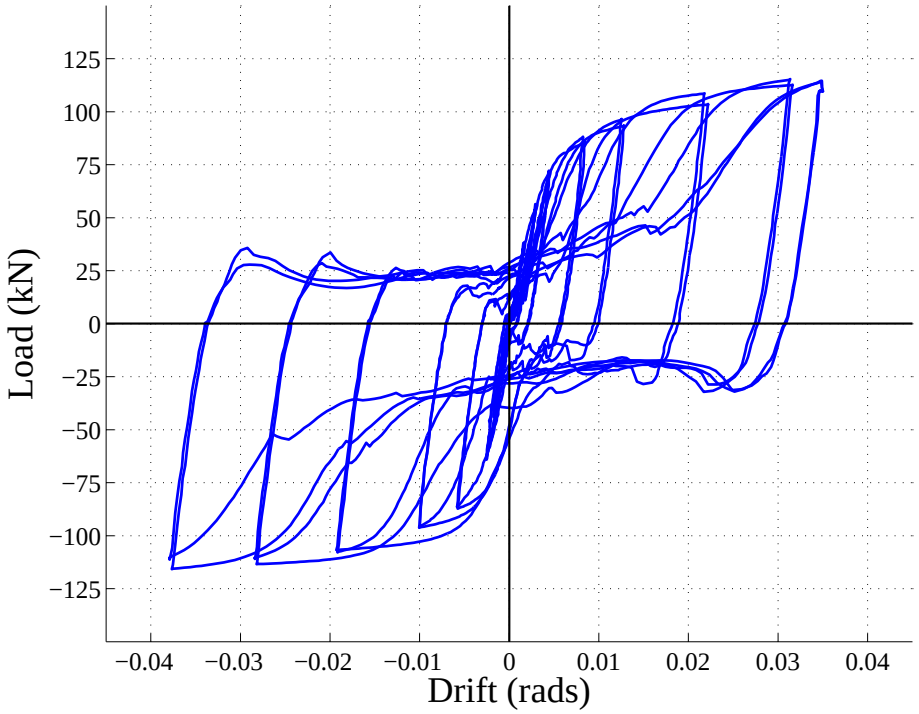

Figure 5.24: Hysteresis Curve for Test #2-18

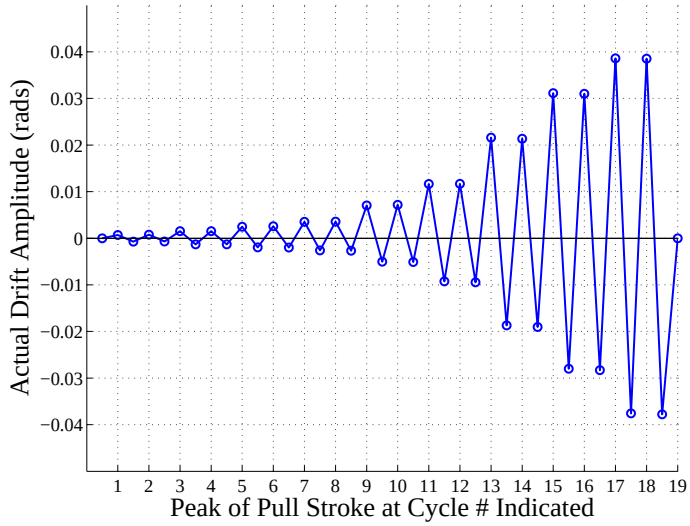

Figure 5.25: Test #3-18 Actual Frame Drift History

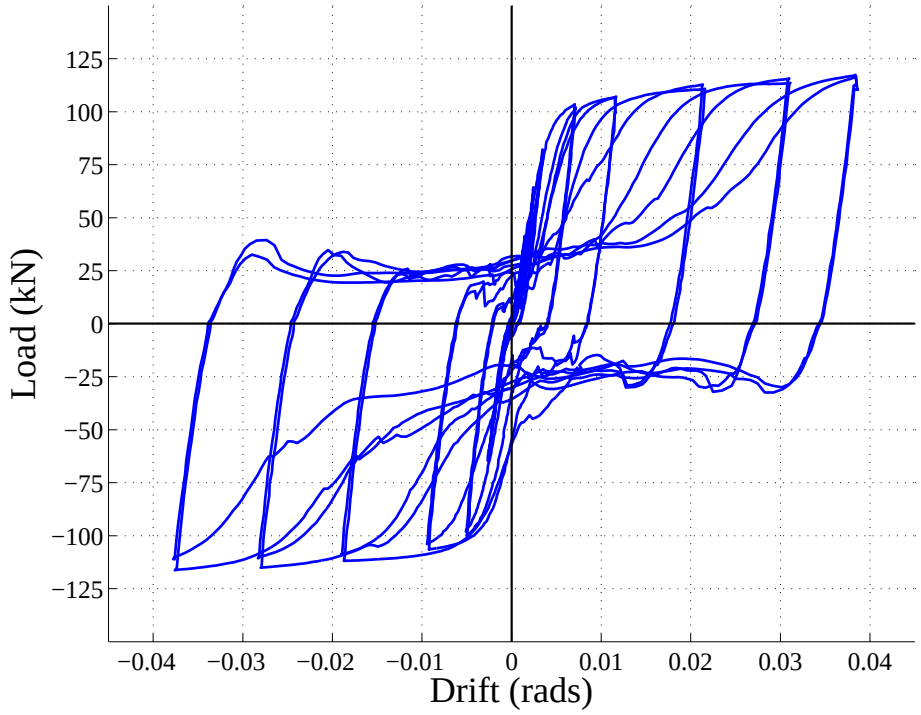

Figure 5.26: Hysteresis Curve for Test #3-18

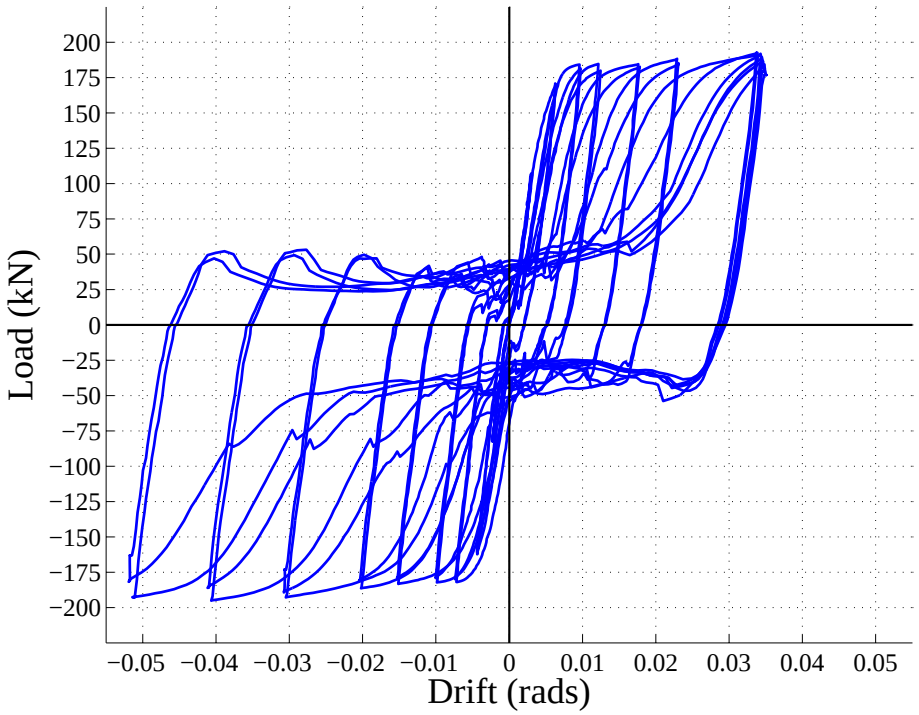

Figure 5.27: Hysteresis Curve for Test #2-16

pull stroke at about 3.4% drift for Test #2-16, so the hysteresis is asymmetric at large amplitudes and the desired drift levels were not achieved. Similarly for Test #3-16 the pull stroke was limited to approximately 3.3% drift. Nonetheless, using methods to be discussed later, the accumulated plastic strain for these tests were estimated to be approximately 0.14 for Test #2-16 and 0.11 for Test #3-16, sufficiently large strain magnitudes to illicit a hardening behavior.

There is a noticeable plateau in the hysteretic backbones of Test #2-16 and #3-16 before 2% drift, particularly in the negative loading. This plateau is approximately 182-183 kN for Test #2-16 and 175-177 kN for Test #3-16. Beyond 2% drift there is a subtle increase in peak strength on the first cycle at each new drift level. This increase beyond the plateau strength is approximately 4% and 7% for Test #2-16 for positive and negative loading respectively. The corresponding increases for Test #3-16 are approximately 7% and 6%

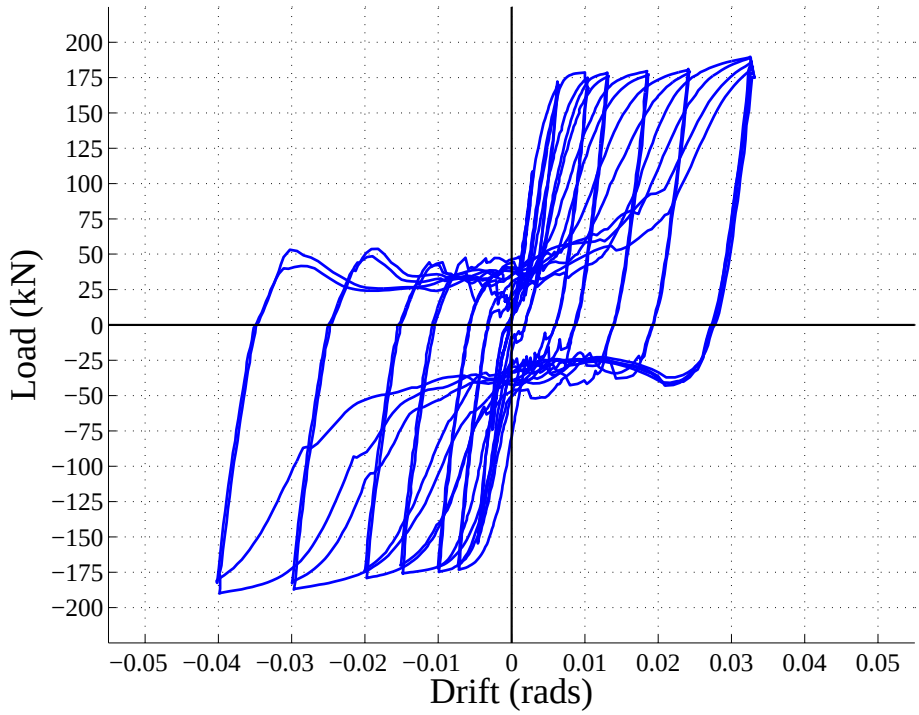

Figure 5.28: Hysteresis Curve for Test #3-16

respectively. For both tests, the 2% drift mark was found to coincide with an accumulated plastic strain of approximately 0.045. This is the strain at the beginning of strain hardening in the coupon tests. Strains of 0.14 and 0.11 coincide approximately with stresses that are 15% and 13% higher respectively, than the yield stress for these tests.

A small amount of slip was detected at the connection between the web plate and the fish plate for Test #2-16. Due to the higher likelihood of slip for the 16 Ga plate, the edge of the Test #3-16 web plate was marked with tape where it aligns with the edge of the clamping bar. See Fig. 5.31. Any tendency of the web plate to slip at the connection would be detected. Some slip was observed and occurred in the last two cycles of loading, but it was limited to areas near the cut-outs and did not exceed 2 mm (3/32 in). Fig. 5.32 shows a corner of the web plate at the completion of Test #3-16 where the tape is no longer exactly aligned with the edge of the clamping bar. No tearing occurred in either web plate.

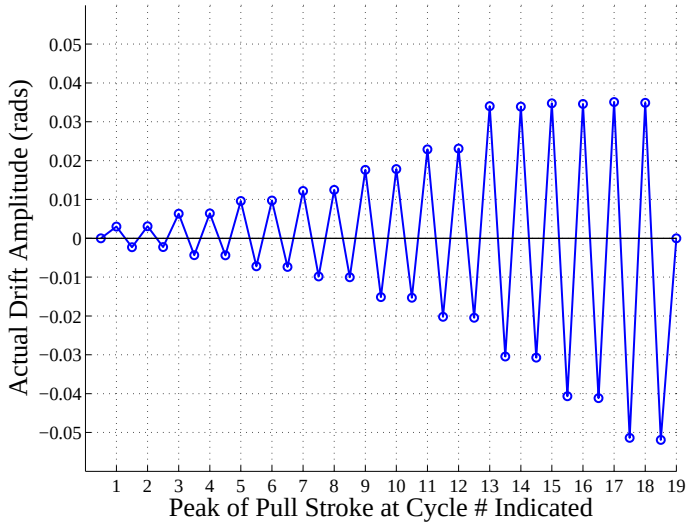

Figure 5.29: Test #2-16 Actual Frame Drift History

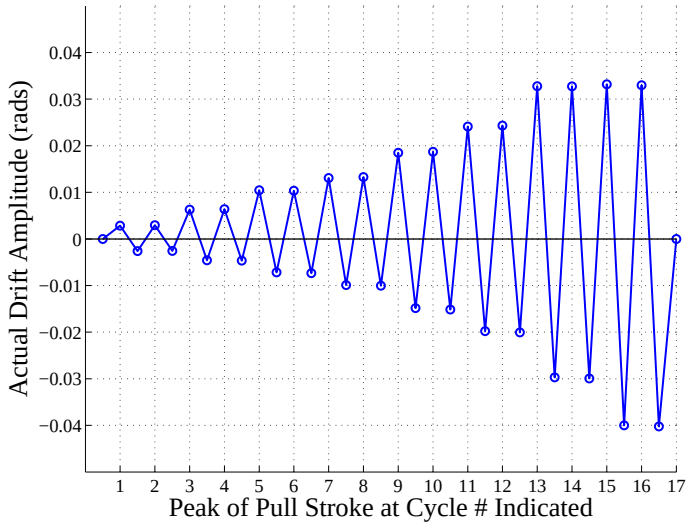

Figure 5.30: Test #3-16 Actual Frame Drift History

5.4.5 Summary of Phase I Tests

All of the Phase I tests had stable hysteretic response, with no load degradation. Where a force reduction is observed on the second cycle at large amplitude (which occurred in all of

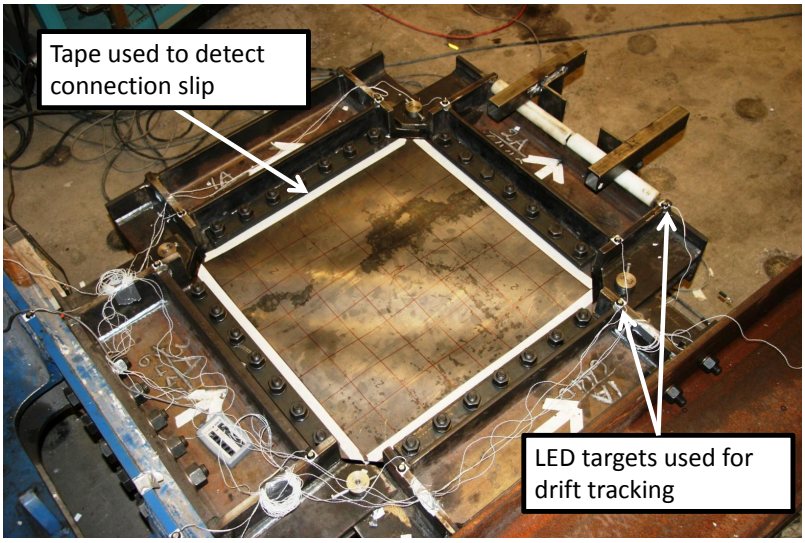

Figure 5.31: Test # 3-16 Peak of pull stroke for cycle #5 showing tape at web plate edge used for detecting connection slip and LED markers for determining drift.

the tests) this is the result of plastic strain accumulation delaying the development of the tension field and is not actually capacity reduction.

Very limited tearing was observed in any of the tested web plates and no brittle behavior was observed at all. Slip at the bolted connection to the fish plate was very limited on all of the tests. Some localized slip of about 2 mm was observed in Test #3-16 near the cut-outs. It is reasonable to assume that a similar slip would have occurred in Tests #1-16 and #2-16, but it was not observed or measured.

The out-of-plane deformations for Tests #1-18 and #1-16 were largely replicated in the 18 Ga and 16 Ga tests that followed. The 16 Ga plate tests had fewer buckled corrugations at peak drift (seven), with lower amplitude (12 mm) than the 18 Ga tests which typically had nine corrugations and amplitude of approximately 16 mm.

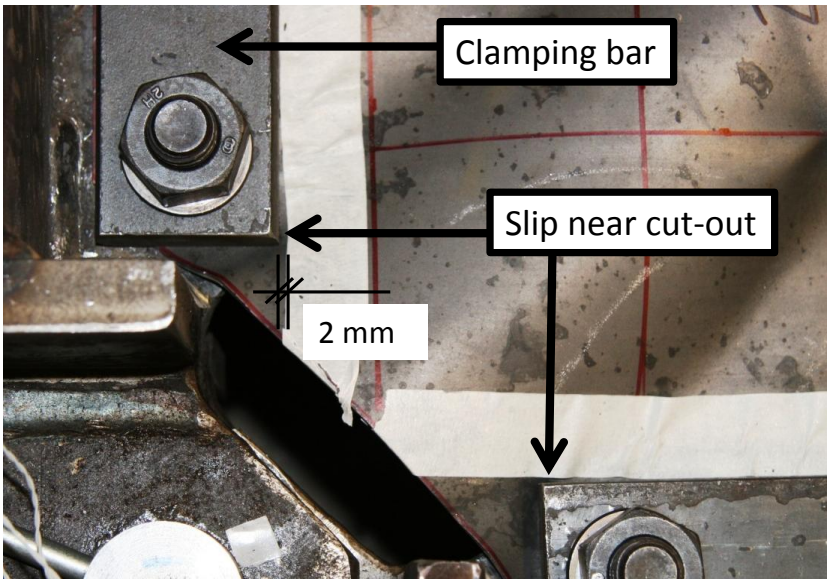

Figure 5.32: Test # 3-16: At end of test showing web plate slip at bolted connection near cut-out.

5.5 Phase II Test Results and Observations

Phase II included Tests #1-22 through #3-22 and used the 22 Ga A1008 plate with the slender VBE sections. The displacement histories and hysteresis curves for these tests are shown in Figs. 5.33 through 5.38. The OptoTrak system was used to track panel deformations, frame drift and VBE flexure, and is shown in Fig. 5.39. Strain gauge rosettes were installed on the top and bottom web plate surface per Fig. 5.40. Strain gauges were also attached to the VBE sections per Figs. 4.6 and 5.41.

The VBE in this series of tests is a composite member and comprises a main VBE section and a clamping bar. For the remainder of this section, VBE-CB refers to the composite member. VBE refers to just the main VBE section that is connected to the other boundary members, and CB to just the clamping bar section. A comprehensive analysis of the data from these tests is presented in section 6.2.

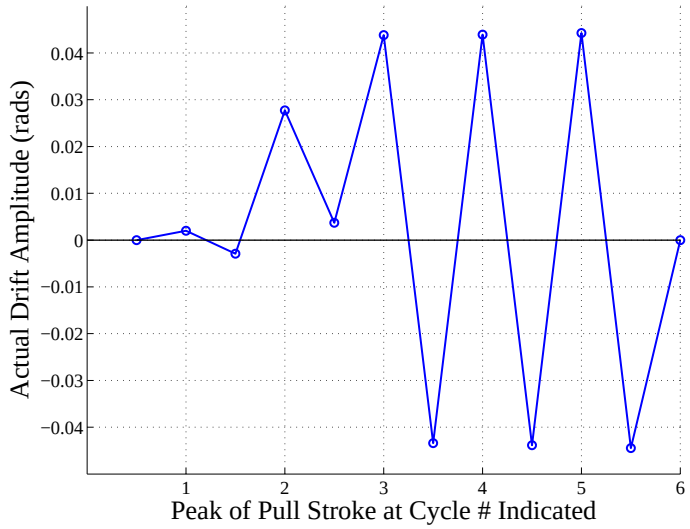

Figure 5.33: Test #1-22 Actual Frame Drift History.

Due to the reduced plate strength, the base rotation for these tests was small but was still accounted for in the force and drift calculations. The reduced base rotation permitted higher drifts at the limit of the actuator stroke. More than 6% drift was attained for Test

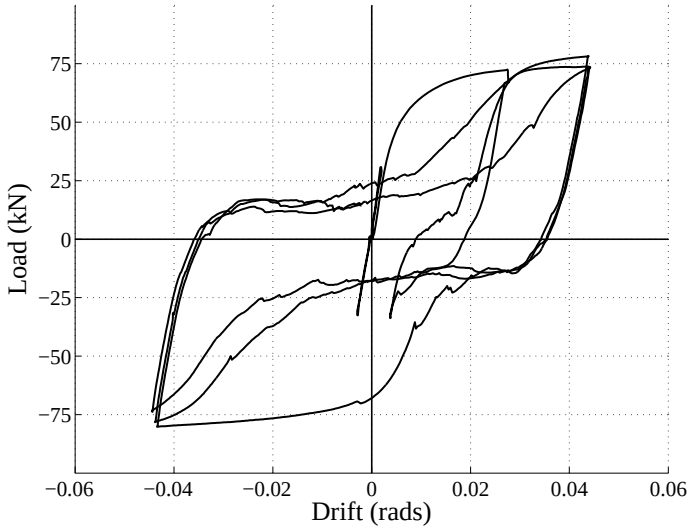

Figure 5.34: Hysteresis Curve for Test #1-22.

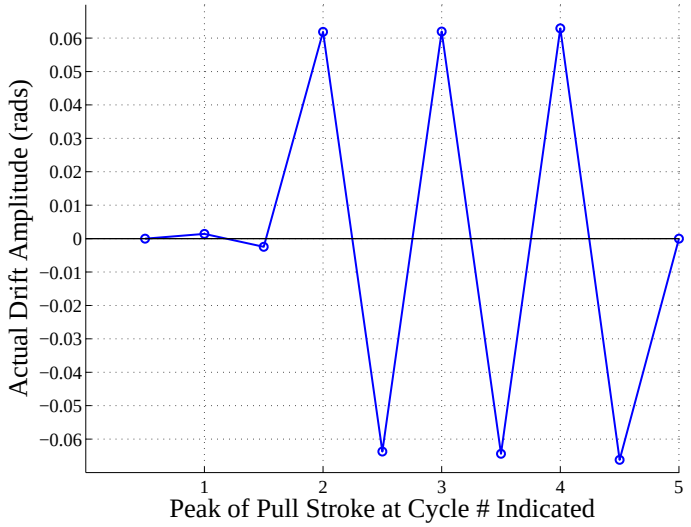

Figure 5.35: Test #2-22 Actual Frame Drift History.

#2-22. The high drifts resulted in some plate tearing at the connection to the fish plate. The buckling corrugations were observed to be inclined between 35 and 45 degrees, as can be seen from the contour plots that follow. On the first half-cycle to a drift of 6% the steep inclination of the corrugations was observed to decrease slightly as the drift increased and

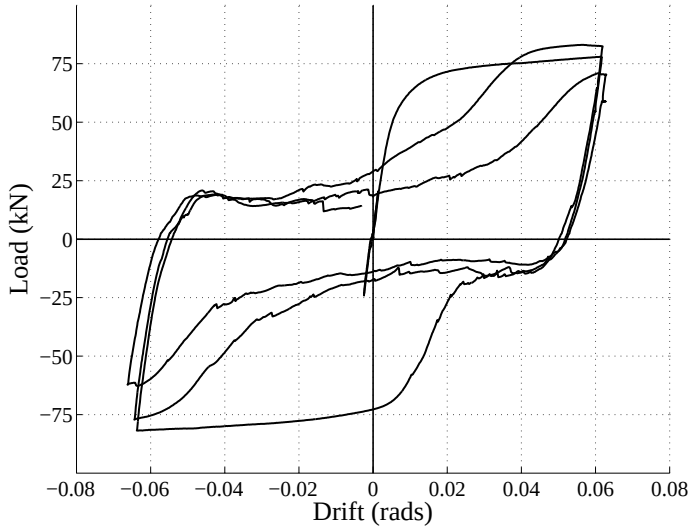

Figure 5.36: Hysteresis Curve for Test #2-22.

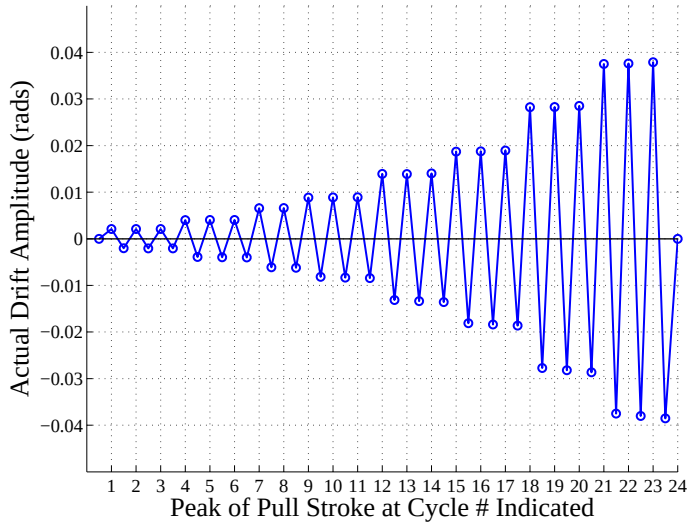

Figure 5.37: Test #3-22 Actual Frame Drift History.

the plate progressively plastified, although the migration was subtle.

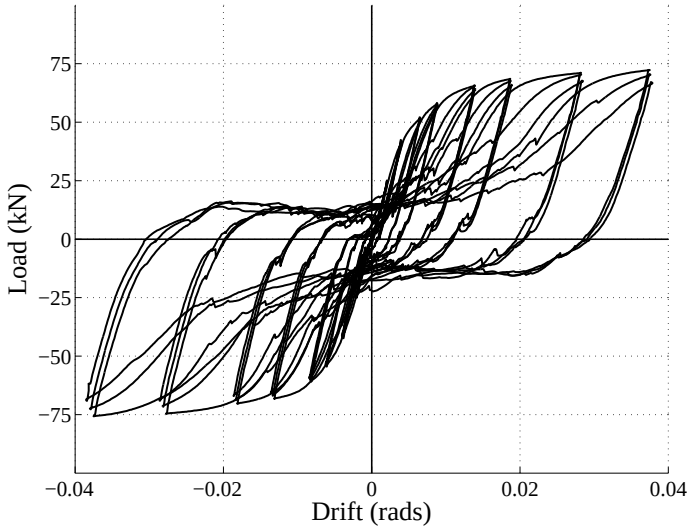

Figure 5.38: Hysteresis Curve for Test #3-22.

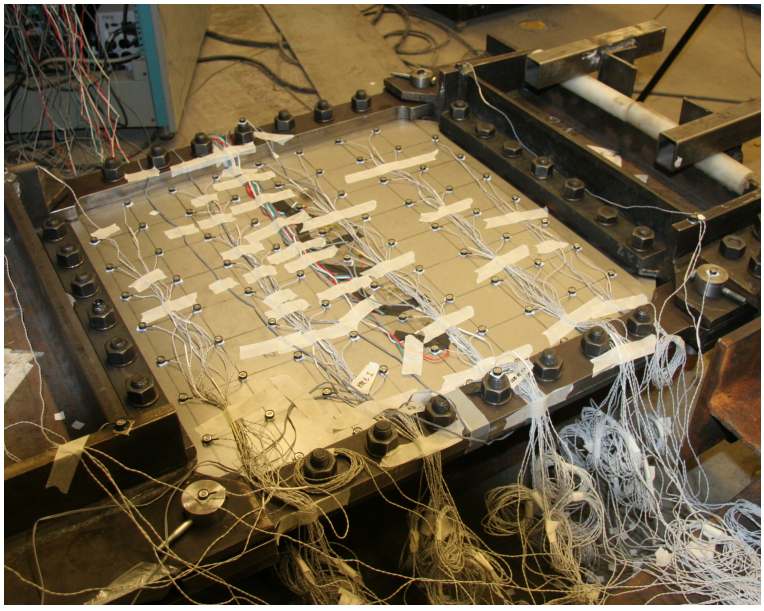

Figure 5.39: Typical LED arrangement for 22 Ga panel tests.

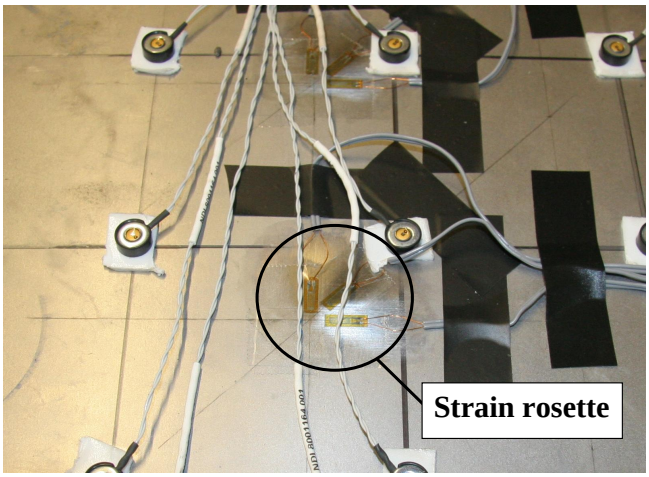

Figure 5.40: Web plate strain gauge rosette for 22 Ga panel tests.

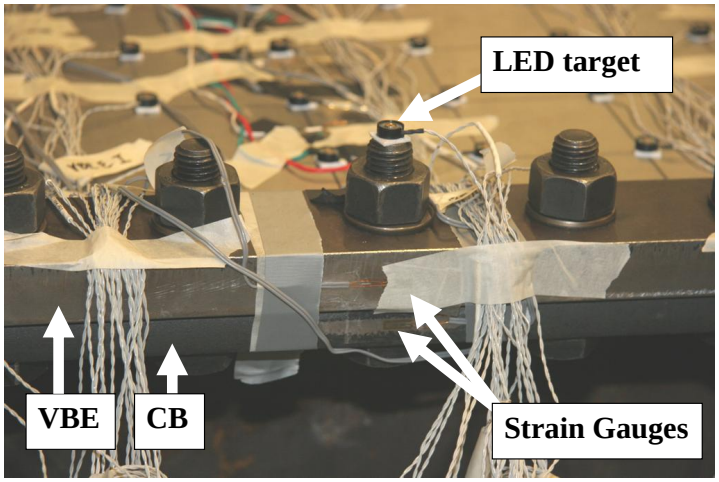

Figure 5.41: VBE and CB strain gauges for 22 Ga panel tests.

5.5.1 Test #1-22

Test #1-22 was the first of the 22 Ga panel tests. This test was designed to measure the elastic tension field inclination angle (α) and the migration of this angle under monotonically increasing lateral load as the drift was applied to more than 4%. It was also designed to investigate the VBE flexural demand under these conditions. This test and Test #2-22 also provide an opportunity to more easily examine the phenomenon of Normal Plastic Contraction (NPC), the tendency for the web plate to plastically contract due to Poisson effects in the direction normal to the principal tensile strains. This effect is difficult to observe in other web plate tests with gradually increasing drift magnitudes. This will be discussed further in the observations of Test #2-22.

Observations

After a single elastic cycle to approximately 0.3% drift, the plate was pushed to a drift of around 2.7% whereupon it was unloaded back to a drift of approximately 0.4%. The specimen was then reloaded out to a maximum drift of approximately 4.4% and then subjected to three more complete cycles to this drift level. The buckled corrugations were generally of lower amplitude and shorter wave length in comparison to the 18 Ga and 16 Ga tests. A comparison between the 16 Ga and 22 Ga buckled corrugations is shown in Fig. 5.42. Analysis of the strain gauge and OptoTrak data is provided later in this chapter.

The small unloading excursion after 2.7% drift provides some insight into how the web plate reloads after a small transient excursion in the opposite direction. Two features of this excursion are noteworthy. First: the trajectory of the stress-strain curve is re-established as the plate reloads in the positive direction with some observable Baushinger effect. Second: even though the plate was elastically unloaded and the tension field in the other direction was only partially engaged, hysteretic energy was dissipated through this excursion. This demonstrates that the web plate underwent plastic deformation even though plastic deformation through tension field action did not occur.

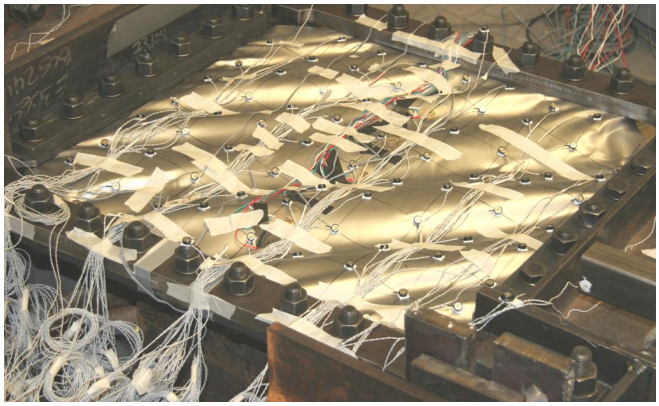

(a)

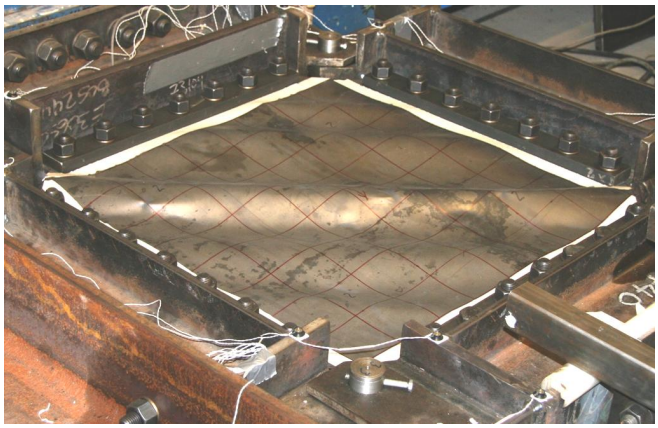

(b)

Figure 5.42: Comparison of buckled corrugations between (a) 16 Ga specimen and (b) 22 Ga specimen.

5.5.2 Test #2-22

Test #2-22 was essentially a repeat of Test #1-22 without the small excursion after 2.7% drift and with larger drift magnitude. This test was necessary because many of the strain gauges on the first test failed to record reliable data. It consisted of an initial elastic cycle

to approximately 0.3% followed by three complete cycles in excess of 6% drift.

Observations

The panel behaved in a similar fashion to Test #1-22, however since the drift cycles were a little larger, some fracturing of the plate occurred. This resulted in some moderate strength degradation in the third cycle.

The fractures initiated after the completion of cycle #4 at the connection to the top HBE, near the corner cut-outs. The right fracture grew to approximately 130 mm (5 inch) in length by the end of the last cycle. A fracture on the left cut-out developed at the same time and was approximately 90 mm (3 1/2 inch) in length at the completion of the test. A noticeable drop in lateral strength can be seen in the last cycle where the peak strength plateaus at between 75% and 85% of the strength reached on the previous cycle. Figs. 5.43 and 5.44 show the fractures at the connection to the top HBE on each side of the web plate.

At the peak of each stroke the deflection of the VBE was perceptible. Fig. 5.45 shows the deflection of the right VBE at the peak of cycle #2 push stroke. This deflection was estimated to be approximately 2 mm (5/64 inch) over the length of the VBE. Analysis of this deformation and the associated flexural forces is presented later in the chapter.

The normal plastic contraction that results from the first inelastic excursion to maximum drift (4.4% for Test #1-22 and 6.1% for Test #2-22) can be estimated by first determining the location of an effective loading point on the first half cycle. This is denoted point A in Fig. 5.46. This point occurs at a load of approximately $0.70V_{max}$ for both tests. By using this value as the reloading point B in the opposite direction, the plastic drift at the point of reloading can be estimated. For both tests the plastic reloading drift was found to be approximately $0.3\Delta\delta^p$, where $\Delta\delta^p$ is the plastic drift on the first half-cycle. This indicates

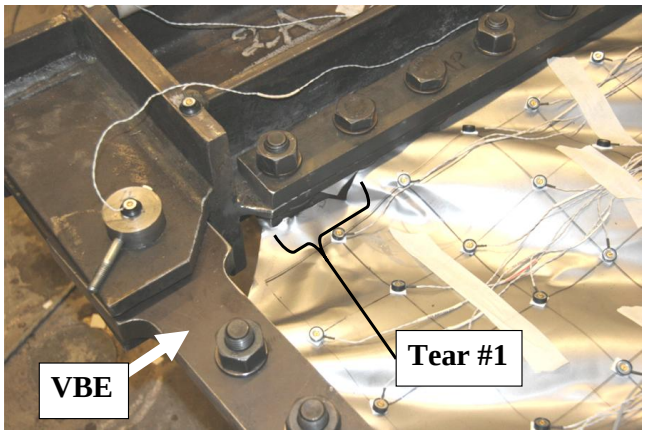

Figure 5.43: Tear in web plate near right VBE at neutral position between cycles #4 and #5 for Test #2-22.

that for both tests the plastic contraction normal to the principal plastic tensile strains of the first inelastic half-cycle were only 30%, rather than 50% as would be predicted assuming a Poissons's ratio of 0.5.

The location of the reloading point B is however somewhat nebulous. It is equally valid to argue that the plate starts to reload as soon as there is an abrupt change in stiffness (point C). If this is done the normal plastic contraction estimate is much closer to the expected value of 0.5. It will be shown towards the end of this chapter that $ABAQUS$ models of the Tests #1-22 and #2-22 predict reloading closer to the theoretical point indicated on Fig. 5.46. It is difficult to attribute this discrepancy between the observed behavior and the theoretical to any single cause, but it may be the result of bolt slippage, VBE rocking (See sections 6.1.4 and 6.1.5) or other behaviors that are not explicitly modeled in ABAQUS. Another explanation is that the plastic contraction in the tests was constrained (and retarded) in regions where moderate tensile stresses act normal to the principal tensile

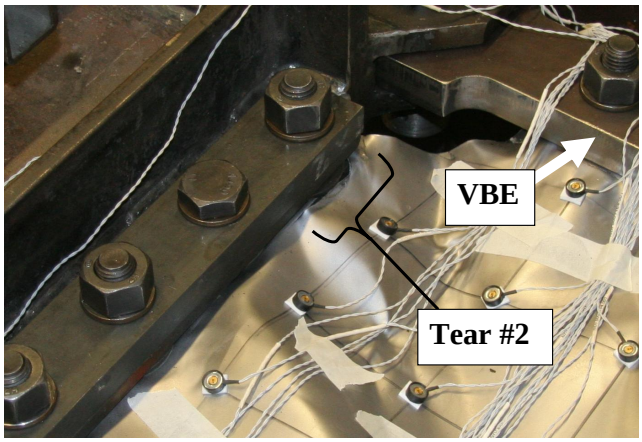

Figure 5.44: Tear in web plate near left VBE at neutral position between cycles #4 and #5 for Test #2-22.

stresses. Where the stresses are compressive, it will have the opposite effect and will exacerbate the contraction. These stresses have been observed in many of the preliminary models. This would delay the onset of reloading point B and soften the reloading stiffness (slope from C to B). The $ABAQUS$ models display this behavior, although it is less pronounced.

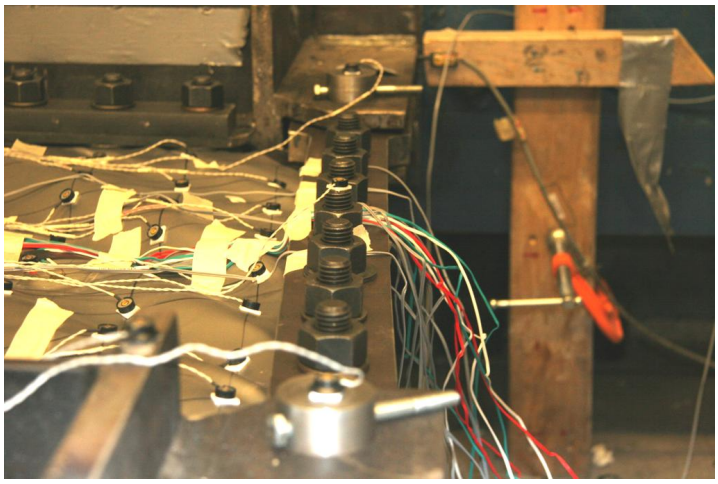

Figure 5.45: VBE curvature at peak of push stroke for cycle #2 for Test #2-22.

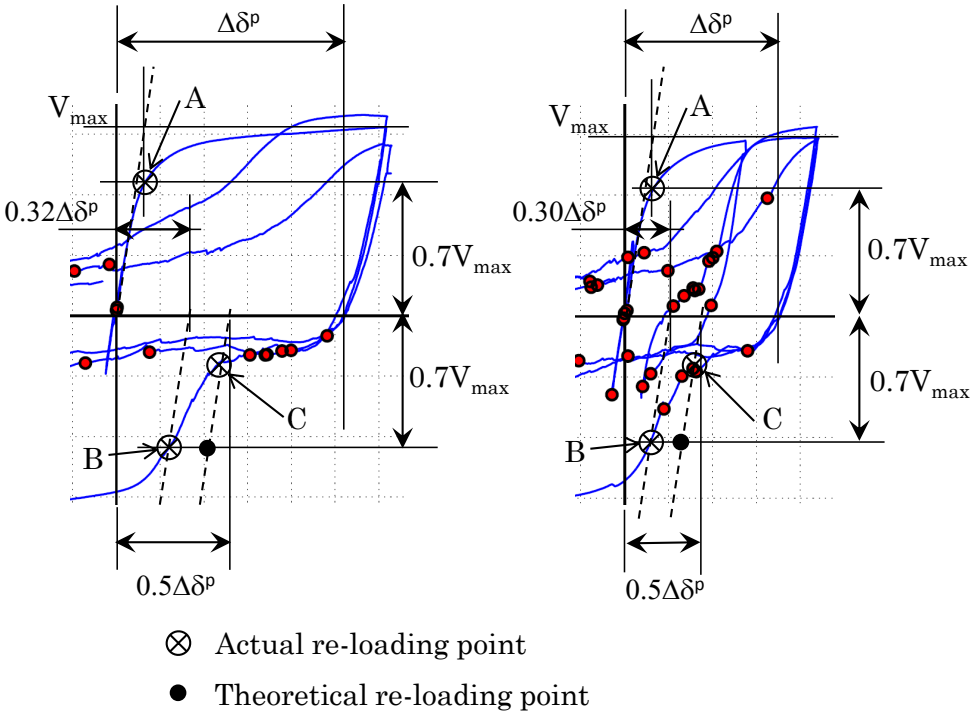

Figure 5.46: Estimating plastic contraction from Tests #1-22 and #2-22 hysteresis curves.

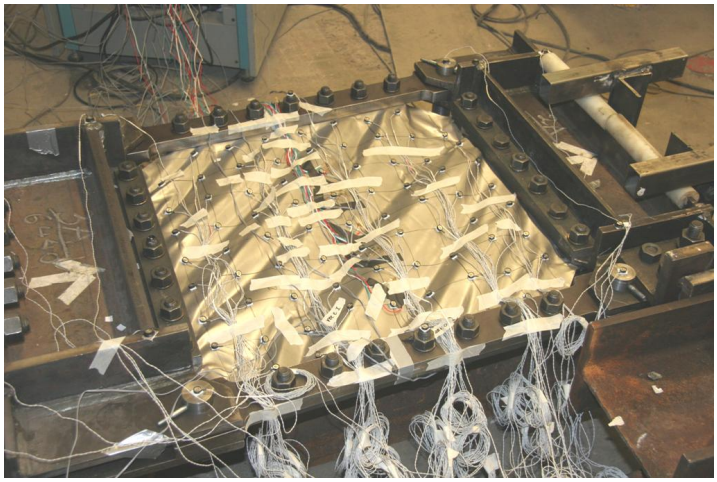

Figure 5.47: Deformed panel at peak of pull stroke between cycles #3 and #4 for Test #2-22.

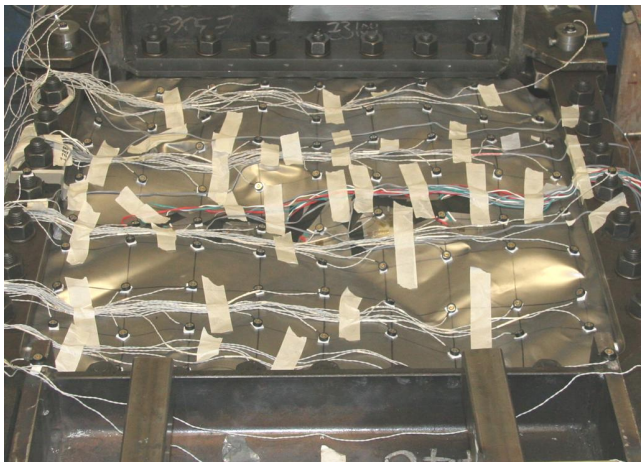

Figure 5.48: Residual deformation at completion of Test #2-22.

5.5.3 Test #3-22

Test #3-22 was designed to examine how the web plate tension field orientation and VBE demand changed under cyclic loading. Figs. 5.38 and 5.38 show, respectively, the frame drift history and the hysteresis curve for this test. The displacement history comprised three cycles each at 0.25, 0.5, 0.75, 1.0, 1.5, 2.0, 3.0 and 4.0% drift.

Observations

The hysteresis trace for the test shows stable behavior with no strength degradation. The hysteresis is approximately symmetrical, with equal elastic stiffnesses in positive and negative loading directions and peak strengths differing by less than 3%. No tearing or other brittle behavior was observed on any part of the plate. The snap-through transitions had noticeably less energy than the 18 Ga and 16 Ga specimens, with snap-through strengths around 16% of the maximum strength and a more rounded snap-through hump. See section 6.5 at end of chapter.

The primary difference between the hysteresis curves for the Phase I tests and the Phase II tests is relative magnitude of the snap-through stiffness, K_{ST}. Fig 5.49 illustrates this for Test #3-22. The quantity Δ_F/Δ_D is approximately 1800 kN/rad for this test. Similar data were obtained from all other tests and are listed in Table 6.1. K_{ST} for the Phase I tests ranges form 10,000 and 16,000 kN/rad. The low value observed in the Phase II specimens is attributed to VBE flexibility.

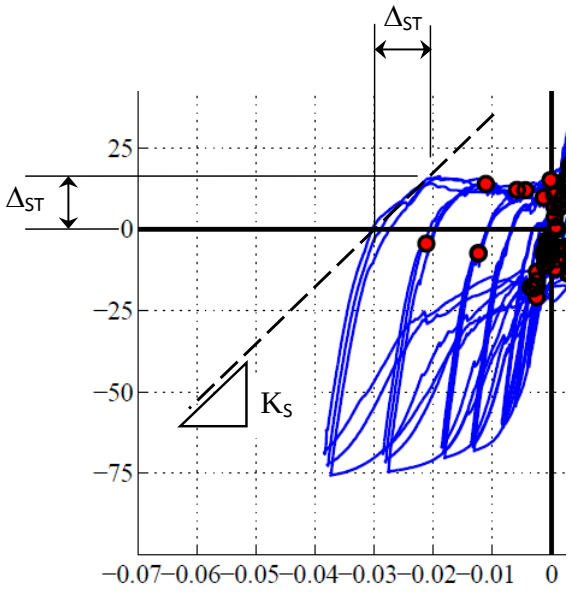

Figure 5.49: Drift from unloading to drift at snap-through drift Test #3-22.

Chapter 6

PRELIMINARY ANALYSIS OF PHASE II TEST RESULTS

Many aspects of the Phase II experimental results require a detailed introduction and discussion before the results are presented in detail and discussed. Much of this concerns the methods and assumptions used to compute the various quantities presented in the figures that follow.

6.0.4 Tension Field Orientation During Reversed Cyclic Loading

In chapter 3, analyses were presented that indicate the tension field inclination angle α changed with monotonically increasing load. A qualitative relationship between drift and α was observed. The way in which α changes under repeated cyclic loading is perhaps more important in the context of seismic design. However, the stretching of the web plate under repeated inelastic cycles makes a simple relationship between the measured drift magnitude and α less meaningful because elastic loading can occur at high drifts and, conversely, plastic loading may occur at very low drifts. The motivation for the analysis of this data is to verify that a) under elastic loading conditions, regardless of load history or the degree of accumulated plastic strain, α correlates with α^{el} and that b) under plastic loading conditions, also after many elastic and inelastic cycles, α is still best approximated using an angle between 40 and 45 degrees.

Therefore, it is necessary to establish suitable criteria that can be used to determine when loading is predominantly elastic and when it is predominantly plastic because, as just discussed, drift magnitude alone is not sufficient. α can then be presented as a function of elastic drift magnitude for elastic loading (relative to its initial loading point for that cycle) and in terms of accumulated plastic drift for plastic loading.

6.0.5 A Note on Stress Trajectory Measurement Using Strain Rosettes

The use of strain rosettes to track principal stresses in web plates should be done under the assumption that the loading is non-proportional i.e., the ratio of the stress components change with drift, as is often the case with the inelastic loading of a web plate. If the stresses in the plate are entirely elastic, which can be determined using the rosette data and detailed knowledge of the material properties, the principal stress trajectories may be determined with reasonable accuracy using Hooke's Law and the standard constitutive relationship for plane stress. However, once plastification begins, computing stress trajectories from strain gauge data requires an alternative approach because the elastic and plastic components of the strain cannot be easily decoupled.

When a web plate is laterally loaded in the post-buckled state and yielding has initiated, the orientation of the principal stresses may change significantly as the lateral drift increases. For isotropic metal plasticity, the plastic strain *increment* $\mathrm{d}\epsilon^p$ is proportional to the total deviatoric stress s_{ij}. This means that if the stress field is changing and plastic straining is occurring, the accumulated resultant strain that is recorded by the strain gauge rosette will not be principally aligned with the final state of stress. If the objective is to determine the orientation of the principal stresses after yielding at a particular point on the web plate, and at a particular drift level, then the most recent strain increments $\Delta\gamma_{xy}$, $\Delta\epsilon_x$ and $\Delta\epsilon_y$ should be used in the tension field angle computation. Furthermore, this is only applicable if the tangent modulus is very low, i.e., the strain is mostly plastic.

To summarize the foregoing discussion in practical terms, the stress trajectories may be computed using total strain and the linear plane-stress equations prior to yielding. Increments in measured strain (rather than total strain) should be used when the strains are predominantly plastic.

6.1 Elastic and Plastic Loading Criteria

In order to detect elastic and plastic loading, the initial elastic tangent stiffness and peak lateral force are first extracted from the test hysteresis. In addition to these quantities, the following are established:

1. minimum tangent stiffness to be considered elastic loading
2. maximum percentage of peak load to be considered elastic loading
3. maximum tangent stiffness to be considered plastic loading
4. minimum percentage of peak load to be considered plastic loading

The criteria noted in items 2 and 4 above are needed because there are several small oscillations in the hysteresis curves (due to snap-though and other similar behavior) where the computed stiffness may be close to or even exceed the initial tangent stiffness. These oscillations sometimes occur at low load levels and well before the tension field has re-established and the computed angle of the stress field is erratic.

The minimum tangent stiffness for elastic loading was set equal to 70% of the initial stiffness of the web plate. The maximum plastic tangent stiffness was set equal to 10% of the initial elastic tangent stiffness of the web plate. Additionally, the transition from elastic to plastic was set equal to 80% of the peak load attained in the direction of loading. That is, to be considered as elastic loading the lateral force had to be less than 80% of the peak load and the tangent stiffness had to be greater than 70% of the initial elastic stiffness. To be considered as plastic loading the lateral force had to be greater than 80% of the peak load and the tangent stiffness had to be less than 10% of the initial elastic stiffness. A simple Matlab program was developed to locate the points on the hysteresis curves that satisfy the above criteria.

The regions of elastic and plastic loading over which tension field inclination was sampled are graphically illustrated in Fig. 6.1 for Test #2-22 and Fig. 6.2 for Test #3-22. In

both cases the elastic behavior is contained largely within the zone close to the origin at low drift levels. The program used to identify these regions accounts for the possibility of elastic re-loading at large drift levels but the stiffness in these regions was generally too low to qualify as elastic.

Although these criteria are arbitrary they do appear to effectively identify and separate the elastic and plastic loading regimes. The initial elastic stiffness was measured directly from the hysteretic response and was determined to be approximately 6000 kN/rad for Test #1-22 and approximately 12000 kN/rad for Tests #2-22 and #3-22.

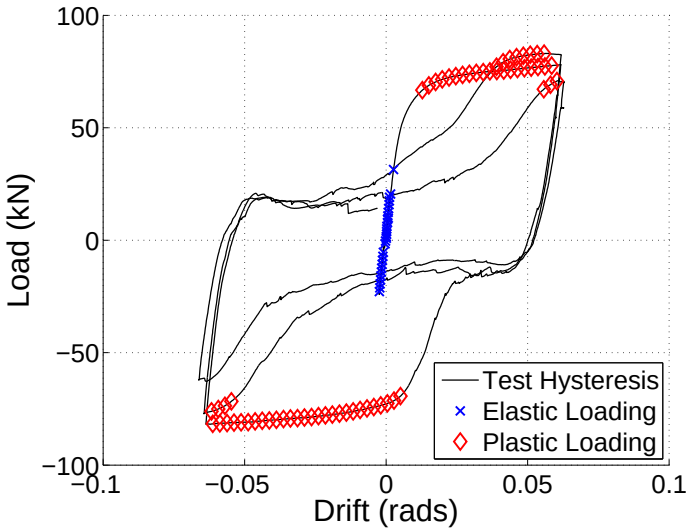

Figure 6.1: Test #2-22: Regions designated as elastic and plastic.

The drift associated with web plate yield, Δ_y, is estimated using Eq. 6.1.

$$\Delta_y = \frac{2\sigma_y}{E_s sin(2\alpha)} \tag{6.1}$$

Where σ_y is the yield stress of the plate and E_s is the elastic modulus of the steel. This quantity is used in some of the plots that follow. This drift is generally *not* the stage at which the plate has fully yielded. Some yielding will have commenced at this drift but it is not complete.

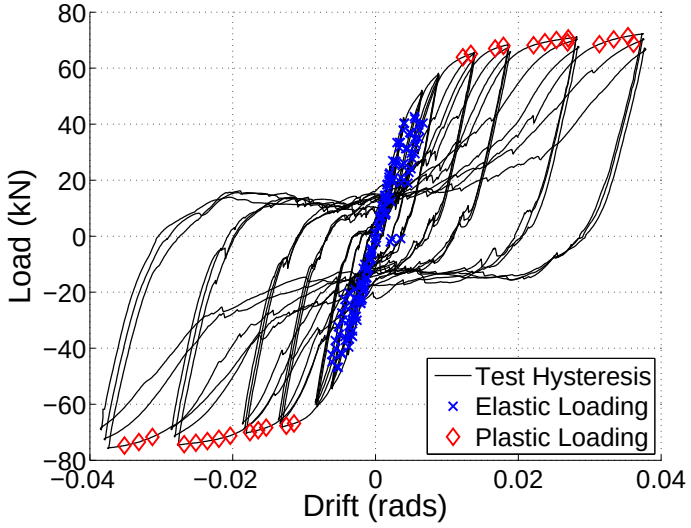

Figure 6.2: Test #3-22: Regions designated as elastic and plastic.

6.1.1 Determination of Yield Drift Using Web Plate Strain Gauge Data

Strains used to compute stress magnitudes and orientations were determined by averaging gauge readings from the bottom and top side of the plate. The von Mises stress was determined by computing the average σ_{eff} for each of the five points. The principal stress components at each of the five locations were computed assuming plane-stress conditions with $\nu = 0.28$. For clarity, the equation for σ_{eff} is reproduced below as Eq. 6.2.

$$\sigma_{eff}^2 = \sigma_1^2 - \sigma_1\sigma_2 + \sigma_2^2 \tag{6.2}$$

Where σ_1 and σ_2 are the in-plane principal stress components. The point where the average computed Mises stress equaled the plate yield stress is shown on Fig. 6.10. Once the specimen drift exceeded approximately 0.04, the web plate strain gauges were no longer reliable as they are only rated to 2%.

6.1.2 Principal Stress Inclination for Elastic and Plastic Loading States

It is necessary to introduce alternative measures for elastic and inelastic drift when measuring the progression of α under cyclic loading so that results from tests with vastly different

loading or drift histories may be objectively compared. It is possible to have a negative drift under positively increasing load and positive drift under negatively decreasing load. Thus, simply using the drift magnitude as the ordinate is inappropriate. In the following sections the elastic drift at point i is shown schematically in Fig. 6.3 and is given by Eq. 6.3

$$\Delta_i^{el} = \frac{|F_i^{el}|}{K_{ti}^{el}} \tag{6.3}$$

Where ${K_{ti}}^{el}$ is the tangent stiffness of the web plate at point i that satisfies the constraints imposed for elastic loading described above in section 6.0.4 and F_i^{el} is the corresponding force. At each drift level the inclination of the principal tensile strain was determined by averaging the angle computed from the five strain rosettes.

If the loading is completely elastic and near the start of the test when accumulated plastic strains are negligible, the difference between this measure of drift and the actual drift magnitude will be very small. As plastic strains accumulate and the panel is stretched and has large out-of-plane deformations it is possible to have additional elastic loading at very large actual drift magnitudes. The drift measure represented by Eq. 6.3 and presented schematically by Fig. 6.3 attempts to compensate for this. In Fig. 6.3, Δ_i^{el} is determined at point "i" on the hysteresis and plotted against α^{el} computed from strain gauge data at that point.

When the loading is substantially plastic, a rational measure of drift to plot against the computed α is the accumulated plastic drift. This is computed by summing the plastic drift increments using the following equation

$$\int |d\Delta^{pl}| = \sum_{i=1} \left(d\Delta - d\Delta^{el}\right) = \sum_{i=1} \left(|\Delta_{i+1} - \Delta_i| - \frac{|{F_{i+1}}^{pl} - F_i^{pl}|}{{K_{in}}^{el}} \right) \tag{6.4}$$

Where Δ_i is the total drift extracted from the hysteresis and F_i^{pl} is the force extracted from the hysteresis that satisfies the criteria assumed for plastic loading as described in section 6.1. ${K_{in}}^{el}$ is the measured initial elastic stiffness of the web plate.

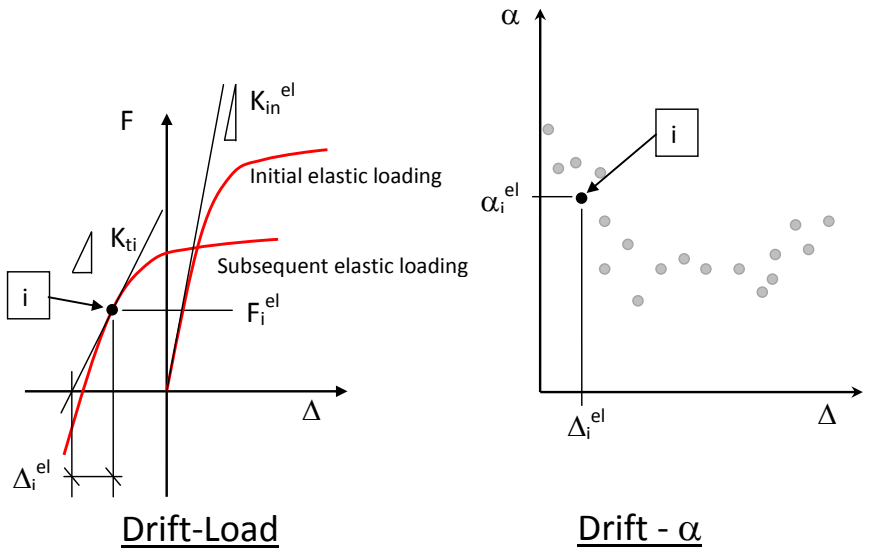

Figure 6.3: Schematic representation of equivalent elastic drift

6.1.3 VBE-CB Flexural Demands from Strain Gauge and NDI Data

The VBE-CB strain gauge and NDI data were analyzed to establish independent estimates for the VBE-CB flexural demand for tests #2-22 and #3-22 and compare these measured demands to those predicted using a conventional tension field analysis. Fig. 6.4 shows the loaded VBE-CB geometry. The actual measured yield stress of the plate determined from the coupon test was used as the expected yield stress, F_e, in place of R_yF_y used by the *Provisions*. The expected yield stress was used to compare the results to those using equations similar to those adopted by the *Provisions*.

The clamping bar (CB) was bolted to the VBE with fully pre-tensioned bolts and the two sections were assumed to act compositely. Strain gauges were attached at midspan of each VBE on the inside and outside of the section, and on the inside and outside of the CB. Prior to loading the specimen, the initial strain in each gauge was removed from the raw strain gauge reading so that a zero strain offset was present at the start of each test. Flexural strains were determined by subtracting the net axial strain in each section from the

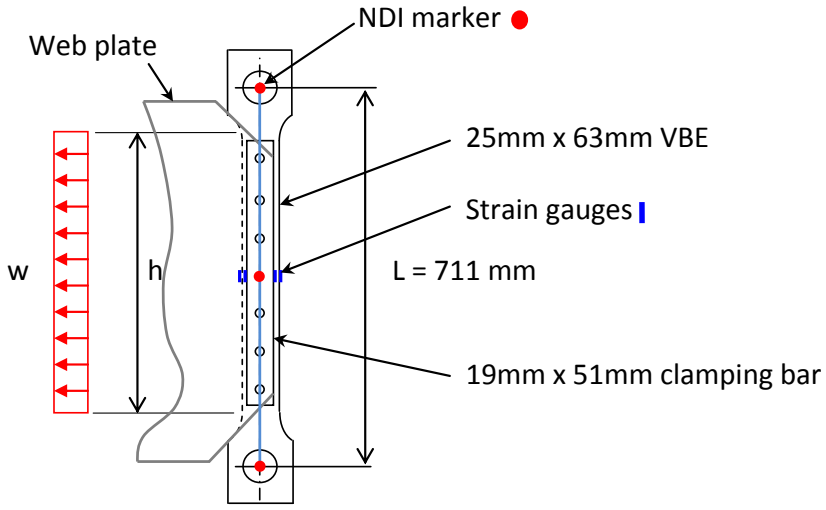

Figure 6.4: Phase II VBE-CB showing loaded length and and instrumentation locations

raw strain data. The resulting flexural strain was used to determine the flexural demand. This procedure was carried out for both of the VBE sections and CB sections. Flexural demands were computed assuming elastic plane-section behavior for the VBE sections and the CBs. Some VBE strains were observed to exceed the expected yield strain, assuming 379 MPa (55 ksi) yield stress. This will be discussed in more detail in the sections that follow.

LED markers were placed at midspan on the top of the center bolt of each VBE-CB and also at the center of each pin at the four corners of the frame. Fig. 6.4 shows the locations of the LED markers. From this array of markers it was possible to compute the midspan deflection, δ_m, of each VBE-CB at every time step. See Fig. 6.5. Some adjustment to the raw data, as discussed below, was required to account for the slight rigid body rotation of the VBE about its own longitudinal axis, and the twist in the section resulting from load eccentricity. The corrected deflection was then used to adjust the computation of the equivalent transverse distributed load and resulting bending moment demand at midspan of the VBE-CB.

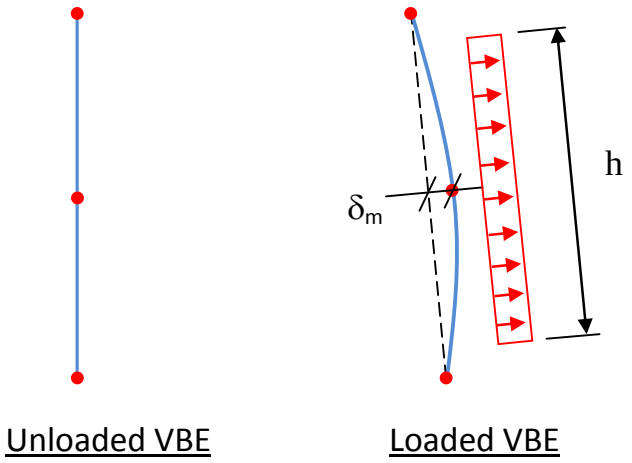

Figure 6.5: Schematic of unloaded and loaded VBE-CB showing measured deflection, δ_m.

6.1.4 VBE-CB Twist About Longitudinal Axis

A SAP model of the VBE-CB assembly was constructed to evaluate precisely the midspan deflection of the composite section due to a unit uniform transverse load and to evaluate the maximum expected bolt shear to help validate the "no slip" assumption. Fig. 6.6 shows a schematic of the SAP model. This model included all of the pertinent geometric and material characteristics. In the experiment, the transverse load from the web plate is applied at the underside of the VBE section which results in a 13 mm (1/2 inch) eccentricity. The deflection is measured at an LED marker approximately 44 mm (1.72 in) above the theoretical shear center of the section. As the section is loaded the twisting of the section displaces the midspan marker, opposing the direction of the primary deflection. In the SAP model, the deflection due to a 113 kN/m (1 kip/in) uniform transverse load was recorded at a marker node located 44 mm above the VBE shear center. The load-deflection ratio (stiffness) extracted from this model is then used to compute the actual midspan bending moment demand from the NDI data. Fig. 6.7 shows schematically how the measured deflection differs from the actual VBE-CB deflection.

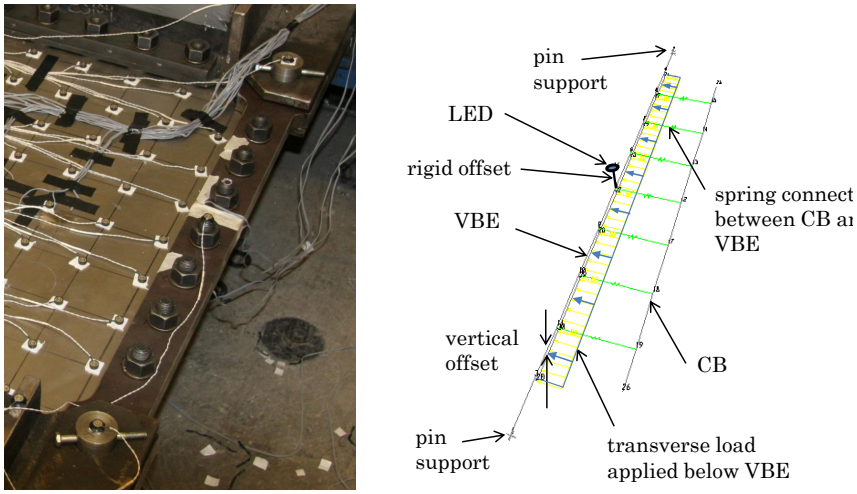

Figure 6.6: SAP model of loaded VBE-CB.

6.1.5 VBE-CB Rocking About Longitudinal Axis

After examining the raw NDI data, there appeared to be an initial lag in the Δ-M plot when compared with that generated using the strain gauge data. It is believed this lag is due to the small amount of play in the VBE connection to the pin. As a result of this observation, the pin outside diameter (OD) and the VBE hole inside diameter (ID) were measured and recorded. The mean pin OD was 42.589 mm, with a standard deviation of 0.10 mm. The mean ID of the VBE hole was 42.926 mm, with a standard deviation of 0.02 mm. The slight oversize of 0.337 mm (0.0133 inch) results in an average rigid body VBE axial rotation of 0.00663 rads upon application of transverse load. Because of the randomness in the exact pin axis and VBE hole axis orientation, this rotation is not expected to occur immediately but at low load levels and will manifest itself as a low initial tangent stiffness. This essentially rigid body rotation results in a mean initial deflection offset of approximately 0.29 mm (0.0114 inch). If this offset is applied to the first main pushover cycle of Test #2-22, the correction aligns the NDI curve and the strain gauge curves at low drift. Fig. 6.8 shows a section through the pin connection where rocking may occur due to hole over-size.

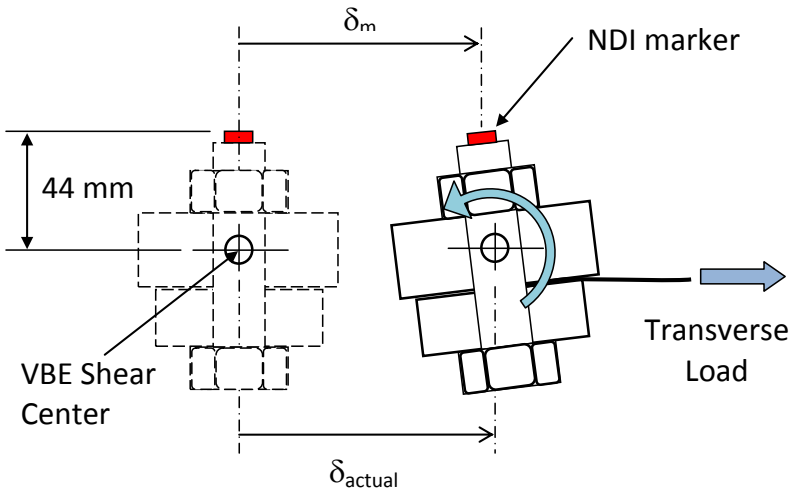

Figure 6.7: Cross section of unloaded and loaded VBE-CB showing exaggerated translation and rotation at mid-span.

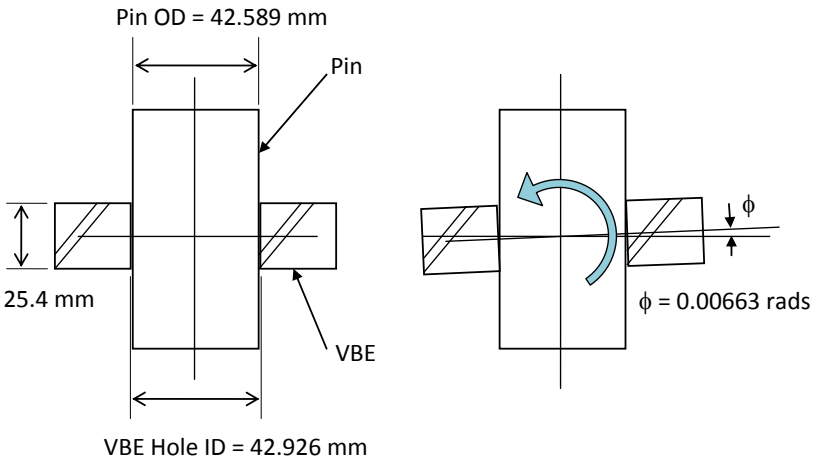

Figure 6.8: Cross section of unloaded and loaded VBE-CB at pin showing exaggerated axial rocking.

6.1.6 VBE-CB Axial Force and Deflection Amplification

Fig. 6.9 shows a schematic representation of the loaded system with free-body-diagrams of the VBE-CBs. Assuming a 45 degree tension field, the axial force, P, at midspan of the VBE-CB switches from a tension of approximately 0.25F to a compression of approximately -0.89F, depending on the direction of the applied lateral load F. Flexural strains are predominantly tensile on the inside of each section and compressive on the outside of each section. Some small excursions in the opposite direction can be observed in the data when the drifts are very low. The presence of axial force will affect the lateral deflection to a small degree. To estimate the influence of axial force on the measured VBE-CB deflection the following simple approximate relationship may be used:

$$\delta_m = \frac{{\delta_m}^{1st}}{\left(1 - \frac{P}{P_{cr}}\right)} \tag{6.5}$$

Where ${\delta_m}^{1st}$ is the first-order deflection resulting from transverse load, P_{cr} is the Euler buckling load of the composite VBE-CB section and P is the axial force in the member, with compression being negative. For the present study, P_{cr} is approximately -2922 kN (-657 kips) and results in a deflection amplification factor of approximately 1.03 in the compressed VBE-CB at peak lateral load. Due to its small effect, it is subsequently ignored for the remainder of the analyses.

6.1.7 VBE-CB Bolt slip

The results of the SAP analysis reveal that under the maximum expected transverse load of 113 kN/m (1 kip/in) the maximum bolt shear is approximately 24.5 kN (5.5 kips). The AISC published value of allowable bolt slip resistance (r_n/Ω_v) for a single shear, slip-critical connection with μ equal to 0.35, is 32.8 kN (7.38 kips). The maximum likely bolt shear is below the service load level slip resistance capacity of a fully pre-tensioned bolt of this size and grade, so full composite behavior is expected.

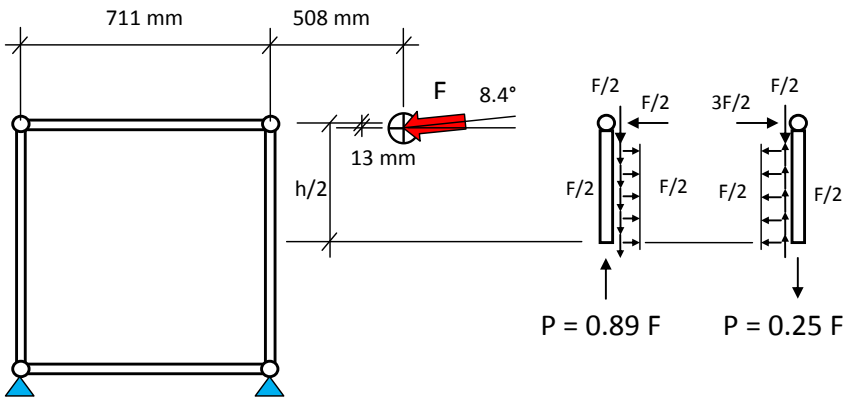

Figure 6.9: Phase II Tests: FBD of VBEs showing approximate axial forces at midspan.

6.1.8 Transverse Load and Bending Demand Estimates

Only a portion of the total VBE-CB length was transversely loaded by the web plate. It was therefore necessary to account for this when computing flexural demands from the strain and deformation data. Numerical analyses of the tests using *ABAQUS* confirmed that the uniform load assumption is valid and the results of this analysis are presented in the next chapter. The equivalent uniform transverse load w_{NDI} (kN/m) determined from the NDI data is computed using Eq. 6.6. Furthermore, no visual indications of bolt slip were observed.

$$w_{NDI} = \kappa \delta_m \tag{6.6}$$

Where δ_m is the deflection (mm) of the VBE-CB measured at midspan with respect to the center of each pin at either end, and κ, a parameter extracted from the SAP analysis that accounts for stiffness distribution and load eccentricity, and equals 16.78 N/mm^2.

Assuming a uniform transverse force distribution over the length h, the bending moment is determined using Eq. 6.7

$$M_{NDI} = \frac{w_{NDI}h}{4}\left(L - \frac{h}{2}\right) \tag{6.7}$$

The equivalent uniform transverse load, w_{SG}, determined using the strain gauges is computed using Eq. 6.8.

$$w_{SG} = \left(\frac{4E}{h}\right)\frac{\left(\epsilon_{cb}S_{cb} + \epsilon_{vbe}S_{vbe}\right)}{\left(L - \frac{h}{2}\right)} \tag{6.8}$$

Assuming elastic section behavior, the bending moment is computed from the strain gauge data using Eq. 6.9.

$$M_{SG} = E\left(\epsilon_{cb}S_{cb} + \epsilon_{vbe}S_{vbe}\right) \tag{6.9}$$

Where ϵ_{cb} and ϵ_{vbe} are the flexural strains in the CB and VBE section respectively. S_{cb} and S_{vbe} are the elastic section moduli of the CB and VBE section. The dimensions L and h are shown on Fig. 6.4. The dimension h is determined by dividing the loaded plate area of 0.420 m^2 (671.5 in^2) by the length of the VBE, which gives h equal to 0.609 m (24.0 inch).

6.2 Tests #2-22 and #3-22 Web Plate Data and Interpretation

This section presents the data obtained from the strain gauge rosettes mounted on the top and underside of the web plate, and the NDI optical tracking system mounted on the top surface of the web plate.

6.2.1 Strain Gauge Estimates of Tension Field Inclination

The migration of the tension field inclination angle measured using strain gauges under monotonically increasing lateral load, or pushover, is presented in Fig. 6.10. This plot shows the migration that occurred for the first loading cycle into the plastic range for Test #2-22. It shows a clear progression of α from a minimum of approximately 35.2 degrees at 0.4% drift to a maximum of approximately 43.8 degrees at 5% drift. This is consistent with the preliminary numerical studies presented in Fig. 3.7 of Chapter 3. The point at which the mean computed von Mises stress reaches the coupon yield stress of 287 MPa (see Tab. 4.2) is also shown on this plot at a drift of 0.65%. This represents the point of significant yield, Δ_{ys}, as distinct from the theoretical yield drift, Δ_y, estimated using Eq. 6.1 which is approximately 0.40% for Test #2-22.

The location of Δ_{ys} coincides with an abrupt increase in the computed α. The tension field inclination angle at zero drift is very close to 45 degrees, which agrees with what theory predicts for the pre-buckled panel. Fig. 6.11 shows the computed tension field inclination angle, α^{el}, for Test #2-22 during each stage of elastic loading, as defined previously, plotted against elastic drift, Δ^{el}. Fig. 6.12 shows the case for plastic loading α^{pl} plotted against accumulated plastic drift, Δ^{pl}. The average measured elastic α starts at close to 45 degrees and migrates towards approximately 36 degrees at a drift of 0.2% and appears to reach a local minimum value at a drift much lower than the drift at significant yield, Δ_{ys}, which is computed as 0.64%, and shown on Fig. 6.10. The angle predicted using elastic least work principles is approximately 37 degrees. This is in good agreement with the angle computed using the strain gauge data. The angle computed when the web plate is plastically loaded

shows almost no dependance of α on the magnitude of the accumulated plastic drift. Fig. 6.12 shows that α^{pl} is close to 42 degrees when the accumulated plastic drift is around 0.5% but only increases to slightly more than 44 degrees at an accumulated plastic drift of 10%.

Similar trends are observed in Fig. 6.13 for Test #3-22 where α^{el} is observed to decrease from an initial value of 45 degrees to a minimum of approximately 37.5 degrees between drifts of 0.2% and 0.3%. The angle increases to nearly 39 degrees as the drift approaches 0.5%. Examination of the mean computed von Mises stress for the five points sampled on the web plate shows that σ_{eff} only reaches approximately 86% of the material yield stress at a drift of 0.51%. This is reasonably consistent with the case for Test #2-22 where the load history was entirely different. A more rapid migration of α towards 45 degrees is observed in this test than for the single monotonic loading case of Test #2-22. The angle computed for plastic loading, shown in Fig. 6.14, is similar to Test #2-22. Once again there is almost no dependance of α^{pl} on the magnitude of the accumulated plastic drift. The mean α^{pl} over the range of plastic drift is approximately 44 degrees.

It can be concluded that for a system with an initial elastic tension field inclination angle significantly less than 45 degrees:

1. The migration of α with increasing elastic drift is largely independent of the loading regime. Prior to buckling it is close to 45 degrees. After buckling it decreases to a value very close to that predicted using elastic least work principles, it then increases to around 40 degrees at just below yield drift.

2. With limited accumulated plastic drift, α rapidly approaches 45 degrees but tends to stabilize at a slightly lower angle. This suggests that when an SPSW web plate is fully yielded, but has limited accumulated plastic drift (around 1%), the tension field will be inclined at between 42-45 degrees, regardless of its initial elastic value. This agrees with the observations of preliminary FE analyses in Chapter 3 which also explored

various VBE properties and panel aspect ratios.

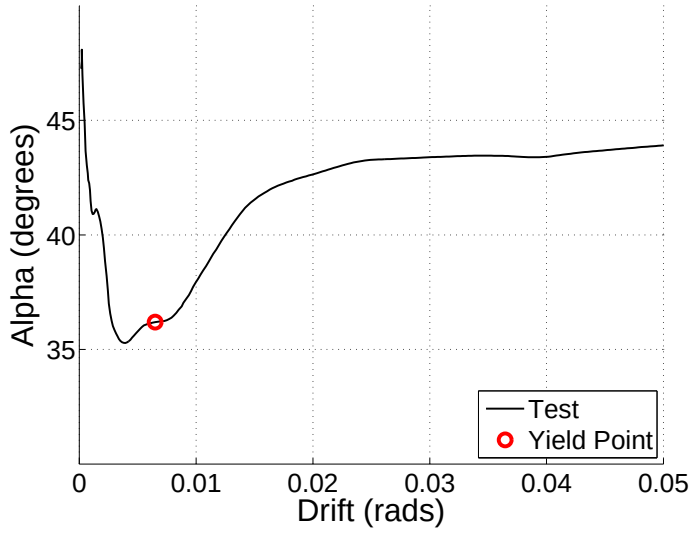

Figure 6.10: Test #2-22: Migration of α under single monotonic load to 5% drift showing the yield point computed from the mean Mises stress.

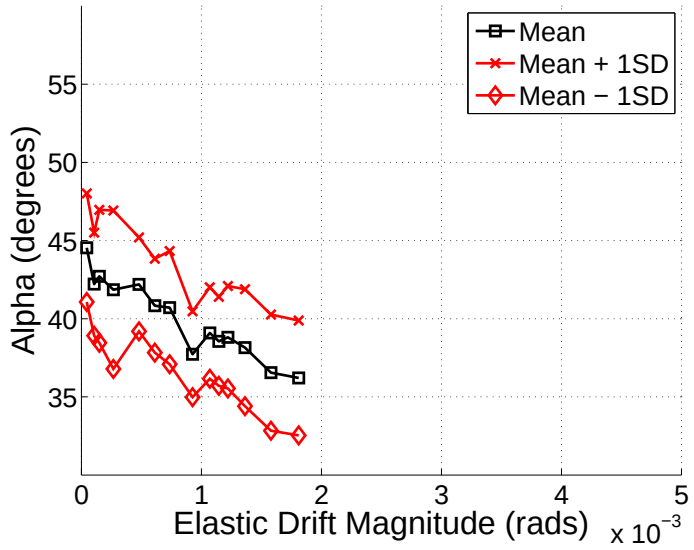

Figure 6.11: Test #2-22: Progression of α under elastic loading.

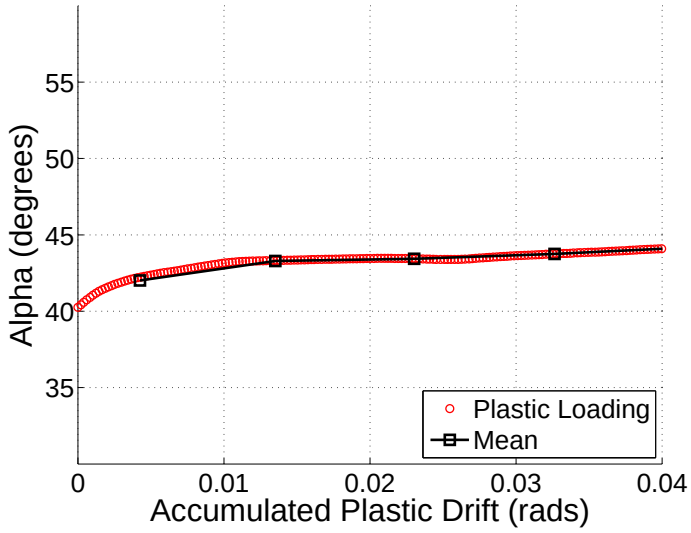

Figure 6.12: Test #2-22: Progression of α under plastic loading.

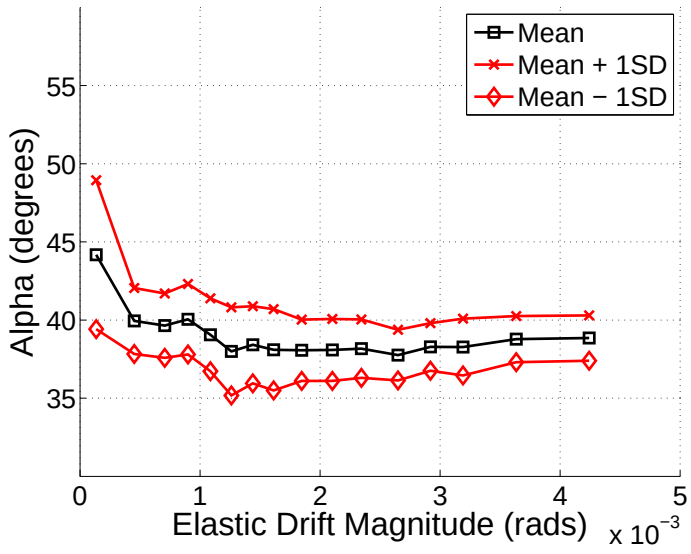

Figure 6.13: Test #3-22: Progression of α under elastic loading.

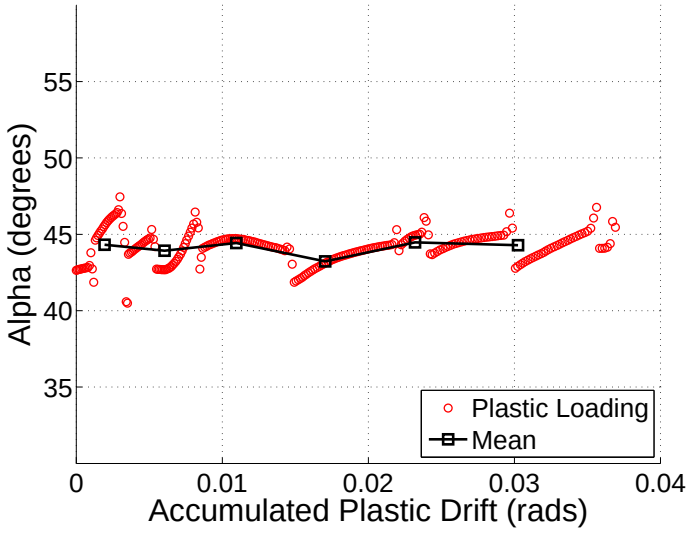

Figure 6.14: Test #3-22: Progression of α under plastic loading.

6.2.2 NDI Estimates of Tension Field Inclination

The array of web plate LED markers was used to track the inclination of the buckled corrugations versus drift. The spatial position (x and y in-plane, and z out-of-plane) of the markers was tracked at every increment in time throughout the test. At every time point, a polynomial function was fitted to the (x,z) components of the data along each horizontal row of markers. This function was used to determine the x and z coordinates of maxima and minima. The y ordinate of each maxima and minima was assumed to lie at its original y position in space, i.e., its row position. Crests and valleys were then constructed by connecting the points of maxima and minima across the rows. The result of this is shown in Figs. 6.15 through 6.17 at various stages of test #2-22.

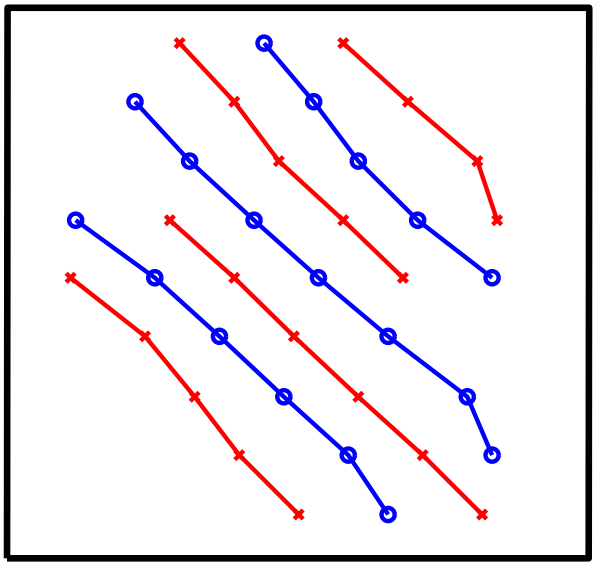

Figure 6.15: Test #2-22: Buckle Ridges and Valleys Computed from NDI Data: Drift = 0.15%

The angle of the buckling corrugations was then computed by linear regression of each crest and valley to find the slope, m, from which the inclination angle could be determined. Prior to averaging, a weighting was applied to the angle determined for each crest and valley in proportion to its total length. Thus, short crests or valleys would not contribute to the

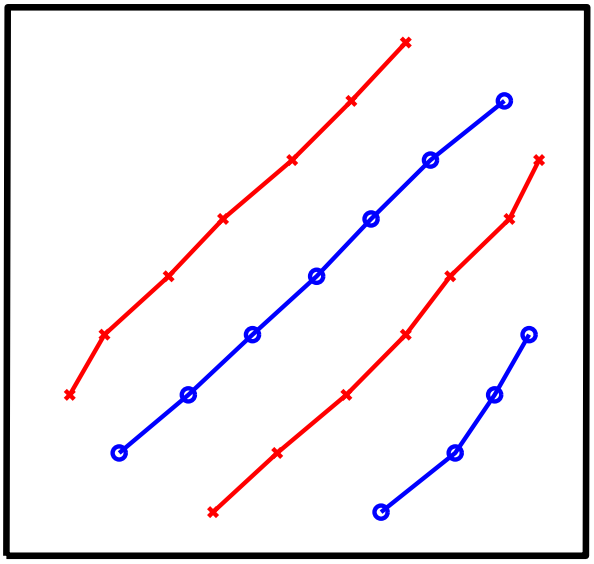

Figure 6.16: Test #2-22: Buckle Ridges and Valleys Computed from NDI Data: Drift = -0.23%

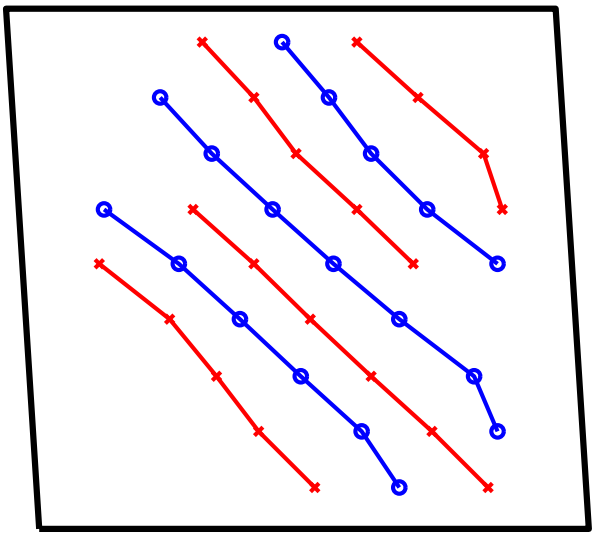

Figure 6.17: Test #2-22: Buckle Ridges and Valleys Computed from NDI Data: Drift = 6.0%

estimated angle as much as long ones.

Figs. 6.18 and 6.19 show how the angle determined form the inclination of the peaks and valleys changes for Test #2-22. The average angle is plotted over the first elastic cycle and the early stages of the first large inelastic cycle (cycle #2). Also shown on this figure is the frame drift (shown on a different scale). In the purely elastic loading cycles, once the tension field had been fully engaged, the measured inclination angle was higher than that predicted using Eq. 4.1 and is seen to be between approximately 38 and 43 degrees. Fig. 6.19 shows the region boxed in Fig. 6.18 showing how the angle progresses for cycle #2, starting at approximately 36 degrees around zero drift (t = 640 sec) and progressing to 46 degrees at 6% drift (t = 715 sec). It appears that the inclination of the buckling corrugations generally followed a similar trend as that determined from the strain gauge data, except that the corrugations change more gradually as the drift increased.

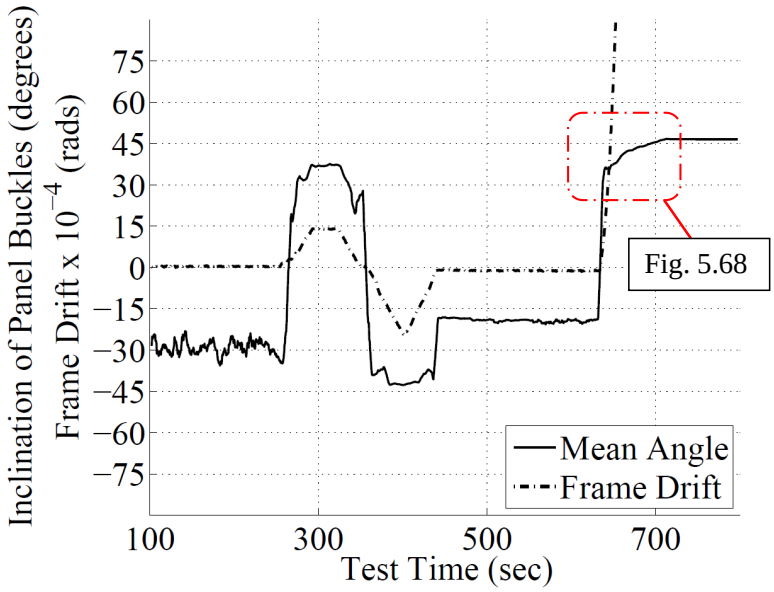

Figure 6.18: Test #2-22: Alpha Computed from Inclination of Panel Buckles

Fig. 6.20 shows the contour plots of Test #3-22 at the pull and push stroke of cycle #5

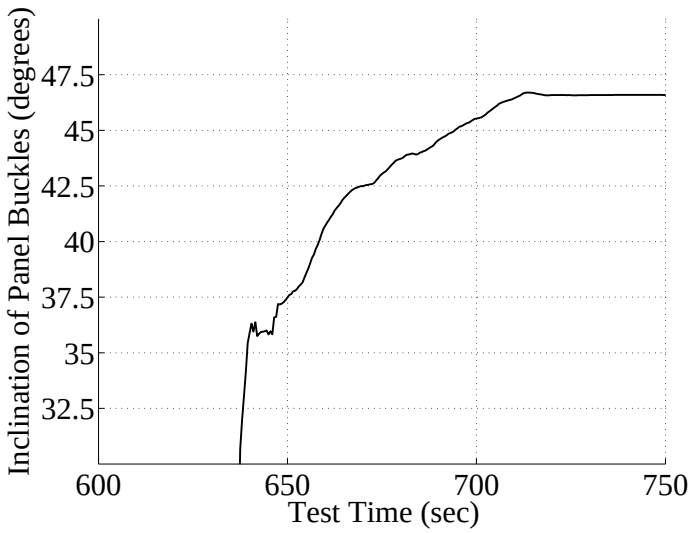

Figure 6.19: Test #2-22: Alpha Computed from Inclination of Panel Buckles

($Drift = 0.40\%$) and cycle #21 ($Drift = 3.75\%$). These contours also show asymmetry in the inclination of the buckled corrugations with pull stroke of cycle #5 being approximately 37 degrees and the push stroke being approximately 40 degrees. The inclination angle measured using the buckled corrugations was observed to be larger for the push strokes than the pull strokes for all cycles up to cycle #7. It is not known what caused this but it is probably due to the asymmetry of the applied loading and boundary conditions. Geometrical imperfections of the web plate itself are not believed to influence this behavior. At cycle #21 the angle settled to approximately 45 degrees in both the push and pull direction.

6.2.3 VBE and CB Section Strains

The total strains are shown in Figs. 6.21 and 6.22. In the legend of these plots; I and O represent Inside and Outside of the section, E and W are East and West member, and the suffixes VBE and CB denote the main VBE section and the CB, respectively. The flexural strains presented in Fig. 6.23 show that the CBs do not appear to be subjected to the same curvature demands at midspan as were the VBE sections. The depth of the CB is

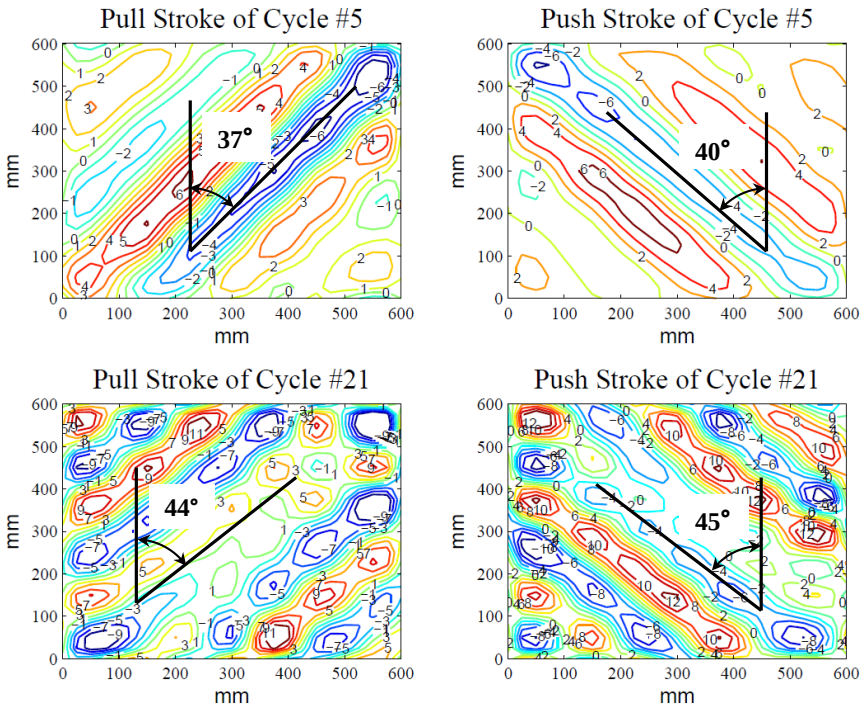

Figure 6.20: Panel Deformed Shapes: Test 3-22.

0.8 times the VBE depth, so with fully composite behavior the VBE flexural strains should be 1.25 times the CB flexural strains. The ratio of ϵ_{vbe} to ϵ_{cb} for the west VBE reduces from an initial value of approximately 1.78 to a value of around 1.5 as the cycles progress. The east VBE shows a similar trend starting at 1.70 and reducing to 1.26 at the last cycle. This reduction in strain ratio appears to be the result of the CBs not completely unloading when the member is fully unloaded, whereas the main VBE sections do. This could be attributed to slip in the connection during the unloading phase of the last five half cycles. Fortunately, the possibility of slip does not affect the estimate of the peak moment demand because any residual elastic flexural strain in the CB will equilibrate with the VBE section. i.e., the residual CB moment should be equal and opposite to the VBE moment when zero transverse load is applied from the web plate.

For both members the initial value of the flexural strain ratio is much higher than ex-

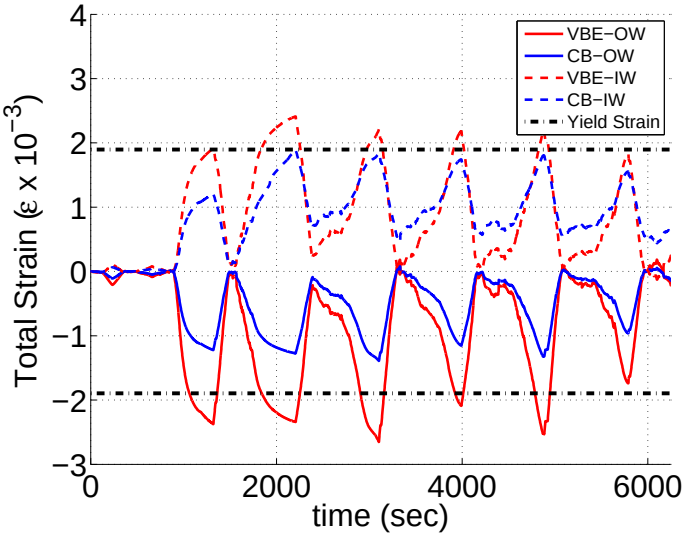

Figure 6.21: Test #2-22: West side VBE and CB total strains.

pected. Examination of the strain ratio over the first two half cycles, where the drift was less than 0.2%, reveals a remarkably constant strain ratio of 1.68 for the west member and 1.77 for the east member. At this drift, the connection should not have undergone any slip and the flexural strain ratio should be very close to the theoretical value of 1.25 predicted using plane section assumptions. Furthermore, the mean ratios of the strain *rates* between the VBE and CB sections are 1.75 and 1.51 for the west and east side and remain close to these values for the entire test. The strain rate cannot be used to indicate slip, as it won't detect it, but assuming the sections remained essentially elastic these ratios should have been constant (as they were) but should have been closer to 1.25.

The similarity in the magnitude of the CB total strains on the inside and outside of the sections, shown in Figs. 6.21 and 6.22, reveals that the CBs did not absorb a measurable proportion of the axial compressive force when the specimen was under lateral load. The VBEs on the other hand show higher magnitude compressive strain (outside of section) than tensile strain on each cycle, as would be expected.

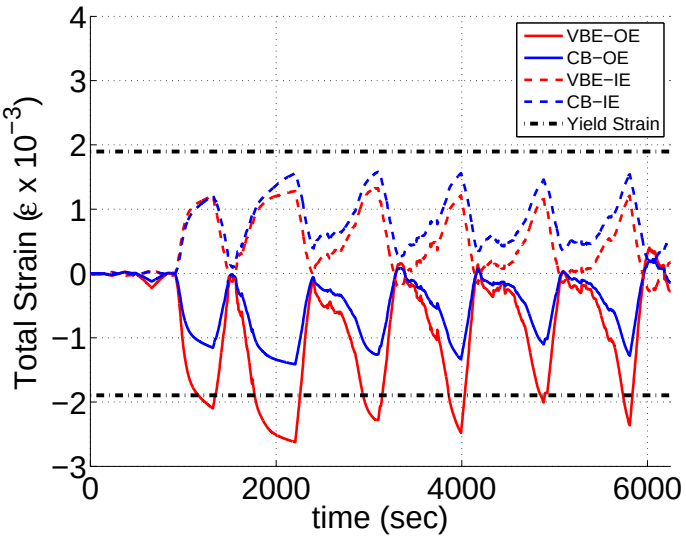

Figure 6.22: Test #2-22: East side VBE and CB total strains.

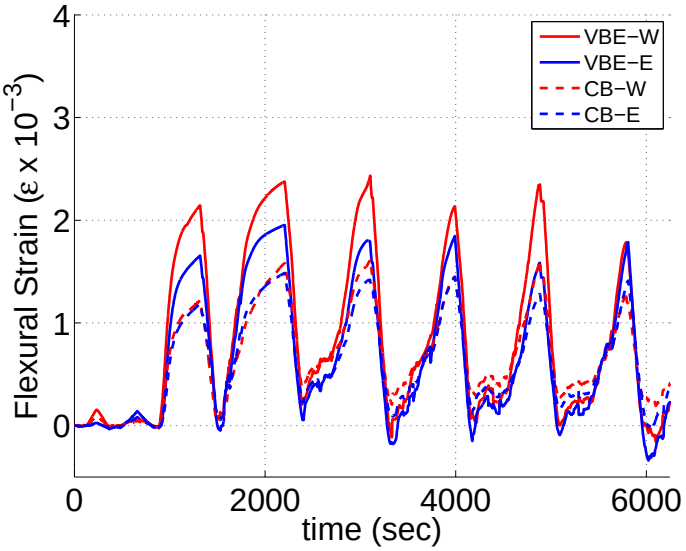

Figure 6.23: Test #2-22: VBE and CB flexural strains.

In conclusion, it appears that the strain gauge data for the VBEs is not entirely reliable because the ratio of the VBE to CB flexural strains and the ratio of VBE to CB strain rates are not consistent with elastic plane section assumptions, even when accounting for the

possibility of non-composite behavior. The CB strains are reasonably close to the theoretically predicted values. The VBE flexural strains are considerably higher than the predicted values.

6.2.4 Estimating Bending Demand from Strain Gauge and NDI Data

The bending moment demand at midspan of each VBE-CB is computed using w_{NDI} from Eq. 6.6. Fig. 6.24 shows the VBE-CB member at peak drift with the LED markers on top of the pins and the center bolt. A slight inward deflection is visible in this image. Fig. 6.25 shows the computed flexural demand for Test #2-22 during the first half-cycle out to a maximum drift of approximately 6%. There is a distinct difference in the calculated demand using the strain gauges and the NDI system, although the overall trend is the same and the post-yield slope of these curves appears to be very similar. For comparison, the peak flexural demands determined from a simple tension field model are shown using α equal to 40 degrees (AISC-40) and 37 degrees (AISC-α) with $R_y F_y$ equal to the actual F_y of the plate. The curve denoted *SG-el* was generated assuming the VBEs behave elastically. The curve denoted *SG-pl* was generated from a fiber analysis of the VBE-CB section using the actual strain gauge readings and an assumed F_y of 379 MPa (55 ksi). The curves diverge slightly at high drift levels where the inside of the VBE section may have yielded at the extreme fibers, however the difference is less than 2% at peak drift.

If it is assumed that the CB strains are correct and the corresponding VBE strains are replaced with a scaled CB strain, the bending and transverse load estimates match the NDI computed values. For comparison, the bending moment demand resulting from the modified VBE strains, denoted *SGmod-el*, are shown in Figs. 6.26 and 6.27 for Test #2-22 and #3-22 respectively. Fig. 6.28 shows the bending demand in the east and west VBEs plotted over time and compares the response assuming elastic and elasto-plastic section properties. The estimated transverse load w_F is derived from the magnitude of the applied lateral force, $F_p(\Delta)$, to the specimen at drift level Δ assuming α equals 45 degrees and the expected proportion of compressive stress present in the plate as a function of drift magnitude. Figs. 6.29 and 6.30 show the measured transverse forces, w_{NDI} and w_{SG}, normalized by the

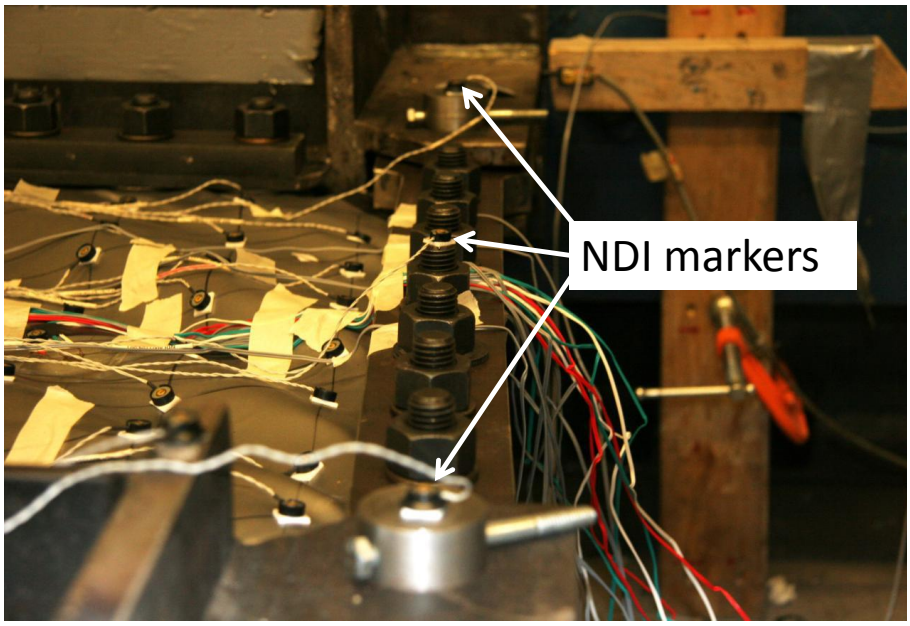

Figure 6.24: Test #2-22: VBE-CB deformation at peak load showing NDI LED marker at top of middle bolt and markers at center-top of each pin.

equivalent transverse force, w_F, form Eq. 6.10 for Tests #2-22 and #3-22 respectively.

$$w_F = \frac{F_p(\Delta)L}{A_p}\left(\frac{1-\eta}{1+\eta}\right) \tag{6.10}$$

Where η is the ratio of mean principal compressive stress magnitude to mean principal tensile stress magnitude in the web plate and is estimated using Eq. 6.11 which was based on results of numerical analyses presented in Fig. 3.21 of Section 3.3.3. A_p is the area of the web plate.

$$\eta = 0.05 + 0.15e^{-60||\Delta||} \tag{6.11}$$

Fig. 6.31 shows the result of normalizing the transverse force by w_{Fa}, where w_{Fa} is

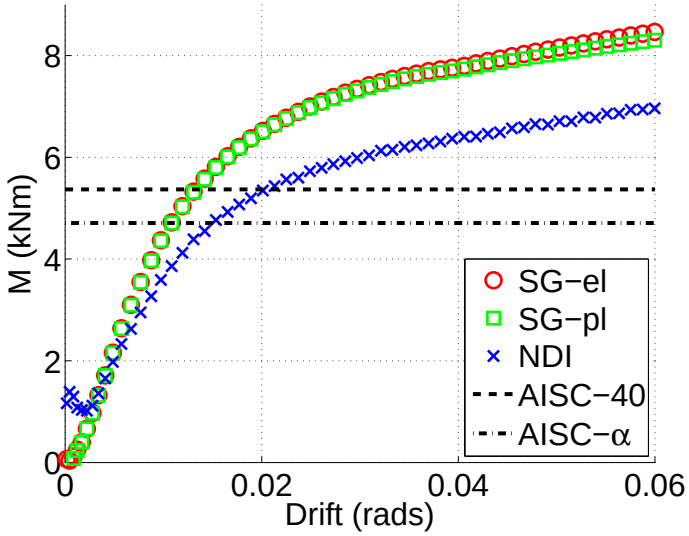

Figure 6.25: Test #2-22: Mean VBE-CB bending moment v's drift for first half-cycle to Δ = 6% determined from strain gauge data (SG) and NDI system.

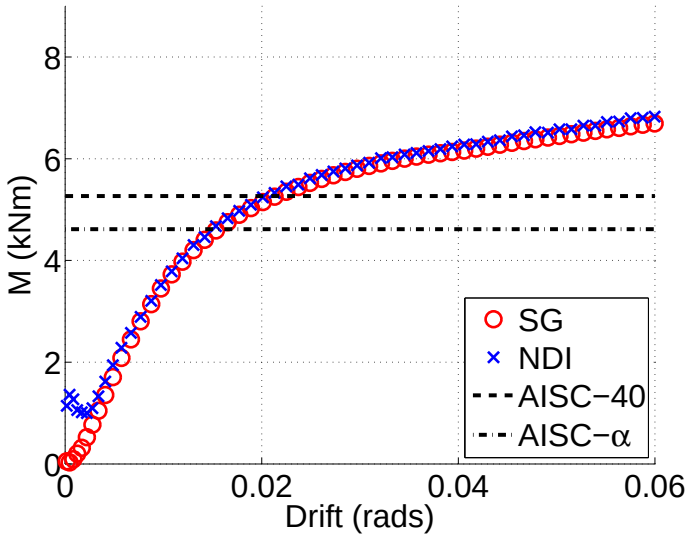

Figure 6.26: Test #2-22: Mean VBE-CB bending moment v's drift for first half-cycle to Δ = 6% determined using modified strain gauge data (SGmod-el) and NDI system.

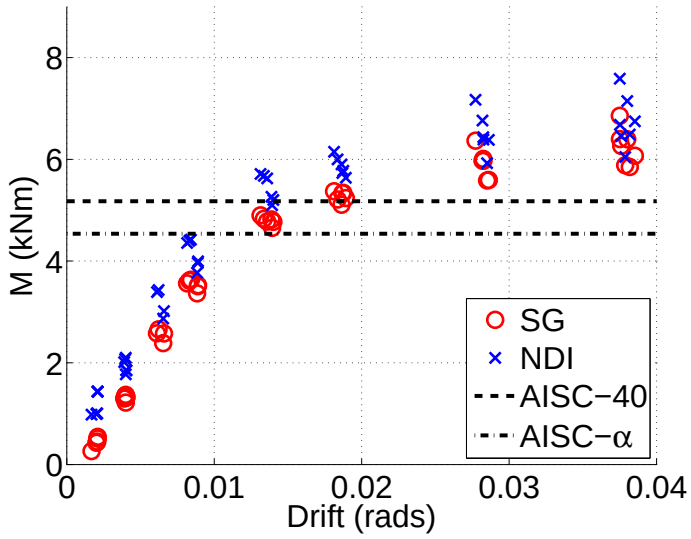

Figure 6.27: Test # 3-22: Mean VBE-CB bending moment v's drift determined using modified strain gauge data (SGmod-el) and NDI system.

computed using Eq. 6.12. Eq. 6.12 uses the actual α measured from the experiment, instead of 45 degrees.

$$w_{Fa} = \frac{2F_p(\Delta)Lsin(2\alpha)}{A_p}\left[\frac{1+\eta}{1+\frac{\eta}{2}}sin^2\alpha - \frac{\eta}{1+\frac{\eta}{2}}\right] \tag{6.12}$$

It is reasonable to expect that this would produce a value of normalized transverse load close to unity at all drift levels. There is still however a tendency for lower than expected transverse loads at drift levels below about 1%.

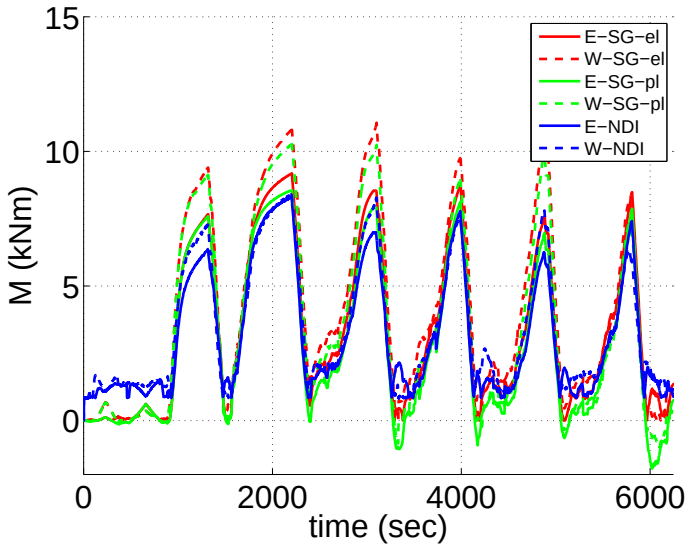

Figure 6.28: Test #2-22: VBE-CB east and west bending moment determined using strain gauge (SG) and NDI data assuming elastic (el) and elasto-plastic (pl) section properties.

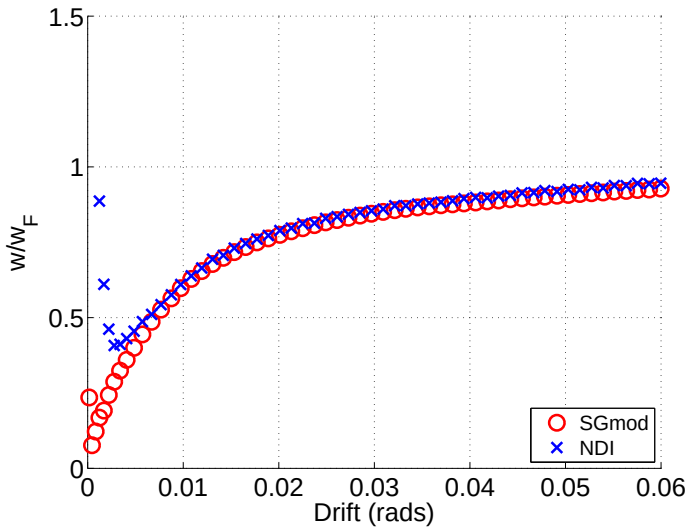

Figure 6.29: Test #2-22: VBE-CB mean transverse distributed load determined from modified strain gauge and NDI data normalized by the computed w_F.

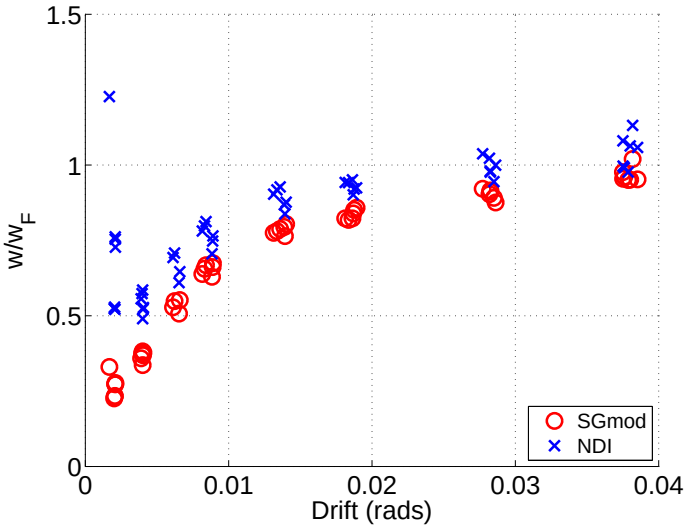

Figure 6.30: Test # 3-22: VBE-CB transverse force demand (w) normalized by equivalent transverse force (w_F).

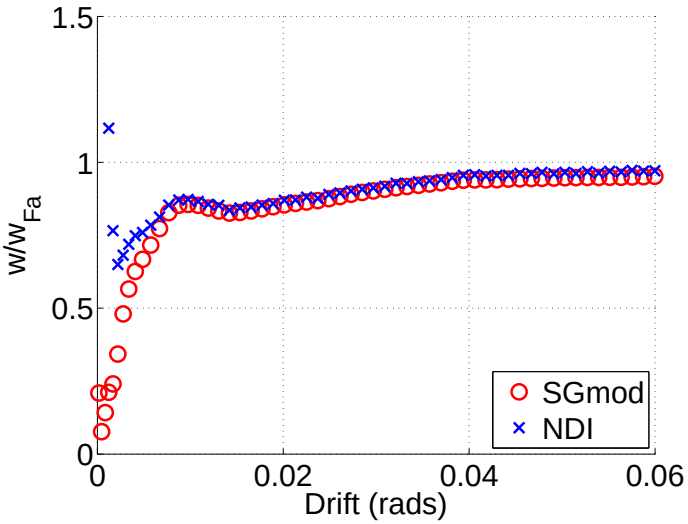

Figure 6.31: Test #2-22: VBE-CB mean transverse distributed load determined from modified strain gauge and NDI data normalized by the computed w_{Fa}.

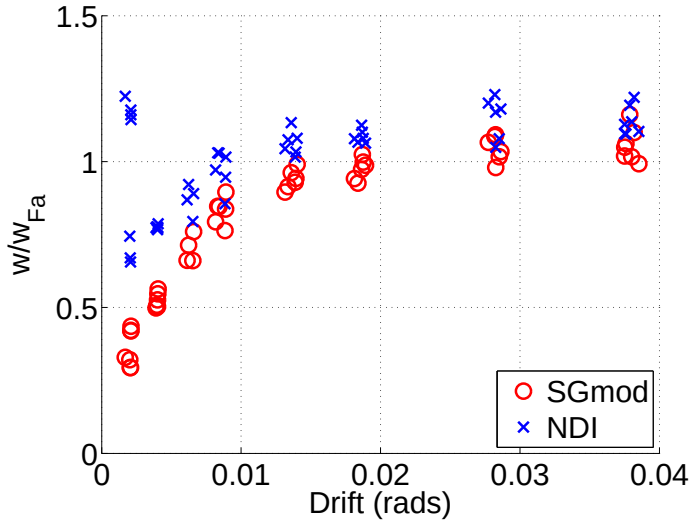

Figure 6.32: Test #3-22: VBE-CB mean transverse distributed load determined from modified strain gauge and NDI data normalized by the computed w_{Fa}.

6.2.5 Summary

The transverse force w_{Fa}, which uses a variable α, provides a better approximation of the measured transverse force than w_F, which used 45 degrees. The improvement however is modest and only at low drift levels. It is also difficult to incorporate a variable α into a FEA model unless continuum elements are used. Certainly, if a strip model approach is adopted it becomes impractical to vary the angle. The most expedient approach is to maintain a constant α value (45 degrees) and tune the material properties of the plate so that the correct lateral force and VBE demand result from given drift history. The challenge then is to develop an equivalent uniaxial truss element that will achieve this. The first step is to devise a method whereby the actual measured (or simulated) stress field may be decomposed into an equivalent 2D stress field, comprising two orthogonal principal stresses that act at 45 and 135 degrees and produce the correct lateral force and VBE transverse force. This would then used to develop the required constitutive properties for the strips.

6.3 Equivalent Web Plate Stress Field

The equivalent web plate stress field, defined here, is one where the actual state of stress is replaced by uniform tensile and compressive stress fields that result in the **same lateral base reaction and the same equivalent VBE bending demand ($\frac{wh^2}{8}$) throughout the load history**. The motivation for this is to determine, in a strip model, the strip constitutive properties that would not only result in the a better estimate of global lateral strength (as a function of drift), but also VBE transverse force demand.

An equivalent uniform web plate stress field, comprising two mutually orthogonal components, may be determined from the experiment by writing expressions for the VBE-CB transverse force, w_{vbe}, and the applied lateral load, $F_p(\Delta)$, in terms of uniform stress field quantities in the web plate. As shown in Fig. 6.33 one component of the field, $\hat{\sigma}_\alpha$, is inclined at α and the other, $\hat{\sigma}_{\frac{\pi}{2}-\alpha}$, is inclined at $\frac{\pi}{2}-\alpha$ (these are later specialized to 45 degrees and 135 degrees). The hat symbol here is used to denote an equivalent uniform stress quantity. The term *equivalent stress* is introduced to distinguish it from the real in-plane web plate stresses, which vary in magnitude and principal orientation throughout the web plate and with drift level. As has been demonstrated in many of the previous figures, using mean values of the real stresses will not result in an accurate estimate of the applied lateral load and VBE transverse force demands simultaneously, particularly at drifts less than 0.75% or greater than (1.25%). Therefore the need for an equivalent stress field is developed.

Assuming a uniform stress field with principal tension inclined at α and principal compression field operating normal to this, the following equations express the magnitude of the lateral load or base reaction, $F_p(\Delta)$, and the transverse force on the VBE, w_{vbe}, in terms of $\hat{\sigma}_{\frac{\pi}{2}-\alpha}$ and $\hat{\sigma}_\alpha$:

$$F_p(\Delta) = \frac{t_w}{2}\left(\hat{\sigma}_\alpha - \hat{\sigma}_{\frac{\pi}{2}-\alpha}\right)\frac{A_p}{L}sin(2\alpha) \tag{6.13}$$

$$w_{vbe} = t_w\left(\hat{\sigma}_\alpha sin^2\alpha + \hat{\sigma}_{\frac{\pi}{2}-\alpha}cos^2\alpha\right) \tag{6.14}$$

In matrix form:

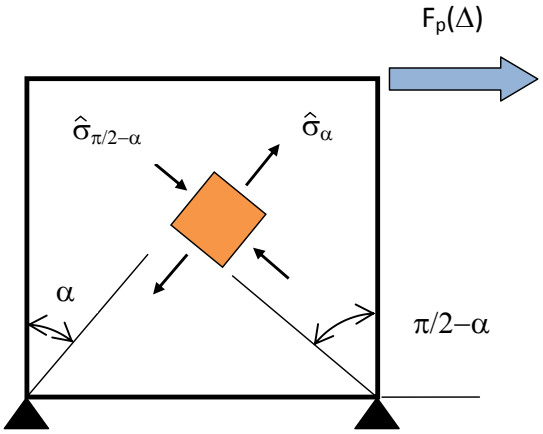

Figure 6.33: Equivalent stress field.

$$\hat{\boldsymbol{\sigma}} = \frac{1}{t_w}\mathbf{A}^{-1}\mathbf{F} \tag{6.15}$$

Where:

$$\hat{\boldsymbol{\sigma}} = \begin{Bmatrix} \hat{\sigma}_\alpha \\ \hat{\sigma}_{\frac{\pi}{2}-\alpha} \end{Bmatrix}$$

$$\mathbf{A} = \begin{bmatrix} \frac{A_p}{2L} sin(2\alpha) & \frac{-A_p}{2L} sin(2\alpha) \\ sin^2(\alpha) & cos^2(\alpha) \end{bmatrix}$$

$$\mathbf{F} = \begin{Bmatrix} F_p(\Delta) \\ w_{vbe} \end{Bmatrix}$$

Since $F_p(\Delta)$ and w_{vbe} are known from the test results, the system can be solved for $\hat{\sigma}_{\frac{\pi}{2}-\alpha}$ and $\hat{\sigma}_\alpha$. This is carried out for both tests by first using α determined from the web plate strain gauges and then using α equal to $\frac{\pi}{4}$. Figs. 6.34 and 6.35 show the principal tensile and compressive stresses in the web plate computed on this basis. Figs. 6.36 and 6.37 show $R_{\hat{\sigma}}$ the ratio of the equivalent uniform principal stress magnitudes, for Tests #2-22 and #3-22 for α determined by the strain gauges and for α equal to $\frac{\pi}{4}$ and $\frac{3\pi}{4}$.

Fig. 6.36 can be compared to Fig. 3.28 in Chapter 3, where for a D/t ratio of 928, R_σ is approximately 0.18 at yield drift and 0.06 at a drift of 3%. $R_{\hat{\sigma}}$ determined from Fig. 6.36 for Test #2-22 is approximately 0.20 at yield drift and 0.06 at 3% drift when using the strain gauge measured α. This system of equations can be solved over the entire load history to develop an equivalent directional hysteretic response of the stress field at $\frac{\pi}{4}$, and at $\frac{3\pi}{4}$. This operation was carried out for Tests #2-22 and #3-22 and the results are shown in Figs. 6.38 and 6.39. In these plots, the sign of the stress for the strip inclined at $\frac{3\pi}{4}$ is reversed so it overlays the one at $\frac{\pi}{4}$. This is done for comparative purposes. Relationships such as these can be used to calibrate strip models.

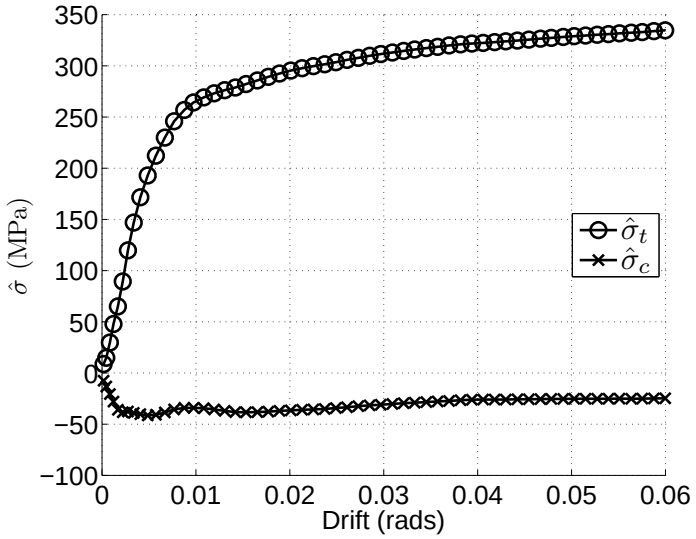

Figure 6.34: Test #2-22: Web plate principal stress magnitudes determined from computed VBE transverse load, w_{vbe}, and applied lateral load to frame, F_p.

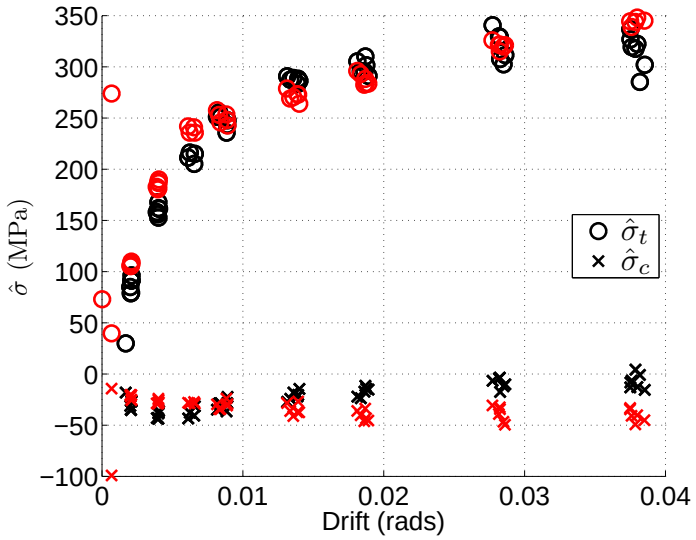

Figure 6.35: Test #3-22: Web plate principal stress magnitudes determined from computed VBE transverse load, w_{vbe}, and applied lateral load to frame, F_p.

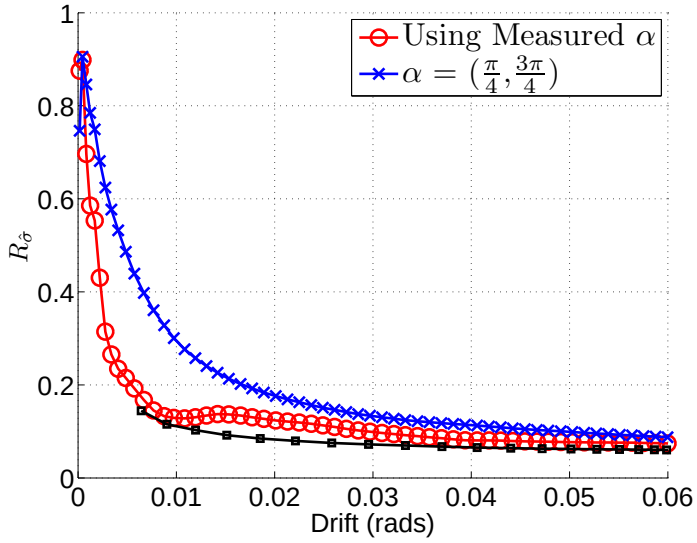

Figure 6.36: Test #2-22: Web plate principal stress magnitude ratio, $R_{\hat{\sigma}}$, determined from computed VBE transverse load, w_{vbe}, and applied lateral load to frame, F_p.

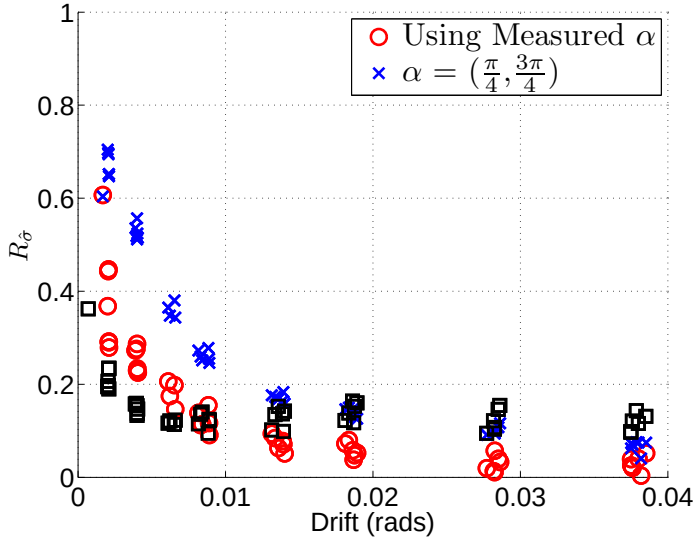

Figure 6.37: Test #3-22: Web plate principal stress magnitude ratio, $R_{\hat{\sigma}}$, determined from computed VBE transverse load, w_{vbe}, and applied lateral load to frame, F_p.

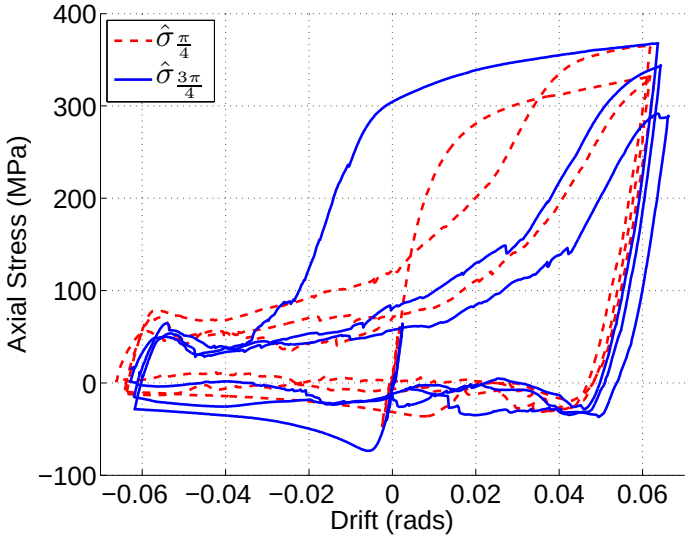

Figure 6.38: Test # 2-22: Directional hysteresis curve showing stress in equivalent 45 degree diagonal uniaxial element.

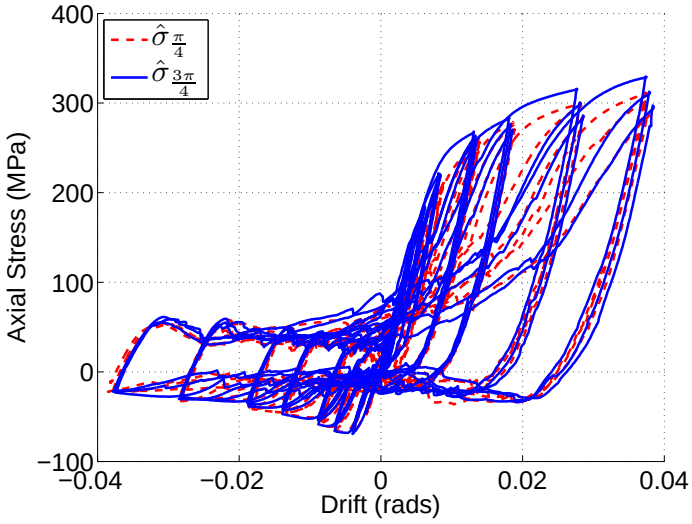

Figure 6.39: Test # 3-22: Directional hysteresis curve showing stress in equivalent 45 degree diagonal uniaxial element.

6.4 Summary of Phase II Tests

The Phase II tests were used to measure the tension field orientation and the effect this has on the VBE bending moment demand. The results of this series of experiments indicate that for this configuration:

- Both pushover and cyclic loading showed the measured tension field orientation angle, α, closely matched that predicted by Eq. 4.1, but only at drifts approximately equal to the theoretical yield drift.

- For pushover loading, α asymptotically approached an angle close 45 degrees as the drift increased and was significantly higher than the elastically predicted angle at design level inter-story drifts, reaching 42 degrees at 1.5% drift.

- The correlation between the inclination of tension field inclination angle measured using the buckled corrugations and the strain gauge data is not very good. The trends are similar but the method tends to be inaccurate.

- For cyclic, plastic loading of the web plate, α maintained a value close to 45 degrees regardless of the degree of accumulated plastic drift.

- For the pushover and the cyclic case, when the drift is less than approximately 0.75%, flexural demands on the VBE-CBs were consistently lower than those predicted using a simple tension field assumption.

- For the pushover and the cyclic case, when the drift is greater than approximately 1.25%, flexural demands on the VBE-CBs were consistently higher than those predicted using a conventional tension field assumption, with α computed per Eq. 4.1. The measured demands were reasonably consistent with predicted demands based on a 45 degree tension field acting in conjunction with the estimated compressive stresses.

- The directional hysteresis of the equivalent uniform stress field may be the most appropriate starting point from which to develop a uniaxial hysteretic element for a web plate strip model.

6.5 Unloaded Shear and Snap-through Strength

Table 6.1 lists approximate values of the mean unloaded strength, F_R, mean snap-through strength, F_{ST}, and max lateral strength F_{max} for each of the Phase I ad Phase II tests. Considerable variation of these quantities can be observed between different cycles within any single panel test, and the observed strengths generally depend on drift level. A bigger source of variation may be the chaotic nature of the residual out-of-plane deformations, as these will effect the stiffness of the web plate as it attempts to snap to a new configuration. Nonetheless, the data are presented here for completeness and the results are valuable. In particular, the snap-through strength observed in the experiments turns out to be significantly less that the predicted snap-through strength obtained from numerical simulations of the tests presented in the next chapter. This is the biggest discrepancy between the test results and the numerical simulations and implies that experimental data are needed to properly estimate this strength. An accurate estimate of the snap-through strength may be important for modeling the performance of self centering systems.

Also listed in Table 6.1 are the ratios of these quantities to the peak strength, F_{max}. It is noteworthy that the ratios, F_R/F_{max} and F_{ST}/F_{max} are a little higher for the thinner plate from the Phase I tests. In these tests relatively rigid pin connected boundary frame members are utilized. This suggests that the snap-through buckling is a more plastic phenomenon for the thicker plate than the thinner plate, in much the same way that the compressive strength P_c of a stocky steel column is a lower proportion of its tensile strength P_t than that for a flexurally slender column. It is believed that the magnitude of F_{ST} is primarily dependent upon VBE stiffness, cut-out geometry, and panel aspect ratio and less so on plate slenderness, plate material properties and displacement history. This is evident in that the Phase II test specimens (with 22 Ga plate) had lower F_{ST}/F_{max} than the 16 Ga tests and also had a much lower ratio of F_{ST} to F_R than the Phase I tests. It is possible that the flexibility of the VBEs heavily influenced the snap-through behavior. The stability of the results for the Phase II test group, using vastly different displacement histories, suggests that the snap though strengths are largely independent of load history. The last column

Table 6.1: Approximate mean unloaded shear strength, mean snap-through strength and mean snap-through stiffness for all tests

Test#	**(kN)** F_R	**(kN)** F_{ST}	**(kN)** F_{max}	F_R/F_{max}	F_{ST}/F_{max}	$(\times 10^3)$ K_{ST}
1-16	28	54	195	0.14	0.28	13
2-16	26	50	192	0.14	0.26	10
3-16	26	48	193	0.13	0.25	10
1-18	18	38	118	0.15	0.32	16
2-18	18	35	117	0.15	0.30	12
3-18	20	35	116	0.17	0.30	12
1-22	12	15	80	0.15	0.19	2.5
2-22	13	16	81	0.16	0.20	2.5
3-22	12	15	74	0.16	0.20	1.8

in the table is the approximate snap-through stiffness at maximum drift, K_{ST}, which is considerably smaller for the 22 Ga specimens than for the 16 and 18 Ga specimens. This is partly due to the increased plate slenderness and partly due to VBE flexibility.

Chapter 7

NUMERICAL SIMULATIONS OF EXPERIMENTAL TESTS

This chapter presents *ABAQUS* numerical simulation results of both the Phase I and Phase II tests. The objectives of this phase of the research are:

1. Through simulation of each test, validate the experimental peak strength, pushover behavior, stiffness and strength degradation.
2. Use numerical simulations to estimate web plate plastic strain accumulation.
3. Use the Phase I test results and *ABAQUS* combined hardening analyses to establish an appropriate hardening law for the A1008 and A36 materials.
4. Examine differences between simulation and experiment in snap-through strength and unloaded shear strength.
5. Validate Phase II test results concerning VBE demand and tension field inclination angle.

In the discussion that follows, frequent reference is made to the equivalent plastic strain, $\bar{\epsilon}^{pl}$, (PEEQ in *ABAQUS* nomenclature). This strain measure is defined in Section 3.1.5 and is a positive scalar quantity.

With regard to item 2 above, an accurate and reliable estimate of plastic strain accumulation is needed if determining the extent of hardening in a web plate undergoing cyclic loading. Without the benefit of a comprehensive continuum model, whereby accumulated plastic strain my be extracted, an estimate based simply on the observed or simulated hysteresis may be possible. Therefore, the simulation estimate of $\bar{\epsilon}^{pl}$ (using ABAQUS) and the two alternative estimates of plastic strain accumulation in the web plate (see section 7.2.2 to follow) are presented. The simulation estimate is used to check the *ABAQUS* force

response for the web plate modeled with an isotropically hardening material. It is also used as a "true" value of $\bar{\epsilon}^{pl}$ against which the alternative estimates may be compared and validated.

7.1 ABAQUS Models

Two *ABAQUS* models were built for the test simulations, one for Phase I and another for Phase II. The primary difference between the models is the VBE section size. For Phase I, the VBEs are modeled with sections equivalent to the W6x25 from the tests. For Phase II, the VBEs are modeled using a rectangular section with equivalent cross-sectional area and gross moment of inertia to the composite VBE-CB used in these experiments. As previously discussed in Chapters 4 and 5, the slender VBE sections used in the Phase II tests were designed to test the migrating tension field inclination angle and the influence of this angle on VBE transverse force demand. Fig. 7.1 shows the basic arrangement for the *ABAQUS* model contrasted with the actual test specimen in a loaded condition. In these models, line elements are used for the boundary elements and S4R shell elements are used for the web plate. These will be discussed in the sections that follow.

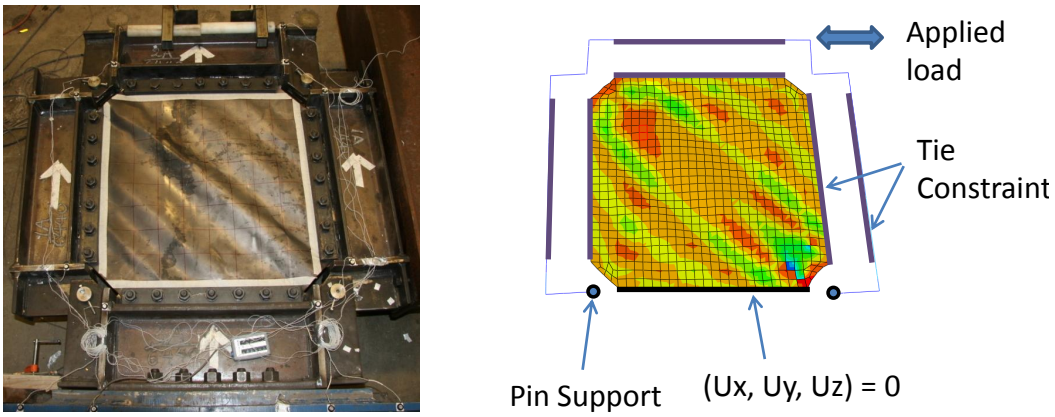

Figure 7.1: Experiment and *ABAQUS* model

7.1.1 Elastic Material Properties

The elastic properties of the web plates used for each simulation were in accordance with the properties detailed in Table. 4.2, with ν set equal to 0.30. The HBE and VBEs were modeled using elastic materials with E_s of 205,000 MPa and ν of 0.30.

7.1.2 Mesh Size, Geometry & Boundary Conditions

Two *ABAQUS* models were built, one for the Phase I series tests and one for the Phase II series tests. Each modeled the web plate using large displacement, finite strain S4R shell elements that extended to the inside edge of the clamping bar. The VBEs and top HBE were modeled using B31 shear deformable line elements located at the centroid of the section. The bottom W8x58 HBE was not explicitly modeled because it formed the bottom boundary to which the boundary frame was pin connected. Tie constraints were used to connect the edge of the web plate to the boundary elements. The VBEs were constrained to the top HBE using multi-point constraints that behave as pin connections between the members. The web plate initial imperfections were seeded using the first two eigenmodes from a buckling analysis, with a total amplitude of approximately 2 mm. This magnitude approximately matches the measured panel imperfection amplitude (See Fig. 5.3) from the experiment. The web plates comprised a 28x28 mesh of elements of approximately equal size. Through the mesh refinement study that follows, this mesh gradation was determined to provide sufficiently accurate results. The shells were modeled with nine integration points through the thickness of the element.

7.1.3 Solution Strategy

All of the simulations employed explicit dynamic analysis. Loads were applied using displacement control of a node at the right end of the top HBE. The displacement amplitude history exactly matched that recorded from each experiment, and was applied using a smooth-step amplitude function. The mass was scaled by a factor of fifty to increase the stable time increment. The time between consecutive amplitude peaks was designed to ensure inertial effects were maintained below approximately 1% of the peak applied lateral

force.

7.1.4 Mesh Refinement Study

To verify the adequacy of the mesh used in the analyses, a convergence study was carried out on a model similar to those developed for the Phase II test simulations using the explicit dynamic solver. Since the mass scaling and the algorithm defining the simulation speed are the same for the Phase I and II simulations, it was not considered necessary to do complete mesh refinement studies on both types of model.

The model used in the refinement study employed a simple bi-linear material model, with isotropic hardening for the web plate. The yield strength, F_y, was set equal to 300 MPa and the strain hardening slope, E_{sh} was set equal to $0.01E_s$, with E_s being set to 140 GPa. The geometry and boundary conditions for the mesh study model were identical to those eventually used in the test simulations that follow. The model was analyzed under cyclic displacement-control, with a displacement history comprising two complete cycles of 0.5%, 1.0%, 2% and 3% drift. The sensitivity to mesh density was evaluated on the basis of the error in maximum load attained at the peak of each cycle and the error in total energy dissipated at the end of the load history, which can be approximated as the error in E_I, the internal energy. Fig. 7.2 shows the results of these analyses using mesh #1, #2a and #3 shown in Table 7.1. Fig 7.3 shows the hystereses for meshes #2a and #2b using the S4R and S4 elements respectively. An energy balance check is presented in the next section. Three different mesh densities were analyzed and the results, including the approximate solution time, are listed in Table 7.1.

Energy Balance Check

It is generally recommended with explicit dynamic analyses that energy quantities be checked. For quasi-static analyses it is important that the kinetic energy (E_K), artificial energy (E_A) and the work done in propelling mass added in mass scaling (E_M) be small in comparison with the internal energy (E_I), which is the sum of the strain energy E_S,

Table 7.1: Mesh Sizes for Sensitivity Study

Mesh #	Mesh Size	Element Type	% error F_{peak}	% error E_I	(mins) Sol. Time
1	19x19	S4R	6.3	29.2	8
2a	28x28	S4R	3.6	8.1	28
2b	28x28	S4	NA	NA	112
3	46x46	S4R	1.0	0.8	120

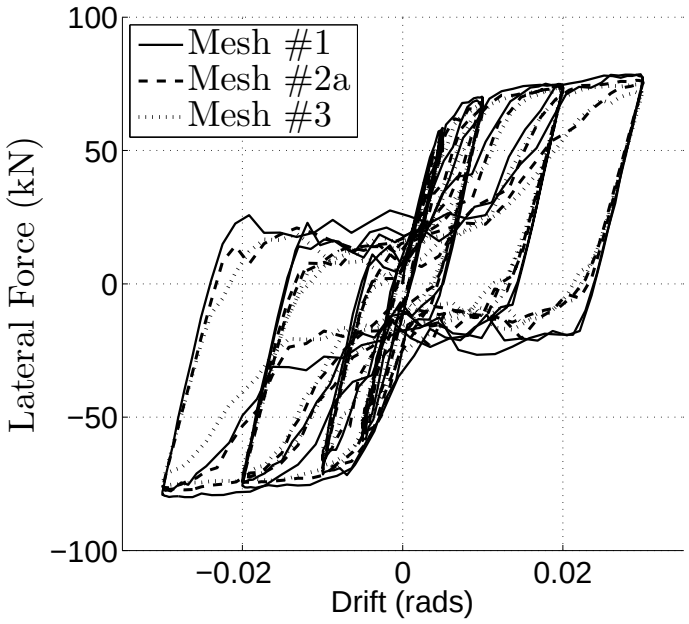

Figure 7.2: Hystereses for mesh #1, #2a and #3.

plastic deformation energy and artificial strain energy, E_A. Figs. 7.4 through 7.7 show the magnitudes of the energy quantities for meshes #1, #2a, #2b and #3 plotted on a Log_{10} scale. E_K should be small, however since the lateral load is measured by reporting base reactions it does not need to be negligibly small. E_K was found to be only 0.1 to 0.3% of E_I for each mesh and between 2 and 10% of E_S throughout the duration of the analysis.

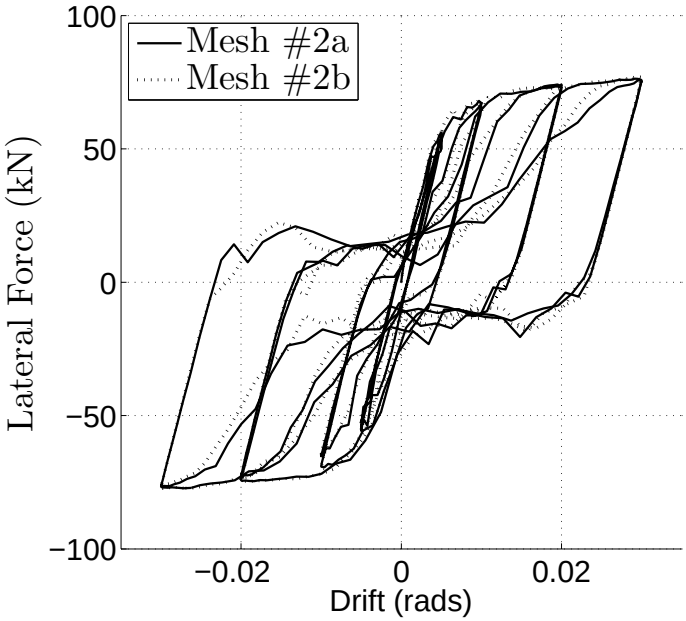

Figure 7.3: Hystereses for mesh #2a and #2b.

For the $S4R$ meshes E_A was believed to be primarily from hourglass control and is between 0.5% and 0.7% of E_I at the end of the simulation, depending on the mesh density. For the mesh #2b, with the $S4$ elements, E_A was only 0.06% of E_I. This slight residual E_A is thought to result from the kinematic constraints applied between the web plate edge and the VBEs and between the VBEs and the top HBE.

The total energy of the system, E_{total}, is defined by Eq. 7.1 and should be approximately zero. Table 7.2 shows the internal, artificial and total energy at the completion of the simulation for the four meshes. E_M was zero for all four meshes.

$$E_{total} = E_K + E_I + E_V - (E_W + E_P + E_C + E_M) \tag{7.1}$$

The remaining terms are: the energy dissipated by viscous effects (E_V), the work done by constraint penalties (E_C), and the external work (E_W). The total energy of the system should be approximately constant. For these simulations the total energy was close to zero

for each mesh.

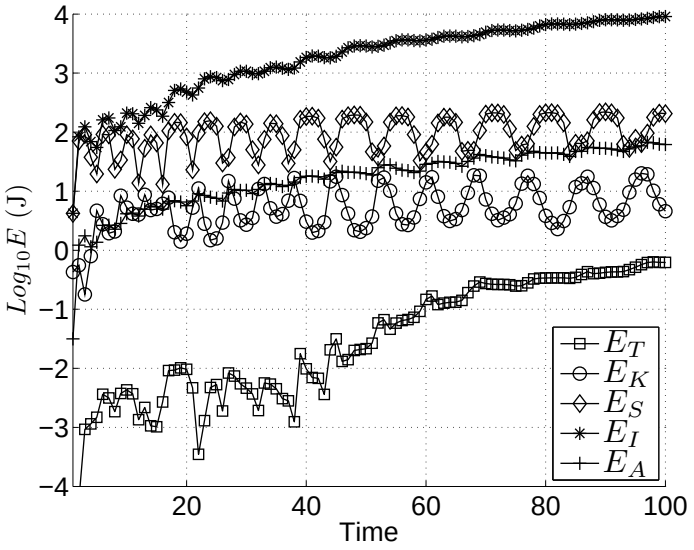

Figure 7.4: Energy quantities for Mesh #1

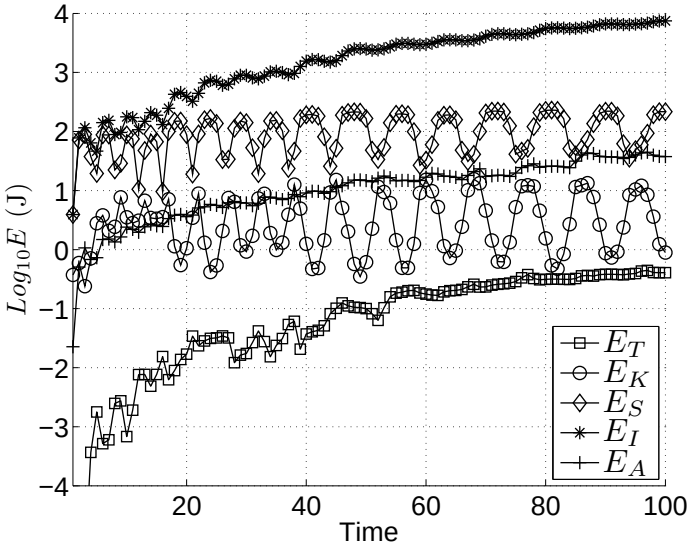

Figure 7.5: Energy quantities for Mesh #2a

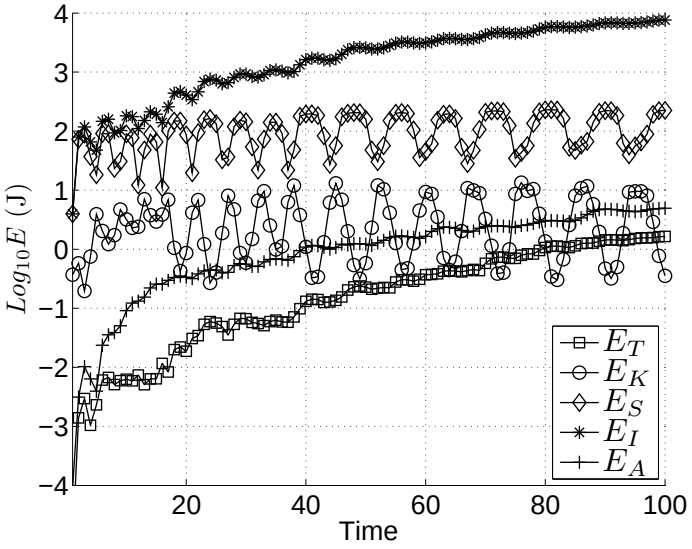

Figure 7.6: Energy quantities for Mesh #2b

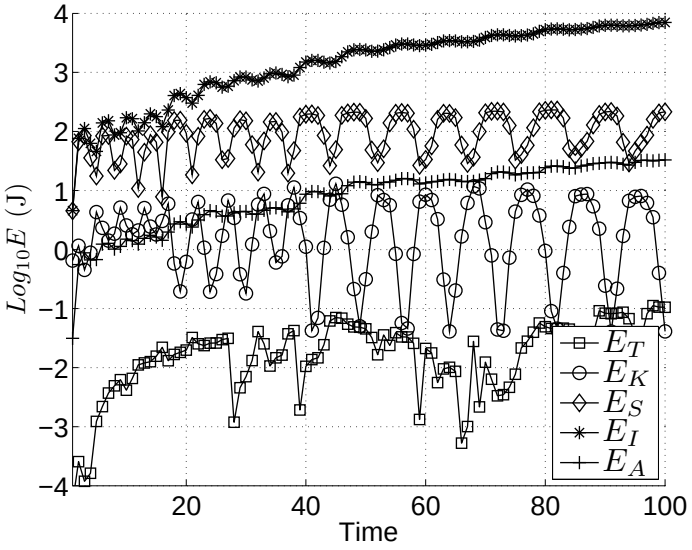

Figure 7.7: Energy quantities for Mesh #3

On the basis of these analyses, a 28x28 mesh of S4R shell elements with enhanced hourglass control was deemed appropriate for the web plate mesh. This mesh density is expected

Table 7.2: Energy Quantities

Mesh #	**Mesh Size**	**Element**	**(Joules)** E_I	**(Joules)** E_A	E_A/E_I	**(Joules)** E_{total}
1	19x19	S4R	9114	61.8	0.0068	-0.62
2a	28x28	S4R	7567	37.5	0.0049	-0.40
2b	28x28	S4	7603	4.9	0.0006	-1.64
3	46x46	S4R	7053	33.0	0.0047	0.10

to overestimate the dissipated energy by 6 to 8%, and overestimate the lateral load at the peak of each cycle by 3 to 4%. Use of a higher mesh density with the significant associated increases in computational time was not deemed to be worth the modest improvements in accuracy. Likewise, the use of S4 elements (mesh #2b) in lieu of the reduced integration S4R elements, does not significantly effect the result, with nearly identical dissipated energy and peak load prediction to mesh #2a.

7.1.5 Web Plate Material Model

For each of the *ABAQUS* analyses, the engineering σ-ϵ relationships derived from the coupon tests were first averaged for the two directions (transverse and longitudinal) then converted to true (Cauchy) stress (σ_{true}) and log plastic strain (ϵ_{ln}^{pl}) per the equations presented in Section 3.1.5. The σ_{true}-ϵ_{ln}^{pl} plots are then curve fitted with exponential functions which are then used with ABAQUS. In the sections that follow, the "true" and "ln" subscripts have been dropped from the stress and strain symbols. Unless stated otherwise, the material stress and strain properties shall be assumed to be true stress and log strain.

The combined hardening option was used for modeling the Phase I cyclic tests in an effort to quantify the proportion of kinematic hardening observed. The material was modeled by fitting a function represented by Eq. 7.2, using a least-squares approach, to the

coupon test data for each test. As just mentioned, this data was first converted to true-stress and log-strain before curve fitting. The material was modeled in $ABAQUS$ using half-cycle combined hardening with two kinematic back-stress components (one linear and one nonlinear, see section 3.1.5 for definitions) and an isotropic component defined precisely by the nonlinear term in the Eqn. 7.2, where $\hat{K}\sigma_{y0}$ is equivalent to Q_∞ and γ is equivalent to b in Eq. 3.15. This results in a material with essentially linear kinematic hardening and nonlinear isotropic hardening. The linear kinematic hardening modulus, H, was varied for each simulation under the assumption that a reasonable match between the observed experimental results and simulation would be found.

Eq. 7.2 describes the fitted $\sigma - \epsilon^{pl}$ curves used in the $ABAQUS$ cyclic analyses.

$$\sigma(\epsilon^{pl}) = \sigma_{y0} + H\epsilon^{pl} + \hat{K}\sigma_{y0}\left(1 - e^{-\gamma\epsilon^{pl}}\right) \tag{7.2}$$

where γ is the isotropic saturation rate parameter, H is the kinematic hardening modulus, $\sigma_{y0} + \hat{K}\sigma_{y0}$ defines the size of the isotropic bounding surface and σ_{y0} is the yield stress.

Figs. 7.8 and 7.9 show the coupon data for each of the six Phase I tests and three Phase II tests with the fitted curves, per Eq. 7.2. The fitted curves overlay the coupon curves in Fig. 7.8 and the match for the 18 Ga specimens was particularly good. The 16 Ga specimen had a long yield plateau and some differences can be seen between the actual coupon test data and the fitted curves, particularly at strains less than 0.05. Also shown on the Phase I plots (Fig. 7.8) are the kinematic back stresses for the four linear kinematic hardening cases analyzed; H = 0 (pure isotropic) and H = 150, 300, 600 MPa. The pure kinematic case is modeled as nonlinear kinematic and utilizes the true stress-log strain data with four backstress components.

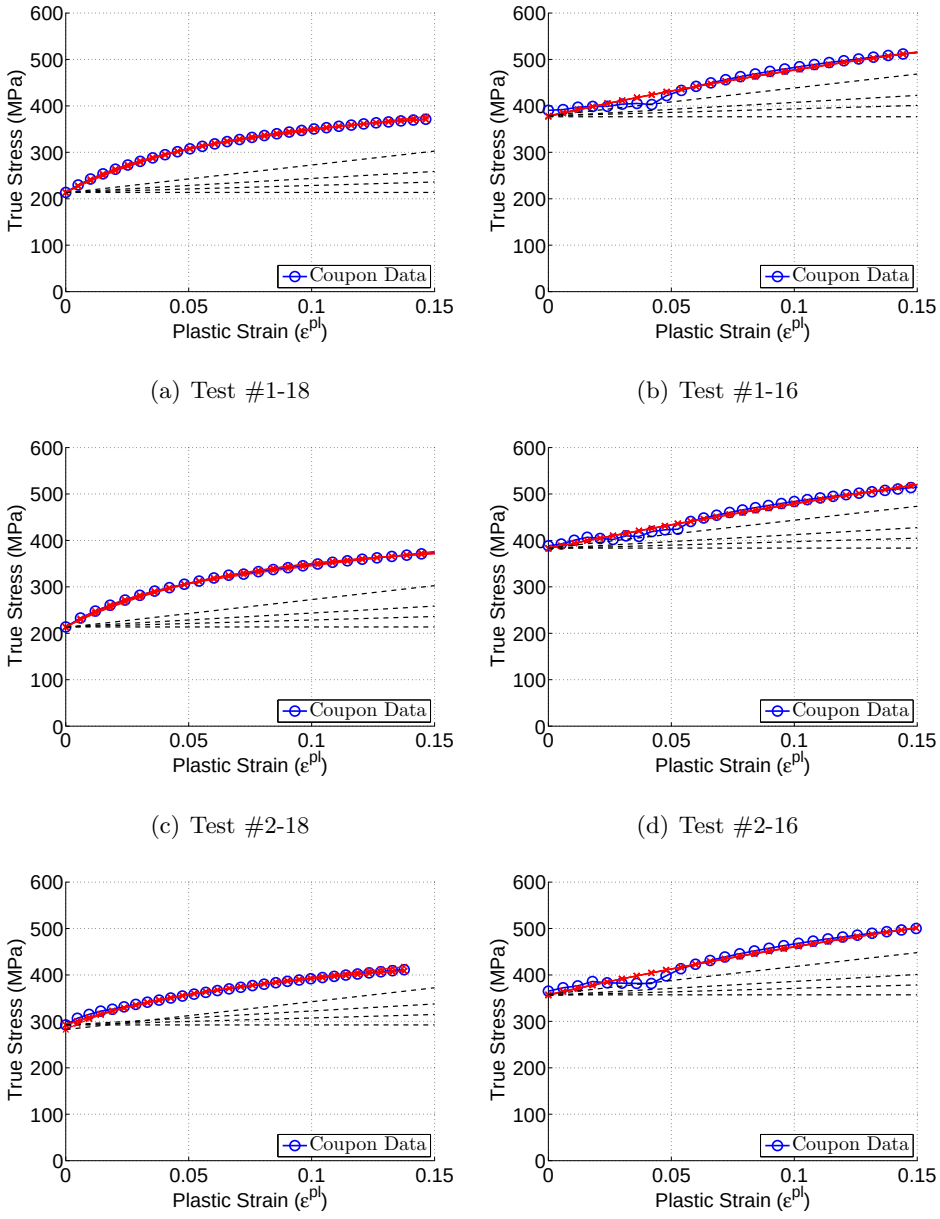

(a) Test #1-18

(b) Test #1-16

(c) Test #2-18

(d) Test #2-16

(e) Test #3-18

(f) Test #3-16

Figure 7.8: True stress-log plastic strain curves for 16 Ga and 18 Ga specimens used in *ABAQUS* analyses showing kinematic hardening back stresses for H = 0, 150, 300 & 600.

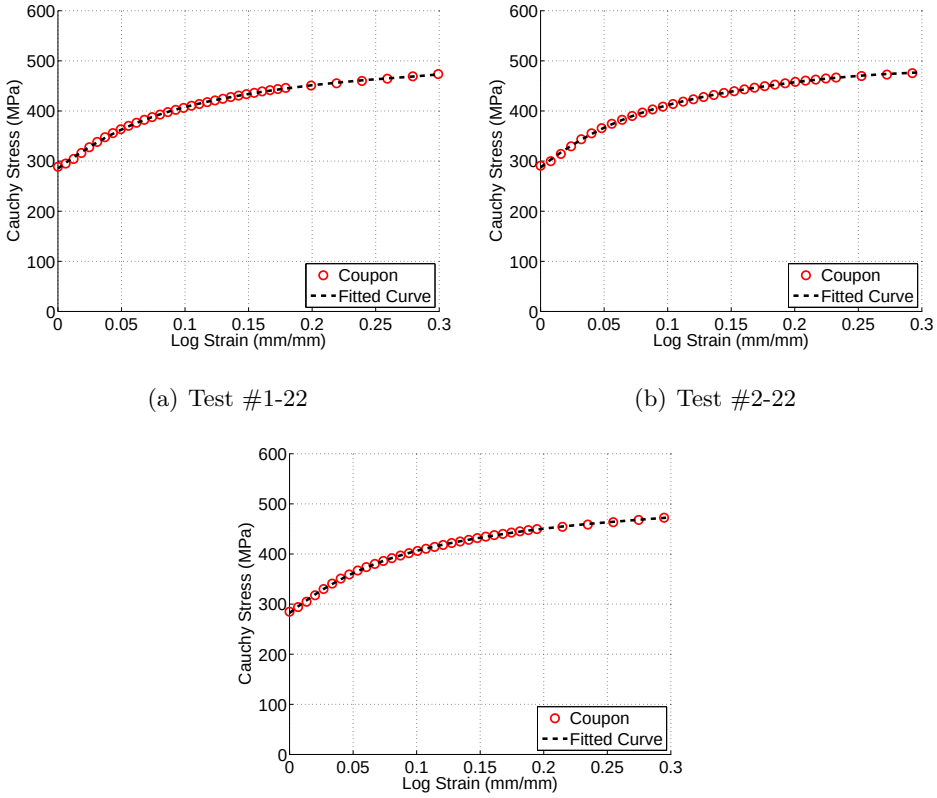

(a) Test #1-22

(b) Test #2-22

(c) Test #3-22

Figure 7.9: True stress-log plastic strain curves for 22 Ga specimens used in *ABAQUS* analyses

7.2 Analysis Results

The analyses performed for each of the nine tests include a single push-over analysis and cyclic analyses. For the Phase I tests the material models include non-linear kinematic, isotropic and three combined hardening cases (as previously discussed) with various levels of linear kinematic hardening. The push-over analysis was used primarily as a check on the validity of the material model and the model kinematics. Should either of these be incorrect, the error was easier to detect and rectify by inspecting the pushover response.

For the Phase I test simulations, the base reaction versus drift response and the mean $\bar{\epsilon}^{pl}$ in the web plate were extracted from the kinematic and the isotropic hardening simulations. For Phase II, where the objective was to study tension field inclination, the cyclic analyses included only the nonlinear kinematic and isotopic material models. For these simulations, in addition to the base reaction versus drift response and mean $\bar{\epsilon}^{pl}$, the VBE bending demand and web plate stresses were also extracted. From the web plate stress components it is possible to determine the migration of the web plate stress inclination angle and the magnitude of web plate compressive stresses.

Fig. 7.10 shows screen captures at various stages of Test #2-16 and the associated *ABAQUS* simulation at the same time. Frame (a) is the residual deformation in the neutral position after the first cycle at 2% drift. Frame (b) and (c) are at the peak of the push and pull stroke at 4% drift. Frame (d) shows the residual deformation of the web plate at the completion of the test.

7.2.1 ABAQUS Pushover Analyses

In Figs. 7.11 and 7.12, the *ABAQUS* pushover response and the positive portion of the experimental hysteresis curve are shown for each test. The measured and simulated strength at 3% drift are listed in Table 7.3. Also listed in this table are the lateral strengths at 3% drift computed from a simple plastic analysis which was carried out to further validate

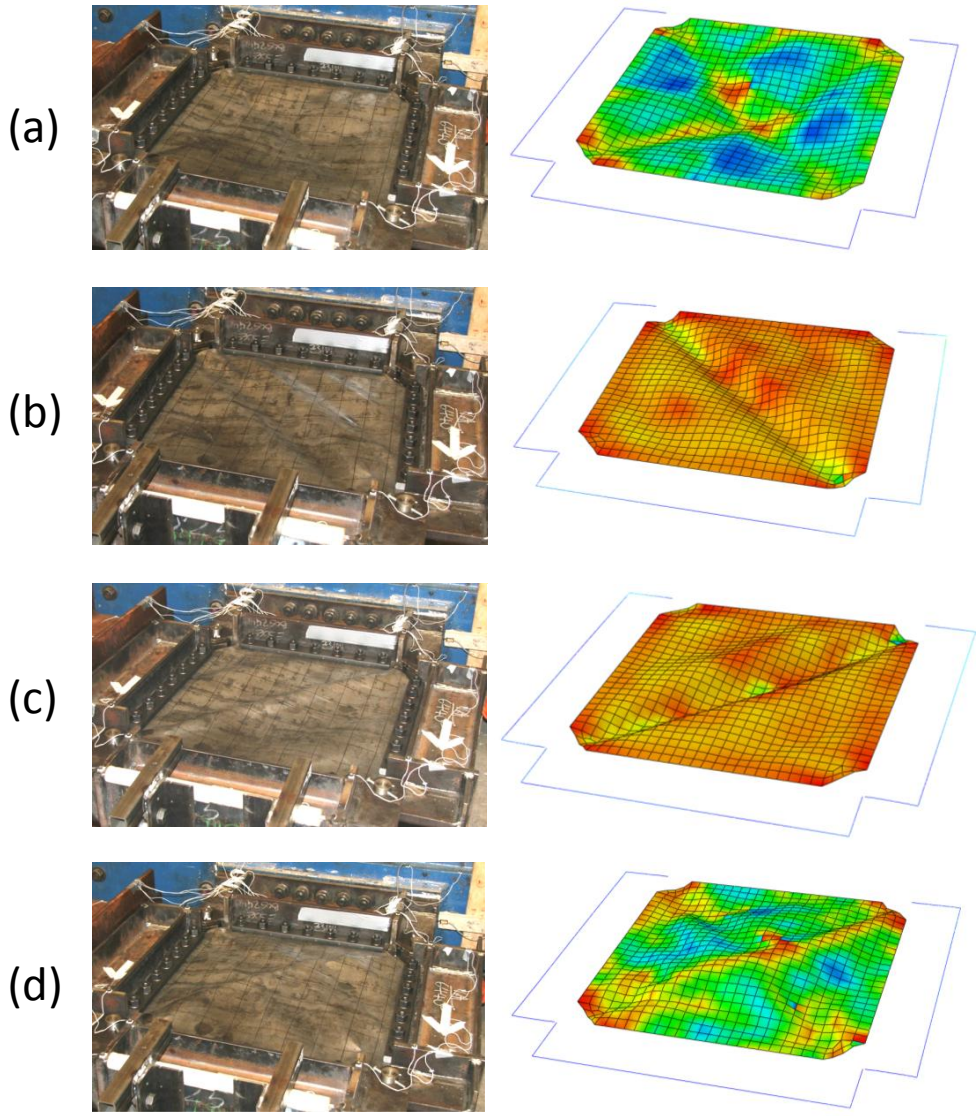

Figure 7.10: Test #2-16: Experimental and *ABAQUS* web plate deformations at various stages of the test.

the pushover response computed with ABAQUS. The plastic analysis considered the actual kinematics of the web plate and the non-uniformity of the principal tensile strain field; at 3% drift the principal tensile strains vary from approximately 0.0221 near the corner cut-out to 0.0156 near the main diagonal. This non-uniformity is due to the offset between the internal edge of the clamping bar and the centers of the pins. To determine the strength at 3% drift, the strains are integrated through the volume of the plate, using a series of thirty-two diagonal strips with volume, V_i. These are then multiplied by the corresponding coupon stress, $\sigma_i(\epsilon)$, to get the internal work. The estimated external force, F_{est}, operates through the displacement h.$\delta\Delta$, where $\delta\Delta$ is a small increment in drift in the vicinity of 0.03, and h is the height of the panel. F_{est} is computed per Eq. 7.3.

$$F_{est} = \frac{\sum_{i=1}^{32} \sigma_i(\epsilon)\epsilon_i^{pl} V_i}{h.\delta\Delta} \tag{7.3}$$

The pushover capacity computed using the above approach is very close to the $ABAQUS$ computed response, F_{ABQ}, at 3% drift. The mean difference is 0.4%, with a COV of 1.9%. Figs. 7.11 and 7.12 show that the initial stiffness (slope) of the $ABAQUS$ push-over curves closely match the initial stiffness from each test. The experimental results for Tests #1-22 and #2-22 show a some premature softening near the yield point (not as obvious as in the Phase I tests) where the experimental curves dip under the simulated curves. It is believed this is due to residual stresses in the plate and is more easily detected in Tests #1-22 and #2-22 where there is an initial pushover cycle. For both these tests the simulated and experimental curves re-align as the drift increase and they differ by less than 1% at a drift of 3%. The data also show that, with the exception of Tests #1-18 and #2-18 (and to some extent Tests #1-22 and #2-22), the pushover curves tend to envelope the test hysteresis curves quite closely. The hysteretic envelopes for Tests #1-18 and #2-18 significantly exceed the pushover capacity curves for these tests. This is due to the nature of the hardening exhibited by these materials.

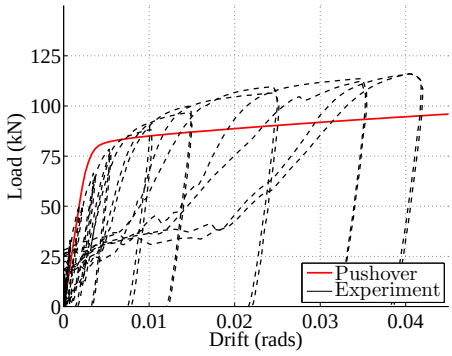

(a) Test #1-18

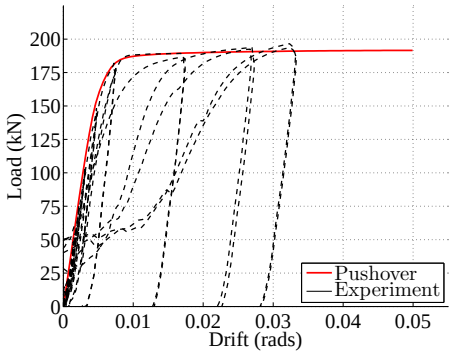

(b) Test #1-16

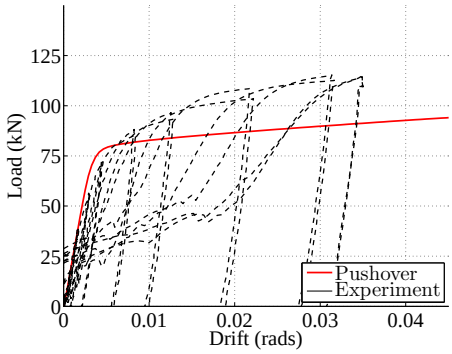

(c) Test #2-18

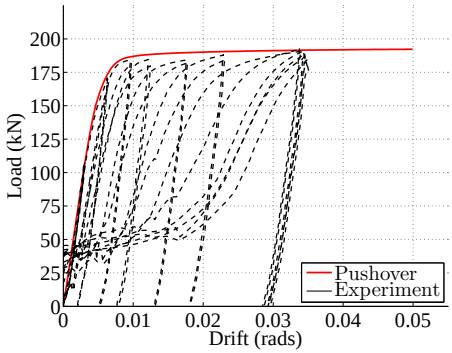

(d) Test #2-16

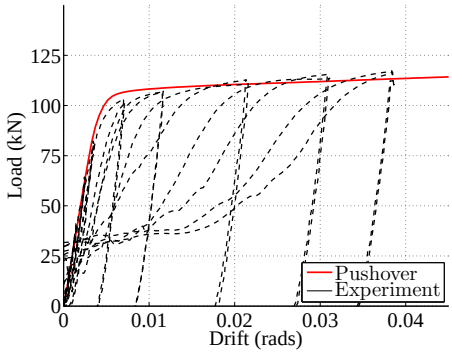

(e) Test #3-18

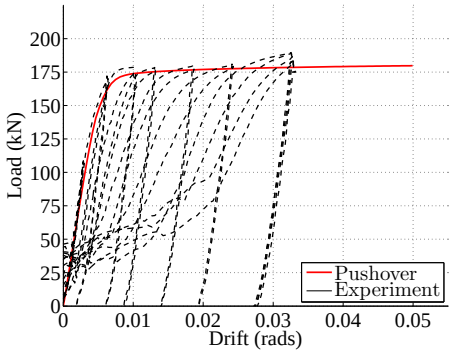

(f) Test #3-16

Figure 7.11: Experimental hysteresis curve with $ABAQUS$ pushover: Phase I.

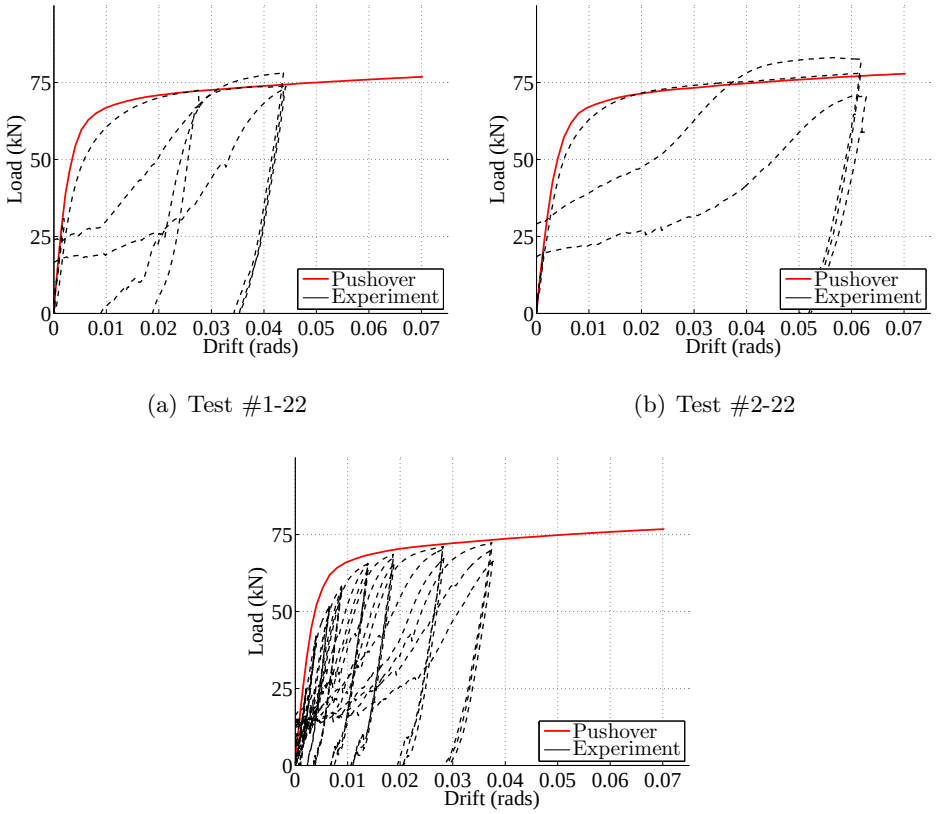

(a) Test #1-22

(b) Test #2-22

(c) Test #3-22

Figure 7.12: Experimental hysteresis curve with $ABAQUS$ pushover: Phase II.

Table 7.3: Estimated and *ABAQUS* Computed Pushover Capacities at 3% Drift

Test #	F_{est} **(kN)**	F_{ABQ} **(kN)**	F_{ABQ}/F_{est}
1-18	91.3	91.8	1.005
2-18	91.7	89.8	0.979
3-18	115.7	111.9	0.967
1-16	185.9	190.8	1.026
2-16	187.4	191.2	1.020
3-16	176.3	178.2	1.011
1-22	71.9	72.6	1.010
2-22	72.6	73.2	1.008
3-22	71.5	72.2	1.010

7.2.2 ABAQUS Cyclic Hardening and Plastic Strain Accumulation

To understand the nature of the hardening evolution for a web plate subjected to repeated cycles of plastic deformation, the cyclic test data from the web plate tests were compared with the results of *ABAQUS* analyses. Figs. 7.13 through 7.21 show *ABAQUS* analyses using isotropic hardening and kinematic hardening overlaying the actual test hysteresis curves. Table 7.5 shows the peak lateral force attained for these analyses, and the peak force from each test. Also shown in Table 7.5 is the mean equivalent plastic strain, $\bar{\epsilon}^{pl}$, as determined by *ABAQUS* for both isotropic and kinematic hardening.

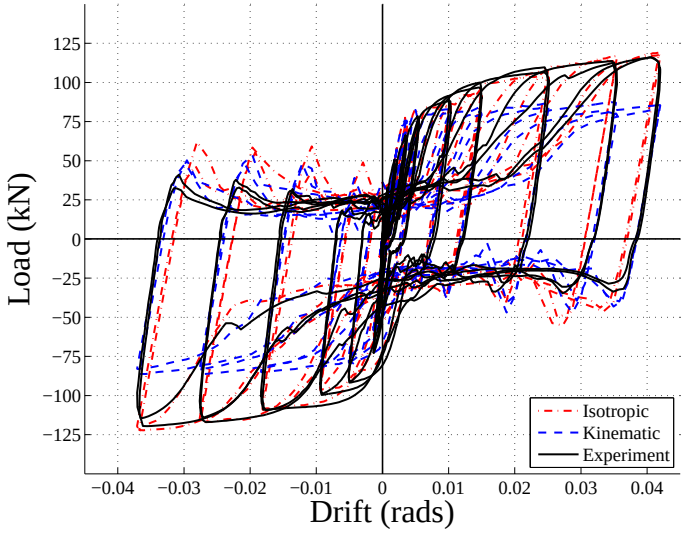

Figure 7.13: Test #1-18: Experimental and $ABAQUS$ hysteresis curves.

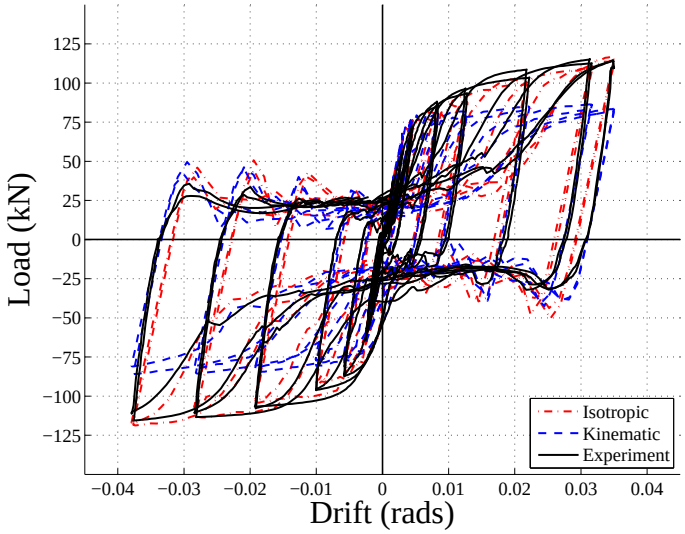

Figure 7.14: Test #2-18: Experimental and $ABAQUS$ hysteresis curves.

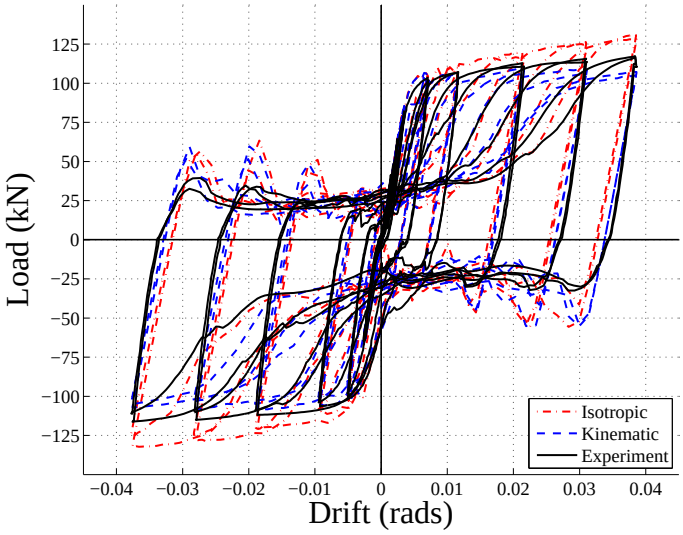

Figure 7.15: Test #3-18: Experimental and $ABAQUS$ hysteresis curves.

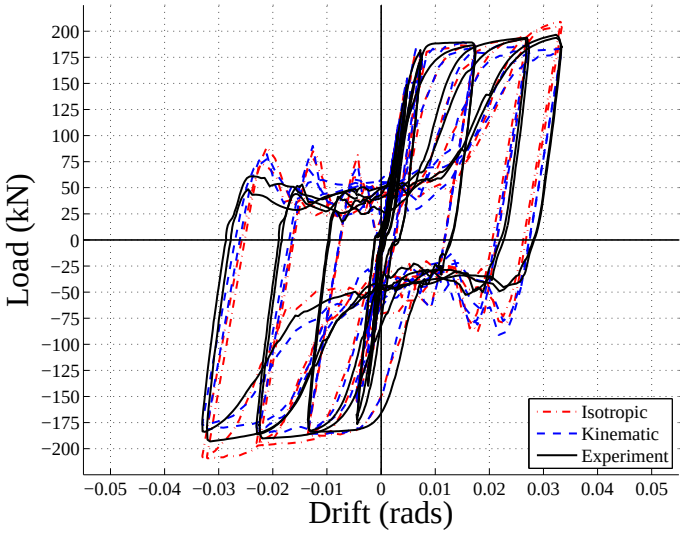

Figure 7.16: Test #1-16: Experimental and $ABAQUS$ hysteresis curves.

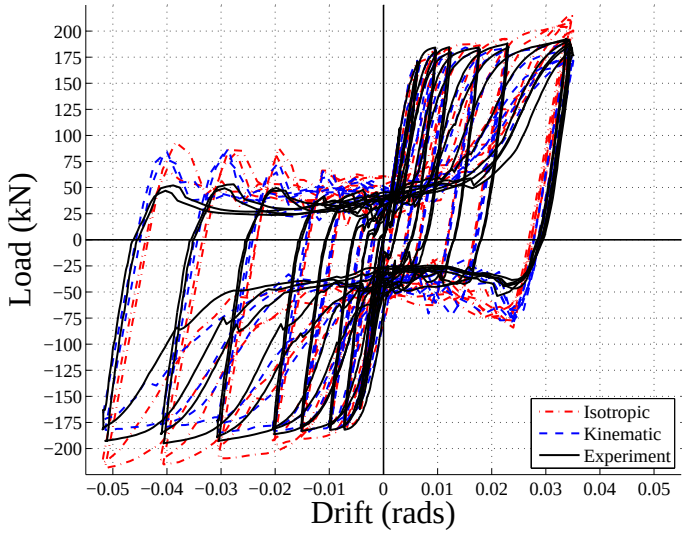

Figure 7.17: Test #2-16: Experimental and $ABAQUS$ hysteresis curves.

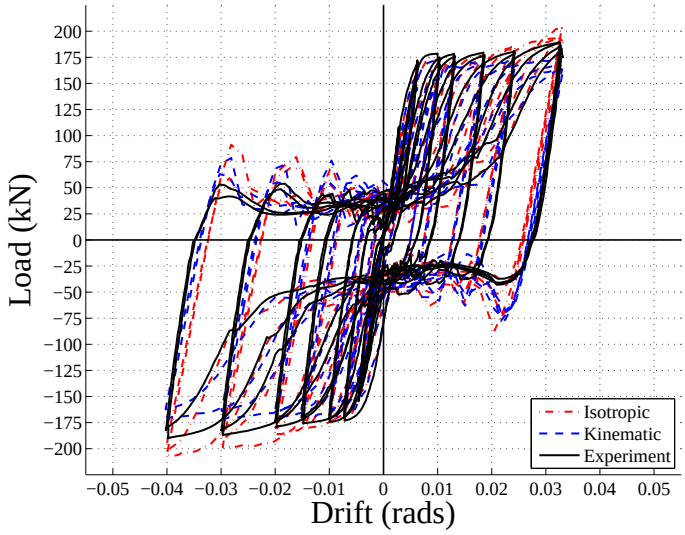

Figure 7.18: Test #3-16: Experimental and $ABAQUS$ hysteresis curves.

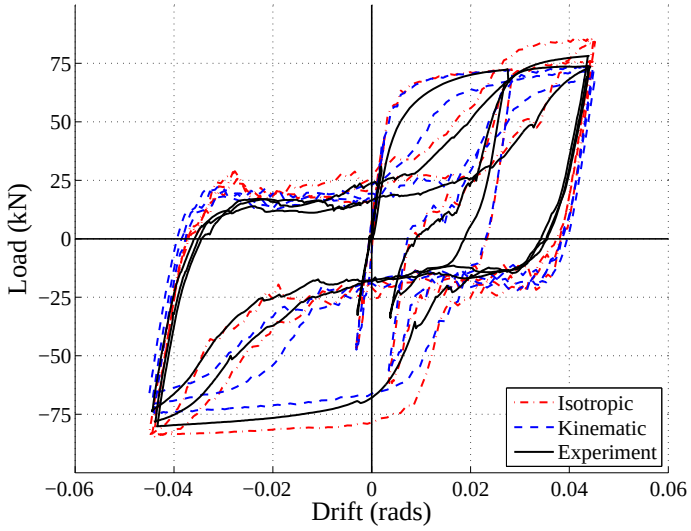

Figure 7.19: Test #1-22: Experimental and $ABAQUS$ hysteresis curves.

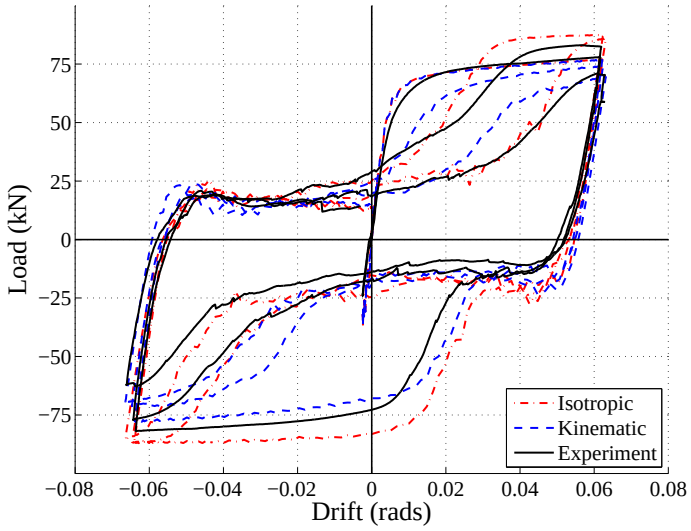

Figure 7.20: Test #2-22: Experimental and $ABAQUS$ hysteresis curves.

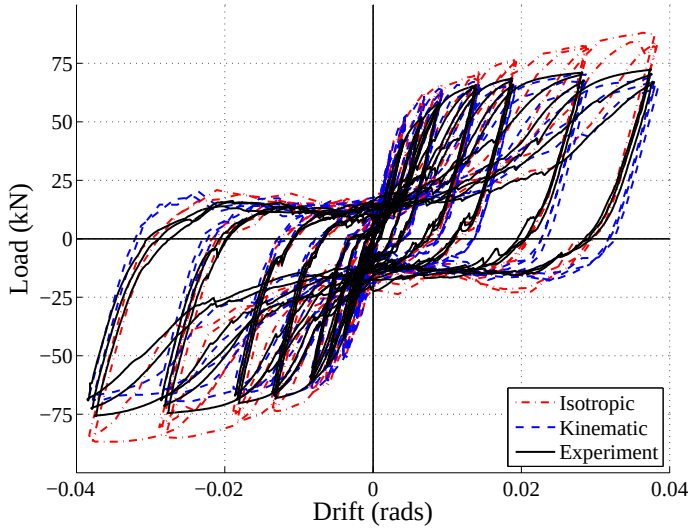

Figure 7.21: Test #3-22: Experimental and $ABAQUS$ hysteresis curves.

The validity of the isotropic hardening response from $ABAQUS$ is checked by computing the stress associated with the engineering strain equivalent of isotropic $\bar{\epsilon}^{pl}$ which is then used to compute an estimate for F_{est} for the cyclic case. The peak load is computed in a similar manner to what was done for the push-over case and is shown in the table as F^c_{est}. The estimated lateral force using the isotropic hardening assumption correlates well with the $ABAQUS$ model for all cases, with a mean difference of 0.6% and a COV of 1.6%. Table 7.5 also shows the peak force attained from the kinematic hardening analyses.

Accumulated Plastic Strain Estimates

The accumulated plastic strain estimate is independently checked by computing the plastic strain directly from the hysteresis curve. This approximation is made by summing the accumulated plastic strain increments on each half cycle. The plastic strain is assumed to commence when the loading curve reaches an inflection point and terminates at the strain associated with peak load of the half cycle. These points are shown for an arbitrary half-cycle of positive loading in Fig. 7.22. In reality, plastic strain also accumulates between these phases of primary loading. Results from these analyses show that approximately 20%

of the total accumulated plastic strain occurs after the plate has unloaded, and prior to reloading in the next phase (Point A to point B in Fig. 7.22). This exercise can be used to gauge how accurately this method predicts accumulated plastic strain for an arbitrary drift history and, if satisfactory, could be used in the development of the "next generation" hysteretic model.

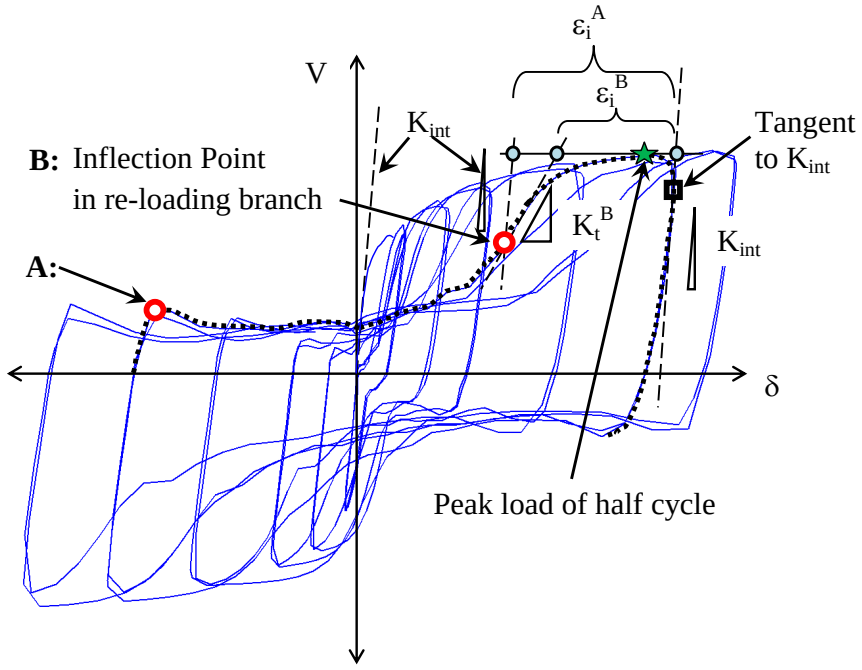

Figure 7.22: Typical hysteresis curve showing transition points and estimates of plastic strain increments for an arbitrary half-cycle

Fig. 7.23 shows the transition points on the hysteresis curves for Tests #1-18 and #1-16. Fig. 7.24 shows the accumulated plastic strain at peak load for Tests #1-18 and #1-16 plotted against the estimated mean web plate tensile stress. The estimate ϵ_i^B is computed from the tangent at the inflection point, K_t^B, of the loading curve. For ϵ_i^A the initial elastic stiffness, K_{int}, is used instead. The results of these analyses for the Phase I tests are summarized in Table. 7.4. The ratios of the computed accumulated plastic strain, $\Sigma\epsilon$, to

$\bar{\epsilon}^{pl}$ from *ABAQUS* are also shown in Table 7.4. It appears that the method "A" estimate does a reasonable job of predicting the $\bar{\epsilon}^{pl}$ strain for the isotropic hardening case with a mean ratio of 0.97 and a COV of 0.097.

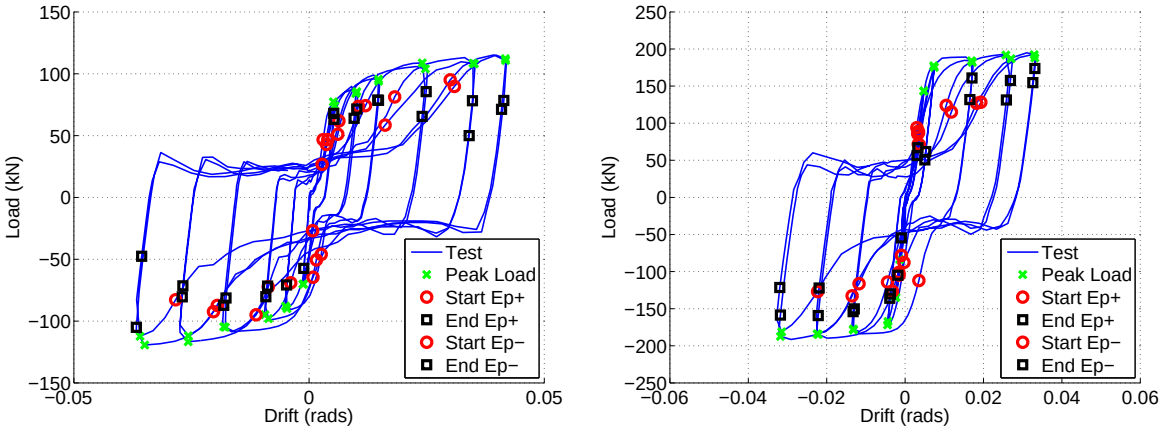

(a) Test #1-18

(b) Test #1-16

Figure 7.23: Transition points for elastic-plastic loading and unloading for (a) Test #1-18 and (b) Test #1-16.

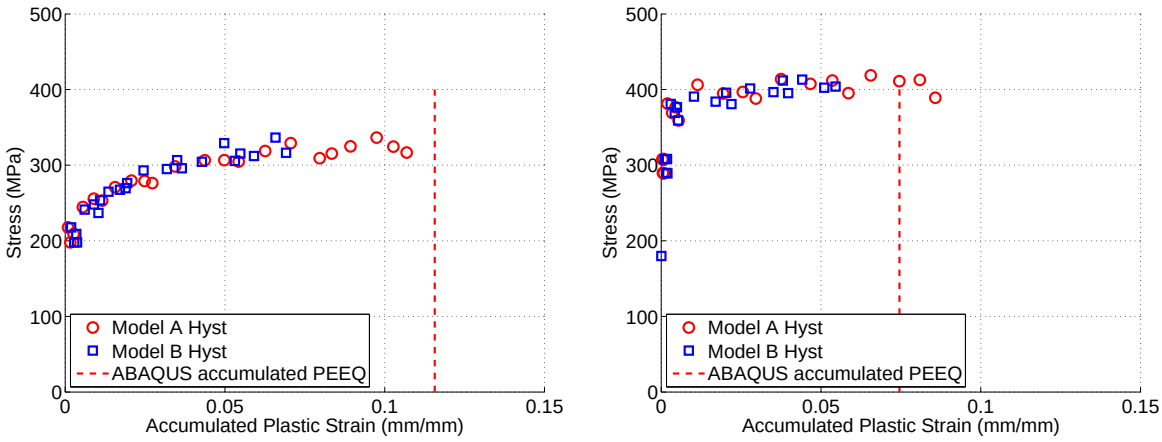

(a) Test #1-18 (b) Test #1-16

Figure 7.24: Accumulated plastic strain estimates using $\Sigma\epsilon^A$ and $\Sigma\epsilon^B$ for (a) Test #1-18 and (b) Test #1-16.

Table 7.4: Estimated and *ABAQUS* Computed Accumulated Plastic Strains for the Phase I Tests

Test #	**ABQ-ISO** $\bar{\epsilon}^{pl}$ **(1)**	**ABQ-KIN** $\bar{\epsilon}^{pl}$	$\sum_i \epsilon_i^B$	$\sum_i \epsilon_i^A$ **(2)**	**(2)/(1)**
1-18	0.1157	0.1586	0.069	0.107	0.924
2-18	0.0959	0.1374	0.063	0.093	0.970
3-18	0.0943	0.12	0.070	0.089	0.944
1-16	0.0746	0.0845	0.055	0.086	1.153
2-16	0.1341	0.1583	0.076	0.117	0.872
3-16	0.0946	0.1197	0.068	0.088	0.930

Table 7.5: Estimated and *ABAQUS* Computed Cyclic Peak Lateral Load (kN) at Maximum Drift

Test #	**ABQ-ISO** F_{iso}	**ABQ-KIN** F_{kin}	**TEST** F_{test}	F^c_{est}	F_{iso}/F^c_{est}	F_{iso}/F^c_{est}	F_{kin}/F_{test}
1-18	124	87	121	124	1.003	1.022	0.719
2-18	120	86	117	118	1.02	1.006	0.735
3-18	133	108	116	133	1.001	1.145	0.931
1-16	211	186	190	212	0.996	1.115	0.979
2-16	218	183	193	220	0.99	1.141	0.948
3-16	207	173	189	205	1.008	1.087	0.915
1-22	86	74	79	87	0.993	1.097	0.937
2-22	89	76	82	85	1.042	1.042	0.927
3-22	88	69	75	88	1.002	1.171	0.920

Preliminary Combined Hardening Study

In this section the nature of the hardening in the test specimens is examined. A more rigorous analysis of the web plate test results is undertaken in Chapter 9 where the extent of hardening expected is quantified for earthquake excitation using a more generic material description.

For each analysis case (i.e., each H value) and for each test simulation, the peak lateral force obtained from the *ABAQUS* simulation, at each maximum and minimum peak drift, is divided by the associated lateral force obtained from the experiment. A perfect match between simulation and test for this data would result in a mean of 1.0 and a SD of zero. Fig. 7.25 shows the result of this normalization for Tests #1-18 and #2-16 where the lateral force ratio (V_S/V_T) is plotted on the vertical axis and the absolute drift magnitude is plotted on the horizontal axis. V_S is the force from the simulation, V_T is the corresponding

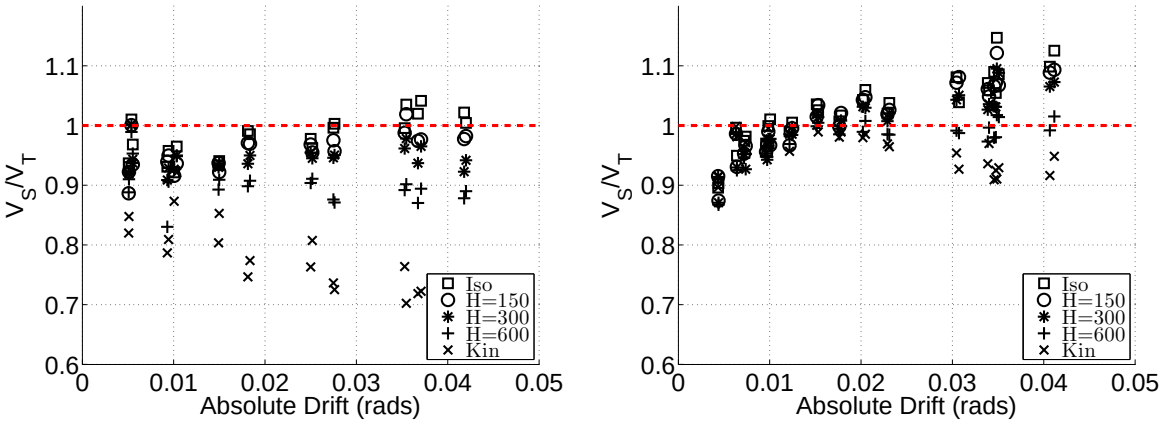

(a) Test #1-18

(b) Test #2-16

Figure 7.25: Normalized force data for Tests #1-18 and #2-16.

force from the test.

Table 7.6 details the statistics of the normalization process (mean and standard deviation), described above, for all six of the Phase I tests.

The data in Table 7.6 show that, for Tests #1-18 and #2-18, the correlation between test and simulation is best for the purely isotropic model. Test #3-18 data suggest that the *H=300* or the *H=600* case provide the best fit.

For the 16 Ga tests, it is more difficult to conclude exactly which hardening parameters provide the best match because so little hardening occurs in these plates. Fig. 7.26 shows histograms for all of the 16 Ga test data, grouped by case. The cases *Iso*, *H=150* and *H=300* have approximately equal mean and provide a good match with the experimental data on this basis. However, the *H=600* case has a much lower μ value,which suggests good correlation across all drift levels and is arguably the best of the five. The case *Kin* is far less likely to provide the correct match.

On the basis of these tests, isotropic hardening is the best option for web plate modeling for two reasons: 1) it provides the best overall match between experimental and simulation

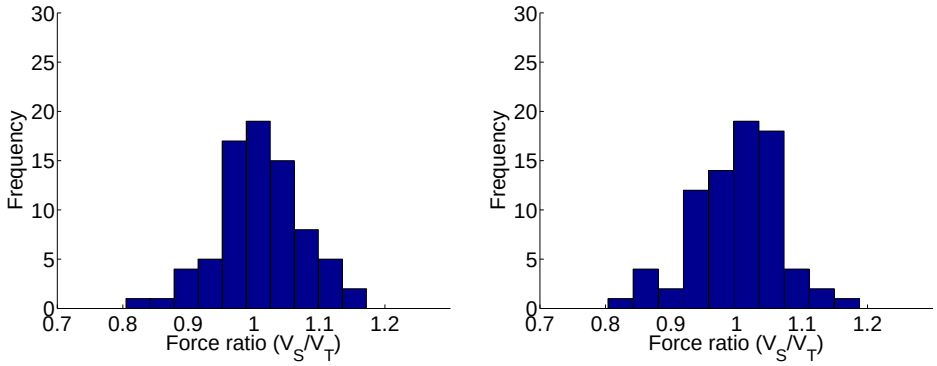

(a) Isotropic

(b) H=150

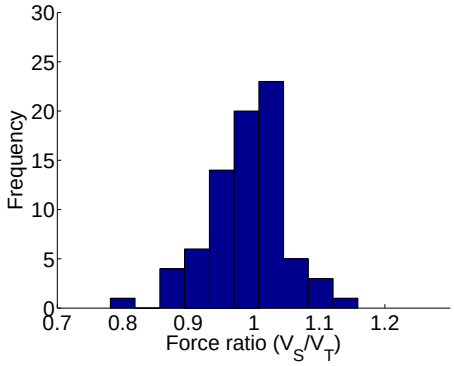

(c) H=300

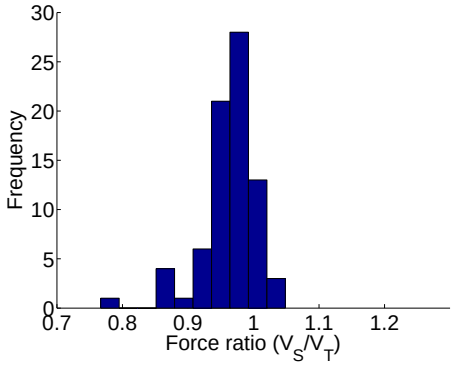

(d) H=600

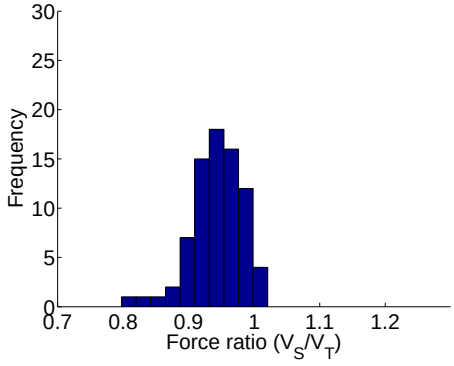

(e) Kinematic

Figure 7.26: Normalized force Histograms for 16 Ga Tests.

Table 7.6: ABAQUS Isotropic, Kinematic and Combined Hardening Analysis Results. Mean and SD of (V_S/V_T) at Peak Load for Each Half-Cycle.

Hardening Statistics						
	Mean		**Combined**			
Test #	**& SD**	**Iso**	**H = 150**	**H = 300**	**H = 600**	**Kin**
1-18	μ	0.9786	0.9571	0.9430	0.9023	0.7984
	σ	0.0364	0.0308	0.0209	0.0326	0.0809
2-18	μ	0.9641	0.9488	0.9307	0.8972	0.8102
	σ	0.0455	0.0342	0.0372	0.0460	0.0910
3-18	μ	1.0427	1.0256	1.0147	0.9871	0.9546
	σ	0.0763	0.0647	0.0590	0.0515	0.0493
1-16	μ	0.9981	0.9828	0.9729	0.9563	0.9506
	σ	0.0735	0.0743	0.0710	0.0638	0.0533
2-16	μ	1.0323	1.0236	1.0109	0.9797	0.9575
	σ	0.0652	0.0673	0.0610	0.0352	0.0294
3-16	μ	0.9929	0.9869	0.9786	0.9530	0.9214
	σ	0.0580	0.0523	0.0448	0.0306	0.0319

data, and 2) it results is a slightly conservative estimate of peak load at any given drift level.

7.3 Analysis of Web Plate Stress Field and VBE Bending for Phase II Tests

The development of the web plate stress field and and its interaction with the VBE sections was examined for Tests #2-22 and #3-22. Figs. 7.29 and 7.30 show the VBE bending demand versus drift for Tests #2-22 and #3-22 and compare these with the results from the experiments using the NDI system. There is a reasonable match between experiment and analysis for both tests, with a force difference at peak drift of approximately 6% for Test #2-22. The result is similar for Test #3-22 and its simulation but with slightly greater

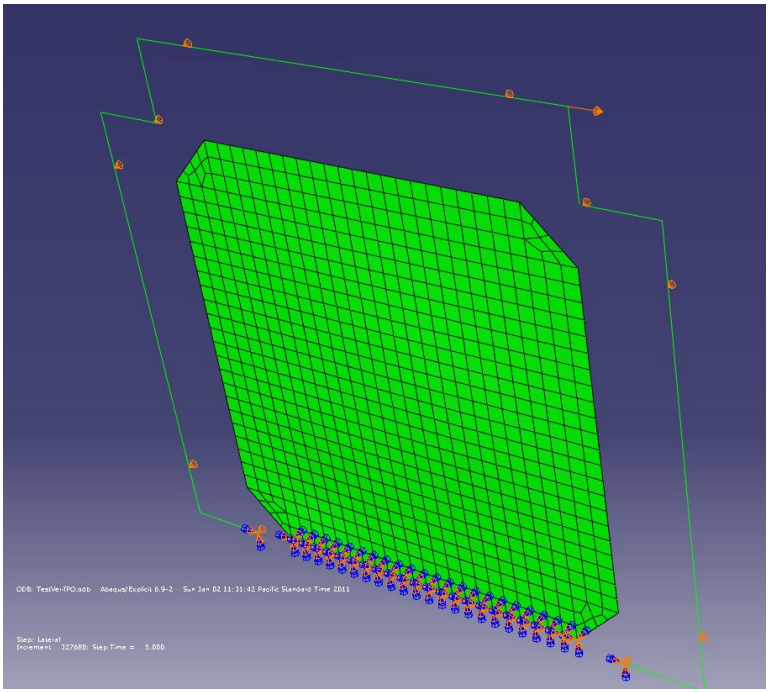

Figure 7.27: ABAQUS model of Phase I test

scatter in the experimental results at high drift.

Fig. 7.31 shows VBE bending moment extracted form the *ABAQUS* analysis normalized by the estimated bending moment, M_{eq}. M_{eq} is computed using the mean in-plane normal stresses at 45 degrees ($\bar{\sigma}_{11}$) and 135 degrees ($\bar{\sigma}_{22}$). These mean field stress quantities are computed using the following equations:

$$\bar{\sigma}_{11} = \frac{1}{n}\sum_{i=1}^{n} \mathbf{n}_1.\boldsymbol{\sigma}_i.\mathbf{n}_1^T \tag{7.4}$$

$$\bar{\sigma}_{22} = \frac{1}{n}\sum_{i=1}^{n} \mathbf{n}_2.\boldsymbol{\sigma}_i.\mathbf{n}_2^T \tag{7.5}$$

$$\bar{\tau}_{12} = \frac{1}{n}\sum_{i=1}^{n} \mathbf{n}_1.\boldsymbol{\sigma}_i.\mathbf{n}_2^T \tag{7.6}$$

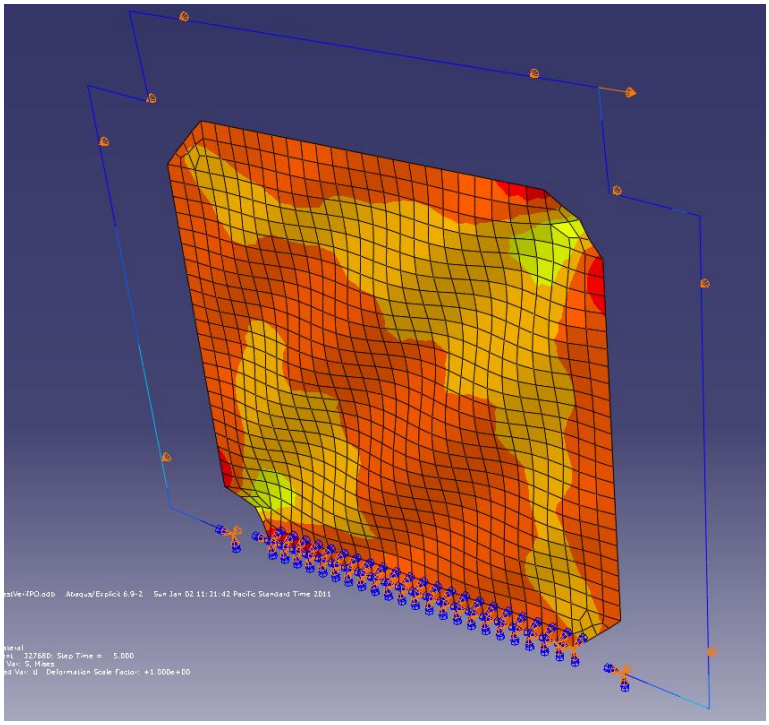

Figure 7.28: ABAQUS model of Phase I test showing Mises stresses and deformed shape from push-over analysis

$$\alpha = \frac{\pi}{4} - tan^{-1}\left(\frac{2\bar{\tau}_{12}}{\bar{\sigma}_{11} - \bar{\sigma}_{22}}\right) \tag{7.7}$$

where n is the number of shell elements in the web plate, $\boldsymbol{\sigma}_i$ is the stress tensor for element "i", $\mathbf{n}_1$ is the unit vector $\frac{1}{\sqrt{2}}\{1,1\}$ at 45 degrees, and $\mathbf{n}_2$ is the unit vector $\frac{1}{\sqrt{2}}\{-1,1\}$ at 135 degrees. M_{eq} is then computed by substituting $\bar{\sigma}_{11}$ and $\bar{\sigma}_{22}$ into Eq. 6.14 and then employing Eq. 6.7 with w_{eq} in place of w_{NDI}. The data presented in Figs. 7.29 and 7.30 show a good agreement between the experimentally derived bending moments and the *ABAQUS* simulated bending moments. Fig. 7.31 shows that the result of normalizing the simulated VBE bending moment by the equivalent stress field suggests that for pushover cases the equivalent stress field can be used to provide a very good estimate of VBE demand. Fig. 7.32 shows that a similar normalization process for the cyclic case significantly exceeds 1.0, peaking at around 1.15. This is consistent with the findings of section 3.3.3 (See

Fig. 3.23) where the normalized VBE bending demands from cyclic loading exceed 1.0 by approximately the same margin.

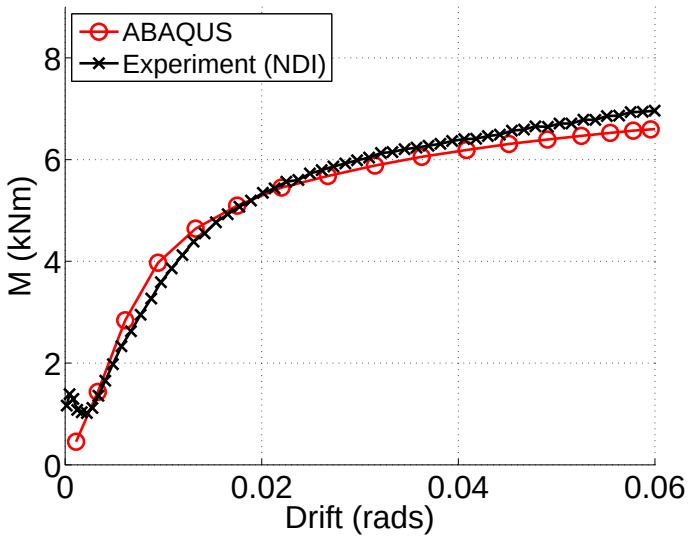

Figure 7.29: Test #2-22: VBE-CB bending demand.

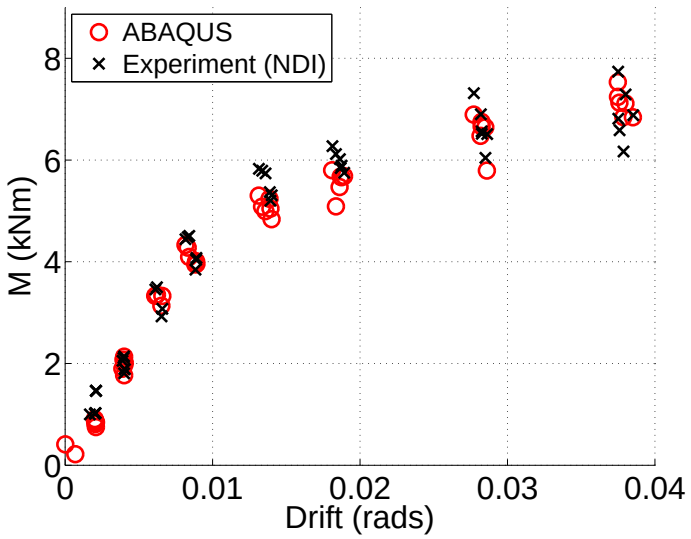

Figure 7.30: Test #3-22: VBE-CB bending demand.

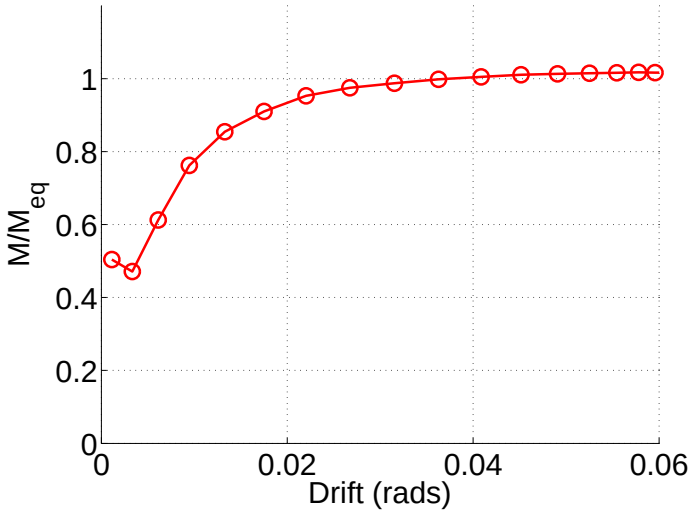

Figure 7.31: Simulation #2-22: VBE bending demand (M) normalized by equivalent moment (M_{eq}) determined from stress field.

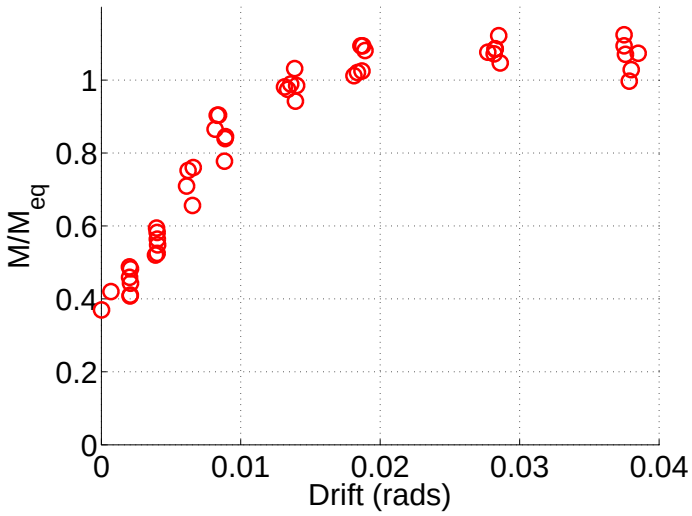

Figure 7.32: Simulation #3-22: VBE-CB bending demand (M) normalized by equivalent moment (M_{eq}) determined from stress field.

Figs. 7.33 and 7.34 show the different measures of stress plotted against drift for Tests #2-22 and #3-22. The stresses $\bar{\sigma}_{p1}$ and $\bar{\sigma}_{p2}$ are the mean principal stresses computed using the conventional 2D plane-stress transformation equations. The stresses $\bar{\sigma}_{11}$, $\bar{\sigma}_{22}$ and $\bar{\tau}_{12}$ are the maximum normal stress, minimum normal stress and shear stress computed at 45 degrees and 135 degrees. The stresses $\hat{\sigma}_t$ and $\hat{\sigma}_c$ are the equivalent tensile and compressive stresses computed using Eqs. 6.13 and 6.14. The equivalent uniform compressive stress for the pushover (Test #2-22) and cyclic case (Test #3-22) significantly exceed the magnitude of the principal compressive stress and projected normal stress magnitudes. This is observed in the experimental data (see Figs. 6.34 and 6.35). Figs. 7.35 and 7.36 show the ratio of compressive stress magnitude to tensile stress magnitude.

7.3.1 Tension Field Inclination

The mean inclination angle, α, of the principal tensile stress is computed using Eq. 7.7. The angle is plotted against drift in Figs. 7.37 and 7.38 for Tests #2-22 and #3-22 respectively. In Fig. 7.38 the angle is plotted only at the peak of each half-cycle. Some scatter can be observed in the experimental result, also shown on this plot, but the general trend is the same and the match between experiment and simulation is very good.

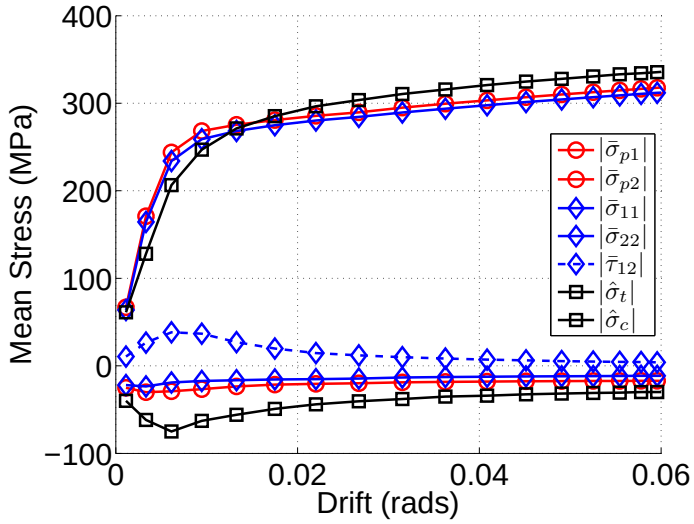

Figure 7.33: Test Simulation #2-22: Mean principal stresses ($\bar{\sigma}_{p1}$ & $\bar{\sigma}_{p2}$), projected normal stresses ($\bar{\sigma}_{11}$ & $\bar{\sigma}_{22}$) and equivalent stresses ($\hat{\sigma}_c$ & $\hat{\sigma}_t$) from Eqs. 6.13 and 6.14.

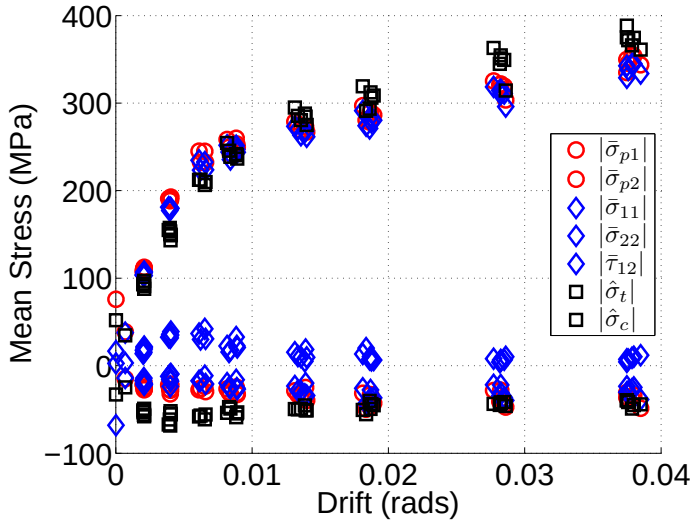

Figure 7.34: Test Simulation #3-22: Mean principal stresses ($\bar{\sigma}_{p1}$ & $\bar{\sigma}_{p2}$), projected normal stresses ($\bar{\sigma}_{11}$ & $\bar{\sigma}_{22}$) and equivalent stresses ($\hat{\sigma}_c$ & $\hat{\sigma}_t$) from Eqs. 6.13 and 6.14.

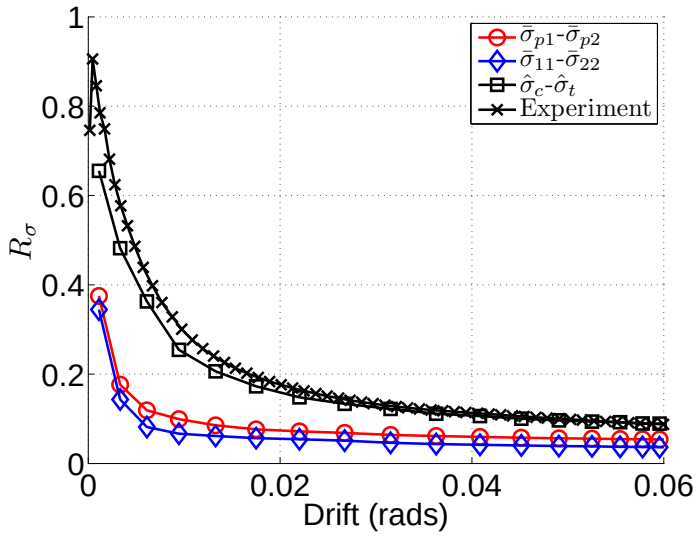

Figure 7.35: Test Simulation #2-22: Principal stress ratio ($\bar{\sigma}_{p2}/\bar{\sigma}_{p1}$), projected normal stress ratio ($\bar{\sigma}_{22}/\bar{\sigma}_{11}$), equivalent stress ratio ($\hat{\sigma}_c/\hat{\sigma}_t$) from Eq. 6.13 and 6.14 and equivalent stress ratio determined from experiment.

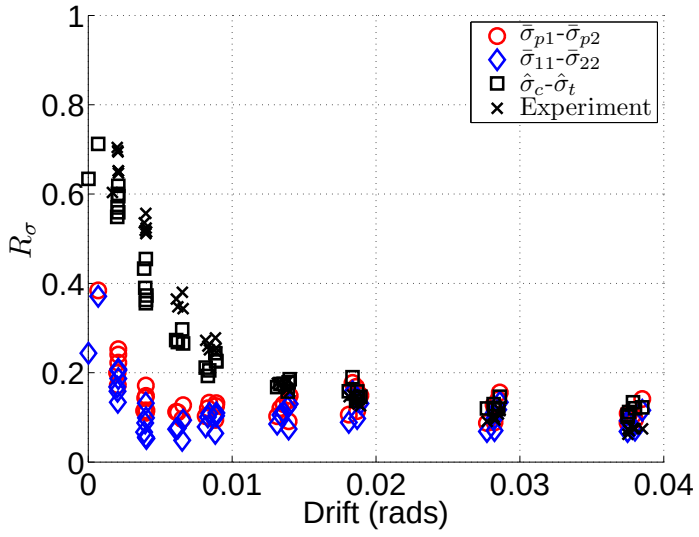

Figure 7.36: Test Simulation #3-22: Principal stress ratio ($\bar{\sigma}_{p2}/\bar{\sigma}_{p1}$), projected normal stress ratio ($\bar{\sigma}_{22}/\bar{\sigma}_{11}$), equivalent stress ratio ($\hat{\sigma}_c/\hat{\sigma}_t$) from Eq. 6.13 and 6.14 and equivalent stress ratio determined from experiment.

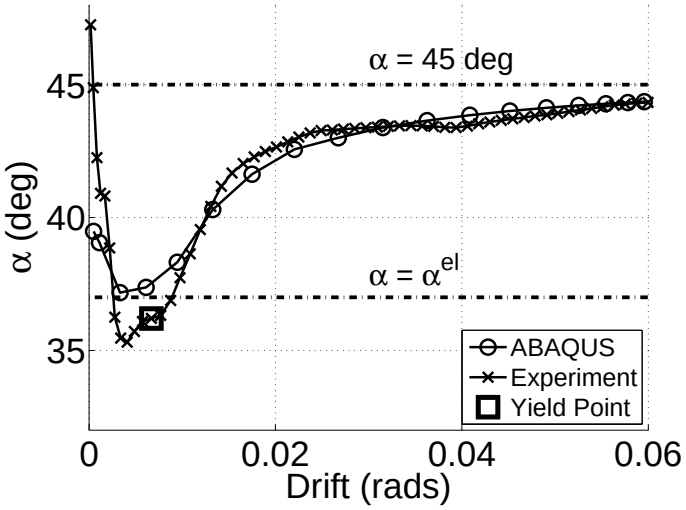

Figure 7.37: Test Simulation #2-22: Inclination angle α.

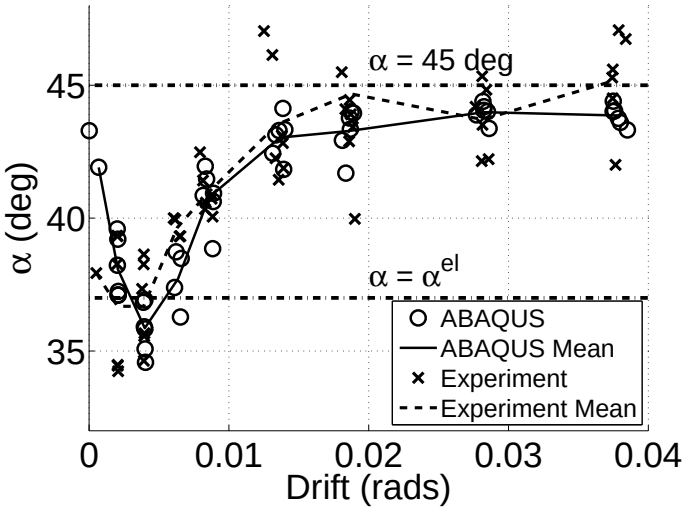

Figure 7.38: Test Simulation #3-22: Inclination angle α at peak of frame drift.

7.3.2 Directional Hysteresis Based on Equivalent Uniform Stress Field

The experimentally derived directional hysteresis curves (see Figs. 6.38 and 6.39) are validated using $ABAQUS$ data from the test simulations. These curves, and others like them, provide a foundation for the development of improved uniaxial hysteretic elements.

The results for the $ABAQUS$ stress field ($\hat{\sigma}_c$ & $\hat{\sigma}_t$) for Tests #2-22 and #3-22 are shown in Figs. 7.39 and 7.41 that follow. These plots have very similar characteristics to those derived from experimental data, though the peak stress values are higher in the simulation. This is entirely due to differences in the hardening model assumed in the simulation (isotropic) and the hardening exhibited in the experiment. Figs. 7.40 and 7.42 show the axial force demands at midspan of the VBEs, where P_{L-ACT} and P_{R-ACT} are the axial forces extracted form the VBE force output and P_{ESF} is computed using the equivalent uniform stress field quantities. Although there are some differences between the simulated VBE axial force and that derived form the equivalent stress field (most notably the unloading stiffness and the response at negative drifts), at the peak of the tension phase the match between the two is very good. Knowledge of these stress fields could be utilized in the development of bi-directional strip models that capture the nuances of web plate post-buckling behavior.

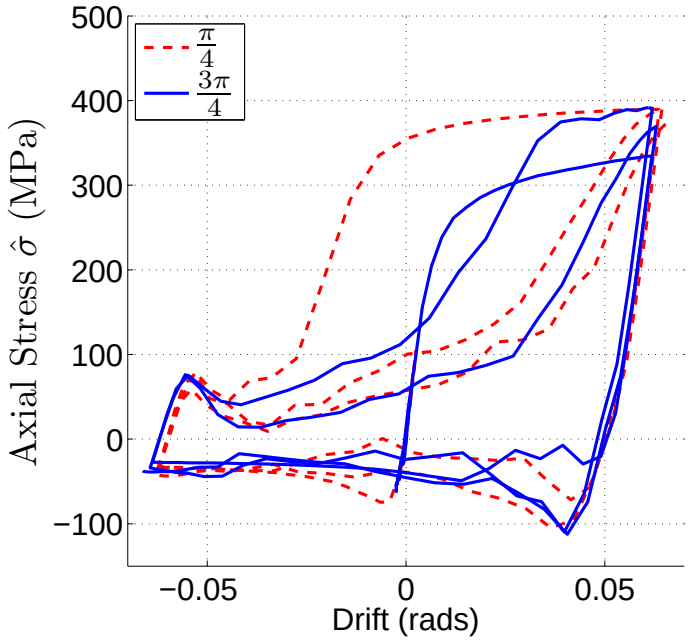

Figure 7.39: Test Simulation #2-22: Stresses in equivalent uniaxial, diagonal truss elements based on equivalent uniform stress field.

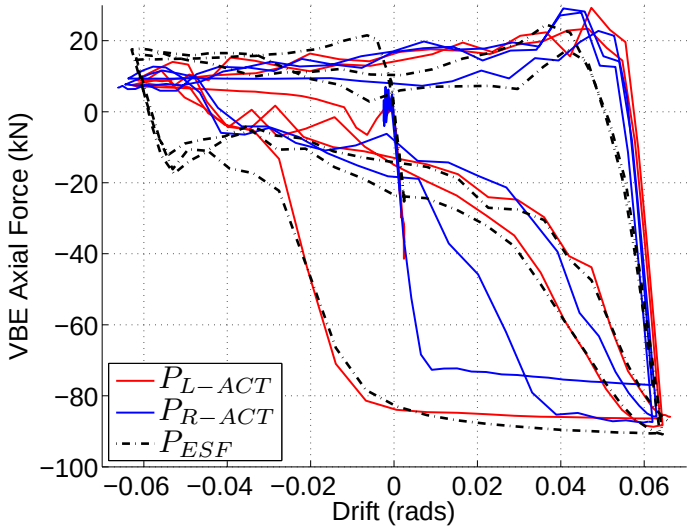

Figure 7.40: Test Simulation #2-22: Actual axial force in left VBE (P_{L-ACT}), right VBE (P_{R-ACT}), and force determined from equivalent stress field (P_{ESF}).

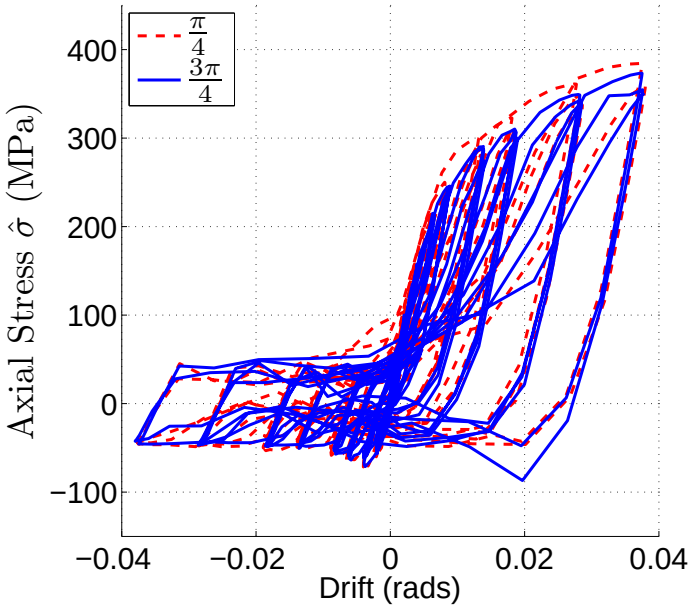

Figure 7.41: Test Simulation #3-22: Stresses in equivalent uniaxial, diagonal truss elements based on equivalent uniform stress field.

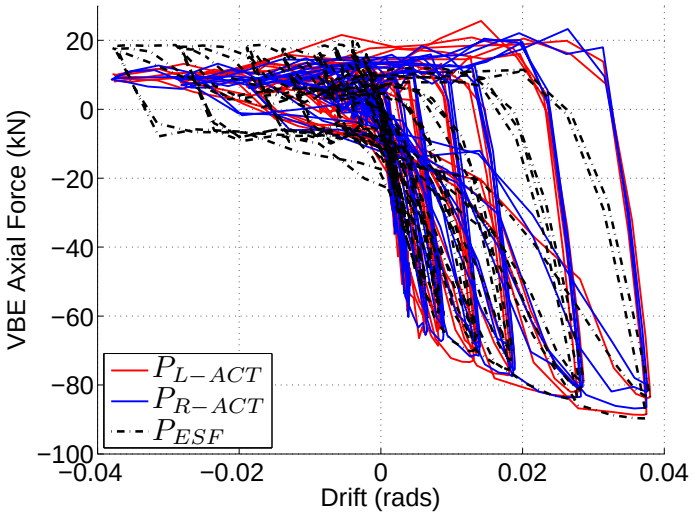

Figure 7.42: Test Simulation #3-22: Actual axial force in left VBE (P_{L-ACT}), right VBE (P_{R-ACT}), and force determined from equivalent stress field (P_{ESF}).

7.3.3 Conclusions

The test simulation results presented in this chapter have validated:

- The progression and magnitude of the tension field inclination angle measured in the experiment.
- The VBE demand measured in the experiment. The "equivalent" web plate stress field can be used to predict VBE bending for push-over analyses but tends to moderately under predict the experimental results for the cyclic analyses.
- The hardening exhibited by the A1008 plate is substantially isotropic, with a minimal kinematic contribution.
- The hardening exhibited by the A36 plate is a mixture of isotropic and kinematic, with approximately 50% contribution from each.
- Isotropic hardening should be assumed for web plate modeling.
- Knowledge only of drift history can be used to accurately predict the accumulation of plastic strains, and therefore provide a means for easily estimating peak VBE demand due to hardening.

Chapter 8

PROPOSED *OPENSEES* UNIAXIAL MATERIAL MODEL *SPSW-WP* FOR SPSW WEB PLATES

8.1 Introduction

This chapter presents the development and validation of a new SPSW web plate material model, *SPSW-WP*. The model, when applied to a series of inclined truss elements, is designed to replicate the behavior of a 2D shell structure subjected to in-plane cyclic shear loading. The *SPSW-WP* model approximates the effects of shear buckling, snap-through, material hardening, stiffness degradation, residual shear strength and normal plastic contraction (NPC). It has been implemented in *OpenSees* as a uniaxial material and is assigned to truss elements in strip model representations of SPSWs. The model only applies to truss elements inclined at 45° because it was calibrated against *ABAQUS* analyses under the assumption that the tension field operates at this angle. Fig. 8.1 shows some of the behaviors just mentioned.

Although the model is designed specifically for SPSWs, it could be used for any slender steel plate cyclically loaded in shear. The model is largely phenomenological, but is underpinned by the basic mechanics of thin plates loaded in shear and plasticity theory. The determination of strip hysteresis comes directly from the concept of the directional hysteresis introduced in Chapter 6. As just noted, the *SPSW-WP* model is calibrated using the directional hysteretic response of single story web plates modeled in *ABAQUS* with a range of panel aspect ratios (L/h), slenderness ratios (h/t_p) and material yield stresses f_y, and subjected to a suite of simple cyclic drift histories. The development of the material model is graphically illustrated in Fig. 8.2.

The calibration process was carried out in the following manner:

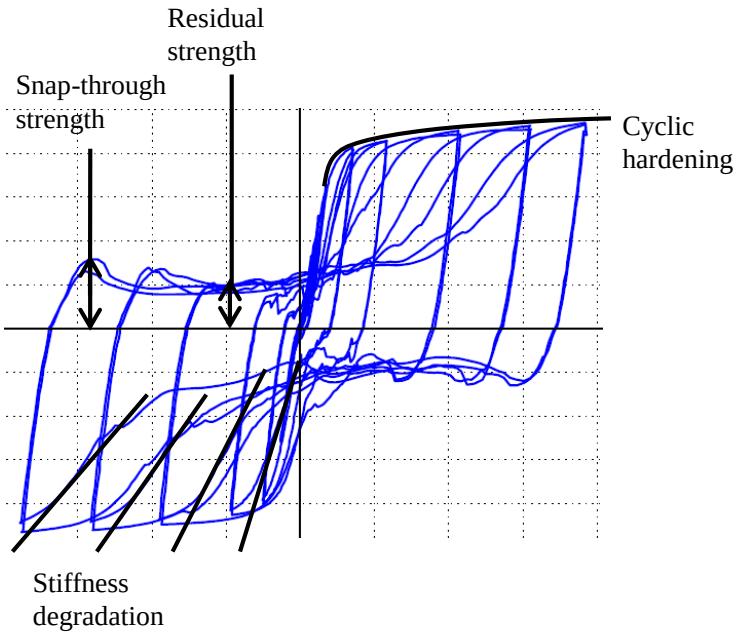

Figure 8.1: Typical SPSW hysteresis showing some of the behaviors

- Select panel aspect ratios (L/h), slenderness ratios (h/t) and material properties (E, fy, etc) that cover a broad range of values encountered in design.

- For each combination of geometrical and material properties, generate an $ABAQUS$ model of a single panel with boundary conditions (i.e., VBE and HBE stiffness) representative of a single story of an SPSW.

- Design/select a set of drift histories to which each $ABAQUS$ model is subjected to. Data from these analyses are used to calibrate the material model.

- Execute $ABAQUS$ analyses and extract state variables that may influence behavior. These include story drift angle, drift range (from last half cycle), mean accumulated plastic strain in web plate, loading and unloading stiffness, etc. Also extract the VBE bending moments at the top, middle and bottom of each VBE, and the total base reaction of the sub-assemblage.

- From VBE moments and base reaction, generate the directional hystereses (See Section 7.3.2 for definition) for each variation of panel h/t, L/h, etc.

- Idealize each phase (or state) of hysteretic behavior with a smooth curve or straight line as appropriate. Many of these functions are determined through regression of data obtained from the *ABAQUS* analyses. Some of the parameters are adjusted manually until a good match is obtained with the observed *ABAQUS* responses.

- Construct an algorithm that can predict the directional hysteretic behavior based on the state variables, accounting for loading and unloading within any state, small perturbations in amplitude and other behaviors that may occur in an actual response history analysis.

The preliminary validation process consisted of the following:

- Assemble series of single panel *OpenSees* bi-directional strip models and apply the *SPSW-WP* material model to the truss elements. These strip models have nominally identical geometries and boundary conditions to the *ABAQUS* models. Each model is subjected to two randomly generated drift histories, similar in drift magnitude and distribution to those that might be expected in a single story of a multi-story structure under earthquake excitation.

- Compare the VBE bending, dissipated energy and hysteretic behavior with *ABAQUS* analyses of identical structures modeled using shell elements. Make the necessary modification and adjustments to hysteretic model as needed.

The final validation process consisted of the following:

- Construct *OpenSees* models of the experimental specimens, including the final version of the *SPSW-WP* material model applied to the truss elements, and subject these to the precise amplitude history recorded from the experiments.

8.1.1 Terminology

Unless noted otherwise within this Chapter, the following apply:

1. loading and unloading refer to positive and negative straining (or drifting) respectively.

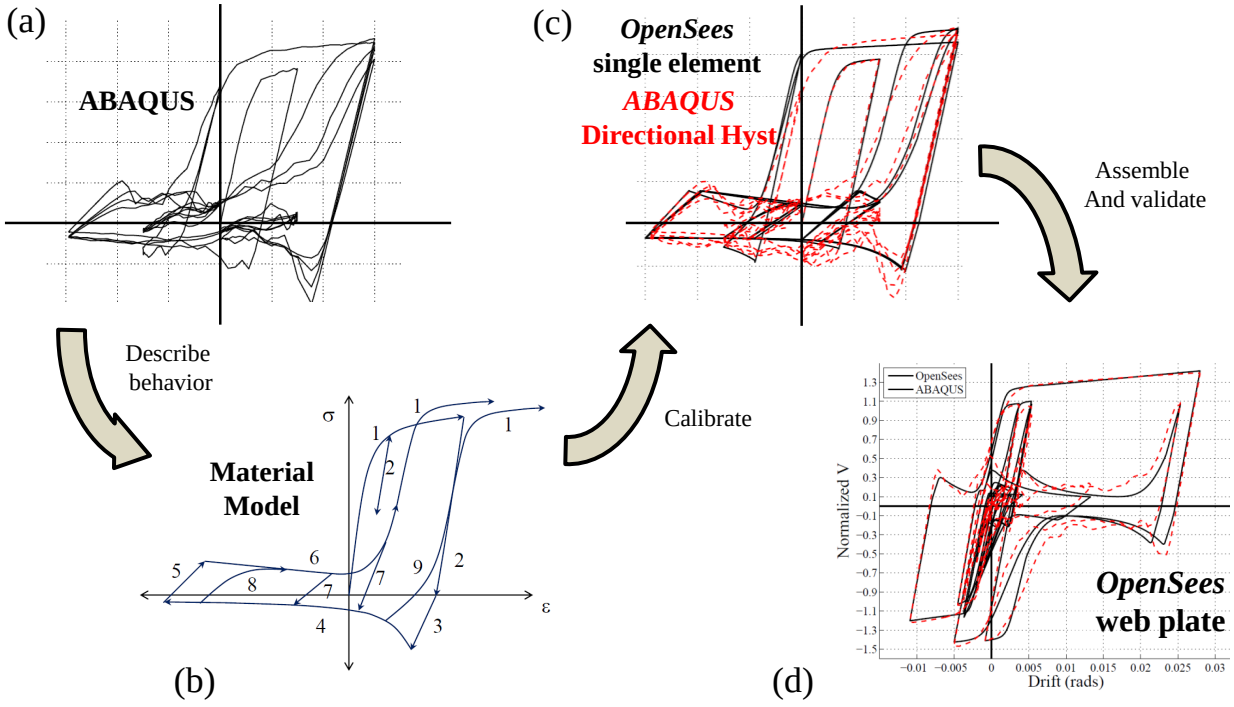

Figure 8.2: Overview of Model Development

8.2 Preliminary OpenSees *Analyses using Existing Uniaxial Material Object*

Comparing some of the results of *ABAQUS* analyses and *OpenSees* analyses that employ commonly used uniaxial material models provides a basis for model development and identifies the shortcomings (if any) of the existing material for SPSW applications. This existing material model is chosen for its simplicity and because it has been adopted for this application in research studies. For this exercise, the *OpenSees* analyses was conducted using the *Hysteretic* uniaxial material. The properties assigned to this material are nominally identical to those of an equivalent structure modeled in *ABAQUS* using shell elements. The parameters $pinchX$ and $pinchY$ (specifying the magnitude of hysteretic pinching on the $drift$ and $load$ axes respectively, are discussed in more detail in the sections that follow) were adjusted until a reasonable match between the *OpenSees* and *ABAQUS* behavior was achieved for a symmetric cyclic load history; a luxury that would not ordinarily be available for calibration purposes. The material is defined in *OpenSees* with the following *tcl* statement

```
uniaxialMaterial Hysteretic tag sp1 ep1 sp2 ep2 sp3 ep3 sn1 en1 sn2 en2 sn3
en3 pinchX pinchY
```

In this statement, (`sp1`, `ep1`) and (`sn1`, `en1`) represent material stress-strain pairs in the positive (tension) and negative (compression) direction of loading.

A total of four cyclic amplitude histories were used, two symmetric ($Amp1$ and $Amp2$) and two asymmetric ($AmpA$ and $AmpB$). These are introduced and discussed later during the validation, but can be seen in Fig. 8.6(a) and (b) and Fig. 8.23(a) and (b).

8.2.1 Analyses Using Symmetric Amplitude Histories

For the models subjected to $Amp1$ and $Amp2$, the hardening was moderate and approximately equivalent to ASTM A36 steel sheet. The pinching parameters, $pinchX$ and $pinchY$, were set to 0.8 and 0.3 respectively for the symmetric amplitude histories. The *OpenSees*

responses were a fair match with *ABAQUS* as shown in Fig. 8.3. The *OpenSees* peak lateral load underestimated the peak *ABAQUS* lateral load by approximately 15%. This is largely due to the use of a monotonic stress-strain relationship (derived from coupon data) to define the backbone of the *OpenSees* model. This is a common approach but one that can lead to significant error. Clearly, this can be compensated for by assuming a steeper strain hardening envelope derived from an assumed cyclic backbone, but the resulting strength becomes drift dependent (i.e., the strength reached at a particular drift is defined entirely by a fixed backbone curve) and selection of the appropriate backbone becomes a matter of judgment and is subjective. It will be demonstrated later, that this dependency does not, in general, exist. For the cases tested here, the VBE bending moments are under-predicted for *Amp*1 and generally over-predicted for *Amp*2.

8.2.2 Analyses Using Asymmetric Amplitude Histories

When the same models are subjected to more random asymmetric amplitude histories, the resulting hystereses are not accurate representations of the *ABAQUS* behavior. Fig. 8.4 shows the result of the analysis using a low strength steel with pronounced strain hardening. In both cases the hysteretic response of the *OpenSees* model is a poor approximation of the *ABAQUS* response and significantly under-predicts peak lateral strength and VBE demand. In both cases the *OpenSees* model using the *Hysteretic* material fails to precisely track the amplitude history, even when employing a small time step. It should be pointed out that the failure of this material to capture the complex behavior of a web plate is to be expected. This material is designed for a range of applications, but is not capable of correctly modeling web plate response for random asymmetric cyclic loading. In view of this, the development of the new *SPSW-WP* material model specifically designed to capture the non-linear cyclic response of a web plate is justified.

8.3 Development of $SPSW-WP$ Model and Calibration

Chapter 6 presented the results of *ABAQUS* analyses of the web plates that were tested as part of the experimental program. These analyses demonstrated that *ABAQUS* can accurately simulate the significant load-displacement characteristics of steel web plates. Chapter

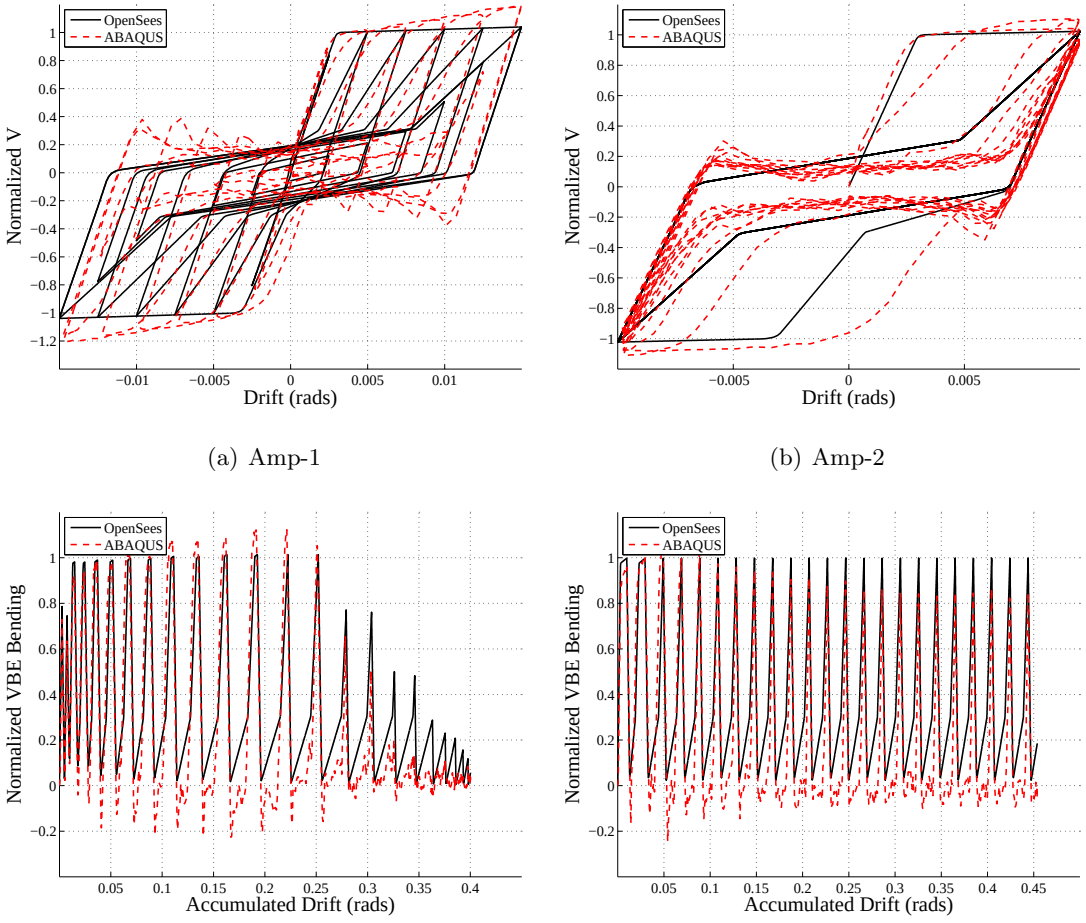

(a) Amp-1

(b) Amp-2

(c) Amp-1

(d) Amp-2

Figure 8.3: Normalized response quantities for *ABAQUS* and *OpenSees* using the existing *Hysteretic* material: Symmetric amplitude histories.

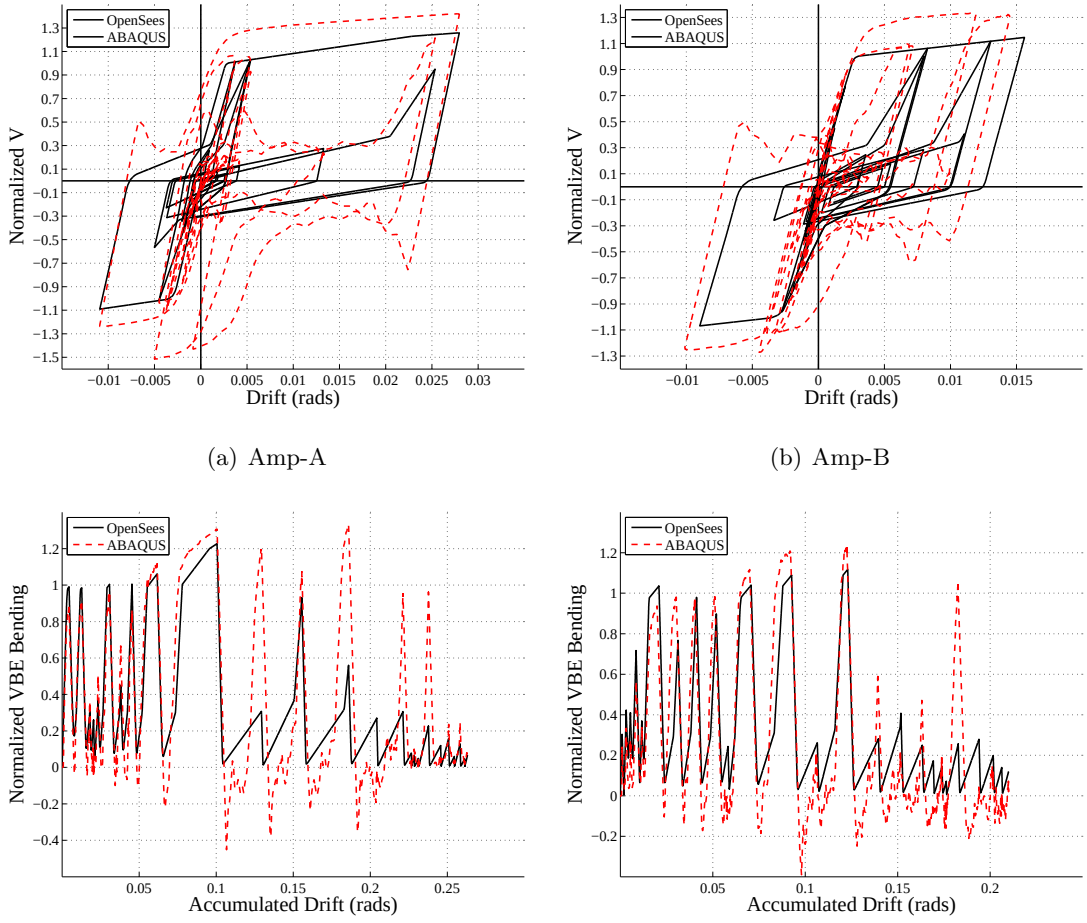

(a) Amp-A

(b) Amp-B

(c) Amp-A

(d) Amp-B

Figure 8.4: Normalized response quantities for *ABAQUS* and *OpenSees* using the existing *Hysteretic* material: Asymmetric amplitude histories.

5 introduced the concept of directional hysteresis that can be used to generate a hysteresis curve for a truss element representation of a 2D continuum, derived either from actual test data or from FE data of web plate shell behavior. On this basis, the directional hysteresis curves derived form the results of $ABAQUS$ analyses are used to calibrate the new material model, rather than experimental data. In this way the range of material properties and drift demands can be expanded beyond the limited range of experimental data to ensure that all behavior modes of interest are captured by the model. The experimental data are then used as part of the model validation process.

Fig. 8.5 shows a typical cycle of the hysteresis for a single truss element. This is an idealization of what is observed in directional hystereses curves derived from $ABAQUS$ data and from experimental data. The element loads in tension with stiffness k_1 and progressively yields. It then unloads along slope k_2 until the stress reaches zero. At this point, the plate has been stretched plastically, but is now unloaded. When loading commences in the opposite direction, the corrugations that formed in the direction of principal tensile stresses as the plate was stretched, promote a snap-through buckling phenomenon with a buckling load (stress) of F_{ST}. This load is governed by plate slenderness, web plate yield strength and web plate aspect ratio. After snap-through at F_{ST}, the load rapidly decays to F_{RES}, which is typically greater than the elastic buckling load of the plate and also a function of plate slenderness. As the load direction changes again, the material typically experiences a rapid increase in the effective tensile strength until it reaches the strength F_{TR}. Further development of tension is delayed until the material reaches the primary tensile reloading drift, at which point the tension field is being reactivated and the cycles continue. The reloading drift is determined by load history but is essentially a function of how much plastic stretch has occurred in the plate in each of the primary directions of tensile loading. It is thus governed mostly by NPC (See Section 8.5.1).

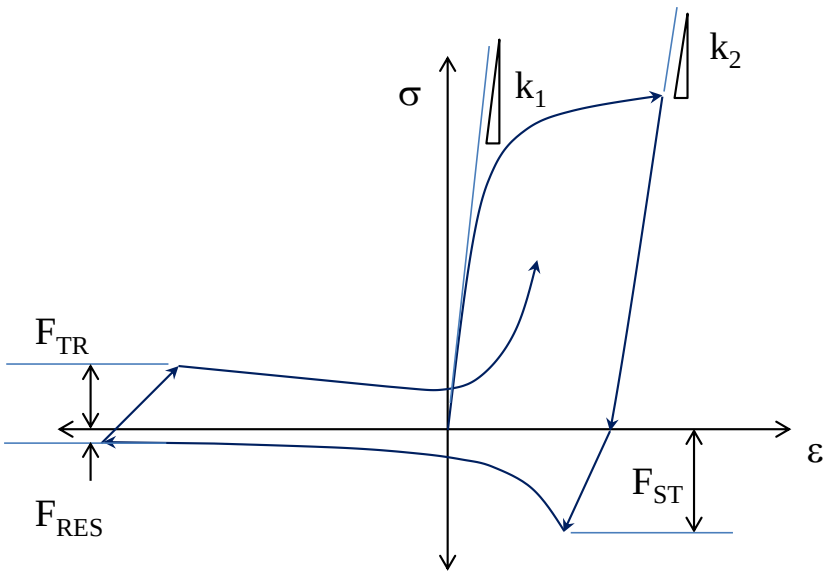

Figure 8.5: Quantities F_{TR}, F_{ST} and F_{RES} from directional hysteresis

This section introduces and details the components of the new material model and the calibration of this model using *ABAQUS* analysis to a selection of drift histories. Two panel aspect ratios (L/h), three slenderness ratios (h/t_p) and two material yield strengths (f_y) were used.

8.3.1 Geometric Parameters and Material Properties used for Parametric Studies

The range of web plate material properties (E, F_y, etc) and geometries (L/h, h/t_p, etc) is selected to provide a balance between efficiency and detail so that key relationships can be adequately quantified. Table 8.1 shows a matrix of the parameters used for calibration. *Amp* is the amplitude number and is introduced in Section 8.3.2.

Table 8.1: Web Plate Model Parameters For *OpenSees* Uniaxial Material Calibration

f_y	$\frac{h}{t}$	$\frac{L}{h}$	*Amp*
250	2000, 1000, 500	1.2, 0.8	1-6
400	1000, 500	1.2, 0.8	1-6

Both the low strength (f_y = 250 MPa) and high strength (f_y = 400 MPa) steels have

multi-linear hardening envelopes defined by the data in in Table 8.2.

Table 8.2: Web Plate Material Stress-Strain Data for Model Calibration

$\frac{f}{f_y}$	ϵ^{pl}
1.0	0.00
1.2	0.03
1.4	0.20
1.5	0.40

8.3.2 Cyclic Amplitude Histories used for Calibration

A total of six drift amplitude histories (*Amp*1 through *Amp*6, shown in Fig. 8.6(a) through (f)) were used in both the *ABAQUS* and *OpenSees* analyses for the purposes of material model calibration. Each history was designed to test different aspects of SPSW response, such as cyclic ratcheting, ramp-up, ramp-down and constant amplitude loading. Each drift history, with the exception of *Amp*2, had a maximum drift of 0.015.

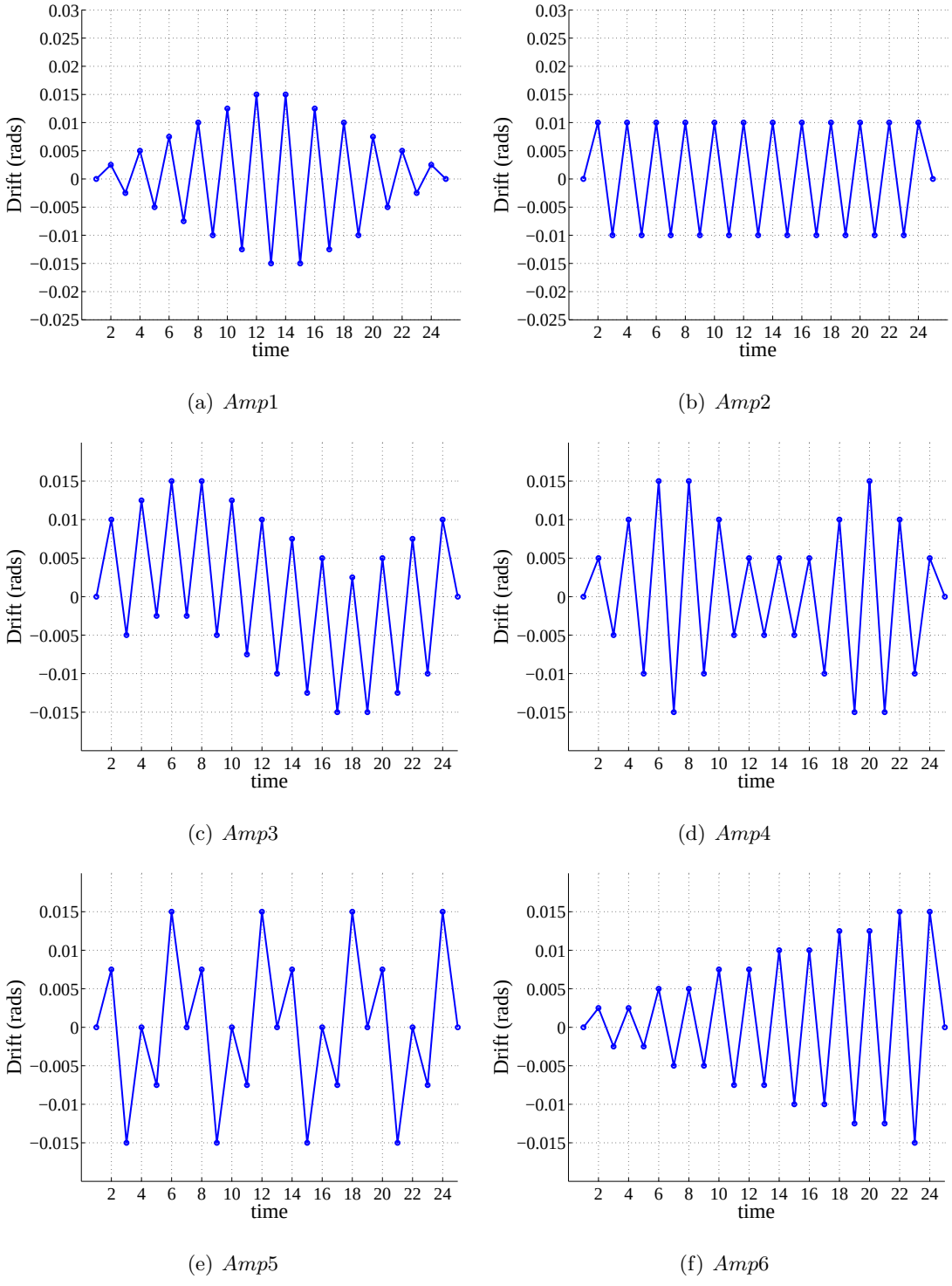

(a) $Amp1$ (b) $Amp2$

(c) $Amp3$ (d) $Amp4$

(e) $Amp5$ (f) $Amp6$

Figure 8.6: Drift Amplitudes Used in Parameter Study.

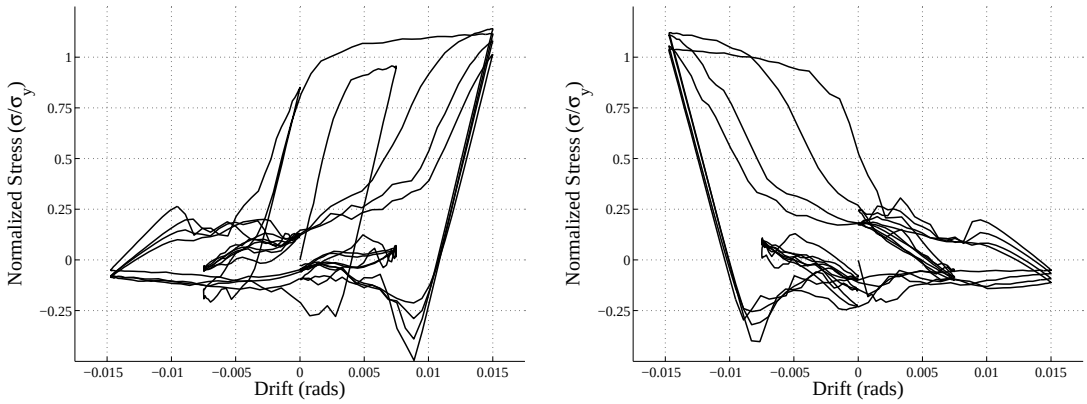

(a) $Direction = 45deg$ (b) $Direction = 135deg$

Figure 8.7: Directional hysteresis curves derived from $ABAQUS$ analyses.

8.3.3 Directional Hysteresis

Most of the hysteretic parameters of interest are derived from the directional hysteresis curves obtained from the $ABAQUS$ response data. Using the equations presented in Section 6.3 of Chapter 5, the hysteresis of an equivalent inclined element can be derived from the $ABAQUS$ data. A sample of the directional hysteresis curves derived from $ABAQUS$ is shown in Fig. 8.7(a) and (b), where (a) is for the direction inclined at 45 degrees to the positive x-axis and (b) is for 135 degrees. These curves were generated for a web plate $h/t = 500$, $L/h = 0.8$ and yield stress $f_y = 250$ MPa (and $Amp5$).

8.4 Model States

The directional hysteresis can logically be divided into a number of *states*. The material can exist in only one state at a time and a series of rules determine the progression of one state to the next. Often the progression is in a sequential manner, i.e., from state "i" to state "i+1", but this is not always the case. The sequence can switch back to a previous state or skip several intermediate states, depending on the strain history. What follows is a brief description of each of the states that define the hysteretic response of the equivalent uniaxial element and the equations that are used to describe them. The states are shown

labeled 1 through 9 in Fig. 8.8. The following itemized list gives a short description of each. These are explained in greater detail later.

1. State 1: Primary tension loading. Commences when tension field is activated at a stress of $0.5\sigma_y$ and transitions into plastic stretching.
2. State 2: Unloading. Occurs immediately after plate is stretched in tension and commences upon unloading.
3. State 3: Snap-through. As plate continues to unload it builds up compressive strength to a peak of F_{ST} along the axis of the (uniaxial) element just prior to snap-through buckling. This is largely the result of corrugations in the plate enhancing compressive strength.
4. State 4: Load decays after snap-through to residual compressive strength, F_{RES}. This is typically higher than the theoretical buckling strength.
5. State 5: Plate undergoes an initial tension reloading up to maximum stress of F_{TR} before the tension field has been activated. This state cannot be easily described by a particular physical phenomenon but exists to provide the correct balance between base shear and VBE transverse load when the plate is outside the primary loading phase.
6. State 6: The transition from initial tension reloading up to the point where the tension field has been fully activated (State 1).
7. State 7: Unloading from State 6.
8. State 8: Reloading from State 4. This occurs if the reloading from State 4 commences at a drift less than the largest negative drift that has occurred so far in the entire history (otherwise State 4 transitions into State 5).
9. State 9: Reloading in tension from State 4. This occurs if the reloading in tension occurs prematurely, just after snap-through has occurred (State 3).

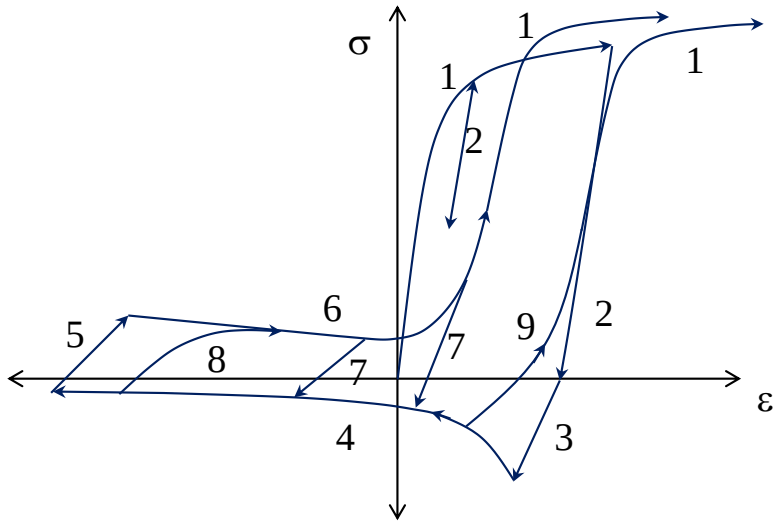

Figure 8.8: SPSW uniaxial strip model hysteresis showing the different loading states

Each of the nine states will now described in more detail, including any equations or other pertinent information that is required. Many of the parameters used to describe the states, are determined through regression of $ABAQUS$ data, while some are simply matched by trial and error. e.g., the curvature parameter, R, used in the Magnegotto-Pinto curves.

8.4.1 State 1

State 1 is primary tensile loading and is represented with a Magnegotto-Pinto hyperbola in Fig. 8.9. State 1 typically commences after the tensile stress exceeds $0.5\sigma_{y0}$, but it does so at zero stress and strain on the very first loading cycle. The Magnegotto-Pinto hyperbola is defined using Eqs. 8.1, 8.2 and 8.3.

$$\epsilon^* = (\epsilon_i - \epsilon_0)/(\epsilon_c - \epsilon_0) \tag{8.1}$$

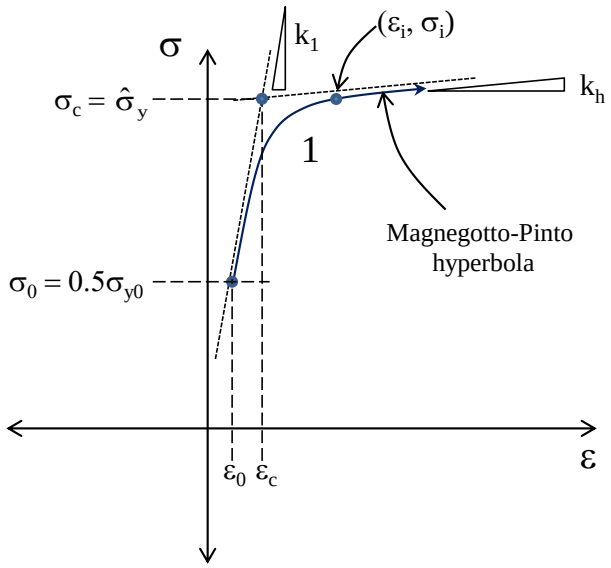

Figure 8.9: State 1, showing key parameters used to describe Magnegotto-Pinto hyperbola

$$\sigma^* = \left(\frac{k_h}{k_1}\right)\epsilon^* + \frac{\left(1 - \left(\frac{k_h}{k_1}\right)\epsilon^*\right)}{\left(1 + \epsilon^{*R}\right)^{\frac{1}{R}}} \tag{8.2}$$

$$\sigma_i = \sigma^*\left(\sigma_c - \sigma_0\right) + \sigma_0 \tag{8.3}$$

The stress and strain terms above are graphically illustrated in Fig. 8.9. The point (σ_c, ϵ_c) is the intersection of the strain hardening branch (with slope k_h) and the loading slope k_1. σ_c is determined by the hardening evolution of the material. The directional hysteretic yield stress $\hat{\sigma}_y$ is the yield stress defined by the hardening model discussed in Section 8.5.3. This stress is a modified form of the actual estimated von Mises stress, which accounts for the presence of compressive stresses. This is equal to the yield stress, σ_{y0}, of the material on the virgin loading branch. The point (σ_0, ϵ_0) is the initial stress and strain at the beginning of the State 1 and (σ_i, ϵ_i) is the stress-strain at some arbitrary point along the hyperbola. The initial strain ϵ_0 is equal to the tension reloading strain ϵ_r defined and discussed in detail in Section 8.5.1. R is a curvature parameter for the hyperbola and was set equal to 6.

The initial tension loading stiffness, k_{1in} (see Fig. 8.9) was found to be correlated primarily with h/t_p of the web plate and is represented by Eq. 8.4 as follows

$$k_{1in} = 0.215E_s\left(\frac{h}{t_p}\right)^{0.19} \tag{8.4}$$

This stiffness is reduced as loading progresses by the additional terms shown in Eq. 8.5.

$$k_1 = k_{1in}\left(0.5 + 0.5exp\left(10^4(\Sigma\dot{\epsilon}^{pl})^2\right)\right)\left(0.5 + 0.5exp\left(10^2(\epsilon_r - \epsilon_4)^2\right)\right) \tag{8.5}$$

In this equation, $(\epsilon_r - \epsilon_4)$ is the strain difference between the last change in loading direction (State 4) and the next tension reloading strain (represented graphically for example by points b and C respectively in Fig. 8.19) and $\Sigma\dot{\epsilon}^{pl}$ is the accumulated plastic strain. Analysis of the measured reloading stiffness in *ABAQUS* parametric studies revealed that there is a slight decrease in k_1 as plastic strain accumulates and as the cyclic drift range increases, although for both cases there is a tremendous amount of scatter in the data. The equation for the evolution of k_1 represented by Eq. 8.4 is developed largely by trial and error, but it matches the *ABAQUS* results reasonably well for the range of parameters and amplitude test cases examined. The stiffness reduction term in Eq. 8.5 is approximately linear out to moderate strain levels and k_1 remains positive at very large strains.

8.4.2 State 2

State 2, with stiffness k_2 shown in Fig. 8.10, follows directly from State 1 and occurs as the plate unloads elastically from peak strain. The unloading stiffness k_2 is more stable than k_1 but maintains a similar relationship with plate slenderness h/t_p and also with aspect ratio. It degrades appreciably with increasing levels of plastic strain accumulation. Accordingly, k_2 is modeled with the following function represented by Eqs. 8.6 and 8.7.

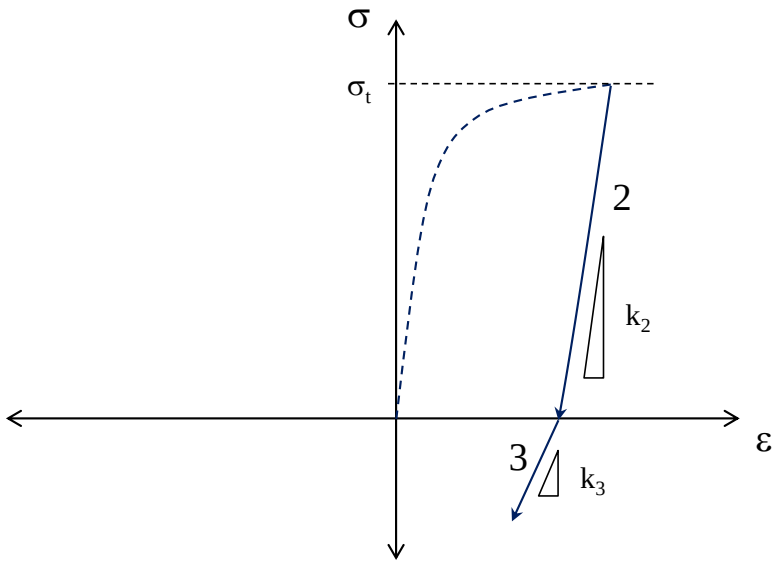

Figure 8.10: States 2 and 3

$$k_{2in} = E\left(\frac{h}{t_p}\right)^{0.1}\left(\frac{L}{h}\right)^{0.15} \tag{8.6}$$

$$k_2 = 0.45 k_{2in} exp\big(-2\Sigma\dot{\epsilon}^{pl}\big) \tag{8.7}$$

With these functions, a large accumulated plastic strain, e.g., 5%, will result in a 10% reduction in k_2 from the initial value. The equations used for k_1 and k_2 were determined largely by trial and error.

8.4.3 State 3

When State 2 reaches zero stress it transitions into State 3, with stiffness k_3, where the unloading plate experiences compression just prior to snap-through buckling into State 4. The unloading stiffness k_3 is defined by Eq. 8.8

$$k_3 = \frac{3}{5}k_2 \tag{8.8}$$

The stress F_{ST} is computed using Eq. 8.15 which is defined in Section 8.5.2. The $\frac{3}{5}$ factor is tuned to the *ABAQUS* analyses by trial and error.

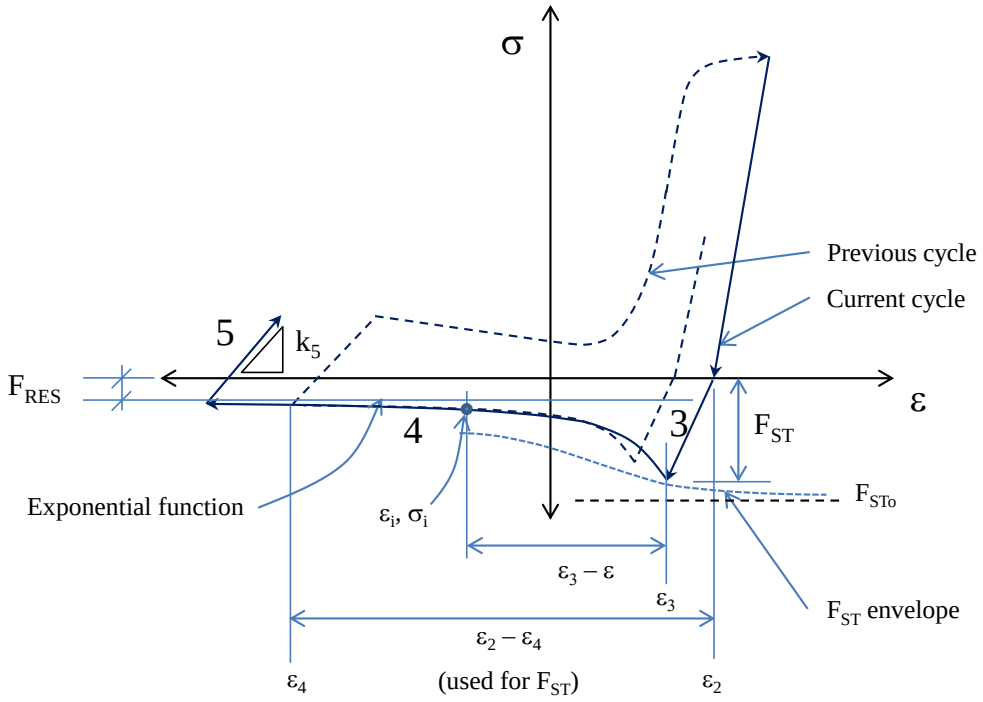

Figure 8.11: State 3, State 4 (exponential) and State 5

8.4.4 State 4

During State 4, shown in Fig. 8.11, the stress decays exponentially out to the maximum drift in the opposite loading direction and asymptotically approaches F_{RES}. The decay of stress σ_i is define by Eq. 8.9.

$$\sigma_i = F_{ST} + \big(F_{RES} - F_{ST}\big)\big(1 - exp(-b(\epsilon - \epsilon_3))\big) \tag{8.9}$$

where ϵ_3 is the strain at the peak of the snap-through stress (i.e., the end of State 3) and the parameter b controls the rate of decay and is set equal to 600. There was a lot of scatter observed in the progression of this decay in the *ABAQUS* analyses. The chosen b factor appeared to adequately match the data for a range of plate thicknesses.

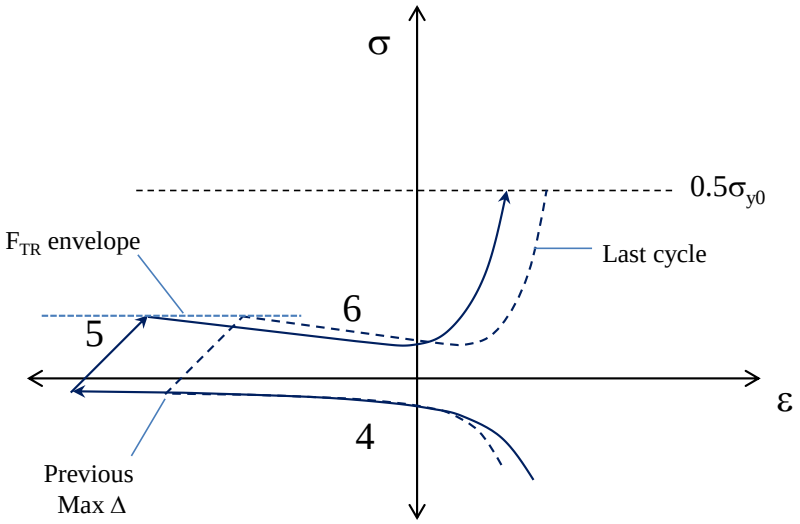

Figure 8.12: State 5 showing previous minimum strain

8.4.5 State 5

After the plate reaches maximum negative drift in State 4, it immediately reloads in tension through State 5, but at a much lower stiffness than the primary tension reloading of State 1. The stiffness of State 5, k_5, is related to the stress and strain quantities experienced in the previous States 2 and 3 and is represented approximately by Eq. 8.10.

$$k_5 = \frac{(F_{TR} - F_{RES})}{\left(\frac{\sigma_t}{k_2} - \frac{F_{ST}}{k_3}\right)} \tag{8.10}$$

The tension reloading strength F_{TR} is computed using Eq. 8.15 which is defined and discussed in Section 8.5.2. Here, σ_t is the stress attained at the end of the last primary loading (State 1) and is illustrated in Fig. 8.10. This equation is is introduced so that the strain at the peak tension reloading strength approximately coincides with the snap-through peak for truss elements in the opposite direction of the web plate. This is illustrated in Fig. 8.19 of Section 8.5.2 by the points p and p'.

8.4.6 State 6

At the end of State 5, the increase in tensile stress is delayed until the strain level reaches the next tension reloading strain, ϵ_r. During State 6, shown in Fig. 8.13, the stress decreases and then progressively increases as the drifts continue to increase in the positive direction. State

6 is also modeled using a Magnegotto-Pinto hyperbola (See State 1), but this time inverted

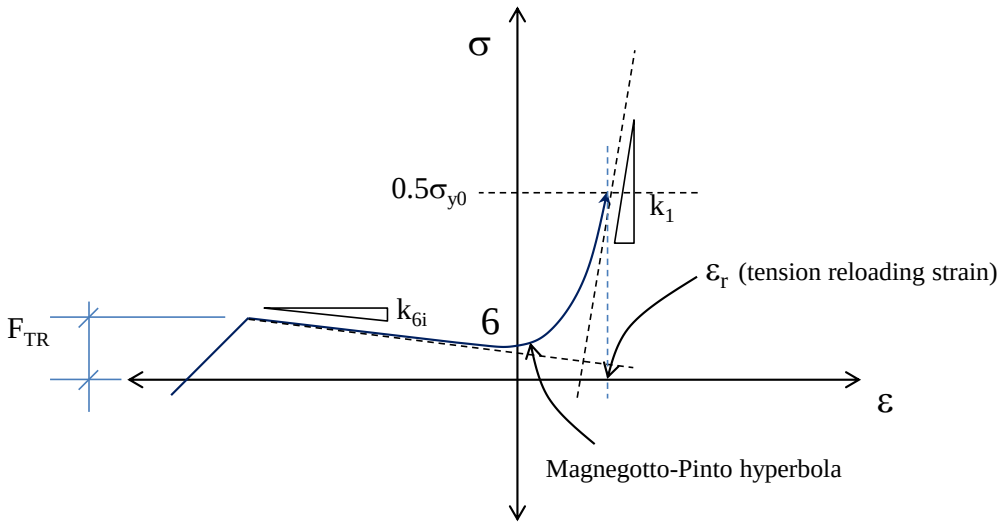

Figure 8.13: State 6 hyperbolic transition to State 1

8.4.7 State 7

State 7, with slope k_7 shown in Fig. 8.14, occurs when the plate unloads from State 6. The slope of k_7 is the maximum of k_7 defined by Eq. 8.11 and the last tangent stiffness attained in State 6. If reloading occurs in State 7 prior to reaching the curve defined by the previous State 4, it reloads along State 7 at a slope of k_7 until it reaches the curve for the previous State 6. If unloading in State 7 reaches the curve for the previous State 4, it transitions into the previous State 4 until positive reloading occurs again. If reloading occurs at a strain less than the last minimum strain attained in State 4, it transitions into a new State 5. This is illustrated in Fig. 8.14. As for State 5, the magnitude of k_7 was chosen by trial and error to match a range of parameters.

$$k_7 = \frac{4}{5}k_5 \tag{8.11}$$

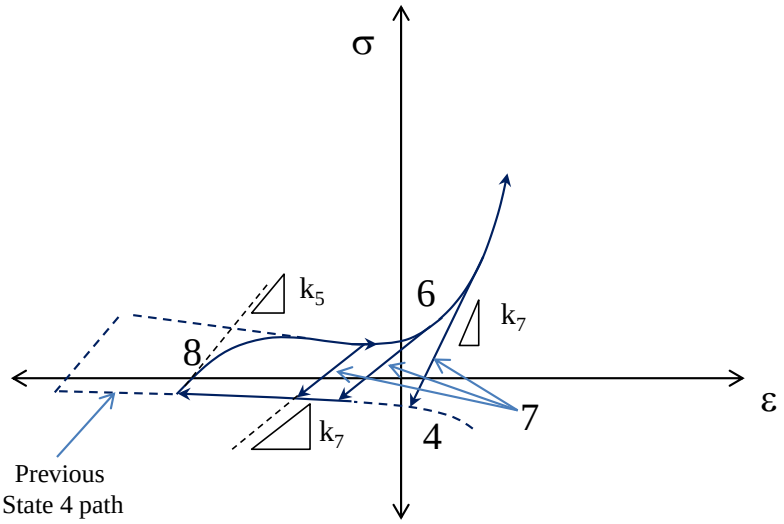

Figure 8.14: State 7 unloading from State 6

8.4.8 State 8

If from State 4 the strain direction switches to positive prior to reaching the previous minimum State 4 strain, it transitions into State 8 shown in Fig. 8.15. State 8 is defined using a cubic polynomial function that has an initial stiffness of k_5 and a final stiffness of k_6 (the last tangent stiffness attained in State 6, if it transitions into State 6) or k_1 (if it transitions into State 1).

8.4.9 State 9

State 9, shown in Fig. 8.16, is also defined bay a Magnegotto-Pinto hyperbola. The initial slope of the hyperbola is set equal to k_5. The final slope is set to k_1 at the reloading strain, ϵ_r, at the beginning of State 1. State 9 is invoked if the plate reloads from State 4 after a short negative drift excursion and transitions directly into State 1.

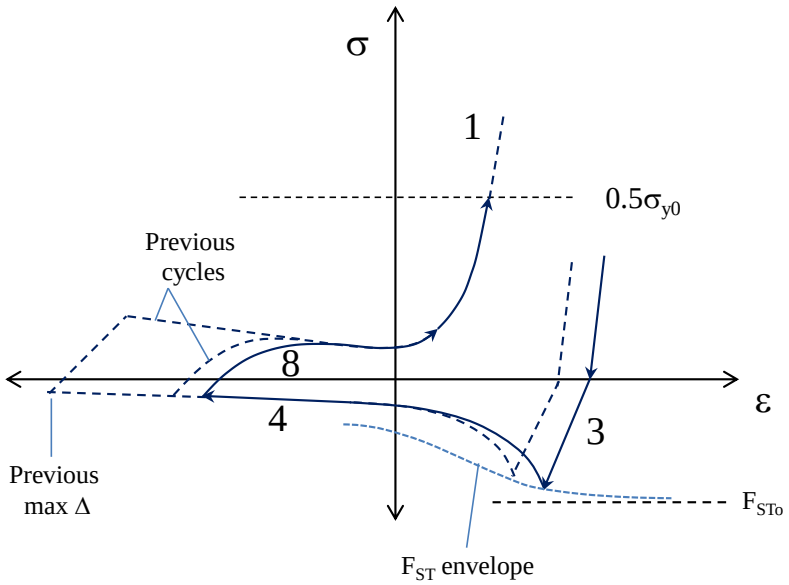

Figure 8.15: State 8 loading from State 4

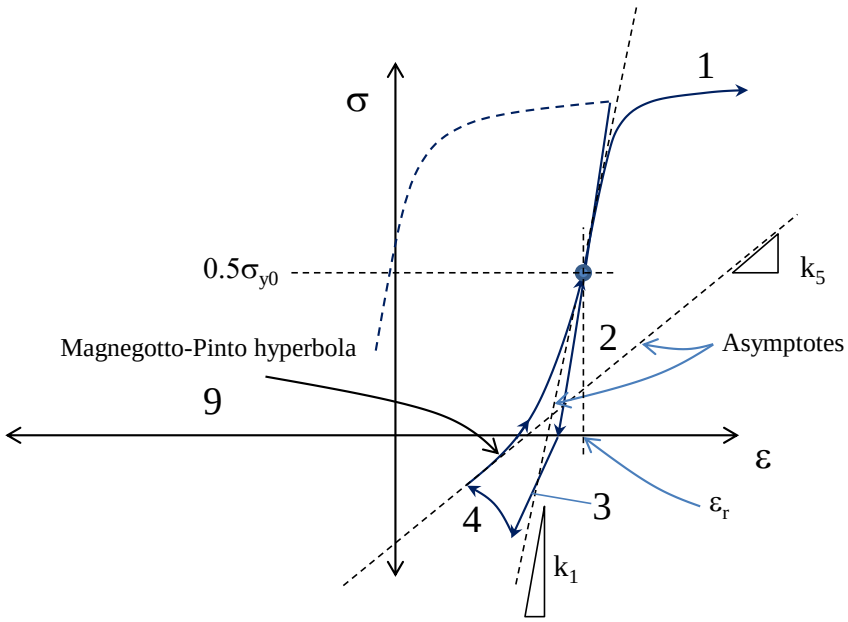

Figure 8.16: State 9 loading from State 4

8.5 Key Parameters Used in Hysteresis

The following sections address details of the key parameters in the hysteresis. These include, F_{ST}, F_{TR}, F_{RES} the reloading strain ϵ_r and the current or instantaneous yield strength, σ_y.

8.5.1 Reloading Strain ϵ_r

The determination of the correct tension reloading strain is a critical step in accurately modeling the hysteretic response of the web plate, because it directly effects the degree of hardening and energy dissipation. Consequently, the tension reloading strain needs to be computed for both directions of loading (i.e., tension and compression). The reason for this becomes clearer when considering the behavior of a web plate as illustrated in Fig. 8.19. The strips in the 45 degree direction need "knowledge" of the strain experienced by the strips in the 135 degree direction. This is not done by recognizing that for a boundary frame with rigid members, the strain in a given strip direction will be uniform across the plate and can be computed exactly from the frame drift. When the VBEs and HBEs are flexible it becomes an approximation, but as will be demonstrated it is a reasonable one.

Fig. 8.19 illustrates how the reloading strain is computed for a single strip. The points A and C are strains for tension reloading, ϵ_r, in the 45 degree direction. The top figure represents the actual stress-strain state of the strip. The bottom figure is the estimated stress-strain state of the strip in the orthogonal direction, which is based on the strain in the strip in the un-primed figure. The quantities of interest in the primed state are the reloading points A' through D'. Starting at the origin, O, the first reloading point occurs at A. As the strip is stretched plastically to point a, the reloading strain moves to point B. The reloading strain for the strips in the opposite direction will move from A' (the initial reloading strain in the 135 degree direction) to B', where $\epsilon_{A'B'}$ is a fraction of ϵ_{AB} (defined here as μ) i.e., $\mu\epsilon_{AB}$. The μ factor is due to normal plastic contraction (NPC) which, in the presence of non-negligible compressive stresses, varies between -0.5 and -1.0, but it is typically between -0.5 and -0.65 for most practical SPSW plate slenderness values. For very slender plates with limited compressive stress development, it is very close to -0.5. For very

stocky plates it can be less than -0.6. For the case where buckling does not occur and the plate yields in shear, μ equals -1.0. The estimation of μ is based in part on the mechanics of a plastically stretching plate and partly on the observed behavior in the $ABAQUS$ models. Eqs. 8.12, 8.13 and 8.14 show the expressions used to compute μ for different L/h and h/t_p ratios.

$$\mu = min\left[0.5 + 0.5exp\left(- 0.01\left[\left(\frac{h}{t_p}\right) - \left(\frac{h}{t_p}\right)_{cr}\right]\right), 1.0\right] \tag{8.12}$$

where

$$\left(\frac{h}{t_p}\right)_{cr} = \sqrt{\frac{\sqrt{3}KE_s}{(1-\nu^2)f_y}} \tag{8.13}$$

$$K = 7.38 + 5.38\left(\frac{L}{h}\right)^{-1.33} \tag{8.14}$$

In Eq. 8.12, $\left(\frac{h}{t_p}\right)_{cr}$ is the critical plate slenderness below which shear yielding will precede shear buckling. The K term in Eq. 8.14 is a shape factor used to compute the shear buckling stress of a rectangular plate. The factor of 0.01 shown in Eq. 8.12 affects the decay rate of the plastic contraction with increasing slenderness.

The plate then unloads from a until the strain in the primed state reaches B' and commences reloading and plastically stretching in the opposite direction until point b' is reached. The positive direction reloading point moves back from B to C, where ϵ_{BC} is $\mu\epsilon_{B'C'}$. The plate then commences positive direction loading and moves from b to C, the next reloading strain. From C to c the plate is again stretched plastically, and the new reloading strain in the positive direction moves to D. As this occurs, the reloading strain in the opposite direction transitions from C' to D', where $\epsilon_{C'D'}$ equals $\mu\epsilon_{CD}$. The process continues in this manner indefinitely.

8.5.2 Snap-through, Tension Reloading and Residual Strength

Strength response quantities F_{ST}, F_{TR} and F_{RES}, which occur outside the primary loading phase, are predicted for the new material model by first assuming a function that can

adequately characterize the observed *ABAQUS* response. These were shown graphically in Fig. 8.5. A dimensionless function is used to describe each response quantity. The function has the general form represented by Eq. 8.15. Examination of *ABAQUS* directional hystereses that have been normalized by web plate yield strength, show that the maximum (roughly 85^{th} percentile) value of these quantities varies with plate slenderness (h/t), aspect ratio (L/h) and elastic modulus to yield strength ratio (E/σ_y). The indicies α, β and γ are determined by minimizing the residual between the observation (*ABAQUS*) and the predicted value using Eq. 8.15. The slope m and intercept C of the line of best fit are determined by linear regression.

$$\bar{F} = m_f \left(\frac{h}{t}\right)^{\alpha_f} \left(\frac{L}{h}\right)^{\beta_f} \left(\frac{E}{F_y}\right)^{\gamma_f} + C_f \tag{8.15}$$

where m_f is the slope of the regressed function and C_f is the intercept.

The normalized snap-through strength $\bar{F}_{ST}$ tends to increase with increasing magnitude of the last drift range $(\epsilon_2 - \epsilon_4)$ and decrease with increasing accumulated plastic strain $\Sigma\dot{\epsilon}^{pl}$. Here, ϵ_4 is the maximum strain in the material when in State 4 of the *previous* cycle. Many functions can adequately capture the degradation of F_{ST}. The differences in predicted web plate response, using a variety of different degradation functions was found to be small. Eq. 8.16 is used to predict F_{ST} with the additional multipliers β_1 and β_2 to better match the observed *ABAQUS* results response.

$$F_{ST} = \beta_1 \beta_2 \sigma_{y0} \bar{F}_{STo} \tag{8.16}$$

Where β_1 and β_2 are described as follows

$$\beta_1 = exp\big(-80(\Sigma\dot{\epsilon}^{pl})^2\big) \tag{8.17}$$

$$\beta_2 = 1 - 0.8exp\big(-2 \times 10^4(\epsilon_2 - \epsilon_4)^2\big) \tag{8.18}$$

The tension reloading stress, F_{TR}, and residual compressive stress, F_{RES}, are defined by Eqs. 8.19 and 8.20 and the values are shown in Table 8.3.

Table 8.3: Regression Data for Key Directional Hysteresis Response Quantities

F	α_f	β_f	γ_f	m_f	C_f
$\bar{F}_{TR}$	-1.08	0.36	0.59	2.59	0.0170
$\bar{F}_{RES}$	-0.83	-0.62	0.26	2.78	0.0032
$\bar{F}_{STo}$	-0.09	-0.23	1.40	$3.5\times\ 10^{-5}$	$0.094 + \bar{F}_{RES}$

$$F_{TR} = \sigma_{y0}\bar{F}_{TR} \tag{8.19}$$

$$F_{RES} = \sigma_{y0}\bar{F}_{RES} \tag{8.20}$$

From the Tables:

$\Sigma\dot{\epsilon}^{pl}$ is the total accumulated plastic strain at the time of interest

t_p is the plate thickness

h is the panel height

E is the plate elastic modulus

σ_{y0} is the web plate yield stress

$\bar{F}_{ST}$ is the normalized snap-through stress at unloading, $\bar{F}_{RES}$ is the normalized compressive stress at peak drift, and $\bar{F}_{TR}$ is the maximum normalized tensile stress, immediately upon tension reloading but before the primary loading phase. These quantities are represented graphically in Figs. 8.11 through 8.13.

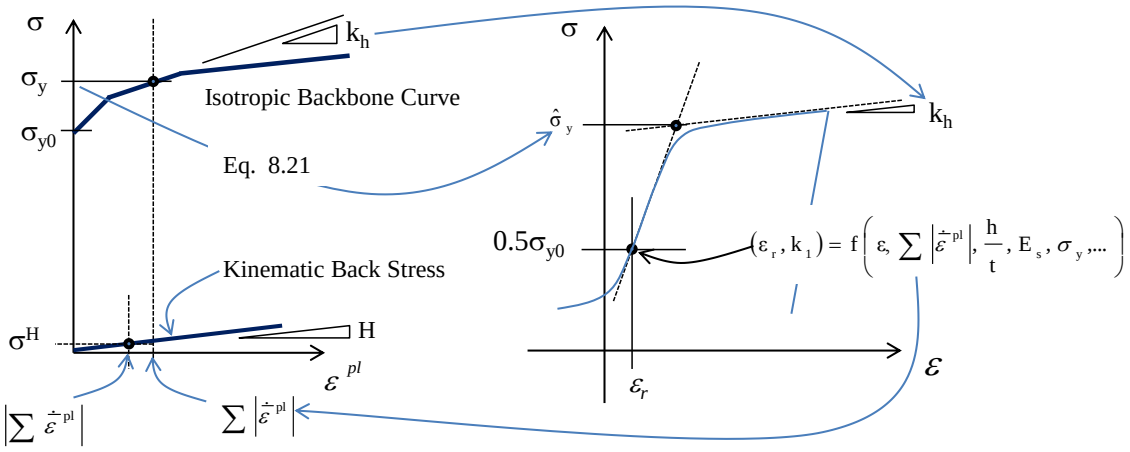

Figure 8.17: Determination of σ_y and k_h

8.5.3 Yield Strength with Hardening

The instantaneous web plate yield stress, σ_y, is governed by the development of material hardening. The yield stress is computed at the end of the reloading state (State 6 or 9) when the transition form State 6 (or 9) to State 1 occurs. σ_y is shown graphically in Fig. 8.17 and is the intercept of the asymptotes of the Magnegotto-Pinto hyperbola. The strain hardening slope, k_h is defined by the slope of the isotropic backbone curve at the accumulated plastic strain at reloading, ϵ_r. If while on the yield plateau of State 1, the accumulated plastic strain transitions from one hardening modulus to a lower modulus, the intercept (ϵ_c, σ_c) is recomputed so that the transition remains smooth in the hysteresis. This is illustrated in Fig. 8.18.

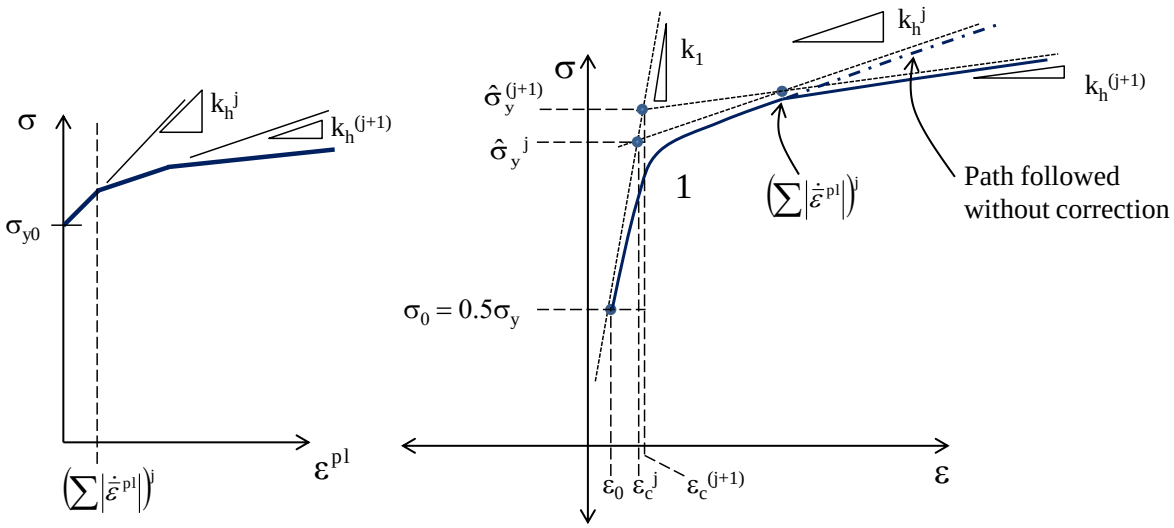

(a) Isotropic Backbone (b) Material Directional Hysteresis

Figure 8.18: Adjustment of k_h during yield plateau

The hardening is handled in the material model by tracking the total accumulated plastic strain ($\Sigma\dot{\epsilon}^p$) in the strip and the location of the tension reloading strain, ϵ_r. The reloading strains (discussed in the next section) represent the points where the web plate tension field is reactivated. This is assumed to be the inflection point on the reloading branch. In the *OpenSees* model, this inflection is assumed to occur at a stress level of $0.5\sigma_{y0}$, to provide a reasonable match to the observed *ABAQUS* behavior reasonably well. The points A, B', C and D' in Fig. 8.19 graphically represent the location of reloading strains for the first two cycles of web plate loading. For purely isotropic hardening, σ_y is determined using the isotropic backbone curve (defined in the previous section). For kinematic hardening the kinematic translation is assumed to occur in the direction of the strain increment $\dot{\epsilon}$ and at a rate proportional to the accumulation of plastic strain. During primary tensile loading (from points A to a or C to c in Fig. 8.19) the kinematic translation in stress space progresses at a rate of $H|\dot{\bar{\epsilon}}^{pl}|$ in the direction of the reduced stress vector per Ziegler's rule (see Section 3.1.5). During unloading, when the tension field is being re-established and

plastic strains are accumulating much more slowly, the translation is set to $0.08H|\dot{\bar{\epsilon}}^{pl}|$ and is also assumed to be in the direction of tensile stress. The unloading phase occurs from a' to B' and c' to D' in Fig. 8.19. The new yield stress in the directional hysteresis, $\hat{\sigma}_y$ is defined by Eq. 8.21

$$\hat{\sigma}_y = \frac{(\sigma_y - \sigma^H)}{\sqrt{1 + \bar{F}_{RES} + \bar{F}_{RES}^2}} + F_{RES} \tag{8.21}$$

where σ_y is interpolated from the isotropic backbone curve as shown in Fig. 8.17, and σ^H is the value of the kinematic back stress at the end of the last loading state (State 1). When H is set to zero, isotropic hardening results. The kinematic back stress is computed by multiplying the kinematic hardening modulus, H, by the sum of the incremental plastic strains for State 1 and the sum of the estimated incremental plastic strains for the orthogonal strips in their State 1. The sign of the strain is retained. Hence, the estimated orthogonal State 1 plastic strain increment will be negative. The regions outside of State 1 accumulate strain at approximately 8% the rate during State 1, but once again, the sign of the strain increment is retained. To illustrate this using Fig. 8.19, the value of σ^H at point D' in the strain history would be computed as:

$$\sigma^H = H(\epsilon_{\bar{AB}} - \epsilon_{\bar{B'C'}} + \epsilon_{\bar{CD}}) + 0.08H(\epsilon_{\bar{BB'}} - \epsilon_{\bar{C'C}} + \epsilon_{\bar{DD'}}) \tag{8.22}$$

here the bar symbol represents the strain from one point to the next, e.g., $\epsilon_{\bar{B'C'}}$ is the plastic strain from point B' to C'. The stress term (σ_y - σ^H)in Eq. 8.21 is divided by the radical term to account for the presence of contemporary compressive stresses (in this case assumed to be F_{RES}). This assumes a von Mises yield criterion. The last F_{RES} term in Eq. 8.21 is added in Eq. 8.21 because the total web plate lateral strength is the sum of the horizontal stress components integrated along the length of the web plate. Thus, $\hat{\sigma}_y$ is always less than σ_y. Note that the total web plate strength includes the strength of the strips in the orthogonal direction. This can be illustrated once again by summing the directional hysteresis curves of Fig. 8.19. Note that the total strength of the web plate at the drift associated with point c on the 45 degree curve is the sum of the stresses at c and at point c' in the 135 degree direction.

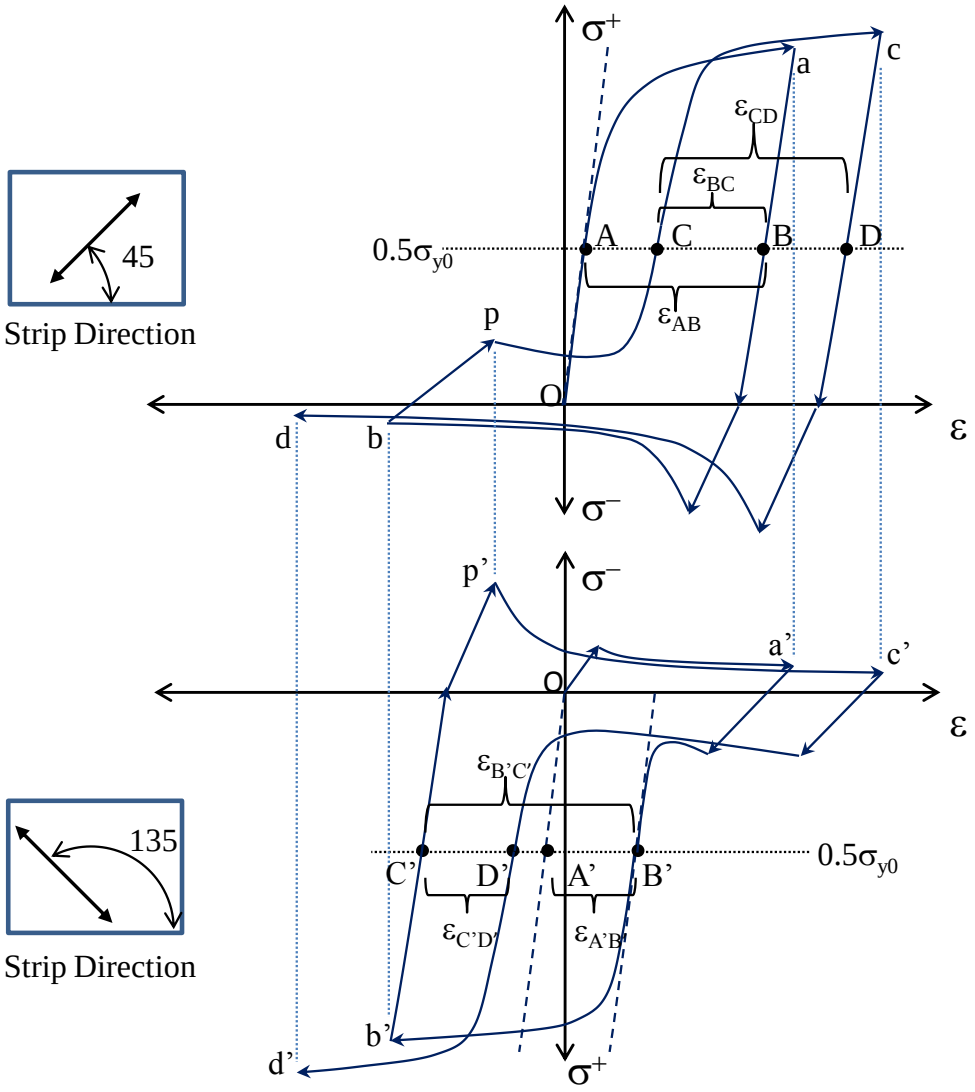

Figure 8.19: Hysteretic response showing progression of tension reloading strains

8.5.4 Summary

Clearly, all of the states used to model the directional hysteresis observed in the *ABAQUS* analyses represent an idealization of the response. A series of smooth curves (rather than an alternative piecewise linear approach) was chosen because (a) it is easier to program, as there are fewer states to consider, (b) it results in a more realistic response, particularly in the reloading phase, and (c) the smooth transitions aid the convergence of the OpenSees solution.

8.6 Material Description in OpenSees

The SPSW web plate material is declared in *OpenSees* with the following tcl statement.

```
uniaxialMaterial SPSW_Web_Plate tag fy Es m1 m2 m3 e1 e2 e3 H L h tp
```

Where `tag` is the material identifier, `fy` is the yield stress, `Es` is the elastic modulus, `m1`, `m2` and `m3` are fractional increases above f_y defining the material isotropic hardening envelope, e.g., $1.2f_y$ would be represented by the fraction 0.2. The strains `e1`, `e2` and `e3` are plastic strains associated with `m1`, `m2` and `m3`. `H` is the kinematic hardening modulus, `L` and `h` are the length and height of the web plate as measured between the insides of the VBE flanges and HBE flanges respectively, and `tp` is the thickness of the web plate.

Web plate hardening is accounted for using the previously mentioned tri-linear backbone, which defines the isotropic yield surface, and a linear kinematic modulus (which may be set to zero) for the kinematic component. The kinematic hardening modulus should be limited per Eq. 8.23 so that the hardening slope remains positive

$$H \leq \frac{f_y(m3 - m2)}{(e3 - e2)} \tag{8.23}$$

8.6.1 Calibrated Directional Hysteresis

Figs. 8.20 and 8.21 show samples of the *OpenSees* normalized hystereses for a single uniaxial element overlaying the hystereses derived from *ABAQUS*. This is for both strip inclinations

(45 deg and 135 deg) but only for $h/t = 500$, $L/h = 1.2$ and $f_y = 250$ MPa. The average solution time for an SPSW panel, shown in Fig. 8.22, subjected to one of the six amplitude histories presented in Fig. 8.6 was only 15 to 20 seconds. The equivalent $ABAQUS$ analyses take approximately 1.5 hours (on the same desktop computer) using the explicit dynamic solver with the aid of mass scaling.

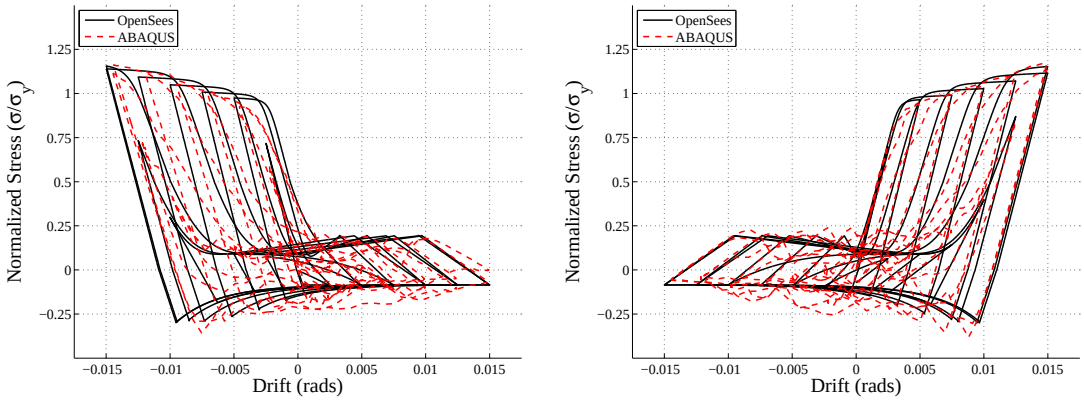

(a) $Amp1 - 45deg$ (b) $Amp1 - 135deg$

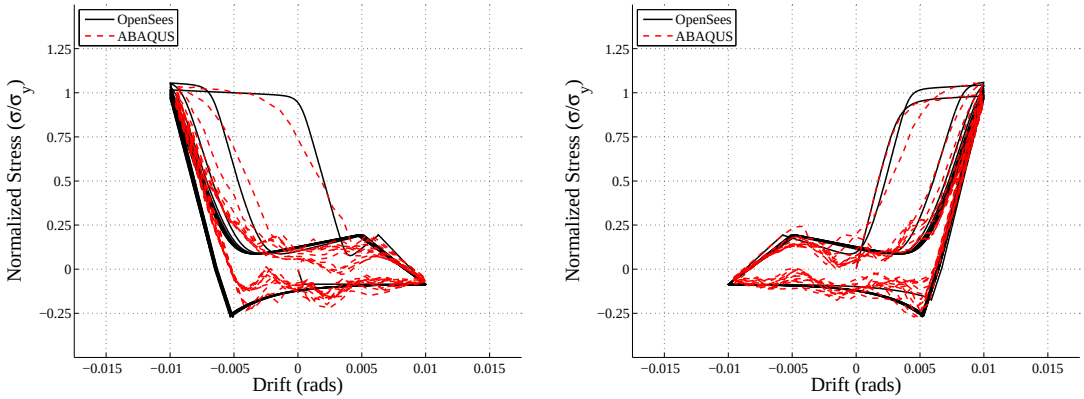

(c) $Amp2 - 45deg$ (d) $Amp2 - 135deg$

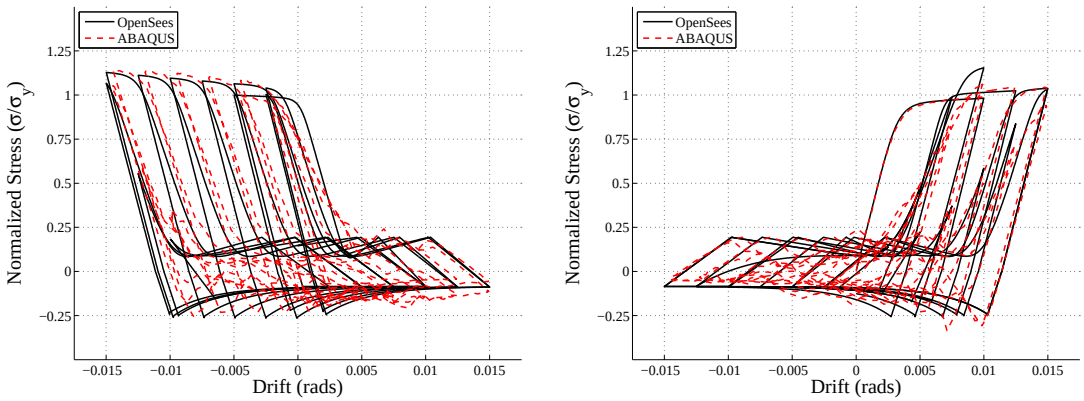

(e) $Amp3 - 45deg$ (f) $Amp3 - 135deg$

Figure 8.20: Directional Hysteresis for $h/t = 500$ and $L/h = 1.2$; $f_y = 250$ MPa.

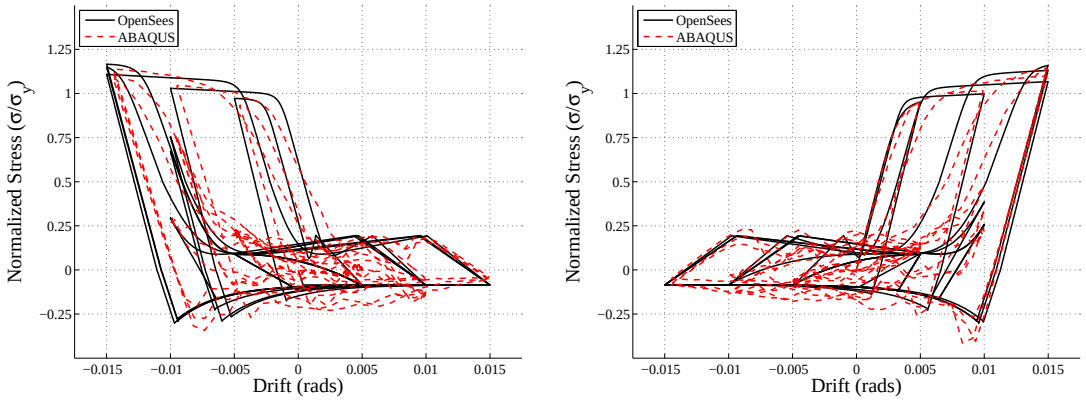

(a) $Amp4 - 45deg$ (b) $Amp4 - 135deg$

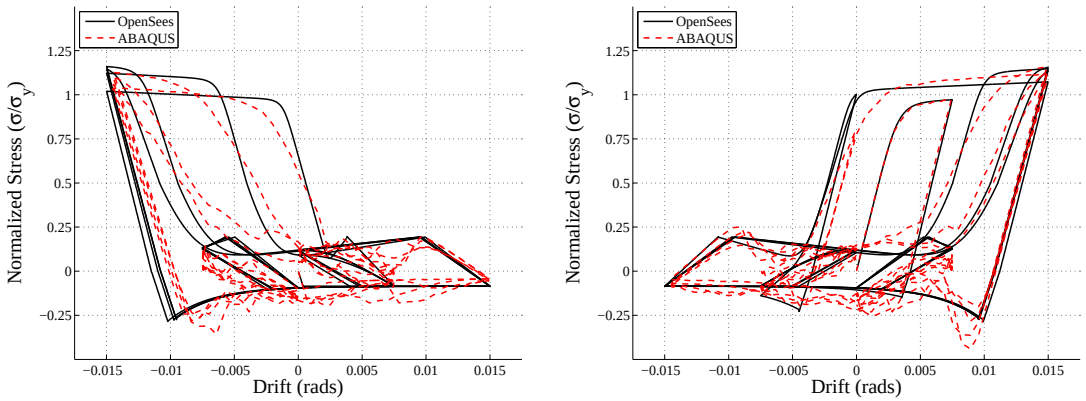

(c) $Amp5 - 45deg$ (d) $Amp5 - 135deg$

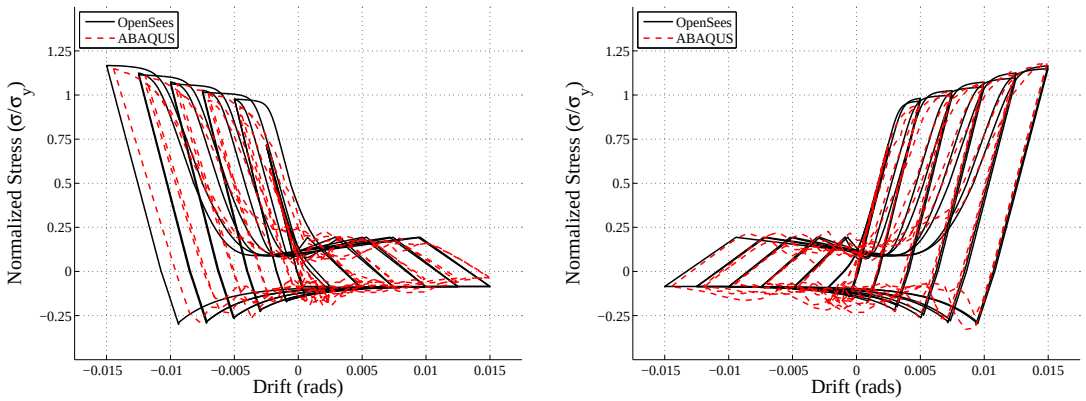

(e) $Amp6 - 45deg$ (f) $Amp6 - 135deg$

Figure 8.21: Directional Hysteresis for $h/t = 500$ and $L/h = 1.2$; $f_y = 250$ MPa.

8.6.2 Model Constraints and Boundary Conditions

Identical member sizes and boundary conditions were applied to the *ABAQUS* and *OpenSees* models. The VBEs were modeled as AISC W24x146 beams using Timoshenko beam elements with elastic material properties. The web plates were modeled as extending to the centroid of each boundary member. The rotations at the top and bottom of each VBE were constrained to mimic flexural continuity at each floor level. The HBEs were pin connected to the VBEs using a system of constraints that forced the adjacent HBE and VBE ends to displace equally in the plane of the wall. The HBEs were also constrained so that midspan vertical deflections were eliminated. A diaphragm constraint was used on the top HBE to prevent differential displacement of the end nodes, thereby approximating a rigid diaphragm. This constraint allowed for some axial extension and contraction between the end nodes, but the net axial extension of the HBE was zero. The bottom of each VBE was pinned to the base support, thereby preventing any net axial extension or contraction of the bottom HBE. In the *ABAQUS* model, corner cut-outs were not included. In the *OpenSees* models, the strips were spaced on the assumption that cut-outs were not included, although the net effect on the *OpenSees* model is clearly more ambiguous and difficult to model accurately.

The *OpenSees* models are represented in Fig. 8.22. For both values of L/h, the height of the panel was set to 3 m and the length L and slenderness h/t_p were varied accordingly. Nine evenly spaced strips were used in each direction to model the web plates. All strips were inclined at 45 degrees to the horizontal.

8.7 Validation of the New Material Model

For validation of the new material model, two randomly generated drift histories were applied to the *ABAQUS* and *OpenSees* models used for calibration, using different panel slenderness ratios, steel yield strengths and hardening properties. The normalized hysteretic response (lateral load vs drift), VBE bending demand and the total dissipated energy were compared for each history. These drifts, *AmpA* and *AmpB* are shown graphically in Fig.

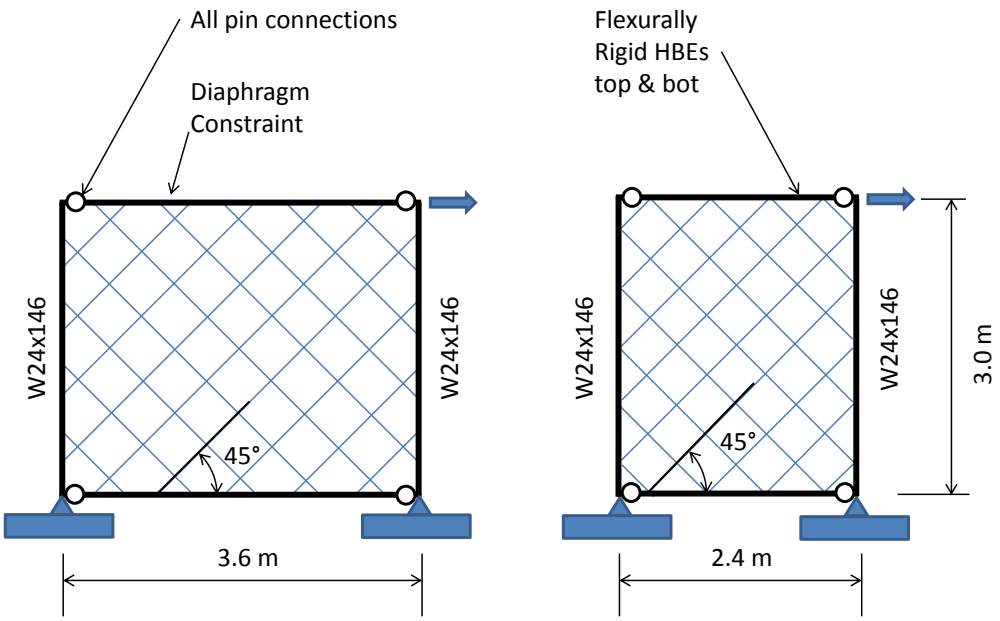

Figure 8.22: *OpenSees* models used for calibration

8.23.

The drift demands were carefully selected and are believed to be a coarse representation of what might result from a response history analysis of a multi-story SPSW. Of the materials selected were: (a) a low yield point (LYP) steel with pronounced strain hardening (high R_{sh}) which was applied to stocky plates, and (b) a high strength steel with limited strain hardening applied to slender plates. A combined hardening model was also analyzed in both *ABAQUS* and *OpenSees* for the LYP steel. The kinematic hardening modulus, H, for these models was set to 800 MPa, or about 0.4% of E_s. This value of H will result in a moderate reduction in web plate shear strength and VBE demand from the purely isotropic case. The material properties are shown in Fig. 8.24. The parameter selection was in some cases purposely outside the range of material properties and geometries against which the new model was initially calibrated.

Another series of analyses was carried out using flexible VBEs to examine the impact this has on the hysteresis. For these analyses, (W14×68) VBEs were used, with all other things remaining unchanged. The section stiffness of a W14×68 is only $1.7_{c,min}$ per the *Provisions*, whereas the default W24×146 is 11.0 $_{c,min}$. Flexible VBEs were not included in the calibration process so this was an important test. A matrix of the validation parameters

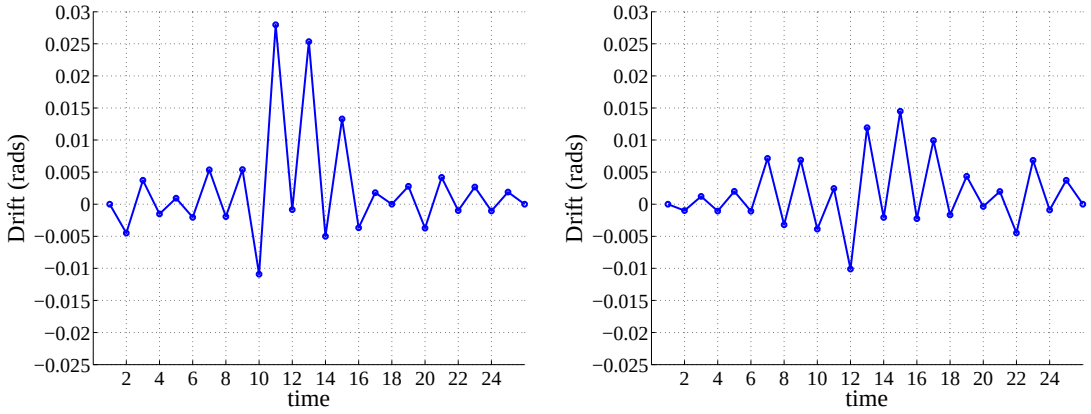

(a) *AmpA* (b) *AmpB*

Figure 8.23: Drift amplitudes used for model validation.

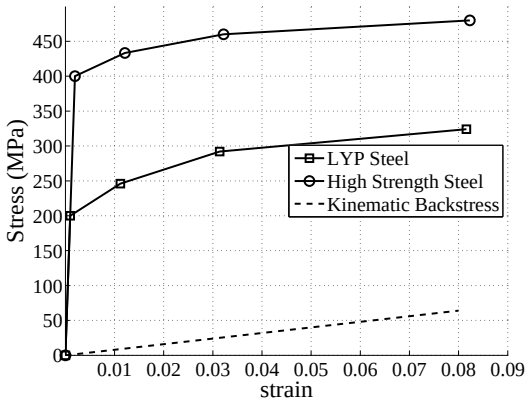

Figure 8.24: Material properties used for validation

Table 8.4: Web Plate Model Parameters for Validation

f_y	R_{sh}	$VBEsize$	$\frac{h}{t}$	Amp	$Hard$
200	0.6	W24x146	300	A	Iso
200	0.6	W24x146	600, 1200	A, B	Iso, Comb
400	0.2	W14x68, W24x146	1200, 2400	A, B	Iso

is shown in Table 8.4.

The model was checked against a selection of experimental hystereses reported in Chapter 5 to finalize the validation exercise. The isotropic material backbone curve is derived directly from the coupon tests and the hardening parameters are taken from Chapter 7. Fig. 8.34 shows the results of *OpenSees* analyses of the Phase I experiments. The new model maintains a good match with the experimental results, but it tends to over-predict the strength of some of the specimens.

8.7.1 VBE Bending Moment Demand

The normalized VBE bending demand shown in Figs. 8.25 through 8.33 match the $ABAQUS$ results very well. This was expected since the development of the directional hysteresis is derived directly from this particular demand.

8.7.2 Energy Dissipation

The energy that web a plate is capable of dissipating through cyclic inelastic loading has an obvious impact on the amount of hysteretic damping of the system. Damping has a significant influence on drift levels, story accelerations and many other related response quantities. For the validation test cases, the degree of hysteretic damping is compared over the full load history and the correlation between the $ABAQUS$ and OpenSees models is generally very good.

8.8 Conclusions

The new SPSW uniaxial material model is capable of mimicking the combined effects snap-through buckling, compressive stress development, normal plastic contraction and material hardening, and manages to track very closely the load-displacement history obtained from *ABAQUS* analyses. The model is stable and runs in a fraction of the time it takes to perform the equivalent *ABAQUS* analysis, typically less than 1 %. The VBE flexural demand matches the demands obtained from *ABAQUS* analyses for a range of plate slenderness ratios, panel aspect ratios and material strengths and generally differs by less than 3 %. The model is simple to implement and does not require the tedious calibration that many of the alternative uniaxial material models do when used for SPSW applications.

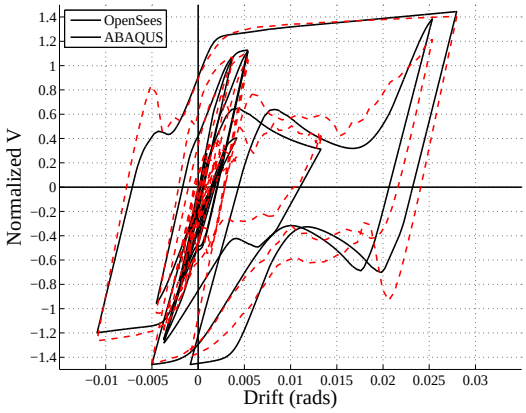

(a) Base Shear: $h/t = 300$

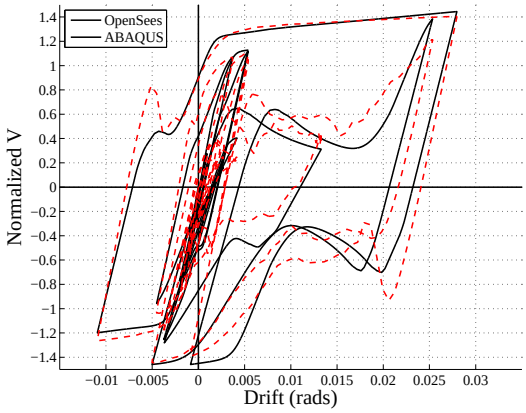

(b) Base Shear: $h/t = 300$

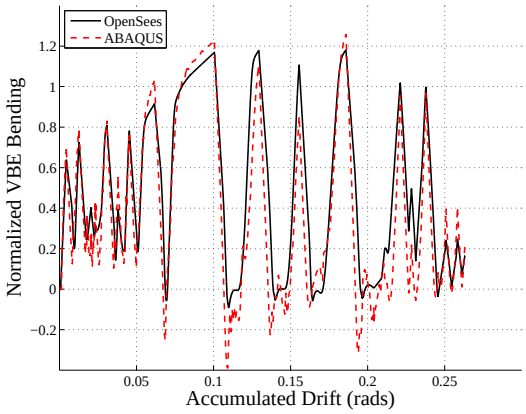

(c) VBE Bending: $h/t = 300$

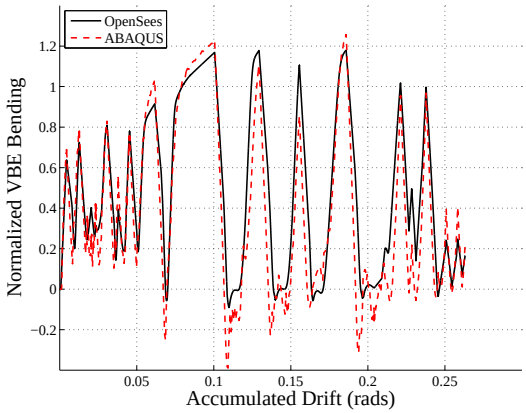

(d) VBE Bending: $h/t = 300$

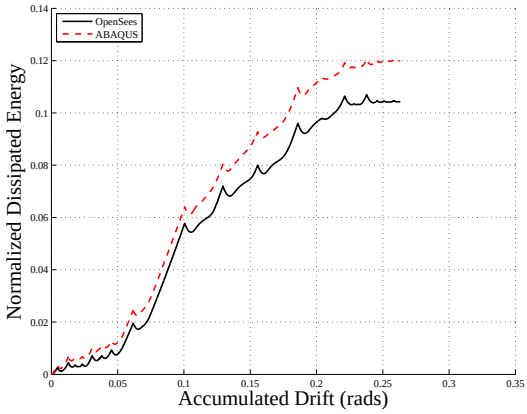

(e) Dissipated E: $h/t = 300$

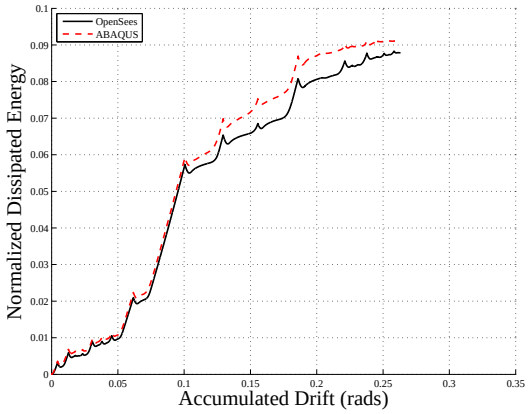

(f) Dissipated E: $h/t = 300$

Figure 8.25: Normalized Response Quantities *AmpA* with $h/t = 300$; $f_y = 400$ MPa; W24x146 VBEs.

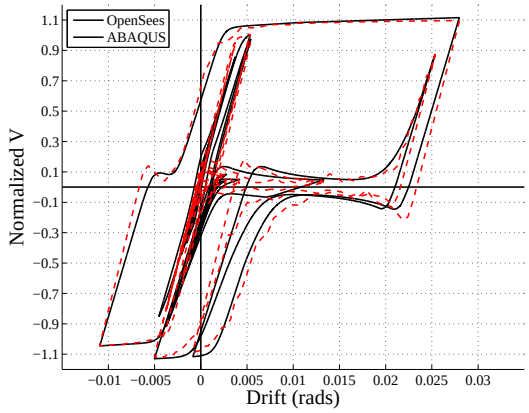

(a) Base Shear: $h/t = 2400$

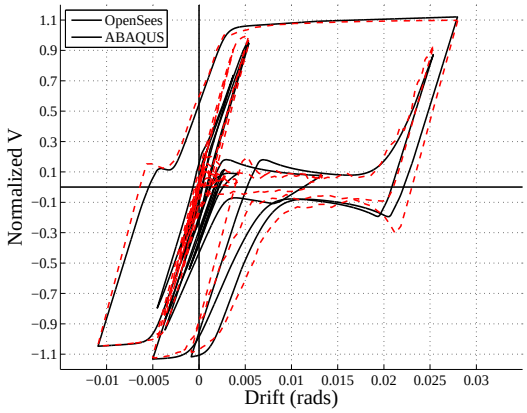

(b) Base Shear: $h/t = 1200$

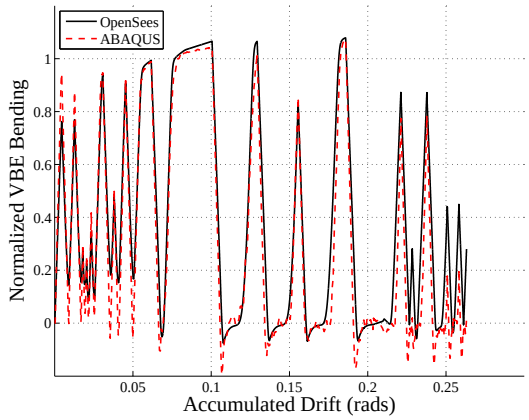

(c) VBE Bending: $h/t = 2400$

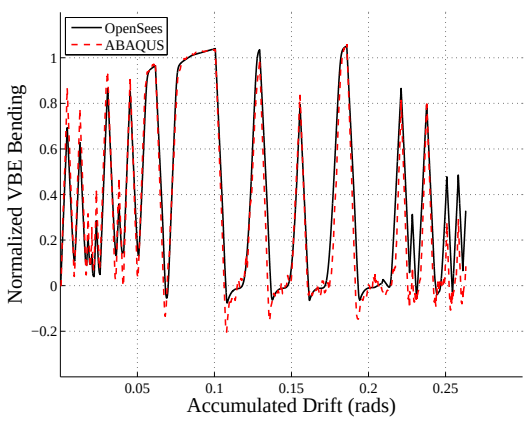

(d) VBE Bending: $h/t = 1200$

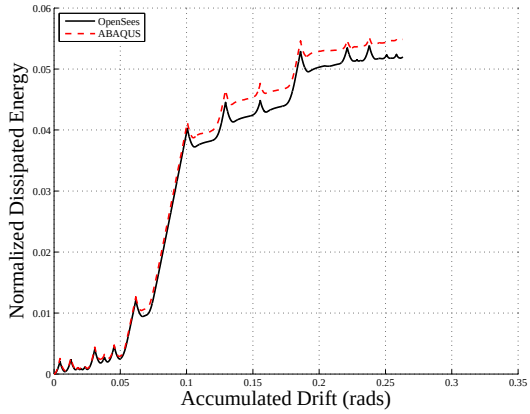

(e) Dissipated E: $h/t = 2400$

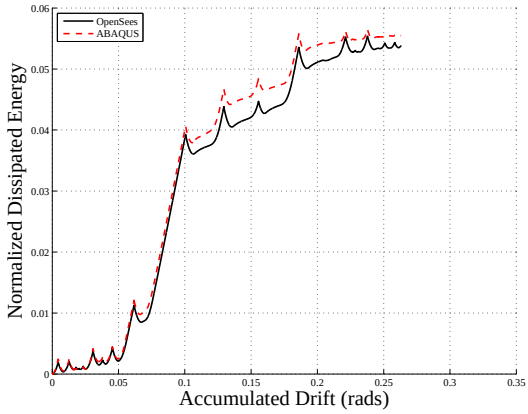

(f) Dissipated E: $h/t = 1200$

Figure 8.26: Normalized Response Quantities *AmpA* with variable h/t; Fy = 400 MPa; W24x146 VBEs.

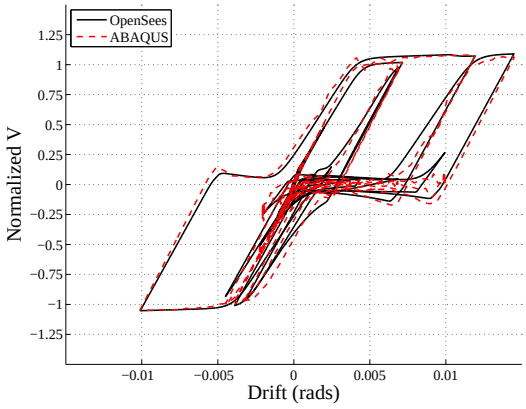

(a) Base Shear: $h/t = 2400$

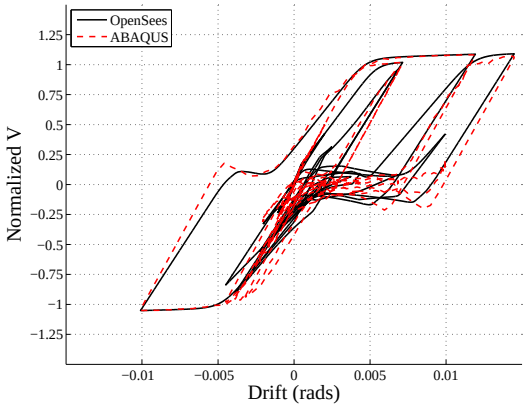

(b) Base Shear: $h/t = 1200$

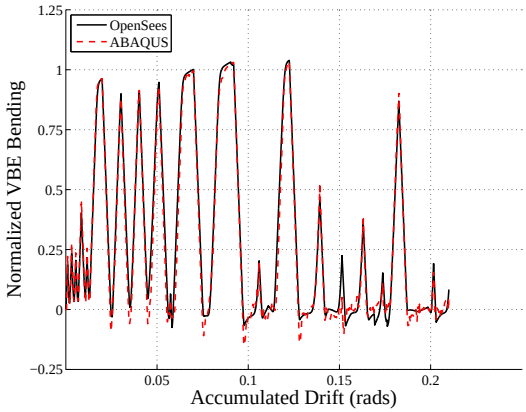

(c) VBE Bending: $h/t = 2400$

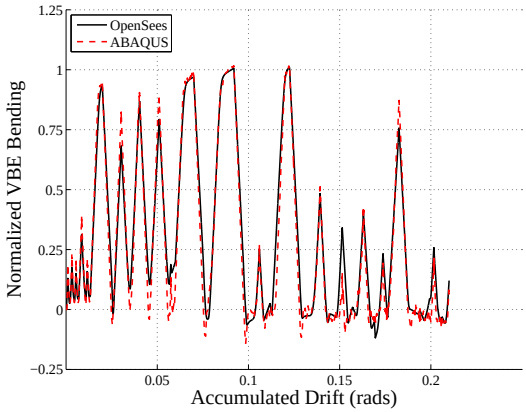

(d) VBE Bending: $h/t = 1200$

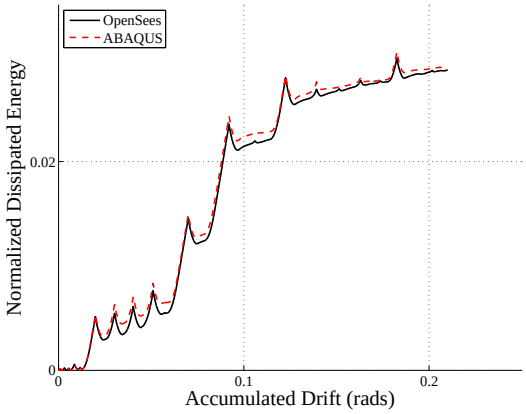

(e) Dissipated E: $h/t = 2400$

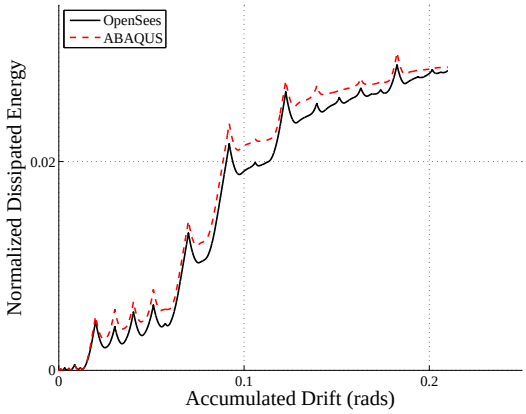

(f) Dissipated E: $h/t = 1200$

Figure 8.27: Normalized Response Quantities *AmpB* with variable h/t; Fy = 400 MPa; W24x146 VBEs.

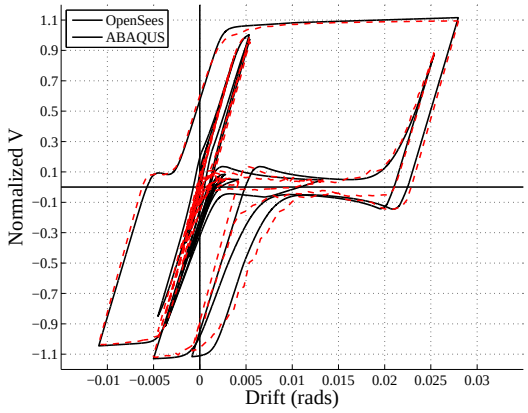

(a) Base Shear: $h/t = 2400$

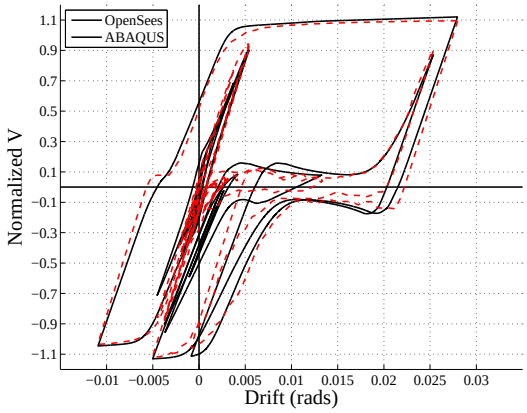

(b) Base Shear: $h/t = 1200$

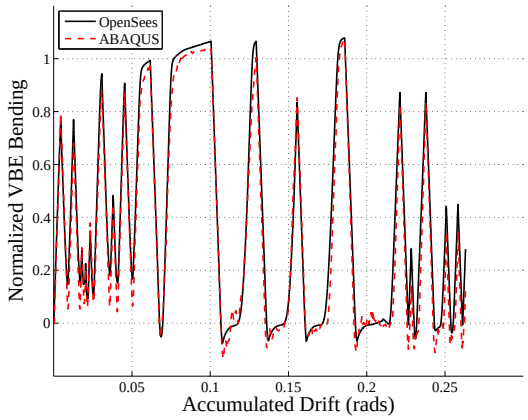

(c) VBE Bending: $h/t = 2400$

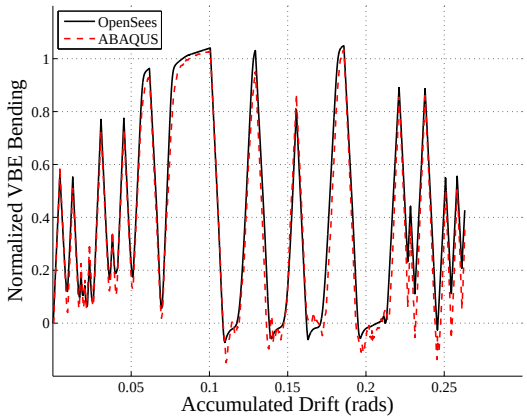

(d) VBE Bending: $h/t = 1200$

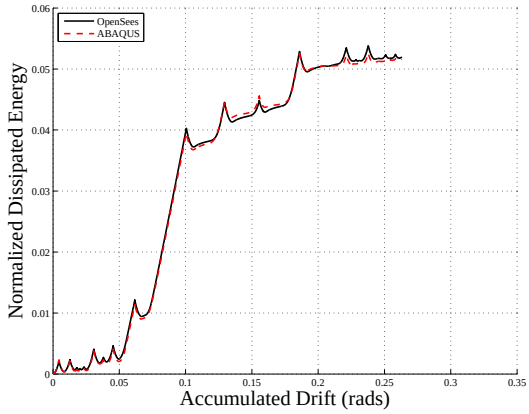

(e) Dissipated E: $h/t = 2400$

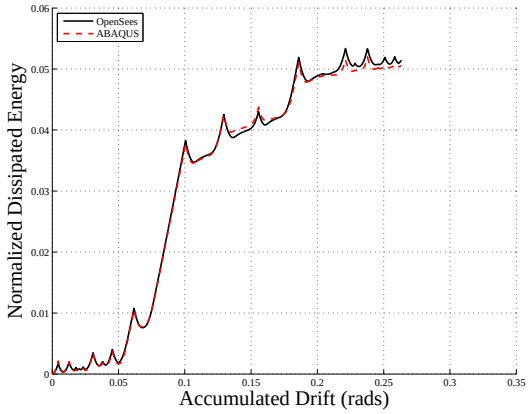

(f) Dissipated E: $h/t = 1200$

Figure 8.28: Normalized Response Quantities *AmpA* with variable h/t; Fy = 400 MPa; W14x68 VBEs.

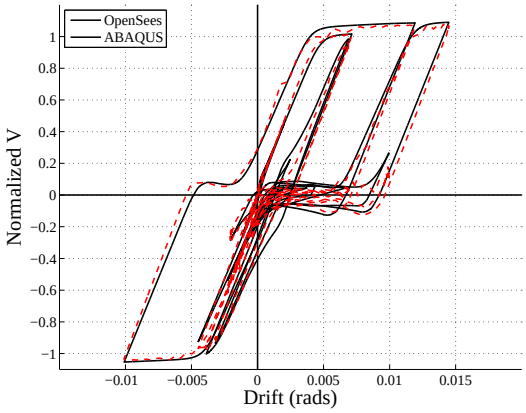

(a) Base Shear: $h/t = 2400$

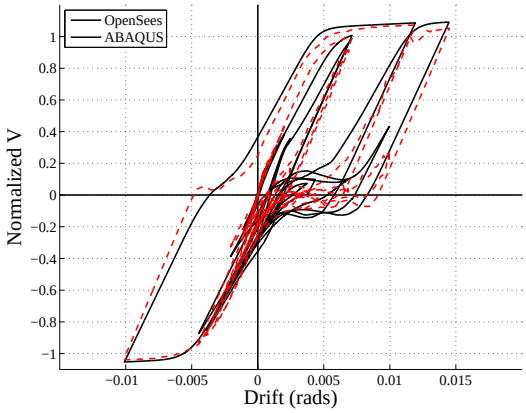

(b) Base Shear: $h/t = 1200$

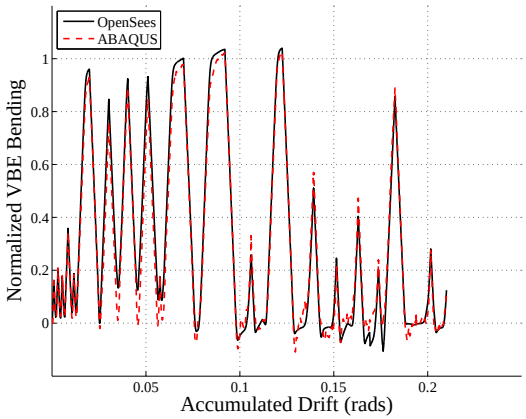

(c) VBE Bending: $h/t = 2400$

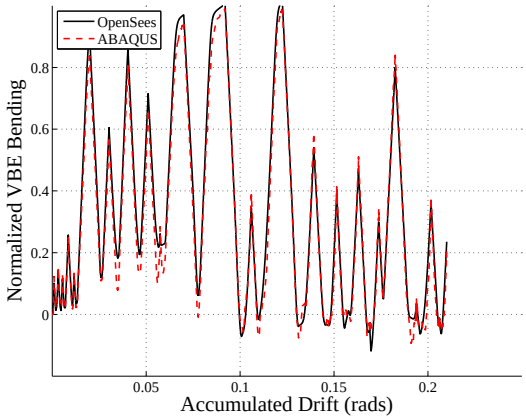

(d) VBE Bending: $h/t = 1200$

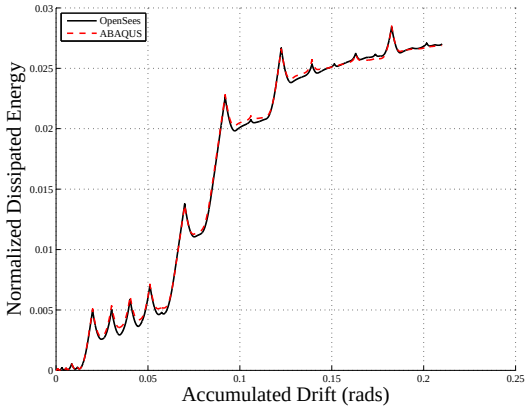

(e) Dissipated E: $h/t = 2400$

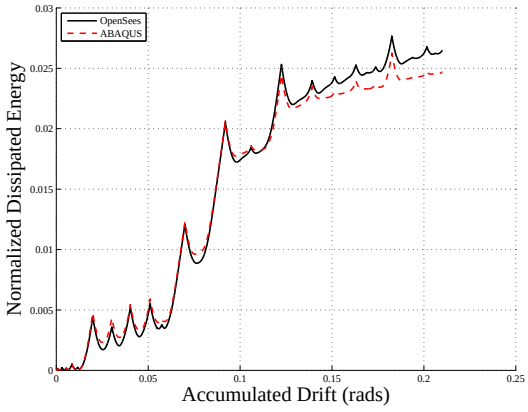

(f) Dissipated E: $h/t = 1200$

Figure 8.29: Normalized Response Quantities *AmpB* with variable h/t; Fy = 400 MPa; W14x68 VBEs.

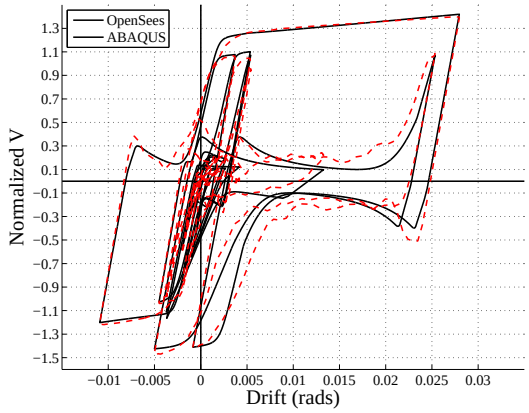

(a) Base Shear: Isotopic

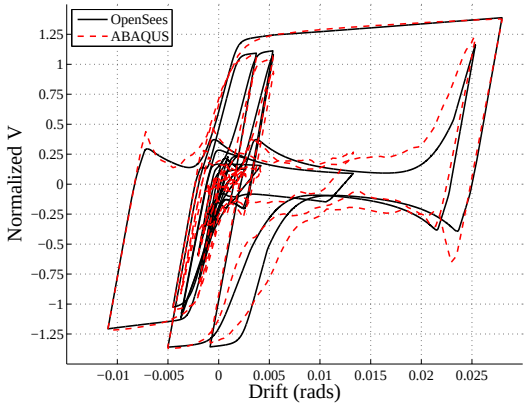

(b) Base Shear: Combined

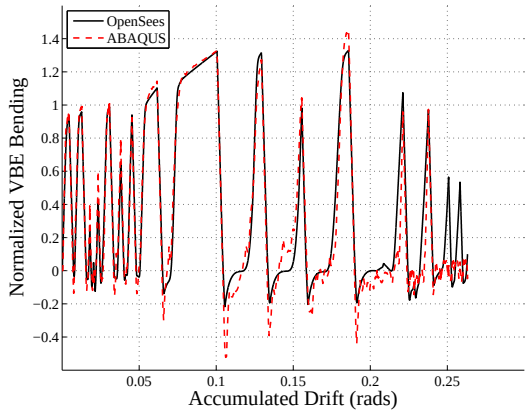

(c) VBE Bending: Isotopic

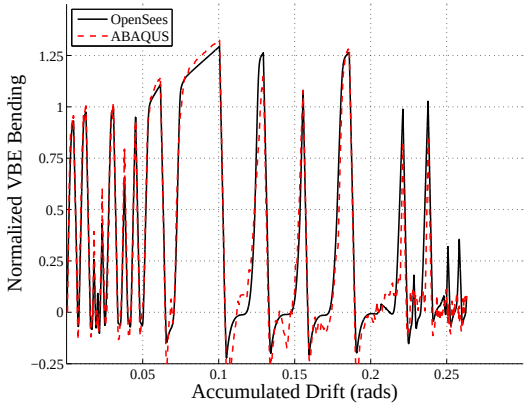

(d) VBE Bending: Combined

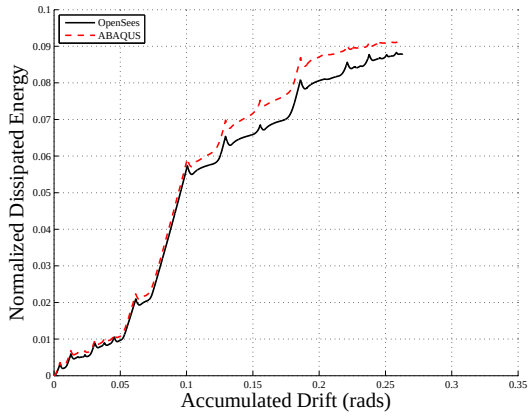

(e) Dissipated E: Isotopic

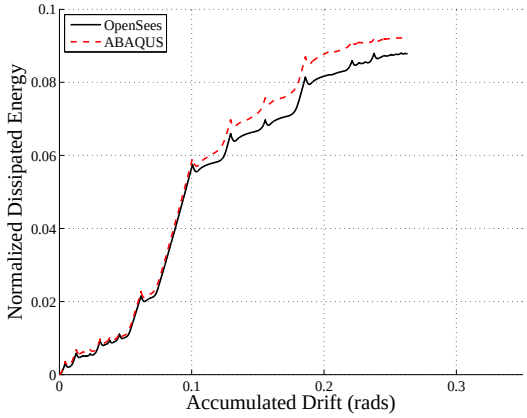

(f) Dissipated E: Combined

Figure 8.30: Normalized Response Quantities $AmpA$ with different hardening laws; $h/t = 1200$; $F_y = 200$ MPa

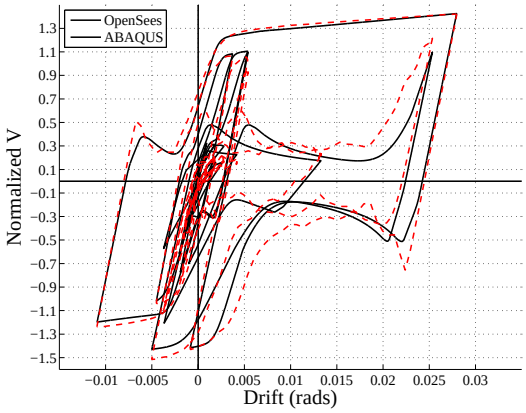

(a) Base Shear: Isotopic

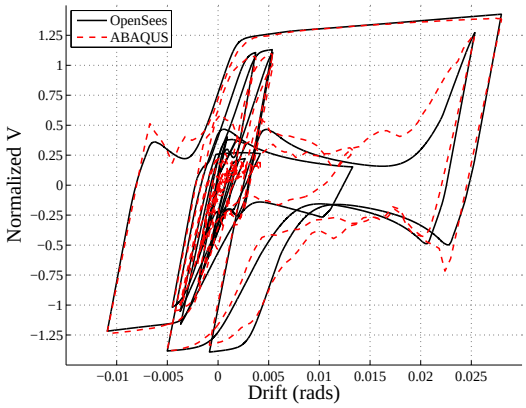

(b) Base Shear: Combined

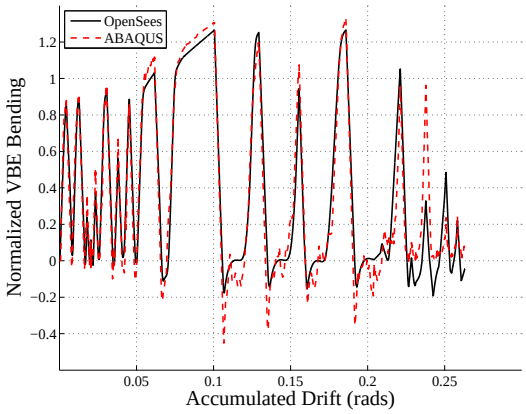

(c) VBE Bending: Isotropic

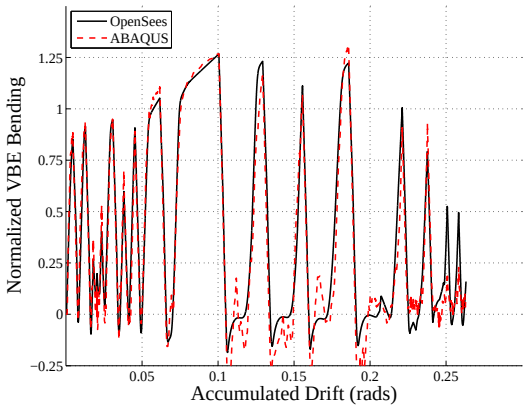

(d) VBE Bending: Combined

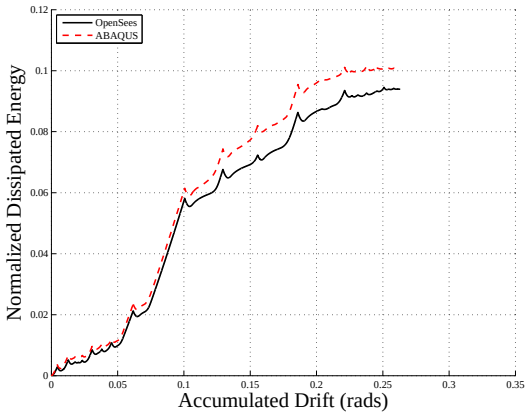

(e) Dissipated E: Isotropic

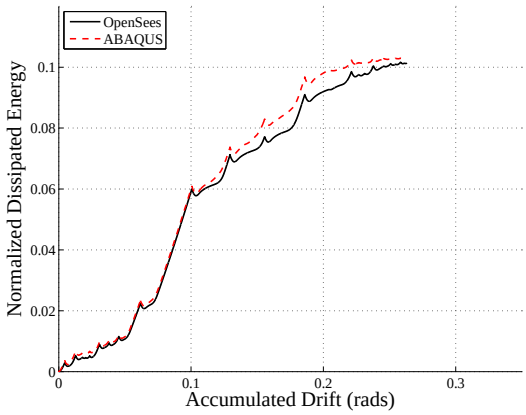

(f) Dissipated E: Combined

Figure 8.31: Normalized Response Quantities $AmpA$ with different hardening laws; $h/t = 600$; $F_y = 200$ MPa

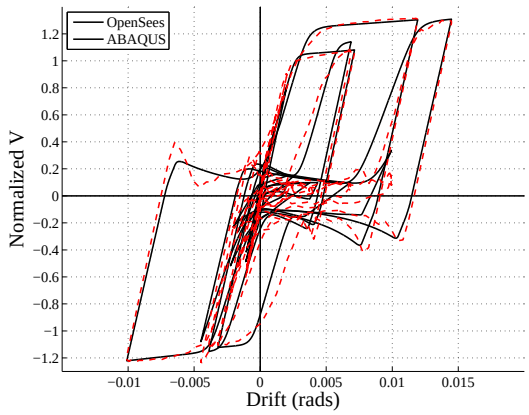

(a) Base Shear: Isotopic

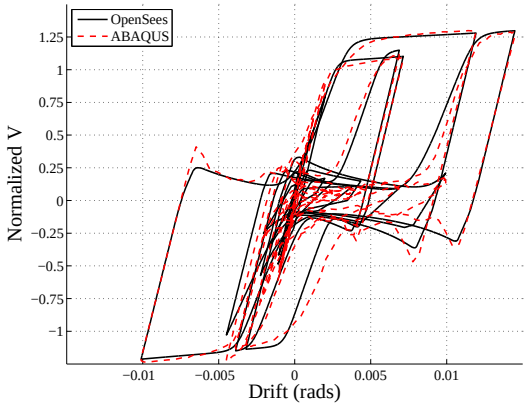

(b) Base Shear: Combined

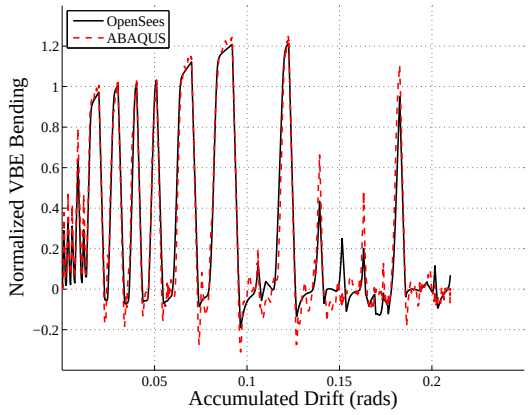

(c) VBE Bending: Isotopic

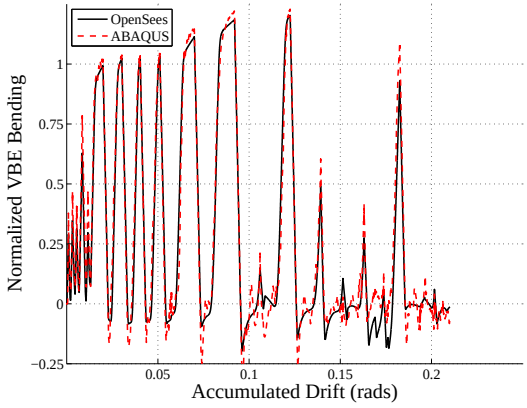

(d) VBE Bending: Combined

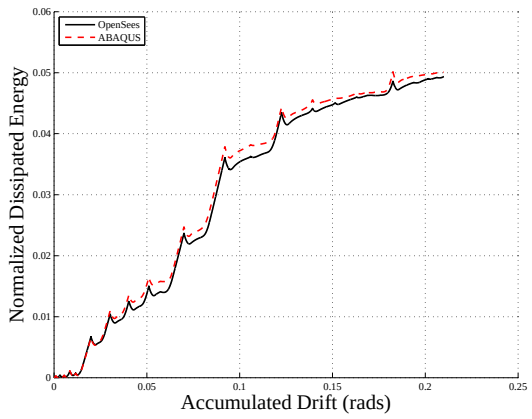

(e) Dissipated E: Isotopic

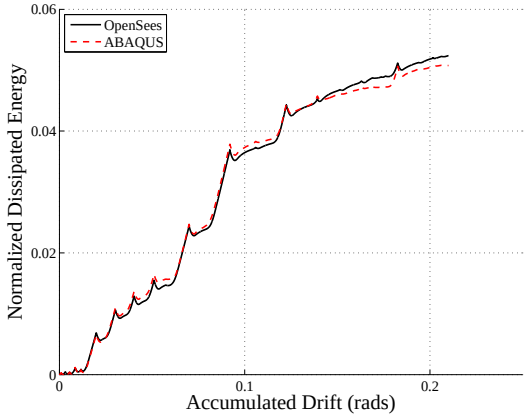

(f) Dissipated E: Combined

Figure 8.32: Normalized Response Quantities *AmpB* with different hardening laws; $h/t = 1200$; $F_y = 200$ MPa

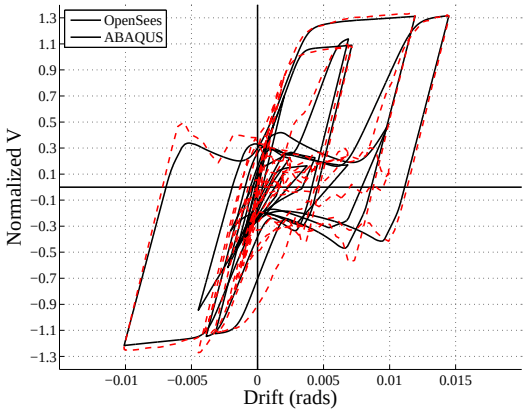

(a) Base Shear: Isotopic

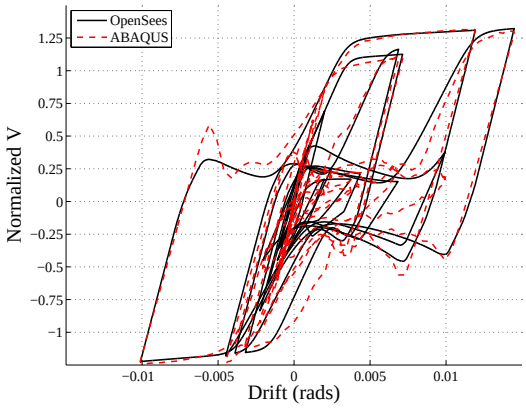

(b) Base Shear: Combined

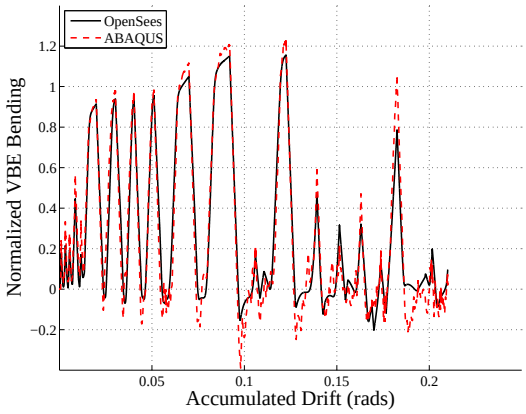

(c) VBE Bending: Isotopic

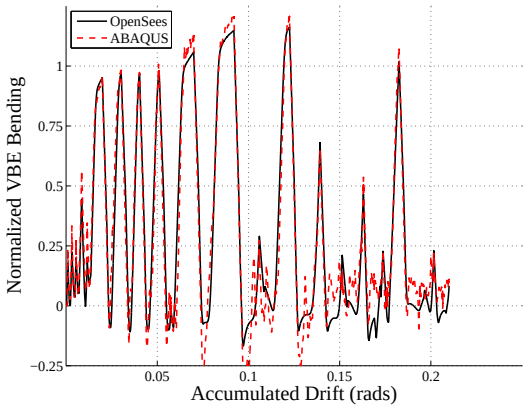

(d) VBE Bending: Combined

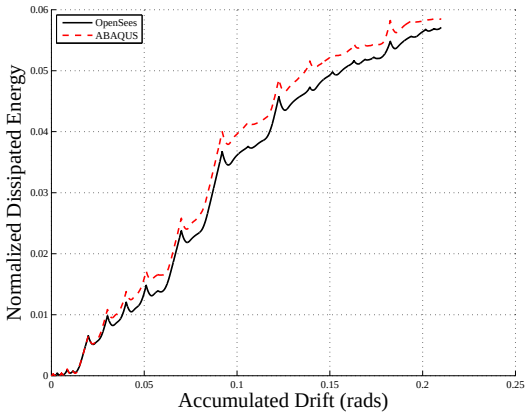

(e) Dissipated E: Isotopic

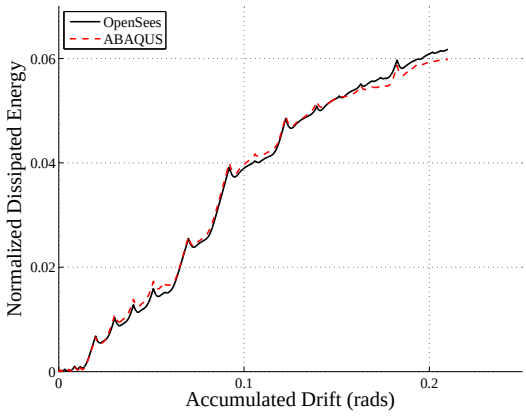

(f) Dissipated E: Combined

Figure 8.33: Normalized Response Quantities *AmpB* with different hardening laws; $h/t = 600$; $F_y = 200$ MPa

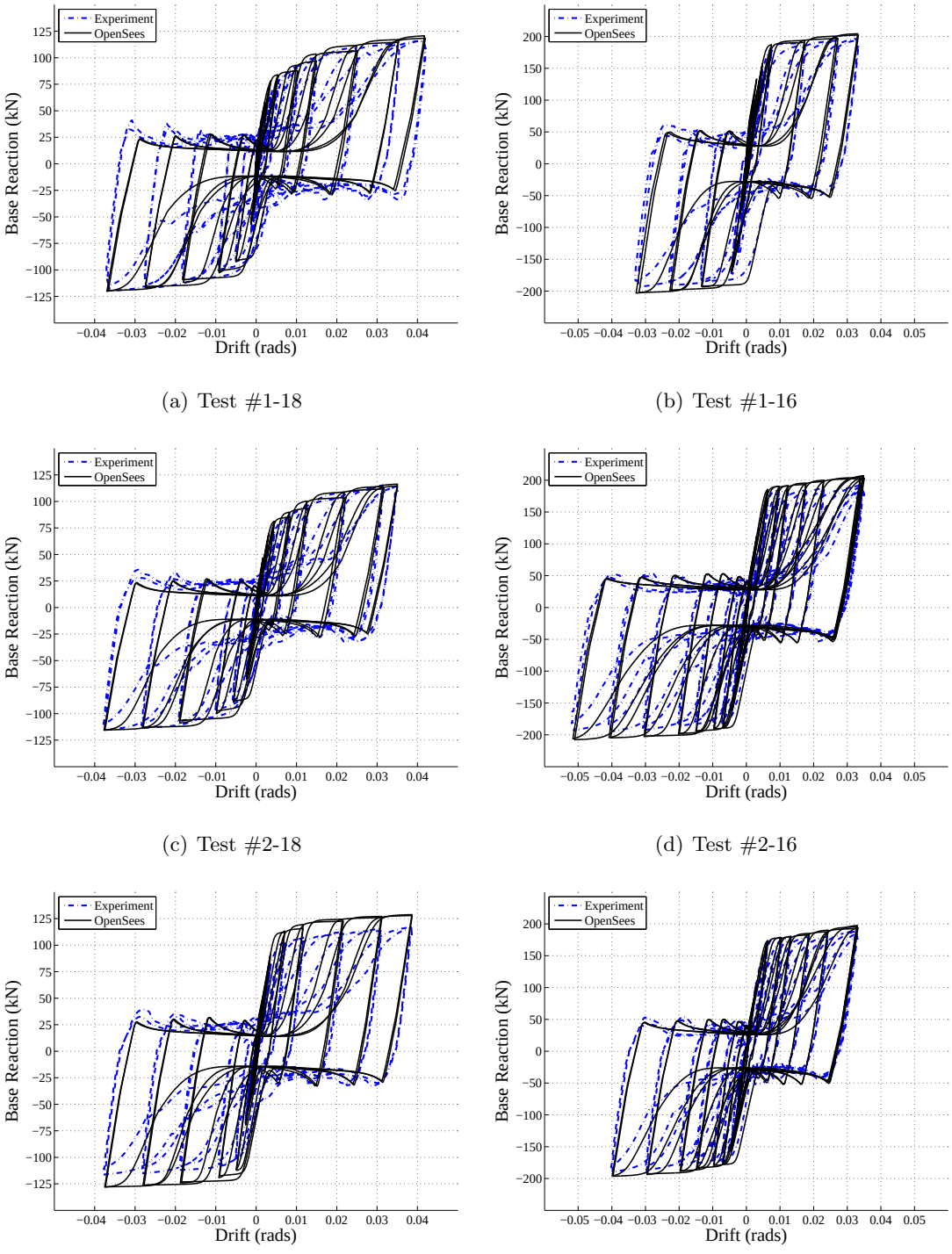

(a) Test #1-18

(b) Test #1-16

(c) Test #2-18

(d) Test #2-16

(e) Test #3-18

(f) Test #3-16

Figure 8.34: OpenSees Analysis of Phase I Experiments.

Chapter 9

HARDENING OF SPSW WEB PLATES

The results of the experimental program, carried out as part of this research, indicate considerable variability in material hardening characteristics under reversed cyclic loading. In some cases the plates were observed to harden in a purely isotropic manner, while in others they displayed a combined kinematic-isotropic behavior with a substantial kinematic component. In numerical simulations, the difference in the peak strength attained by the plate was found to be sensitive to the type of hardening assumed and used. The strength of the web plate is important to the assessment of boundary element force demands, and may be a critical determinant of SPSW performance in general. Web plate tensile stresses significantly higher than $R_y F_y$ could result in transverse force demands on the VBEs that adversely alter the progression of yielding in the structure. Excessive *pull-in* of the VBEs, resulting from web plate hardening and a migration of the tension field towards 45° (Webster, Berman and Lowes 2013), may concentrate deformation at a single story and initiate a hinge or soft story at that level. Concentrated inelastic behavior at a single story has been shown by Tsai et al. (2010) to be stable under cyclic loading. However, this response mechanism results in minimal energy dissipation. The intent of the Seismic Provisions is to distribute yielding over as many stories as possible to maximize energy dissipation. This will be examined further in Chapter 10. The main objective of this chapter is to estimate an appropriate period (T) dependent strength amplification factor for SPSW web plates to be used with capacity design and/or pushover procedures.

While the experiments were useful for calibrating material models and validating other simplified models used to predict plastic strain accumulation, they do not quantify the extent to which hardening may affect actual earthquake response or its relative importance

in predicting behavior. The drift history and the magnitude of accumulated plastic strains in experimental cyclic tests will differ substantially from those actually encountered in an earthquake. In an earthquake, building story drift histories are random, with small and large drift cycles occurring throughout the record and with asymmetric positive/negative drift magnitude distribution. Therefore to improve the understanding of the impact of plate hardening on system response and component demands, a statistical analysis was conducted to quantify, using experimentally validated material properties, the degree of material hardening expected for common steel plate materials under design level seismic demands. Using the newly developed OpenSees materiel model, the effect of hardening on VBE demand is examined for low to mid-rise SPSWs.

The consideration of strain hardening in SPSW web plates naturally raises the question of whether it should also be considered in the design of other LFRS components, such as special and intermediate moment resisting frames (IMF and SMRF respectively) and special concentrically braced frames (SCBF). Braces in Eccentric Braced Frames (EBFs) are required to be designed for amplified link strength of between 1.25 (wide flange (WF) sections) and 1.4 (box sections) due to strain hardening, but the inelastic strain demands on EBF links is very high. The Seismic Provisions require that the shear strength of IMF and SMF beam-column connections be designed for *the effects of limited strain hardening of the beam and other sources of over-strength* by amplifying the nominal plastic flexural strength by 10% to $1.1R_yF_yZ_x$. However, for design of columns in SCBFs, beams and connections are required to be designed only for the expected yield strength of the brace, $R_yF_yA_g$, with no amplification for strain hardening.

To investigate the impact of hardening analysis of SCBF braces under the equivalent seismic drift demands the SPSWs were subjected to (presented in the sections that follow) suggest that the Seismic Provisions are only slightly unconservative as the maximum tensile force developed in a SCBF brace generally does not exceed the expected yield strength of

the brace by more than 2-5%, even if conservative assumptions are made regarding hardening law (isotropic) and strength degradation (none), and in contrast to the SPSW web plate, hardening of a SCBF brace need not be considered in design. In terms of accumulated plastic strain and strain hardening, the SPSW web plate sits somewhere between the SCBF and EBF.

9.1 General Outline of this Chapter

This focus of this chapter is on the estimation of the maximum expected (equivalent uniform) web plate stress under actual earthquake excitation. As just mentioned, this is an important aspect of SPSW strength, boundary element force demands, etc. To achieve this, a description (or model) of the drift demands imposed on a SPSW web plate is required. The model comprises two basic components: 1) a probability density function Q_{Δ}, which characterizes the drift as a random variable, and 2) the number of cycles or inelastic excursions, N_{Δ}.

The analysis begins with an assessment of drift demands for low to mid-rise SPSWs. First, nine low rise SPSWs are designed for the LA region and built in *OpenSees*. These buildings include 3 variations of 3, 6 and 9 story SPSWs. Each SPSW is subjected to a selection of ten ground motions from the SAC-97 suite of MCE level events. From these response history analyses, the probability density function that describes story drift is determined. The number of inelastic excursions is also determined and expressed as a function of building period, T.

A simple *Matlab* script, named *PeakStress*, that describes the hardening evolution of a single story web plate is then developed and is validated against *ABAQUS* models of continuum FE models. In simple terms, the *PeakStress* model is used to predict the maximum equivalent uniform web plate stress resulting from an arbitrary drift history for a particular hardening model i.e., isotropic, kinematic or combined. *PeakStress* is then used

to estimate the maximum web plate stress (or strength) in Monte-Carlo simulations of thousands of random drift sequences generated from the probability density function, Q_Δ and number of cycles N_Δ. The resulting maximum stress is then expressed as a function of T and the probability of exceedance, P.

9.2 Introduction

In conventional static analysis procedures, such as those presented in the Commentary of the Seismic Provisions and adopted by the Canadian Standards Association Limit States Design of Steel Structures (CSA 2001), VBEs are capacity designed assuming a web plate material with strength $R_y F_y$ (the expected yield strength of the web plate), but with no explicit consideration for hardening. A commonly adopted approach in pushover analyses is to use the coupon stress-strain properties of the material or set a bilinear stress-strain curve with the hardening modulus, E_{sh}, to some fraction of the elastic modulus, usually 1 or 2%. Although the later approach may acknowledge strain hardening, it can be inadequate for representing the inelastic cyclic hardening behavior of the web plate. Table 9.1 shows some typical steel hardening properties of commonly used SPSW web plate materials. In table 9.1, the quantity R_{sh} is given by Eq. 9.1.

$$R_{sh} = \frac{R_t F_u}{R_y F_y} - 1 \tag{9.1}$$

where R_y and R_t are factors that convert nominal yield stress and tensile stresses to expected yield stress and tensile stress respectively. F_y and F_u are the nominal yield strength and tensile strength of the material.

9.3 Prior Research

To date, web plate hardening has not been considered of primary importance in research addressing SPSW analysis or in experimental studies of SPSW behavior. Neither the AISC Provisions nor CAN/CSA S16-09 require consideration of cyclic material hardening when designing the boundary elements for web plate strength. Several investigators have developed hysteretic models for SPSW web plates (Roberts and Sabouri-Ghomi 1991; Elgaaly,

Table 9.1: Typical Material Strengths and Over-Strength Factors for SPSW Web Plates

Material ASTM	(MPa) F_y	R_y	(MPa) F_u	R_t	R_{sh}
A36	248	1.3	400	1.2	0.49
A1011	207	ND	338	ND	0.63
A572-Gr 42	290	1.3	414	1.0	0.10
A572-Gr 50	345	1.1	448	1.2	0.42

Caccese and Du 1993; Xue 1995; Driver et al. 1997; Rezai 1999; Shishkin, Driver and Grondin 2005; Choi and Park 2010). Most did not address hardening in their models.

A review of this and other research shows that kinematic hardening is typically assumed (Driver et al 1997; Behbahanifard 2003; Kharrazi 2005; Choi and Park 2010). Two of those surveyed used an isotropic hardening model for the web plate (Qu et al 2008; Berman 2010).

As with the present experimental study, Roberts (1991) and Jalali (2006) both tested web plates bolted within pin connected boundary frames, isolating the web plate behavior. Neither reported on or investigated the hardening evolution of the panel and only reported yield strength of the material. Notably, hardening is given consideration in the seismic design of other systems, e.g., Eccentric Braced Frames (EBF) and Special Concentric Braced Frames (SMRF).

9.3.1 Other Strain Hardening Phenomena

Multi-directional non-proportional loading of isotropic and orthotropic crystalline materials, including steel, has been extensively studied for applications in sheet metal forming processes, where precise modeling of material under arbitrary loading is required to predict behavior. For bi-directional orthogonal cyclic loading, a phenomenon known as cross-hardening can increase the yield stress above that predicted by von Mises criterion upon

reloading in the orthogonal direction (Wang et al. 2006). This may be followed by hardening stagnation, which is the subsequent reduction in the hardening modulus immediately after cross-hardening. Both of these phenomena likely affected the response of cyclically loaded web plates studied here. However, they are not modeled explicitly in the present study.

Material hardening may also result from strain aging and strain rate effects. Neither of these is addressed here, but are worthy of consideration. High strain rates increase the yield strength of steels. According to Bruneau et al (2011), at typical earthquake induced strain rates this amounts to an increase in F_y of between 5% and 10%. Although one could argue that this also may be applied to the resisting elements (VBEs and HBEs) and has limited overall impact. Strain aging is another strain hardening phenomenon that can substantially increase the yield strength of A572, A992 and A36 steels. Kaufmann (2001) found that under monotonic loading, with 10 hours of strain aging and 2% plastic pre-strain, the yield strength of A36 steel increased by 25%. Ultimate strengths may also increase by more than 25%, with a concomitant decrease in ductility. This has consequences for the aftershock performance of not only SPSWs, but all steel and reinforced concrete lateral systems.

9.3.2 Response of Inelastic Systems

As an inelastic system is cycled, only the inelastic component of deformation is of interest with regard to material hardening of a particular component. For SPSWs, the inelastic component of story drift is of interest because this can be used to provide an accurate estimate of web plate inelastic demand.

In general, the story drift demand for a generic lateral system is related to the ductility demand and the period of the building, T. The Applied Technology Council ATC-24 (1992) presents data showing how the number of inelastic excursions, N, is related to the

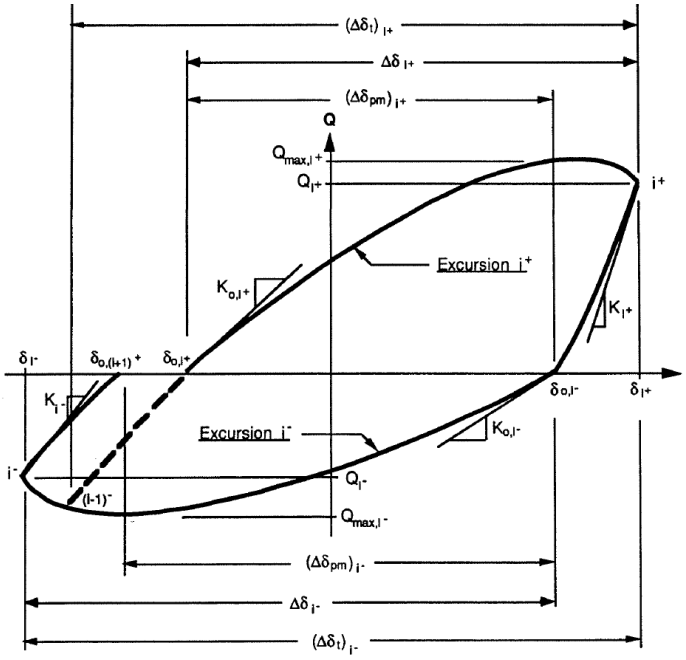

Figure 9.1: Generic deformation history for inelastic structure (from ATC-24).

displacement ductility demand, μ_d, and T. An excursion is defined as *a load or deformation history unit that starts and finishes at zero load, and contains a loading and unloading branch.* Depending on the building period, and assuming a ductility ratio equal to the R-factor used for design, N may vary from as little as 5 for a tall building to more than 30 for a low-rise structure. ATC-24 cites research by Hadidi-Tamjed [35] who analyzed simple inelastic SDOF structures and found that the plastic deformation range (peak-to-valley plastic drift) $\Delta\delta_i$ is both log-normally distributed and has a median value *usually less than 15% of the maximum* plastic drift range, $\Delta\delta_{i,max}$. Basing an analysis of SPSW systems on a distribution with imprecise median and maximum quantities may not be appropriate and would require verification. The document does however provide a useful baseline for comparison.

9.3.3 Plastic Strain Accumulation

An accurate estimate of web plate stress, i.e., the extent to which hardening increases the strength of the plate beyond the expected yield strength, requires an accurate prediction of accumulated plastic strain. SPSW web plates accumulate plastic strain in both directions of loading. The majority of this strain occurs when the tension field has fully activated and is undergoing plastic stretching, denoted here as *primary loading*. It also accumulates outside the phases of primary loading but at a much lower rate; on average approximately 8% of that during the primary loading phase, as has been observed from FE analyses of web plates.

The equivalent plastic strain (also referred to as accumulated plastic strain) is the integral of the equivalent plastic strain rate over the entire history. For a uniaxial stress state this reduces to the uniaxial plastic strain. This should be distinguished from the plastic strain, $\bar{\bar{\epsilon}}^{pl}$, which is tensorial and may be negative. Note that the *ABAQUS* simulations use J_2 plasticity with associated flow.

An accurate and reliable estimate of plastic strain accumulation is required for determining the instantaneous yield stress in a web plate. As just mentioned, an algorithm was developed to estimate an equivalent uniform tensile. The equivalent uniform tensile stress is defined in Section 6.3. This stress is a function of the accumulated plastic strain $\bar{\epsilon}^{pl}$ for isotropic hardening and also of strain history when a kinematic contribution is present. The plastic strain is computed from drift by assuming the boundary frame sways as a rigid pin connected structure. This is a reasonable assumption for the purposes of estimating strain and stress quantities but clearly doesn't recognize localized effects or account for VBE flexibility. The algorithm was validated by comparing the estimate of $\bar{\epsilon}^{pl}$ to the *ABAQUS* $\bar{\epsilon}^{pl}$ estimates and the maximum equivalent uniform stress for several randomly generated histories. For a illustrative description of the approach applied here, see Section 8.5.3.

A characteristic behavior of SPSW web plates is the plastic contraction that occurs in the direction normal to the principal plastic tensile strains. If unconstrained plastic stretch-

ing is assumed, the contraction in the orthogonal direction will be approximately half the magnitude of the plastic stretch ($\nu = 0.5$) and will tend to draw the reloading drift for the opposite direction back and reduce hysteretic pinching. However, SPSW web plates are not entirely unconstrained. As the plate slenderness is reduced, localized compressive stresses (normal to the principle stretch direction) will increase the magnitude of the contraction. This contraction, referred to here for convenience as Normal Plastic Contraction (NPC), has been recognized in other SPSW research and some authors have included various forms of it in web plate hysteretic models. NPC reduces the pinching in the hysteresis but also contributes to higher accumulated strains in the web plate than a simple uniaxial element model would predict.

Using an approach discussed in more detail in Section 9.7.1, an analysis was conducted using a large suite of synthetic story drift histories representing strong ground shaking (SAC-97: LA 2% in 50 year hazard) and a material model that accounts for NPC, bi-directional straining and strain accumulation outside the primary loading phase. The median accumulated plastic strain in a web plate was found to be 0.028, with a 95th percentile value of 0.050. In SPSW modeling, the backbone curve used to define the web plate material response should reflect this. Note, in pushover analysis, the web plate strain at 2% drift will be approximately 0.01.

9.3.4 Possible Consequences of Amplified Tensile Stresses

The plastic web plate strain in a pushover analysis (displaced to the target story drift) will be much lower than the accumulated plastic strain expected in a large seismic event. In nonlinear dynamic analysis, a similar situation may arise if the backbone curve used to describe the web plate force-deformation or stress-strain response mirrors the monotonic stress-strain curve. Again, this is because the bi-axial nature of the plastic strain accumulation is neglected.

In pushover analyses, arguably the prevailing static nonlinear procedure in commercial practice, an underestimate of the web plate strength may identify an incorrect pattern of damage or yield hierarchy for an SPSW, particularly if the steel has significant hardening characteristics and these are not included in the model. This is a key objective of any static pushover analysis.

9.4 ABAQUS Simulations

The results of *ABAQUS* simulations were used to: 1) to examine and quantify the hardening exhibited by the web plates tested in the experimental program, and 2) validate an algorithm, *PeakStress*, developed to estimate the peak equivalent uniform web plate tensile stress attained due to an arbitrary cyclic drift history. This will be presented later in the chapter.

In ABAQUS, the equivalent plastic strain, $\bar{\epsilon}^{pl}$ (PEEQ in *ABAQUS* nomenclature) is the integral of the equivalent plastic strain rate defined by Eq. 9.2,

$$\dot{\bar{\epsilon}}^{pl} = \sqrt{\frac{2}{3}\dot{\bar{\epsilon}}^{pl} : \dot{\bar{\epsilon}}^{pl}} \tag{9.2}$$

where $\dot{\bar{\epsilon}}^{pl}$ is the plastic component of the strain rate tensor.

ABAQUS supports the simulation of material response using isotropic and kinematic hardening as well as a combination of the two, combined hardening. The results of *ABAQUS* simulations of the test specimens suggest that combined hardening provides the most accurate description of the observed response. Isotropic, kinematic and combined hardening models can be calibrated from the results of actual test data to determine the contribution from each to the total hardening response. The degree to which each of these contributes to the overall hardening depends upon, amongst other things, the stress-strain history and the material properties. Although combined hardening provides the best description of the response, analysis of the experimental tests were conducted using only nonlinear isotropic

and nonlinear kinematic hardening (independently) to illustrate the differences between the two. For the simulations that were used to validate the *PeakStress* algorithm, both isotropic and combined nonlinear kinematic-isotropic hardening were used.

9.4.1 Analysis of Experimental Specimens

ABAQUS models for the web plate tests were created using the web plate coupon data. This data is summarized in Table 9.2. Poisson's ratio of 0.30 was assumed for the web plate steel. The HBE and VBEs were modeled using elastic materials with an E of 205,000 MPa also with Poisson's ratio of 0.30. Web plate inelastic material properties were developed form the coupon test data. The engineering stress-strain relationships derived from the coupon tests were averaged for the two directions of each web plate specimen, then fitted with a smooth function per Eq. 9.3, before being converted to true-stress log strain for use with *ABAQUS*.

$$\sigma_{yI} = \sigma_{y0}\left[1 + R_{sh}\left(\beta_1\left(1 - e^{\alpha_1 \bar{\epsilon}^{pl}}\right) + \beta_2\left(1 - e^{\alpha_2 \bar{\epsilon}^{pl}}\right)\right)\right] \tag{9.3}$$

Where σ_{y0} is the initial yield stress, R_{sh} is the degree of strain hardening, $\bar{\epsilon}^{pl}$ the plastic strain and α_1, α_2, β_1 and β_2 are parameters required for curve fitting.

9.4.2 Mesh Refinement Study, Geometry and Boundary Conditions

A mesh refinement study was conducted to determine an appropriate mesh size and element formulation. On the basis of these analyses, a 28×28 mesh of large displacement, finite strain $S4R$ (4-noded reduced integration) shell elements with nine integration points through the thickness of the plate and enhanced hourglass control was deemed appropriate for the web plate mesh. A finer mesh resulted in significantly increased computational demand and a modest improvement in accuracy. The use of $S4$ elements, in lieu of the reduced integration $S4R$ elements, did not significantly affect the result, with nearly identical dissipated energy

and peak load prediction to the same mesh of $S4R$ elements.

The shell elements extended to the inside edge of the clamping bar, as shown in Figure 9.2. The VBEs and top HBE were modeled using $B31$ shear deformable line elements located at the centroid of the section. The bottom W8x58 HBE was not modeled. Tie constraints were used to connect the edge of the web plate to the boundary elements. The VBEs were constrained to the top HBE using multi-point constraints that behave as pin connections between the members. The web plate initial imperfections were seeded with the first two buckling modes with a total amplitude of approximately 2 mm. This magnitude approximately matches the measured panel imperfection amplitude from the experiment.

9.4.3 Solution Strategy

All of the finite element simulations utilized explicit dynamic analysis. Loads were applied using displacement control of a node at the right end of the top HBE, as was the case in the physical tests. The displacement amplitude history exactly matched that recorded from each experiment, and was applied using a smooth-step amplitude function. The model mass was scaled by a factor of fifty to increase the stable time increment. The time between consecutive amplitude peaks was moderated to ensure inertial effects were maintained below 1% of the peak applied lateral force. As is typically recommended with explicit analyses, an energy balance check was performed using this mesh to verify that the kinetic energy, artificial energy and the work done in propelling mass added in mass scaling were small in comparison with the internal energy.

Each plate was modeled for two cases of hardening: 1) pure isotropic hardening, and 2) pure nonlinear kinematic hardening. The nonlinear kinematic hardening used two back-stress components, one linear and one nonlinear (computed internally by ABAQUS). The backbones of the response histories generated using the isotropic and kinematic models represent an upper bound (purely isotropic) and lower bound (purely kinematic) on the experimental results. Fig. 9.2 shows a single experimental specimen at peak drift with the $ABAQUS$ model of the specimen at the same drift.

Table 9.2: Material properties of Experimental Specimens

Test #	**ASTM**	t_w	F_y	F_u	F_u/F_y	E
1-16	A36	1.47	388	450	1.161	183,900
2-16	A36	1.46	391	450	1.151	191,400
3-16	A36	1.46	367	438	1.193	179,800
1-18	A1008	1.12	218	322	1.475	153,700
2-18	A1008	1.14	218	326	1.496	151,100
3-18	A1008	1.12	298	364	1.221	173,400
3-22	A1008	0.80	287	373	1.30	163,500

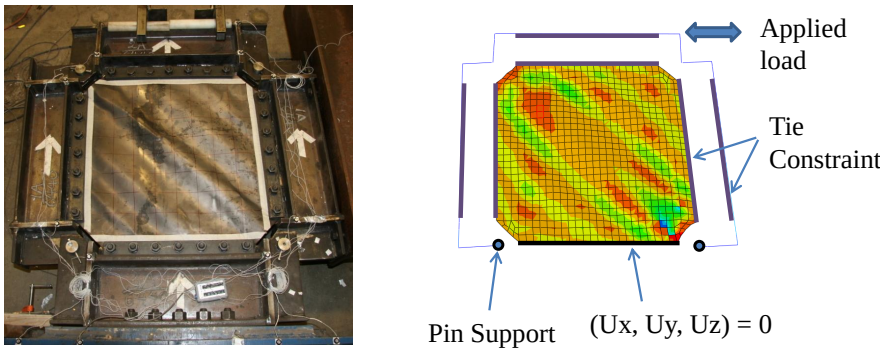

Figure 9.2: Experimental specimen and *ABAQUS* model of Specimen

9.5 Web Plate PeakStress *Model*

To facilitate efficient generation of estimates of the maximum web plate stress though random drift histories, an algorithm was developed and implemented in Matlab that can accurately predict the magnitude of the maximum stress attained at maximum drift of each loading cycle. This model computes the accumulated plastic strain, the growth of the isotropic yield surface and the translation of the kinematic backstress. The stress at cycle

i is represented by Eq. 9.4, which is based on the combined hardening model proposed by Lemaitre (1990).

$$\sigma_{PS} = abs\left[\nu\frac{C}{\gamma} + \left(H_{(i-1)} - \nu\frac{C}{\gamma}\right)e^{[-\nu\gamma(\epsilon_i{}^{pl} - \epsilon_{(i-1)}{}^{pl})]} + \nu\left[\sigma_{y0} + Q\left(1 - e^{-b\bar{\epsilon}_i^{pl}}\right)\right]\right] \quad (9.4)$$

In Eq. 9.4, ν is ± 1 and depends on the direction of loading, σ_{y0} is the initial yield stress (F$_y in Table 9.2$),C$and \gamma$ are kinematic hardening parameters which are set to 840 MPa and 15 respectively for validation purposes. $H_{(i-1)}$ is the kinematic shift or back stress at the end of excursion *i-1*, $\epsilon_i{}^{pl}$ is the plastic strain at the end of excursion i (and may be negative), $\bar{\epsilon}_i^{pl}$ is the accumulated plastic strain at the end of excursion i and Q is the radius of the yield surface at saturation, also determined from cyclic test data. b is an isotropic saturation rate parameter (71 MPa and 11 respectively for the verification). The plastic strain, $\epsilon_i{}^{pl}$, and accumulated plastic strain, $\bar{\epsilon}_i^{pl}$, are both initial zero.

Note: The values assigned to Q and b were selected to give a reasonable representation of hardening parameters for a steel with moderate isotropic strain hardening behavior. For the combined hardening runs, C and γ were similarly selected so that a web plate exhibited a significant kinematic shift on cyclic loading. The exact values assigned for these parameters is not important. They are used to assess the accuracy of the *PeakStress* model. Fig. 9.3 illustrates the process undertaken by *PeakStress*.

9.5.1 PeakStress Model Verification

The *PeakStress* algorithm is verified against a series of eight *ABAQUS* analyses of a web plate subjected to eight randomly generated drift histories. The histories each comprised twenty full cycles with a log-normal amplitude distribution. The median and 99^{th} percentile drifts were set to 0.3% and 2% respectively, in accordance with Hadidi Tamjed [35]. The *ABAQUS* analyses procedures were nominally identical to those used for the web plate specimen. The *ABAQUS* model comprised a pin-connected *B*31 wire element boundary

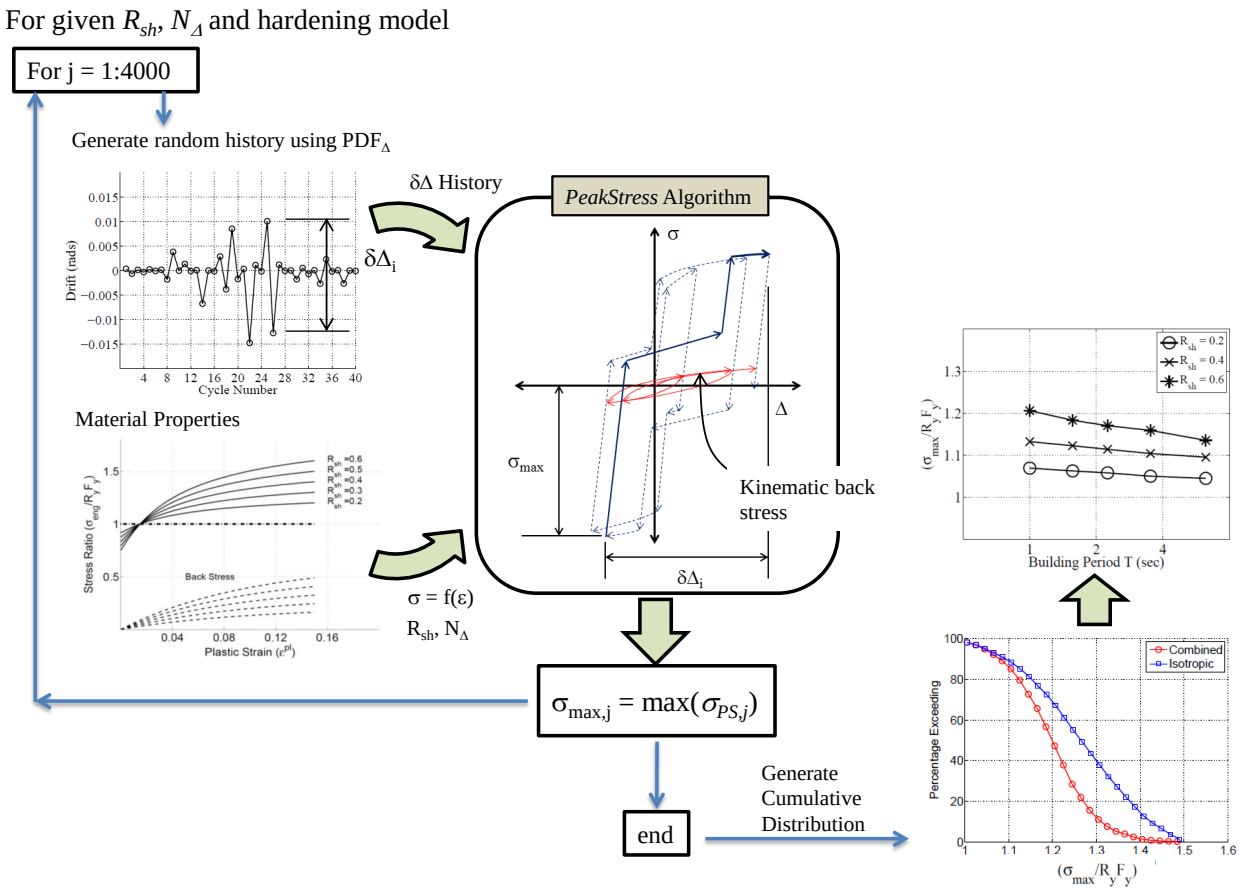

Figure 9.3: Flow diagram for *PeakStress* algorithm

frame with a web plate aspect ratio, L/h, of 1.2 and web plate slenderness, h/t_w, of 1000. The VBEs and HBEs each had flexural stiffness exceeding nine times the AISC permitted minimum. The web plate was modeled using a 30×36 mesh of $S4R$ shell elements. All analyses were conducted using *ABAQUS Explicit*. Web plate stresses were determined by extracting the average web plate von Mises stress sampled over a uniformly spaced 10×10 grid of elements.

Primary plastic straining (or loading) is assumed to commence after the inflection point

of the drift-load curve and terminate at peak drift whereupon the load direction reverses. As previously discussed, plastic strain also accumulates outside primary loading but at a lower rate, approximately 8% of that during primary loading. Translation of the kinematic backstress is assumed to occur only under primary loading because the orientation of plastic strains are highly non-uniform over the web plate during the transition between sequential phases of primary loading. This approximation of plastic strain accumulation predicts ${\epsilon_i}^{pl}$ for the isotropic hardening case (for the eight drift histories examined) with a mean ratio of the estimated to $ABAQUS$ computed values equal to 0.97 and a COV of 0.097.

An analysis of the maximum web plate stress predicted by $PeakStress$, σ_{PS}, and by $ABAQUS$, σ_{ABQ}, shows that for combined hardening the $ABAQUS$ estimate ranged from $1.042F_y$ to $1.114F_y$, depending on the history, and the mean ratio (over the eight histories) of the predicted maximum stress from $PeakStress$ and $ABAQUS$ was 0.997 with a coefficient of variation $CV = 0.010$. For isotropic hardening σ_{ABQ} ranged from $1.085F_y$ to $1.206F_y$ and the mean ratio of the stress estimates was 0.995 with a $CV = 0.013$. Thus for a reasonably broad range of maximum stresses developed by the web plate, the algorithm $PeakStress$ predicted the outcome of the $ABAQUS$ simulations extremely well for both hardening types.

9.6 Hardening Properties of Experimental Specimens

In order to determine how the web plate specimens harden, an accurate estimate of the accumulated plastic strain and of the equivalent uniform stress are required. The accumulated plastic strain is estimated from the $PeakStress$ algorithm. The measured "actual" stress in the web plate is computed form knowledge of the lateral load and the loading configuration. The peak lateral load attained at the maximum drift of each cycle was used to compute an estimate of the average von Mises stress in the web plate assuming plane stress conditions. This estimate is based on Eq. 9.5 which assumes that elastic properties are maintained up to the point of yield.

$$\sigma_{vm} = \frac{2hV}{t_w A_p (1 - 0.3\beta)\sqrt{(1 - \beta + \beta^2)}} \tag{9.5}$$

Where h is the vertical distance between the pin centers, V is the load at peak drift corrected for actuator orientation and base rotation, t_w is the thickness of the web plate, A_p is the area of the web plate (L_{cf}) and β is the average ratio of compressive stress to tensile stress in the plate. From finite element simulations this ratio was found to vary with plate slenderness h/t_w and is approximately -0.08, -0.06 and -0.05 for the 16 Ga, 18 Ga and 22 Ga plate respectively.

Fig. 9.4 shows σ_{vm} plotted against $\bar{\epsilon}^{pl}$ for Tests $\#1-18$, $\#3-18$, $\#2-16$ and $\#3-22$. Also shown is the result of running the test drift history simulation through the *Peak-Stress* algorithm. The kinematic hardening parameters, C and γ, shown in Table 9.3 were determined by trial and error by running the actual test cyclic drift history through the $PeakStress$ algorithm. Q and b were determined from the idealized coupon data (excluding yield plateau). The cyclic hardening parameters, C, γ were manually adjusted until a good match was found between the experimental data and the maximum stress predicted by $PeakStress$. The experimental points below the envelope are cases of peak load where the tension field has not fully developed and are typically the 2nd cycle at a particular drift level. For reference, a fully isotropic hardening case is also shown in Fig. 9.4. The resulting cyclic hardening parameters are shown in Table 9.3.

From Table 9.3 the parameters $\frac{Q}{R_{sh}F_y}$ and $\frac{F_{max}-F_y}{F(\epsilon^{pl})-F_y}$ are independent measures of the degree of isotropic hardening. These values will approach 1.0 as the contribution of kinematic hardening to the total response diminishes. F_{max} is the computed maximum equivalent uniform stress attained in the test, $F(\epsilon^{pl})$ is the maximum stress computed from the coupon stress-strain data using the estimate of ϵ^{pl}. Included in this table are the computed estimates for the ATLSS tests of A36 and A572 Gr. 50 steel. It is clear from this table that the A1008

Table 9.3: Results of Hardening Analysis of Experimental Specimens

Test #	ASTM	F_y	C	γ	Q	b	$R_{sh}F_y$	$\frac{Q}{R_{sh}F_y}$	ϵ^{pl}	$F(\epsilon^{pl})$	F_{max}	$\frac{F_{max}-F_y}{F(\epsilon^{pl})-F_y}$
1-18	A1008	216	0	NA	105	30	107	**0.98**	0.111	317	316	**0.99**
2-18	A1008	216	0	NA	100	32	106	**0.94**	0.103	314	306	**0.92**
3-18	A1008	297	120	10	52	20	64	**0.81**	0.103	354	338	**0.72**
3-22	A1008	287	250	10	63	25	88	**0.72**	0.139	373	347	**0.70**
1-16	A36	382	340	10	34	25	69	**0.49**	0.078	426	410	**0.64**
2-16	A36	381	400	10	29	15	64	**0.45**	0.141	444	407	**0.41**
3-16	A36	363	300	10	44	15	68	**0.65**	0.109	423	397	**0.57**
ATLSS	A36	255	850	8	60	40	166	**0.36**	0.138	428	321	**0.38**
ATLSS	A572	396	880	20	78	25	122	**0.64**	0.132	520	477	**0.65**

steel has predominantly isotropic hardening behavior, particularly Tests #1-18 and #2-18, whereas the A36 and A572 steel specimens appear to have roughly equal contributions from each.

9.6.1 Selection of Cyclic Hardening Parameters

Before the selection of hardening parameters for the experimental results and FE simulations are discussed, some results of an earlier study by Kaufmann et al. (2001) on strain aging of structural steels are examined. In these tests ASTM A36 and A572 Gr. 50 steel coupons were cyclically tested. The material properties are shown in Table 9.2. Though it is understood that uniaxial cyclic data are not directly applicable to web plate hardening, an analysis of the hardening of these specimens is instructive. Moreover, the results may serve as a reasonable lower bound estimate of web plate response. That is, more kinematic hardening is expected in uniaxial cyclic loading than in bi-directional cyclic loading. A greater proportion of kinematic hardening will tend to reduce the maximum stress attained.

The method outlined by Lemaitre [**?**] was used to determine the hardening parameters for the tests. This method uses the stabilized cyclic data (the envelope of the hysteresis

curves for a particular strain level) from all tests out to ±4% strain. A reasonable match is obtained for the larger strain amplitudes (2%, 3% and 4%) but the 1% strain test is inaccurately represented at low strain levels. Since the 1% test is compatible with the strains expected in a SPSW, it alone was used.

The results of the experiments indicate considerable variability in material hardening characteristics under reversed cyclic loading. In some cases, namely the A1008 specimens, the plates display isotropic hardening behavior, while in others a combined kinematic-isotropic behavior was observed. It should be noted that even though some plates appeared to harden isotropically (Test $\#1-18$ and $\#2-18$ in particular), and that this model best describes the observed behavior, this may not true of the material. Pure isotropic hardening will only occur in cases of proportional loading in mild steels and this is not the case for any of the web plate tests. It is believed that the close match observed here may be attributed to a combination of significant isotropic hardening, exacerbated by cross hardening. Regardless, for the purposes of determining the peak stress, the isotropic assumption appears to be a good predictor for some steels.

9.7 Expected Hardening of Web Plates in Seismic Events

While the experiments were useful for calibrating material models, they do not quantify the extent to which hardening may affect actual earthquake response, or its relative importance in predicting behavior. The drift history and the magnitude of accumulated plastic strains in experimental cyclic tests will differ substantially from those actually encountered in an earthquake and are both typically much higher in a cyclic test. In an earthquake, story drifts are random with large drift cycles clustering in one or more regions of the history, but otherwise occurring randomly throughout the record. Drifts also typically have asymmetric positive/negative magnitude distributions.

Therefore, to understand the impact of web plate hardening on system response and

component demands, an accurate quantification of actual earthquake demands on SPSW web plates under severe seismic action is desirable. This is accomplished using Monte-Carlo simulations of expected drift demands. These synthetically generated drift demands are based on the drift response characteristics of SPSW FE models to actual recorded MCE level ground motions.

These Monte-Carlo simulations used a broad range of hardening behaviors and drift demands that reflect actual expected drifts from thousands of synthetic earthquakes. Variations of the material properties E, F_y, and the strain hardening modulus, E_{sh}, were not included. It is expected that inclusion of this material variability will not substantially alter the reported mean or median quantities but will tend to increase the variance.

9.7.1 Estimating Inelastic Drift Demand

Monte-Carlo simulations are used for the present study. In order to quantify web plate hardening, a reasonable estimate of likely story drift demand is required. i.e., a statistical description of the probability distribution and the number of cycles. To do this, a statistical model of the expected inelastic drift demand was developed from response history analyses of multi-story SPSWs.

OpenSees is used to analyze a series of 3-story, 6-story and 9-story SPSWs with three variations of bay width for each wall height (L = 3.05 m, 4.57 m and 6.10 m). Fig. 9.5 shows the typical configuration of the OpenSees models. The 3-story and 9-story models are identical to those analyzed by Berman [10] and are loosely based on the SAC moment frame building configurations from FEMA 353 [33]. The 6-story SPSWs were designed according to the Seismic Provisions and the AISC Specification. The VBEs were sized using capacity design principles and were modeled as elastic beam-columns, but permitted to form flexural hinges at their base. The HBEs were also sized using capacity design

principles and were permitted to hinge over their entire length. In all SPSW models, the web plates were modeled using truss elements and utilized the new SPSW web plate uniaxial material model per Chapter 8. The web plates were modeled assuming A36 sheet steel with $R_y F_y = 46.8$ ksi and isotropic strain hardening behavior with an R_{sh} of 1.3.

Each SPSW was subjected to a set of ten earthquake ground motions, scaled to the 2% in 50 year hazard level for LA, obtained from the SAC-97 suites (per Somerville [**?**]). From these analyses, the distribution and number of inelastic excursions (defined in Section 9.3.2) can be obtained for each story web plate. The probability density function can then be generated representing the inelastic demand. A curve representing the median of the aggregate data is shown in Fig. 9.6(a) and is defined by Eq. 9.6.

$$f(\Delta\delta) = 1.3 \times 10^4 exp(-22.5(\Delta\delta)^{0.25}) \tag{9.6}$$

where $\Delta\delta$ is the inelastic drift range and the constant terms were obtained by curve fitting.

Somewhat surprisingly, the probability density functions for each building height (3-, 6- and 9-stories) were essentially identical. This fact is illustrated in Fig. 9.6(a) where the 3-, 6- and 9-story data are overlain. From these analyses, the mean (over all ground motions) of the maximum story drift was between 1.6% and 2.6% for the 3-story walls, 1.1% and 2.6% for the 6-story walls and between 0.9% and 3.1% for the 9-story walls.

Although the probability distribution of inelastic drift range for different wall heights is invariant, the average number of inelastic excursions N that a web plate undergoes is not. The mean value of N was found to be 42.9 for the 3-story walls, 29.6 for the 6-story walls and 27.3 for the 9-story walls. The fundamental periods of these buildings were computed from eigenvalue analyses and ranged from 0.45-0.55 seconds for the 3-story SPSWs, 0.84-0.95 seconds for the 6-story and 1.11-1.42 seconds for the 9-story SPSWs. Accordingly, an

approximate relationship between T and N for low-rise SPSWs can be made using Eq. 7.

$$N = \frac{30}{\sqrt{T}} \tag{9.7}$$

The invariance of the probability density function (for maximum inelastic story drift) with T and dependency of N on T are both consistent with the findings of Hadidi-Tamjed (1988) who studied generic SDOF inelastic systems, although, the shape of the function proposed by Hadidi-Tamjed is different. For SPSWs it appears to be weighted more heavily at the very low end of inelastic drift range. The shape of the function, it is suspected, has more to do with how the inelastic drift distribution is determined rather than any system related dependency.

Also, it should be noted that the *OpenSees* computed periods are considerably longer than those computed using equation 12.8-7 of ASCE-7 10. The difference is due primarily to the presence of leaner columns in the analysis.

9.7.2 Generation of Synthetic Drift Histories and Statistical Validation

The density function presented in the previous section provides a basis for generating synthetic drift histories. Before implementation, two additional constraints are introduced:

1. Randomly generated sequences of inelastic drift range ($\Delta\delta_i$) are shuffled so that the large drifts tend to cluster (though not exclusively) in one segment of the record, typically the middle. This is consistent with response history observations.

2. The histories are generated so that the web plate always comes back to zero drift at the end of the record.

Item 2 is introduced because of the difficulty encountered when attempting to generate realistic synthetic records by simply adding *top-to-tail* a sequence of randomly generated drift range values with alternating sign. Although this maintains the correct distribution of drift range, it has a tendency to accumulate very large residual drifts at the end of the record, sometimes exceeding 20%. Instead, each drift sequence was generated by assuming

a random inelastic **drift** statistic, (rather than drift range statistic) of $0.5\Delta\delta_i$. The sequence was then shuffled so that large drifts had a higher probability of occurring in the middle of the record. The result of this approach was checked by generating a sequence of 5000 histories (each with 20 full cycles or $N = 40$) and extracting the drift range distribution. The resulting distribution was in very good agreement with Eq.9.6.

In the *OpenSees* analyses of multi-story SPSWs using ground motions representing the 2% in 50 year hazard level for LA, moderate to severe residual story drifts were often observed, sometimes exceeding 3%. The rate of residual drift accumulation typically correlated with drift magnitude, i.e., large residuals accumulated rapidly when drift demands were highest. Ignoring this feature of the actual response histories will result in a slight underestimate of the web plate hardening in the Monte-Carlo simulations. However, it is programmatically expedient to introduce this modification and unrealistically high residual drifts are avoided.

9.7.3 Material Model used for Monte-Carlo Simulations

The material model used in this study is designed to represent the stress-strain properties exhibited by typical A36, A572 (Gr. 50 and Gr. 42) and A1011 steel sheet and flat plate. These data, with the following constraints based on other available published data, are used to construct the idealized stress-strain curves for the simulations:

- the strain at initiation of strain hardening, ϵ_{sh}, equals 0.015
- the initial slope of the strain hardening branch, E_{sh}, is between $E/20$ and $E/75$
- the ultimate engineering stress, σ_{ult}, occurs at an ultimate strain, ϵ_{ult}, of 0.15.

The material model assumes a hot rolled plate with a yield plateau although the material model used in *PeakStress* does not include the plateau. To account for the potential for delayed onset of hardening, the normalized yield stress at zero strain is reduced below 1.0 so that at $\epsilon = \epsilon_{sh}$ it equals 1.0. Figure 12 shows the curves for different magnitudes of hardening. This figure also shows the 1-D kinematic backstress for each value of R_{sh}. The higher back stresses are associated with higher R_{sh} values. Items 1 and 2 above are

based on recommendations from Bruneau (2011) for typical structural steels. Examination of monotonic stress-strain curves by Kaufmann (2001) for ASTM A36 and A572 steel shows E_{sh} of approximately $E/50$ and $E/70$ respectively. Item 3 is also based on the work by Kaufmann.

The analysis is conducted for several cases of strain hardening magnitude, R_{sh}, defined by Eq. 9.1. The over-strength factors are included in the estimate of R_{sh} because the primary interest is expected hardening derived from an estimate of drift magnitude, drift distribution and accumulated plastic strain. R_{sh} varies from 0.1 for ASTM A572-Gr 42 to as much as 0.63 for ASTM A1011 steel.

In the Monte-Carlo simulations, the normalized monotonic engineering stress-strain curves for steel are described by Eq. 9.3 but are normalized by $R_y F_y$. The parameters C, γ, Q and b are contrived so that: 1) at $\epsilon_{ult} = 0.15$, the normalized stress, $\hat{\sigma}$, equals $1 + R_{sh}$, and 2) the contribution to the monotonic hardening at 4% strain is shared equally between the isotropic component and the kinematic component, i.e., 50% isotropic hardening. The saturation rate parameters γ and b are set to 10 and 40 respectively and are based on results presented in Table **??**. It is most important to get the correct relationships between the parameters up to about 8% plastic strain. Results of the Monte-Carlo simulations verified that SPSW web plates will typically not accumulate strains in excess of 6% (50th percentile = 0.028; 95th percentile = 0.050). A sample distribution from the Monte-Carlo simulations is shown in Fig. 9.7 for $N = 20$ cycles.

The parameter b was selected so that it generated a sufficiently high E_{sh} and was also within the range determined experimentally. For the prescribed R_{sh} values used in the simulations, the resulting E_{sh} (determined by finding the slope of Eq. 9.3 at $\epsilon = \epsilon_{sh}$) varied from $E/66$ to $E/197$. These are lower than typical steel grades and will generally lead to an underestimate of the peak stress.

Table 9.4: Parameters for Eq. 9.8

Hardening Model	a	b	d	e	f
Isotropic	-0.07	0.25	0.191	-0.599	0.504
Combined	-0.03	0.21	0.086	-0.273	0.225

9.7.4 Results of Hardening Study

Figs. 9.9 (a) through (f) present the normalized maximum stress attained (σ_{max}/R_yF_y) in the web plate versus the approximate period of the building, T, for different degrees of hardening magnitude R_{sh}. These plots are for the case of probability $P = 10\%$, 50% and 90% of exceeding σ_{max}/R_yF_y. The data in these figures is generated from 4000 synthetic histories with the number of inelastic drift ranges N varied from 24 to 60 (12 to 30 full cycles). The building period T is computed using Eq. 9.7

For the hardening parameters used in these simulations, the expected maximum web plate stress can be expressed as a function of T, R_{sh} and P for $0.05 < P < 0.95$ and $0.5 < T < 2$ seconds. This is represented by Eq. 9.8 which has a standard error of less than 0.5% within the limits stated.

$$\frac{\sigma_{max}}{R_yF_y} = mlog_e(T) + c \tag{9.8}$$

Where m and c are functions of R_{sh} and P given by Eqs. 9.9 and 9.10:

$$m = aR_{sh}(1-P)^b \tag{9.9}$$

$$c = 1 + (dP^2 + eP + f)R_{sh} \tag{9.10}$$

For example; for the case where $T = 0.5$ seconds, and $R_{sh} = 0.49$ (A36 hot-rolled steel plate) and assuming isotropic hardening, for any web plate there is a 50% probability that the maximum equivalent uniform tensile stress will exceed $1.12R_yF_y$. Table 9.9 shows the calculated stress amplification due to hardening for both the isotropic case and the combined case and for varying levels of exceedance probability. e.g., from Fig. 9.9(c) there is a 50% probability that for a building with $T = 2$ seconds and $R_{sh} = 0.4$, σ_{max} will exceed approximately $1.1R_yF_y$.

It should be clearly acknowledged that these equations are simply a closed form representation of the data generated from the analyses, they do not constitute a design recommendation. Also, the data were generated from a specific set of scaled strong ground motion records for the LA region and are not representative of equivalent hazard levels in other regions of the U.S. The full impact of this potential increase beyond R_yF_y is yet to be established.

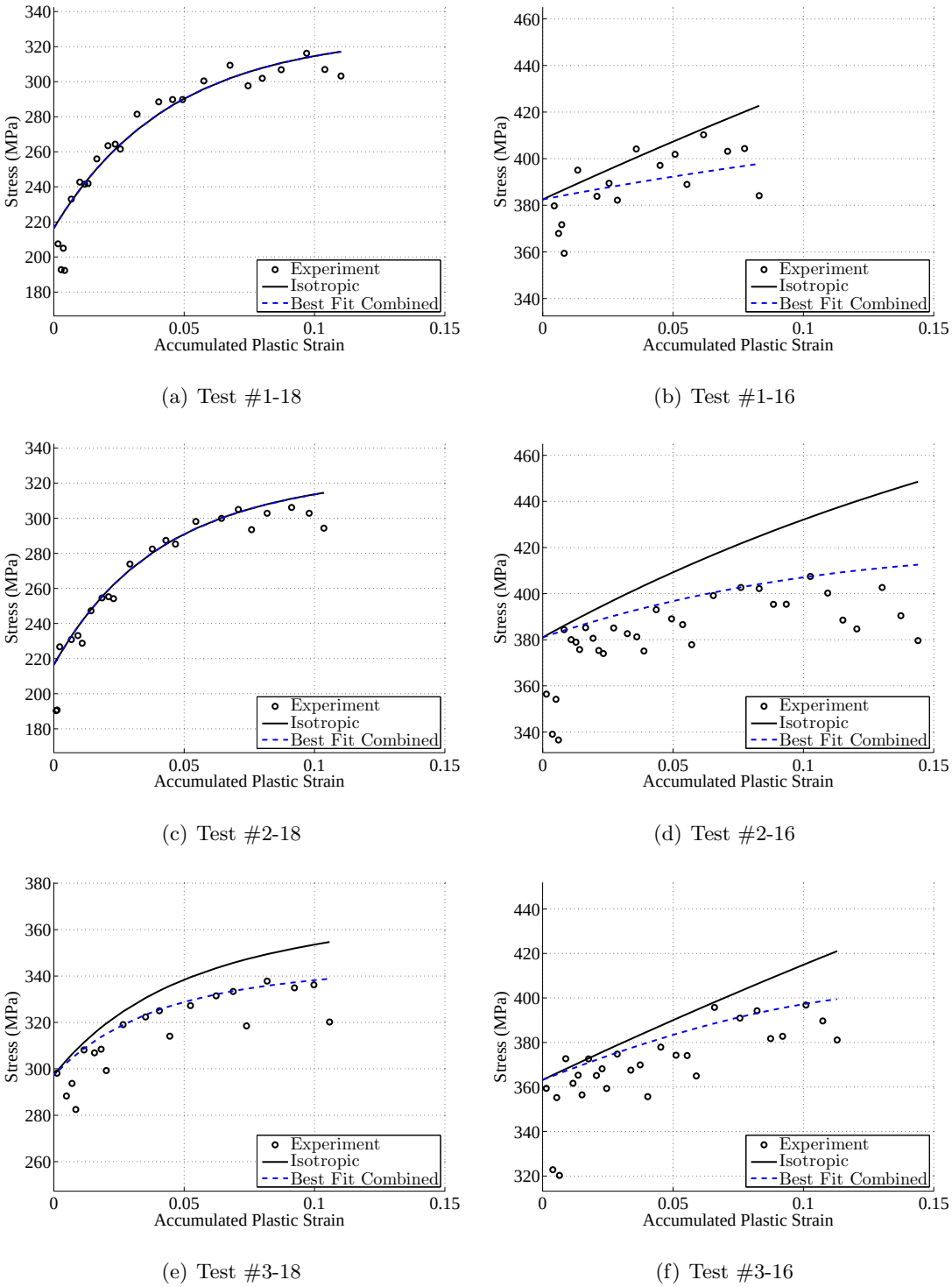

(a) Test #1-18

(b) Test #1-16

(c) Test #2-18

(d) Test #2-16

(e) Test #3-18

(f) Test #3-16

Figure 9.4: Relationship between the maximum equivalent uniform stress in web plate versus the the predicted stress assuming pure isotropic hardening and combined hardening.

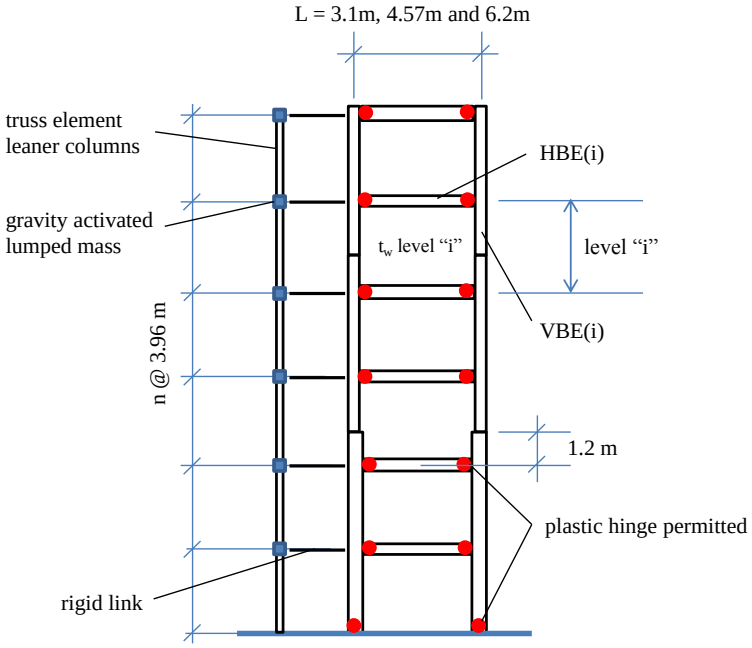

Figure 9.5: *OpenSees* SPSW model configuration used for drift determination

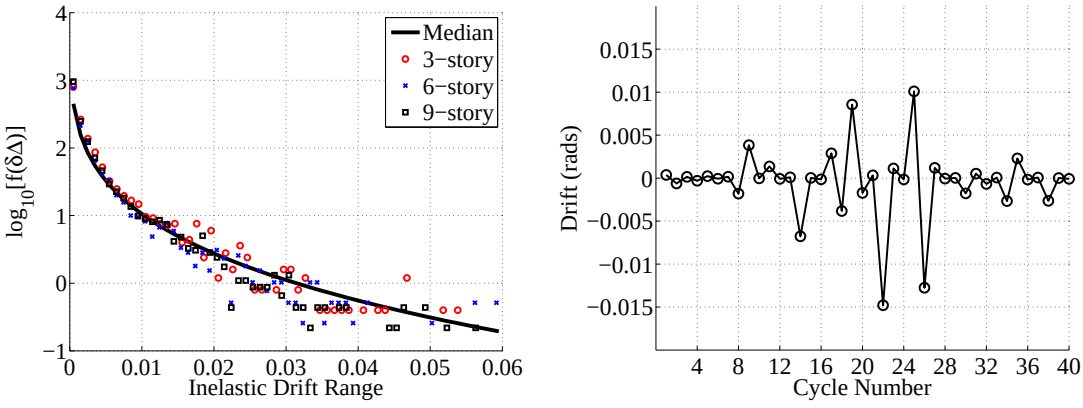

(a) Probability Density Function

(b) Sample Random Drift Sequence

Figure 9.6: (a) Probability density function used for Monte-Carlo simulations showing data from response history analyses and (b) sample random inelastic drift sequence (N = 20 cycles) used in the simulations.

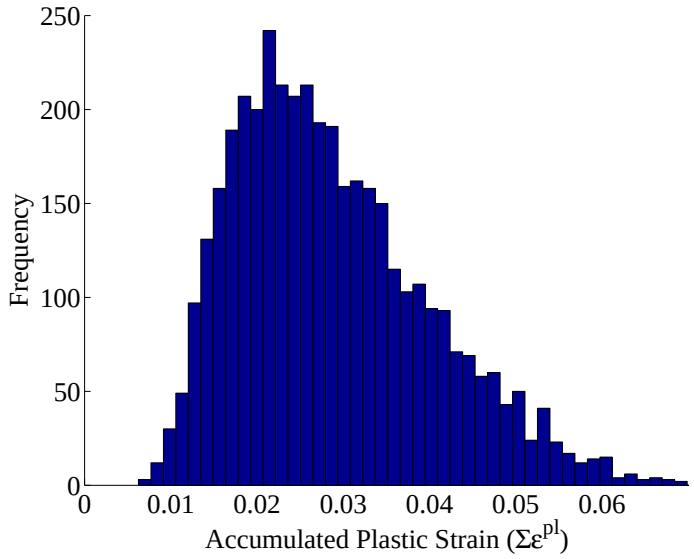

Figure 9.7: Sample distribution of accumulated plastic strain for $N = 20$ excursions.

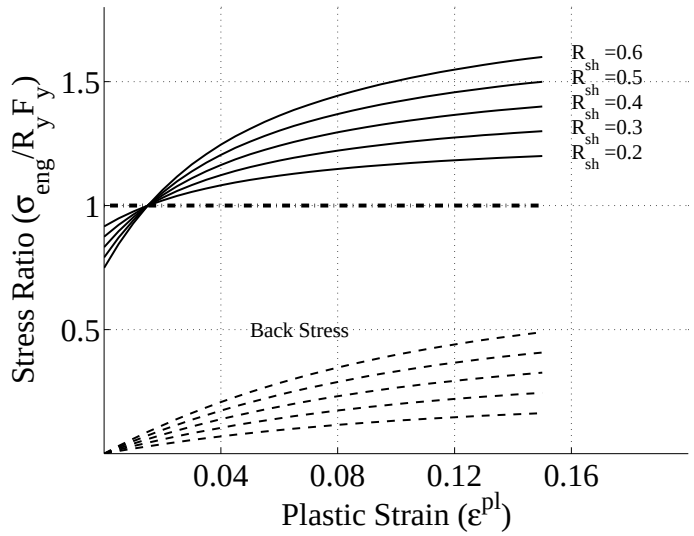

Figure 9.8: Stress-strain curves used in Monte-Carlo simulations showing different cases of R_{sh}. Increasing back stress magnitude corresponds with increasing R_{sh}.

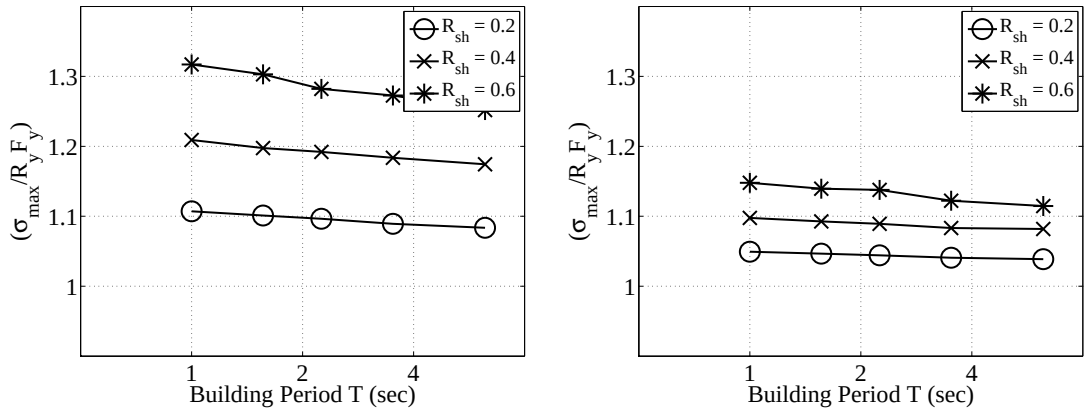

(a) P = 10%; Isotropic

(b) P = 10%; Kinematic

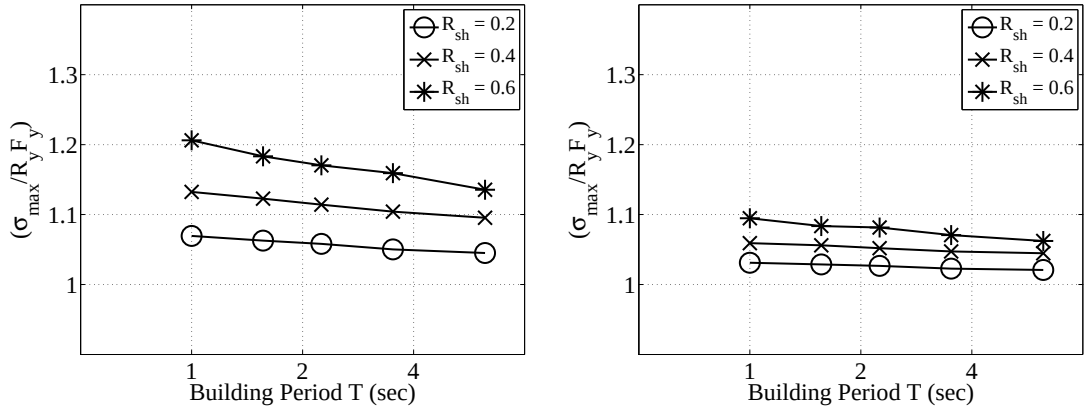

(c) P = 50%; Isotropic

(d) P = 50%; Kinematic

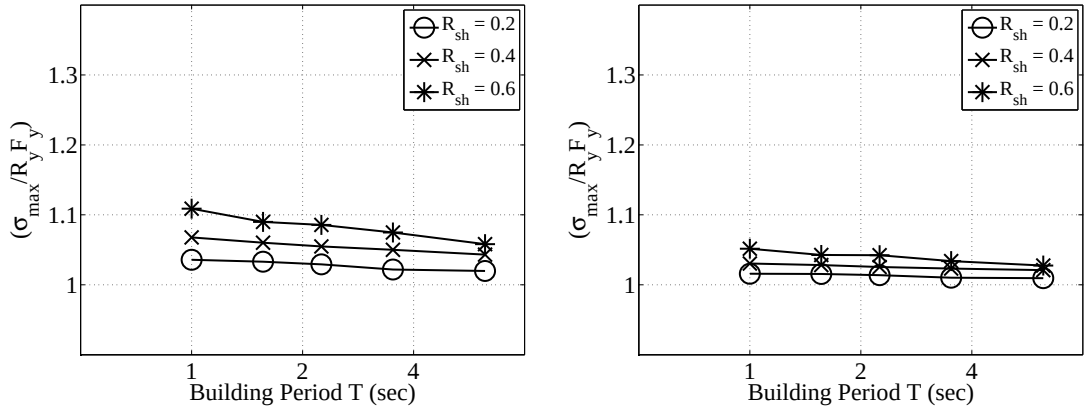

(e) P = 90%; Isotropic

(f) P = 90%; Kinematic

Figure 9.9: Stress amplification attained for different hardening values (R_{sh}) and different probabilities of exceedance (P).

9.8 Case Study of 6-Story SPSWs With and Without Amplified Web Plate Strength Due to Hardening

The net impact of SPSW web plate hardening is now examined by comparing the nonlinear static response of a series of six-story SPSWs analyzed using *OpenSees*. The web plates are modeled in each SPSW using two different elasto-plastic materials and tension only truss elements with different angles of inclination; these being (a) α (per AISC Eq. F5-2), (b) 40 degrees and (c) 45 degrees.

The web plate materials were selected to be representative of (a) a typical web plate steel (A36) with moderate hardening characteristics, and (b) Low Yield Point steel (LYP), a steel that is gaining popularity in seismic regions, notably Japan and Taiwan. These Low Yield Point steels have particular advantages in SPSW construction. LYP100 steel has an expected yield strength of around 110 MPa (16 ksi) and no yield plateau, but has substantial hardening with an F_u of approximately 260-270 MPa (37-39 ksi) [79].

The naming convention for the SPSW models analyzed is shown in Table 10.3. Table 9.6 shows the tension field inclination angle α for the two wall types, as computed using equation F5-2 of the Provisions.

Table 9.5: Models used for Pushover Analyses

		Hardening	
Steel	Angle	Yes	No
A36	α	$A36_{\alpha H}$	$A36_{\alpha}$
	40°	$A36_{40H}$	$A36_{40}$
	45°	$A36_{45H}$	$A36_{45}$
LYP	α	$LYP_{\alpha H}$	LYP_{α}
	40°	LYP_{40H}	LYP_{40}
	45°	LYP_{45H}	LYP_{45}

Table 9.6: Six-Story Tension Field α Values

Story #	(deg) A36	(deg) LYP
1	39.7	36.0
2	41.5	38.5
3	40.8	37.8
4	42.2	39.8
5	42.3	39.9
6	43.1	41.3

9.8.1 SPSW Designs

The design of the A36 walls is identical to those introduced at the beginning of this chapter. The bay size is 4.57 m (15 ft) and the story height is 3.96 m (13 ft). The required design base shear for these walls was determined using ASCE-7 10 for the LA region and is approximately 2410 kN. The lateral load is applied using the ASCE-7 load distribution per the Equivalent Lateral Force procedure of Section 12.8. The design of the LYP walls is carried out in the same manner and the web plate thicknesses are determined by scaling the A36 plate thickness up by the ratio of the expected $R_y F_y$ values.

9.8.2 Analysis Particulars

Pushover analysis is used for this exercise because it provides a convenient way of assessing capacity design demands on the VBEs for a given "expected" web plate strength. It is acknowledged that pushover analysis is not always the best tool for determining system behavior and does have drawbacks; however to make a simple objective comparison between VBE force demands using different material models, it is deemed adequate. The VBEs and HBEs are modeled using displacement based nonlinear beam-column elements with fiber cross-section and linear kinematic hardening with an effective hardening modulus of 0.5%

Table 9.7: Six-Story Web Plate Effective Yield Strength ($\beta_H R_y F_y$) used in Pushover Analyses

Material	(MPa) No Hardening	(MPa) Hardening
A36	322	370
LYP	110	174

E. The yield strength of the HBEs and VBEs was set at 379 MPa (55 ksi), although the HBEs are only permitted to hinge at their ends and the VBEs at their base. The web plates are modeled using the uniaxial *Hysteretic* material and, as discussed previously, have bi-linear elsto-plastic behavior. A diaphragm tie constraint is introduced between the ends of each HBE to prevent axial shortening.

The cases with hardening use an amplified expected strength $\beta_H R_y F_y$ in lieu of $R_y F_y$, where the factor β_H is determined on the basis of the web plate material used. For these analyses, the target drift of the first floor is set at 2%. The β_H factors are 1.15 for A36 steel and 1.58 for LYP100 steel. These are computed using the strength magnification in accordance with section 9.7.4 of this chapter. The β_H factor of 1.58 is based on assumed isotropic hardening using $T = 0.9$ seconds and $R_{sh} = 1.6$ in Eq. 9.1. Some liberty is taken here in the equivalency of R_{sh} and F_u/F_y-1 (they are not strictly the same) and in the extrapolation of Eq. 9.1 for a very high value of F_u/F_y. However, the analysis is carried out for the purposes of determining the impact on the system behavior using a reasonable estimate of the magnification of yield strength due to hardening under the same displacement demands.

9.8.3 Computed DCR Quantities

The Demand Capacity Ratios (DCR) are computed for each model using the AISC Specification equations H1-1a and H1-1b for flexure-compression interaction. For the interaction

Table 9.8: Six-Story SPSW Member Sizes and Web Plate Thicknesses

Story #	VBE	HBE	A36 t_w (mm)	LYP t_w (mm)
1	W14×550	W18×86	4.8	12.7
2	W14×550	W18×158	4.8	12.7
3	W14×342	W18×86	3.2	9.5
4	W14×342	W18×158	3.2	9.5
5	W14×221	W18×86	1.6	4.0
6	W14×221	W18×158	1.6	4.0

check, the VBEs are assumed to have a yield strength of 379 MPa (55 ksi) and a strength reduction factor ϕ of 1.0. DCRs are checked at the bottom, middle and top of each VBE on both sides of the wall, at each story. Thus for a single 6-story wall, 18 DCRs are computed. In Tables 9.8.3 through 9.8.3 that follow, TB is the mean DCR of the top-left, bottom-left, top-right and bottom right of the VBEs at that story. M is the maximum of the left and right DCR at mid-height. TB_R and M_R are respectively the ratios of the TB and M quantities to the reference case DCRs where α is per Table 9.6 and no stress magnification is used (i.e., $\beta_H = 1.0$). The TB_R and M_R quantities simply indicate the relative effect on TB and M of changing the strip angle and/or introducing a $\beta_H > 1.0$ to account for the expected hardening. The last three columns of each table show P_R the relative change from the reference case in maximum axial compressive force at that story. The bottom row of each table shows the mean value of the quantities in the rows above.

9.9 Discussion of Results

The DCRs for the $A36_{40}$ walls, where hardening is not considered (Table 9.8.3), show only a slight change relative to the reference case where the strips are inclined per Table 9.6. For the $A36_{45}$ walls the change in DCR is between -3 and 9%, with an average between 3 and 5%. The change in the contribution to the DCR from axial compression is less than 1%. The change in computed base shear, shown in Table 9.13, is also very small and also typically less than 1%. These trends are very similar for the LYP models but the increases are generally larger. The change in DCR for LYP_{45} walls are between -3 and 14% with a mean of around 6%. The effect of inclining the strips at 45 degrees is moderate for flexure-compression interaction, typically between 3-10% but this depends on many factors. The changes are large enough to be worthy of further consideration.

When the effect of hardening is included in the estimate of the expected web plate strength, the impact on VBE demands is more significant. For the A36 models, the increase in the DCR ranges from -1% to 10% for the $A36_{\alpha H}$ and from 0% to 13% for $A36_{45H}$, depending the story and location. The mean change for the $A36_{45H}$ is between 6% and 8%. Thus for pushover response of the A36 models, the effect of tension field inclination and material hardening appears to be modest but localized significant increases in DCR were observed.

For the LYP_{45H} models, the relative increase in DCR is between 10% and 28% with an overall mean of around 19%.

9.10 Additional Considerations

The transverse anchorage forces imposed on the VBEs resulting from cyclic hardening is tempered by the presence of a non-negligible compressive stress field operating normal to the tension field, which is typically ignored in design. These compressive stresses may exceed 10% of the yield strength for thick plates ($h/t_w \leq 400$). Therefore, for high-rise structures with stocky web plates and a low target drift, web plate hardening is not likely to have a significant impact on the boundary frame forces. However, for a low-rise structure with

slender web plates designed using $\alpha \leq 40^{\circ}$ the combined effect of web plate over-strength and tension field migration towards 45 degrees may be significant.

The preceding analyses of six-story structures is limited in that it utilized pushover procedures to assess the increased demand on elastic VBE demands. The extent to which a magnified web plate strength influences the performance under dynamic loading is not fully understood but will be examined for the same structures in the next chapter.

It is worth acknowledging once again that variability in material yield and ultimate strength was not considered in this analysis. Material over-strength factors, R_y and R_t determined as part of the Structural Shape Producers Council survey, are approximate and will change over time as steel production is influenced by many external factors. According to A.3 of the Provisions commentary, in some instances the yield over-strength factor R_y may already include an allowance for strain hardening or may be heavily skewed by small sections with high R_y values. This analysis should be considered with this in mind.

9.11 Conclusions

This analysis used synthetically generated drift histories and realistic material properties based on published data and seven small scale physical tests to estimate the maximum stress developed in a web plate under strong ground motion. The following general conclusions can be made:

- Cold-rolled A1008 sheet appears to have a high isotropic cyclic hardening contribution, sometimes approaching 100%.

- The magnification of web plate yield strength due to hardening depends heavily on the ratio of ultimate strength to yield strength (F_u/F_y) of the material, the bi-directional hardening evolution of the plate (isotropic component) and, to a lesser extent, on the number of inelastic cycles to which it is subjected.

- Under cyclic loading characteristic of strong ground motion for low rise SPSWs, the median magnitude of maximum equivalent uniform web plate stress is between $(1 + 0.25R_{sh})R_yF_y$ and $(1 + 0.35R_{sh})R_yF_y$.

- For the six-story walls subjected to pushover, the net increase in VBE demand capacity ratios due to magnified web plate yield strength appears to be approximately 25% of the increase in web plate strength (i.e., $0.25\beta_H$), or 6% of R_{sh}. This translates to an increase in VBE demand of around 4% for slender A36 web plate and 12% for slender LYP100 web plate steel. When this is coupled with a potentially large change in the tension field angle and the presence of web plate compressive stresses, the changes may be more subtle and heavily dependent on other factors (i.e., plate slenderness).

9.12 Recommendations

The following general recommendations are made:

- The cyclic hardening behavior of thick (6.4 mm (0.25 inch)) hot-rolled plates should be studied. The tests carried out as part of this research used thin hot-rolled plate with unusual hardening properties.

- The influence of web plate over-strength on total system behavior should be examined. This analysis only assessed how much hardening might be expected in a web plate subjected to severe seismic loading, not the impact this over-strength has on system performance.

Table 9.9: DCR and DCR Ratios for A36 with No Hardening

	$A36_\alpha$		$\frac{A36_\alpha}{A36_\alpha}$		$A36_{40}$		$\frac{A36_{40}}{A36_\alpha}$		$A36_{45}$		$\frac{A36_{45}}{A36_\alpha}$		P_R		
Story	TB	M	TB_R	M_R	TB	M	TB_R	M_R	TB	M	TB_R	M_R	α	40	45
1	0.867	1.067	1.000	1.000	0.873	1.075	1.007	1.007	0.907	1.126	1.045	1.055	1.000	0.999	1.007
2	0.526	0.738	1.000	1.000	0.537	0.744	1.022	1.009	0.546	0.762	1.039	1.033	1.000	1.000	1.006
3	0.453	0.793	1.000	1.000	0.457	0.801	1.009	1.011	0.491	0.780	1.085	0.985	1.000	0.995	0.999
4	0.437	0.341	1.000	1.000	0.438	0.344	1.003	1.009	0.444	0.330	1.017	0.969	1.000	1.004	1.006
5	0.541	0.448	1.000	1.000	0.537	0.437	0.992	0.976	0.561	0.470	1.037	1.050	1.000	1.005	1.011
6	0.478	0.472	1.000	1.000	0.487	0.466	1.019	0.987	0.503	0.510	1.053	1.081	1.000	1.019	0.986
mean	0.550	0.643	1.000	1.000	0.555	0.645	1.009	1.000	0.575	0.663	1.046	1.029	1.000	1.004	1.003

Table 9.10: DCR and DCR Ratios for A36 with Hardening

	$A36_{\alpha H}$		$\frac{A36_{\alpha H}}{A36_{\alpha}}$		$A36_{40H}$		$\frac{A36_{40H}}{A36_{\alpha}}$		$A36_{45H}$		$\frac{A36_{45H}}{A36_{\alpha}}$		P_R		
Story	TB	M	TB_R	M_R	TB	M	TB_R	M_R	TB	M	TB_R	M_R	α	40	45
1	0.879	1.095	1.014	1.026	0.886	1.104	1.021	1.034	0.922	1.156	1.063	1.083	1.096	1.095	1.104
2	0.564	0.773	1.073	1.049	0.558	0.780	1.062	1.057	0.585	0.793	1.112	1.076	1.089	1.090	1.094
3	0.498	0.833	1.099	1.051	0.501	0.846	1.106	1.067	0.512	0.825	1.131	1.041	1.085	1.081	1.088
4	0.442	0.351	1.012	1.030	0.445	0.356	1.018	1.046	0.449	0.339	1.027	0.995	1.074	1.079	1.075
5	0.557	0.462	1.030	1.030	0.553	0.451	1.023	1.008	0.581	0.483	1.074	1.079	1.067	1.073	1.072
6	0.471	0.472	0.987	1.001	0.483	0.465	1.011	0.987	0.496	0.510	1.039	1.082	1.064	1.033	1.026
mean	0.569	0.664	1.036	1.031	0.571	0.667	1.040	1.033	0.591	0.685	1.074	1.059	1.079	1.075	1.077

Table 9.11: DCR and DCR Ratios for LYP100 with No Hardening

	LYP_α		$\frac{LYP_\alpha}{LYP_\alpha}$		LYP_{40}		$\frac{LYP_{40}}{LYP_\alpha}$		LYP_{45}		$\frac{LYP_{45}}{LYP_\alpha}$		P_R		
Story	TB	M	TB_R	M_R	TB	M	TB_R	M_R	TB	M	TB_R	M_R	α	40	45
1	0.850	1.023	1.000	1.000	0.871	1.044	1.024	1.020	0.902	1.109	1.061	1.084	1.000	1.015	1.024
2	0.523	0.717	1.000	1.000	0.558	0.705	1.066	0.983	0.555	0.760	1.060	1.060	1.000	1.012	1.017
3	0.438	0.797	1.000	1.000	0.458	0.767	1.045	0.962	0.453	0.790	1.036	0.991	1.000	1.008	1.011
4	0.439	0.324	1.000	1.000	0.438	0.288	0.996	0.890	0.455	0.309	1.035	0.956	1.000	1.011	1.012
5	0.530	0.434	1.000	1.000	0.539	0.408	1.016	0.940	0.561	0.475	1.058	1.092	1.000	1.018	1.022
6	0.511	0.488	1.000	1.000	0.541	0.526	1.059	1.077	0.557	0.557	1.090	1.140	1.000	0.987	0.985
mean	0.549	0.631	1.000	1.000	0.567	0.623	1.034	0.979	0.580	0.666	1.056	1.054	1.000	1.009	1.012

Table 9.12: DCR and DCR Ratios for LYP100 with Hardening

	$LYP_{\alpha H}$		$\frac{LYP_{\alpha H}}{LYP_{\alpha}}$		LYP_{40H}		$\frac{LYP_{40H}}{LYP_{\alpha}}$		LYP_{45H}		$\frac{LYP_{45H}}{LYP_{\alpha}}$		P_R		
Story	TB	M	TB_R	M_R	TB	M	TB_R	M_R	TB	M	TB_R	M_R	α	40	45
1	0.889	1.114	1.046	1.089	0.916	1.161	1.078	1.135	0.957	1.218	1.126	1.190	1.354	1.375	1.382
2	0.618	0.847	1.182	1.182	0.648	0.870	1.237	1.213	0.657	0.881	1.256	1.230	1.324	1.340	1.342
3	0.544	0.954	1.243	1.197	0.546	0.987	1.248	1.238	0.557	0.961	1.273	1.206	1.310	1.321	1.323
4	0.487	0.364	1.109	1.124	0.499	0.376	1.136	1.163	0.502	0.372	1.142	1.151	1.270	1.284	1.282
5	0.616	0.483	1.162	1.112	0.631	0.496	1.190	1.142	0.637	0.528	1.201	1.215	1.244	1.266	1.268
6	0.510	0.506	0.999	1.036	0.550	0.537	1.076	1.100	0.560	0.584	1.097	1.196	1.250	1.272	1.220
7	0.611	0.711	1.123	1.123	0.632	0.738	1.161	1.165	0.645	0.757	1.182	1.198	1.292	1.310	1.303

Table 9.13: Six-Story Max Base Shear (kN)

Hardening	Model #	(kN) V_b
No	$A36_{\alpha}$	5035
	$A36_{40}$	5000
	$A36_{45}$	5040
Yes	$A36_{\alpha H}$	5449
	$A36_{40H}$	5404
	$A36_{45H}$	5444
No	LYP_{α}	4662
	LYP_{40}	4706
	LYP_{45}	4742
Yes	$LYP_{\alpha H}$	6040
	LYP_{40H}	6089
	LYP_{45H}	6138

Chapter 10

COMPARISON BETWEEN *OPENSEES* AND *ABAQUS* FOR TWO SIX-STORY PROTOTYPE SPSWS

10.1 Introduction

This chapter presents a comparison between *OpenSees* and *ABAQUS* response history analyses of two prototype six-story SPSWs. This is partly intended to be a comprehensive validation exercise for the new material model presented in Chapter 8. More generally it is an assessment of how well strip models, when compared to shell models, predict the multi-story SPSW behavior and member forces. It is also a closer examination of the VBE demands and story drifts predicted using response history analyses of multi-story SPSWs, and how these compare with pushover analyses. The performance of the LYP web plate SPSWs is of particular interest because capacity design procedures may over predict VBE demands for stocky web plates.

It has been well established that pushover analyses are often not a reliable predictor of system behavior under dynamic loading, particularly if higher modes are prevalent in the response. A six story structure was chosen because it is tall enough to have significant higher mode contribution to the response without the computational expense of a very tall structure. Thus the number of ground motions and web plate models can be expanded.

Two variations of an otherwise identical SPSW design are analyzed. These are:

1. six story SPSW with slender A36 type web plates throughout
2. six story SPSW with stocky, low strength LYP100 type web plates throughout

The designs have the same member sizes, bay size, story height, etc. Fig. 10.1 shows each SPSW design and indicates the thickness of the web plates at each story. The story height

for both walls is 3.96 m (13 ft) and the bay width is 4.57 m (15 ft). The columns from the floor below are transitioned at approximately 1.22 m (4 ft) above the HBE centerline. The HBE and VBE sizes for both walls are identical, only the plate thickness and web plate material properties are altered.

Each SPSW is designed in accordance with the AISC Seismic Specification to lateral forces determined from the ASCE-7 equivalent lateral force procedure. The VBEs are permitted to yield at their base, but otherwise are capacity designed and proportioned using capacity design methods. The HBEs are sized to preclude flexural hinging between the beam ends and to satisfy the minimum flexural stiffness per the *Provisions*. Story masses, plan dimensions, and dead and live loads were consistent with the SAC buildings with the 6 story building being similar to the 9 story building. The SPSWs were designed for a site class D soil and adjusted maximum considered earthquake spectral response parameters at 0.2 and 1 second periods, S_{MS} and S_{M1}, were 1.61g and 1.19g respectively. Resulting design spectral acceleration parameters at 0.2 and 1 seconds, S_{DS} and S_{D1}, were 1.07g and 0.79g, respectively.

There are several broad objectives for these analyses. They are:

- to compare and contrast the performances of the new SPSW truss element material model and the existing *Hysteretic* material model to the equivalent *ABAQUS* shell element model and identify any limitations
- to compare and contrast the performance of SPSWs with slender web plates and stocky web plates
- to compare and contrast VBE demands and story drift using response history analyses with those from pushover analyses

10.1.1 Limitations of Adopted Methodology

There are limitations in the adopted methodology. Firstly, the response of the *ABAQUS* models is assumed to be a benchmark against which the accuracy of the *OpenSees* truss

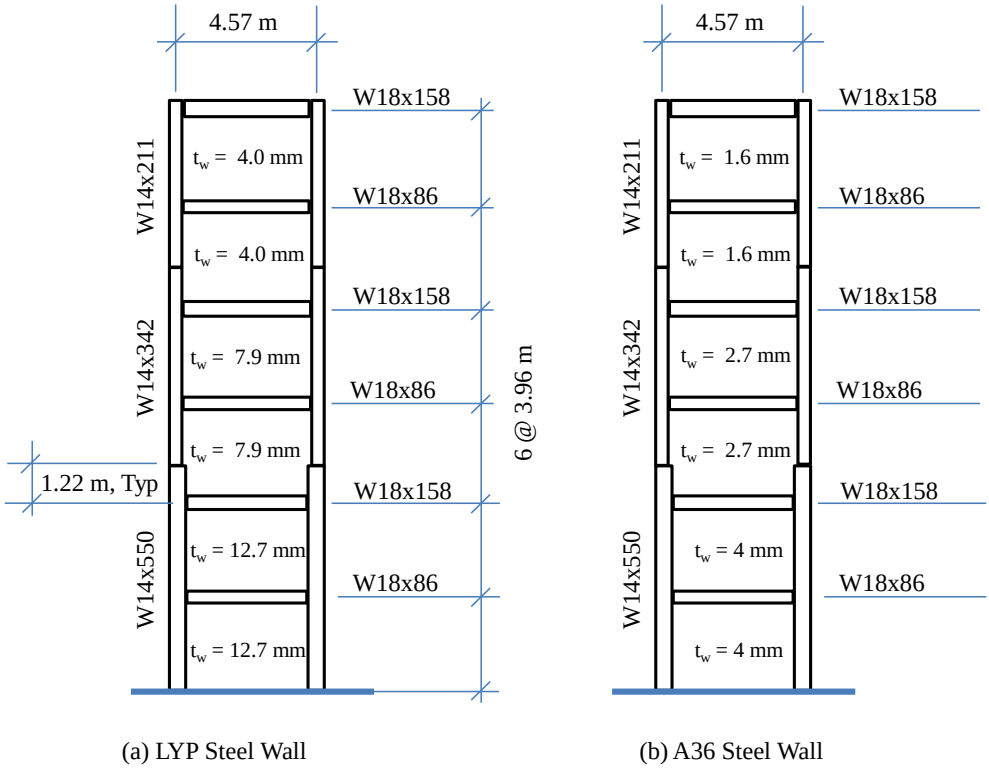

(a) LYP Steel Wall (b) A36 Steel Wall

Figure 10.1: Dimensions and member sizes for A36 an LYP Walls

models is measured. This implies that the *ABAQUS* model accurately represents the "real" structure, which may not be the case. However, the *ABAQUS S4R* shell element has proved to be a reliable predictor of strength and stiffness of an actual web plate under cyclic load. With careful implementation, the *ABAQUS* shell model will be a better approximation of a real structure than any available strip model. Secondly, the analyses are conducted for a limited number of ground motions and SPSW configurations. It is not comprehensive enough to draw conclusions about performance of other configurations, but it is believed to be sufficient in detail and scope to make observations about average performance quantities and behavioral trends (drifts, DCRs, etc) with reasonable certainty.

10.2 Input Ground Motions

Each wall is analyzed over 12 seconds of the strong motion portion of eight SAC-97 LA scaled ground motions developed by Somerville et. al. (1997). From FEMA 355C:

The ground motions are scaled such that, on average, their spectral values match with a least square error fit to the United States Geological Surveys (USGS) mapped values at 0.3, 1.0, and 2.0 seconds, and an additional predicted value at 4.0 seconds. The weights ascribed to the four period points are 0.1 at the 0.3 second period point and 0.3 for the other three period points. The target spectra provided by USGS are for the SB/SC soil type boundaries, which have been modified to be representative for soil type SD (stiff soil - measured shear wave velocity between 600 to 1200 ft/sec).

Since the primary interest is peak member demand, for computational efficiency only the strong motion portion is analyzed. The first 0.5 seconds of each 12 second ground motion segment is de-amplified with a smooth sinusoidal ramp function so that the acceleration record starts at zero g. Four records are taken from the 2% in 50 year hazard level suite; these are:

1. Kobe 1995 (LA21: 6 to 18 seconds)
2. Northridge 1994 (LA27: 3 to 15 seconds)
3. Tabas 1974 (LA29: 7 to 19 seconds)
4. Palos Verdes (simulated) (LA37: 7 to 19 seconds)

Four ground motions are taken from the 10% in 50 year suite; These are:

1. Imperial Valley 1979 (LA05: 2 to 14 seconds)
2. Landers 1992 (LA10: 11 to 23 seconds)
3. Loma Prieta 1989 (LA11: 2 to 14 seconds)

4. North Palm Springs 1992 (LA19: 0 to 12 seconds)

The 2% in 50 year ground motions are used to assess the performance of the walls under extreme events where drift demands are very large. The 10% in 50 year motions are used to assess the performance of the SPSWs when the demands are moderate, with maximum drifts typically in the range 0.75% to 1.5%. The motions are purposefully selected to have different frequency content to elicit a variety of responses. The ground motion acceleration histories for the 10% in 50 year and 2% in 50 year events are shown in Figs. 10.2 and 10.3. Note the different vertical axis scales on the ground motion traces. Also, some of the 10% in 50 year motions appear to have stronger ground shaking than many of the 2% in 50 year motions. Notably, the North Palm Springs ground motion (Fig. 10.2(d)) has stronger shaking than either Northridge, Tabas or Palos Verdes, although the frequency content is noticeably shifted towards very short periods.

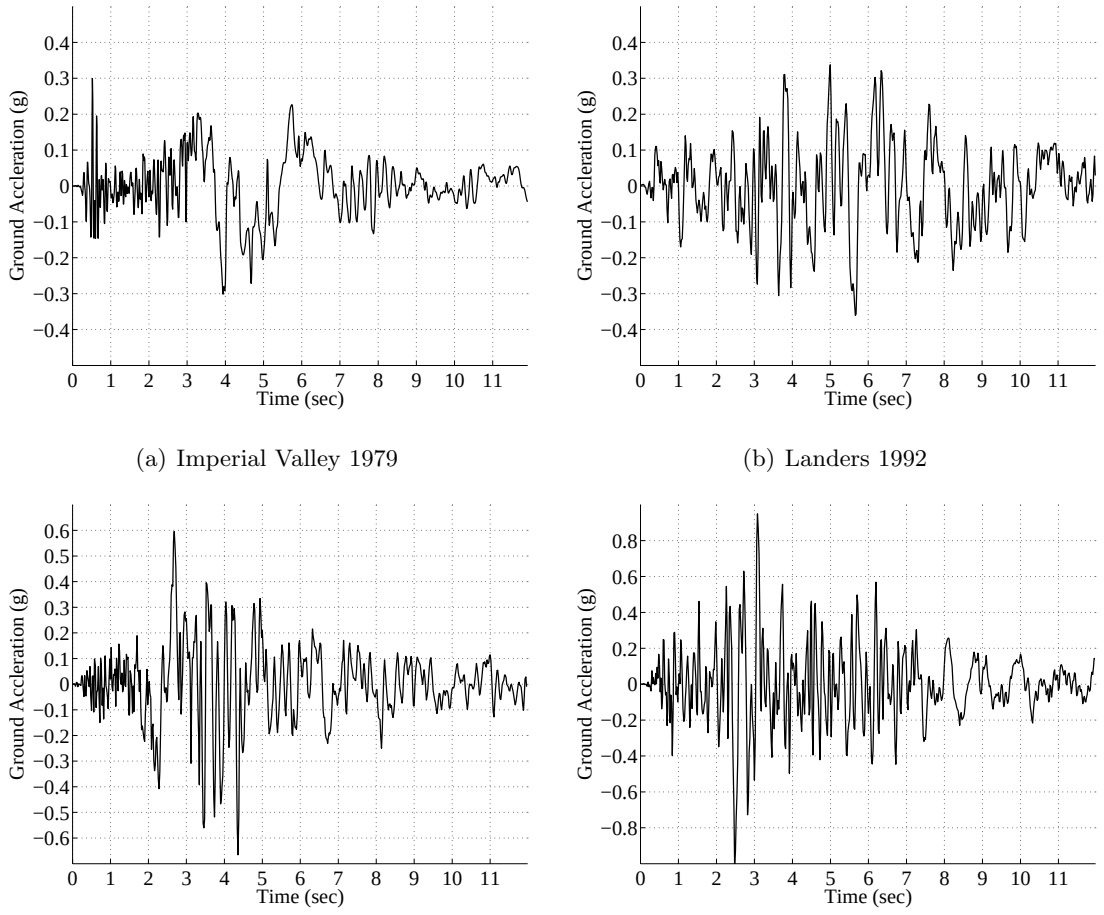

(a) Imperial Valley 1979

(b) Landers 1992

(c) Loma Prieta 1989

(d) North Palm Springs 1986

Figure 10.2: 10% in 50 year Ground Motions

10.3 Finite Element Models

In order to make an objective comparison between the *ABAQUS* and *OpenSees* response quantities for the different web plate models (member DCRs, drifts, etc.), it is important to model all other aspects of the SPSWs in the same or similar manner. Accordingly, except for the web plates, the *ABAQUS* and *OpenSees* models have identical geometry, material properties, member sizes, gravity loads, added masses, rigid offsets, plastic hinge locations and applied loading. However, the element formulation, effective damping and solution algorithms are different.

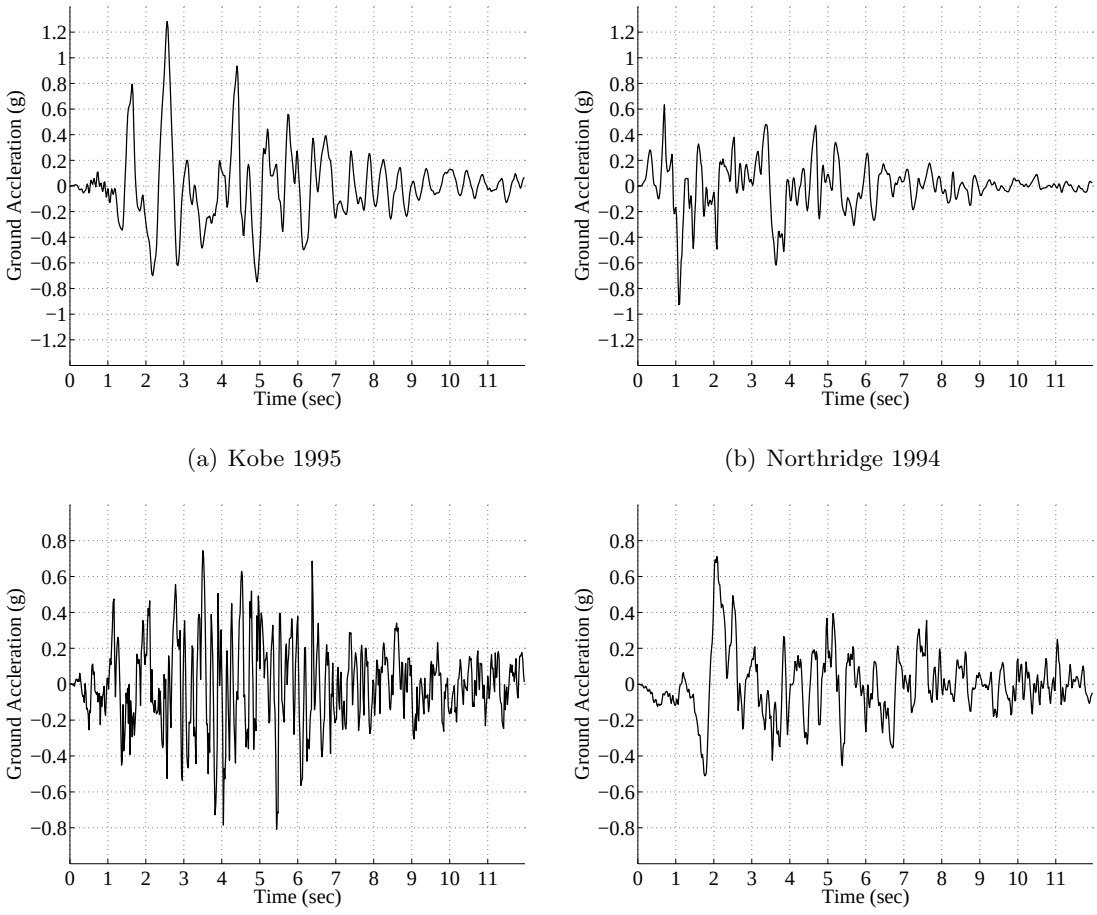

(a) Kobe 1995

(b) Northridge 1994

(c) Tabas 1974

(d) Palos Verdes (simulated)

Figure 10.3: 2% in 50 year Ground Motions

In both the *ABAQUS* and *OpenSees* analyses the VBEs are modeled as elastic, shear-deformable beam-columns, except at the base where they may form a plastic hinge. The HBEs are permitted to hinge at their ends. Rigid offsets are modeled between the web plate edge and the face of the boundary members. Neither the *ABAQUS* nor *OpenSees* models include panel zone deformation. All models include a continuous W14x550 leaning column with lumped translational masses at the story level. The leaning column is oriented with the weak axis in the plane of the SPSW and is intended to represent the stiffness provided

Table 10.1: Added Mass

Mass	**(kg)**
M	2×10^5
M_R	2×10^5

by the gravity columns. Distributed translational masses of the SPSW is included in both *ABAQUS* and *OpenSees* models at each node by lumping tributary masses at each element end node. At each level, concentrated vertical loads are applied at the leaning columns to account for floor weight tributary to the SPSW. Vertical concentrated loads are also applied at the intersection of the SPSW beam-column joints to account for weight tributary to the VBEs at each level. A vertical uniformly distributed load is applied to each HBE at each level to account for tributary slab weight. In all models, gravity load is applied before the ground motion, and it is maintained throughout the duration of the response history. The masses and applied gravity loads are shown graphically in Fig. 10.4 and the magnitudes of the added masses and gravity loads are shown in Tables 10.1 and 10.2. For simplicity, the self weight of the SPSW components is not gravity activated in the gravity load case for either the *ABAQUS* models or the *OpenSees* models.

Damping in *ABAQUS* and *OpenSees* is handled differently. In the six-story *ABAQUS* analyses, damping is introduced at the element level using bulk viscosity. In *OpenSees*, Rayleigh damping is used. These will be discussed a little more in the following sections.

As previously mentioned, both the *ABAQUS* and *OpenSees* models incorporate rigid offsets between the VBEs and web plate elements. In *OpenSees* the offset is modeled using rigid elements that connect the boundary member nodes to the ends of the web plate truss elements. In *ABAQUS* the same is achieved through use of multi-point edge-to-surface constraints. The offsets are located half of the HBE or VBE member depth away from the

Table 10.2: Distributed and Concentrated Gravity Loads

Load	**(N or N/m)**
P_L	1.6×10^5
P_{LR}	1.6×10^5
w	4×10^4
w_R	4×10^4

respective center-line of the elements. The member connectivity and offsets for the models are shown in Fig. 10.6. It is clear that the connection of the *OpenSees* truss elements to the VBEs will introduce a concentrated bending moment in the VBE. The magnitude of this was computed and is typically less than 1% of the member capacity. It can result in an error in computed flexural DCR, but when averaging over multiple locations and ground motions, the error is entirely obscured by noise i.e., differences in integration scheme, solution method, discretization, rounding errors, etc.

10.3.1 OpenSees Models

Two versions of the *OpenSees* SPSW truss element model are analyzed. The first, model type H, uses the existing *OpenSees Hysteretic* material model with the truss elements inclined per Eq. F5-2 of the *Provisions*. The second, model type S, uses the new SPSW web plate material model developed in Chapter 7 with truss elements inclined at 45 degrees. Fig 10.8 shows the *OpenSees* model H (for A36 and LYP100) and model S.

The *OpenSees* VBEs and HBEs are modeled using displacement based nonlinear beam-column elements and $n = 3$ Gauss-Labatto quadrature. The member sections are analyzed with 16 fibers across the width of the flange, 16 fibers through the depth of the web, 4 fibers through the thickness of the flange and 2 through the thickness of the web.

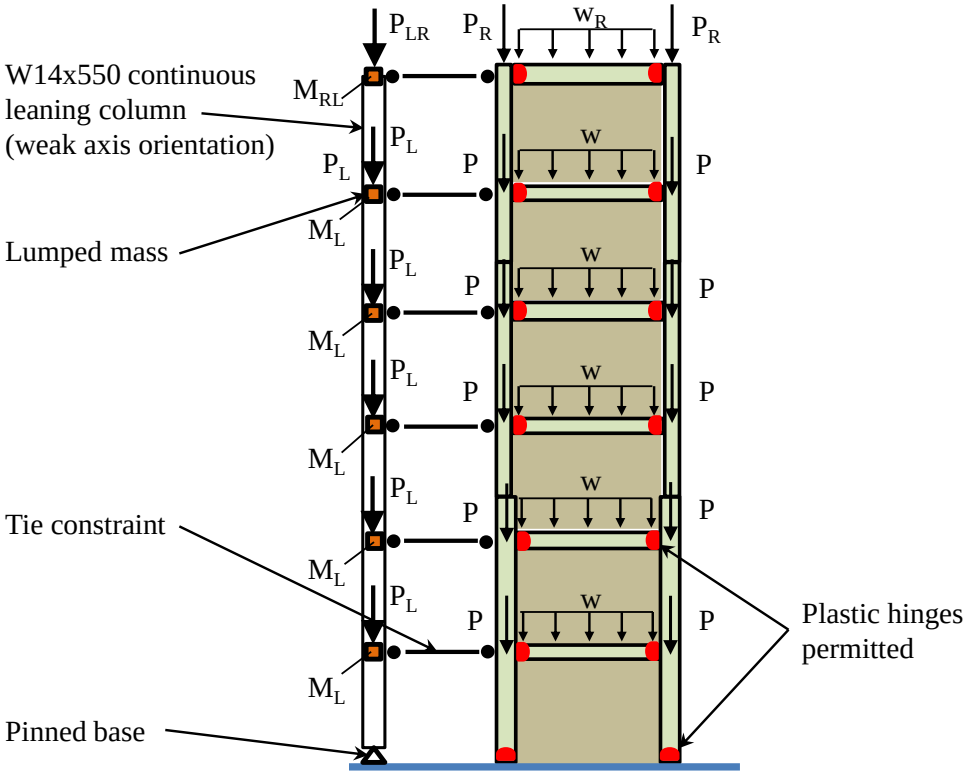

Figure 10.4: Gravity loads and added masses for six-story SPSWs

OpenSees Solution Strategy

All *OpenSees* models utilize several solution algorithms for obtaining a converged solution, these include Newton, Modified Newton, Broydon and Newton Line-Search. Displacements are integrated using the *OpenSees* Newmark average acceleration method ($= 0.5$, $\gamma = 0.25$) with a convergence tolerance of 1×10^{-8}. The maximum time step permitted is 0.002 seconds.

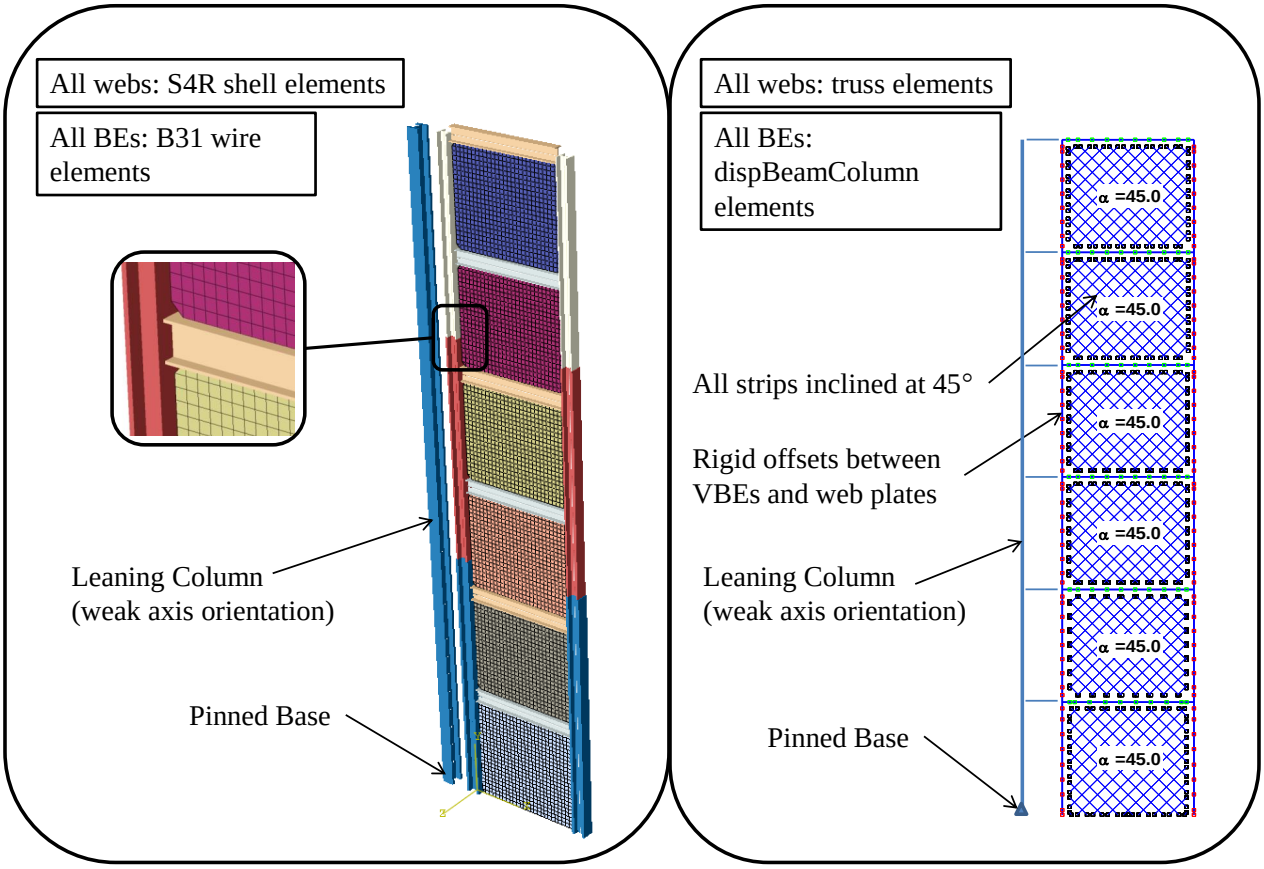

Figure 10.5: *ABAQUS* and *OpenSees* models of six-story SPSW

Viscous Damping

Damping in the *OpenSees* models is applied using Rayleigh (mass and stiffness proportional) damping. For the six-story models, 3% damping is applied to the first and third modes. This will result in damping lower than 3% for the 2nd mode and higher than 3% for modes higher than three. The majority of the effective structural damping will come from the hysteretic damping resulting web plate yielding and, to a lesser extent, from beam-column hinging.

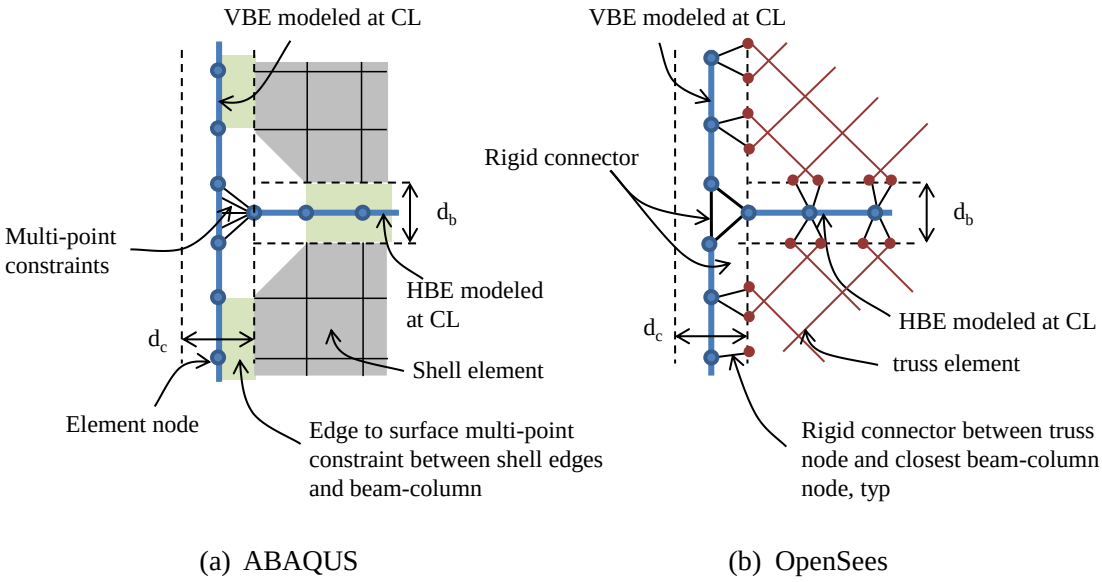

(a) ABAQUS (b) OpenSees

Figure 10.6: Element connectivity and rigid offsets

Type H Models

The hysteretic response of the *OpenSees* type *H* model web plates are shown in Fig. 10.9. For these models isotropic hardening is assumed. The envelope used to define the cyclic hardening is determined using the values used in Section 9.8 of Chapter 9 for the pushover analyses. i.e., at 2% drift (roughly 1% strain) the A36 web plate hardens to $1.15R_yF_y$, approximately 371 MPa, and the LYP100 steel hardens to $1.58R_yF_y$, approximately 174 MPa. The transition to these stress magnitudes is modeled with a tri-linear approximation for implementation in *OpenSees*. The *PinchX* and *PinchY* parameters for the *Hysteretic* material model in *OpenSees* were set to 0.8 and 0.2 respectively to approximate hysteretic pinching characteristic of SPSWs.

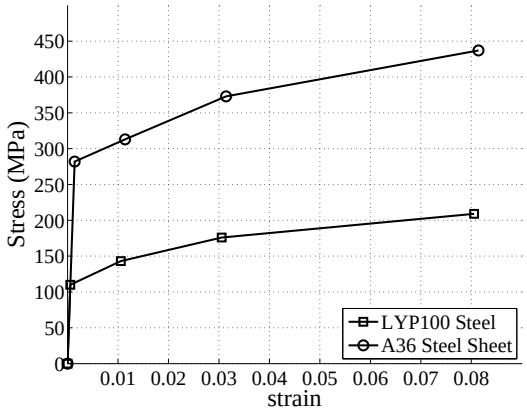

Figure 10.7: Web plate material properties

A common practice in web plate modeling is to use the coupon data to describe the cyclic backbone of the material. Therefore, an additional set of analyses is run for the four 10% in 50 year ground motions using the Hysteretic model and a hardening envelope defined by the monotonic stress-strain behavior. Both of these can be seen in Fig. 10.9(b) where *Backbone* is based on the findings of Chapter 9 and *Coupon* is based on the assumed monotonic stress-strain response.

Type S Models

Model type S uses the proposed web plate material model $SPSW - WP$ from Chapter 8 and the material properties shown in Fig. 10.7. Isotropic hardening is selected for both the A36 and LYP100 web plates. The pinching and hardening parameters are history dependent and are computed internally by the material model throughout the response history.

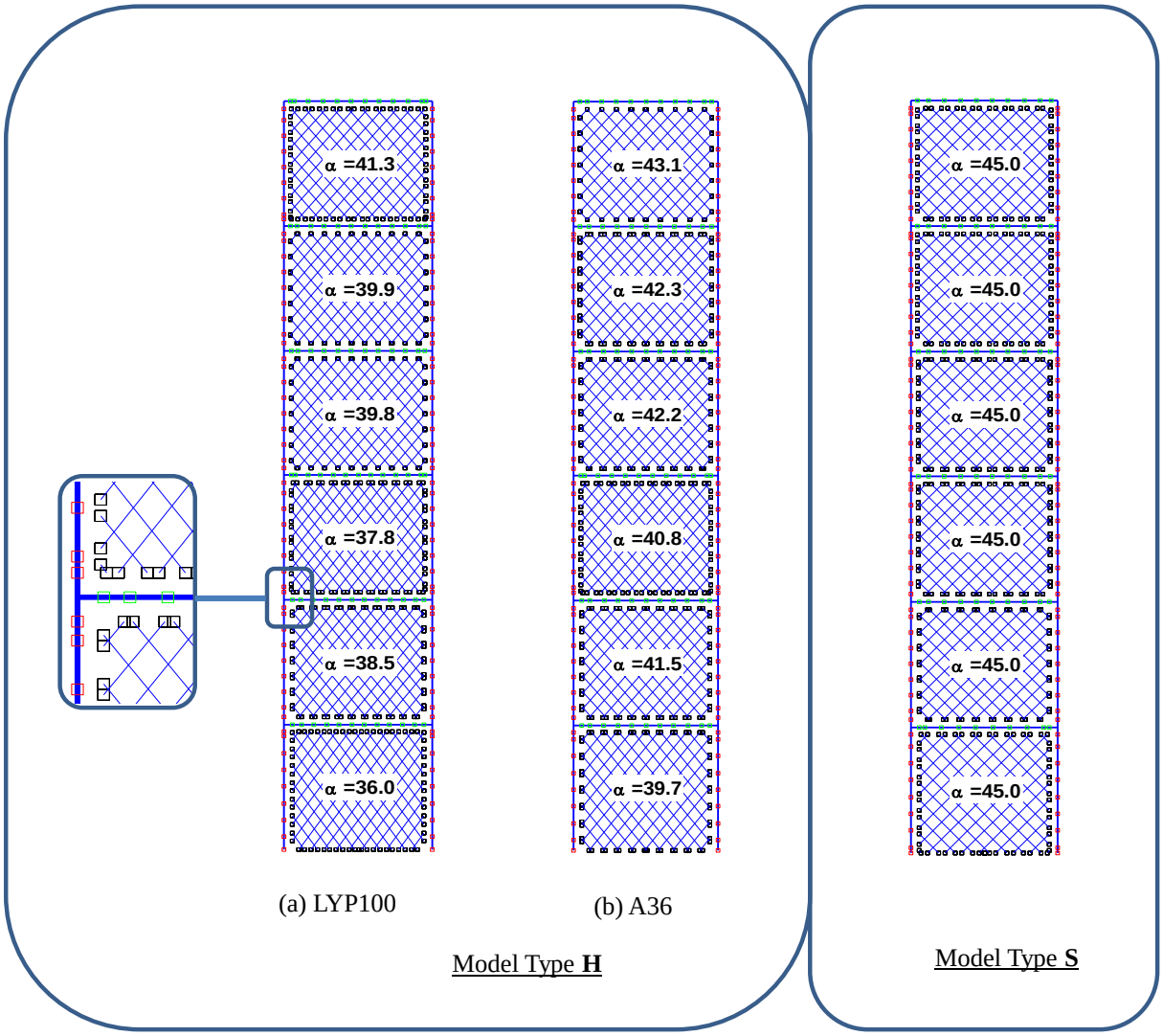

Figure 10.8: *OpenSees* SPSW models showing truss element inclination

10.3.2 ABAQUS Models

As with the single panel models used in the material model calibration and the experimental modeling, the solution strategy adopted for the six-story *ABAQUS* SPSWs uses explicit dynamic time stepping. However, unlike the single panel models, the six-story model mass is not scaled up to reduce the stable time increment. A description of the dynamic explicit

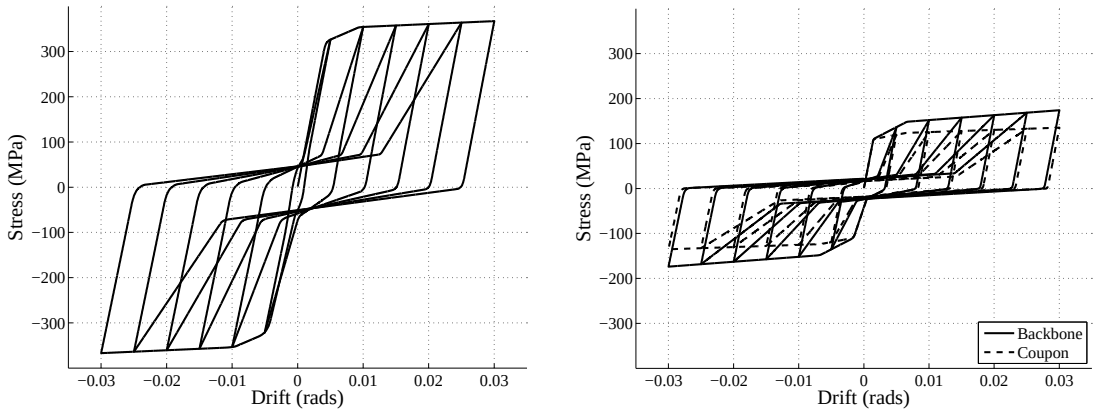

(a) A36 (b) LYP100

Figure 10.9: *OpenSees* single panel response to symmetric cyclic loading using the *Hysteretic* material for (a) A36 steel with $f_y = 322$ MPa and (b) LYP100 steel with $f_y = 110$ MPa. Base reaction normalized by $0.5Lt_w$

method is detailed in Section 3.1.3.

Damping

Damping is handled in *ABAQUS explicit* at the element level through linear and nonlinear bulk viscosity. In the six-story analyses, the quadratic bulk viscosity coefficient, b_2, was set to zero. The linear bulk viscosity coefficient, b_1, was set to 0.05, resulting in 5% critical damping, but this is only applied to the dilatational modes of the elements. The damping from bulk viscosity is a function of the volumetric strain rate, so pure shear straining will induce no effective damping at the element level. As with the *OpenSees* models, the majority of the effective structural damping results from material hysteresis. The slightly elevated linear damping used for the *ABAQUS* analyses is an attempt to account for this difference. It should be possible to determine a damping coefficient that provides the best match with the assumed *OpenSees* damping, by examining the rate of decay in displacement amplitude of materially linear (no yielding) six-story SPSW model subjected to a single pulse load. Due to restrictions in available time, this was not done.

Element Formulation

The *ABAQUS* models utilize reduced integration *S*4*R* shell elements for the web plates and *B*31 shear deformable wire elements for the VBEs and HBEs. The wire element sections are defined by a series of points in the cross-section of the beam. Each fiber is integrated numerically along the axis of the section so that the section can be used with nonlinear material behavior. The sections comprise five integration points (default) across the beam flanges and five through the web depth. The web plates are tied to the boundary elements using multi-point constraints.

10.4 Properties of Web Plate Materials used in Analyses

The assumed A36 and LYP100 steel material properties are shown in Fig. 10.7. In both cases, and for both the *ABAQUS* and *OpenSees* models, the material is modeled as piece-wise linear. The A36 steel stress-strain curve is loosely based on published data and is representative of typical A36 steel sheet or plate. The LYP100 stress-strain curve follows that provided by Zirakian and Zhang (2012).

In both the *ABAQUS* models and *OpenSees* type *S* models, the A36 web plate material is modified to have a yield strength of 282 MPa (rather than 322 MPa). The yield stress at $\epsilon_{sh} = 0.012$ (approximately the onset of strain hardening) is 322 MPa. This simply facilitates a better tri-linear approximation of the stress-strain response beyond ϵ_{sh}. The removal of the yield plateau has negligible impact on the cyclic response. A similar approach was adopted for modeling the materials in the hardening study carried out in Chapter 7.

10.5 Results

The results of the analyses are presented in tabular format and as a series of time-drift traces for comparing drift response. There are three objectives in the examination of the response data. These were introduced at the beginning of the chapter, but they will be reiterated

here. These are: (1) to assess the performance of the new *OpenSees* material model using *ABAQUS* shell models as the benchmark, (2) to assess and contrast the performance of SPSWs modeled with slender and stocky web plates, and (3) to contrast the predicted drifts and VBE demands from response history analyses to those from pushover analyses.

The demand capacity ratios (DCRs) are tracked throughout the entire response history using the AISC compression-flexure interaction equations; H1-1a and H1-1b. These are repeated here (excluding the weak-axis term) as Eq. 10.1 and 10.2 for convenience.

For $\frac{P_r}{P_c} \geq 0.2$

$$\frac{P_r}{P_c} + \frac{8}{9}\left(\frac{M_{rx}}{M_{cx}}\right) \leq 1.0 \tag{10.1}$$

For $\frac{P_r}{P_c} < 0.2$

$$\frac{P_r}{2P_c} + \left(\frac{M_{rx}}{M_{cx}}\right) \leq 1.0 \tag{10.2}$$

Fig. 10.10 shows the DCR sampling locations and associated nomenclature at an arbitrary story in the SPSW.

In the *ABAQUS* models, the member demands are sampled at the integration point located at the center of the element length approximately 75 mm (3 in) above the top of the HBE for the BR and BL sections and 75 mm below the HBE flange for the TR and TL sections. This differs slightly from the OpenSees models that sample internal member demands at the 1st and 3rd Gauss-Labatto integration point for the bottom and top elements respectively. This can result in as much as 4-5% difference in the reported bending moment demand but typically less than 2% difference in the overall AISC flexure-compression interaction value.

Only the maximum interaction value recorded over the entire history is reported at each of the section locations indicated on Fig. 10.10. As for the pushover analyses presented in Chapter 8, these are at the bottom, middle and top of each VBE. A yield stress of 379 MPa (55 ksi) is used to compute the VBE strength with no strength reduction factor. i.e., $\phi =$

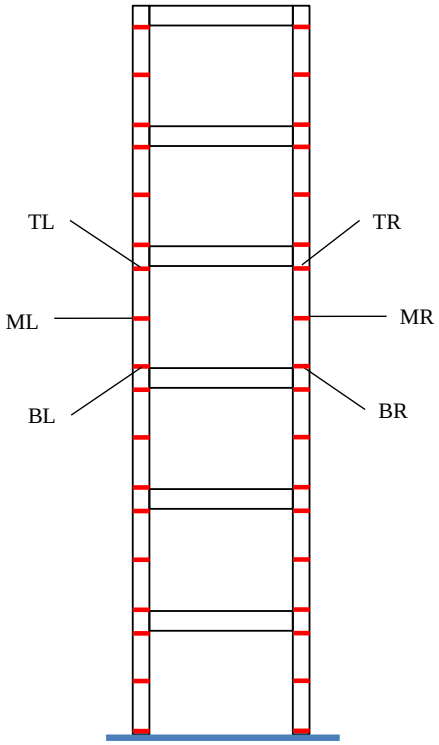

Figure 10.10: DCR sample locations at each floor (labeling nomenclature indicated at 3rd floor)

1.0.

10.5.1 Demand Capacity Ratios (DCR)

For the purposes of gauging the accuracy of the new material model, the relationship between the *ABAQUS* and *OpenSees* predicted DCR at each section location (BL, BR, ML, MR, TL and TR) is of interest. However, in order to consolidate data, only the mean and standard error (CV) will be reported in the tables.

In the equations that follow, DCR_{XX} is the maximum DCR computed at location XX over the duration of the response history. Quantities denoted R_{DCR} are the ratio of the *OpenSees* predicted DCR to that predicted by *ABAQUS*.

The average value of maximum DCR at story "j" for the ends (TB: top & bottom) and middle (M: middle) of the VBEs is computed using Eqs. 10.3 and 10.4 respectively. The closer DCR_{TB} is to unity the higher the likelihood of a plastic collapse mechanism. Eq. 10.4 is a measure of the potential for a within-span hinge in the VBE. In the equations that follow, i is the ground motion number, n is the total number of ground motions and j is the story number.

For top and bottom of story j, ground motion i:

$$DCR^i_{TBj} = \frac{1}{4}\left(DCR_{TL} + DCR_{TR} + DCR_{BL} + DCR_{BR}\right)^i_j \tag{10.3}$$

For the midspan locations:

$$DCR^i_{Mj} = \frac{1}{2}\left(DCR_{ML} + DCR_{MR}\right)^i_j \tag{10.4}$$

The maximum DCR in story j may be computed per Eq. 10.5

$$DCR^i_{maxj} = max\left[DCR_{TL}, DCR_{TR}, DCR_{BL}, DCR_{BR}, DCR_{ML}, DCR_{MR}\right]^i_j \tag{10.5}$$

This averaging process obviously removes some of the variation observed when comparing demands at the section level. However, these mean and maximum response values

are a more succinct representation of the net demand and are sufficiently localized (at the story level rather than at the section level) for assessing model performance (*OpenSees* vs *ABAQUS*) and system performance (A36 vs LYP100).

Before averaging over the number of ground motions, each of these may be normalized by the equivalent quantity determined from the *ABAQUS* analyses. That is, for VBE top and bottom, story j, ground motion i:

$$R^i_{DCR_{TBj}} = \frac{\left(DCR^i_{TBj}\right)_{OS}}{\left(DCR^i_{TBj}\right)_{ABQ}} \tag{10.6}$$

For midspan:

$$R^i_{DCR_{Mj}} = \frac{\left(DCR^i_{Mj}\right)_{OS}}{\left(DCR^i_{Mj}\right)_{ABQ}} \tag{10.7}$$

These quantities indicate the relative difference between the mean DCRs computed from *OpenSees* and *ABAQUS*. A similar calculation may be done for DCR_{max} quantity, thus:

$$R^i_{DCR_{maxj}} = \frac{\left(DCR^i_{maxj}\right)_{OS}}{\left(DCR^i_{maxj}\right)_{ABQ}} \tag{10.8}$$

The mean (over all ground motions) of the DCR ratios for story j are computed using the following:

$$R_{DCR_{TBj}} = \frac{1}{n}\left(\sum_{i=1}^{n} R^i_{DCR_{TBj}}\right) \tag{10.9}$$

$$R_{DCR_{Mj}} = \frac{1}{n}\left(\sum_{i=1}^{n} R^i_{DCR_{Mj}}\right) \tag{10.10}$$

$$R_{DCR_{maxj}} = \frac{1}{n}\left(\sum_{i=1}^{n} R^i_{DCR_{maxj}}\right) \tag{10.11}$$

The average R_{DCR} values over all stories and all ground motions are then:

$$R_{DCR_{TB}} = \frac{1}{6}\left(\sum_{j=1}^{6} R_{DCR_{TBj}}\right) \tag{10.12}$$

$$R_{DCR_M} = \frac{1}{6}\left(\sum_{j=1}^{6} R_{DCR_{Mj}}\right) \tag{10.13}$$

$$R_{DCR_{max}} = \frac{1}{6}\left(\sum_{j=1}^{6} R_{DCR_{maxj}}\right) \tag{10.14}$$

The coefficient of variation (CV) is used as another measure of the predictive quality of Models S and H. For any given normalized quantity (e.g., $R_{DCR_{TB}}$), an unbiased estimate of CV (assuming normally distributed data) is as follows:

$$CV = \frac{\sigma}{\mu}\left(1 + \frac{1}{4n}\right) \tag{10.15}$$

where n is the sample size, σ is the sample standard deviation and μ is the mean. In the tables that follow, n may be the number of ground motions or the number of stories. It will be obvious from the structure of the table which applies. In some cases the CV is computed across certain ground motions and the average CV (over the number of stories) is presented at the bottom of the table.

10.5.2 Discussion of DCR results

Comparing Model S and Model H over all Ground Motions

Table 10.3 shows the $R_{DCR_{max}}$ values computed using Eq. 10.5 for P-M, compression and flexural interaction, where the averaging is performed over all eight ground motions and over all stories. For model S (with new material model), the P-M interaction ratio of *OpenSees* to *ABAQUS* for the A36 SPSW has a mean of 0.969 and a CV of 0.085. For model H the mean and CV are 1.029 and 0.107. The S and H models predict the mean DCRs with approximately equal accuracy, though there is more spread in the H model estimates. By contrast, the S model provides a significant improvement in the prediction of the *ABAQUS* maximum DCR values for the LYP100 SPSW, where the mean and CV are 1.005 and 0.086. The H model mean and CV are 1.182 and 0.174 respectively. In an average sense, the S model is slightly better at predicting the A36 SPSW demands but considerably better at predicting the LYP100 demands.

Table 10.3: $R_{DCR_{max}}$ values ($OpenSees/ABAQUS$) for $OpenSees$ models S and H. Averaging performed over all ground motions and all stories

Wall Type	Int	Model S		Model H	
		Mean	CV	Mean	CV
All	P-M	0.986	0.085	1.106	0.151
	P_u/P_n	0.987	0.059	1.108	0.094
	M_u/M_n	1.033	0.145	1.112	0.181
A36	P-M	0.969	0.092	1.029	0.108
	P_u/P_n	0.974	0.067	1.081	0.082
	M_u/M_n	0.958	0.150	1.057	0.130
LYP100	P-M	1.004	0.072	1.182	0.151
	P_u/P_n	0.999	0.053	1.135	0.101
	M_u/M_n	1.055	0.125	1.166	0.208
overall mean & CV		**0.996**	**0.094**	**1.180**	**0.134**

Comparing LYP100 and A36 Type H Models Under Pushover Analyses

Table 10.4 shows the results of pushover analyses for the two SPSWs using the type H model. For this comparison the Type H model uses 45 degree truss elements and accounts for hardening with the factor β_H introduced in Chapter 9. The values in columns labeled TB and M are computed in accordance with Eq. 10.3 and 10.4 except that the index i is for a single pushover case. The last two columns show the ratio of the LYP100 to A36 SPSW DCRs. Note that there is an increase in predicted DCR for the LYP100 SPSW when pushed to the same target drift, in this case 2% at the 1st floor. The average increase (approximately 11%) in story DCR for the LYP100 SPSW is lower than the ratio of the web plate strengths (approximately 26%) computed using $\beta_H t_w F_y$. This suggests that a large contribution of the demand comes from frame action. The important point to note here is that pushover analysis predicted DCRs that were on average 10-11% higher for the LYP100 SPSW than for the A36 SPSW.

Table 10.4: DCR_{TB} and DCR_M for Model H Under Pushover Analyses

	A36		LYP100		LYP100/A36	
Story	TB	M	TB	M	TB	M
1	0.922	1.156	0.957	1.218	1.038	1.054
2	0.585	0.793	0.657	0.881	1.123	1.111
3	0.512	0.825	0.557	0.961	1.088	1.165
4	0.449	0.339	0.502	0.372	1.118	1.097
5	0.581	0.483	0.637	0.528	1.096	1.093
6	0.496	0.510	0.560	0.584	1.129	1.145
				mean	**1.099**	**1.111**

Comparing the $LYP100$ SPSW and the $A36$ SPSW from $ABAQUS$ Response History Analyses

Table 10.5 presents DCR values for the $LYP100$ and $A36$ SPSWs computed from the $ABAQUS$ model results and separated into the two ground motion hazard levels. The values in columns labeled $A36$ and $LYP100$ are computed using Eqs. 10.3 and 10.4 where the index i runs from 1 to 4. The columns labeled $LYP100/A36$ are the ratio of the computed DCR values in the adjacent columns immediately to the left. It is clear from these results that the mean $ABAQUS$ response history analyses predict significantly lower DCRs for both the $A36$ and $LYP100$ SPSWs when compared with the pushover analysis (see Table 10.4). Also of note is the ratio of $LYP100$ SPSW to $A36$ SPSW DCRs. For the 10% in 50 year hazard, the $LYP100$ SPSW DCRs are between 77-79% of those for the $A36$ SPSW, even though the $LYP100$ system has higher net web plate strength $\beta_H t_w F_y$. Compare this with the 10-11% increase observed for the pushover case (see Table 10.4). A similar observation can be made for the 2% in 50 year hazard where the LYP100 SPSW DCRs are between 90-92% of those for the $A36$ SPSW system. The contradictory results of the pushover and response history analyses can be attributed to two things: 1) the stocky $LYP100$ plate has much greater energy dissipation on cyclic loading. This reduces peak drifts and consequently reduces the frame action contribution to the DCR, particularly for

the higher modes, and 2) the principal compressive stresses (and subsequently lower tensile yield stress) will tend to reduce the net transverse loads on the VBEs. Since the pushover analyses used the *Hysteretic* material, web plate compression is not present. The lower ratio observed for the reduced hazard level suggests that for hazard levels below 10% in 50 years, the ratio of $LYP100$ to $A36$ DCRs will be lower still. This has significant design implications.

Table 10.5: Mean $ABAQUS$ response history analyses DCR_{TB} and DCR_M values for A36 and LYP100 SPSWs at different hazard levels

Story	10in50						2in50					
	A36		LYP100		LYP100/A36		A36		LYP100		LYP100/A36	
	TB	M	TB	M	TB	M	TB	M	TB	M	TB	M
1	0.567	0.549	0.455	0.447	0.802	0.815	0.766	0.756	0.734	0.728	0.959	0.964
2	0.420	0.373	0.324	0.338	0.772	0.906	0.600	0.551	0.538	0.512	0.897	0.929
3	0.470	0.504	0.392	0.444	0.834	0.881	0.632	0.697	0.620	0.636	0.980	0.913
4	0.430	0.323	0.331	0.274	0.771	0.848	0.612	0.401	0.573	0.388	0.936	0.968
5	0.512	0.384	0.396	0.284	0.774	0.741	0.710	0.513	0.647	0.437	0.911	0.852
6	0.467	0.219	0.307	0.121	0.657	0.551	0.671	0.462	0.563	0.355	0.838	0.769
				mean	**0.768**	**0.790**				mean	**0.920**	**0.905**
				CV	**0.081**	**0.172**				CV	**0.057**	**0.088**

Comparing the $LYP100$ and the $A36$ Response History Analyses at 2% in 50 Year to Pushover Analyses

Table 10.6 shows the ratio the pushover DCRs to the mean DCRs obtained from the 2% in 50 year ground motions for the $A36$ and $LYP100$ SPSWs modeled in $ABAQUS$. A value below 1.0 indicates that the pushover analysis under-predicts the mean DCR obtained form the response history. The pushover analysis clearly over-predicts the DCRs in the lower

stories and under-predicts DCRs at mid-height. This is the result of higher modes, not captured by pushover analysis, influencing the response of the wall and ultimately the demands on the VBEs.

Table 10.6: Ratio of pushover DCRs to mean 2% in 50 year *ABAQUS* response history analysis DCRs

	A36		LYP100	
Story	TB	M	TB	M
1	1.204	1.530	1.304	1.672
2	0.976	1.440	1.221	1.722
3	0.810	1.184	0.899	1.512
4	0.734	0.846	0.876	0.960
5	0.818	0.941	0.985	1.208
6	0.739	1.104	0.995	1.644
mean	**0.880**	**1.174**	**1.047**	**1.453**
CV	**0.215**	**0.239**	**0.175**	**0.218**

OpenSees Model S Response History Analyses Results and Comparison With ABAQUS

Table 10.7 is similar to Table 10.5 except that the DCRs are obtained from *OpenSees* analyses of model S (new model). Table 10.8 presents the R_{DCR} values for the model S; the ratio of Model S DCRs to *ABAQUS* DCRs. The closer these values are to one the better the predictive capability of the Type S model. Model S tends to underestimate the DCRs for the $A36$ SPSWs and slightly overestimate those for the LYP100 SPSWs. The average R_{DCR} over all section locations, stories and hazard levels is 1.008.

Table 10.7: Model S: Mean *OpenSees* response history values of DCR_{TBj} and DCR_{Mj} for A36 and LYP100 SPSWs at different hazard levels

Story	10in50						2in50					
	A36		LYP100		LYP100/A36		A36		LYP100		LYP100/A36	
	TB	M	TB	M	TB	M	TB	M	TB	M	TB	M
1	0.555	0.558	0.481	0.485	0.867	0.870	0.775	0.790	0.758	0.791	0.978	1.002
2	0.379	0.356	0.334	0.354	0.882	0.994	0.534	0.520	0.535	0.533	1.001	1.025
3	0.392	0.526	0.383	0.481	0.978	0.915	0.551	0.724	0.564	0.727	1.025	1.004
4	0.405	0.368	0.330	0.324	0.816	0.880	0.574	0.438	0.568	0.430	0.990	0.981
5	0.500	0.487	0.399	0.345	0.797	0.708	0.662	0.591	0.636	0.523	0.960	0.885
6	0.459	0.186	0.300	0.115	0.653	0.616	0.622	0.353	0.579	0.320	0.930	0.905
				mean	**0.832**	**0.830**				mean	**0.981**	**0.967**
				CV	**0.136**	**0.176**				CV	**0.035**	**0.062**

Table 10.8: Model S: Ratio of mean *OpenSees* to *ABAQUS* response history analysis values $R_{DCR_{TBj}}$ and $R_{DCR_{Mj}}$ for $A36$ and $LYP100$ SPSWs at different hazard levels

Story	10in50				2in50			
	A36		LYP100		A36		LYP100	
	TB	M	TB	M	TB	M	TB	M
1	0.978	1.016	1.057	1.084	1.012	1.045	1.032	1.086
2	0.903	0.954	1.032	1.046	0.891	0.944	0.993	1.042
3	0.834	1.043	0.977	1.083	0.870	1.040	0.910	1.144
4	0.942	1.139	0.998	1.182	0.937	1.094	0.992	1.108
5	0.977	1.270	1.007	1.214	0.933	1.152	0.983	1.196
6	0.984	0.849	0.977	0.949	0.927	0.765	1.029	0.900
mean	**0.936**	**1.045**	**1.008**	**1.093**	**0.928**	**1.007**	**0.990**	**1.079**
CV	**0.065**	**0.146**	**0.033**	**0.091**	**0.055**	**0.142**	**0.047**	**0.099**

OpenSees Model H Response History Analysis Results and Comparison With ABAQUS

A similar situation arises for model H where the $A36$ SPSW DCRs are closer to the *ABAQUS* DCRs than model S. For the $LYP100$ SPSW the H model DCRs are sig-

nificantly higher than those predicted by *ABAQUS*, exceeding them by an average factor of 1.13.

Table 10.9: Model H: Mean *OpenSees* response history analysis values of DCR_{TB} and DCR_M for $A36$ and $LYP100$ SPSWs at different hazard levels

Story	10in50						2in50					
	A36		LYP100		LYP100/A36		A36		LYP100		LYP100/A36	
	TB	M	TB	M	TB	M	TB	M	TB	M	TB	M
1	0.583	0.583	0.553	0.552	0.949	0.947	0.767	0.787	0.760	0.782	0.991	0.994
2	0.405	0.397	0.394	0.399	0.972	1.005	0.554	0.561	0.547	0.559	0.988	0.996
3	0.416	0.564	0.419	0.567	1.008	1.005	0.585	0.821	0.605	0.837	1.034	1.020
4	0.439	0.393	0.417	0.384	0.950	0.978	0.634	0.487	0.643	0.495	1.013	1.016
5	0.501	0.526	0.488	0.520	0.974	0.988	0.691	0.608	0.693	0.642	1.003	1.056
6	0.454	0.192	0.420	0.165	0.923	0.859	0.676	0.434	0.642	0.395	0.950	0.909
				mean	**0.963**	**0.964**				mean	**0.996**	**0.999**
				CV	**0.031**	**0.060**				CV	**0.030**	**0.051**

Lastly, the influence of the different hysteretic envelope assumptions for Model H is examined for the $LYP100$ SPSW under the 10% in 50 year ground motions. Table 10.11 shows the DCR_{TB} and DCR_M values for the assumed hysteretic behaviors shown in Fig. 10.9(b). It also shows the ratio of the predicted DCRs. The DCRs for the $LYP100$ material that use the *Coupon* envelope are on average 4-6% lower than those for the *Backbone* envelope where hardening is properly considered. The net reduction for a similar analysis of the $A36$ SPSWs is expected to be lower.

Table 10.10: Model H: Ratio of mean *OpenSees* to *ABAQUS* response history analysis values $R_{DCR_{TBj}}$ and $R_{DCR_{Mj}}$ for $A36$ and $LYP100$ SPSWs at different hazard levels

Story	10in50				2in50			
	A36		LYP100		A36		LYP100	
	TB	M	TB	M	TB	M	TB	M
1	1.027	1.063	1.215	1.235	1.002	1.041	1.036	1.073
2	0.966	1.062	1.216	1.178	0.923	1.019	1.016	1.093
3	0.884	1.118	1.068	1.276	0.925	1.178	0.976	1.317
4	1.022	1.215	1.260	1.401	1.036	1.216	1.122	1.277
5	0.979	1.371	1.233	1.829	0.974	1.185	1.072	1.468
6	0.974	0.875	1.368	1.365	1.006	0.940	1.141	1.111
mean	**0.975**	**1.117**	**1.227**	**1.381**	**0.978**	**1.097**	**1.060**	**1.223**
CV	**0.055**	**0.155**	**0.028**	**0.177**	**0.049**	**0.106**	**0.062**	**0.134**

Table 10.11: Ratio of mean DCRs for *OpenSees Hysteretic* models using *Backbone* and *Coupon* assumptions

Story	Backbone (1)		Coupon (2)		(2)/(1)	
	TB	M	TB	M	TB	M
1	0.553	0.552	0.511	0.526	0.924	0.952
2	0.394	0.399	0.369	0.365	0.938	0.916
3	0.419	0.567	0.395	0.530	0.943	0.935
4	0.417	0.384	0.404	0.336	0.969	0.874
5	0.488	0.520	0.464	0.478	0.951	0.919
6	0.420	0.165	0.448	0.174	1.067	1.057
				mean	**0.965**	**0.942**
				CV	**0.051**	**0.063**

Table 10.12 shows how the inclination of the web plate strips effects the DCR magnitude. In this table the DCRs for the $A36$ SPSW $Hysteretic$ model with the strips inclined at 45 degrees ($H45$) are normalized by those for the regular $Hysteretic$ model (Model H) where the strips are inclined at α per eq. F5-2 of the $Provisions$. The total interaction value, per Eqs. 10.1 and 10.2 is shown in the $P-M$ column. The maximum axial and flexural DCRs recorded over the response history are also shown. The $H45$ DCRs are also normalized by the $ABAQUS$ DCRs and shown in the 3rd and 4th rows. The strip inclination angles for the $A36$ SPSW Model H are shown in Fig. 10.8.

Table 10.12: Ratio of mean DCRs for $OpenSees$ Model H with strips at 45 deg to Model H with strips at α and $OpenSees$ Model H with strips at 45 deg to $ABAQUS$

R_{DCR}		$P-M$		P_u/P_n		M_u/M_n	
		TB	M	TB	M	TB	M
H45/H	mean	1.017	0.997	0.981	0.982	1.030	1.011
	CV	0.008	0.018	0.018	0.018	0.035	0.036
H45/ABQ	mean	1.002	1.114	1.026	1.056	0.998	1.253
	CV	0.034	0.107	0.034	0.056	0.048	0.170

Table 10.13: Mean Axial-Flexure (P-M) and Axial-Shear (P-V) DCRs for $OpenSees$ Model S under 10% in 50 year ground motions

	A36		LYP100	
Story	P-M	P-V	P-M	P-V
1	0.567	0.312	0.455	0.237
2	0.420	0.256	0.324	0.188
3	0.470	0.316	0.392	0.285
4	0.430	0.351	0.331	0.294
5	0.512	0.426	0.396	0.377
6	0.467	0.401	0.307	0.319

Within the bottom three stories, the average increase in transverse VBE force magni-

tude resulting from the larger inclination angle (45 degrees) is approximately 17%, yet the increase in the mean VBE bending (M_z) DCR is less than 2%. Comparing this change with the $ABAQUS$ DCRs ($H45/ABQ$) it is clear that the influence of strip inclination is minor with respect to differences associated with modeling technique, in this case the use of shell elements.

10.5.3 Story Drifts

Story drifts are a critical determinant of building lateral system performance. For each model, the story drift is tracked and recorded through time and the maximum value obtained for each story. The trace of story drifts though time is presented in Figs. 10.12 through 10.27. Figs. 10.12, 10.14, 10.16 and 10.18 show the ABAQUS, S model and H model story drifts for the $A36$ SPSW under the 10% in 50 year ground motions. Figs. 10.13, 10.15, 10.17 and 10.19 show the same for the $LYP100$ SPSWs. Figs. 10.20, 10.22, 10.24 and 10.26 show the ABAQUS, S model and H model story drifts for the $A36$ SPSW under the 2% in 50 year ground motions. Figs. 10.21, 10.23, 10.25 and 10.27 show the same for the $LYP100$ SPSWs.

From these figures, Model S appears to approximate the $ABAQUS$ story drifts more accurately than Model H. The similarities between Model S and $ABAQUS$ are particularly strong up to and during the strong motion portion of the records, after that Model S and H are roughly equivalent. Model S, with the stocky $LYP100$ web plate, typically mimics the $ABAQUS$ model drifts very closely, whereas the Model H drifts are often too high. There are notable differences in the frequency content in the drift response of the H models also. The increased pinching and delayed onset of tension reloading for Model H result in a softer structure which leads to increased drifts and longer periods for the lower vibration modes.

Table 10.11 presents the average (mean) maximum and CV of the normalized story drifts for Model S and H for different hazard levels and for different web plate materials. The normalized average maximum and CVs are computed per Eqs. 10.16 and 10.17. For the $A36$ SPSW, the average maximum story drift predicted by Model H is closer to $ABAQUS$ than Model S, although the CV is higher for Model H. Model S tends to under-predict the A36 average maximum story drift by 7-9%, depending on the hazard level.

The mean values presented in Table 10.14 are computed as follows:

$$R_{\Delta_{max}} = \frac{1}{24}\left(\sum_{j=1}^{6}\sum_{i=1}^{4}\frac{\left(\Delta_{max}{}_j^i\right)_{OS}}{\left(\Delta_{max}{}_j^i\right)_{ABQ}}\right) \tag{10.16}$$

The mean coefficient of variation (CV) is computed as follows:

$$CV_{\Delta_{max}} = \frac{1}{6}\sum_{j=1}^{6} CV\left(\frac{\left(\Delta_{max}{}_j^i\right)_{OS}}{\left(\Delta_{max}{}_j^i\right)_{ABQ}}\right) \tag{10.17}$$

The CV is computed for the normalized maximum drifts obtained from the four ground motions at each hazard level. These CVs are then averaged over the number of stories to get an average $CV_{\Delta_{max}}$ for the particular model type (S or H).

Fig. 10.11 shows the average maximum story drift recorded for each hazard level and web plate. Within each plot is the response obtained from $ABAQUS$, Model S and Model H. These plots don't show the scatter in the data observed from different ground motions (embodied in the CV presented in Table 10.14) so the performance of Model H for the $A36$ SPSW appears to be a little better than it actually is. Model S of the $LYP100$ SPSW (Fig. 10.11(c) and (d)) very closely match the average maximum story drifts obtained from $ABAQUS$.

For the $LYP100$ SPSW, Model S is considerably better at predicting average maximum $ABAQUS$ story drift than Model H. The average normalized story drift for Model S is 0.98, with a CV of between 0.09 and 0.11. By contrast, Model H over-predicts the mean average story drift by a factor of between 1.20 and 1.35 with a CV of approximately 0.24.

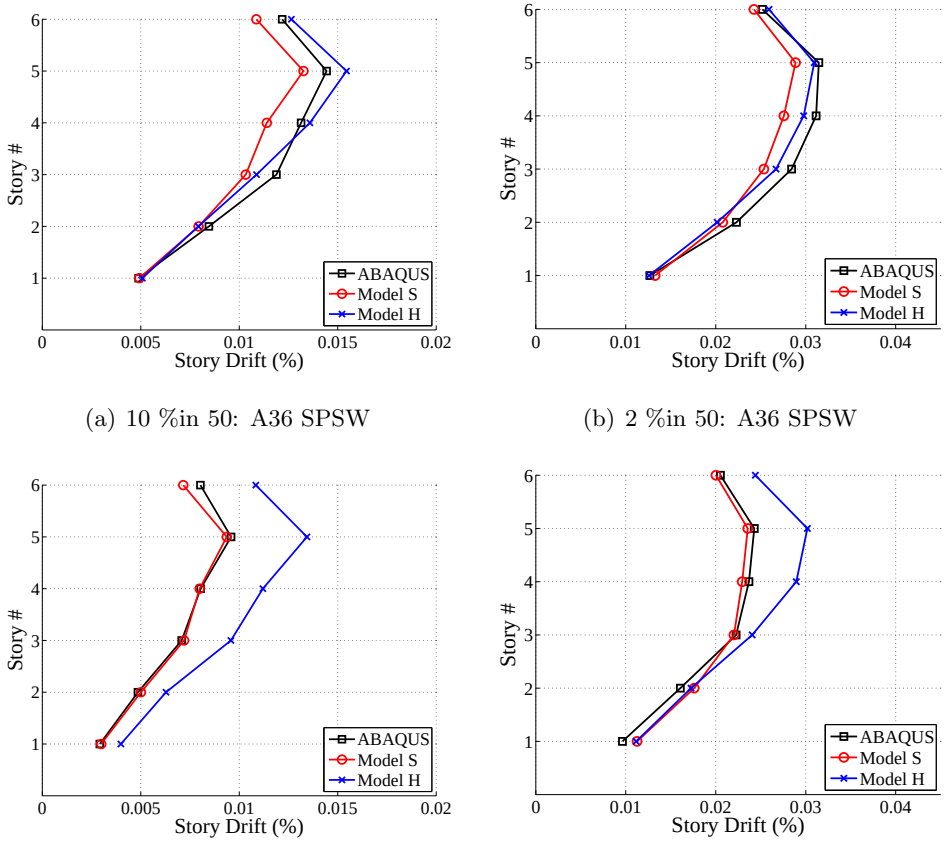

(a) 10 %in 50: A36 SPSW

(b) 2 %in 50: A36 SPSW

(c) 10 %in 50: LYP100 SPSW

(d) 2 %in 50: LYP100 SPSW

Figure 10.11: Mean value of maximum story drift for $ABAQUS$, Model S and Model H for different hazard levels (10% in 50 and 2% in 50) and different web plates (A36 and LYP100)

Table 10.14: Normalized story drift and CV of normalized story drift for *OpenSees* Models S and H

Model	Model S (new)				Model H (hyst)			
Hazard	10% in 50		2% in 50		10% in 50		2% in 50	
Web Plate	A36	LYP100	A36	LYP100	A36	LYP100	A36	LYP100
mean	**0.910**	**0.982**	**0.930**	**0.980**	**0.992**	**1.353**	**0.954**	**1.201**
$CV_{\Delta_{max}}$	**0.114**	**0.090**	**0.076**	**0.090**	**0.143**	**0.231**	**0.112**	**0.241**

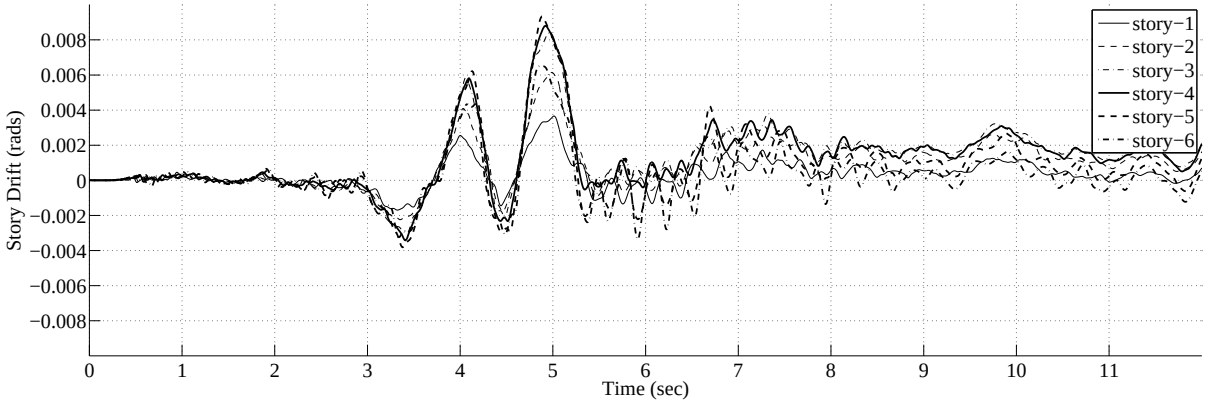

(a) *ABAQUS*

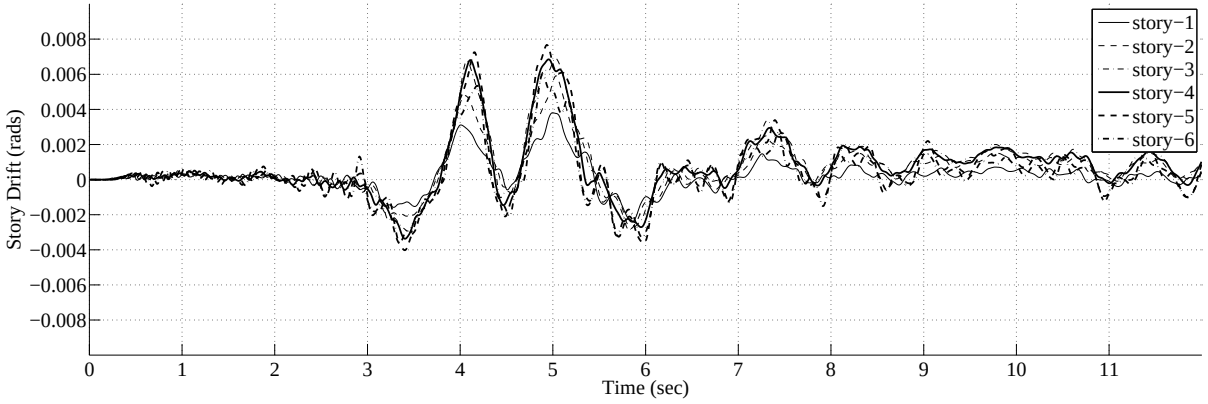

(b) *OpenSees* with $SPSW - WP$ material model

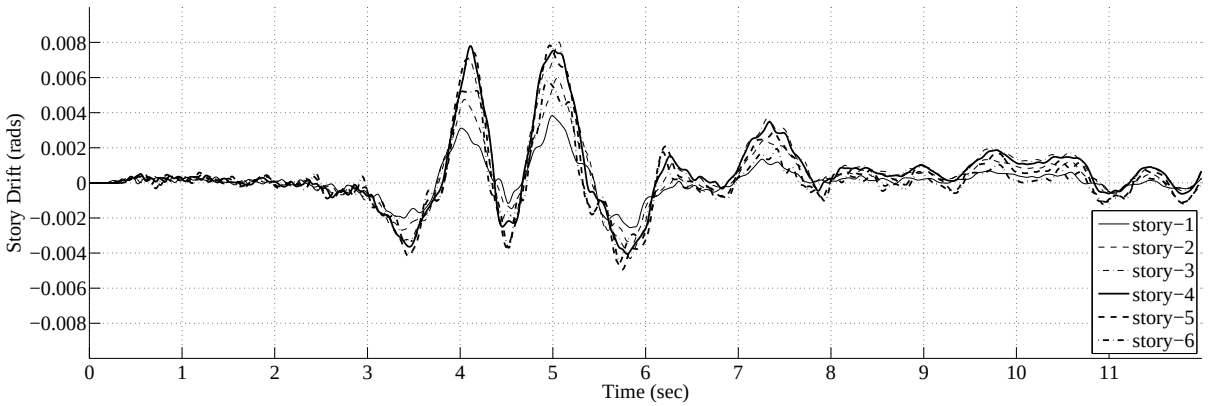

(c) *OpenSees* with *Hysteretic* material model

Figure 10.12: Story Drifts: A36 SPSW under Imperial Valley 1979 (LA05) ground motion from 2 to 14 sec.

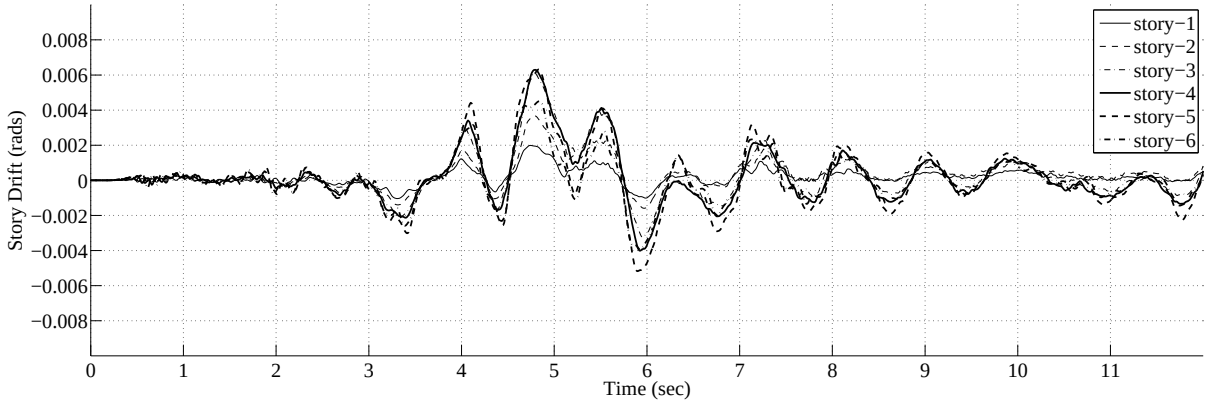

(a) $ABAQUS$

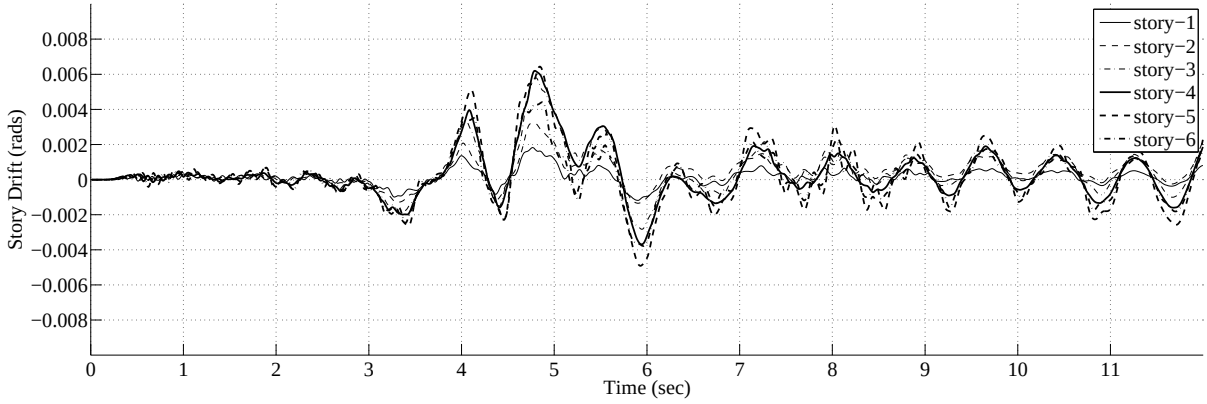

(b) *OpenSees* with $SPSW - WP$ material model

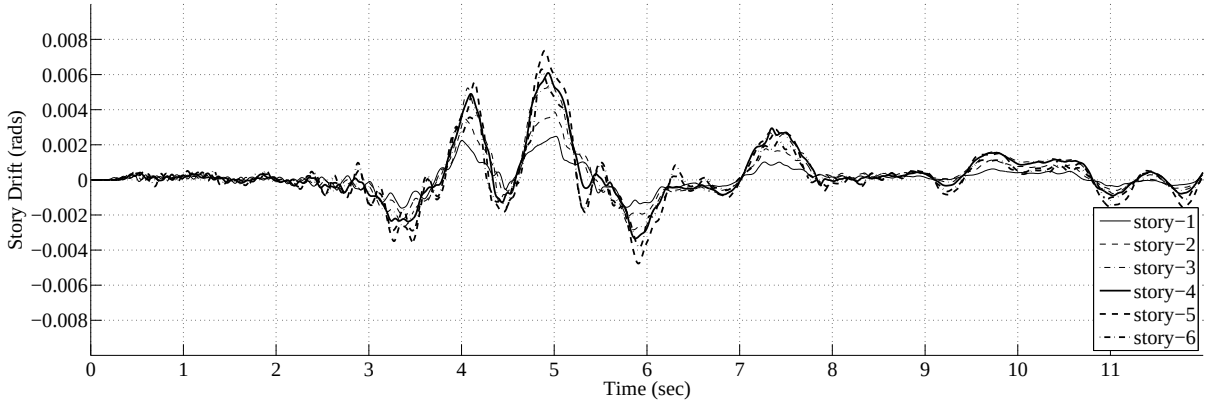

(c) *OpenSees* with *Hysteretic* material model

Figure 10.13: Story Drifts: LYP100 SPSW under Imperial Valley 1979 (LA05) ground motion from 2 to 14 sec.

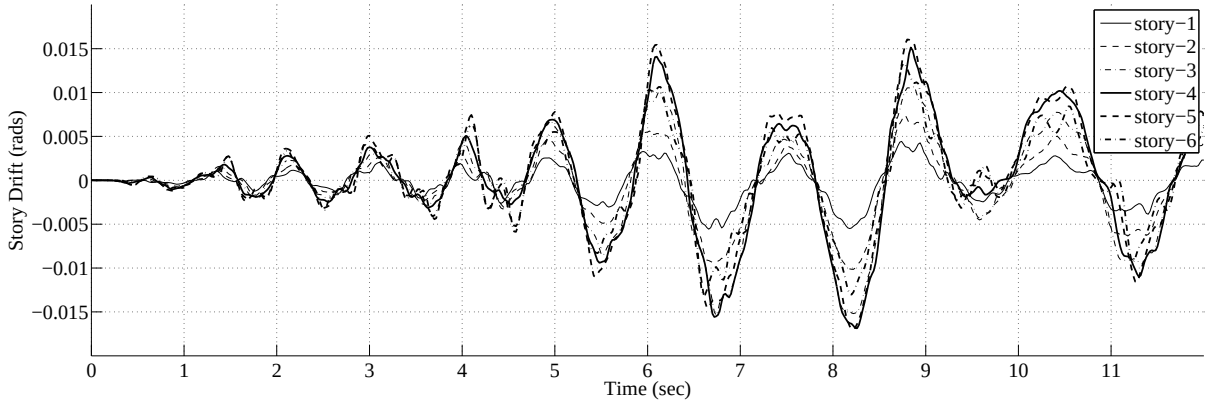

(a) *ABAQUS*

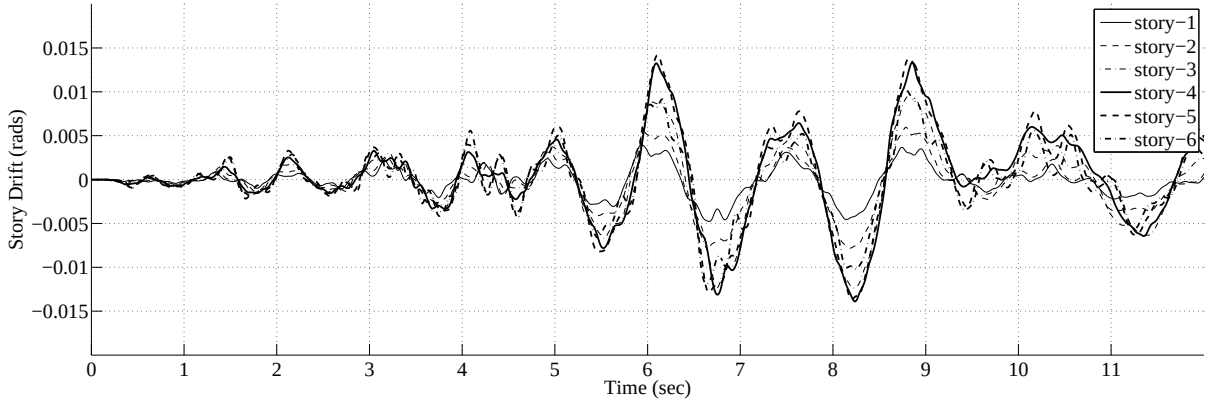

(b) *OpenSees* with $SPSW - WP$ material model

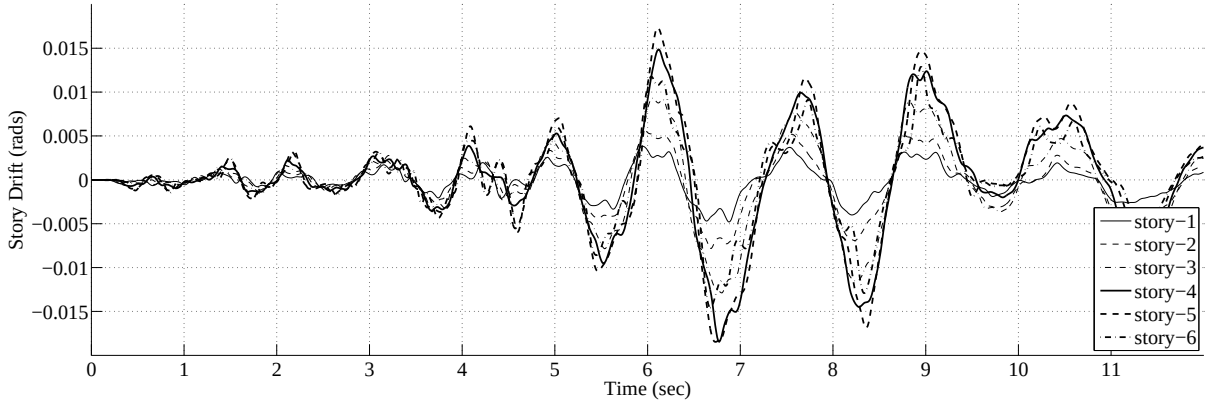

(c) *OpenSees* with *Hysteretic* material model

Figure 10.14: Story Drifts: A36 SPSW under Landers 1992 (LA10) ground motion from 11 to 23 sec.

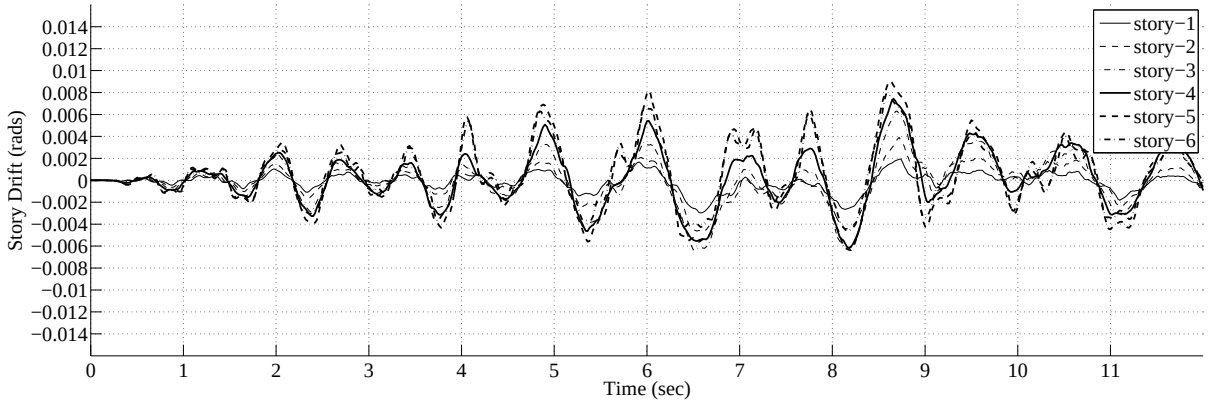

(a) *ABAQUS*

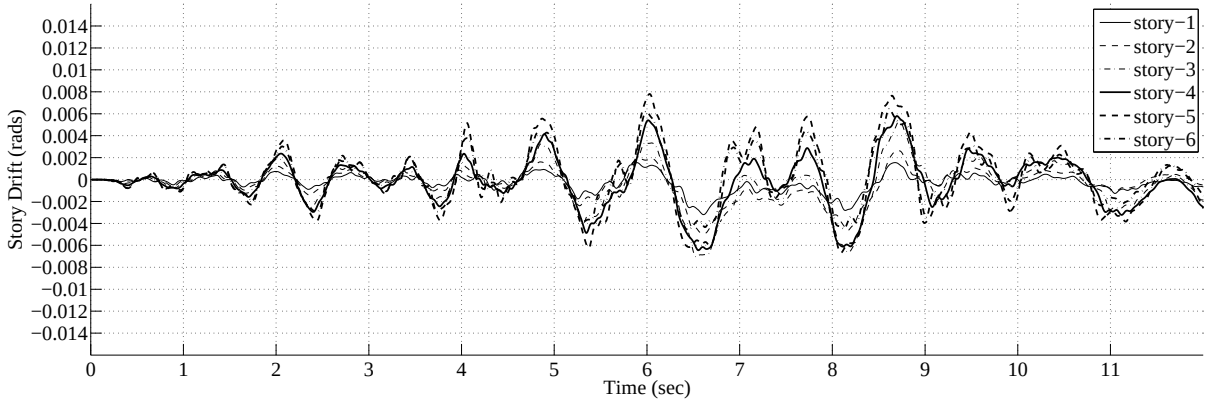

(b) *OpenSees* with $SPSW - WP$ material model

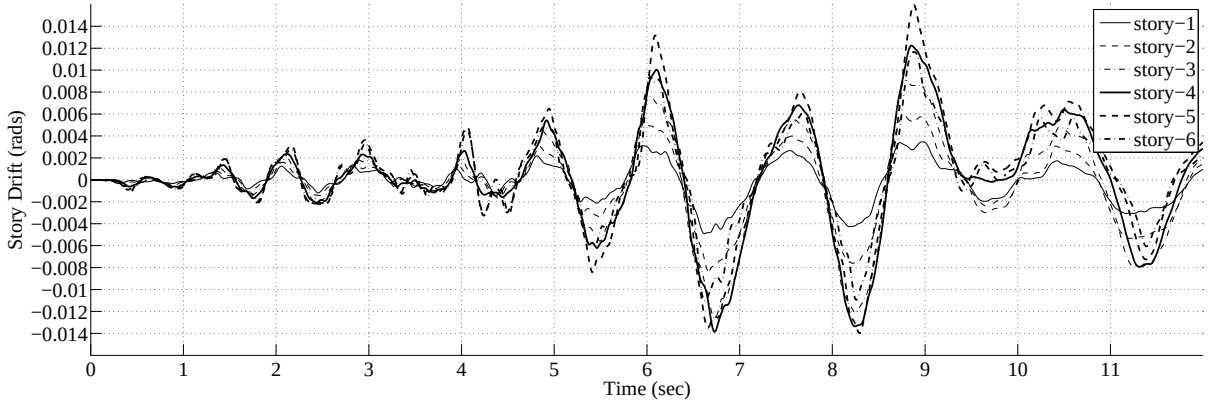

(c) *OpenSees* with *Hysteretic* material model

Figure 10.15: Story Drifts: LYP100 SPSW under Landers 1992 (LA010) ground motion from 11 to 23 sec.

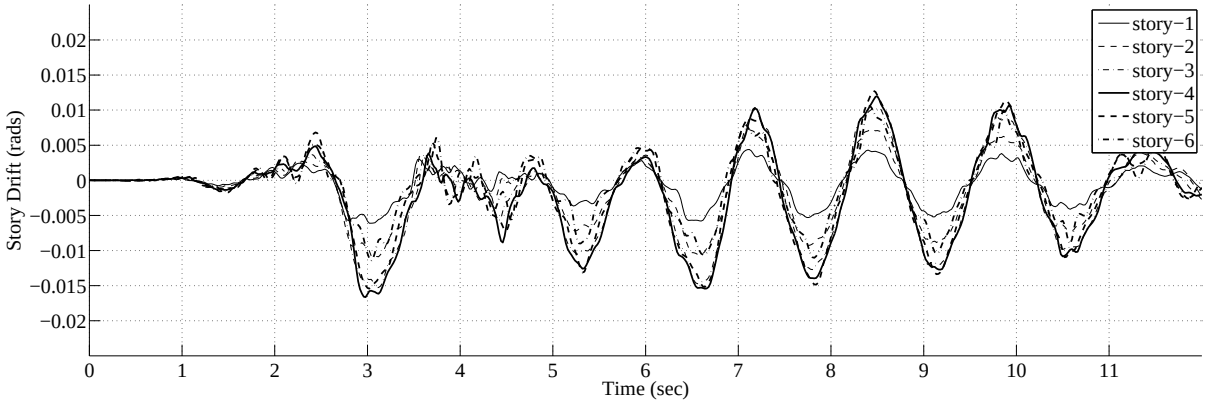

(a) *ABAQUS*

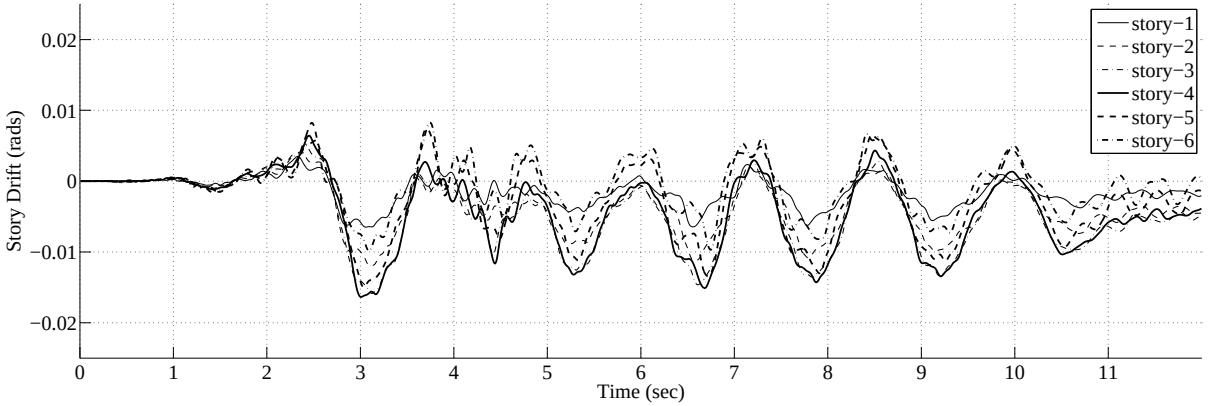

(b) *OpenSees* with $SPSW - WP$ material model

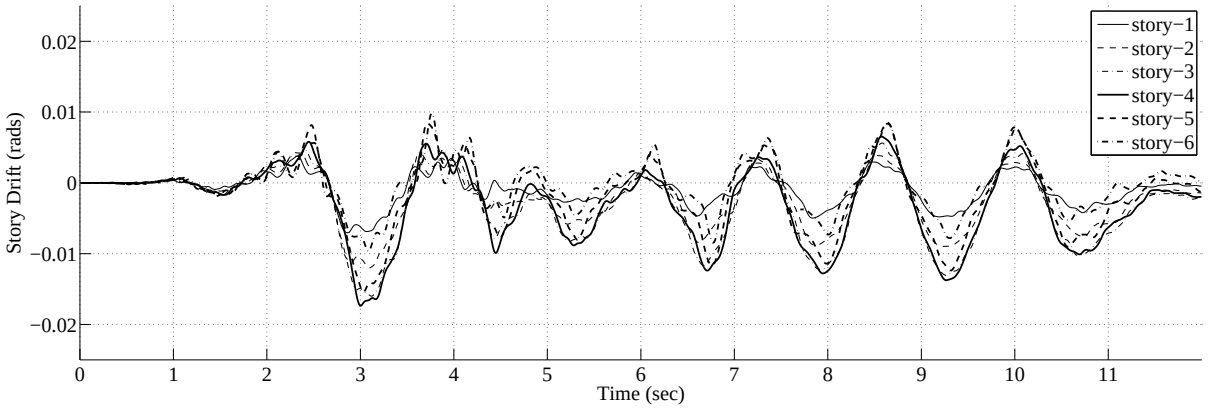

(c) *OpenSees* with *Hysteretic* material model

Figure 10.16: Story Drifts: A36 SPSW under Loma Prieta 1989 (LA11) ground motion from 2 to 14 sec.

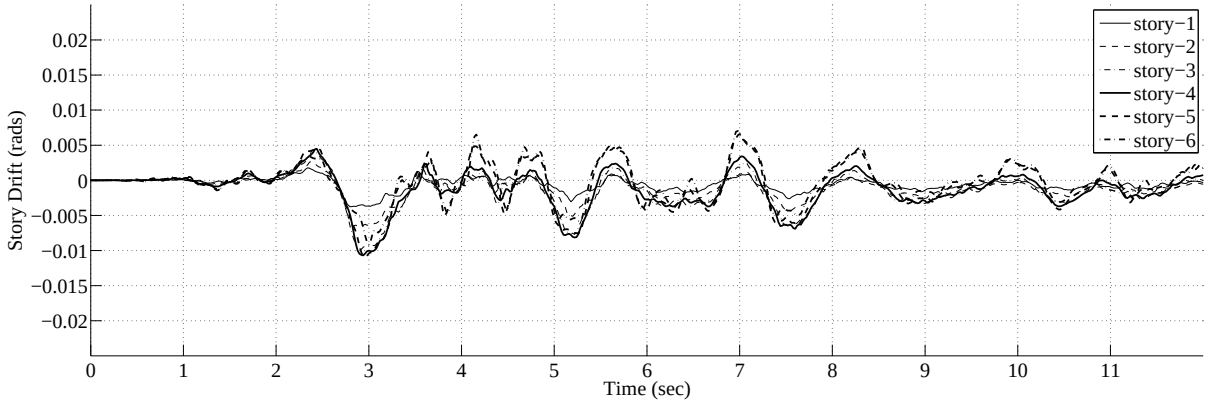

(a) *ABAQUS*

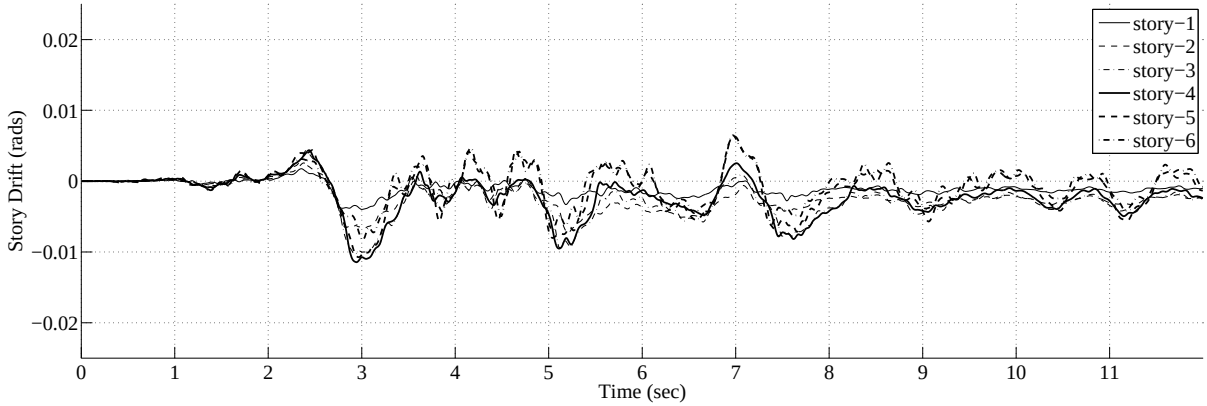

(b) *OpenSees* with $SPSW - WP$ material model

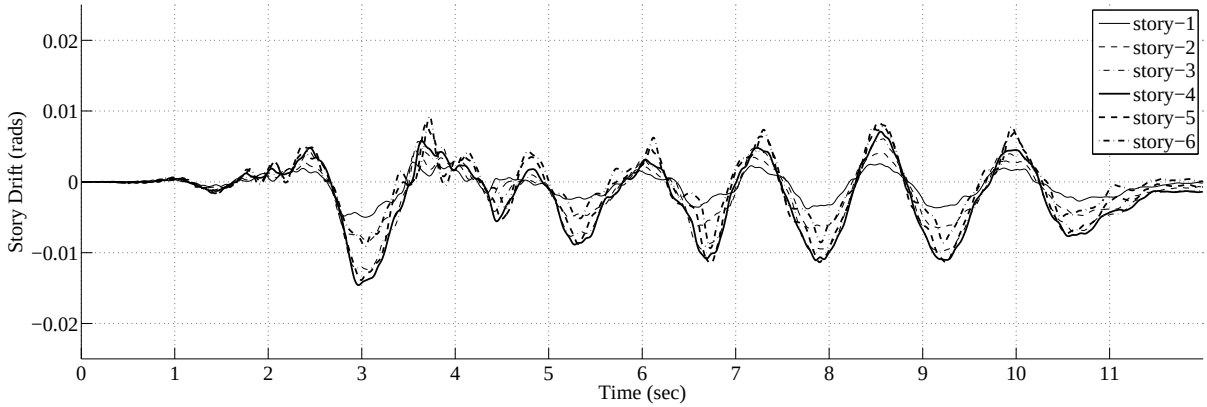

(c) *OpenSees* with *Hysteretic* material model

Figure 10.17: Story Drifts: LYP100 SPSW under Loma Prieta 1989 (LA11) ground motion from 2 to 14 sec.

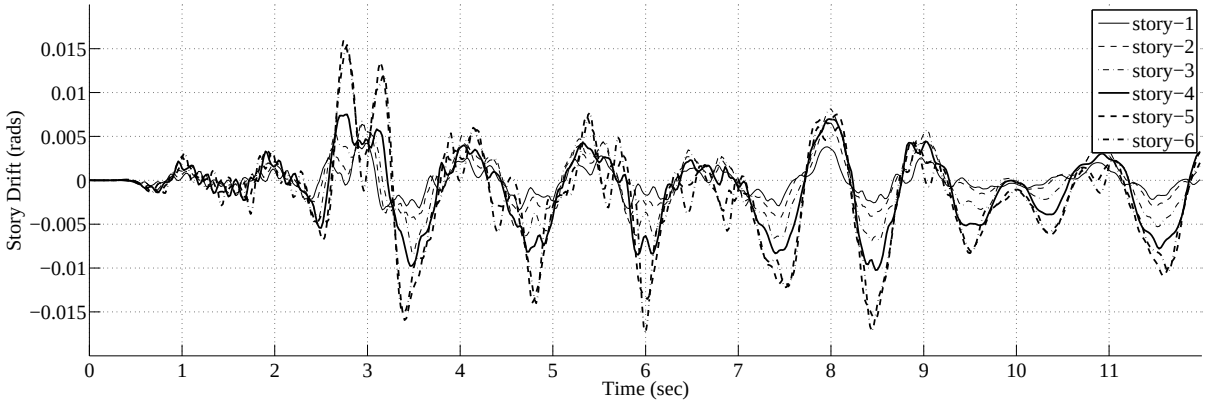

(a) *ABAQUS*

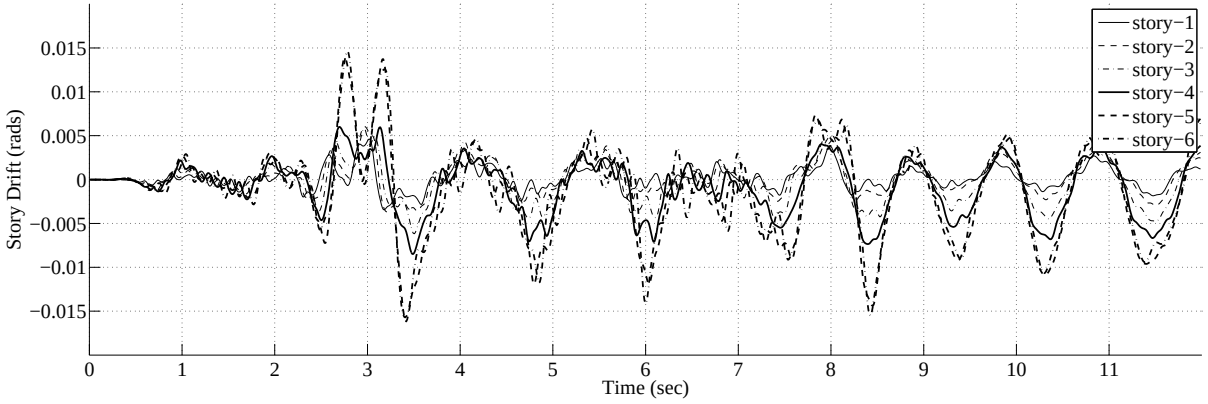

(b) *OpenSees* with $SPSW - WP$ material model

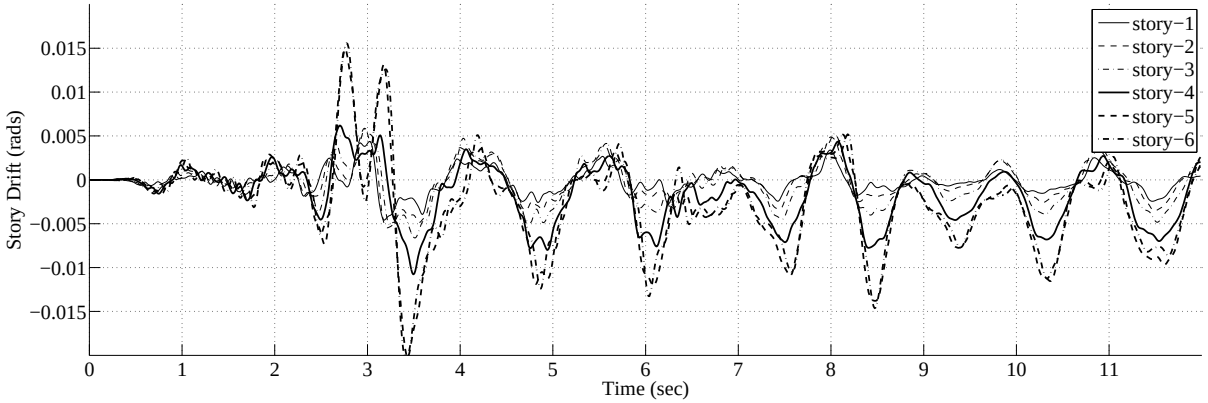

(c) *OpenSees* with *Hysteretic* material model

Figure 10.18: Story Drifts: A36 SPSW under North Palm Springs 1992 (LA19) ground motion from 0 to 12 sec.

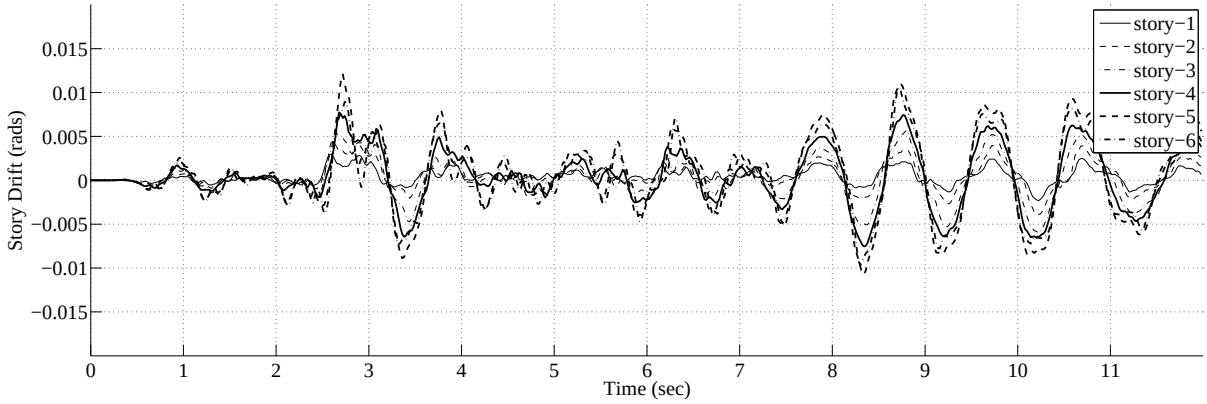

(a) *ABAQUS*

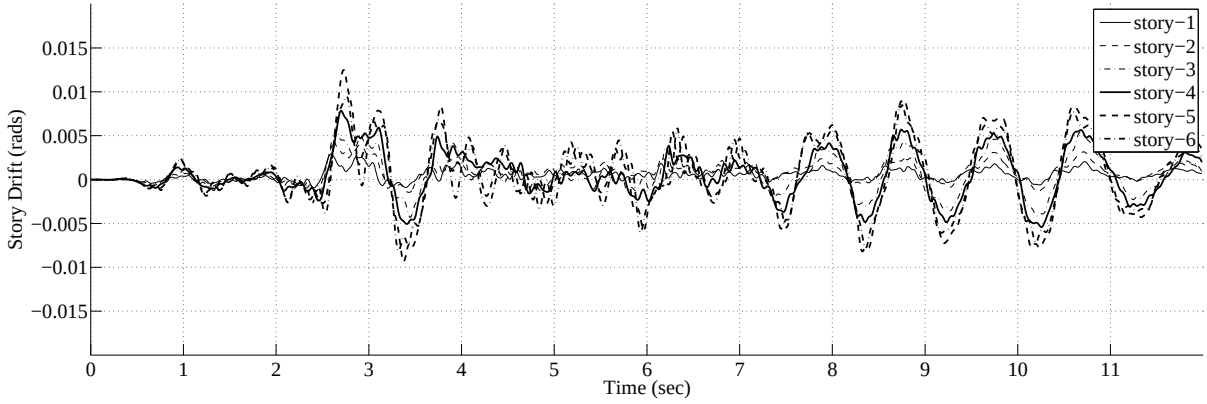

(b) *OpenSees* with $SPSW - WP$ material model

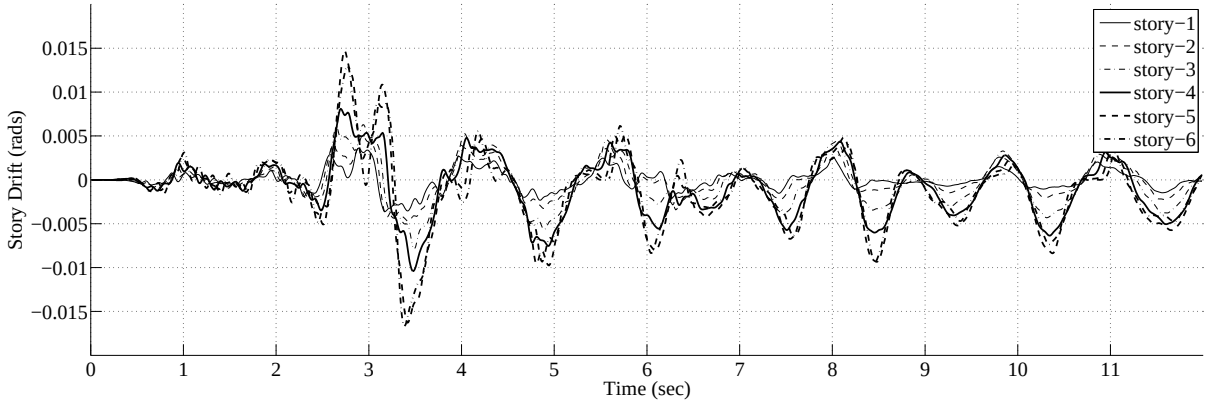

(c) *OpenSees* with *Hysteretic* material model

Figure 10.19: Story Drifts: LYP100 SPSW under North Palm Springs 1992 (LA19) ground motion from 0 to 12 sec.

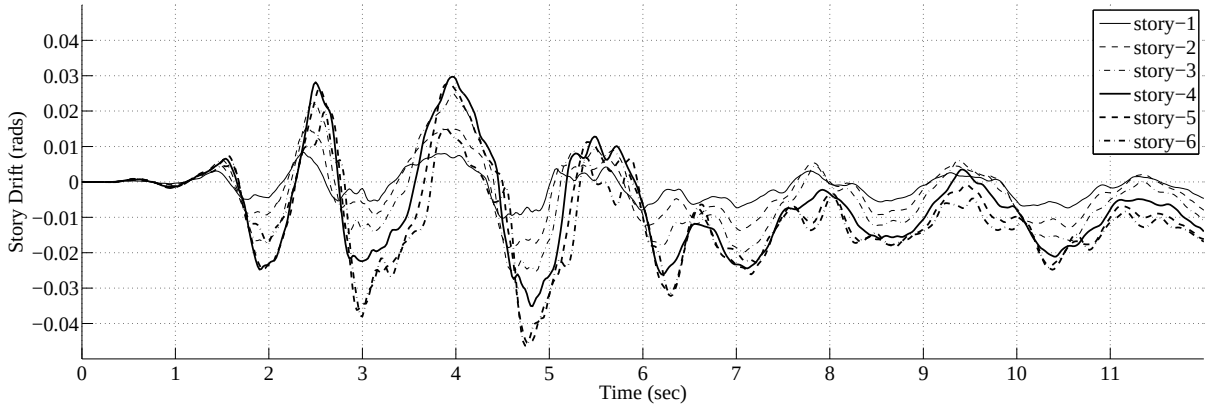

(a) *ABAQUS*

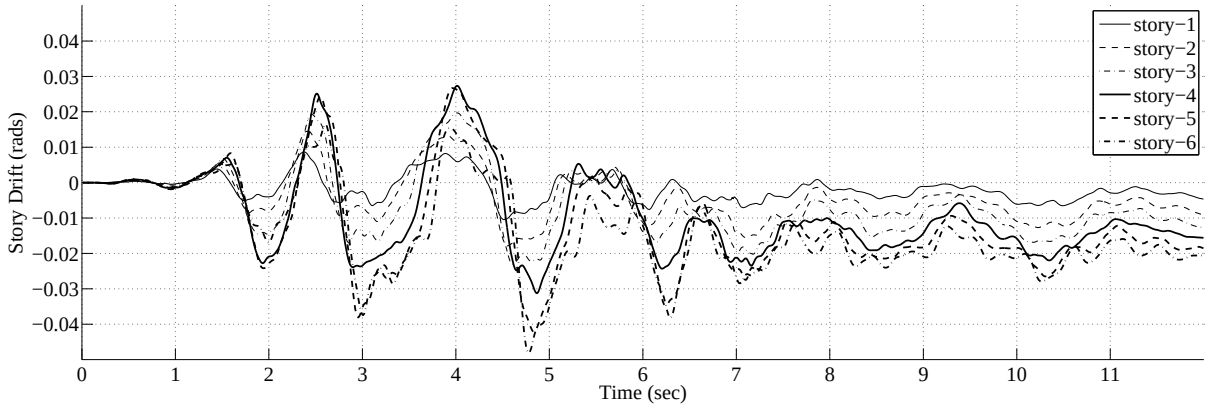

(b) *OpenSees* with $SPSW - WP$ material model

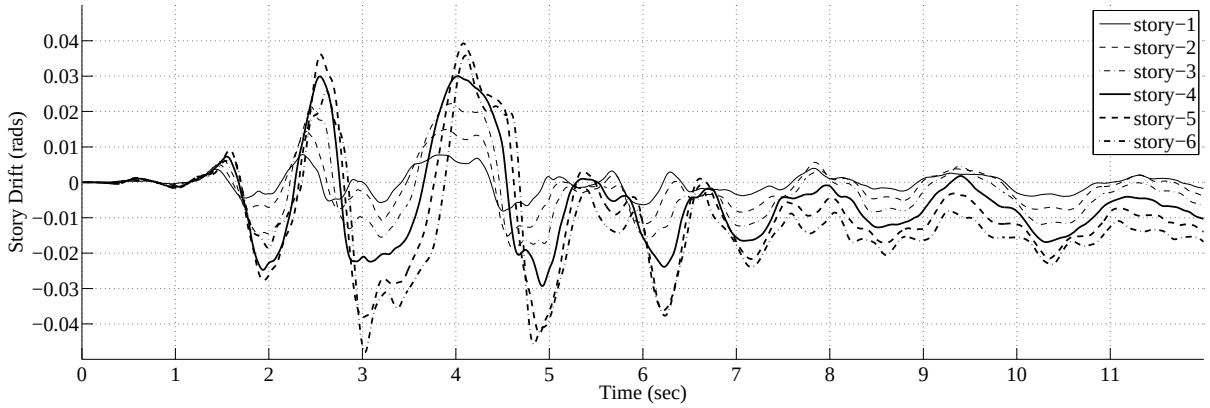

(c) *OpenSees* with *Hysteretic* material model

Figure 10.20: Story Drifts: A36 SPSW under Kobe 1995 (LA21) ground motion from 6 to 18 sec.

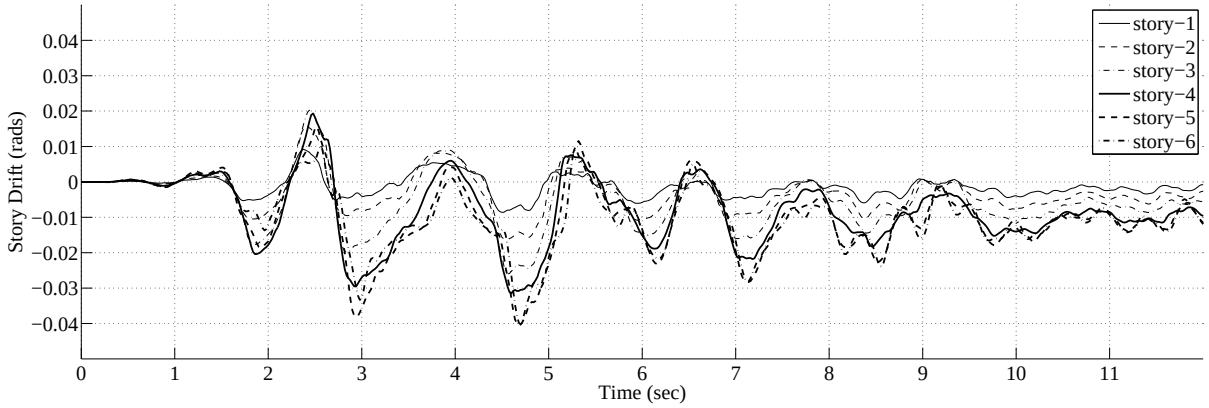

(a) *ABAQUS*

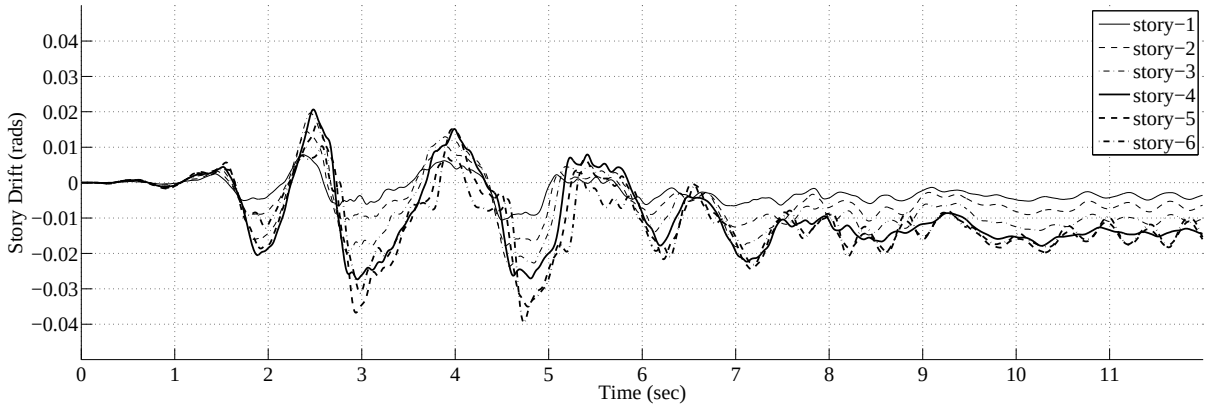

(b) *OpenSees* with $SPSW - WP$ material model

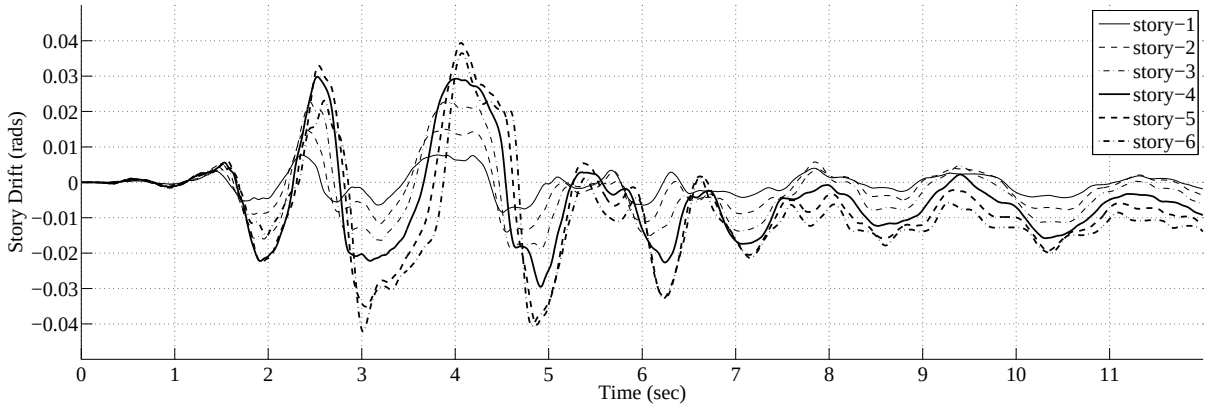

(c) *OpenSees* with *Hysteretic* material model

Figure 10.21: Story Drifts: LYP100 SPSW under Kobe 1995 (LA21) ground motion from 6 to 18 sec.

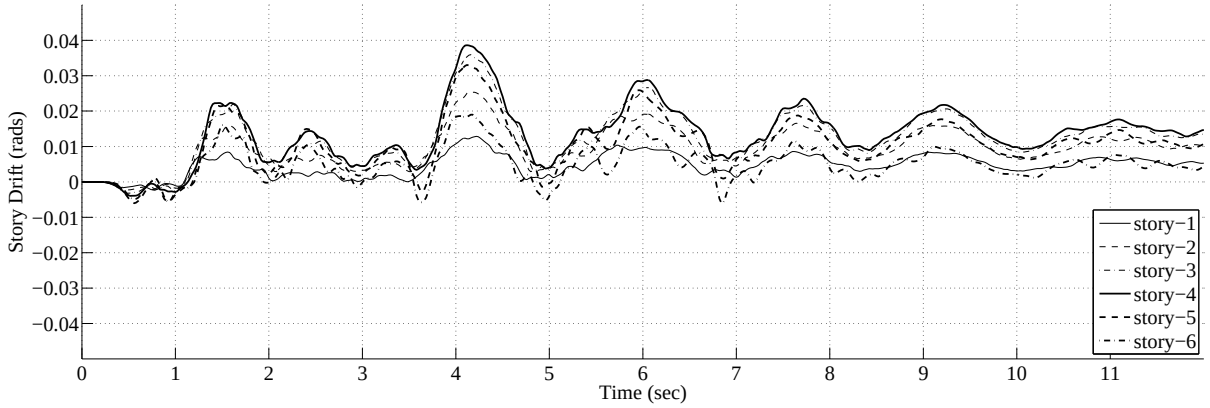

(a) $ABAQUS$

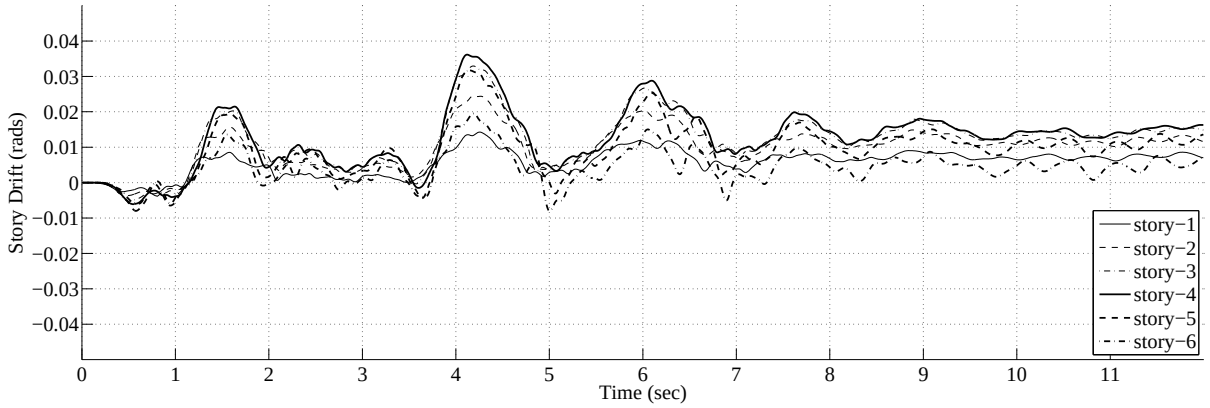

(b) *OpenSees* with $SPSW - WP$ material model

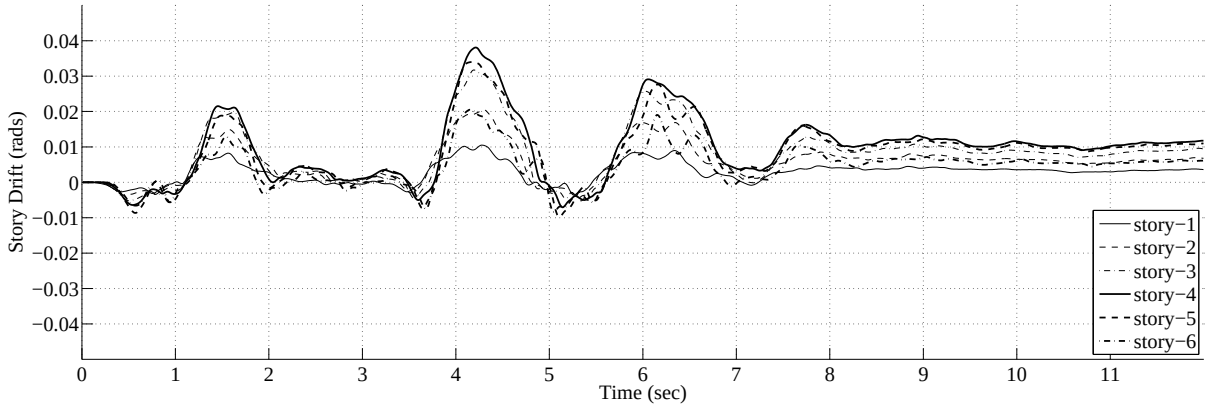

(c) *OpenSees* with *Hysteretic* material model

Figure 10.22: Story Drifts: A36 SPSW under Northridge 1994 (LA27) ground motion from 3 to 15 sec.

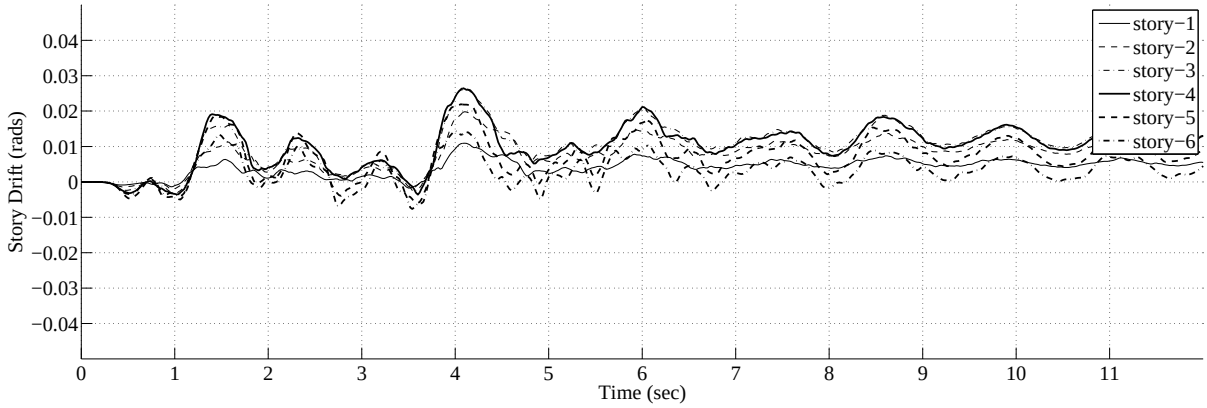

(a) *ABAQUS*

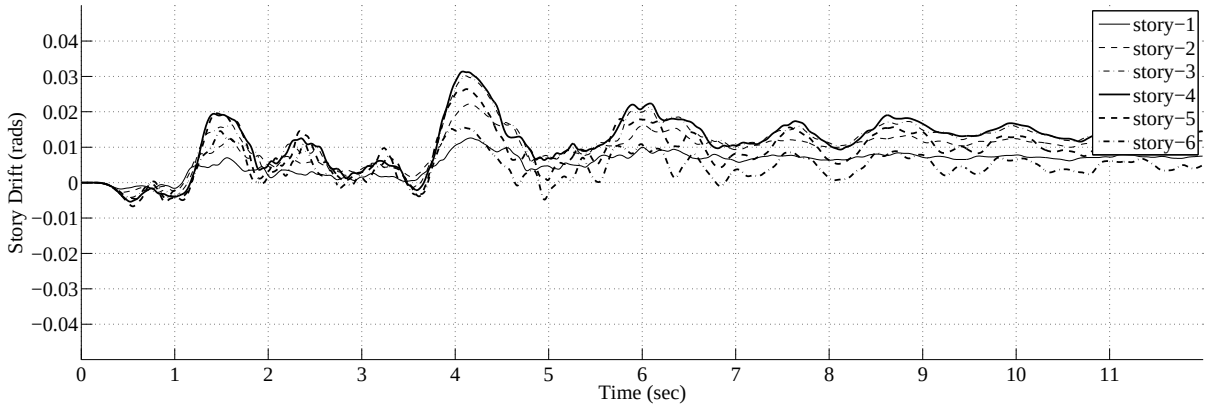

(b) *OpenSees* with $SPSW - WP$ material model

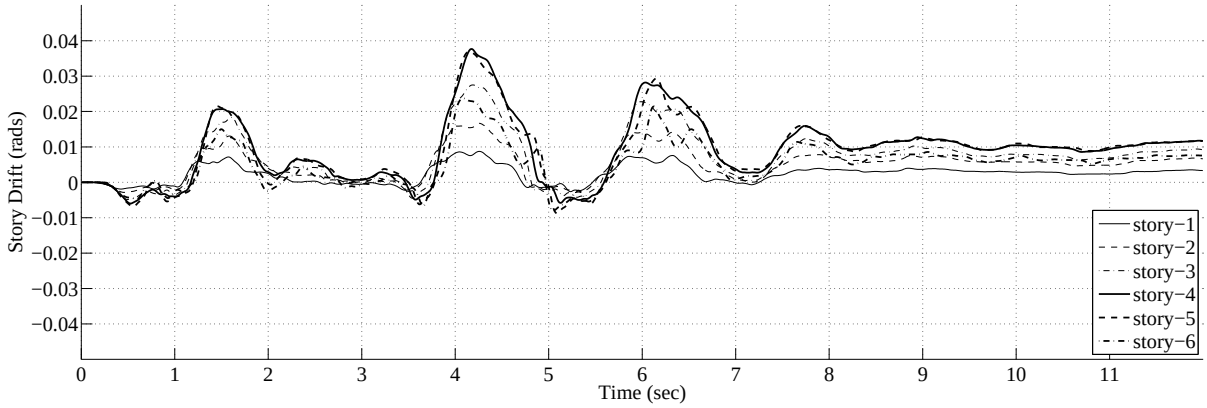

(c) *OpenSees* with *Hysteretic* material model

Figure 10.23: Story Drifts: LYP100 SPSW under Northridge 1994 (LA27) ground motion from 3 to 15 sec.

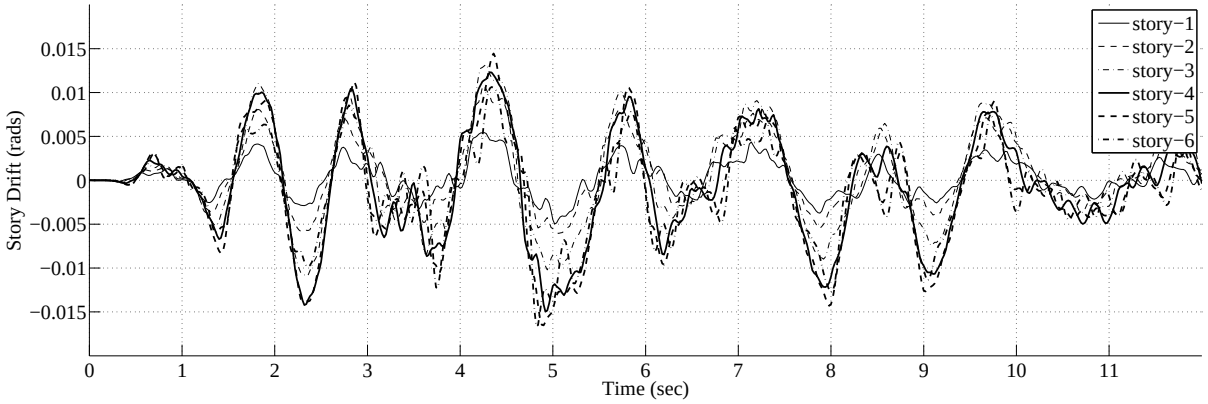

(a) $ABAQUS$

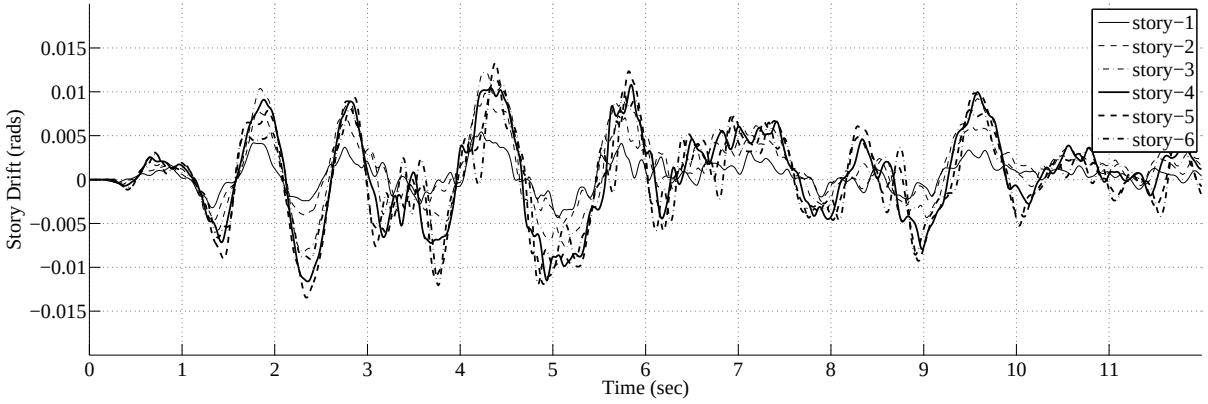

(b) *OpenSees* with $SPSW - WP$ material model

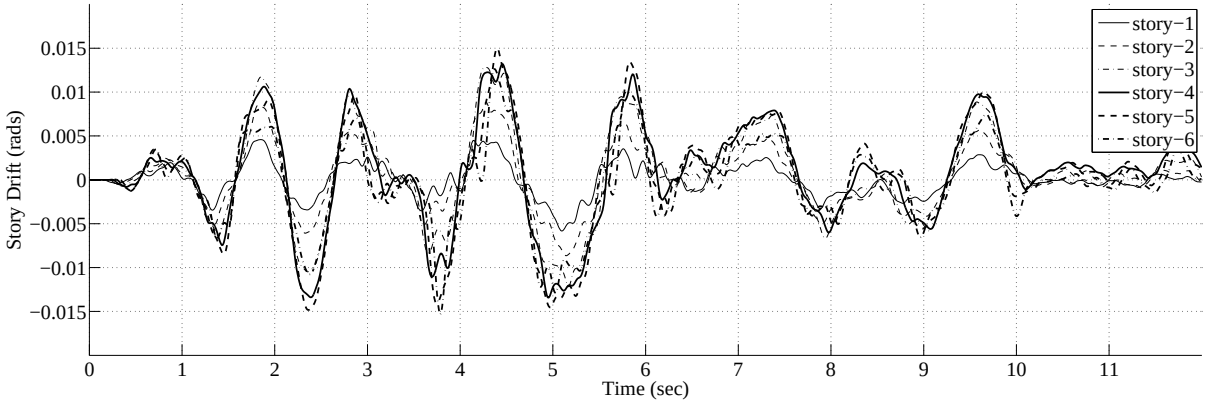

(c) *OpenSees* with *Hysteretic* material model

Figure 10.24: Story Drifts: A36 SPSW under Tabas 1974 (LA29) ground motion from 7 to 19 sec.

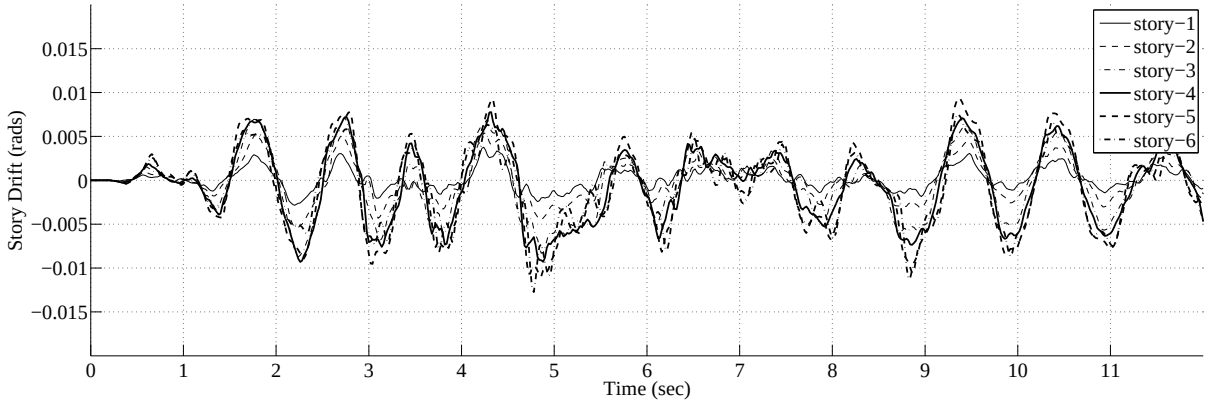

(a) $ABAQUS$

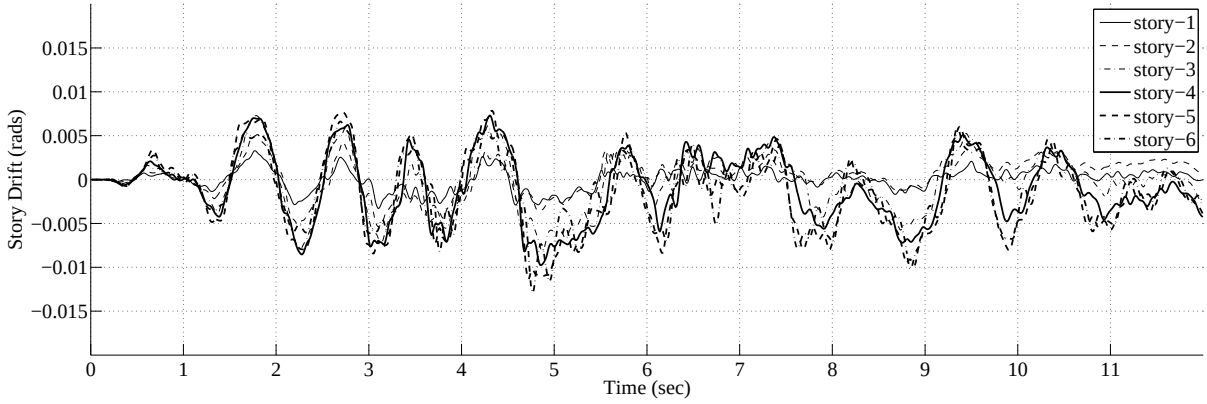

(b) *OpenSees* with $SPSW - WP$ material model

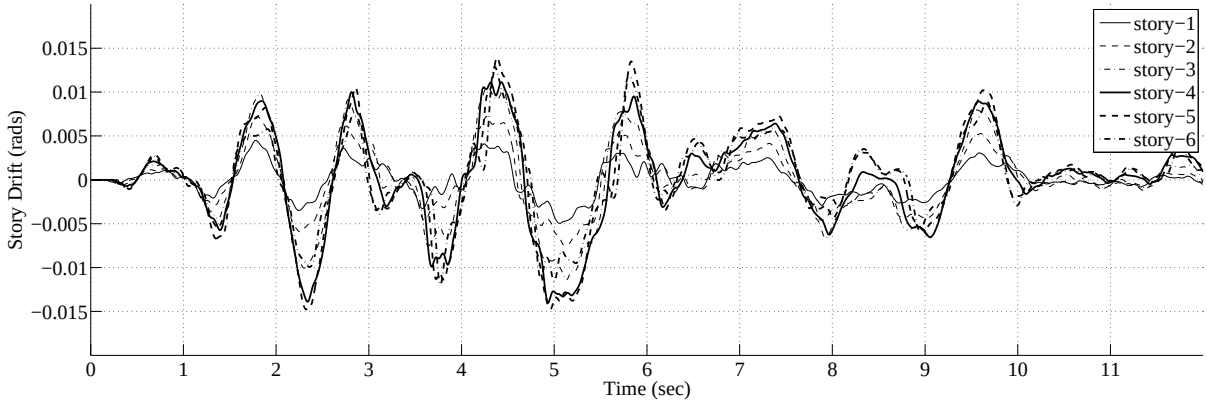

(c) *OpenSees* with *Hysteretic* material model

Figure 10.25: Story Drifts: LYP100 SPSW under Tabas 1974 (LA29) ground motion from 7 to 19 sec.

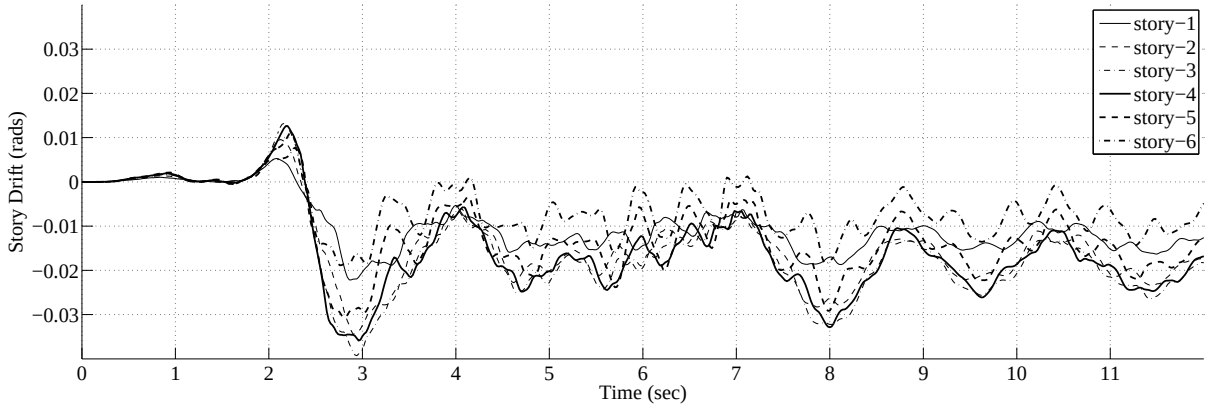

(a) *ABAQUS*

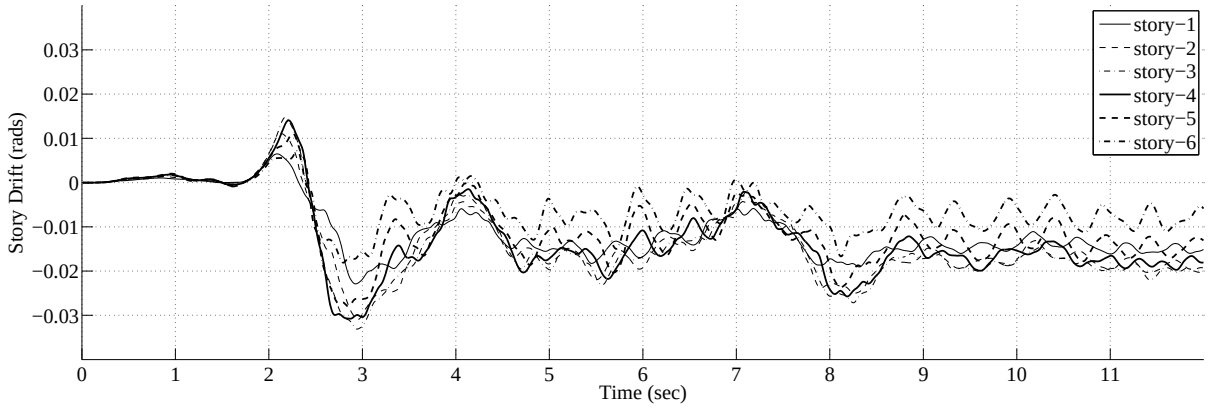

(b) *OpenSees* with $SPSW - WP$ material model

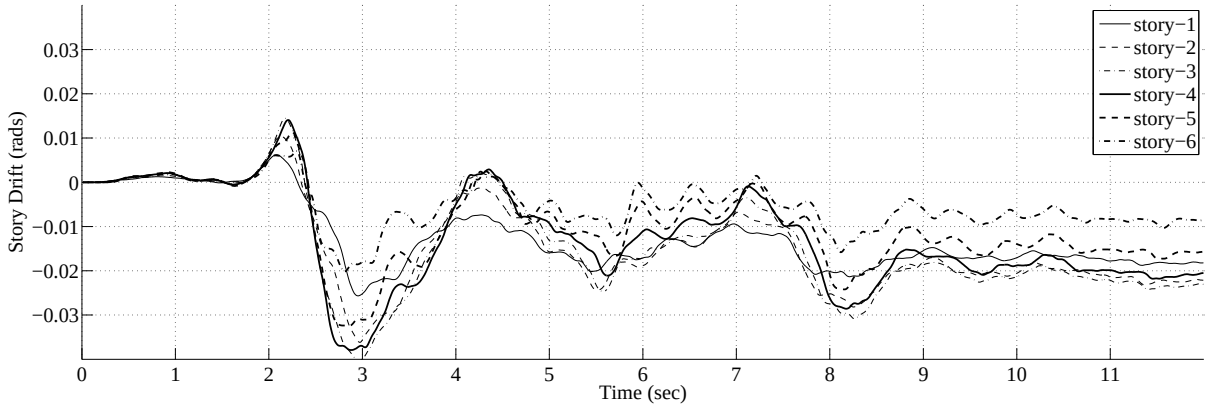

(c) *OpenSees* with *Hysteretic* material model

Figure 10.26: Story Drifts: A36 SPSW under Palos Verdes (simulated) (LA37) ground motion from 7 to 19 sec.

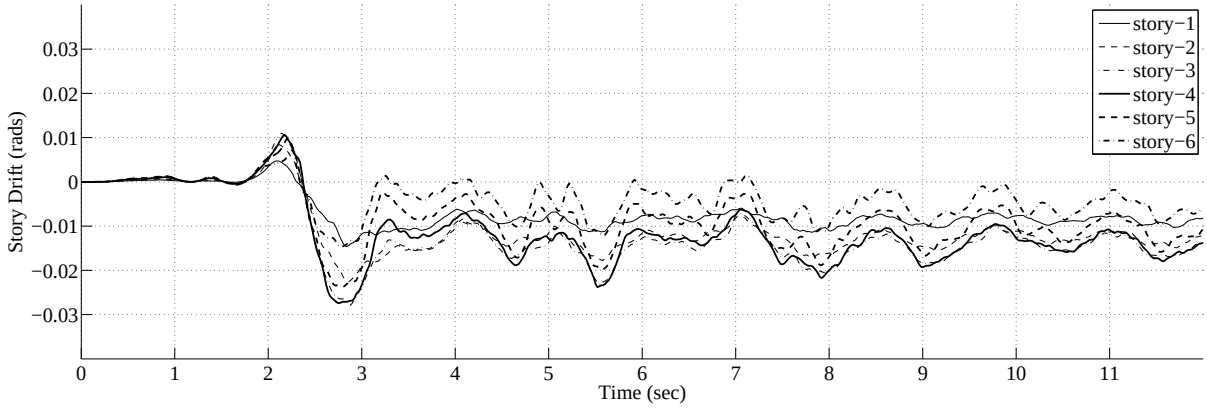

(a) *ABAQUS*

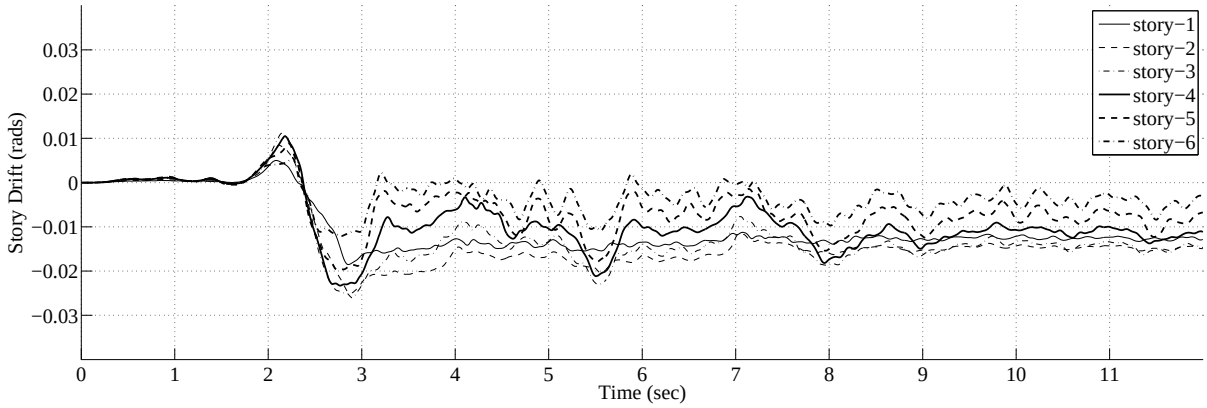

(b) *OpenSees* with $SPSW - WP$ material model

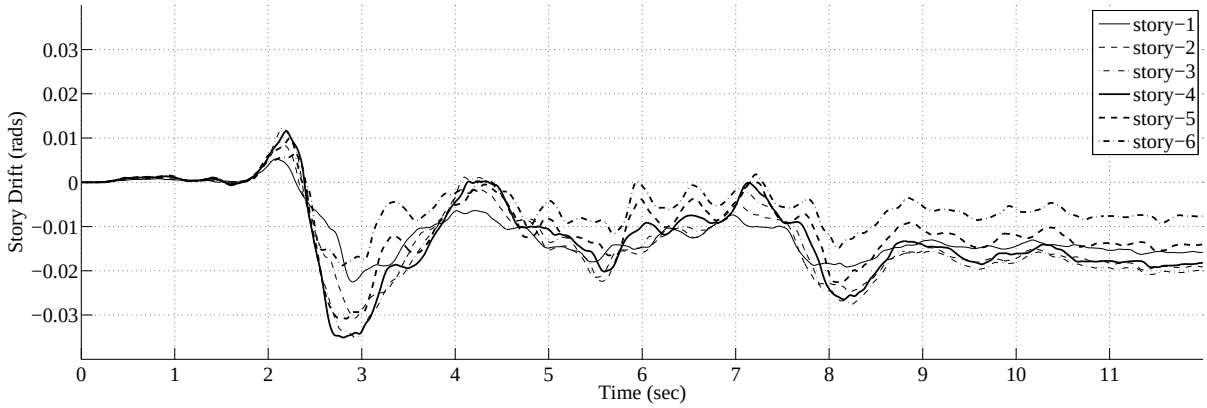

(c) *OpenSees* with *Hysteretic* material model

Figure 10.27: Story Drifts: LYP100 SPSW under Palos Verdes (simulated) (LA37) ground motion from 7 to 19 sec.

10.6 Conclusions

The conclusions drawn from these analyses are as follows:

1. The effect of material hardening on VBE demand is moderate. When the low yield point steel ($LYP100$) web plate is modeled using two versions of the existing *OpenSees* *Hysteretic* material (*one with the hysteretic envelope described by the monotonic coupon curve and the other described by the expected cyclic hardening response*) the average increase in VBE demand capacity ratio (DCR) for the four 10% in 50 year ground motions was typically less than 30% of the increase in enveloped web plate stress at 1% drift. i.e., the percentage increase in VBE demand was less than one-third of the percentage increase in web plate strength.

2. The pushover analyses carried out in Chapter 7 predict an average increase in VBE DCR of around 10% when comparing the $LYP100$ SPSW to the $A36$ SPSW. This increase results from a higher net strength $\beta_H F_y t_w$ in the $LYP100$ web plates. Using the identical models, the response history analyses predict a reduction in the average maximum VBE DCRs of nearly 20% for the 10% in 50 year ground motions and a reduction of around 10% for the 2% in 50 year ground motions. The enhanced hysteretic damping of the LYP web plate is largely responsible for this difference.

3. The 2% in 50 year ground motions predict a different pattern of demand up the height of the structure compared with the PO analyses. Typically, the PO analyses over-predicts the VBE DCRs at the lower two stories and under-predicts them at mid-height. This is due to higher modes having a significant contribution to the response.

4. The *OpenSees* $SPSW - WP$ uniaxial material model for truss elements is slightly better at predicting VBE DCRs than the *Hysteretic* material applied to trusses inclined at α per the Seismic Provisions. Normalized by $ABAQUS$, the new model had a mean DCR ratio of approximately 1.00 with a CV of 0.094. The *OpenSees* model employing the *Hysteretic* material had a mean DCR ratio of 1.18 with a CV of 0.134.

5. The story drifts predicted using the *OpenSees* SPSW material model were evaluated

for slender ($A36$) and stocky ($LYP100$) web plates under 10% in 50 and 2% in 50 year ground motions. The new model tends to slightly under-predict drifts for the slender web plate system but matches the $ABAQUS$ drifts very closely for the stocky web plate system. The *OpenSees Hysteretic* model does a good job at predicting mean story drift for the slender web plate system, but has higher variability (CV) than the new model. The *Hysteretic* model also significantly over-predicts the drifts for the stocky web plate SPSWs and has a high CV.

Chapter 11

CONCLUSIONS AND RECOMMENDATIONS

11.1 Conclusions

This chapter summarizes the conclusions drawn from the work carried out for this research.

1. Both experimental and numerical studies showed that when a SPSW web plate is loaded either monotonically or cyclically (well into the inelastic range), the inclination of the web plate tension field migrated towards 45 degrees, regardless of SPSW geometry or boundary element sizes.

2. Experimental tests revealed that A1008 steel sheet displays isotropic hardening behavior upon reversed cyclic loading and A36 material displays a combined kinematic-isotropic hardening.

3. An investigation of the magnitude of the expected web plate hardening due to earthquake excitation showed that:

   - the number of inelastic cycles is building period dependent

   - the inelastic drift range probability density function that describes the drift range distribution (for buildings from three to nine stories) is invariant to changes in building period and can be described by a single function as:

     $$f(\Delta\delta) = 1.3 \times 10^4 exp(-22.5(\Delta\delta)^{0.25}) \tag{11.1}$$

     where $\Delta\delta$ is the inelastic drift range

   - using this density function, the magnitude of expected web plate hardening from design level earthquake excitation can be expressed as a function of the material parameter R_{sh}, the building period T and the probability of exceedance P.

4. When modeling SPSW web plates with inclined truss elements and subjecting to pushover, the effect on VBE DCRs for elements inclined at 45° (in lieu of 40° or α determined from Eq. F5-2 of the Seismic Provisions) is small. The 45° assumption typically leads to a slight increase in VBE flexural demand ($< 6\%$) and a very small increase in VBE axial demand and base shear ($< 1\%$). These differences are completely obscured by differences in the demands obtained from pushover and response history analyses.

5. From pushover analyses of six-story SPSWs, the impact of hardening on boundary element demand was found to be moderate. The mean increase in VBE demand was approximately 6% of R_{sh}, i.e., a 4% increase for A36 web plate and 12% increase for LYP100 web plate above what would be determined from capacity design using $R_y F_y$.

6. When subjected to a small suite of 2% in 50 year ground motions, the distribution of VBE demand up the height of a six-story SPSW differs significantly from that predicted using PO analysis. Typically, the PO analyses over-predicts the VBE DCRs at the lower two stories and under-predicts them at mid-height. This is due to higher modes having a significant contribution to the response.

7. The implementation of a new *OpenSees* uniaxial material model, specifically designed for SPSW web plates, was able to provide a reasonable match with the results of *ABAQUS* analyses of six story SPSWs. The model provides an improvement over the existing *OpenSees Hysteretic* material in predicting VBE demands for SPSWs with A36 web plates and a significant improvement in predicted VBE demands for SPSWs modeled with stocky LYP100 web plates. The model is able to match drift demands of the *ABAQUS* analyses well and the accuracy improves with decreasing web plate slenderness.

8. Response history analyses of six-story SPSWs showed that the VBE demand capacity to ratios (DCRs) for SPSWs with stocky web plates are significantly lower than those using slender web plates and that the mean reduction in demand could be as much as 30%.

11.2 Design Implications and Recommendations

1. When modeling SPSW web plates with truss elements and performing inelastic pushover or response history analyses, it is recommended for simplicity that the elements be inclined at 45°.

2. Pushover analysis is not recommended for SPSWs above three stories in height because it does not adequately capture higher mode effects.

3. There are significant benefits in the application of low yield point (LYP) web plate steel in SPSW construction. These include but are not limited to:

   - the enhanced ductility of LYP steel enhances deformation capacity
   - the reduced web plate slenderness reduces hysteretic pinching which subsequently reduces story drift demands
   - the reduced slenderness promotes higher web plate compressive stresses which reduce transverse loads on the VBEs

4. Though the influence of hardening is generally small, it should be properly accounted for in the modeling of web plates. For analysis and design purposes, an isotropic hardening assumption is recommended. If using a simple material model to describe the web plate (such as the *OpenSees Hysteretic* material), the web plate strength at 2% drift can be approximated using:

$$\sigma_{(\Delta=2\%)} = (1 + 0.35R_{sh})R_yF_y \tag{11.2}$$

   where $R_{sh} = \dfrac{R_tF_u}{R_yF_y}$ - 1

5. Using reasonable assumptions, it is recommended that a strain hardening value of 1.1 be considered for capacity design of SPSW boundary elements.

Appendix A

SOURCE CODE FOR $SPSW - WP$ MATERIAL MODEL

A.1 Introduction

The following $C++$ code was used within the OpenSees Development environment to test and implement the $SPSW - WP$ material model. A detailed description of the model is contained within Chapter 8.

```
#include <elementAPI.h>
#include "SPSW_Web_Plate.h"
#include <iostream>
#include <Vector.h>
#include <Channel.h>
#include <math.h>
#include <float.h>
using namespace std;
#ifdef _USRDLL
#define OPS_Export extern "C" _declspec(dllexport)
#elif _MACOSX
#define OPS_Export extern "C" __attribute__((visibility("default")))
#else
#define OPS_Export extern "C"
#endif

static int numSPSW_Web_Plate = 0;

OPS_Export void *
OPS_SPSW_Web_Plate()
{
  // Pointer to a uniaxial material that will be returned
  UniaxialMaterial *theMaterial = 0;

  int    iData[1];
  double dData[12];
  int numData = 1;
```

```
29    if (OPS_GetIntInput(&numData, iData) != 0) {
        opserr << "WARNING invalid uniaxialMaterial SPSW_Web_Plate tag" << endln;
31      return 0;
      }
33
      numData = 12;
35    if (OPS_GetDoubleInput(&numData, dData) != 0) {
        opserr << "WARNING invalid parameters\n";
37      return 0;
      }
39
       //create a new material
41
      theMaterial = new SPSW_Web_Plate(iData[0], dData[0], dData[1], dData[2], dData[3],
        dData[4], dData[5], dData[6], dData[7],
43              dData[8], dData[9], dData[10], dData[11]);

45    if (theMaterial == 0) {
        opserr << "WARNING could not create uniaxialMaterial of type SPSW_Web_Plate\n";
47      return 0;
      }
49
      // return the material
51    return theMaterial;
}
53
SPSW_Web_Plate::SPSW_Web_Plate(int tag, double FY, double ES, double MF1, double MF2,
       double MF3, double EN1, double EN2, double EN3, double KIN, double LEN, double
      HT, double TP)
55 :UniaxialMaterial(tag, 0),
    fy(FY), Es(ES), mf1(MF1), mf2(MF2), mf3(MF3), en1(EN1), en2(EN2),
57  en3(EN3), kin(KIN), len(LEN), ht(HT), tp(TP)
{
59  // Declare Constants
    ////////////////////////////////////////////////////////////////////
61  mu = 0.3; // elastic poisson's ratio
    beta = -0.045-0.08*exp(-0.003*(ht/tp-300)); // Residual compressive strength
63  Kb = 7.38+5.38*pow((ht/len),1.33); // Shear buckling parameter
    hont_cr = sqrt(1.732*Kb*Es/((1-pow(mu,2))*fy));  // Critical slenderness ratio fro
      shear buckling
65  Ftr = fy*(2.59*pow((ht/tp),-1.08)*pow((len/ht),0.36)*pow((Es/fy),0.59) + 0.017);
      // Tension reloading strength
```

```
    Fres = -fy*(2.78*pow((ht/tp),-0.83)*pow((len/ht),-0.62)*pow((Es/fy),0.26) + 0.0032)
      ; // Residual compressive stress
67  Fst = Fres; // Initial snap-thru stress
    Ft = fy + Fres/2; // Initial modified tensile stress
69  R = 6; // Magnegotto-Pinto parameter for State 1
    R6 = 12; // Magnegotto-Pinto parameter for State 6
71  ct = 0; // counter
    togp = 1; // Positive loading toggle
73  togn = 1; // Negative loading toggle

75  k1in = Es*(0.215*pow((ht/tp),0.19)); // Initial tangent stiffness for State 1
    k1 = k1in;
77  k1f = 0.7*Es; // Minimum value of tangent stiffness for state 1 at large strain
      accumulation
    k2in = Es*pow((ht/tp),0.1)*pow((len/ht),0.15); // Unloading stiffness
79  k3in = 0.6*k2in; // Initial tangent stiffness for State 3
    kv = 0.0;
81  b = 600; // Decay rate parameter for State 4

83  sigcr = 0.25*Ftr;  // Stress at intersection of asymptotes for State 6
    s_exp = 0.0;
85
    nu = min(0.5 + 0.5*exp(-0.01*(ht/tp-hont_cr)),1.0); // Plasic contraction parameter
87  xia = 1.0; // Plastic strain accumulation factor (1 for State 1, 0.08 otherwise)
    xib = 0.08;
89  ////////////////////////////////////////////////////////////////////////

91  // Parameters for State 1 Magnegotto-Pinto curve
    Kn = 0.0;
93  kh = 0.0;
    khold = 0.0;
95  Kp = 0.0;
    k1hyp = k1in;
97  kt = 0.0;
    estar = 0.0;
99  sigstar = 0.0;
    gamma = 0.0;
101 ds = 0.0;
    dep = 0.0;
103
    // Parameters used for construction of State 8 cubic polynomial
105 X1 [0] = 0.0; X1 [1] = 0.0; X1 [2] = 0.0; X1 [3] = 0.0;
```

```
    X2 [0] = 0.0; X2 [1] = 0.0; X2 [2] = 0.0; X2 [3] = 0.0;
107 X3 [0] = 0.0; X3 [1] = 0.0; X3 [2] = 0.0; X3 [3] = 0.0;
    X4 [0] = 0.0; X4 [1] = 0.0; X4 [2] = 0.0; X4 [3] = 0.0;
109 Y [0] = 0.0; Y [1] = 0.0; Y [2] = 0.0; Y [3] = 0.0;
    f1 = 0.0;
111 f2 = 0.0;
    f3 = 0.0;
113 kq1 = 0.0;
    kq2 = 0.0;
115 sq1 = 0.0;
    sq2 = 0.0;
117 eq1 = 0.0;
    eq2 = 0.0;
119
    // Initialize History Variables
121 TS_exp [0] = 0.0;
    TS_exp [1] = 0.0;
123 TS_exp [2] = 0.0;
    TS_exp [3] = 0.0;
125 CS_exp [0] = 0.0;
    CS_exp [1] = 0.0;
127 CS_exp [2] = 0.0;
    CS_exp [3] = 0.0;
129
    Tss [0] = 0.0;
131 Tss [1] = 0.0;
    Tss [2] = 0.0;
133 Tss [3] = 0.0;
    Tss [4] = 0.0;
135 Tss [5] = 0.0;

137 Css [0] = 0.0;
    Css [1] = 0.0;
139 Css [2] = 0.0;
    Css [3] = 0.0;
141 Css [4] = 0.0;
    Css [5] = 0.0;
143
    TS [0] = 0.0;
145 TS [1] = 0.0;
    TS [2] = 0.0;
147 TS [3] = 0.0;
```

```
    TS [4] = 0.0;
149 TS [5] = 0.0;
    TS [6] = 0.0;
151 CS [0] = 0.0;
    CS [1] = 0.0;
153 CS [2] = 0.0;
    CS [3] = 0.0;
155 CS [4] = 0.0;
    CS [5] = 0.0;
157 CS [6] = 0.0;

159 TA1 = 0.0;
    TA2 = 0.0;
161 TA3 = 0.0;
    TA4 = 0.0;
163 CA1 = 0.0;
    CA2 = 0.0;
165 CA3 = 0.0;
    CA4 = 0.0;
167
    TK1l = 0.0;
169 TK4l = 0.0;
    TK5l = 0.0
171 TK6i = 0.0;
    TK6l = 0.0;
173 TK7l = 0.0;
    TK8l = 0.0;
175 TK9l = 0.0;
    CK1l = 0.0;
177 CK4l = 0.0;
    CK5l = 0.0;
179 CK6i = 0.0;
    CK6l = 0.0;
181 CK7l = 0.0;
    CK8l = 0.0;
183 CK9l = 0.0;

185 Tev = 1e+6;
    Tsv = 1e+6;
187 Cev = 1e+6;
    Csv = 1e+6;
189 Tep = 0.0;
```

```
    Tdec = 0.0;
191 Tepk = 0.0;
    Terp = fy/(2*k1in);
193 Tern = -fy/(2*k1in);
    Cep = 0.0;
195 Cdec = 0.0;
    Cepk = 0.0;
197 Cerp = fy/(2*k1in);
    Cern = -fy/(2*k1in);
199
    TKrl = k1in;
201 TKul = k2in;
    CKrl = k1in;
203 CKul = k2in;

205 Temin = 0.0;
    Cemin = 0.0;
207
    Te0 = 0.0;
209 Tec = (fy+Fres/2)/k1in;
    Tsig0 = 0.0;
211 Tsigc = fy+Fres/2;
    Ce0 = 0.0;
213 Cec = (fy+Fres/2)/k1in;
    Csig0 = 0.0;
215 Csigc = fy;

217 Te0p = 0.5*fy/k1in;
    Tsig0p = fy/2;
219 Tecp = fy/k1in;
    Tsigcp = fy;
221 Ce0p = 0.5*fy/k1in;
    Csig0p = fy/2;
223 Cecp = fy/k1in;
    Csigcp = fy;
225
    Te0n = -0.5*fy/k1in;
227 Tsig0n = -fy/2;
    Tecn = -fy/k1in;
229 Tsigcn = -fy;
    Ce0n = -0.5*fy/k1in;
231 Csig0n = -fy/2;
```

```
    Cecn = -fy/k1in;
    Csigcn = -fy;

    // Trial and committed strains and stresses for each State
    Te1 = 0.0;
    Te2 = 0.0;
    Te3 = 0.0;
    Te4 = 0.0;
    Te5 = 0.0;
    Te6 = 0.0;
    Te7 = 0.0;
    Te8 = 0.0;
    Te9 = 0.0;
    Ce1 = 0.0;
    Ce2 = 0.0;
    Ce3 = 0.0;
    Ce4 = 0.0;
    Ce5 = 0.0;
    Ce6 = 0.0;
    Ce7 = 0.0;
    Ce8 = 0.0;
    Ce9 = 0.0;

    Ts1 = 0.0;
    Ts2 = 0.0;
    Ts3 = 0.0;
    Ts4 = 0.0;
    Ts5 = 0.0;
    Ts6 = 0.0;
    Ts7 = 0.0;
    Ts8 = 0.0;
    Ts9 = 0.0;
    Cs1 = 0.0;
    Cs2 = 0.0;
    Cs3 = 0.0;
    Cs4 = 0.0;
    Cs5 = 0.0;
    Cs6 = 0.0;
    Cs7 = 0.0;
    Cs8 = 0.0;
    Cs9 = 0.0;

```

```
    LCstress = 0.0;
    LCS = 0; // last committed state

  // State variables
    TState = 0;
    Tstrain = 0.0;
    Tstress = 0.0;
    Ttangent = k1in;

    CState = 0;
    Cstrain = 0.0;
    Cstress = 0.0;
    Ctangent = k1in;

}

SPSW_Web_Plate::SPSW_Web_Plate()
:UniaxialMaterial(0, 0),
 fy(0.0), Es(0.0), mf1(0.0), mf2(0.0), mf3(0.0), en1(0.0), en2(0.0),
  en3(0.0), kin(0.0), len(0.0), ht(0.0), tp(0.0)
{
  mu = 0.3;
  beta = -0.045-0.08*exp(-0.003*(ht/tp-300));
  Kb = 7.38+5.38*pow((ht/len),1.33);
  hont_cr = sqrt(1.732*Kb*Es/((1-pow(mu,2))*fy));
  Ftr = fy*(2.59*pow((ht/tp),-1.08)*pow((len/ht),0.36)*pow((Es/fy),0.59) + 0.017);
  Fres = -fy*(2.78*pow((ht/tp),-0.83)*pow((len/ht),-0.62)*pow((Es/fy),0.26) + 0.0032)
    ;
  Fst = Fres;
  Ft = fy + Fres/2;
  R = 6;
  R6 = 12; //R6 = 12;
  ct = 0;
  togp = 1;
  togn = 1;

  k1in = Es*(0.215*pow((ht/tp),0.19));
  k1 = k1in;
  k1f = 0.7*Es;
  k2in = Es*pow((ht/tp),0.1)*pow((len/ht),0.15);
  k3in = 0.6*k2in;
  kv = 0.0;
```

```
315   b = 600;

317

      sigcr = 0.25*Ftr; //sigcr = 0.125*Ftr;
319   s_exp = 0.0;

321   nu = min(0.5 + 0.5*exp(-0.01*(ht/tp-140)),1.0);
      xia = 1.0; //plastic sctrain accumulation factor (1 for State 1, 0.08 otherwise)
323   xib = 0.08;
      ////////////////////////////////////////////////////////////////////////

325

      Kn = 0.0;
327   kh = 0.0;
      khold = 0.0;
329   Kp = 0.0;
      k1hyp = k1in;
331   kt = 0.0;
      estar = 0.0;
333   sigstar = 0.0;
      gamma = 0.0;
335   ds = 0.0;
      dep = 0.0;
337

      X1 [0] = 0.0; X1 [1] = 0.0; X1 [2] = 0.0; X1 [3] = 0.0;
339   X2 [0] = 0.0; X2 [1] = 0.0; X2 [2] = 0.0; X2 [3] = 0.0;
      X3 [0] = 0.0; X3 [1] = 0.0; X3 [2] = 0.0; X3 [3] = 0.0;
341   X4 [0] = 0.0; X4 [1] = 0.0; X4 [2] = 0.0; X4 [3] = 0.0;
      Y [0] = 0.0; Y [1] = 0.0; Y [2] = 0.0; Y [3] = 0.0;
343   f1 = 0.0;
      f2 = 0.0;
345   f3 = 0.0;

347   kq1 = 0.0;
      kq2 = 0.0;
349   sq1 = 0.0;
      sq2 = 0.0;
351   eq1 = 0.0;
      eq2 = 0.0;
353

      // Initialize History Variables
355   TS_exp [0] = 0.0;
      TS_exp [1] = 0.0;
```

```
357   TS_exp [2] = 0.0;
      TS_exp [3] = 0.0;
359   CS_exp [0] = 0.0;
      CS_exp [1] = 0.0;
361   CS_exp [2] = 0.0;
      CS_exp [3] = 0.0;
363
      TS [0] = 0.0;
365   TS [1] = 0.0;
      TS [2] = 0.0;
367   TS [3] = 0.0;
      TS [4] = 0.0;
369   TS [5] = 0.0;
      TS [6] = 0.0;
371   CS [0] = 0.0;
      CS [1] = 0.0;
373   CS [2] = 0.0;
      CS [3] = 0.0;
375   CS [4] = 0.0;
      CS [5] = 0.0;
377   CS [6] = 0.0;

379   Tss [0] = 0.0;
      Tss [1] = 0.0;
381   Tss [2] = 0.0;
      Tss [3] = 0.0;
383   Tss [4] = 0.0;
      Tss [5] = 0.0;
385
      Css [0] = 0.0;
387   Css [1] = 0.0;
      Css [2] = 0.0;
389   Css [3] = 0.0;
      Css [4] = 0.0;
391   Css [5] = 0.0;

393   TA1 = 0.0;
      TA2 = 0.0;
395   TA3 = 0.0;
      TA4 = 0.0;
397   CA1 = 0.0;
      CA2 = 0.0;
```

```
399   CA3 = 0.0;
      CA4 = 0.0;
401
      TK1l = 0.0;
403   TK4l = 0.0;
      TK5l = 0.0;
405
      TK6i = 0.0;
407
      TK6l = 0.0;
409   TK7l = 0.0;
      TK8l = 0.0;
411   TK9l = 0.0;
      CK1l = 0.0;
413   CK4l = 0.0;
      CK5l = 0.0;
415
      CK6i = 0.0;
417
      CK6l = 0.0;
419   CK7l = 0.0;
      CK8l = 0.0;
421   CK9l = 0.0;

423   Tev = 1e+6;
      Tsv = 1e+6;
425   Cev = 1e+6;
      Csv = 1e+6;
427
      Tep = 0.0;
429   Tepk = 0.0;
      Terp = fy/(2*k1in);
431   Tern = -fy/(2*k1in);
      Cep = 0.0;
433   Cdec = 0.0;
      Cepk = 0.0;
435   Cerp = fy/(2*k1in);
      Cern = -fy/(2*k1in);
437
      TKrl = k1in;
439   TKul = k2in;
      CKrl = k1in;
```

```
441   CKul = k2in;

443   Temin = 0.0;
      Cemin = 0.0;
445
      Te0 = 0.0;
447   Tec = (fy+Fres/2)/k1in;
      Tsig0 = 0.0;
449   Tsigc = fy+Fres/2;
      Ce0 = 0.0;
451   Cec = (fy+Fres/2)/k1in;
      Csig0 = 0.0;
453   Csigc = fy;

455   Te0p = 0.5*fy/k1in;
      Tsig0p = fy/2;
457   Tecp = fy/k1in;
      Tsigcp = fy;
459   Ce0p = 0.5*fy/k1in;
      Csig0p = fy/2;
461   Cecp = fy/k1in;
      Csigcp = fy;
463
      Te0n = -0.5*fy/k1in;
465   Tsig0n = -fy/2;
      Tecn = -fy/k1in;
467   Tsigcn = -fy;
      Ce0n = -0.5*fy/k1in;
469   Csig0n = -fy/2;
      Cecn = -fy/k1in;
471   Csigcn = -fy;

473   Te1 = 0.0;
      Te2 = 0.0;
475   Te3 = 0.0;
      Te4 = 0.0;
477   Te5 = 0.0;
      Te6 = 0.0;
479   Te7 = 0.0;
      Te8 = 0.0;
481   Te9 = 0.0;
      Ce1 = 0.0;
```

```
483   Ce2 = 0.0;
      Ce3 = 0.0;
485   Ce4 = 0.0;
      Ce5 = 0.0;
487   Ce6 = 0.0;
      Ce7 = 0.0;
489   Ce8 = 0.0;
      Ce9 = 0.0;
491
      Ts1 = 0.0;
493   Ts2 = 0.0;
      Ts3 = 0.0;
495   Ts4 = 0.0;
      Ts5 = 0.0;
497   Ts6 = 0.0;
      Ts7 = 0.0;
499   Ts8 = 0.0;
      Ts9 = 0.0;
501   Cs1 = 0.0;
      Cs2 = 0.0;
503   Cs3 = 0.0;
      Cs4 = 0.0;
505   Cs5 = 0.0;
      Cs6 = 0.0;
507   Cs7 = 0.0;
      Cs8 = 0.0;
509   Cs9 = 0.0;

511   // Set trial values
        this->revertToLastCommit();
513 }

515 SPSW_Web_Plate::~SPSW_Web_Plate()
    {
517   // Do Nothing
    }
519
    int SPSW_Web_Plate::setTrialStrain (double strain, double strainRate)
521 {
        double dstrain = strain - Cstrain;
523     if (fabs(dstrain) < DBL_EPSILON) {
          return 0;
```

```
525     }
        else {
527       Tstrain = strain;
          if (ct == 1) {
529         k1 = k1in*(0.5+0.5*exp(-1e+4*pow(Cep,2)))*(0.5+0.5*exp(-100*(pow((Cerp-Ce4)
    ,2))));
          }
531       else {
          }
533       k2 = k2in*0.45*exp(-2*Cep);
          k3 = 0.6*k2;
535
    //
      ////////////////////////////////////////////////////////////////////////////////////////////

537 // Positive strain increment
    //
      ////////////////////////////////////////////////////////////////////////////////////////////

539
          if (dstrain > 0) {
541                 togn = 1;
            if (TState == 0) {
543           Determine_kh();
              estar = (Tstrain-Ce0)/(Cec-Ce0);
545           sigstar = (kh/k1)*estar + (1-(kh/k1))*estar/pow((1+pow(estar,R)),(1/R));
              Tstress = sigstar*(sigcr-Csig0) + Csig0;
547           Ttangent = k1in;
              TKrl = k1in;
549           TKul = k3;
              TState = 1;
            }
551         else if (TState == 1) {
553             ct = ct + 1;
              if (LCS != 1){
555           k1hyp = k1;
            }
557           else {
            }
559           khold = kh;
              Determine_kh();
561
```

```
        //opserr << "khold = " << khold;
563     //opserr << "k1 = " << k1 << endln;
        Tdec = ((k1hyp-khold)*Tec + (khold-kh)*Tstrain)/(k1hyp-kh) - Tec;
565     Tsigc = Tsigc + Tdec*k1hyp;
                estar = (Tstrain-Te0)/(Tec-Te0);
567             sigstar = (kh/k1hyp)*estar + (1-(kh/k1hyp))*estar/pow((1+pow(
    estar,R)),(1/R));
                Tstress = sigstar*(Tsigc-Tsig0) + Tsig0;
569             Determine_Ft();
        Ttangent = ((Tsigc-Tsig0)/(Tec-Te0))*(kh/k1hyp + (1-kh/k1hyp)*pow((1+pow(
    estar,R)),(-1/R)) - (1-kh/k1hyp)*pow(estar,R)*pow((1+pow(estar,R)),(-1-1/R)));
571     Te1 = Tstrain; // last strain in State 1
        Ts1 = Tstress; // last stress in State 1
573     TState = 1;
        TKrl = Ttangent;  // last positive tangent stiffness
575     TKul = k2; // unloading stiffness
        }
577   else if (TState == 2) {
        if (Tstress < Ts1) {
579       ds = k2*dstrain;
          Ttangent = k2;
581       Tstress = Cstress + ds;
          TState = 2;
583     }
        else    {
585       ds = TK1l*dstrain;
          Ttangent = TK1l;
587       Tstress = Cstress + ds;
          TState = 1;
589     TKrl = k2;
        TKul = k2;
591     }
      }
593   else if (TState == 3) {
        ds = k1*dstrain;
595     Tstress = Cstress + ds;
        Ttangent = k1;
597     Te3 = Tstrain; // last strain in State 1
        Ts3 = Tstress; // last stress in State 1
599     Te0 = Te3;
        Tsig0 = Ts3;
601     Tec = Te0 + (Ft-Ts3)/k2;
```

```
        Tsigc = Ft;
603     TState = 1;
        TKrl = k1;
605     TKul = k3;
      }
607
      else if (TState == 4)  {
609     TS_exp[0] = Cstress;
        TS_exp[1] = Cstrain;
611     TS_exp[2] = Ce3;
        TS_exp[3] = b*(Fst-Fres);
613     k5 = (Ftr-Fres)/(Ft/k2 - Fst/k3);
        k7 = 0.8*k5;
615     if (Terp > (Ce4 + (Ftr-Cs4)/k5 + (0.5*fy-Ftr)/k1 + 0.0005) && Ce4 <= Temin)
    {

617       ds = k5*dstrain;
          Tstress = Cstress + ds;
619       Ttangent = k5;
          Tec = Terp - (fy/(2*k1)-sigcr/k1);
621       Te0 = Ce4 + (Ftr-Cs4)/k5;
          //Te0 = Ce4 + (Ftr-Fres)/k5;
623       Tsig0 = Ftr;
          Te4 = Cstrain; //last strain in State 4
625       Ts4 = Cstress; // last stress in State 4
          TState = 5;
627       TKrl = k5;
          TKul = k5;
629     }
        else if (Terp > (Ce4 + (Ftr-Cs4)/k5 + (0.5*fy-Ftr)/k1 + 0.0005) && Ce4 >
    Temin) {
631
          ds = k7*dstrain;
633       Tstress = Cstress + ds;
          Ttangent = k7;
635       Determine_Ft();
          Te4 = Cstrain;  // last strain in State 4
637       Ts4 = Tstress;  // last stress in State 4
          TState = 8;
639       TKrl = k7;
          TKul = k7;
641     }
```

```
        else {
643       Te0 = TS_exp[1];
          Tsig0 = TS_exp[0];
645       Tec = (0.5*fy-k1*Terp-Tsig0+k5*Te0)/(k5-k1);
          Tsigc = Tsig0+k5*(Tec-Te0);
647       estar = (Tstrain-Te0)/(Tec-Te0);
          sigstar = (k1/k5)*estar + (1-(k1/k5))*estar/pow((1+pow(estar,R)),(1/R));
649       Tstress = sigstar*(Tsigc-Tsig0) + Tsig0;
          Ttangent = ((Tsigc-Tsig0)/(Tec-Te0))*(k1/k5 + (1-k1/k5)*pow((1+pow(estar,
    R)),(-1/R)) - (1-k1/k5)*pow(estar,R)*pow((1+pow(estar,R)),(-1-1/R)));
651       Determine_Ft();
          Te4 = Tstrain; // last strain in State 4
653       Ts4 = Tstress; // last stress in State 4
          TS[0] = Tsig0;
655       TS[1] = Te0;
          TS[2] = Tsigc;
657       TS[3] = Tec;
          TS[4] = k5;
659       TS[5] = k5;
          TS[6] = Terp;
661       TState = 9;
          TKrl = k7;
663       TKul = k5;
        }
665   }
      else if (TState==5) {
667     if (Tstress < Ftr) {
          ds = k5*dstrain;
669       Tstress = Cstress+ds;
          TState = 5;
671     }
        else {
673       TK6i = max((sigcr-Ftr)/(Terp-(0.5*fy-sigcr)/k1-Te0),-k5/2);
          Te0 = Te4 + (Ftr-Cs4)/k5;
675       Tec = (0.5*fy-Ftr+TK6i*Te0-k1*Terp)/(TK6i-k1);
          Tsigc = 0.5*fy-(Terp-Tec)*k1;
677       ds = TK6i*dstrain;
          Tstress = Cstress + ds;
679       Tsv = 1e6;
          Tev = 1e6;
681       TS[0] = Tsig0;
          TS[1] = Te0;
```

```
683             TS[2] = Tsigc;
                TS[3] = Tec;
685             TS[4] = TK6i;
                TS[5] = TK6i;
687             TS[6] = Terp;
                TState = 6;
689           }

691           Determine_Ft();
              Temin = Te4;
693           Ttangent = k5;
              Te5 = Tstrain; // last strain in State
695           Ts5 = Tstress; // last stress in State
              TKrl = k5;
697           TKul = k5;
            }
699         else if (TState==6) {
              if (Tstress < 0.5*fy && (LCS == 5 | LCS == 7)) {
701             Te0 = Te4 + (Ftr-Cs4)/k5;
                Tec = (0.5*fy-Ftr+TK6i*Te0-k1*Terp)/(TK6i-k1);
703             Tsigc = 0.5*fy-(Cerp-Tec)*k1;
                estar = (Tstrain-Te0)/(Tec-Te0);
705             sigstar = (k1/TK6i)*estar + (1-(k1/TK6i))*estar/pow((1+pow(estar,R6)),(1/
    R6));
                Tstress = sigstar*(Tsigc-Tsig0) + Tsig0;
707             Determine_Ft();
                TK6l = ((Tsigc-Tsig0)/(Tec-Te0))*(k1/TK6i + (1-k1/TK6i)*pow((1+pow(estar,
    R6)),(-1/R6)) - (1-k1/TK6i)*pow(estar,R6)*pow((1+pow(estar,R6)),(-1-1/R6)));
709             Ttangent = TK6l;

711             TS[0] = Tsig0;
                TS[1] = Te0;
713             TS[2] = Tsigc;
                TS[3] = Tec;
715             TS[4] = TK6l;
                TS[5] = TK6i;
717             TS[6] = Terp;
                TState = 6;
719             LCS = 5;
              }
721           else if (Tstress < 0.5*fy && LCS == 8) {
                Te0 = Te8;
```

```
723             Tsig0 = Ts8;
                Tec = (0.5*fy-Tsig0+TK8l*Te0-k1*Terp)/(TK8l-k1);
725             Tsigc = 0.5*fy-(Cerp-Tec)*k1;
                estar = (Tstrain-Te0)/(Tec-Te0);
727             sigstar = (k1/TK8l)*estar + (1-(k1/TK8l))*estar/pow((1+pow(estar,R6)),(1/
    R6));
                Tstress = sigstar*(Tsigc-Tsig0) + Tsig0;
729             Determine_Ft();
                TK6l = ((Tsigc-Tsig0)/(Tec-Te0))*(k1/TK8l + (1-k1/TK8l)*pow((1+pow(estar,
    R6)),(-1/R6)) - (1-k1/TK8l)*pow(estar,R6)*pow((1+pow(estar,R6)),(-1-1/R6)));
731             Ttangent = TK6l;
                TS[0] = Tsig0;
733             TS[1] = Te0;
                TS[2] = Tsigc;
735             TS[3] = Tec;
                TS[4] = TK6l;
737             TS[5] = TK6i;
                TS[6] = Terp;
739             TState = 6;
                LCS = 8;
741           }
              else   {
743             ds = k1*dstrain;
                Tstress = Cstress+ds;
745             Tec = Te6+(Ft-fy/2)/k1;
                Te0 = Cstrain;
747             Tsig0 = Cstress;
                Tsigc = Ft;
749             Determine_Ft();
                Determine_kh();
751             Ttangent = k1;
                TState = 1;
753             LCS = 6;
              }
755           if (Ttangent >= 0.0 && Ctangent <= 0.0) {
                Tsv = Cstress;
757             Tev = Cstrain;
              }
759           else {
              }
761           Te6 = Tstrain; // last strain in State
              Ts6 = Tstress; // last stress in State
```

```
763             TKrl = Ttangent;
                if (k7 > TK6l){
765               TKul = k7;
                }
767             else {
                  TKul = TK6l;
769             }
              }
771         else if (TState == 7) {
              if (LCS == 6) {
773             if (Tstress < Ts6) {
                  if (k7 > TK7l){
775               Kn = k7;
                  }
777               else {
                    Kn = TK7l;
779               }
                  //cout << "K1 = "; cout << Kn; cout << "\n";
781               ds = Kn*dstrain;
                  Tstress = Cstress + ds;
783               Ttangent = Kn;
                  TState = 7;
785             }
                else {
787               Kn = TS[5];
                  ds = Kn*dstrain;
789               Tstress = Cstress+ds;
                  Tec = TS[3];
791               Tsigc = TS[2];
                  Te0 = TS[1];
793               Tsig0 = TS[0];
                  Ttangent = Kn;
795               TState = 6;
                  LCS = 7;
797             }
              }
799           else if (LCS == 8) {
                 if (Tstress < Ts8) {
                  if (k7 > TK7l){
801               Kn = k7;
                  }
803               else {
```

```
805                 Kn = TK7l;
                   }
807                ds = Kn*dstrain;
                   Tstress = Cstress+ds;
809                Ttangent = Kn;
                   TState = 7;
811               }
                  else {
813                ds = TK8l*dstrain;
                   Tstress = Cstress+ds;
815                Ttangent = TK8l;
                   TState = 8;
817                LCS = 7;
                  }
819            }
               else if (LCS == 9) {
821               if (Tstress < Ts9) {
                   if (k7 > TK7l){
823                Kn = k7;
                   }
825                else {
                     Kn = TK7l;
827                }
                   ds = Kn*dstrain;
829                Tstress = Cstress+ds;
                   Ttangent = Kn;
831                TState = 7;
                  }
833               else {
                   ds = TK9l*dstrain;
835                Tstress = Cstress + ds;
                   Ttangent = TK9l;
837                TState = 9;
                   LCS = 7;
839               }
               }
841            else {
               }
843         TK7l = Ttangent;
            Te7 = Tstrain;  // last strain in State
845         Ts7 = Tstress;  // last stress in State
            TKrl = TK7l;
```

```
847         TKul = TK7l;
            }
849         else if (TState == 8) {
              if (Tsv != 1e+6) {
851             kv = (Tsv-Ts4)/(Tev-Te4);
                if (Te4 > Tev - (Tsv-Ts4)/k7 && Tstress < Ts6) {
853               Tss [0] = k7;
                  Tss [1] = TK6l;
855               Tss [2] = Ts4;
                  Tss [3] = Ts6;
857               Tss [4] = Te4;
                  Tss [5] = Te6;
859               Determine_cubic_coeff();
                  Tstress = TA1 + TA2*Tstrain + TA3*pow(Tstrain,2) + TA4*pow(Tstrain,3);
861               Ttangent = TA2 + 2*TA3*Tstrain + 3*TA4*pow(Tstrain,2);
                  TState = 8;
863             }
                else if (Te4 > Tev - (Tsv-Ts4)/k7 && Tstress > Ts6) {
865               ds = TK6l*dstrain;
                  Tstress = Cstress+ds;
867               Ttangent = TK6l;
                  TState = 6;
869               LCS = 8;
                }
871             else if (Te4 < Tev - (Tsv-Ts4)/k7 && Tstrain < Tev) {
                  Tss[0] = k7;
873               Tss[1] = 0.0;
                  Tss[2] = Ts4;
875               Tss[3] = Tsv;
                  Tss[4] = Te4;
877               Tss[5] = Tev;
                  Determine_cubic_coeff();
879               Tstress = TA1 + TA2*Tstrain + TA3*pow(Tstrain,2) + TA4*pow(Tstrain,3);
                  Ttangent = TA2 + 2*TA3*Tstrain + 3*TA4*pow(Tstrain,2);
881               TState = 8;
                }
883             else if (Te4 < Tev - (Tsv-Ts4)/k7 && Tstrain > Tev) {
                  ds = 0;
885               Tstress = Cstress+ds;
                  Ttangent = 1e-3;
887               TState = 6;
                  LCS = 8;
```

```
889             }
              }
891           else if (Tsv == 1e+6 && Tstrain < Te6) {
                Tss[0] = k7;
893             Tss[1] = TK6l;
                Tss[2] = Ts4;
895             Tss[3] = Ts6;
                Tss[4] = Te4;
897             Tss[5] = Te6;
                Determine_cubic_coeff();
899             Tstress = TA1 + TA2*Tstrain + TA3*pow(Tstrain,2) + TA4*pow(Tstrain,3);
                Ttangent = TA2 + 2*TA3*Tstrain + 3*TA4*pow(Tstrain,2);
901             TState = 8;
              }
903           else {
                ds = TK6l*dstrain;
905             Tstress = Cstress + ds;
                            Ttangent = TK6l;
907             TState = 6;
                LCS = 8;
909           }
              TK8l = Ttangent;
911           Te8 = Tstrain; // last strain in State
              Ts8 = Tstress; // last stress in State
913           TKrl = TK8l;
              TKul = TK7l;
915         }
          else if (TState == 9) {
917         if (Tstress < 0.5*fy) {
              Te0 = TS[1];
919           Tec = TS[3];
              Tsigc = TS[2];
921           estar = (Tstrain-Te0)/(Tec-Te0);
              sigstar = (k1/k5)*estar + (1-(k1/k5))*estar/pow((1+pow(estar,R)),(1/R));
923           Tstress = sigstar*(Tsigc-Tsig0) + Tsig0;
              Ttangent = ((Tsigc-Tsig0)/(Tec-Te0))*(k1/k5 + (1-k1/k5)*pow((1+pow(estar,
    R)),(-1/R)) -
925             (1-k1/k5)*pow(estar,R)*pow((1+pow(estar,R)),(-1-1/R)));
              TK9l = Ttangent;
927           TS[0] = Tsig0;
              TS[1] = Te0;
929           TS[2] = Tsigc;
```

```
            TS[3] = Tec;
            TS[4] = TK9l;
            TS[5] = k5;
            TS[6] = Terp;
            TState = 9;
          }
          else {
            ds = k1*dstrain;
            Tstress = Cstress+ds;
            Ttangent = k1;
            Tec = Cstrain + (Ft-fy/2)/k1;
            Te0 = Cstrain;
            Tsig0 = Cstress;
            Tsigc = Ft;
            Determine_kh();
            TState = 1;
            LCS = 9;
          }

          Te9 = Tstrain; // last strain in State
          Ts9 = Tstress; // last stress in State
          Temin = TS_exp[1];
          TKrl = TK9l;
          TKul = TK9l;
        }
        else {
        }
        //Determine_Ft();
        if  (Tstrain < Cerp)  {
          gamma = 0.0;
          dep = xib*fabs(dstrain); // increment in accumulated plastic strain
          Tepk = Tepk + dep; // strain used to compute kinematic back stress
          Tep = Cep + dep;
          togp = 1;
        }
        else if ((Tstrain > Cerp) && togp == 1) {
          Determine_Ft();
          Determine_kh();
          gamma = 0.0;
          dep = xib*fabs(dstrain);
          Tep = Cep + dep;
          Te0p = Terp;
```

```
          Tecp = Terp + (Ft-0.5*fy)/k1;
973       togp = 0;
        }
975     else if ((Tstrain >= Cerp) && togp == 0) {

977       //Determine_kh();
          estar = (Cstrain-Te0p)/(Tecp-Te0p);
979
          kt = ((Ft-0.5*fy)/(Tecp-Te0p))*(kh/k1 + (1-kh/k1)*pow((1+pow(estar,R)),(-1/
    R)) - (1-kh/k1)*pow(estar,R)*pow((1+pow(estar,R)),(-1-1/R)));
981       gamma = fabs(kt/k1);
          //opserr << "gamma = " << gamma << endln;
983       dep = (1-gamma)*dstrain;
          derp = dep;
985       dern = nu*dep;
          Tep = Cep + dep;
987       Terp = Cerp + derp;
          Tern = Cern + dern;
989       Tepk = Cepk + dep;
        }
991     else {
          gamma = 0;
993     }

995   }

997 //
    ////////////////////////////////////////////////////////////////////////////////////////////

    // Negative strain increment
999 //
    ////////////////////////////////////////////////////////////////////////////////////////////

    else if (dstrain < 0) {
1001            togp = 1;
      if (TState == 0) {
1003
          Tstress = dstrain*k1;
1005      Fst = Fres;
          Ttangent = k1in;
1007      TKrl = k1in;
          TKul = k3;
```

```
1009            TState = 3;
                ct = ct + 1;
1011          }
                      if (TState == 1) {
1013
                ds = k2*dstrain;
1015            Tstress = Cstress + ds;
                Ttangent = k2;
1017            TState = 2;
                Te1 = Tstrain; // last strain in State
1019            Ts1 = Tstress; // last stress in State
                TKrl = k1;
1021            TKul = k2;
              }
1023              else if (TState == 2) {
                ct = 0;
1025                  if (Tstress > 0) {
                          ds = k2*dstrain;
1027              Tstress = Cstress + ds;
                  Ttangent = k2;
1029              TState = 2;
                }
1031              else    {
                      Fst = -fy*(3.5e-5*pow((ht/tp),-0.09)*pow((len/ht),-0.23)*pow((Es/fy)
    ,1.4))*exp(-80*(pow(Cep,2)))*(1-0.8*exp(-20000*(pow(fabs(Te2-Ce4),2)))) + Fres;
1033
                      k5 = k2in*(Ftr-Fres)/(fy-Fst);
1035                  k7 = 0.8*k5;
                      ds = k3*dstrain;
1037                  Tstress = Cstress + ds;
                      Ttangent = k3;
1039                  Tsigc = Ft;
                      TState = 3;
1041            }
                      Determine_Ft();
1043                  Te2 = Tstrain; // last strain in State
                      Ts2 = Tstress; // last stress in State
1045                  TKrl = k2;
                      TKul = k2;
1047          }
              else if (TState==3) {
1049          if (Tstress > Fst) {
```

```
            Kn = k3;
            ds = Kn*dstrain;
            Tstress = Cstress + ds;
            Ttangent = k3;
            TState = 3;
          }
          else {
            Kn = b*(Fst-Fres);
            ds = Kn*dstrain;
            Tstress = Cstress + ds;
            Ttangent = Kn;
            Temin = 1;
            Te3 = (Fst-Cstress)/k3 + Cstrain;
            TS_exp[0] = Tstress;
            TS_exp[1] = Tstrain;
            TS_exp[2] = Te3;
            TS_exp[3] = Kn;
            TState = 4;
          }
          TKrl = k1;
          TKul = Kn;
        }
        else if (TState==4) {
          Tstress = Fst + (Fres-Fst)*(1-exp(b*(Tstrain-Te3)));
          Determine_Ft();
          TK4l = -b*(Fres-Fst)*exp((Tstrain-Te3));
          Te4 = Tstrain; // last strain in State
          Ts4 = Tstress; // last stress in State
          TS_exp[0] = Ts4,
          TS_exp[1] = Te4,
          TS_exp[2] = Te3,
          TS_exp[3] = TK4l;
          TKrl = k5;
          TKul = TK4l;
          Ttangent = TK4l;
          TState = 4;
        }
      ////////////////////////////////////
        else if (TState == 5) {
          if (Tstress > TS_exp[0]) {
            ds = k5*dstrain;
            Tstress = Cstress + ds;
```

```
            Ttangent = k5;
1093        TState = 5;
          }
1095      else {
            Kn = TS_exp[3];
1097        ds = Kn*dstrain;
            Tstress = Cstress + ds;
1099        Ttangent = Kn;
            TState = 4;
1101      }
          TK5l = k5;
1103      Te5 = Tstrain; // last strain in State
          Ts5 = Tstrain; // last stress in State
1105      TKrl = k5;
          TKul = k5;
1107    }
        else if (TState == 6) {
1109
          if (k7 > TS[4]){
1111        Kn = k7;
          }
1113      else {
            Kn = TS[4];
1115      }
          ds = Kn*dstrain;
1117      Determine_Ft();
          Tstress = Cstress + ds;
1119      Ttangent = Kn;
          TState = 7;
1121      TKrl = TS[4];
          TKul = k7;
1123    }
        else if (TState == 7) {
1125      s_exp = Fst + (Fres-Fst)*(1-exp(b*(Tstrain-Te3)));
          if (Tstress > s_exp) {
1127        if (k7 > TS[4]){
            Kn = k7;
1129        }
            else {
1131          Kn = TS[4];
            }
1133        ds = Kn*dstrain;
```

```
            Tstress = Cstress + ds;
            Ttangent = Kn;
            TState = 7;
          }
          else if (Tstress <= s_exp) {

            ds = TK4l*dstrain;
            Tstress = Cstress + ds;
            Ttangent = TK4l;
            TState = 4;
          }
          Determine_Ft();
          TK7l = Kn;
          Te7 = Tstrain; // last strain in State
          Ts7 = Tstress; // last stress in State
          TKrl = k7;
          TKul = TK7l;
        }
        else if (TState == 8) {
          if (Tstress > s_exp) {

            if (k7 > TS[4]){
            Kn = k7;
            }
            else {
              Kn = TS[4];
            }
            ds = Kn*dstrain;
            Tstress = Cstress + ds;
            Ttangent = Kn;
            TState = 7;
          }
          else {
          }
          TKrl = TK8l;
          TKul = k7;
        }
        else if (TState == 9) {
          if (k7 > TS[4]){
          Kn = k7;
          }
          else {
```

```
            Kn = TS[4];
1177      }
          ds = Kn*dstrain;
1179      Determine_Ft();
          Tstress = Cstress + ds;
1181      Ttangent = Kn;
          Te9 = Tstrain;
1183      Ts9 = Tstress;
          TState = 7;
1185      TKrl = TK9l;
          TKul = Kn;
1187    }
//
  ////////////////////////////////////////////////////////////////////////////////////////

1189    if ((Tstrain > Cern) && (Tstrain < Cerp))  {
          gamma = 0;
1191      dep = xib*fabs(dstrain); // increment in accumulated plastic strain
          Tep = Cep + dep;
1193      Tepk = Cepk - dep; // strain used to compute kinematic back stress
        }
1195    else if (((Tstrain < Cern) && (Cstrain >= Cern)) | ((Tstrain <= Cern) && (
  Cstrain > Cern))) {
          Determine_Ft();
1197      Determine_kh();
            gamma = 0.0;
1199      dep = xib*fabs(dstrain);
          Tep = Cep + dep;
1201      Te0n = Tern;
          Tecn = Tern - (Ft-0.5*fy)/k1;
1203    }
        else if (Tstrain <= Cern )  {
1205
          estar = (Cstrain-Te0n)/(Tecn-Te0n);
1207      kt = -((Ft-0.5*fy)/(Tecn-Te0n))*(kh/k1 + (1-kh/k1)*pow((1+pow(estar,R)),(-1/R
  )) - (1-kh/k1)*pow(estar,R)*pow((1+pow(estar,R)),(-1-1/R)));

1209      gamma = fabs(kt/k1);
          dep = (1-gamma)*fabs(dstrain);
1211      derp = -nu*dep;
          dern = -dep;
1213
```

```
        Tep = Cep + dep;
        Terp = Cerp + derp;
        Tern = Cern + dern;
        Tepk = Cepk - dep;
      }
      else {
        gamma = 0;
      }
  //
    ////////////////////////////////////////////////////////////////////////////////////////

       }
    else if (dstrain == 0) {
    }
//
    ////////////////////////////////////////////////////////////////////////////////////////

// If Ttangent is zero or bigger than initial stiffness, reassign.
    if (Ttangent == 0.0) {
      Ttangent = 1e-3;
    }
    else if (Ttangent > k2in) {
      Ttangent = k2in;
    }
    if (TState != CState) {
      LCS = CState;
    }
    else {
    }
   }
   return 0;
}
void SPSW_Web_Plate::Determine_kh() {
    if (Tep < en1) {
      kh = fy*(mf1)/(en1);
    }
    else if (Tep >= en1 && Tep < en2) {
      kh = fy*(mf2-mf1)/(en2-en1);
    }
    else if (Tep >= en2) {
      kh = fy*(mf3-mf2)/(en3-en2);
    }
```

```
}
void SPSW_Web_Plate::Determine_Ft() {
    if (Tep < en1) {
      Ft = (fy*(1 + mf1*Tep/en1)-kin*(Tep-fabs(Tepk)))/pow((1-fabs(Fres/fy)+pow(fabs(
    Fres/fy),2)),0.5) + Fres;
    }
    else if (Tep >= en1 && Tep < en2) {
      Ft = (fy*((1+mf1) + (mf2-mf1)*(Tep-en1)/(en2-en1))-kin*(Tep-fabs(Tepk)))/pow
    ((1-fabs(Fres/fy)+pow(fabs(Fres/fy),2)),0.5) + Fres;
    }
    else if (Tep >= en2) {
      Ft = (fy*((1+mf2) + (mf3-mf2)*(Tep-en2)/(en3-en2))-kin*(Tep-fabs(Tepk)))/pow
    ((1-fabs(Fres/fy)+pow(fabs(Fres/fy),2)),0.5) + Fres;
    }
}
void SPSW_Web_Plate::Determine_cubic_coeff() {
  // This routine finds the coeff of cubic equation describing transition
  kq1 = Tss[0];
  kq2 = Tss[1];
  sq1 = Tss[2];
  sq2 = Tss[3];
  eq1 = Tss[4];
  eq2 = Tss[5];

  X1[0] = 1.0; X1[1] = eq1; X1[2] = pow(eq1,2); X1[3] = pow(eq1,3);
  X2[0] = 1e-10; X2[1] = 1.0; X2[2] = 2*eq1; X2[3] = 3*pow(eq1,2);
  X3[0] = 1.0; X3[1] = eq2; X3[2] = pow(eq2,2); X3[3] = pow(eq2,3);
  X4[0] = 1e-10; X4[1] = 1.0; X4[2] = 2*eq2; X4[3] = 3*pow(eq2,2);
  Y[0] = sq1; Y[1] = kq1; Y[2] = sq2; Y[3] = kq2;

  f1 = -X1[0]/X2[0];
  f2 = -X1[0]/X3[0];
  f3 = -X1[0]/X4[0];
  X2[1] = f1*X2[1]+X1[1]; X2[2] = f1*X2[2]+X1[2]; X2[3] = f1*X2[3]+X1[3];
  X3[1] = f2*X3[1]+X1[1]; X3[2] = f2*X3[2]+X1[2]; X3[3] = f2*X3[3]+X1[3];
  X4[1] = f3*X4[1]+X1[1]; X4[2] = f3*X4[2]+X1[2]; X4[3] = f3*X4[3]+X1[3];
  Y[1] = f1*Y[1]+Y[0]; Y[2] = f2*Y[2]+Y[0]; Y[3] = f3*Y[3]+Y[0];

  f1 = -X2[1]/X3[1];
  f2 = -X2[1]/X4[1];
  X3[2] = f1*X3[2]+X2[2]; X3[3] = f1*X3[3]+X2[3];
  X4[2] = f2*X4[2]+X2[2]; X4[3] = f2*X4[3]+X2[3];
```

```
1291    Y[2] = f1*Y[2] + Y[1];   Y[3] = f2*Y[3] + Y[1];

1293    f1 = -X3[2]/X4[2];
        X4[3] = f1*X4[3]+X3[3];
1295    Y[3] = f1*Y[3]+Y[2];

1297    TA4 = Y[3]/X4[3];
        TA3 = (Y[2]-TA4*X3[3])/X3[2];
1299    TA2 = (Y[1]-TA4*X2[3]-TA3*X2[2])/X2[1];
        TA1 = (Y[0]-TA4*X1[3]-TA3*X1[2]-TA2*X1[1])/X1[0];
1301
}
1303 double SPSW_Web_Plate::getStrain ()
{
1305    return Tstrain;
}
1307 double SPSW_Web_Plate::getStress ()
{
1309    return Tstress;
}
1311 double SPSW_Web_Plate::getTangent ()
{
1313    return Ttangent;
}
1315 int SPSW_Web_Plate::commitState ()
{
1317    // Reset trial history variables to last committed state
        LCstress = Cstress;
1319    //LCS = CState;

1321     CState = TState;
         Cstrain = Tstrain;
1323     Cstress = Tstress;
         Ctangent = Ttangent;
1325     CS_exp [0] = TS_exp [0];
         CS_exp [1] = TS_exp [1];
1327     CS_exp [2] = TS_exp [2];
         CS_exp [3] = TS_exp [3];
1329     Css [0] = Tss [0];
         Css [1] = Tss [1];
1331     Css [2] = Tss [2];
         Css [3] = Tss [3];
```

```
1333    Css [4] = Tss [4];
        Css [5] = Tss [5];
1335    CS [0] = TS [0];
        CS [1] = TS [1];
1337    CS [2] = TS [2];
        CS [3] = TS [3];
1339    CS [4] = TS [4];
        CS [5] = TS [5];
1341    CS [6] = TS [6];
        CA1 = TA1;
1343    CA2 = TA2;
        CA3 = TA3;
1345    CA4 = TA4;
        CK1l = TK1l;
1347    CK4l = TK4l;
        CK5l = TK5l;
1349    CK6i = TK6i;
        CK6l = TK6l;
1351    CK7l = TK7l;
        CK8l = TK8l;
1353    CK9l = TK9l;
        Cev = Tev;
1355    Csv = Tsv;
        Cep = Tep;
1357    Cepk = Tepk;
        Cerp = Terp;
1359    Cern = Tern;
        CKrl = TKrl;
1361    CKul = TKul;
        Cemin = Temin;
1363    Ce0 = Te0;
        Cec = Tec;
1365    Csig0 = Tsig0;
        Csigc = Tsigc;
1367    Ce0p = Te0p;
        Csig0p = Tsig0p;
1369    Cecp = Tecp;
        Csigcp = Tsigcp;
1371    Ce0n = Te0n;
        Csig0n = Tsig0n;
1373    Cecn = Tecn;
        Csigcn = Tsigcn;
```

```
1375      Ce1 = Te1;
          Ce2 = Te2;
1377      Ce3 = Te3;
          Ce4 = Te4;
1379      Ce5 = Te5;
          Ce6 = Te6;
1381      Ce7 = Te7;
          Ce8 = Te8;
1383      Ce9 = Te9;
          Cs1 = Ts1;
1385      Cs2 = Ts2;
          Cs3 = Ts3;
1387      Cs4 = Ts4;
          Cs5 = Ts5;
1389      Cs6 = Ts6;
          Cs7 = Ts7;
1391      Cs8 = Ts8;
          Cs9 = Ts9;
1393     return 0;
    }
1395
    int SPSW_Web_Plate::revertToLastCommit ()
1397 {
       // Reset trial state variables to last committed state
1399      TState = CState;
          Tstrain = Cstrain;
1401      Tstress = Cstress;
          Ttangent = Ctangent;
1403      TS_exp [0] = CS_exp [0];
          TS_exp [1] = CS_exp [1];
1405      TS_exp [2] = CS_exp [2];
          TS_exp [3] = CS_exp [3];
1407      Tss [0] = Css [0];
          Tss [1] = Css [1];
1409      Tss [2] = Css [2];
          Tss [3] = Css [3];
1411      Tss [4] = Css [4];
          Tss [5] = Css [5];
1413      TS [0] = CS [0];
          TS [1] = CS [1];
1415      TS [2] = CS [2];
          TS [3] = CS [3];
```

```
    TS [4] = CS [4];
    TS [5] = CS [5];
    TS [6] = CS [6];
    TA1 = CA1;
    TA2 = CA2;
    TA3 = CA3;
    TA4 = CA4;
    TK1l = CK1l;
    TK4l = CK4l;
    TK5l = CK5l;
    TK6i = CK6i;
    TK6l = CK6l;
    TK7l = CK7l;
    TK8l = CK8l;
    TK9l = CK9l;
    Tev = Cev;
    Tsv = Csv;
    Tep = Cep;
    Tepk = Cepk;
    Terp = Cerp;
    Tern = Cern;
    TKrl = CKrl;
    TKul = CKul;
    Temin = Cemin;
    Te0 = Ce0;
    Tec = Cec;
    Tsig0 = Csig0;
    Tsigc = Csigc;
    Te0p = Ce0p;
    Tsig0p = Csig0p;
    Tecp = Cecp;
    Tsigcp = Csigcp;
    Te0n = Ce0n;
    Tsig0n = Csig0n;
    Tecn = Cecn;
    Tsigcn = Csigcn;
    Te1 = Ce1;
    Te2 = Ce2;
    Te3 = Ce3;
    Te4 = Ce4;
    Te5 = Ce5;
    Te6 = Ce6;
```

```
1459      Te7 = Ce7;
          Te8 = Ce8;
1461      Te9 = Ce9;
          Ts1 = Cs1;
1463      Ts2 = Cs2;
          Ts3 = Cs3;
1465      Ts4 = Cs4;
          Ts5 = Cs5;
1467      Ts6 = Cs6;
          Ts7 = Cs7;
1469      Ts8 = Cs8;
          Ts9 = Cs9;
1471
          return 0;
1473  }

1475  int SPSW_Web_Plate::revertToStart ()
      {
1477     // State variables
         TState = 0;
1479     Tstrain = 0.0;
         Tstress = 0.0;
1481     Ttangent = k1in;
         CState = 0;
1483     Cstrain = 0.0;
         Cstress = 0.0;
1485     Ctangent = k1in;
         //History Variables
1487      TS_exp [0] = 0.0;
          TS_exp [1] = 0.0;
1489      TS_exp [2] = 0.0;
          TS_exp [3] = 0.0;
1491      CS_exp [0] = 0.0;
          CS_exp [1] = 0.0;
1493      CS_exp [2] = 0.0;
          CS_exp [3] = 0.0;
1495      TS [0] = 0.0;
          TS [1] = 0.0;
1497      TS [2] = 0.0;
          TS [3] = 0.0;
1499      TS [4] = 0.0;
          TS [5] = 0.0;
```

```
    TS [6] = 0.0;
    CS [0] = 0.0;
    CS [1] = 0.0;
    CS [2] = 0.0;
    CS [3] = 0.0;
    CS [4] = 0.0;
    CS [5] = 0.0;
    CS [6] = 0.0;
    Tss [0] = 0.0;
    Tss [1] = 0.0;
    Tss [2] = 0.0;
    Tss [3] = 0.0;
    Tss [4] = 0.0;
    Tss [5] = 0.0;
    Css [0] = 0.0;
    Css [1] = 0.0;
    Css [2] = 0.0;
    Css [3] = 0.0;
    Css [4] = 0.0;
    Css [5] = 0.0;
    TA1 = 0.0;
    TA2 = 0.0;
    TA3 = 0.0;
    TA4 = 0.0;
    CA1 = 0.0;
    CA2 = 0.0;
    CA3 = 0.0;
    CA4 = 0.0;
    TK1l = 0.0;
    TK4l = 0.0;
    TK5l = 0.0;
    TK6i = 0.0;
    TK6l = 0.0;
    TK7l = 0.0;
    TK8l = 0.0;
    TK9l = 0.0;
    CK1l = 0.0;
    CK4l = 0.0;
    CK5l = 0.0;
    CK6i = 0.0;
    CK6l = 0.0;
    CK7l = 0.0;
```

```
1543    CK8l = 0.0;
        CK9l = 0.0;
1545    Tev = 1e+6;
        Tsv = 1e+6;
1547    Cev = 1e+6;
        Csv = 1e+6;
1549    Tep = 0.0;
        Tepk = 0.0;
1551    Terp = fy/(2*k1in);
        Tern = -fy/(2*k1in);
1553    Cep = 0.0;
        Cepk = 0.0;
1555    Cerp = fy/(2*k1in);
        Cern = -fy/(2*k1in);
1557    TKrl = k1in;
        TKul = k2in;
1559    CKrl = k1in;
        CKul = k2in;
1561    Temin = 0.0;
        Cemin = 0.0;
1563    Te0 = 0.0;
        Tec = (fy+Fres)/k1in;
1565    Tsig0 = 0.0;
        Tsigc = fy+Fres;
1567    Ce0 = 0.0;
        Cec = (fy+Fres)/k1in;
1569    Csig0 = 0.0;
        Csigc = fy;
1571    Te0p = 0.0;
        Tsig0p = fy/2;
1573    Tecp = fy/k1in;
        Tsigcp = fy;
1575    Ce0p = 0.0;
        Csig0p = fy/2;
1577    Cecp = fy/k1in;
        Csigcp = fy;
1579    Te0n = 0.0;
        Tsig0n = -fy/2;
1581    Tecn = -fy/k1in;
        Tsigcn = -fy;
1583    Ce0n = 0.0;
        Csig0n = -fy/2;
```

```
1585      Cecn = -fy/k1in;
          Csigcn = -fy;
1587      Te1 = 0.0;
          Te2 = 0.0;
1589      Te3 = 0.0;
          Te4 = 0.0;
1591      Te5 = 0.0;
          Te6 = 0.0;
1593      Te7 = 0.0;
          Te8 = 0.0;
1595      Te9 = 0.0;
          Ce1 = 0.0;
1597      Ce2 = 0.0;
          Ce3 = 0.0;
1599      Ce4 = 0.0;
          Ce5 = 0.0;
1601      Ce6 = 0.0;
          Ce7 = 0.0;
1603      Ce8 = 0.0;
          Ce9 = 0.0;
1605      Ts1 = 0.0;
          Ts2 = 0.0;
1607      Ts3 = 0.0;
          Ts4 = 0.0;
1609      Ts5 = 0.0;
          Ts6 = 0.0;
1611      Ts7 = 0.0;
          Ts8 = 0.0;
1613      Ts9 = 0.0;
          Cs1 = 0.0;
1615      Cs2 = 0.0;
          Cs3 = 0.0;
1617      Cs4 = 0.0;
          Cs5 = 0.0;
1619      Cs6 = 0.0;
          Cs7 = 0.0;
1621      Cs8 = 0.0;
          Cs9 = 0.0;
1623
      return 0;
1625  }
```

```
1627 UniaxialMaterial* SPSW_Web_Plate::getCopy()
     {
1629   SPSW_Web_Plate* theCopy = new SPSW_Web_Plate(this->getTag(), fy, Es, mf1, mf2, mf3,
         en1, en2, en3, kin, len, ht, tp);

1631   /*// Converged state variables*/
       theCopy->CState = CState;   theCopy->Cstrain = Cstrain;   theCopy->Cstress =
         Cstress;   theCopy->Ctangent = Ctangent;
1633
       /*// Converged history variables*/
1635   theCopy->LCstress = LCstress; theCopy->LCS = LCS;
       theCopy->CS_exp [0] = TS_exp [0];
1637   theCopy->CS_exp [1] = CS_exp [1];
       theCopy->CS_exp [2] = CS_exp [2];
1639   theCopy->CS_exp [3] = CS_exp [3];
       theCopy->Css [0] = Css [0];
1641   theCopy->Css [1] = Css [1];
       theCopy->Css [2] = Css [2];
1643   theCopy->Css [3] = Css [3];
       theCopy->Css [4] = Css [4];
1645   theCopy->Css [5] = Css [5];
       theCopy->CS [0] = CS [0];
1647   theCopy->CS [1] = CS [1];
       theCopy->CS [2] = CS [2];
1649   theCopy->CS [3] = CS [3];
       theCopy->CS [4] = CS [4];
1651   theCopy->CS [5] = CS [5];
       theCopy->CS [6] = CS [6];
1653   theCopy->CA1 = CA1;
       theCopy->CA2 = CA2;
1655   theCopy->CA3 = CA3;
       theCopy->CA4 = CA4;
1657   theCopy->CK1l = CK1l;
       theCopy->CK4l = CK4l;
1659   theCopy->CK5l = CK5l;
       theCopy->CK6i = CK6i;
1661   theCopy->CK6l = CK6l;
       theCopy->CK7l = CK7l;
1663   theCopy->CK8l = CK8l;
       theCopy->CK9l = CK9l;
1665   theCopy->Cev = Cev;
       theCopy->Csv = Csv;
```

```
    theCopy->Cep = Cep;
    theCopy->Cepk = Cepk;
    theCopy->Cerp = Cerp;
    theCopy->Cern = Cern;
    theCopy->CKrl = CKrl;
    theCopy->CKul = CKul;
    theCopy->Cemin = Cemin;
    theCopy->Ce0 = Ce0;
    theCopy->Cec = Cec;
    theCopy->Csig0 = Csig0;
    theCopy->Csigc = Csigc;
    theCopy->Ce0p = Ce0p;
    theCopy->Csig0p = Csig0p;
    theCopy->Cecp = Cecp;
    theCopy->Csigcp = Csigcp;
    theCopy->Ce0n = Ce0n;
    theCopy->Csig0n = Csig0n;
    theCopy->Cecn = Cecn;
    theCopy->Csigcn = Csigcn;
    theCopy->Ce1 = Ce1;
    theCopy->Ce2 = Ce2;
    theCopy->Ce3 = Ce3;
    theCopy->Ce4 = Ce4;
    theCopy->Ce5 = Ce5;
    theCopy->Ce6 = Ce6;
    theCopy->Ce7 = Ce7;
    theCopy->Ce8 = Ce8;
    theCopy->Ce9 = Ce9;
    theCopy->Cs1 = Cs1;
    theCopy->Cs2 = Cs2;
    theCopy->Cs3 = Cs3;
    theCopy->Cs4 = Cs4;
    theCopy->Cs5 = Cs5;
    theCopy->Cs6 = Cs6;
    theCopy->Cs7 = Cs7;
    theCopy->Cs8 = Cs8;
    theCopy->Cs9 = Cs9;

    return theCopy;
}

int SPSW_Web_Plate::sendSelf (int commitTag, Channel& theChannel)
```

```
1709 {
     int res = 0;
1711 static Vector data(85);
      data(0) = this->getTag();
1713 // Material properties
      data(1) = fy;
1715  data(2) = Es;
      data(3) = mf1;
1717  data(4) = mf2;
      data(5) = mf3;
1719  data(6) = en1;
      data(7) = en2;
1721  data(8) = en3;
      data(9) = kin;
1723  data(10) = len;
      data(11) = ht;
1725  data(12) = tp;
    // History variables from last converged state
1727  data(13) = LCstress;
      data(14) = LCS;
1729  data(15) = CState;
      data(16) = Cstrain;
1731  data(17) = Cstress;
      data(18) = Ctangent;
1733  data(19) =  CS_exp[0];
      data(20) =  CS_exp[1];
1735  data(21) =  CS_exp[2];
      data(22) =  CS_exp[3];
1737  data(23) =  CS[0];
      data(24) =  CS[1];
1739  data(25) =  CS[2];
      data(26) =  CS[3];
1741  data(27) =  CS[4];
      data(28) =  CS[5];
1743  data(29) =  CS[6];
      data(30) =  Css[0];
1745  data(31) =  Css[1];
      data(32) =  Css[2];
1747  data(33) =  Css[3];
      data(34) =  Css[4];
1749  data(35) =  Css[5];
      data(36) =  CA1;
```

```
1751      data(37) =  CA2;
          data(38) =  CA3;
1753      data(39) =  CA4;
          data(40) =  CK1l;
1755      data(41) =  CK4l;
          data(42) =  CK5l;
1757      data(43) =  CK6i;
          data(44) =  CK6l;
1759      data(45) =  CK7l;
          data(46) =  CK8l;
1761      data(47) =  CK9l;
          data(79) =  Cev;
1763      data(80) =  Csv;
          data(48) = Cep;
1765      data(49) = Cepk;
          data(50) = Cerp;
1767      data(51) = Cern;
          data(52) = CKrl;
1769      data(53) = CKul;
          data(54) =  Cemin;
1771      data(55) =  Ce0;
          data(56) = Cec;
1773      data(57) = Csig0;
          data(58) = Csigc;
1775      data(59) = Ce0p;
          data(60) = Csig0p;
1777      data(61) = Cecp;
          data(62) = Csigcp;
1779      data(63) = Ce0n;
          data(64) = Csig0n;
1781      data(65) = Cecn;
          data(66) = Csigcn;
1783      data(67) = Ce1;
          data(68) = Ce2;
1785      data(69) = Ce3;
          data(70) = Ce4;
1787      data(71) = Ce5;
          data(72) = Ce6;
1789      data(73) = Ce7;
          data(74) = Ce8;
1791      data(75) = Ce9;
          data(76) = Cs1;
```

```
1793     data(77) = Cs2;
         data(78) = Cs3;
1795     data(79) = Cs4;
         data(80) = Cs5;
1797     data(81) = Cs6;
         data(82) = Cs7;
1799     data(83) = Cs8;
         data(84) = Cs9;
1801
1803    // Data is only sent after convergence, so no trial variables
        // need to be sent through data vector
1805
        res = theChannel.sendVector(this->getDbTag(), commitTag, data);
1807    if (res < 0)
           opserr << "SPSW_Web_Plate::sendSelf() - failed to send data\n";
1809    return res;
}
1811
int SPSW_Web_Plate::recvSelf (int commitTag, Channel& theChannel,
1813                                FEM_ObjectBroker& theBroker)
{
1815    int res = 0;
        static Vector data(85);
1817    res = theChannel.recvVector(this->getDbTag(), commitTag, data);

1819    if (res < 0) {
           opserr << "SPSW_Web_Plate::recvSelf() - failed to receive data\n";
1821       this->setTag(0);
        }
1823    else {
           this->setTag(int(data(0)));
1825
        // Material properties
1827       fy = data(1);
           Es = data(2);
1829       mf1 = data(3);
           mf2 = data(4);
1831       mf3 = data(5);
           en1 = data(6);
1833       en2 = data(7);
           en3 = data(8);
```

```
1835        kin = data(9);
            len = data(10);
1837        ht = data(11);
            tp = data(12);
1839    // History variables from last converged state
            LCstress = data(13);
1841        LCS = data(14);
        // State variables from last converged state
1843        CState = data(15);
            Cstrain = data(16);
1845        Cstress = data(17);
            Ctangent = data(18);
1847        data(19) =  CS_exp[0];
            data(20) =  CS_exp[1];
1849        data(21) =  CS_exp[2];
            data(22) =  CS_exp[3];
1851        data(23) =  CS[0];
            data(24) =  CS[1];
1853        data(25) =  CS[2];
            data(26) =  CS[3];
1855        data(27) =  CS[4];
            data(28) =  CS[5];
1857        data(29) =  CS[6];
            data(30) =  Css[0];
1859        data(31) =  Css[1];
            data(32) =  Css[2];
1861        data(33) =  Css[3];
            data(34) =  Css[4];
1863        data(35) =  Css[5];
            data(36) =  CA1;
1865        data(37) =  CA2;
            data(38) =  CA3;
1867        data(39) =  CA4;
            data(40) =  CK1l;
1869        data(41) =  CK4l;
            data(42) =  CK5l;
1871        data(43) =  CK6i;
            data(44) =  CK6l;
1873        data(45) =  CK7l;
            data(46) =  CK8l;
1875        data(47) =  CK9l;
            data(79) =  Cev;
```

```
1877        data(80) =  Csv;
            data(48) = Cep;
1879        data(49) = Cepk;
            data(50) = Cerp;
1881        data(51) = Cern;
            data(52) = CKrl;
1883        data(53) = CKul;
            data(54) =  Cemin;
1885        data(55) =  Ce0;
            data(56) = Cec;
1887        data(57) = Csig0;
            data(58) = Csigc;
1889        data(59) = Ce0p;
            data(60) = Csig0p;
1891        data(61) = Cecp;
            data(62) = Csigcp;
1893        data(63) = Ce0n;
            data(64) = Csig0n;
1895        data(65) = Cecn;
            data(66) = Csigcn;
1897        data(67) = Ce1;
            data(68) = Ce2;
1899        data(69) = Ce3;
            data(70) = Ce4;
1901        data(71) = Ce5;
            data(72) = Ce6;
1903        data(73) = Ce7;
            data(74) = Ce8;
1905        data(75) = Ce9;
            data(76) = Cs1;
1907        data(77) = Cs2;
            data(78) = Cs3;
1909        data(79) = Cs4;
            data(80) = Cs5;
1911        data(81) = Cs6;
            data(82) = Cs7;
1913        data(83) = Cs8;
            data(84) = Cs9;
1915    }
    return res;
1917}
    void SPSW_Web_Plate::Print (OPS_Stream& s, int flag)
```

```
1919 {
     s << "SPSW_Web_Plate tag: " << this->getTag() << endln;
1921 s << "  fy:   " << fy << " ";
     s << "  Es:   " << Es << " ";
1923 s << "  mf1:  " << mf1 << " ";
     s << "  mf2:  " << mf2 << " ";
1925 s << "  mf3:  " << mf3 << " ";
     s << "  e1:   " << en1 << " ";
1927 s << "  e2:   " << en2 << " ";
     s << "  e3:   " << en3 << " ";
1929 s << "  kin:  " << kin << " ";
     s << "  len:  " << len << " ";
1931 s << "  ht:   " << ht << " ";
     s << "  tp:   " << tp << " ";
1933 }
```

BIBLIOGRAPHY

[1] AISC. 2010. "Seismic Provisions for Structural Steel Buildings." *ANSI/AISC 341-10* American Institute of Steel Construction, Inc., Chicago, IL.

[2] AISC. 2010. "Specification for Structural Steel Buildings." *ANSI/AISC 360-10* American Institute of Steel Construction, Inc., Chicago, IL.

[3] Alinia M. M., Gheitasi, A. S. E. 2009. "Plastic Shear Buckling of Unstiffened Stocky Plates." *Journal of Constructional Steel Research* No. 65, 1631-1643.

[4] Applied Technology Council. 1992. "Guidelines for Cyclic Seismic Testing of Components of Steel Structures." *ATC* Proj. No. 88-6604 NSF Grant No. BCS-8912602

[5] Basler K. 1961. "Strength of Plate Girders in Shear." *Journal of the Structural Division, ASCE* Vol. 87, No. ST7, Paper 2967.

[6] Behbehanifard M. R. 2003. "Cyclic Behavior of Unstiffened Steel Plate Shear Walls." *PhD Dissertation* University of Alberta, Canada.

[7] Berman J. W., Bruneau M. 2003. "Experimental Investigation of Light-Gage Shear Walls for the Seismic Retrofit of Buildings." *Technical Report MCEER-03-0001*, University at Buffalo,

[8] Berman J.W., Bruneau, M. 2003. "Plastic Analysis and Design of Steel Plate Shear Walls." *Journal of Structural Engineering, ASCE* Vol. 129, No. 11, 14481456.

[9] Berman J. W., Bruneau M. 2008. "Capacity Design of Vertical Boundary Elements in Steel Plate Shear Walls." *Engineering Journal*, First Quarter 47-71.

[10] Berman J. W. 2010. "Seismic Behavior of Code Designed Steel Plate Shear Walls." *Engineering Structures*, No. 33 230-244.

[11] Bhowmick A. K., Driver R. G., Grondin G. Y. 2009. "Seismic Analysis of Steel Plate Shear Walls Considering Strain Rate and P-delta Effects." *Journal of Constructional Steel Research.* No. 65, 1149-1159.

[12] Bloom F., Coffin D. 2001. *Handbook of Thin Plate Buckling and Postbuckling*, Chapman & Hall/CRC

[13] Bruneau M., Uang C., Sabelli R. 2011. *Ductile Design of Steel Structures*, 2nd Ed. McGraw Hill

[14] Cassese V., Elgaaly M., Chen R. 1993. "Experimental Study of Thin Steel-Plate Shear Walls under Cyclic Load." *Journal of Structural Engineering* Vol. 119, No. 2, 573-587.

[15] Chen W., Han D. 2007. *Plasticity for Structural Engineers.* J. R. Ross Publications

[16] Chen R. 1991. "Cyclic Behavior of Unstiffened Thin Steel Plate Shear Walls." *PhD Dissertation* University of Maine.

[17] Chen S., Jhang C. 2011. "Experimental Study of Low-Yield-Point Steel Plate Shear Wall Under In-Plane Load." *Journal of Constructional Steel Research.* No. 67, 977-985.

[18] Chen B., Sivakumaran K. 2011. "Post-Buckling Shear Strength of Thin Steel Plates." *The Twelfth East Asia-Pacific Conference on Structural Engineering and Construction.* Procedia Engineering No. 14, 641647.

[19] Choi I., Park H. 2008. "Ductility and Energy Dissipation Capacity of Shear-Dominated Steel Plate Walls." *Journal of Structural Engineering* Vol. 134, No. 9, 1495-1507.

[20] Choi I., Park H. 2009. "Steel Plate Shear Walls with Various Infill Plate Designs." *Journal of Structural Engineering* Vol. 135, No. 7, 785-796.

[21] Choi I., Park H. 2010. "Hysteresis Model of Thin Infill Plate for Cyclic Nonlinear Analysis of Steel Plate Shear Walls." *Journal of Structural Engineering* Vol. 136, No. 11, 1423-1434.

[22] CSA. 2009. "Design of Steel Structures.". *CAN/CSA S16-09* Canadian Standards Association, Mississauga, ON, Canada.

[23] Crisfiled M. A. 1991. *Non-linear Finite Element Analysis of Solids and Structures: Vol I.* John Wiley & Sons,

[24] Dafalias Y. F. 1991. "Bounding Surface Plasticity Model for Steel under Cyclic Loading". *Stability and Ductility of Steel Structures under Cyclic Loading*, Fukumoto and Lee, CRC Press.

[25] 2009. *ABAQUS Documentation Collection. Version 6.9* Dassault Systèmes Simulia Corp. Providence, RI, USA.

[26] Deylami A., Rowghani-Kashani J. 2011. "Analysis and Design of Steel Plate Shear Walls Using Orthotropic Membrane Model". *Proceedings of The Twelfth East Asia-Pacific Conference on Structural Engineering and Construction*, Procedia Engineering No. 14, 33383345

[27] Driver R.G., Kulak G.L., Kennedy D.J.L, Elwi A.E. 1997. "Seismic Behavior of Steel Plate Shear Walls". *Structural Engineering Report No. 215*, University of Alberta, Canada.

[28] Driver R.G., Kulak G.L., Elwi A.E. Kennedy D.J.L 1998. "FE and Simplified Models of Steel Plate Shear Walls". *Journal of Structural Engineering*, Vol. 124, No. 2, 121-130.

[29] Technical Working Group No. 8, Editors: Dubas P., Gehri E. 1986. "Behavior and Design of Steel Plated Structures." *Applied Statics and Steel Structures.* Swiss Federal Institute of Technology, Zurich. No. 44.

[30] Elgaaly M., Caccese V., Du R. 1993. "Post-Buckling Behavior of Steel Plate Shear Walls Under Cyclic Loads". *Journal of Structural Engineering* Vol. 119, No. 2, 588-605.

[31] Elgaaly M., Liu Y. 1997. "Analysis of Thin-Steel-Plate Shear Walls". *Journal of Structural Engineering* Vol. 123, No. 11, 1487-1496.

[32] Federal Emergency Management Agency (FEMA) 2003. "NEHRP Recommended Provisions for Seismic Regulations for New Buildings and Other Structures" FEMA 450, SAC Joint Venture for FEMA, Washington, D.C.

[33] Federal Emergency Management Agency (FEMA) 2000. "State of the Art Report on Systems Performance of Steel Moment Frames Subject to Earthquake Ground Shaking" FEMA 353, SAC Joint Venture for FEMA, Washington, D.C.

[34] Ghosh S., Farooq A., Anirudha D. 2009. "Design of Steel Plate Shear Walls Considering Inelastic Drift Demand" *Journal of Constructional Steel Research* No. 65, 1431-1437.

[35] Hadidi-Tamjed H. 1987. "Statistical Response of Inelastic SDOF Systems Subjected to Eartquakes" *PhD Dissertation*, Stanford University.

[36] Jalali A., Sazgari A. 2006. "Experimental and Theoretical Post-Buckling Study of Steel Shear Walls". *Proceedings of the 4th International Conference on Earthquake Engineering* Paper No. 114.

[37] Kaufmann E. J., Metrovich B., Pense A. W. 2001. "Characterization of Cyclic Inelastic Strain Behavior On Properties of A572 Gr. 50 and A913 Gr. 50 Rolled Sections". *ATLSS Report No. 01-13*, Lehigh University

[38] Kharrazi M. H. K. 2005 "Rational Method for Analysis and Design of Steel Plate Walls" *PhD Dissertation*, University of British Columbia, Canada.

[39] Kollar L., Dulacska E. 1984. *Buckling of Shells for Engineers*, John Wiley & Sons

[40] Krawinkler H. 2009. "Loading Histories for Cyclic Tests in Support of Performance Assessment of Structural Components". Stanford University

[41] Kuhn P. 1933. "A Summary of Design Formulas for Beams Having Thin Webs in Diagonal Tension.". *NACA Technical Note #469*

[42] Lemaitre J., Chaboche J. L. 1990. "Mechanics of Solid Materials." English Translation Edition., Cambridge University Press, Cambridge, UK. 161-252

[43] Levy S., Fienup K.L., Woolley R.M. 1945. "Analysis of Square Shear Web Above Buckling Load". *NACA Technical Note #962*

[44] Levy R., Spillers W.R. 2003. "Analysis of Geometrically Nonlinear Structures, 2nd Edition". *Kluwer Academic Publishers*

[45] Li C., Tsai K., Lin C., Tsai C., Chen P. 2010 "Cyclic tests of four two-story narrow steel plate shear walls. Part 2: Experimental results and design implications". *Earthquake Engineering and Structural Dynamics*, No. 39, 801-826.

[46] Li C.H., Tsai K.C., Chang J.T., Lin C.H. 2011. "Cyclic Test of a Coupled Steel Plate Shear Wall Substructure." *Proceedings of the 12th East-Asia Pacific Conference on Structural Engineering and Construction*

[47] Lin C., Tsai K., Qu B., Bruneau M. 2010. "Sub-Structural Pseudo-Dynamic Performance of Two Full-Scale Two-story Steel Plate Shear Walls." *Journal of Constructional Steel Research.* No. 66, 1467-1482

[48] Lubell A.S. 1997. "Performance of Unstiffened Steel Plate Shear Walls Under Cyclic Quasi-Static Loading". *Masters Thesis*, University of British Columbia.

[49] Lubell A.S., Ventura C.E., Prion H., Rezai M. 2000. "Unstiffened Steel Plate Shear Wall Performance Under Cyclic Loading". *Journal of Structural Engineering*, Vol. 126, No. 4 453-460,

[50] Lubliner J. 2006. *Plasticity Theory.* Revised Edition (PDF)

[51] Park H., Kwack J., Jeon S., Kim W., Choi I. 2007. "Framed Steel Plate Wall Behavior under Cyclic Lateral Loading" *Journal of Structural Engineering* Vol. 133, No. 3, 378-389

[52] Qu B., Bruneau M., Lin C., Tsai K. 2008. "Testing of Full-Scale Two-Story Steel Plate Shear Wall with Reduced Beam Section Connections and Composite Floors". *Journal of Structural Engineering*, Vol. 134, No. 3 364-373.

[53] Qu B., Bruneau M. 2008. "Seismic Behavior and Design of Boundary Frame Members of Steel Plate Shear Walls". *Technical Report MCEER-08-0012*, University of Buffalo, New York.

[54] Rezai M. 1999 "Seismic Behavior of Steel Plate Shear Walls by Shake Table Testing" *PhD Dissertation*, University of British Columbia.

[55] Roberts T. M., Sabouri-Ghomi S. 1991. "Hysteretic Characteristics of Unstiffened Plate Shear Panels". *Thin-Walled Structures*, Vol 12, Issue 2, 145-162.

[56] Roberts T. M. 1995. "Seismic Resistance of Steel Plate Shear Panels". *Engineering Structures*, Vol 17, No. 5, 344-351.

[57] Rockey K. C., Skaloud M. 1972. "The Ultimate Load Behavior of Plate Girders Loaded in Shear". *The Structural Engineer*, Vol 50, No. 1, 47.

[58] Sabelli R., Bruneau M. 2007. "Steel Design Guide 20". *Steel Plate Shear Walls* American Institute of Steel Construction, Inc., Chicago, IL.

[59] Sabouri-Ghomi S., Roberts T. M. 1991. "Nonlinear Dynamic Analysis of Thin Steel Plate Shear Wall". *Computers & Structures*, Vol. 39, No. 1/2, 121-127.

[60] Shishkin J.J., Driver R.G., Grondin G.Y. 2005. "Analysis of Steel Plate Shear Walls Using the Modified Strip Model". *Structural Engineering Report No. 261*, University of Alberta, Canada.

[61] Skaloud M., Zörnerova M. 1972. "Post-Buckled Behavior of Webs in Shear". *Transactions of the Czechoslovak Academy of Sciences*, Series "Technical Sciences". No.3/1972

[62] Somerville P., Smith N., Punyamurthula S., Sun J. 1997. "Development of ground motion time histories for phase 2 of the FEMA/SAC steel project. SAC background document." Report no. SAC/BD-97/04. SAC Joint Venture

[63] Stein M., Neff J. 1947. "Buckling Stresses of Rectangular Flat Plates in Shear". *NACA Technical Note #1222*,

[64] Stowell E.Z. 1948. "Critical Shear Stress of an Infinitely Long Plate in the Plastic Region". *NACA Technical Note #1661*,

[65] Stowell E.Z. 1949. "Plastic Buckling of Long Flat Plates Under Combined Shear and Longitudinal Compression". *NACA Technical Note #1990*,

[66] Thornburn L. J., Kulak G. L., Montgomery C. J. 1983. "Analysis of Steel Plate Shear Walls". *Structural Engineering Report No. 107*, University of Alberta,

[67] Timler P. A., Kulak G. L. 1983. "Experimental Study of Steel Plate Shear Walls". *Structural Engineering Report No. 114*, University of Alberta, Canada

[68] Timler P. A., Ventura C.E., Prion H., Anjam R. 1998. "Experimental and Analytical Studies of Steel Plate Shear Walls as applied to Tall Buildings". *The Structural Design of Tall Buildings*, 7, 233-249,

[69] Timoshenko S.P 1936. *Theory of Elastic Stability*, McGraw-Hill Book Company, Inc.

[70] Timoshenko S.P 1940. *Theory of Plates and Shells*, McGraw-Hill Book Company, Inc.

[71] Topkaya C., Kurban C. O. "Natural Periods of Steel Plate Shear Wall Systems" *Journal of Constructional Steel Research.* No. 65, 542-551.

[72] Topkaya C., Atasoy M. "Lateral Stiffness of Steel Plate Shear Wall Systems" *Thin-Walled Structures.* No. 47, 827-835.

[73] Tromposch E.W., Kulak G. L. 1987. "Cyclic and Static Behavior of Thin Panel Steel Plate Shear Walls". *Structural Engineering Report No. 145*, University of Alberta, Canada.

[74] Tsai K., Li C., Lin C., Tsai C., Yu Y. 2010 "Cyclic tests of four two-story narrow steel plate shear walls: Part 1: Analytical studies and specimen design". *Earthquake Engineering and Structural Dynamics*, No. 39, 775-799.

[75] Wagner H. 1931. "Flat Sheet Metal Girders with Very Thin Metal Webs". *NACA Technical Memo #604*,

[76] Webster D.J., Berman J.W., Lowes L.N. 2012. "The Elastic and Inelastic Post-Buckling Behavior of Steel Plate Shear Wall Web Plates and their Interaction with Vertical Boundary Elements". *Proceedings of the Annual Stability Conference, Grapevine, Texas*,

[77] Xue M. 1995. "Behavior of Steel Shear Wall Panels and Frame-Wall Systems". *PhD Dissertation*, Lehigh University

[78] Ziegler H. 1959. "A modification of Pragers's Hardening Rule ". *Quarterly of Applied Mathematics*, No. 17 55-65.

[79] Zirakian T., Zhang J. 2012. "Structural Performance of SPSWs with Unstiffened Slender, Moderate, and Stocky LYP Steel Infill Plates". *Proceedings of the 15th World Conference in Earthquake engineering, Lisbon, Portugal*,